Exploration fonctionnelle du cortex cérébral : De la caractérisation de neurones uniques vers l'étude des dynamiques spatiotemporelles de l'activité corticale

Isabelle Ferezou

Mémoire présenté pour l'obtention du
Diplôme d'Habilitation à Diriger les Recherches
par

Isabelle Férézou

Equipe Traitement sensoriel, Neuromodulation et Plasticité Neuronale (Dir. Daniel Shulz)
Unité de Neurosciences Information et Complexité FRE 3693
CNRS, Gif sur Yvette, France (Dir. Daniel Shulz)

Exploration fonctionnelle du cortex cérébral : De la caractérisation de neurones uniques vers l'étude des dynamiques spatiotemporelles de l'activité corticale

Date de soutenance : 21 décembre 2018

Composition du jury :

Rapporteurs :

Frédéric CHAVANE	(DR, CNRS), Institut de Neurosciences de la Timone, Marseille, France.
Antoine DEPAULIS	(DR, INSERM), Institut de Neurosciences de Grenoble, Grenoble, France.
Martin DESCHENES	(Professeur, Université de Laval), Département de Psychiatrie et de Neurosciences, Québec, Canada.

Examinateurs :

Jean-Marc EDELINE	(DR, CNRS), Institut des Neurosciences Paris-Saclay, Orsay, France.
Patricia GASPAR	(DR, INSERM), Institut du Fer à Moulin, Paris, France.

Résumé

Le néocortex est une structure complexe qui joue un rôle d'intégration indispensable aux fonctions cognitives qui régissent nos interactions avec notre environnement, depuis l'analyse sensorielle jusqu'à la genèse de commandes motrices. L'ensemble des travaux que j'ai réalisés à ce jour était centré sur l'étude de cette structure cérébrale.

Au cours de mon doctorat (Laboratoire de Neurobiologie et Diversité Cellulaire, ESPCI, Paris), je me suis intéressée aux propriétés fonctionnelles d'une population d'interneurones inhibiteurs du néocortex. Mon travail, effectué sous la supervision de Bertrand Lambolez, était basé sur une méthode permettant l'analyse des caractéristiques électrophysiologiques, pharmacologiques, moléculaires et morphologiques de neurones ciblés, à partir de tranches de cortex de rat maintenues en survie ex vivo. Cette approche m'a permis de montrer que les interneurones sensibles aux agonistes nicotiniques, qui expriment le peptide vasoactif intestinal et la cholecystokinine, peuvent être activés de manière rapide, synaptique, par les fibres sérotoninergiques afférentes, via le récepteur à la sérotonine de type 3 (5-HT3). La mise en évidence de l'expression sélective du récepteur opioïde de type μ et de la préproenképhaline dans cette population neuronale m'a conduit à démontrer par la suite l'existence d'une boucle d'autorégulation enképhalinergique, spécifique de ces interneurones.

Au cours de mon post-doctorat, effectué sous la supervision de Carl Petersen (Laboratoire LSENS, Brain Mind Institute, EPFL, Lausanne), j'ai abordé l'étude du cortex cérébral de manière plus intégrée. Mes travaux étaient centrés sur le traitement cortical de l'information sensorielle, en utilisant pour modèle le système des vibrisses chez la souris. J'ai développé une méthode pour observer l'activité du cortex somatosensoriel primaire à l'aide de l'imagerie sensible au potentiel chez l'animal éveillé et libre de ses mouvements. J'ai ainsi pu montrer que l'activité évoquée par des stimuli tactiles au niveau du cortex somatosensoriel primaire dépend fortement du comportement de la souris. Par la suite, j'ai élargi l'observation de l'activité corticale induite par les stimulations tactiles à toute la partie dorsale du cortex cérébral, chez des souris éveillées "tête fixée". Cette approche m'a permis de visualiser pour la première fois l'activation du cortex moteur primaire consécutive à la réponse du cortex somatosensoriel primaire qui est régulée par le comportement de l'animal, et corrélée avec la génération de mouvements évoqués.

De retour en France, dans le laboratoire de Neurobiologie de l'ESPCI ParisTech (équipe "Physiologie des Interneurones" dirigée par Jean Rossier), j'ai été recrutée au CNRS, avec pour projet l'étude des mécanismes cellulaires et moléculaires impliqués dans la modulation du traitement cortical de l'information sensorielle en combinant approches *ex vivo* et *in vivo*. Sachant que les interneurones exprimant le récepteur 5-HT3 représentent un point de convergence remarquable entre les voies neuromodulatrices sérotoninergiques et cholinergiques au niveau cortical, je m'intéressai plus particulièrement à l'implication de ces interneurones dans la modulation du traitement de l'activité sensorielle tactile au niveau du cortex en tonneaux chez la souris. L'utilisation de souris transgéniques exprimant une protéine fluorescente verte sous le contrôle du promoteur récepteur 5-HT3 nous a notamment permis d'aller plus loin dans la caractérisation de cette population neuronale en

déterminant son origine embryonnaire. Dans le cadre de collaborations, j'ai mené en parallèle des études visant à montrer les conséquences fonctionnelles d'altérations de la circuiterie thalamo-corticale ou cortico-corticale, en analysant les réponses corticales évoquées par des stimulations tactiles à l'aide de l'imagerie sensible au potentiel.

J'ai décidé par la suite de rejoindre l'Unité de Neurosciences Information et Complexité dont les thématiques de recherche, axées sur la modulation des états corticaux, le traitement de l'information sensorielle et la perception, étaient en parfaite adéquation avec mes centres d'intérêts. La mise au point par l'équipe de Daniel Shulz d'une matrice de stimulation tactile avait en effet ouvert de nouvelles perspectives dans l'étude de l'intégration corticale de stimuli tactiles complexes. Elle a permis de révéler notamment que le cortex « en tonneaux » est capable d'intégrer les informations multi-vibrissales afin d'extraire les propriétés globales des objets rencontrés. Mon arrivée dans l'équipe, renforcée par l'obtention d'une ANR Jeune Chercheur, offrait donc la possibilité de combiner l'imagerie sensible au potentiel à cette méthode de stimulation tactile, ce qui représente un moyen unique d'étudier, à l'échelle mésoscopique, la propagation et l'intégration de l'information neuronale dans le cortex somatosensoriel primaire, en réponse à des stimulations spatialement distribuées sur la surface réceptrice.

Nous avons tout d'abord mis au point une méthode permettant l'alignement des signaux enregistrés par imagerie sensible au potentiel avec la carte cytoarchitecturale du réseau cortical sous-jacent. Nous avons ensuite étudié, chez la souris anesthésiée, la sélectivité à la direction globale d'une stimulation tactile générée par la déflection séquentielle de l'ensemble des vibrisses, avec María Eugenia Vilarchao, dont j'ai supervisé le travail de doctorat (co-direction avec Daniel Shulz). Nous avons ainsi observé que dans l'ensemble, le cortex « en tonneaux » répond préférentiellement aux mouvements globaux caudo-ventraux. Cette préférence directionnelle est organisée spatialement à l'échelle supra-colonnaire, les colonnes correspondant aux vibrisses rostrales étant plus sélectives à la direction globale que les colonnes associées aux vibrisses caudales.

Je cherche à présent à élargir l'étude de l'intégration des stimuli tactiles complexes au cortex somatosensoriel secondaire, dont le rôle dans le traitement de l'information sensorielle tactile est encore mal connu.

J'ai également pour projet de mettre en évidence l'implication fonctionnelle de ces mécanismes d'intégration et leur importance perceptive et comportementale, en utilisant la fibroscopie chez l'animal éveillé, dans un paradigme expérimental impliquant l'extraction des propriétés globales d'un objet par l'animal. Ce projet fait l'objet d'un doctorat que je vais co-encadrer avec Daniel Shulz à partir d'octobre 2018.

Enfin, je m'intéresse à la capacité des cortex somatosensoriels primaire et secondaire à générer des signaux d'attente en fonction du contexte sensorimoteur. En effet, l'activité du cerveau n'est pas déterminée uniquement par les stimuli externes, mais émerge d'un processus actif, visant à comparer les entrées sensorielles avec leurs anticipations. Je souhaite étudier les signaux physiologiques centraux sous-tendant la capacité d'anticipation, dans le contexte d'une tâche sensorimotrice où une souris est entrainée à contacter avec ses vibrisses de façon répétée, un objet qui est enlevé de façon inattendue. Ce projet s'inscrit dans le cadre d'une collaboration avec les groupes de Laurent Bourdieu et Clément Léna à l'IBENS, financée par une ANR dédiée. Dans ce contexte, je co-encadre avec Laurent Bourdieu le travail de doctorat de Sophie Hubatz, qui a débuté en octobre 2017.

Table des matières

Introduction

Le cortex cérébral est considéré comme le sommet hiérarchique du système nerveux central chez les mammifères. L'extraordinaire complexité de cette structure apparue relativement tardivement au cours de l'évolution et son implication dans les activités cognitives les plus complexes en font un sujet de recherche central dans la neurophysiologie actuelle qui vise à comprendre les bases neuronales du comportement.

Mon parcours scientifique, tout comme mes projets de recherche en cours et à venir révèlent ma fascination inexhaustible pour ce réseau de neurones dense et complexe. Parmi les multiples fonctions dans lesquelles il est impliqué, j'ai choisi d'axer mes travaux sur le traitement des informations sensorielles tactiles : mon but est de mieux comprendre comment les signaux originaires de la périphérie sont intégrés au sein du réseau cortical, en fonction de l'expérience sensorielle vécue et du contexte comportemental pour générer un percept, élément essentiel à l'interaction de l'individu avec son environnement.

1. Le système vibrissal du rongeur, un modèle privilégié pour l'étude fonctionnelle du cortex cérébral

Article de revue : Estebanez L, **Férézou I**, Ego-Stengel V, Shulz DE. Representation of tactile scenes in the rodent barrel cortex. ***Neuroscience***. 2018, 368:81-94.

1.1. Une organisation anatomo-fonctionnelle remarquable

Parce que l'étude du cortex cérébral nécessite une approche intégrée, de la cellule au réseau de neurones, il est essentiel de l'aborder au sein d'un système bien défini qui peut être analysé quantitativement. Le rongeur représente un modèle expérimental de choix du fait qu'il autorise l'utilisation de manipulations cellulaires, moléculaires et génétiques, tout en offrant un comportement riche et complexe.

De plus, le cortex cérébral des rongeurs a la propriété d'être dépourvu de circonvolutions tout en partageant une structure laminaire comparable à celle des primates. Cette lissencéphalie offre un accès optique privilégié à de nombreuses aires corticales ce qui est un véritable atout à l'heure où les méthodes optiques sont devenues incontournables, que ce soit pour enregistrer (Lin and Schnitzer, 2016) ou contrôler (Deisseroth, 2015) expérimentalement l'activité d'assemblées de neurones.

Les rongeurs sont des animaux nocturnes dont la vie est essentiellement souterraine : ils utilisent leurs "moustaches", ou vibrisses mystaciales, pour collecter des informations sur leur environnement proche. La représentation corticale des vibrisses occupe chez ces animaux une large part des aires corticales somatosensorielles primaire et secondaire (S1 et S2, respectivement, **figure 1a**, Woolsey and Van der Loos, 1970).

Au sein du cortex S1, la zone qui reçoit l'information sensorielle relative aux vibrisses est communément appelée cortex "en tonneaux", du fait de son organisation cytoarchitecturale remarquable. Celle-ci contient des agrégats cellulaires, nommées "tonneaux", au niveau de la couche

IV, qui sont organisées de la même manière que les vibrisses sur le museau de l'animal (**figure 1b**). Chaque colonne neuronale correspondant à un tonneau traite en premier lieu l'information provenant de la vibrisse qui lui correspond (Armstrong-James et al., 1992; Brecht and Sakmann, 2002a; Moore and Nelson, 1998; Simons, 1978; Zhu and Connors, 1999).

Dès leur première description chez la souris par Woolsey et Van der Loos en 1970, ces tonneaux ont été considérés comme une manifestation morphologique des colonnes corticales, unités fonctionnelles jusqu'alors décrites uniquement sur la base de résultats d'enregistrements électrophysiologiques (Mountcastle, 1957, 1997).

Cette possibilité unique de lier cytoarchitecture et fonction au niveau d'une région corticale relativement dorsale et donc facile d'accès expérimentalement a dès lors fait du système vibrissal des rongeurs un modèle privilégié en neurophysiologie intégrative.

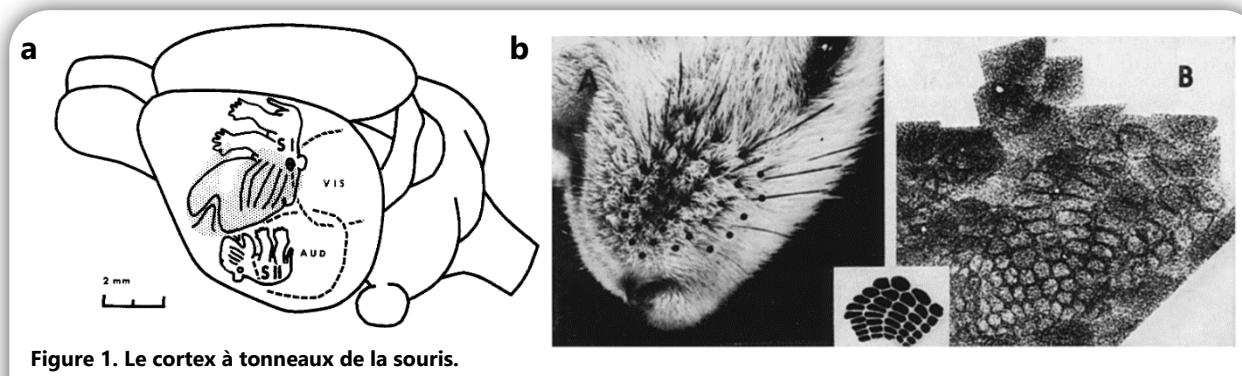

Figure 1. Le cortex à tonneaux de la souris.

a. Dessin d'un cerveau de souris illustrant la zone corticale de représentation des vibrisses au sein du cortex S1 et S2 en relation avec les aires sensorielles visuelles (VIS) et auditives (AUD) primaires déterminées par des enregistrements de potentiels évoqués. **b.** Figure illustrant l'organisation anatomo-fonctionnelle remarquable du cortex en tonneaux chez la souris. A l'organisation spatiale des vibrisses photographiées à gauche, correspond l'arrangement des "tonneaux" observés en coupe tangentielle de cortex au niveau de la couche 4 après coloration de Nissl.

Woolsey & Van der Loos, 1970.

Près de cinquante ans après ces premières observations, les voies de transmission de l'information sensorielle tactile depuis la périphérie jusqu'au cortex S1 sont assez bien décrites, notamment grâce au travail remarquable effectué par Martin Deschênes et collaborateurs sur la base de reconstructions anatomiques de neurones uniques chez le rat (pour revues, voir Deschênes et al., 1998 ; Deschenes & Urbain, 2009). L'information sensorielle tactile est transmise, depuis les terminaisons nerveuses situées dans les follicules qui entourent la base des vibrisses, vers le cortex en tonneaux, via des noyaux situés au niveau du tronc cérébral et du thalamus (**figure 2**). De manière générale, l'aspect discret inhérent aux vibrisses est remarquablement conservé de la périphérie jusqu'au cortex. Ainsi, à une vibrisse correspondent : des tonnelets (« barrelet ») dans le noyau trigeminal principal (PrV) et le noyau trigéminal spinal interpolaris (SpVi) du tronc cérébral, un tonneloïde (« barreloïde ») au niveau du noyau ventro-postero-médian (VPM) du thalamus, et un tonneau (« barrel ») dans le cortex S1.

Quatre voies de transmission de l'information sensorielle tactile de la périphérie au cortex S1 ont été décrites à ce jour : deux voies dites lemniscales, une voie paralemniscale et une voie extralemniscale (Deschenes & Urbain, 2009; Yu et al., 2006).

Les voies lemniscales passent par le PrV, puis par la région dorso-médiane du VPM, pour atteindre enfin principalement la couche 4, mais aussi le haut de la couche 6 du cortex S1. La voie lemniscale la

plus classiquement décrite est portée par des neurones du PrV dont le champ récepteur est dominé par une vibrisse principale (Minnery, 2003), qui se projettent sur les neurones du "cœur" des tonneloïdes du VPM (Haidarliu, 2008). Ces derniers sont à l'origine d'une innervation dense des tonneaux de la couche 4 et se projettent de manière plus diffuse en couche 6 (Arnold et al., 2001; Jensen and Killackey, 1987; Pierret et al., 2000). Une seconde voie lemniscale, décrite plus récemment (Urbain and Deschenes, 2007), est portée par des neurones du PrV présentant de larges champs récepteurs multivibrissaux (Veinante and Deschênes, 1999) qui se projettent à l'extrémité dorso-médiane du VPM, au niveau de la "tête" des tonneloïdes. Ces neurones innervent préférentiellement les septa, zones situées entre les tonneaux de la couche 4 (Furuta et al., 2009). Ces deux voies lemniscales semblent donc porter différents types d'informations vibrissales vers le cortex S1. Des expériences de lésion du PrV ont mené à une suppression quasi-totale des réponses du cortex en "tonneaux" aux stimulations vibrissales, soulignant la place prépondérante occupée par ces voies dans la transmission de l'information tactile (Furuta et al., 2009).

La voie paralemniscale, plus diffuse et caractérisée par de larges champs récepteurs multivibrissaux, passe par la partie rostrale du noyau SpVi qui n'est pas organisée en tonnelets, puis par le noyau postéro médian du thalamus (Po), pour finalement atteindre les septa en couche 4, ainsi que les couches 1 et 5a (Koralek et al., 1988; Veinante and Deschênes, 1999; Veinante et al., 2000a).

Enfin, la voie extralemniscale, qui présente également des champs récepteurs multivibrissaux, passe par la partie caudale de SpVi, où les neurones organisés en tonnelets se projettent sur la partie ventrolaterale du VPM au niveau de la "queue" des tonneloïdes. Les axones des neurones situés à ce niveau se projettent de manière éparse vers le cortex S1, à l'extérieur des tonneaux, en couches 3, 4 et 6 et le cortex S2 en couche 4 et 6 (Pierret et al., 2000; Veinante et al., 2000a).

Ces voies "ascendantes" de transmission de l'information ne sont pas totalement parallèles : il existe d'importantes interconnections au niveau des noyaux trigeminaux (Furuta et al., 2008; Jacquin et al., 1990; Voisin et al., 2002). En outre, des voies "descendantes", depuis les couches profondes du cortex S1 vers le thalamus et les noyaux trigéminaux, interviennent également dans le traitement de l'information (Bokor et al., 2008; Bourassa et al., 1995; Veinante et al., 2000b; Welker et al., 1988), voir Deschenes & Urbain (2009) pour revue.

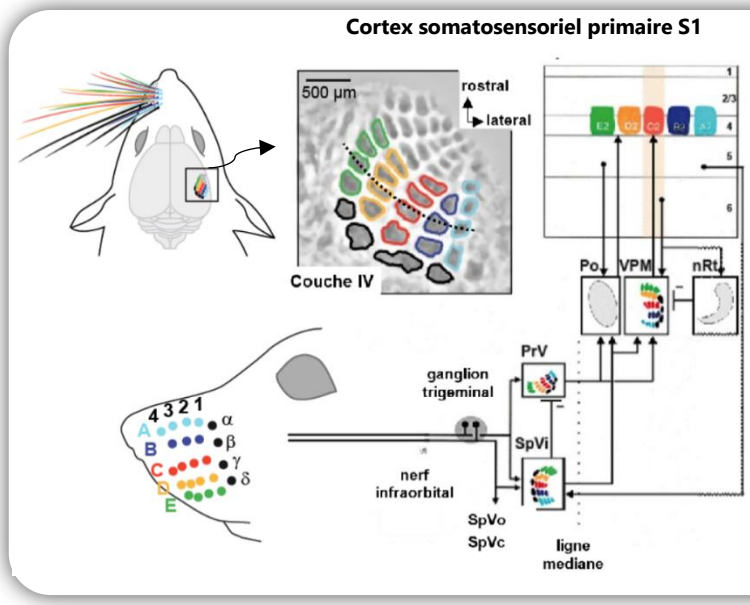

Figure 2. De la périphérie au cortex « en tonneaux ».

Les vibrisses sont organisées selon une matrice composée de rangées A, B, C, D, E et d'arcs 1, 2, 3,... etc. Les vibrisses caudales aussi appelées « straddlers » car elles sont intercalées par rapport aux rangées (en noir sur le schéma), sont désignées par des lettres grecques. On retrouve des matrices d'agrégats cellulaires suivant la même organisation spatiale au niveau du tronc cérébral (PrV et SpVi), du thalamus (VPM) et du cortex S1. L'image centrale (en haut) montre une coupe tangentielle du cortex S1 au niveau de la couche 4, au sein de laquelle les tonneaux sont bien visibles, le schéma (en haut à droite) montre dans un plan pseudo-coronal l'arrangement des tonneaux le long de l'arc 2 (représenté en pointillé à gauche).

Adapté de Deschênes et al., 1998.

1.2. Une microcircuiterie dédiée de mieux en mieux décrite

La cytoarchitecture particulière de la représentation corticale des vibrisses au niveau de S1 chez les rongeurs permet donc de délimiter les colonnes corticales, considérées comme unités fonctionnelles du cortex cérébral. Les propriétés des neurones qui constituent les colonnes du cortex en tonneaux, leurs connections synaptiques et leurs réponses à des stimulations sensorielles ont été largement étudiées à l'aide d'enregistrements électrophysiologiques, de marquages neuroanatomiques et d'imagerie fonctionnelle réalisés *in vitro* ou *in vivo*, chez l'animal anesthésié (voir Petersen, 2007; Schubert et al., 2007; Feldmeyer et al., 2013 pour revues).

On notera la contribution remarquable de Bert Sakmann, pionnier dans ce domaine, instaurant la pipette de patch comme un outil incontournable de collecte systématique de données électrophysiologiques et morphologiques sur les composants cellulaires des colonnes corticales du cortex en tonneaux de rat (Helmstaedter et al., 2007; Sakmann, 2017).

Grâce à l'ensemble des travaux qui en ont découlé, nous avons aujourd'hui une idée assez précise de l'organisation cellulaire d'une colonne type (**figure 3**), même si l'on note que toutes les colonnes ne sont pas équivalentes (**figure 3a**, Meyer et al., 2013). Une colonne compterait ainsi approximativement 87% de neurones excitateurs pour 13% d'interneurones inhibiteurs (**figure 3b**) avec au total environ 19 700 neurones chez le rat (Meyer et al., 2011) et 6 500 neurones chez la souris (Lefort et al., 2009).

Les neurones excitateurs glutamatergiques sont pour la plupart des cellules dites pyramidales, caractérisées par la forme triangulaire de leur soma, leur dendrite apicale proéminente qui s'étend verticalement vers la surface du néocortex, et leurs dendrites basales qui émergent latéralement de la base du corps cellulaire (**figure 3c**, DeFelipe and Fariñas, 1992; Narayanan et al., 2015).

Les données quantitatives dont on dispose sur la morphologie des cellules pyramidales (**figure 3c,d**) et leur connectivité au sein des colonnes corticales permettent de tenter de reconstituer la cascade d'évènements synaptiques excitateurs mise en jeu lors de la stimulation de vibrisses (Bureau et al., 2006; Feldmeyer, 2012; Feldmeyer et al., 2006; Lefort et al., 2009; Narayanan et al., 2015, 2017).

Figure 3. Organisation cellulaire du cortex en tonneaux de rat.

a. Projections de tous les corps cellulaires du cortex vibrissal chez un animal : à gauche sur un plan tangentiel, à droite sur un plan pseudo-coronal (région délimitée par la ligne pointillée à gauche). *Meyer et al., 2013.*

b. Projection 2D de la densité 3D des neurones excitateurs (à gauche), et inhibiteurs (à droite). *Meyer et al., 2013.*

c. Neuf types cellulaires identifiés sur la base de leurs propriétés morphologiques. L'étendue verticale de la localisation des corps cellulaires est indiquée pour chaque type par les rectangles colorés. *Oberlaender et al., 2012.*

d. Distribution des corps cellulaires (à gauche), des arbres dendritiques (au centre) et des axones (à droite) des différents types cellulaires excitateurs au sein d'une colonne type. *Narayanan et al., 2017.*

e. La diversité morphologique des interneurones inhibiteurs est illustrée par des exemples de reconstruction dans différentes couches. Les axones sont indiqués en bleu, les corps cellulaires et dendrites en rouge. *Feldemeyer et al., 2018.*

Abréviations : L2py : cellule pyramidale de couche 2, L3py : cellule pyramidale de couche 3, L4sp : cellule pyramidale étoilée, L4ss : cellule étoilée épineuse, L4py : cellule pyramidale de couche 4, L5st : celle pyramidale svelte-touffue, L5tt : cellule épaisse-touffue, L6cc : cellule pyramidale cortico-corticale, L6ct : cellule pyramidale corto-thalamique. L6inv : cellule pyramidale inversée. ChC : cellule en chandelier/axo-axonique, BC : cellule en panier, VIP : cellule exprimant le peptide vasoactif intestinal, NGFC : cellule neurogliaforme, MC : cellule de Martinotti.

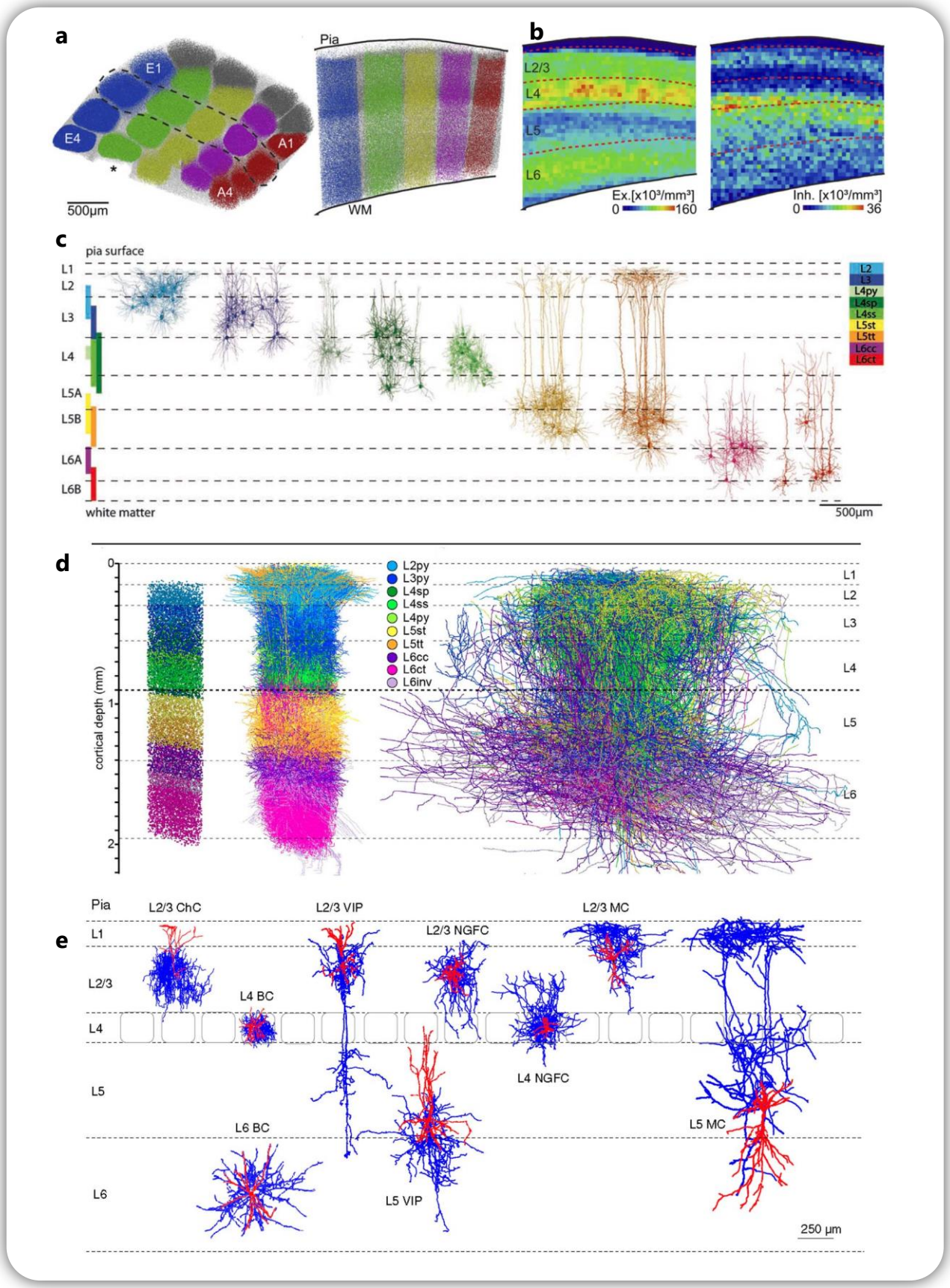
a
E1
E4
A1
A4
*
500µm
Pia
WM
b
L2/3
L4
L5
L6
Ex.[x10³/mm³]
0
160
Inh. [x10³/mm³]
0
36
c
pia surface
L1
L2
L3
L4
L5A
L5B
L6A
L6B
white matter
L2
L3
L4py
L4sp
L4ss
L5st
L5tt
L6cc
L6ct
500µm
d
cortical depth (mm)
0
1
2
L2py
L3py
L4sp
L4ss
L4py
L5st
L5tt
L6cc
L6ct
L6inv
L1
L2
L3
L4
L5
L6
e
Pia
L1
L2/3
L4
L5
L6
L2/3 ChC
L4 BC
L6 BC
L2/3 VIP
L5 VIP
L2/3 NGFC
L4 NGFC
L2/3 MC
L5 MC
250 µm

Cependant, l'activité de ce réseau excitateur est constamment régulée par les interneurones GABAergiques inhibiteurs du cortex. Contrairement aux neurones excitateurs, ces interneurones présentent des propriétés électrophysiologiques, moléculaires et morphologiques très diverses (**figure 3e,** Cauli et al., 1997; DeFelipe, 2002). De nombreux travaux ont par conséquent cherché à décrire des populations d'interneurones distinctes sur la base de leurs caractéristiques intrinsèques (Ascoli et al., 2008; DeFelipe et al., 2013; Markram et al., 2004 ;Tremblay et al., 2016).

Si la classification fonctionnelle des interneurones est en soi une problématique complexe, la manière dont les différents types d'interneurones interviennent dans les réponses sensorielles corticales est encore assez mal connue. En effet, comme il est difficile de cibler *in vivo* l'enregistrement d'interneurones spécifiques, les données dont on dispose aujourd'hui ont été, pour la plupart, obtenues grâce au développement de préparations de tranches de cerveaux au sein desquelles les connections entre le thalamus et le cortex en tonneaux sont préservées (Agmon and Connors, 1991). Ces études menées *ex vivo* ont montré que différents types d'interneurones reçoivent directement des entrées sensorielles provenant du thalamus (Porter et al., 2001). Ils sont donc impliqués dans le traitement cortical de l'information sensorielle.

Cependant, il semble que leur rôle dans la modulation des réponses corticales diffère selon leurs propriétés physiologiques et morphologiques spécifiques (Cruikshank et al., 2010; Gabernet et al., 2005; Kapfer et al., 2007; Porter et al., 2001; Tan et al., 2008; Sun et al., 2006). Le développement de souris transgéniques permettant l'expression spécifique (He et al., 2016; Madisen et al., 2012; Taniguchi et al., 2011) de marqueurs fluorescents, de protéines photosensibles ou de senseurs fluorescents d'activité neuronale ont permis un apport conséquent de données dans ce domaine au cours de ces dernières années (pour revue voir Feldmeyer et al., 2018).

1.3. Interactions sensorimotrices inhérentes à la collecte d'informations tactiles

L'acquisition et le traitement des informations sensorielles tactiles sont des processus actifs qui nécessitent des interactions étroites entre mouvements et sensations, du fait de la nécessité d'un contact physique, dynamique, entre l'objet appréhendé et le senseur (la vibrisse dans le modèle qui nous intéresse ici).

Lorsqu'ils explorent leur environnement, les rongeurs développent des stratégies motrices leurs permettant d'optimiser la collecte d'informations tactiles. On observe chez le rat et la souris un comportement typique dit de thigmotactisme (Milani et al., 1989; Simon et al., 1994; Whishaw and Kolb, 2005), c'est-à-dire une forte propension à se déplacer le long des murs. En outre, lorsqu'ils explorent leur environnement, les rongeurs ont un comportement typique dit de "whisking" qui consiste à bouger leurs vibrisses de l'avant vers l'arrière de manière rythmique et stéréotypée (**figure 4a**, Carvell and Simons, 1990; Fu and Zuo, 2011; Kleinfeld and Deschênes, 2011; Voigts et al., 2015; Jin, 2004).

La composante motrice essentielle à la collecte d'informations sensorielles tactiles fait du système vibrissal du rongeur un modèle de choix pour l'étude de l'intégration sensorimotrice (Kleinfeld et al., 2006). On peut considérer qu'il fonctionne en boucle fermée, étant donné que les entrées sensorielles tactiles induisent un ajustement des commandes motrices qui en retour vont avoir un impact sur les entrées sensorielles (Ahissar and Assa, 2016), et cette boucle met en jeu un grand nombre de structures cérébrales (**Figure 4b**, Ahissar and Assa, 2016; Bosman et al., 2011).

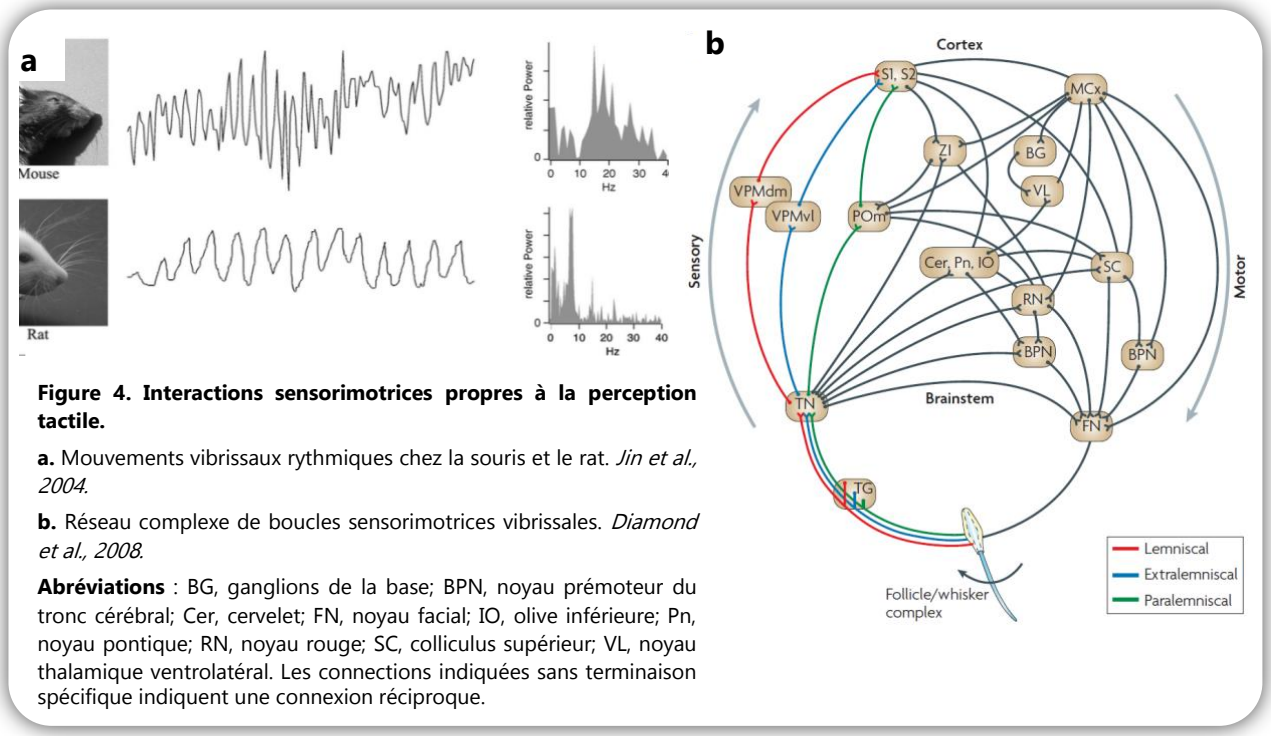

Figure 4. Interactions sensorimotrices propres à la perception tactile.

a. Mouvements vibrissaux rythmiques chez la souris et le rat. *Jin et al., 2004.*

b. Réseau complexe de boucles sensorimotrices vibrissales. *Diamond et al., 2008.*

Abréviations : BG, ganglions de la base; BPN, noyau prémoteur du tronc cérébral; Cer, cervelet; FN, noyau facial; IO, olive inférieure; Pn, noyau pontique; RN, noyau rouge; SC, colliculus supérieur; VL, noyau thalamique ventrolatéral. Les connections indiquées sans terminaison spécifique indiquent une connexion réciproque.

Rapidement, je mentionnerai que les muscles impliqués dans les mouvements vibrissaux sont contrôlés par des motoneurones du noyau moteur facial et que les commandes à l'origine des mouvements vibrissaux rythmiques sont générés au niveau d'un oscillateur neuronal situé dans la formation réticulée intermédiaire, à proximité de l'oscillateur contrôlant la phase inspiratrice de la respiration, le complexe pre-Bötzinger (Moore et al., 2013). Une connexion unilatérale de ce dernier vers l'oscillateur vibrissal, récemment mise en évidence (Deschênes et al., 2016), semble être à l'origine du couplage étroit existant entre les rythmes respiratoires et vibrissaux. Au niveau cortical, la relation entre l'activité du cortex moteur primaire et les mouvements vibrissaux est complexe et fait actuellement l'objet de nombreuses études (Ebbesen and Brecht, 2017; Ebbesen et al., 2017; Sreenivasan et al., 2016). Enfin, les denses connections réciproques qui existent au niveau cortical entre les cortex somatosensoriel et moteur primaires (Mao et al., 2011) jouent probablement un rôle clé dans l'extraction d'informations sensorielles pertinentes qui requiert l'intégration des commandes motrices générées pour les collecter.

2. Dynamiques corticales et traitement de l'information sensorielle

Article de revue : **Ferezou I**, Deneux T. Review: How do spontaneous and sensory-evoked activities interact? ***Neurophotonics***. 2017,4(3):031221.

Chapitre de livre : Crochet S, **Ferezou I**, Petersen CCH. Spontaneous activity in the rodent primary somatosensory cortex. In: "Mechanisms of spontaneous active states in the neocortex" edited by Igor Timofeev. Publishers: Research Signpost (Kerala, India). ISBN 81-308-0175-2.

Tout au long de la vie, le dense réseau neuronal que constitue le cortex cérébral est constamment actif. Cette activité est caractérisée par des dynamiques spatiotemporelles qui varient en fonction du niveau de vigilance et du comportement de l'animal (Harris and Thiele, 2011). Elle résulte d'une balance entre entrées excitatrices glutamatergiques d'origine majoritairement intracorticale et

l'activité des interneurones inhibiteurs locaux, mais elle est également constamment sous l'influence d'entrées neuromodulatrices telles que les afférences cholinergiques, sérotoninergiques, noradrenergiques ou dopaminergiques qui proviennent, respectivement, des noyaux de la base, des noyaux du raphé, du locus coeruleus et de l'aire tegmentale ventrale. Ces substances neuromodulatrices sont impliquées dans de nombreux processus cognitifs tels que l'attention, la motivation, l'apprentissage et la mémoire. La manière dont elles influent sur l'activité du réseau cortical est complexe car elles peuvent avoir des effets très différents selon les types de récepteurs qu'elles activent et la nature de leurs cibles cellulaires (pour revue, voir Gu, 2002).

La modulation des dynamiques corticales en fonction des états de vigilance et du comportement, est de ce fait un domaine de recherche foisonnant. Non seulement du fait de la complexité des mécanismes cellulaires et moléculaires sous-jacents, mais aussi parce que le rôle fonctionnel de cette activité neuronale dite "spontanée" reste encore mal compris.

Je tiens à souligner ici à quel point il est indispensable de considérer l'influence de cette activité de base du réseau cortical sur la manière dont celui-ci va répondre à une stimulation sensorielle donnée. Réciproquement, l'activation spécifique du réseau induite par une stimulation sensorielle est susceptible de provoquer un changement d'état cortical. Certains aspects seront évoqués dans les chapitres suivants, mais le lecteur est invité à lire une revue récente (Ferezou & Deneux, 2017), pour une description plus approfondie de ces interactions.

3. Le traitement des informations sensorielles tactiles n'est pas restreint au cortex somatosensoriel primaire

Si le cortex S1 est la première aire corticale activée lors d'une stimulation sensorielle tactile, ce n'est pas pour autant le seul acteur intervenant dans le traitement des informations tactiles (**figure 5**).

Les informations provenant de l'entrée en contact des vibrisses avec un objet font tout d'abord l'objet d'un traitement pré-neuronal dépendant des propriétés physiques des vibrisses elles-mêmes. La manière dont la vibrisse va transmettre un signal mécanique depuis son extrémité jusqu'à sa base pour entraîner l'activation des mécanorécepteurs (Boubenec et al., 2012, 2014; Campagner et al., 2018) va donc être susceptible de varier d'une vibrisse à l'autre mais aussi dans le temps, car les vibrisses poussent et son remplacées tout au long de la vie de l'animal selon un cycle régulier (Ibrahim and Wright, 1975).

L'activité générée au niveau des mécanorécepteurs est ensuite transmise vers le cortex via les noyaux du tronc cérébral et du thalamus, qui ne sont pas de simples relais mais bien de premières stations d'intégration de l'information puisqu'ils sont, comme mentionné plus haut, interconnectés entre eux et reçoivent des projections descendantes originaires du cortex.

Enfin, au niveau cortical, les entrées sensorielles atteignent le cortex S1 mais aussi S2 avec une latence à peine plus importante (Carvell and Simons, 1986; Kwegyir-Afful and Keller, 2004; Le Merre et al., 2018; Mao et al., 2011; Minamisawa et al., 2018), puis comme nous le verrons plus en détail ci-après, le cortex moteur primaire (M1), une dizaine de millisecondes plus tard (Ferezou et al., 2007; Le Merre et al., 2018; Mohajerani et al., 2013). Une représentation des caractéristiques des objets contactés (position, forme, texture) serait donc susceptible d'émerger d'une interaction entre ces zones corticales (Chen et al., 2013, 2016; Diamond et al., 2008; Yamashita and Petersen, 2016; Yamashita et al., 2013; Zuo et al., 2015).

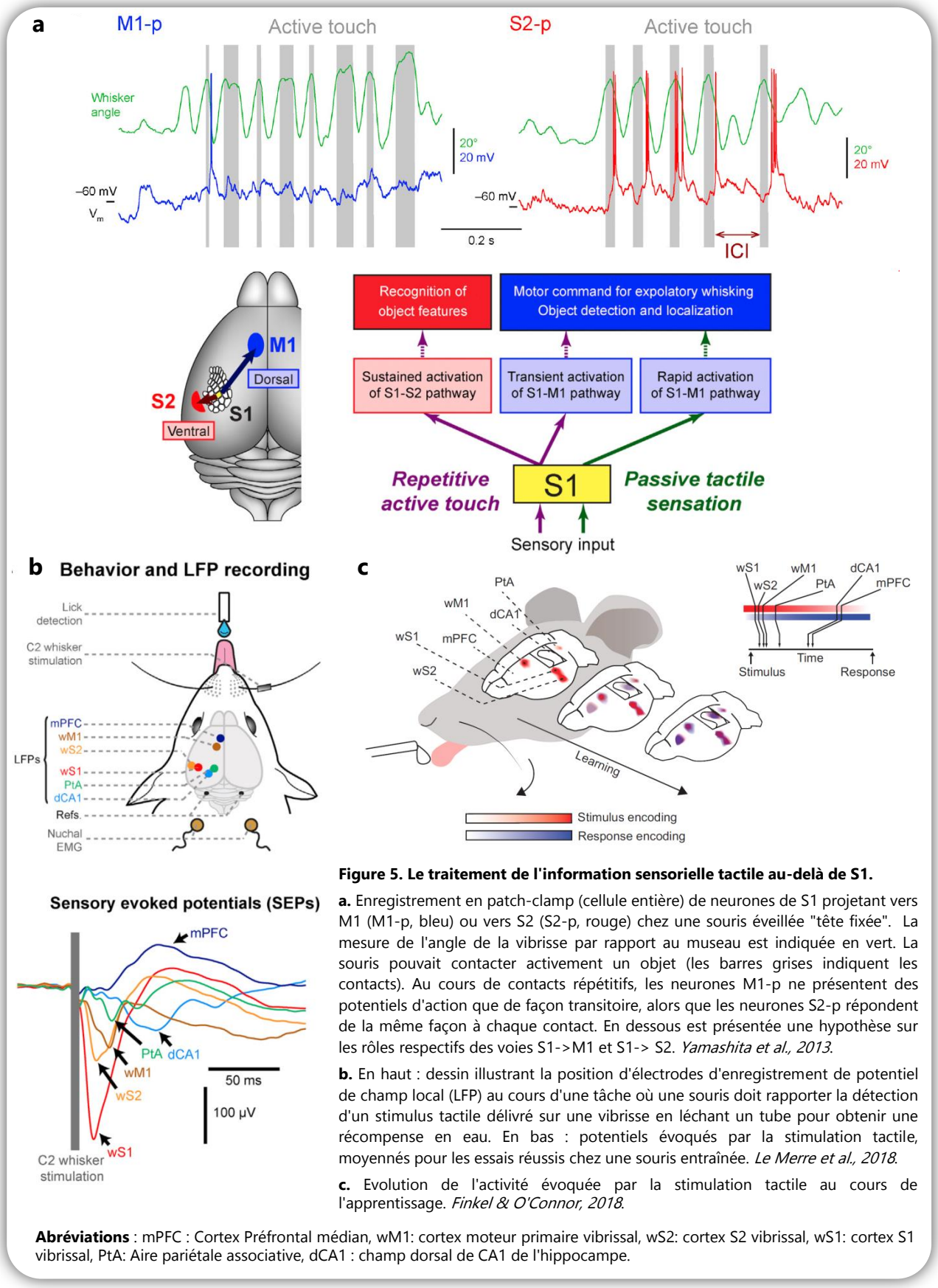

Figure 5. Le traitement de l'information sensorielle tactile au-delà de S1.

a. Enregistrement en patch-clamp (cellule entière) de neurones de S1 projetant vers M1 (M1-p, bleu) ou vers S2 (S2-p, rouge) chez une souris éveillée "tête fixée". La mesure de l'angle de la vibrisse par rapport au museau est indiquée en vert. La souris pouvait contacter activement un objet (les barres grises indiquent les contacts). Au cours de contacts répétitifs, les neurones M1-p ne présentent des potentiels d'action que de façon transitoire, alors que les neurones S2-p répondent de la même façon à chaque contact. En dessous est présentée une hypothèse sur les rôles respectifs des voies S1->M1 et S1-> S2. *Yamashita et al., 2013*.

b. En haut : dessin illustrant la position d'électrodes d'enregistrement de potentiel de champ local (LFP) au cours d'une tâche où une souris doit rapporter la détection d'un stimulus tactile délivré sur une vibrisse en léchant un tube pour obtenir une récompense en eau. En bas : potentiels évoqués par la stimulation tactile, moyennés pour les essais réussis chez une souris entraînée. *Le Merre et al., 2018*.

c. Evolution de l'activité évoquée par la stimulation tactile au cours de l'apprentissage. *Finkel & O'Connor, 2018*.

Abréviations : mPFC : Cortex Préfrontal médian, wM1: cortex moteur primaire vibrissal, wS2: cortex S2 vibrissal, wS1: cortex S1 vibrissal, PtA: Aire pariétale associative, dCA1 : champ dorsal de CA1 de l'hippocampe.

L'analyse différentielle des propriétés des neurones de S1 projetant vers M1 ou S2 a notamment permis d'émettre des hypothèses quant aux rôles respectifs de ces deux voies de traitement de l'information (**figure 5a**, Chen et al., 2016, 2013; Yamashita et al., 2013; Yamashita and Petersen, 2016).

Des expériences récentes ont montré que les neurones de S1 sont extrêmement sélectifs aux stimulations temporellement structurées de multiples vibrisses (Estebanez et al., 2012, 2016; Ramirez et al., 2014). Parmi ces neurones, seuls ceux qui se projettent vers S2 sont capables de suivre des séquences temporelles de contacts actifs d'une vibrisse avec un objet avec une faible adaptation (Yamashita et al., 2013). Ils seraient aussi plus performants pour discriminer des textures, alors que les neurones se projetant vers M1 seraient plus performants pour coder la position d'un objet (Chen et al., 2013).

Mes co-équipiers ont récemment montré que les neurones de S2 sont susceptibles d'intégrer des informations sensorielles sur des échelles temporelles et spatiales plus larges que les neurones de S1 (Goldin, Harrel et al., 2018). D'autres travaux récents, menés chez la souris en comportement, suggèrent qu'une représentation de l'objet appréhendé pourrait émerger d'une activité coordonnée entre S1 et S2 (Kwon et al., 2016 ; Yamashita et Petersen, 2016 ; Zuo et al., 2015).

Les signaux transmis de S1 à M1 ne seraient pas indispensables pour la détection tactile (Yamashita et Petersen, 2016; Le Merre et al., 2018). Cependant, il a été démontré que les axones originaires de M1 projetant vers S1 portent des informations sur plusieurs aspects du mouvement des vibrisses, y compris le contact avec un objet. Il est intéressant de noter qu'un tel contact évoque une activité dans M1 qui persiste pendant des secondes, facilitant ainsi l'intégration sensorimotrice dans S1 (Petreanu et al., 2012).

Au-delà de ces trois aires corticales dont les réponses aux stimuli tactiles sont rapides et robustes (il est possible de les observer chez l'animal anesthésié ou éveillé), d'autres aires corticales semblent entrer en jeu dès lors que la stimulation tactile a été associée à une réponse comportementale au cours d'un apprentissage dans un protocole de conditionnement opérant (**figure 5 b, c**, Gilad et al., 2018; Le Merre et al., 2018).

4. Comment générer un percept global à partir de contacts discrets ?

De nombreuses études sur le système vibrissal du rongeur se sont concentrées sur les réponses neuronales aux déflections de vibrisses individuelles, soit pour décrire les champs récepteurs neuronaux, soit pour explorer la sélectivité des réponses neuronales aux différentes caractéristiques des déflections de vibrisses.

Cependant, de telles déflections de vibrisses unitaires sont rarement rencontrées dans un environnement naturel où les rongeurs explorent leur environnement avec l'ensemble de leurs vibrisses. Dans notre équipe, nous cherchons à comprendre comment le système vibrissal peut extraire les propriétés globales de scènes tactiles complexes à partir de telles séquences de déflexions multi-vibrissales (Estebanez et al., 2018). Le développement d'un stimulateur multivibrissal unique, doté de 24 déflecteurs piezoélectriques a constitué un apport déterminant pour aborder cette question (**figure 6**, Jacob et al., 2010).

Malgré une apparente organisation en lignes dédiées au sein de laquelle chaque vibrisse est successivement représentée par un tonnelet, un tonneloïde, puis un tonneau, plusieurs observations nous invitent à penser qu'une intégration multivibrissale est susceptible d'avoir lieu au niveau de S1. En effet, des neurones répondant à de multiples vibrisses ont été observés au niveau du noyau trigéminal principal (Veinante and Deschênes, 1999) et du noyau VPM thalamique, en particulier sous faible dose d'anesthésie (Armstrong-James and Callahan, 1991). Il a également été observé qu'une proportion non négligeable de neurones thalamo-corticaux pourrait bifurquer pour envoyer l'information à plus d'une seule colonne au sein du cortex en tonneaux (Arnold et al., 2001). Au niveau cortical, une étude morphométrique systématique récente réalisée dans le cortex en tonneaux de rat a révélé que la majorité des axones intracorticaux se projettent latéralement bien au-delà de la colonne corticale (Narayanan et al., 2015). Ceci expliquant probablement les larges champs récepteurs des neurones de S1.

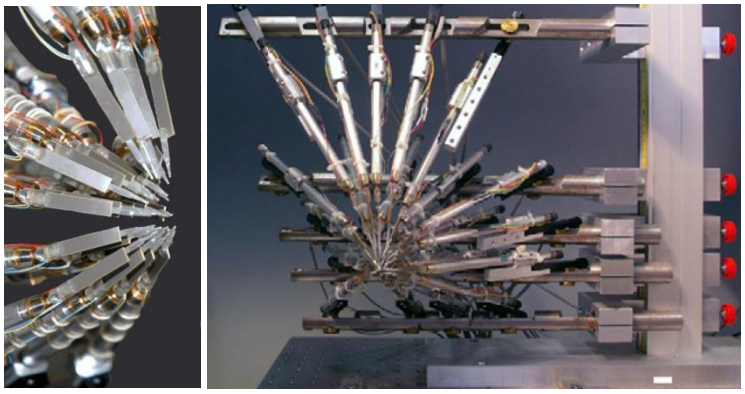

Figure 6. Matrice de stimulation vibrissale dotée de 24 stimulateurs piezoélectriques unidirectionnels.

Photographies de la première génération de matrice de stimulation multi-vibrissale développée par l'équipe de Daniel Shulz. Cette matrice, adaptée à une utilisation chez le rat anesthésié, a permis de révéler des propriétés d'intégration insoupçonnées des neurones de S1 (Jacob et al., 2008, Estebanez et al., 2012).

Adapté de Jacob et al., 2010.

Il a en effet été démontré que dans les couches 2 et 5 de S1, les neurones reçoivent des informations non seulement de leur vibrisse dite principale, mais aussi de plusieurs vibrisses adjacentes (Brecht and Sakmann, 2002b; Brecht et al., 2003; Manns et al., 2004; Moore and Nelson, 1998; Zhu and Connors, 1999). Sur le plan fonctionnel, plusieurs études, dont celles de notre équipe, ont démontré que les réponses des vibrisses adjacentes ne sont pas traitées linéairement par les neurones du cortex en tonneaux (Brumberg et al., 1996; Simons, 1985; Simons and Carvell, 1989; Ego-Stengel et al., 2005; Goldreich et al., 1998; Shimegi et al., 1999). Bien que de fortes interactions supra-linéaires aient été signalées chez les jeunes animaux, elles sont principalement sous-linéaires à des stades ultérieurs (Borgdorff et al., 2007; Ego-Stengel et al., 2005). On notera enfin que la structure de ces champs récepteurs est susceptible de varier en fonction de la direction de la déflexion des vibrisses individuelles (Le Cam et al., 2011).

Il semblerait donc qu'une intégration multivibrissale non linéaire puisse avoir lieu au niveau de S1. Pour vérifier cette hypothèse, notre équipe a étudié la manière dont les neurones de S1 appartenant à la colonne centrale C2 sont susceptibles de coder la direction d'une stimulation séquentielle de l'ensemble des macro-vibrisses, que nous appellerons un "mouvement global", imitant une barre se déplaçant à travers l'ensemble des vibrisses (**figure 7**), tout en gardant la direction de déflection des vibrisses individuelles invariante. Les réponses à des stimulations de type "mouvement global" présentées dans 8 directions différentes ont été enregistrées chez le rat anesthésié (Jacob et al., 2008).

Si les neurones sommaient linéairement les réponses aux différentes vibrisses, étant donné que les différents mouvements globaux impliquent que les 24 vibrisses soient défléchies une fois dans une direction donnée, la réponse intégrée pour chaque direction devrait être identique, donnant une courbe de sélectivité à la direction globale isotrope. En revanche, il a été constaté que 70% des unités enregistrées dans la colonne C2 montraient une sélectivité à la direction globale significative (voir deux exemples **figure 7 b,c**), favorisant, à l'échelle de la population, une préférence pour la direction caudo-ventrale.

Dans la même étude, il a été montré que la direction préférée pour les mouvements globaux ne dépend pas de la direction préférée pour les déflections locales de la vibrisse principale, indiquant différents modes de traitement de l'information locale vs globale dans le cortex en tonneaux.

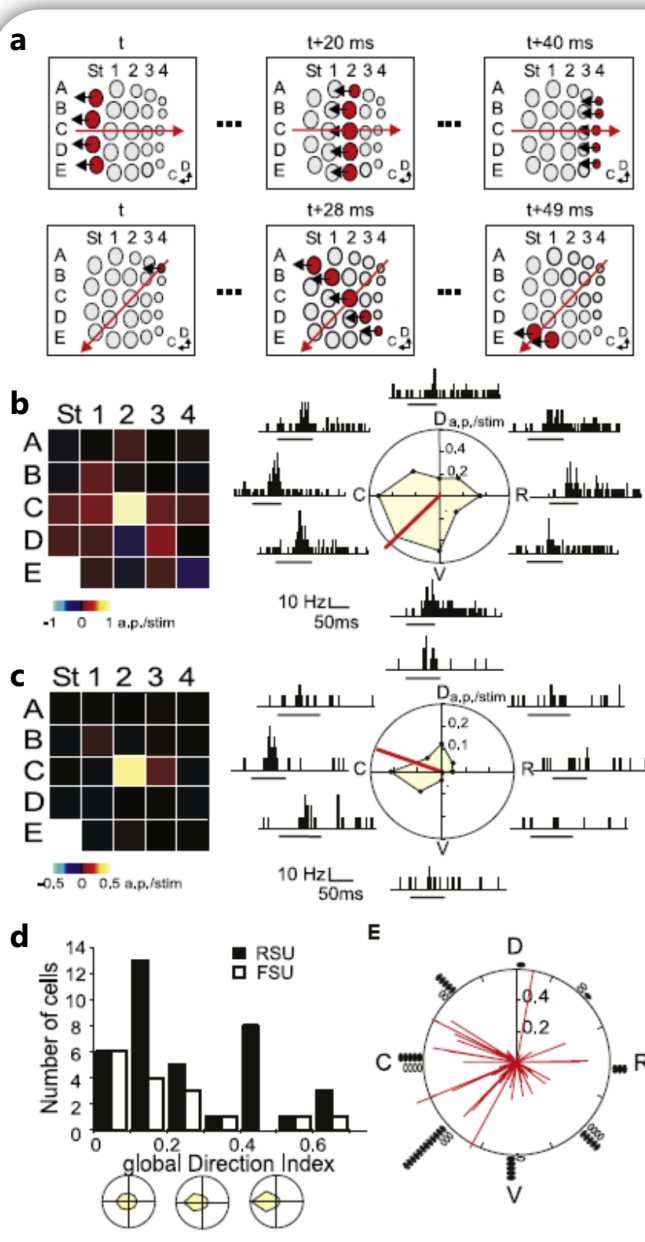

Figure 7. Sélectivité à la direction d'un mouvement global dans S1.

a. Trois étapes du protocole de stimulation de type "mouvement global" pour deux directions sur les huit présentés (mouvement global rostral (0°) en haut, et caudoventral (225°) en bas), illustrées sur un schéma de l'implantation des vibrisses (St, straddlers ; C, caudal ; D, dorsal). Les flèches noires indiquent le mouvement local des vibrisses (rostro-caudal, 180 °). Les vibrisses en rouge sont stimulées simultanément au temps indiqué, dans le cadre du mouvement global (flèche rouge).

b. Gauche : Champ récepteur d'une cellule à décharge régulière de la couche 5 présenté sous la forme d'une carte de l'activité évoquée (10-60 ms post stimulus). L'amplitude des réponses est illustrée par une échelle de couleur. Droite : diagramme polaire des réponses (25-105 ms à partir du début du stimulus) aux 8 directions du mouvement global. Le segment en rouge représente la somme vectorielle des 8 réponses il pointe vers la direction globale préférée de ce neurone. Les réponses à chacun des 8 mouvements globaux sont illustrées sous forme d'histogrammes péri-stimulus (les barres noires illustrent la durée de la stimulation). L'indice de sélectivité à la direction globale pour cette cellule était de 0.24.

c. Réponse d'une cellule à décharge rapide de la couche 5. Mêmes conventions qu'en (**b**). L'indice de sélectivité à la direction globale pour cette cellule était de 0.,41.

d. Gauche: Distribution de l'indice de sélectivité à la direction globale pour les cellules à décharge régulière (RSU, barres noires, n = 37) et rapide (FSU, barres blanches, n = 16) des courbes représentatives avec un indice de direction de 0.1, 0.3, et 0.5 sont représentés sous l'histogramme. Droite : Distribution des vecteurs de direction. Chaque vecteur représente la direction globale préférée pour une seule unité, et sa longueur représente l'indice de sélectivité. L'histogramme autour du graphique montre la distribution des directions préférées par tranche de 45° pour les FSU (points blancs, n = 16) et RSU (points noirs, n = 37).

Jacob et al., 2008.

Abréviations : C, caudal ; R, rostral ; D, dorsal ; V, ventral.

Enfin, des travaux réalisés par la suite ont montré que cette sélectivité à la direction de mouvements globaux apparait au niveau du noyau VPM thalamique, puis est amplifiée au niveau cortical (Ego-Stengel et al., 2012).Nous avons par la suite décidé de poursuivre sur ce thème en élargissant l'étude des réponses corticales aux mouvements globaux à l'ensemble de la carte des tonneaux afin d'explorer si l'ensemble des colonnes corticales partageaient ces propriétés d'intégration.

5. Cortex cérébral et anticipation sensorielle tactile

Un autre aspect particulièrement intriguant de la physiologie du cortex cérébral est la manière dont il est susceptible de générer des prédictions en fonction du contexte comportemental et de l'expérience sensorielle d'un individu. En effet, le cerveau n'est pas un dispositif passif d'entrée-sortie, mais plutôt un système générateur qui produit continuellement des attentes prospectives sur le monde extérieur. Ainsi, l'anticipation est une fonction majeure du système nerveux qui prépare l'organisme à réagir de manière significative au flux sensoriel en fonction du contexte interne et externe récent (Bullock et al., 1994; Engel et al., 2001). Elle est nécessaire pour un grand nombre de processus : de l'optimisation du traitement des signaux sensoriels dans un environnement bruyant à la détection d'entrées sensorielles inattendues et au déclenchement de réponses comportementales appropriées.

Les prédictions sur les entrées sensorielles peuvent être générées dans des situations relativement passives, par exemple à l'écoute de séquences régulières de sons (Chen et al., 2015) ou en observant des séquences de stimuli visuels (Gavornik and Bear, 2014), mais dans le cas de la modalité tactile, les commandes motrices gouvernant les mouvements des organes sensoriels sont impliquées dans le processus de perception, et donc d'anticipation. Ainsi, des contacts actifs répétés avec un objet fixe devraient être à l'origine de l'émergence de jugements prospectifs sur les contacts futurs lors de la réalisation d'un programme moteur ciblé.

La perception sensorielle tactile devrait ainsi impliquer : 1) Une représentation de l'attente sensorielle tactile émanant de l'intégration de la mémoire des événements sensoriels passés avec la commande motrice, capable de s'étendre sur un certain intervalle de temps, jusqu'à ce que l'événement en cours soit perçu. 2) La génération d'une représentation précise du stimulus perçu. 3) La comparaison entre la représentation du stimulus perçu et celui attendu, un processus qui semble se dérouler dans le système vibrissal comme en témoignent les réponses adaptatives déclenchées par un retrait abrupt d'une cible (Voigts et al., 2015). La détection d'une violation de l'attente se produit lorsqu'il y a discordance entre la représentation des événements sensoriels perçus et ceux qui sont attendus (Harms et al., 2016). Chacune de ces trois opérations putatives, qui se déroulent donc probablement dans le système vibrissal, est censée avoir ses propres corrélats neuronaux.

Comme exposé plus bas, l'un de mes projets consiste à étudier quelles sont les bases neuronales de cette forme d'anticipation sensorimotrice au sein du réseau cortical, avec une attention particulière portée aux régions S1-S2-M1.

6. Contributions personnelles

Dans la suite de ce document, je vais tout d'abord présenter brièvement les plus importantes contributions que j'ai apportées à l'étude fonctionnelle du cortex cérébral, avec un focus particulier sur le traitement de l'information tactile. Puis je présenterai mes principaux projets de recherche qui, je l'espère, continueront à contribuer à une meilleure compréhension de la physiologie corticale et des bases neuronales du comportement.

Ces travaux passés et à venir ont bien souvent impliqué et impliquerons la formation, la supervision et l'encadrement d'étudiants stagiaires et doctorants. Cet aspect de mon activité sera indiqué le cas échéant par un rond bleu ●.

1ère Partie : Réalisations scientifiques

1. Interroger la diversité cellulaire du cortex cérébral

Travaux réalisés essentiellement au cours de mon doctorat (2000-2003) et après mon post-doctorat (2007-2010) au sein du Laboratoire de Neurobiologie de l'École Supérieure de Physique et de Chimie Industrielles de la ville de Paris, ESPCI ParisTech, sous la direction du Dr Bertrand Lambolez et du Pr. Jean Rossier.

1.1. Vers une classification fonctionnelle des interneurones corticaux ?

Le cortex cérébral est impliqué dans des processus sensori-moteurs, cognitifs et émotionnels. Les aires corticales et les systèmes de neurotransmission mis en jeu dans ces processus complexes sont de mieux en mieux connus grâce aux études neurochimiques comportementales, aux progrès de l'imagerie fonctionnelle, et à l'émergence des outils optogénétiques. Cependant, les populations neuronales spécifiquement impliquées dans les fonctions corticales, ainsi que leurs modes d'activation, restent largement inconnus du fait de la grande hétérogénéité du tissu cérébral. Mes travaux visaient à contribuer à l'exploration fonctionnelle du néocortex par la compréhension des mécanismes contrôlant l'activation de populations neuronales spécifiques au sein du réseau cortical.

Le néocortex comprend deux grandes populations de neurones : les cellules pyramidales glutamatergiques excitatrices qui constituent les principales efférences du néocortex, et les interneurones, pour la plupart GABAergiques inhibiteurs, impliqués dans la modulation des signaux au niveau des circuits locaux. Ces interneurones sont très hétérogènes du point de vue de leurs propriétés électrophysiologiques, moléculaires et morphologiques. Cette grande diversité a donné cours à de nombreux travaux visant à caractériser des populations d'interneurones distinctes sur la base de leurs propriétés intrinsèques (Ascoli et al., 2008; Cauli et al., 1997, 2000; DeFelipe, 1993; DeFelipe et al., 2013; Gupta et al., 2000; Kawaguchi, 1995; Markram et al., 2004; Rudy et al., 2011; Tremblay et al., 2016). La définition d'une classification fonctionnelle des interneurones inhibiteurs apparait en effet comme une étape clef dans l'établissement de modèles canoniques de traitement de l'information au sein des unités fonctionnelles que sont les colonnes corticales (Douglas and Martin, 2004; Jiang et al., 2015). Malgré les efforts fournis en ce sens, il est malheureusement encore difficile de faire émerger une classification et nomenclature faisant l'unanimité car les différents types d'interneurones définis par ces différentes études dépendent des critères de classification utilisés qui sont eux-mêmes contraints par des limitations techniques.

Les approches émergentes de transcriptomique sur cellules uniques à grande échelle vont sans doute apporter des données précieuses dans ce domaine (Tasic et al., 2016; Zeisel et al., 2015). Cependant il est essentiel de garder en tête que, quels que soient les critères utilisés pour la classification, les propriétés des neurones restent variables au sein d'une population donnée et les frontières entre populations neuronales ne sont pas dessinées de manières très nettes. Il semble donc que la meilleure manière de dépeindre cette diversité est un continuum organisé autour d'archétypes donnés (Battaglia et al., 2013). L'étude de l'origine embryonnaire et des mécanismes de

différentiation des interneurones peut apporter des indications précieuses sur les liens existants entre les populations neuronales ainsi décrites (Vitalis and Rossier, 2011; Wonders and Anderson, 2006).

1.2. Stratégie expérimentale : analyse multiparamétrique de neurones uniques

La combinaison des techniques de patch-clamp, de RT-PCR sur cellule unique et de marquages histochimiques (**figure 8**, Lambolez et al., 1992), a permis d'établir chez le rat, une classification basée sur des paramètres multiples, définissant ainsi des populations d'interneurones caractérisés à la fois par leurs propriétés électrophysiologiques, moléculaires et morphologiques (Cauli et al., 1997, 2000).

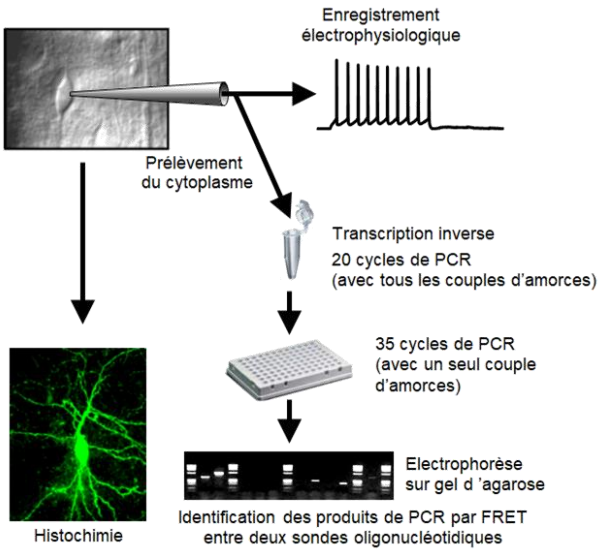

Figure 8. La RT-PCR sur cellule unique après patch-clamp.

Les enregistrements électrophysiologiques de potentiel ou de courants membranaires sont effectués suivant la méthode de patch-clamp en configuration cellule entière sur des tranches de cortex maintenues en survie *ex vivo*. De la biocytine placée dans le milieu intracellulaire contenu dans la pipette d'enregistrement permet d'étudier la morphologie du neurone d'intérêt après fixation de la tranche et révélation histochimique. A la fin de chaque enregistrement, une pression négative appliquée dans la pipette permet d'aspirer une portion du cytoplasme du neurone enregistré. Le contenu de la pipette est ensuite collecté dans un tube afin de procéder à une transcription inverse des ARN messagers par la reverse transcriptase, puis à l'amplification des ADN complémentaires par réaction en chaîne de l'ADN polymérase (RT-PCR). Les produits ainsi obtenus sont analysés par électrophorèse sur gel d'agarose, et leur nature confirmée par transfert résonant d'énergie de fluorescence (FRET) entre deux sondes oligonucléotidiques adjacentes (pour détails, voir Férézou et al., 2002).

Grace à cette approche expérimentale, j'ai pu apporter des données fonctionnelles sur une population d'interneurones corticaux caractérisés par l'expression de la sous unité 5HT3A du récepteur à la sérotonine de type 3 (que nous appellerons interneurones 5HT3 par la suite). Cette population représenterait ~30% des interneurones corticaux chez la souris (Lee et al., 2010; Rudy et al., 2011).

1.3. Excitation synaptique rapide des interneurones VIP/CCK via les récepteurs 5HT3

Ferezou I, Cauli B, Hill E, Rossier J, Hamel E, Lambolez B. 5-HT3 receptors mediate serotonergic fast synaptic excitation of neocortical VIP/CCK interneurons. ***J Neurosci***. 2002, 22(17):7389–7397.

La combinaison du patch-clamp à la RT-PCR sur cellule unique m'a tout d'abord permis de caractériser les neurones néocorticaux exprimant le récepteur 5HT3 (seul récepteur canal activé par la sérotonine). La sous-unité 5HT3A était sélectivement exprimée dans les interneurones VIP/CCK alors que la sous-unité 5HT3B n'a jamais été détectée, indiquant que les récepteurs 5HT3 exprimés par les neurones néocorticaux ne contiennent pas cette sous-unité. Chez les interneurones exprimant la sous-unité 5HT3A, la sérotonine induisait des dépolarisations de potentiel de membrane rapides dues à l'activation d'un courant entrant qui était bloqué par un antagoniste sélectif du récepteur 5HT3, le tropisetron (**figure 9a**).

De plus, j'ai observé des appositions entre les fibres sérotoninergiques originaires des noyaux du raphé et les dendrites et corps cellulaires de neurones sensibles à la sérotonine, suggérant l'existence d'une excitation synaptique rapide des interneurones VIP/CCK par les fibres sérotoninergiques afférentes (**figure 9b**). L'enregistrement de courants postsynaptiques excitateurs sensibles au tropisetron, en réponse à des stimulations électriques locales dans des neurones sensibles à la sérotonine, m'a permis de démontrer par la suite l'existence d'un tel mode de transmission (**figure 9c**). Enfin, les interneurones exprimant le récepteur 5HT3 étaient également excités par un agoniste nicotinique, suggérant une convergence des transmissions synaptiques rapides sérotoninergiques et nicotiniques sur les interneurones VIP/CCK.

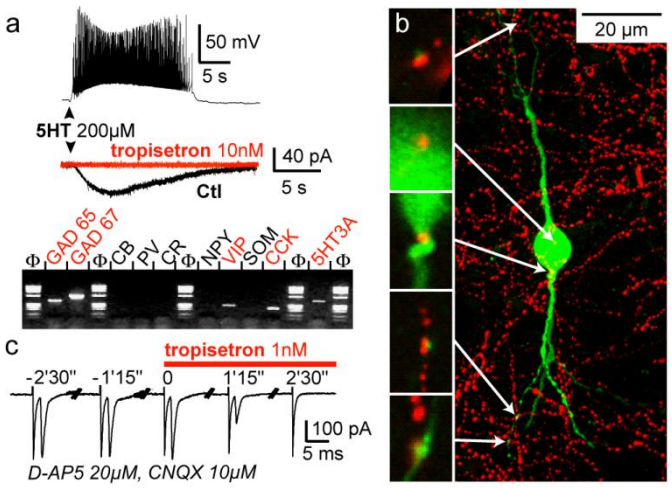

Figure 9. Excitation synaptique rapide des interneurones VIP/CCK via les récepteurs 5HT3.

a. Expression fonctionnelle du récepteur 5HT3 dans un interneurone VIP/CCK. Ce neurone a répondu à l'application locale de sérotonine (5HT) par une longue décharge de potentiels d'actions (en haut). Le large courant entrant induit par la 5HT était bloqué en présence de tropisetron (au milieu). La caractérisation moléculaire de ce neurone a mis en évidence l'expression des enzymes de synthèse du GABA (GAD 65 et GAD 67), des neuropeptides VIP et CCK ainsi que de la sous-unité 5HT3A du récepteur 5HT3 (en bas).

b. Fibres sérotoninergiques (marquage immuno-cytochimique de la 5HT, en rouge) formant des appositions avec le corps cellulaire et les dendrites d'un neurone répondant à la 5HT (marquage histochimique de la biocytine, en vert).

c. Réponse d'un neurone sensible à la 5HT induite par une stimulation électrique locale et son blocage par le tropisetron.

Ces résultats ont permis de mettre en évidence la présence de la sous-unité 5HT3A dans les interneurones GABAergiques inhibiteurs de type VIP/CCK, son expression fonctionnelle et son activation synaptique par les fibres sérotoninergiques afférentes provenant des noyaux du raphé (Férézou et al., 2002).

1.4. Intégration des signaux nicotiniques et opioïdergiques au sein du néocortex

Ferezou I, Hill EL, Cauli B, Gibelin N, Kaneko T, Rossier J, Lambolez B. Extensive Overlap of µ-Opioid and Nicotinic Sensitivity in Cortical Interneurons. ***Cereb Cortex***. 2007, 17(8):1948-57.

Les données présentées jusqu'ici indiquent que les interneurones VIP/CCK jouent un rôle spécifique dans la modulation de l'activité du réseau néocortical par les systèmes cholinergiques et sérotoninergiques ascendants. J'ai observé par la suite que le récepteur opioïde de type µ est exprimé de manière sélective par les interneurones VIP/CCK et les interneurones de la couche I du néocortex. Les données de RT-PCR sur cellule unique ont révélé que les interneurones VIP/CCK (et non les interneurones de la couche I) expriment fréquemment l'enképhaline, agoniste endogène du récepteur µ-opioïde, ce qui suggère l'existence d'une boucle d'autorégulation opioïdergique de type autocrine ou paracrine au sein de cette population neuronale. La fonctionnalité des récepteurs µ-opioïdes exprimés par ces neurones a été testée à l'aide d'un agoniste sélectif de ce récepteur. Les

interneurones exprimant le récepteur μ-opioïde répondaient à l'application de cet agoniste par une hyperpolarisation inhibitrice, due à l'activation d'un courant sortant potassique. En outre, j'ai observé une colocalisation quasiment totale des récepteurs post-synaptiques μ-opioïdes et nicotiniques (nACh) dans le néocortex. J'ai enfin montré que l'excitation des interneurones sensibles à la nicotine peut induire une libération d'enképhaline endogène qui activerait alors les récepteurs μ-opioïdes. La transmission μ-opioïde corticale agirait donc comme une boucle de rétroaction négative sur les neurones sensibles à la nicotine, ce qui modifierait l'excitabilité du réseau lors d'une excitation cholinergique (Férézou et al., 2007). Ainsi, ce mécanisme cellulaire rend compte de l'implication des récepteurs opioïdes de type μ dans les effets de la nicotine, au niveau néocortical.

1.5. Caractérisation des interneurones 5HT3 et de leur origine embryonnaire chez la souris

Vucurovic K*, Gallopin T*, **Ferezou I***, Rancillac A, Chameau P, van Hooft JA, Geoffroy H, Monyer H, Rossier J, Vitalis T. Serotonin 3A receptor subtype as an early and protracted marker of cortical interneuron subpopulations. ***Cereb Cortex***. 2010, 20(10):2333-47.
** Ces auteurs ont contribué de manière égale au travail.*

Nous avons mené par la suite une étude systématique des interneurones 5HT3 ex vivo, à l'aide de souris transgéniques exprimant la GFP sous le contrôle du promoteur 5-HT3A (Vucurovic, Gallopin, Ferezou et al., 2010). L'expression précoce de la sous-unité 5-HT3A nous a permis d'étudier les interneurones 5HT3 depuis leur naissance jusqu'à leur phénotype fonctionnel final.

La combinaison d'enregistrements électrophysiologiques (patch clamp) à des analyses moléculaires, histochimiques et statistiques nous a permis de montrer l'existence de deux populations d'interneurones exprimant le récepteur 5-HT3. La première population étant caractérisée par l'expression fréquente de VIP et une morphologie bipolaire/bitouffue typique, alors que la deuxième population exprime de façon prédominante le neuropeptide Y et présente une arborisation dendritique plus complexe. La plupart des interneurones de ce deuxième groupe possèdent des caractéristiques morphologiques élecrophysiologiques et moléculaires de cellules dites neurogliaformes (Gong et al., 2006; Hestrin and Armstrong, 1996; Jiang et al., 2015; Kawaguchi, 1995).

Des injections de 5-bromo-2-deoxyuridine combinées avec la détection de l'ARNm 5-HT3A ont montré que les interneurones 5-HT3A corticaux sont générés autour du jour embryonnaire 14.5. Bien qu'à ce stade, la sous-unité 5-HT3A s'exprime à la fois dans l'éminence ganglionnaire caudale et l'aire entopédonculaire, des expériences de greffes homochroniques in utero ont révélé que les interneurones 5-HT3 corticaux sont principalement générés dans l'éminence ganglionnaire caudale.

Nous avons ainsi montré que les interneurones 5HT3 forment deux populations distinctes qui partagent une origine embryonnaire commune.

L'ensemble de ces résultats, ainsi que les données dont on dispose sur la population des interneurones 5HT3, indiquent que ces derniers représentent un point de convergence remarquable entre de nombreuses voies de neuromodulation/neurotransmission impliquées dans la régulation des états émotionnels et motivationnels. En effet, diverses études neurochimiques comportementales, basées sur l'administration d'agonistes des récepteurs nACh, 5HT3 et μ-opioïdes, ont mis en évidence leur implication dans les phénomènes de stress et d'anxiété (Brioni et al., 1993; Costall et al., 1990; Irvine et al., 2001; Jones et al., 1988; Ragnauth et al., 2001; Roychoudhury and Kulkarni, 1997).

2. Visualiser les dynamiques corticales à l'échelle mésoscopique

Lebeuf R, **Férézou I**, Rossier J, Arseniyadis S, Cossy J. Straightforward synthesis of the near-infrared fluorescent voltage-sensitive dye RH1691 and analogues thereof. ***Org Lett.*** 2009, 11(21):4822-5.

Chapitre de livre : **Ferezou I**, Matyas F, Petersen CCH. Imaging the brain in action - real-time voltage-sensitive dye imaging of sensorimotor cortex of awake behaving mice. In: "In vivo optical imaging of brain function" edited by Ron Frostig. Publishers: CRC Press (Boca Raton, USA), 2009.

Berger T, Borgdorff A, Crochet S, Neubauer FB, Lefort S, Fauvet B, **Ferezou I**, Carleton A, Lüscher HR, Petersen CCH. Combined voltage and calcium epifluorescence imaging in vitro and in vivo reveals subthreshold and suprathreshold dynamics of mouse barrel cortex. ***J Neurophysiol.*** 2007, 97(5):3751-62.

Souhaitant aller plus loin dans la compréhension des bases neuronales du comportement, de la cellule au réseau de neurones, j'ai souhaité aborder par la suite l'étude du cortex cérébral de manière plus intégrée, passant d'une approche *ex vivo* à l'échelle des neurones uniques vers une approche *in vivo*, visant à analyser les dynamiques spatiotemporelles de l'activité du réseau qui sous-tendent certaines fonctions corticales. J'ai choisi de concentrer mes efforts sur l'intégration de l'information sensorielle par le néocortex en utilisant pour modèle de la voie sensorielle des vibrisses chez la souris. Afin d'étudier la manière dont le réseau cortical est activé en réponse à des stimuli tactiles, j'ai décidé de mettre en œuvre sur ce modèle, l'imagerie sensible au potentiel qui permet de suivre les dynamiques corticales avec une résolution temporelle de l'ordre de la milliseconde et une résolution spatiale allant de la dizaine à la centaine de microns, afin de travailler à une échelle dite mésoscopique (**figure 10**, Chemla et al., 2017).

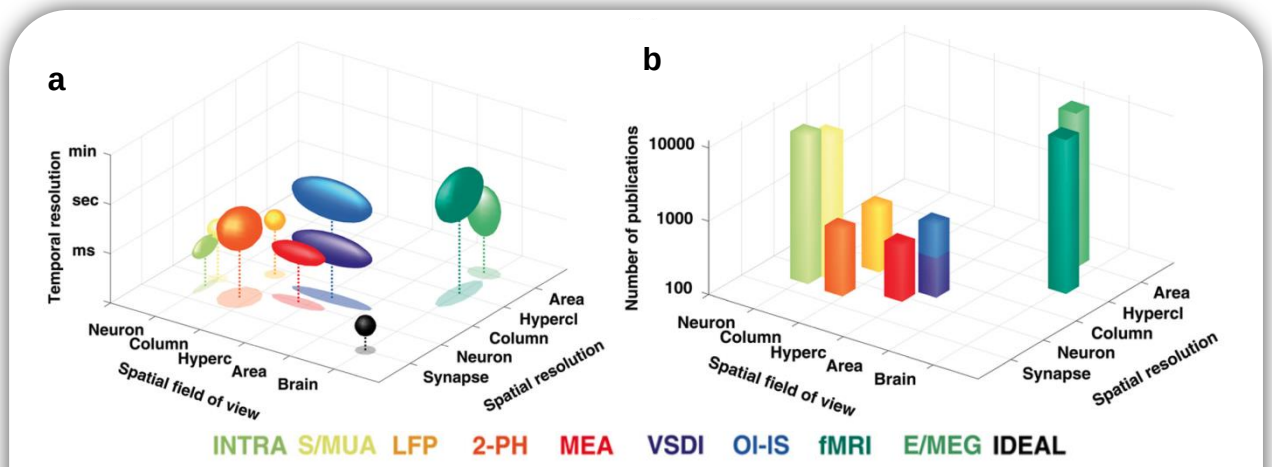

Figure 10. Résolution spatio-temporelle et échelles des méthodes d'enregistrement neuronal

a. Représentation tridimensionnelle de 10 familles de méthodes d'enregistrement neuronal en fonction de leur résolution spatiale, de leur résolution temporelle et du champ de vision spatial qu'elles peuvent atteindre.

b. Histogramme de la quantité de publications référencées dans PubMed avec le mot "cortex" et l'une de ces méthodes. La ligne de recherche générique était : (TECHNIQUE_NAME[Titre/Abstract]) AND (cortex[Titre/Abstract] OU cortical[Titre/Abstract]). Le cas échéant, le nom de la technique a été écrit en entier et abrégé.

Chemla et al., 2017.

Abréviations : INTRA, enregistrements intracellulaires ; S/MUA, enregistrements extracellulaires d'activité unitaire ou multi-unitaire ; LFP, potentiels de champ local ; 2-PH, microscopie à deux photons ; MEA : réseau d'électrodes multiples ; **VSDI, imagerie sensible au potentiel** ; OI-IS, imagerie optique de signaux intrinsèques ; fMRI, imagerie par résonance magnétique fonctionnelle ; E/MEG, électro-encéphalogramme ou magnéto-encéphalogramme ; IDEAL, technique idéale.

Cette résolution est particulièrement attractive car elle autorise la distinction entre les unités fonctionnelles du réseau que sont les colonnes corticales. Cette méthode d'imagerie fonctionnelle est basée sur l'utilisation de colorants sensibles au potentiel (ou VSD pour *Voltage Sensitive Dyes)*. Il s'agit de molécules fluorescentes qui s'insèrent dans la membrane plasmique des cellules et modifient leurs propriétés de fluorescence en fonction des variations de la différence de potentiel qui existe de part et d'autre de la bicouche lipidique. Ces changements de fluorescence suivent les variations de potentiel membranaire de manière parfaitement linéaire, avec une résolution temporelle inférieure à la milliseconde (Berger et al., 2007). Alors que les signaux d'imagerie calcique varient en fonction de l'émission de potentiels d'action et permettent donc de suivre exclusivement l'activité neuronale dite supraliminaire, les VSDs permettent l'imagerie en temps réel de l'activité du potentiel membranaire des neurones, qu'il se trouve en dessous ou au-delà du seuil de décharge de potentiels d'action.

On soulignera ici le rôle essentiel joué par Rina Hildesheim et Amiram Grinval dans le développement de cette méthode d'imagerie fonctionnelle appliquée aux neurosciences (Grinvald & Hildesheim, 2004). Cette contribution a été collectivement honorée dans un numéro spécial de la revue *Neurophotonics* en 2017 (Frostig and Petersen, 2017). Les premiers enregistrements d'imagerie VSD réalisés *in vivo* dans le but d'étudier la dynamique de réponses sensorielles ont été obtenus dans le tectum visuel de la grenouille (Grinvald et al., 1984), puis dans le cortex somatosensoriel et visuel du rat (Orbach et al., 1985) et dans le cortex visuel du macaque (Blasdel and Salama, 1986). Historiquement, le principal inconvénient de cette technique résidait dans la présence d'artefacts liés au rythme cardiaque en raison non seulement des mouvements produits par la pulsation physique des vaisseaux sanguins, mais aussi du spectre d'absorption de l'hémoglobine qui varie en fonction du niveau d'oxygénation, contaminant les signaux enregistrés. Pour minimiser ce dernier, le groupe d'Amiram Grinvald a développé des colorants fluorescents dotés de spectres d'absorption et d'émission dans le rouge lointain, au-delà de 600 nm (Grinvald and Hildesheim, 2004; Shoham et al., 1999). Ceux-ci ont été utilisées avec succès pour étudier les dynamiques spatio-temporelles de l'activité corticale au sein du cortex visuel chez le chat anesthésié, mais aussi chez le singe vigile (Arieli et al., 1996; Tsodyks et al., 1999). Le RH1961 que j'utilise est l'un des colorants de cette nouvelle série de VSDs (**Figure 11a**).

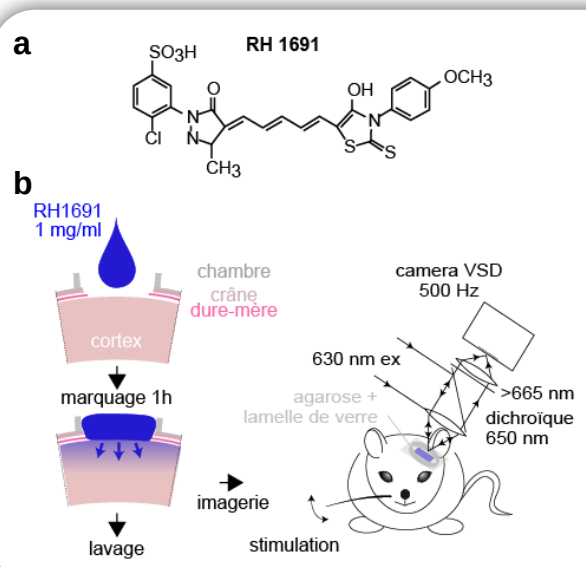

Figure 11. Imagerie des signaux de fluorescence émis par le colorant RH1691.

a. Structure chimique du colorant RH1691.

b. Utilisation du RH1691 chez la *souris in vivo*. L'os du crâne doit être ôté au niveau de la zone d'intérêt. La dure-mère doit ensuite être retirée avec précaution, puis le colorant est appliqué sur le cerveau. Au bout d'une heure, le colorant non fixé est lavé, la craniotomie protégée avec de l'agarose et une lamelle de verre, puis l'animal transféré sur le poste d'imagerie où les signaux peuvent être recueillis à l'aide d'une caméra rapide. A la fin de la session d'enregistrement, le cerveau de la souris peut être prélevé après fixation au paraformaldéhyde, et coupé en tranches tangentielles. Un marquage à la cytochrome oxydase permet alors de révéler la carte somatotopique du cortex en "tonneaux" et de la superposer avec les enregistrements optiques.

Il s'agit d'un composé d'oxonol aromatique soluble dans l'eau, ses changements de conformation sont exécutés par transfert d'électrons. Il s'insère dans la bicouche lipidique de la membrane plasmique des cellules où il peut être excité par la lumière à ~630 nm, et émet des photons fluorescents avec des longueurs d'onde >665 nm. Sa mise en œuvre est illustrée **figure 11b**.

Sachant que l'imagerie sensible au potentiel n'avait jamais été effectuée sur la souris auparavant, j'ai effectué des expériences visant à vérifier la nature des signaux obtenus avec ce VSD. J'ai tout d'abord observé par imagerie confocale que la pénétration du colorant dans le cortex de la souris conduisait à un marquage préférentiel des couches 2/3 (**figure 12a**). De plus, des enregistrements simultanés de potentiel de membrane de neurones de la couche 2/3 et de la fluorescence du colorant, m'ont permis de montrer une très bonne corrélation entre ces deux types de signaux. Les potentiels d'action spontanés n'étaient cependant pas accompagnés de larges déflections de fluorescence, suggérant que ces évènements n'avaient pas lieu simultanément dans une large population de neurones (**figure 12b**, Ferezou et al., 2006).

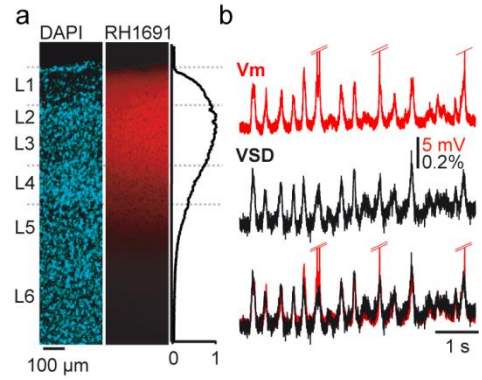

Figure 12. Corrélation de la fluorescence du VSD (RH1691) avec le potentiel de membrane des neurones des couches 2/3.

a. Après une session d'imagerie sensible au potentiel, le cerveau de la souris a été fixé et coupé en tranches parasagittales (100 µm d'épaisseur) qui étaient contremarquées au DAPI (di aminido phenyl indol) afin de distinguer les différentes couches corticales. Les images en microscopie confocale de ces tranches ont révélé un marquage préférentiel des couches 2/3 du néocortex par le RH1691.

b. Enregistrement du potentiel de membrane (Vm) d'un neurone (couche 2/3) de la colonne C2 (en rouge) effectué simultanément avec la mesure de la fluorescence du VSD (en noir) chez une souris anesthésiée (uréthane). La superposition des deux traces révèle une forte corrélation des changements de fluorescence avec le potentiel membranaire sous liminaire du neurone.

Brièvement, les atouts de cette méthode résident essentiellement dans 1) la possibilité d'observer le potentiel membranaire moyen des neurones avec une excellente résolution spatiotemporelle, et un relativement bon rapport signal sur bruit 2) la très faible contamination des signaux de fluorescence par les constantes physiologiques telles que les battements cardiaques et la respiration, en particulier chez la souris. Ainsi, il est possible d'analyser les dynamiques corticales sans avoir à moyenner les signaux issus de plusieurs séquences d'acquisition, ce qui est un atout essentiel lorsque l'on veut lier dynamiques corticales et comportement. En revanche, il s'agit d'une méthode invasive, qui ne permet pas de réaliser des expériences de manière répétée chez un même animal au cours d'un apprentissage par exemple. Une autre limitation de cette approche réside dans le fait que le colorant s'insère de manière non spécifique dans les membranes cellulaires. Il est par conséquent difficile d'évaluer la contribution respective des différents types cellulaires et compartiments subcellulaires dans les signaux enregistrés.

Il est à noter qu'un travail de modélisation de la colonne corticale a été effectué dans le but de fournir des estimations et faciliter l'interprétation des données d'imagerie VSD (Chemla and Chavane, 2010). Ce travail suggère une contribution majeure de l'activité dendritique (77%) des neurones excitateurs (83%) dans les couches superficielles (81%). Cependant, les interneurones inhibiteurs (17%), l'émission de potentiels d'action (23%) et les couches profondes (19%) contribueraient à

hauteur de 20 % au signal total. Enfin cette étude a révélé que ces contributions respectives ne seraient pas figées mais susceptibles de varier en fonction du niveau d'activation du réseau.

Ces limitations devraient être levées par l'émergence de sondes sensibles au potentiel protéiques, efficaces, pouvant être encodées génétiquement (Inagaki and Nagai, 2016; Xu et al., 2017). De tels outils permettraient en effet, non seulement de pratiquer ce type d'imagerie de manière chronique dans des études longitudinales au travers d'une fenêtre implantée dans le crâne de l'animal, mais aussi de cibler l'expression de sondes dans des types cellulaires et/ou des compartiments subcellulaires choisis et donc de mieux comprendre la manière dont les vagues d'activation sont générées et se propagent au sein du réseau cortical.

3. Influence du contexte comportemental sur le traitement cortical des informations sensorielles tactiles

Travaux réalisés essentiellement au cours de mon post-doctorat (2004-2007) au sein du Laboratory of Sensory Processing, Brain Mind Institute, École Polytechnique Fédérale de Lausanne, Suisse. Direction : Pr. Carl Petersen.

La souris utilise ses vibrisses de manière active pour explorer son environnement avec des mouvements rythmiques. Ce comportement, encore appelé "whisking", contribue à l'excellente performance de cette voie sensorielle, primordiale pour ces rongeurs nocturnes qui doivent, dans maintes circonstances, prélever des informations sur leur environnement dans l'obscurité.

Au cours de mon post-doctorat, j'ai développé des approches expérimentales novatrices, basées sur l'imagerie sensible au potentiel, qui m'ont permis d'effectuer des observations utiles à la compréhension du traitement cortical de l'information chez l'animal éveillé. J'ai en effet : 1) développé une méthode pour enregistrer l'activité corticale chez l'animal éveillé et libre de ses mouvements afin d'étudier l'impact du comportement sur le traitement de l'information corticale (Ferezou et al., 2006); 2) élargi à toute la partie dorsale du cortex cérébral l'observation de l'activité neuronale induite par les stimulations sensorielles afin d'étudier les interactions sensorimotrices (Ferezou et al., 2007).

3.1. Impact de l'activité motrice sur les dynamiques corticales évoquées par des stimuli tactiles

Ferezou I, Bolea S, Petersen CCH. Visualising the cortical representation of whisker touch: voltage-sensitive dye imaging in freely moving mice. ***Neuron***. 2006, 50(4):617-29.

Afin d'adapter la technique d'imagerie sensible au potentiel à la souris éveillée, libre de ses mouvements, nous avons utilisé un faisceau de fibres optiques reliant le système d'épifluorescence (équipé d'une caméra ultra rapide) à la tête de la souris. Les fibres optiques (longues de 50 cm) étaient suffisamment légères et flexibles pour permettre à la souris de bouger librement dans une "chambre de comportement". Pour travailler sur une vibrisse unique, toutes les vibrisses étaient coupées au début de l'expérience à l'exception de la vibrisse C2. La colonne corticale correspondant à cette vibrisse était localisée, à travers l'os, par imagerie des signaux optiques intrinsèques (Grinvald et al., 1986). Une craniotomie était ensuite effectuée de manière à placer cette colonne corticale au centre de la zone exposée. L'extrémité du faisceau de fibres (3x3 mm) était alors placée en contact

avec le cortex S1, préalablement marqué au VSD. Pendant l'expérience, la souris était illuminée par des diodes électroluminescentes (LEDs) infrarouges, et son comportement était enregistré à l'aide d'une seconde caméra (**figure 13a**).

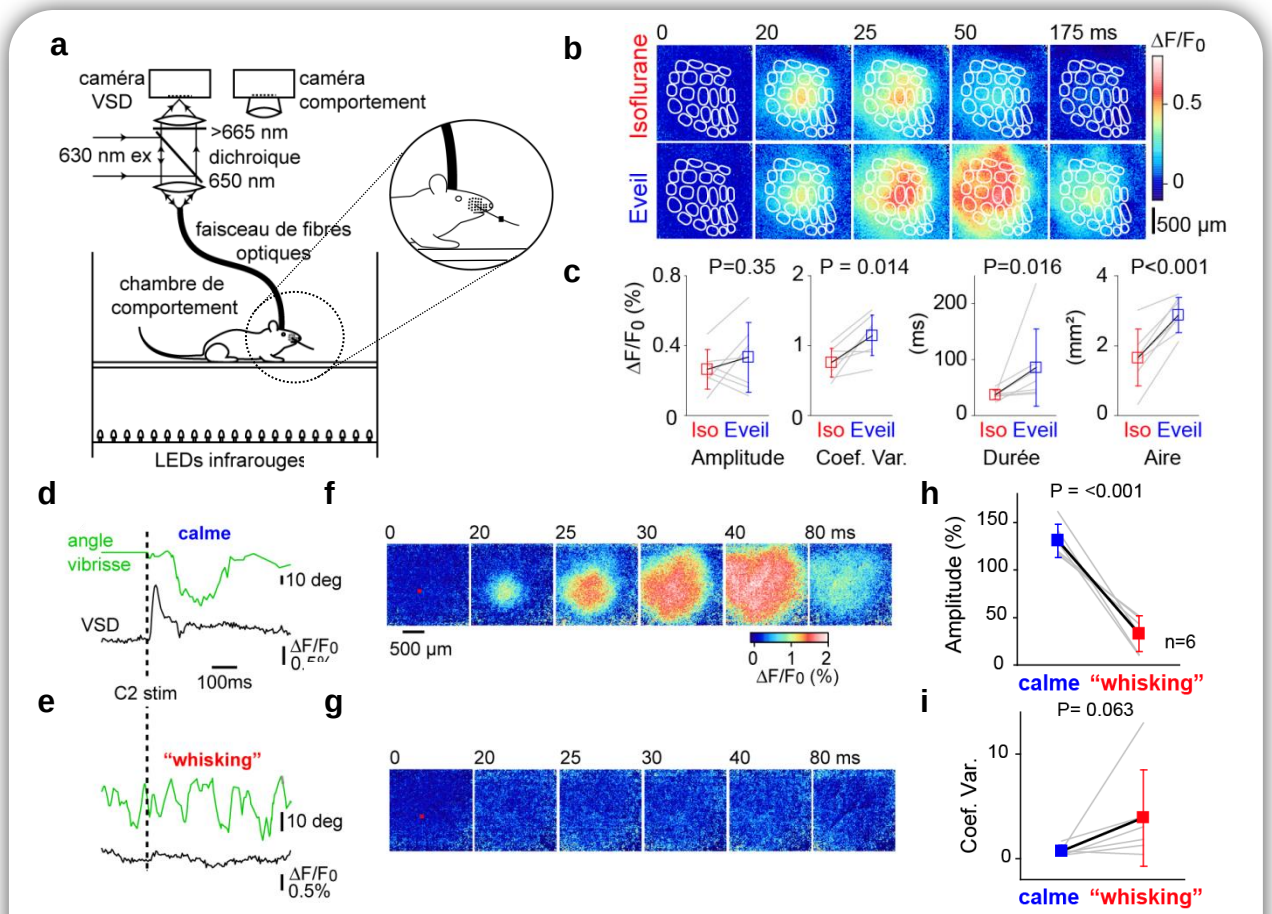

Figure 13. Les réponses sensorielles évoquées dépendent fortement du comportement de la souris.

a. Schéma illustrant le poste de travail utilisé. Pour stimuler la vibrisse C2 chez les souris éveillées de manière reproductible, une petite particule métallique était attachée à la vibrisse et un bref champ magnétique était délivré à l'aide une bobine électromagnétique.

b. Comparaison des réponses corticales évoquées par la déflection de la vibrisse C2, enregistrées par imagerie sensible au potentiel, chez une souris sous anesthésie à l'isoflurane ou éveillée (moyennes de 30 réponses pour chaque condition, les contours blancs indiquent la carte des tonneaux en couche 4 reconstruite *post hoc*).

c. L'amplitude maximale de la réponse sensorielle chez les animaux éveillés était en moyenne plus grande que sous anesthésie à l'isoflurane (bien que cette différence ne soit pas significative). Le coefficient de variation, la durée et l'étendue de la réponse sensorielle étaient significativement plus importants chez les animaux éveillés.

d. Exemple d'une réponse à la stimulation de la vibrisse C2 enregistrée par imagerie sensible au potentiel alors que la souris était immobile et ne bougeait pas sa vibrisse (comme l'indique la trace montrant l'angle de la vibrisse en vert). La fluorescence (en noir) était mesurée à partir de la région indiquée en rouge en f.

e. Lors de la stimulation suivante, la souris bougeait ses vibrisses activement ("whisking"). Seule une très faible réponse a alors été enregistrée.

f-g. Séquences d'images correspondant aux réponses illustrées en d et e, respectivement.

h. L'amplitude maximale des réponses a été quantifiée au niveau de la colonne C2 pour chaque essai individuel et classée en fonction du comportement de la souris au moment du stimulus (calme vs "whisking"). Les amplitudes de réponse ont été normalisées en fonction de la réponse moyenne évoquée pour chaque expérience (n = 6). Lors d'un comportement calme, l'amplitude de réponse était supérieure à la moyenne, alors qu'elle était fortement réduite pendant le "whisking"

g. Les réponses évoquées étaient plus variables pendant le "whisking" que lors d'un comportement calme, comme le suggèrent les coefficients de variation.

J'ai ainsi observé que les réponses corticales à la stimulation d'une vibrisse étaient plus amples, plus longues et plus variables chez la souris éveillée que sous anesthésie (**figure 13b-c**).

Cependant, le profil global d'activation est comparable entre ces deux situations ; la réponse apparaît dans la dizaine de millisecondes consécutive à la stimulation au niveau de la colonne corticale correspondante, puis l'activation corticale s'étend largement jusqu'à couvrir l'intégralité du cortex "en tonneaux" (voir exemple **figure 13b**). Chez la souris éveillée, les stimulations passives de la vibrisse induisaient des réponses corticales de large amplitude lorsque la souris était calme, et des répon ses plus variables, de très faible amplitude, lorsque la souris était en train de bouger activement sa vibrisse (**figure 13d-i**).

Cette suppression de la réponse sensorielle pendant le "whisking" indique que le comportement a un impact important sur le traitement cortical de l'information, et souligne l'importance de l'étude de l'intégration sensorielle chez l'animal éveillé. Cette technique nous a également permis de décrire l'activité corticale spontanée chez l'animal éveillé et d'observer l'activité corticale lorsque la souris allait toucher d'elle-même un objet avec sa vibrisse (Ferezou et al., 2006).

3.2. Activation séquentielle des aires sensorimotrices corticales en réponse à une stimulation tactile

Ferezou I, Haiss F, Gentet L, Aronoff R, Weber B, Petersen CCH. Spatiotemporal dynamics of cortical sensorimotor integration in behaving mice. ***Neuron***. 2007, 56(5):907-923.

Par la suite j'ai voulu élargir l'observation de l'activité corticale afin d'étudier les interactions sensorimotrices. En effet, l'information sensorielle est acquise de manière active et ceci est particulièrement évident pour le sens du toucher, où les entrées sensorielles dépendent des mouvements que l'on fait lorsque l'on touche un objet et où les mouvements sont eux-mêmes sans arrêt ajustés en fonction des entrées sensorielles. J'ai donc entrepris d'utiliser l'imagerie sensible au potentiel pour observer une surface corticale plus importante, comprenant à la fois le cortex somatosensoriel primaire et le cortex moteur, en effectuant des craniotomies plus étendues (**figure 14**).

Avec de telles préparations, il était préférable de travailler avec des souris "tête fixée". Les souris étaient donc habituées à être fixées par la tête au cours de plusieurs sessions d'entraînement précédant le jour de l'expérience. J'ai ainsi pu filmer l'activité corticale alors que la souris touchait activement un objet avec sa vibrisse (**figure 14a-b**).

Comme précédemment, la réponse était localisée au niveau de la colonne C2 du cortex somatosensoriel primaire pendant les premières millisecondes consécutives au contact. Puis, ~8-10 ms plus tard, apparaissait un second site d'activation plus rostral, au niveau du cortex moteur. Enfin, ces deux zones d'activation s'étendaient largement, jusqu'à couvrir toute la partie visible du cortex dorsal. Cette activation du cortex moteur consécutive à la stimulation d'une vibrisse a été observée de manière très robuste chez des souris éveillées et anesthésiées. Des expériences menées sous anesthésie m'ont permis de montrer que l'injection ciblée d'antagonistes des récepteurs glutamatergiques au niveau de la colonne C2 du cortex "en tonneaux" bloque l'activation du cortex somatosensoriel induite par la stimulation de la vibrisse C2, mais aussi la réponse observée au niveau du cortex moteur. En outre, des micro-stimulations électriques effectuées au niveau du tonneau C2 entraînent une activation du cortex moteur similaire à celle observée à la suite d'une déflection de la

vibrisse C2. L'ensemble de ces résultats indique que l'activation du cortex moteur observée à la suite de stimuli sensoriels est dépendante de projections directes provenant du cortex "en tonneaux". Des marquages anatomiques antérogrades basés sur l'induction de l'expression de la *green fluorescent protein* par injections ciblées de virus au niveau de la colonne C2 du cortex en "tonneaux" nous ont effectivement permis d'observer de denses projections axonales vers le cortex moteur, qui participeraient à son activation lors de stimulations sensorielles. Enfin, la stimulation de différentes vibrisses m'a conduit à mettre en évidence une organisation somatotopique des réponses sensorielles au niveau du cortex moteur.

Chez les souris éveillées, j'ai également observé les réponses corticales induites par la stimulation passive de la vibrisse C2. Ces réponses étaient fortement dépendantes du comportement de la souris, avec une suppression de la réponse sensorielle pendant le "whisking", telle qu'observée précédemment. En l'absence de "whisking", certaines stimulations évoquaient un mouvement volontaire de la vibrisse, alors que d'autres ne modifiaient pas le comportement de la souris (**figure 14c-d**).

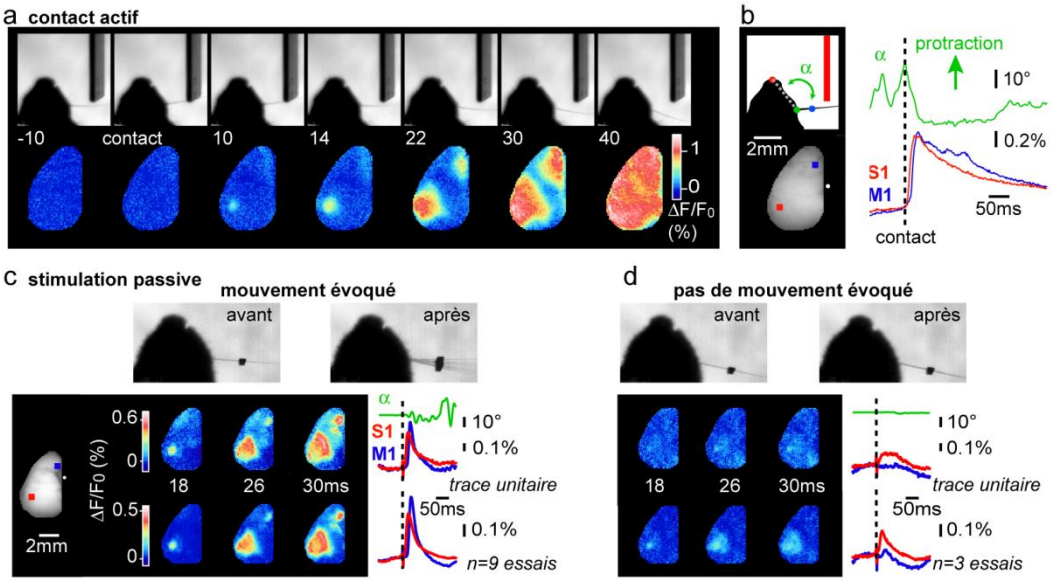

Figure 14. L'imagerie sensible au potentiel de la partie dorsale du cortex permet l'étude des interactions sensorimotrices chez la souris éveillée.

a. Images de la position de la vibrisse (en haut) et de la fluorescence du VSD (en bas) enregistrées simultanément alors que la souris touchait activement un objet avec sa vibrisse.

b. Quantification, pour la même séquence, de l'angle de la vibrisse (α, en vert) et des variations de fluorescence au niveau du cortex somatosensoriel primaire (S1, en rouge) et du cortex moteur primaire (M1, en bleu). Les régions d'intérêt utilisées pour la quantification des variations de fluorescence sont indiquées par des carrés sur l'image (en bas à gauche) montrant la fluorescence de base.

c. La stimulation passive de la vibrisse C2 induisait, dans certains cas, un mouvement évoqué de la vibrisse. Les images du haut montrent la superposition de 25 clichés correspondant à une période de 100 ms avant et après la stimulation. Les images du milieu indiquent que cette stimulation a induit une large réponse corticale, d'abord au niveau de S1, puis au niveau de M1. Les images du bas illustrent la réponse moyenne obtenue pour toutes les stimulations ayant induit un mouvement de la vibrisse chez cette souris.

d. Dans d'autres cas, la stimulation passive de la vibrisse C2 n'induisait pas de mouvement de la vibrisse. La réponse corticale enregistrée était alors beaucoup plus faible et plus localisée au niveau du cortex S1.

Les réponses corticales étaient significativement plus grandes lorsque nous observions un mouvement évoqué de la vibrisse. La propagation de l'information sensorielle vers le cortex moteur est donc régulée par le comportement de l'animal, et corrélée avec la génération de mouvements évoqués. Cette voie neuronale représente donc un mécanisme de contrôle sensoriel de l'activité motrice qui pourrait jouer un rôle clef dans la perception sensorielle tactile (Ferezou et al., 2007).

L'ensemble de ces travaux nous a permis de montrer que l'imagerie sensible au potentiel chez la souris éveillée est un outil de choix pour étudier l'impact du comportement sur l'activité corticale en temps réel, avec une résolution temporelle de l'ordre de la milliseconde. Les résultats ainsi obtenus indiquent que le traitement cortical de l'information sensorielle tactile est fortement dépendant du comportement de l'animal.

4. Traitement cortical des scènes tactiles complexes

Travaux réalisés au sein de l'équipe Traitement sensoriel, neuromodulation et plasticité neuronale de l'unité de Neurosciences Information et Complexité (UNIC CNRS FRE 3693), Gif sur Yvette, France. Direction : Dr. Daniel Shulz.

Le développement récent, au sein de l'équipe de Daniel Shulz, d'une matrice de stimulation multivibrissale dotée de 24 stimulateurs multidirectionnels (Jacob et al., 2010) a permis de mettre en évidence, à l'aide d'enregistrements électrophysiologiques unitaires, des propriétés jusqu'alors insoupçonnées du cortex S1. Il a été notamment démontré qu'une majorité des neurones d'une colonne donnée est capable d'extraire les propriétés émergentes d'une stimulation multivribrissale (Jacob et al., 2008). Ces propriétés d'intégration semblent émerger au niveau du thalamus et sont ensuite amplifiées au niveau du cortex S1 (Ego-Stengel et al., 2012).

Depuis que j'ai rejoint l'équipe en 2011, une grande part de mon activité a été consacrée à l'étude de l'intégration de stimuli tactiles multivibrissaux à l'échelle mésoscopique, couvrant l'ensemble de la représentation vibrissale dans S1.

L'association de l'imagerie sensible au potentiel à la matrice de stimulation multivibrissale offrant une opportunité unique pour étudier la manière dont sont intégrées les scènes tactiles complexes.

4.1. Stratégie expérimentale : imagerie des dynamiques corticales évoquées par des stimulations tactiles complexes chez la souris anesthésiée

- *Travail réalisé avec **María Eugenia Vilarchao,** doctorante que j'ai co-encadrée avec Daniel Shulz (Ecole Doctorale « Frontières du Vivant » - Paris Descartes Paris Diderot PhD Program in Life Sciences).*

A mon arrivée dans l'équipe, j'ai monté un nouveau poste d'imagerie fonctionnelle, doté d'une matrice de stimulation composée de 24 stimulateurs piezoélectriques multidirectionnels. Cette matrice "seconde génération" (Jacob et al., 2010) n'avait, jusqu'à présent, été utilisée que chez le rat. La qualité des signaux optiques obtenus chez la souris, ainsi que la disponibilité d'un nombre croissant de souris transgéniques permettant l'expression spécifique d'outils optogénétiques dans des populations neuronales choisies, nous ont poussés à développer l'utilisation de ce modèle dans l'équipe : il fallait donc adapter la matrice de stimulation multivibrissale au museau de la souris (**figure 15**).

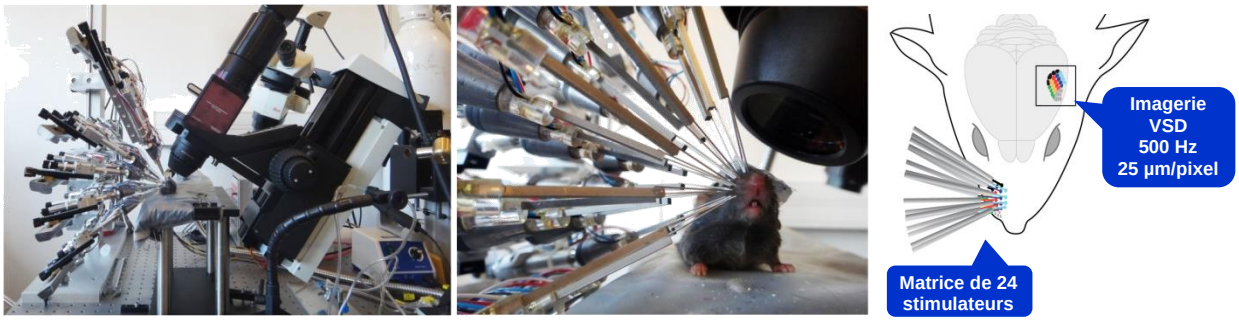

Figure 15. Poste expérimental combinant imagerie sensible au potentiel et matrice de stimulation multi-vibrissale.

La matrice de stimulation vibrissale "seconde génération", dotée de 24 stimulateurs piezoélectriques multidirectionnels a été adaptée pour une utilisation chez la souris. Elle est ici montée sous un système d'imagerie sensible au potentiel qui comporte un macroscope d'épifluorescence équipé de deux objectifs montés dos à dos, offrant une distance de travail compatible avec l'usage de la matrice.

4.2. Développement méthodologique : alignement semi-automatique des images fonctionnelles avec la carte des tonneaux

● *Travail réalisé avec **Lorraine Perronnet** stagiaire de Master 2 "Mathématiques et Informatique", spécialité "Mathématiques Appliquées", parcours "Mathématiques, Vision, Apprentissage" de l'ENS Cachan que j'ai co-encadrée avec Gabriel Peyré, alors chercheur au CEREMADE (CEntre de REcherche en MAthématiques de la Décision) CNRS-Université Paris-Dauphine UMR 7534.*

Perronnet L*, Vilarchao ME*, Hucher G, Shulz DE, Peyré G, **Ferezou I**. An automated workflow for the anatomo-functional mapping of the barrel cortex. ***J Neurosci Methods.*** 2016, 263:145-54.
** Ces auteurs ont contribué de manière égale au travail.*

L'alignement des signaux enregistrés par imagerie sensible au potentiel avec la carte cytoarchitecturale du réseau cortical sous-jacent est très précieux pour l'analyse des données obtenues par ce type d'approche, tout particulièrement lorsque l'on s'intéresse aux réponses induites par des stimulations multivibrissales complexes. A la fin des expériences d'imagerie, le cerveau de l'animal est fixé et un marquage histologique de la cytochrome oxydase est réalisé sur des coupes tangentielles afin de visualiser les tonneaux en couche 4 (**figure 16a**). L'expérimentateur doit ensuite procéder au réalignement des coupes histologiques pour reconstituer l'ensemble de la carte des tonneaux et la superposer avec celle formée par les vaisseaux sanguins superficiels qui sera utilisée pour aligner les données histologiques avec les données d'imagerie fonctionnelle (**figure 16b-e**).

Nous avons développé une procédure visant à automatiser le réalignement des coupes histologiques et la reconstitution de la carte des tonneaux afin d'optimiser ces étapes de l'analyse des expériences d'imagerie (tant d'un point de vue du temps qui leur est imparti, que de leur précision). Celle-ci repose sur un algorithme Matlab permettant d'effectuer le recalage rigide de coupes histologiques du cortex en tonneaux de la souris. Le recalage de deux coupes successives est obtenu par le calcul d'une transformation rigide permettant d'aligner deux ensembles de sections de vaisseaux sanguins détectés automatiquement. Ceci est réalisé grâce à l'utilisation d'une variante robuste de la méthode d'ICP (*iterative closest point*), qui vise à minimiser itérativement la distance entre deux nuages de points. Ensuite, la reconstruction de la carte des tonneaux consiste à fusionner les sections en une image unique obtenue par un mélange non-linéaire de gradients (**figure 16b**). L'outil final fournit une interface souple pour l'utilisateur avec peu de paramètres à régler (Perronnet et al., 2016).

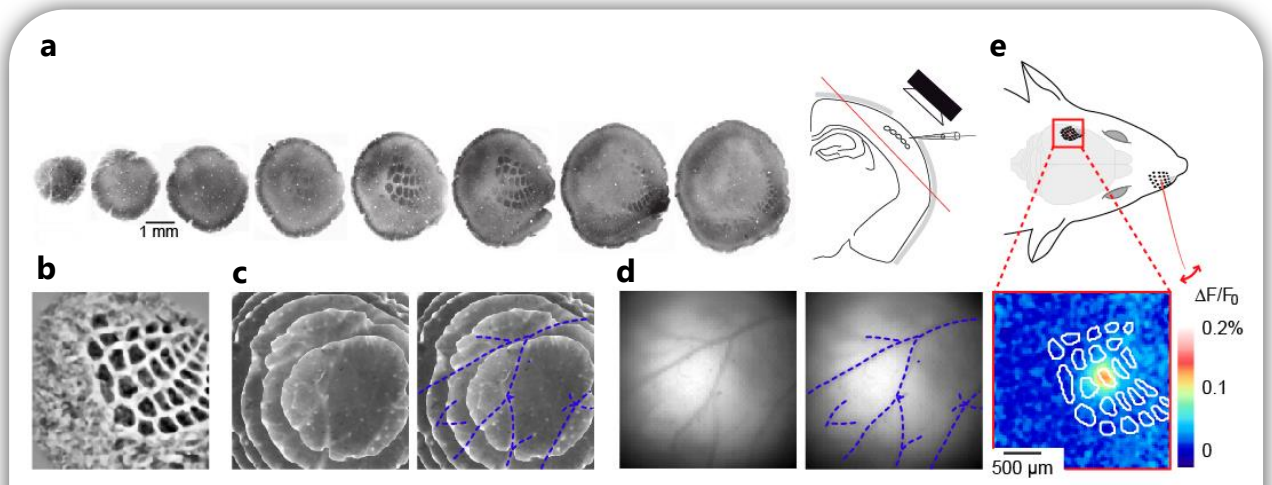

Figure 16. Procédure d'alignement des données fonctionnelles avec la reconstruction de la carte des tonneaux en couche 4.

a. Série de sections histologiques marquées à la cytochrome oxydase. Les vaisseaux sanguins de surface sont bien visibles sur la première section. Sur les autres sections, les vaisseaux plongeants apparaissent comme des taches circulaires ou ellipsoïdales blanches. Les tonneaux de la couche 4 sont apparents sur un certain nombre de sections, en fonction du plan exact de coupe (illustré en rouge sur le schéma à droite représentant une vue coronale du cortex S1.

b. Reconstruction de la carte des tonneaux en couche 4 après réalignement des sections histologiques.

c. Superposition des coupes histologiques réalignées permettant le tracé des vaisseaux de surface.

d. Vaisseaux de surface tels qu'ils apparaissent *in vivo* sur les images fluorescentes enregistrées pendant la session d'imagerie. Il est ainsi possible d'aligner la carte structurelle des tonneaux avec les images focntionnelles.

e. Image de l'activité corticale enregistrée 10 ms après la déflection de la vibrisse C2 par imagerie VSD sous anesthésie. Les tonneaux sont indiqués par les lignes blanches.

4.3. Etude de la sélectivité à la direction d'un mouvement global au sein du cortex en tonneaux chez la souris

● *Travail réalisé avec **María Eugenia Vilarchao,** doctorante que j'ai co-encadrée avec Daniel Shulz (Ecole Doctorale « Frontières du Vivant » - Paris Descartes Paris Diderot PhD Program in Life Sciences).*

Vilarchao ME, Estebanez L, Shulz DE, **Férézou I**. Supra-barrel Distribution of Directional Tuning for Global Motion in the Mouse Somatosensory Cortex. ***Cell Rep.*** 2018 Mar 27;22(13):3534-3547.

Tirant parti de la possibilité de stimuler les 24 vibrisses principales tout en enregistrant les dynamiques corticales au niveau de la représentation corticale de l'ensemble de ces vibrisses, nous avons décidé d'étudier les réponses corticales induites par des séquences structurées de stimulations multivibrissales. En stimulant les vibrisses (de manière localement invariante) selon des séquences spatiotemporelles qui génèrent un mouvement apparent global dans huit directions (**figure 17a**), nous avons voulu vérifier s'il existe une organisation spatiale de la sélectivité à la direction d'un mouvement global au niveau de S1.

En réponse à un mouvement global rostral, nous avons observé une activation corticale (initiée au niveau des colonnes correspondant aux premières vibrisses stimulées) qui s'étendait rapidement pour couvrir l'ensemble du cortex en tonneaux (**figure 17b**). Les colonnes corticales successives étaient ainsi activées avant même que leurs vibrisses correspondantes ne soient stimulées.

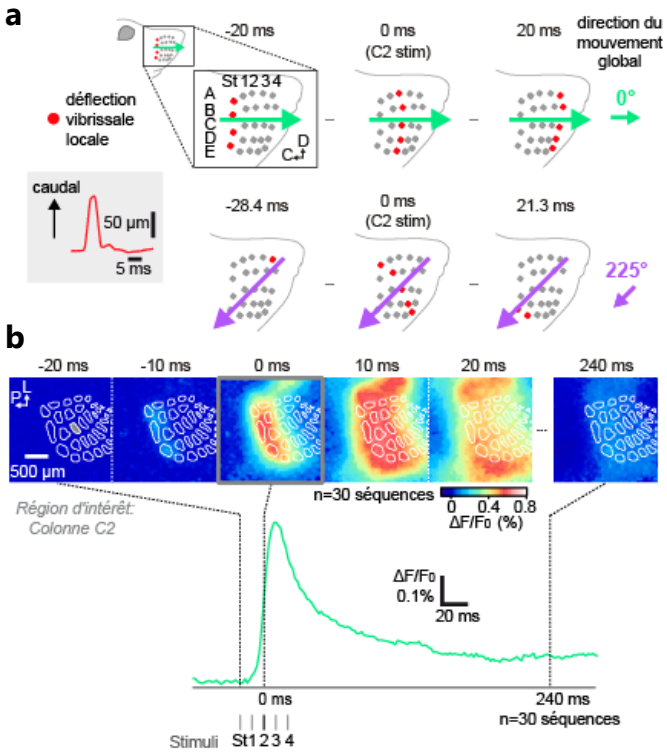

Figure 17. Imagerie des réponses corticales évoquées par des stimulations multivibrissales.

a. Protocole de mouvement global. Les rangées de vibrisses sont nommées avec des lettres, les arcs avec les nombres, sauf l'arc le plus caudal qui correspond aux quatre "straddlers" (St). Trois étapes correspondant à deux directions du protocole de mouvement global (0 ° et 225 °) sont illustrées à titre d'exemples. Les points rouges indiquent les vibrisses qui sont défléchies au moment indiqué au-dessus. L'encart gris montre la déflection locale des vibrisses mesurée à l'aide d'un télémètre laser à la pointe d'un stimulateur.

b. Images du signal de fluorescence moyen (n = 30 séquences) pour un cas représentatif à six instants différents par rapport à la déflection de la vibrisse centrale C2 pour la direction globale rostrale (0 °). La carte des tonneaux en couche 4, reconstruite à partir d'une révélation histologique de la cytochrome oxydase et superposée aux signaux de fluorescence (voir figure 16), est représentée sous forme de contours blancs. Le profil de fluorescence mesuré à partir de la région correspondant au tonneau C2 (indiquée en gris sur la première image) est illustré plus bas. Les lignes en pointillés indiquent les temps de stimulation du premier arc de vibrisses (-20 ms), de l'arc C (0 ms, l'image correspondante est entourée en gris), et des dizaines de millisecondes après la stimulation (+240 ms), correspondant à la dernière image.

Ainsi au temps 0 correspondant au début de la stimulation de la vibrisse centrale C2, un niveau important d'activité était déjà présent au niveau de la colonne C2.

La propagation latérale de l'activité dans le cortex est donc plus rapide que la stimulation vibrissale en périphérie, ce qui suggère que les réponses corticales à la déflexion de la vibrisse C2 sont conditionnées par cette propagation latérale.

Ce type de séquence d'activation corticale a été observé pour les 8 directions de mouvement global (**figure 18a**). Une quantification du signal mesuré au niveau de la colonne centrale C2 a cependant révélé que bien que la déflection de la vibrisse C2 soit identique pour toutes les stimulations globales, cette colonne répond préférentiellement pour les mouvements globaux caudaux (**figure 18b**, voir Jacob et al., (2008) pour une observation similaire chez le rat). En calculant ainsi la direction globale préférée de chaque colonne, nous avons pu montrer que la sélectivité à la direction globale est spatialement organisée dans le cortex en tonneaux à l'échelle supra-colonnaire (**Figure 19**, Vilarchao et al., 2018).

Les colonnes correspondant aux vibrisses rostrales sont en effet plus sélectives à la direction globale que les colonnes associées aux vibrisses caudales. En outre, les colonnes correspondant aux vibrisses dorsales répondent préférentiellement aux directions globales ventrales, tandis que les colonnes associées aux vibrisses ventrales répondent préférentiellement aux directions globales caudales (**Figure 19 a-b**). Enfin, les réponses induites par des directions globales caudo-ventrales sont en moyenne les plus fortes pour toutes les colonnes.

Des enregistrements électrophysiologiques ciblés sur les colonnes alpha, C2 et C4 nous ont permis de renforcer ces observations : non seulement en montrant que les neurones du cortex en tonneaux

de la souris présentent une sélectivité directionnelle pour le mouvement global au niveau de leur activité de décharge de potentiels d'actions (comme observé auparavant chez le rat, Jacob et al., 2008), mais aussi en confirmant, à ce niveau de lecture de l'activité neuronale supraliminaire, l'organisation spatiale de cette sélectivité à la direction globale.

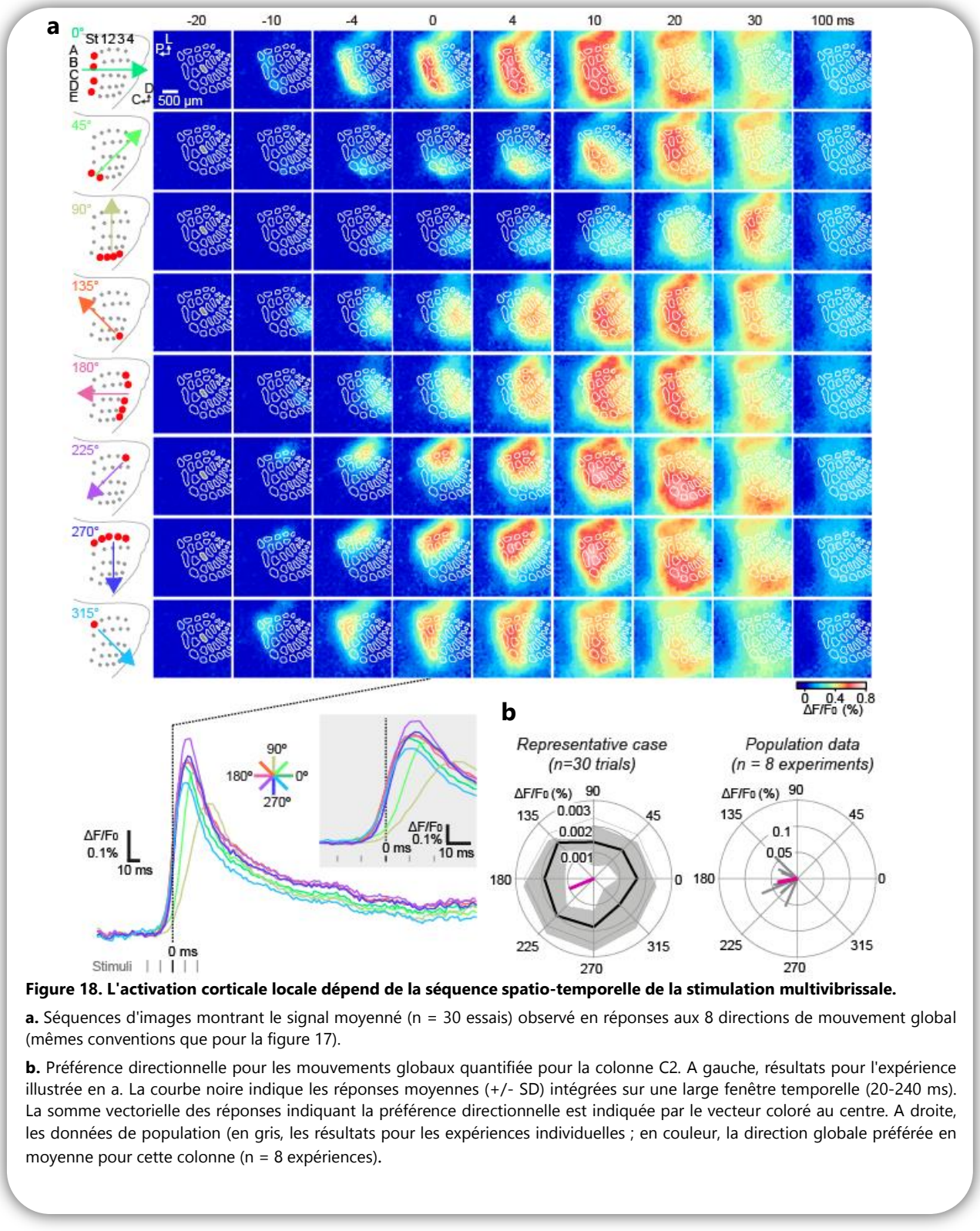

Figure 18. L'activation corticale locale dépend de la séquence spatio-temporelle de la stimulation multivibrissale.

a. Séquences d'images montrant le signal moyenné (n = 30 essais) observé en réponses aux 8 directions de mouvement global (mêmes conventions que pour la figure 17).

b. Préférence directionnelle pour les mouvements globaux quantifiée pour la colonne C2. A gauche, résultats pour l'expérience illustrée en a. La courbe noire indique les réponses moyennes (+/- SD) intégrées sur une large fenêtre temporelle (20-240 ms). La somme vectorielle des réponses indiquant la préférence directionnelle est indiquée par le vecteur coloré au centre. A droite, les données de population (en gris, les résultats pour les expériences individuelles ; en couleur, la direction globale préférée en moyenne pour cette colonne (n = 8 expériences).

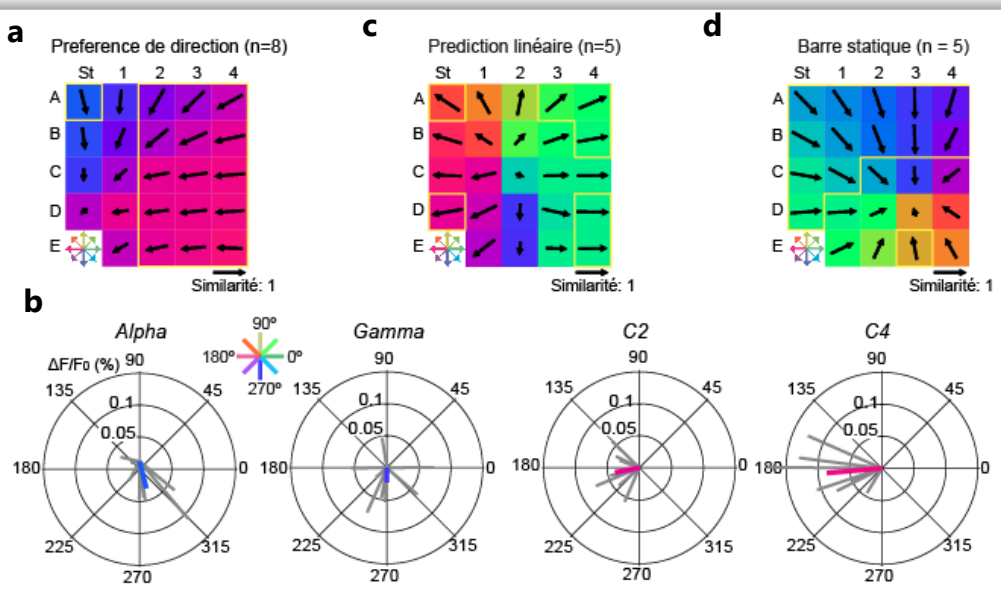

Figure 19. Distributions spatiales des préférences directionnelles au sein du cortex en tonneaux.

a. Matrice des préférences directionnelles aux mouvements globaux (n = 8 expériences). Pour chaque colonne corticale, la direction préférée (Dpref) est illustrée par sa couleur et la direction de la flèche qu'elle contient. La longueur des flèches représente l'index de similarité (une similarité de 0 indique des Dpref différents entre les expériences alors qu'une similarité de 1 indique des Dprefs identiques). L'anisotropie de la distribution des Dpref a été évaluée avec un test de Rayleigh. Les colonnes montrant une distribution significativement anisotropique sont indiquées par un encadrement jaune. Ces conventions sont valables pour toute la figure.

b. Distribution des vecteurs de direction globale pour chaque expérience (en gris) présentée pour les colonnes correspondant aux vibrisses alpha (StA), gamma (StC), C2 et C4. Les vecteurs de couleur indiquent la somme vectorielle pour les 8 expériences.

c. Matrice de préférence directionnelle obtenue à partir des prédictions linéaires (n = 5 expériences).

d. Matrice de préférence directionnelle obtenue à partir des "barres statiques" (n = 5 expériences).

Nous avons tout d'abord émis l'hypothèse que la sélectivité à la direction globale et son organisation spatiale pourraient être déterminées par les mécanismes de suppression bien décrits lors de stimulations séquentielles de vibrisses adjacentes (Brumberg et al., 1996; Ego-Stengel et al., 2005; Higley and Contreras, 2003; Kleinfeld and Delaney, 1996; Shimegi et al., 1999, 2000; Simons, 1985; Simons and Carvell, 1989)

Afin de tester cette hypothèse, nous avons utilisé un autre protocole dans lequel nous avons alterné les mêmes stimulations globales dans quatre directions cardinales, avec des déflections de vibrisses de rangées ou d'arcs individuels, aussi appelées "barres statiques". Par sommation linéaire séquentielle des réponses aux "barres statiques", nous avons construit des prédictions linéaires des réponses aux mouvements globaux et ainsi observé que les réponses aux stimulations globales de l'ensemble des vibrisses sont en effet fortement sous-linéaires, mais indépendamment de la direction de la stimulation.

Nous avons calculé la carte de sélectivité directionnelle à partir des prédictions linéaires (**Figure 19c**). Cette carte est qualitativement différente de celle obtenue avec les stimulations globales (**Figure 19a**) : seules quelques colonnes - situées principalement en périphérie - ont une direction préférée significative (test de Rayleigh, p <0,05, contour jaune), pointant vers l'extérieur. Étant donné que les prédictions linéaires sont obtenues en ajoutant successivement les réponses aux barres statiques, il n'est pas surprenant d'observer une réponse plus importante pour les directions ayant débuté du

côté opposé. En outre, lors de cette série d'expériences, nous avons observé que les réponses corticales induites par des stimuli globaux semblaient similaires à celles évoquées par des "barres statiques" correspondant au point de départ de la stimulation globale. Afin d'évaluer si la sélectivité directionnelle globale pourrait être expliquée par la saillance de cette position de départ, nous avons calculé une carte direction de sélectivité en utilisant les réponses aux "barres statiques" : Arc St, Arc 4, Rangée A, et en rangée E (**Figure 19d**). Cette carte montre une distribution des directions préférées en "pinwheel", dont le centre se situe à proximité de la colonne D3.

Cette carte de sélectivité diffère qualitativement de celle obtenue avec les stimuli globaux (**Figure 19a**). Toutefois, les colonnes correspondant aux vibrisses plus rostrales et dorsales ont des directions préférées similaires dans les deux conditions. Ces résultats suggèrent que la saillance de la position de départ du stimulus global pourrait participer à l'émergence de la distribution spatiale de la sélectivité à la direction globale, en plus de mécanismes dépendants du déplacement de la barre.

En conclusion, nous avons montré ici que le cortex en tonneaux de la souris est capable d'extraire la direction globale d'un stimulus multivibrissal. Cette forme de sélectivité directionnelle émerge à partir d'interactions non linéaires et se répartit spatialement, de manière supra-colonnaire, sur l'ensemble de la représentation des vibrisses dans S1. La manière dont cette organisation spatiale participe à faire émerger un percept global à partir de séquences de stimulations multivibrissales complexes reste à éclaircir. Cette topographie pourrait être avantageuse pour la transmission d'informations vers des aires corticales de plus haut niveau (Thivierge et Marcus, 2007). Elle pourrait ainsi être exploitée lors de la discrimination certaines caractéristiques d'une scène tactile, telles que l'orientation des mouvements d'un objet (Polley et al., 2005) ou encore le mouvement de l'animal lui-même au sein de son environnement. Des aires de plus haut niveau telles que le cortex somatosensoriel secondaire, qui semble pouvoir intégrer des informations sensorielles tactiles à plus grande échelle spatiale et temporelle (Goldin, Harrell, et al., 2018), pourraient jouer un rôle clef dans cette lecture fonctionnelle. De nouvelles études mettant l'accent sur l'intégration des entrées multivibrissales dans cette aire corticale sont nécessaires pour approfondir la compréhension du traitement cortical de scènes tactiles complexes.

5. Travaux collaboratifs

En parallèle des travaux présentés ci-dessus, j'ai effectué plusieurs études dans le cadre de collaborations. En effet, le fait d'être la seule à développer ce type d'imagerie fonctionnelle permettant de suivre les dynamiques corticales à l'échelle mésoscopique chez la souris en Ile de France, a très vite été suivi de nombreuses sollicitations de collaborations, parmi lesquelles j'ai privilégié celles qui restaient centrées sur mes préoccupations premières, à savoir l'étude fonctionnelle du cortex cérébral basée sur le modèle du système vibrissal chez la souris.

Je vais me contenter ici de résumer très brièvement ces différentes études car, pour la plupart d'entre elles, je n'étais pas initialement porteuse du projet. Je tiens cependant à les mentionner car les interactions scientifiques et humaines qu'elles ont générées ont enrichi mon parcours scientifique.

On notera que le projet effectué en collaboration avec le Dr. Sophie Pezet (*cf. paragraphe 5.4*) s'est déroulé alors que nous faisions partie de la même équipe scientifique (au sein du laboratoire de Neurobiologie de l'ESPCI PartisTech), ce qui explique une interaction plus forte : nous avons mené

ensemble ce projet, co-encadré un étudiant de Master 2, et co-signé en dernier auteur l'article rapportant les résultats obtenus.

5.1. Impact de la transmission synaptique thalamocorticale sur le développement du cortex somatosensoriel

Collaboration avec Nicolas Narboux Nème & Patricia Gaspar (équipe Neuroplasticité et Développement dirigée par Patricia Gaspar - Institut du Fer à Moulin - INSERM UPMC UMR-S 839)

> Narboux-Nême N, Evrard A, **Ferezou I**, Erzurumlu RS, Kaeser PS, Lainé J, Rossier J, Ropert N, Südhof TC, Gaspar P. Neurotransmitter release at the thalamocortical synapse instructs barrel formation but not axon patterning in the somatosensory cortex. ***J Neurosci.*** 2012, 32(18):6183-96.

L'utilisation de l'imagerie sensible au potentiel m'a permis de caractériser l'altération des réponses corticales induites par des stimulations sensorielles tactiles à l'âge adulte, chez des souris transgéniques pour lesquelles la transmission synaptique thalamocorticale est déficiente (Narboux-Nême et al., 2012).

5.2. Etude des mécanismes impliqués dans l'hyperexcitabilité sensorielle associée au Syndrome du X Fragile, basée sur l'utilisation d'un modèle de souris transgéniques (Fmr1 knockout)

Collaboration avec Melanie Ginger & Andreas Frick (équipe AVENIR: Circuit and dendritic mechanisms underlying cortical plasticity dirigée par Andreas Frick - Neurocentre Magendie INSERM U 862 Université Bordeaux 2).

> Zhang Y, Bonnan A, Bony G, **Ferezou I**, Pietropaolo S, Ginger M, Sans N, Rossier J, Oostra B, LeMasson G, Frick A. Dendritic channelopathies contribute to neocortical and sensory hyperexcitability in Fmr1(-/y) mice. ***Nat Neurosci.*** 2014, 17(12):1701-9.

Ma contribution à ce travail a consisté à comparer les réponses corticales induites par des stimulations tactiles entre ces souris mutantes et des souris contrôles. Les résultats ont mis en évidence, chez les souris Fmr1 Knockout, une propagation plus rapide de l'activation corticale dans la direction medio-latérale que chez leurs contrôles (Zhang et al., 2014).

5.3. Développement d'une méthode de détection optique pour l'imagerie hémodynamique cérébrale

Collaboration avec Michaël Atlan (Institut Langevin CNRS UMR 7587, ESPCI ParisTech).

> Magnain C, Castel A, Boucneau T, Simonutti M, **Ferezou I**, Rancillac A, Vitalis T, Sahel JA, Paques M, Atlan M. Holographic laser Doppler imaging of microvascular blood flow. ***J Opt Soc Am A Opt Image Sci Vis***. 2014, 31(12):2723-35.

Dans le cadre d'un travail de développement d'une méthode de détection optique pour l'imagerie hémodynamique cérébrale, nos expériences étaient basées sur l'utilisation d'un laser Doppler sur caméra CCD utilisant une détection holographique qui permet d'imager la perfusion sanguine de surface au niveau du cortex somatosensoriel chez la souris. Ma contribution à ce travail a été principalement de fournir une préparation biologique adaptée à la validation de cette approche holographique (Magnain et al., 2014).

5.4. Etude de la plasticité moléculaire et fonctionnelle dans un modèle de douleur neuropathique orofaciale

Collaboration avec Sophie Pezet qui dirige actuellement l'équipe Douleur et Adaptation Neurale au Laboratoire Plasticité du Cerveau de l'ESPCI ParisTech CNRS UMR 8249.

- *Travail réalisé avec **Sébastien Rivière**, stagiaire de Master 2, Biologie Intégrative et Physiologie, Spécialité Neurosciences de l'UPMC que j'ai co-encadré avec Sophie Pezet.*

Thibault K, Rivière S, Lenkei Z, **Férézou I***, Pezet S*. Orofacial Neuropathic Pain Leads to a Hyporesponsive Barrel Cortex with Enhanced Structural Synaptic Plasticity. ***PLoS One.*** 2016, 11(8):e0160786.
** Ces auteurs ont contribué de manière égale au travail.*

Cette étude se focalisait sur la plasticité corticale liée à la douleur chronique orofaciale, induite par une ligature du nerf infra-orbitaire chez la souris. Après validation du protocole expérimental par vérification de la mise en place de l'hypersensibilité mécanique au niveau de la zone orofaciale, la plasticité du cortex somatosensoriel en tonneaux a été étudiée par imagerie intrinsèque, une méthode de détection de l'activité corticale basée sur les changements hémodynamiques. Nous avons ainsi observé une diminution de l'aire corticale activée ainsi que de l'intensité maximale de la réponse après stimulation d'une vibrisse chez les animaux ligaturés. Cette diminution apparente des signaux évoqués pourrait résulter d'une hausse de l'activité spontanée des neurones du cortex en tonneaux, modifiant les propriétés intégratives du réseau. L'augmentation de l'expression de marqueurs liés à l'activité cellulaire et à la plasticité synaptique dans cette aire corticale est en faveur de cette hypothèse et confirment l'existence d'une plasticité corticale liée à la douleur chronique orofaciale dans le cortex somatosensoriel en tonneaux, mais aussi au niveau des cortex moteur et cingulaire (Thibault et al., 2016).

5.5. Impact de l'absence ou de l'activation prénatale de la microglie sur la mise en place du réseau cortical et son fonctionnement

Collaboration avec Morgane Thion & Sonia Garel (équipe Développement et Plasticité du Cerveau dirigée par Sonia Garel, IBENS ENS-CNRS UMR8197, Inserm U1024), et avec Coralie-Anne Mosser & Etienne Audinat (équipe Interactions Neurone-Glie dirigée par Etienne Audinat, Institut de Génomique Fonctionnelle, Montpellier).

Les infections prénatales sont des facteurs de risque pour la schizophrénie et l'autisme et il semblerait que ce soit la réaction immunitaire maternelle qui pourrait être à l'origine de ces pathologies neuropsychiatriques (Estes and McAllister, 2016). Or il a été montré que la microglie, macrophage du tissu cérébral, joue un rôle déterminant dans la mise en place de la circuiterie corticale au cours du développement, notamment dans le positionnement de certains types d'interneurones GABAergiques (Squarzoni et al., 2014, 2015). Nous avons ici cherché à établir les conséquences fonctionnelles de l'absence ou de l'activation prénatale de la microglie sur l'excitabilité du réseau cortical. Ma contribution à ce projet a consisté à étudier les dynamiques corticales évoquées par des stimuli tactiles dans des modèles murins de déplétion ou d'activation microgliale. J'ai observé, chez des jeunes souris âgées de 3 semaines, un ralentissement de la propagation latérale des réponses corticales, reflétant les aberrations de connectivité observées *in vitro* dans ces mêmes modèles (article en préparation).

2ème partie : Projets Scientifiques

1. Rôle fonctionnel du cortex somatosensoriel secondaire (S2) dans le traitement des informations sensorielles tactiles

● *Travail amorcé lors du stage de Master 2 d'Ingénierie Biomédicale, spécialité Bioingénierie et Innovation en Neurosciences (Université Paris Descartes et ESPCI ParisTech) de* ***Sophie Hubatz*** *que j'ai encadré.*

Comme nous l'avons vu jusqu'ici, le cortex en tonneaux des rongeurs est devenu un modèle d'étude incontournable du traitement cortical de l'information sensorielle, du fait de son organisation cellulaire remarquable. Cependant, lors d'une stimulation sensorielle tactile, l'information est transmise au cortex en tonneaux, mais aussi, presque simultanément, au cortex somatosensoriel secondaire S2 (Kwegyir-Afful and Keller, 2004; Le Merre et al., 2018). Or, les connaissances concernant cette aire corticale et son implication dans l'intégration des informations sensorielles tactiles sont encore très limitées.

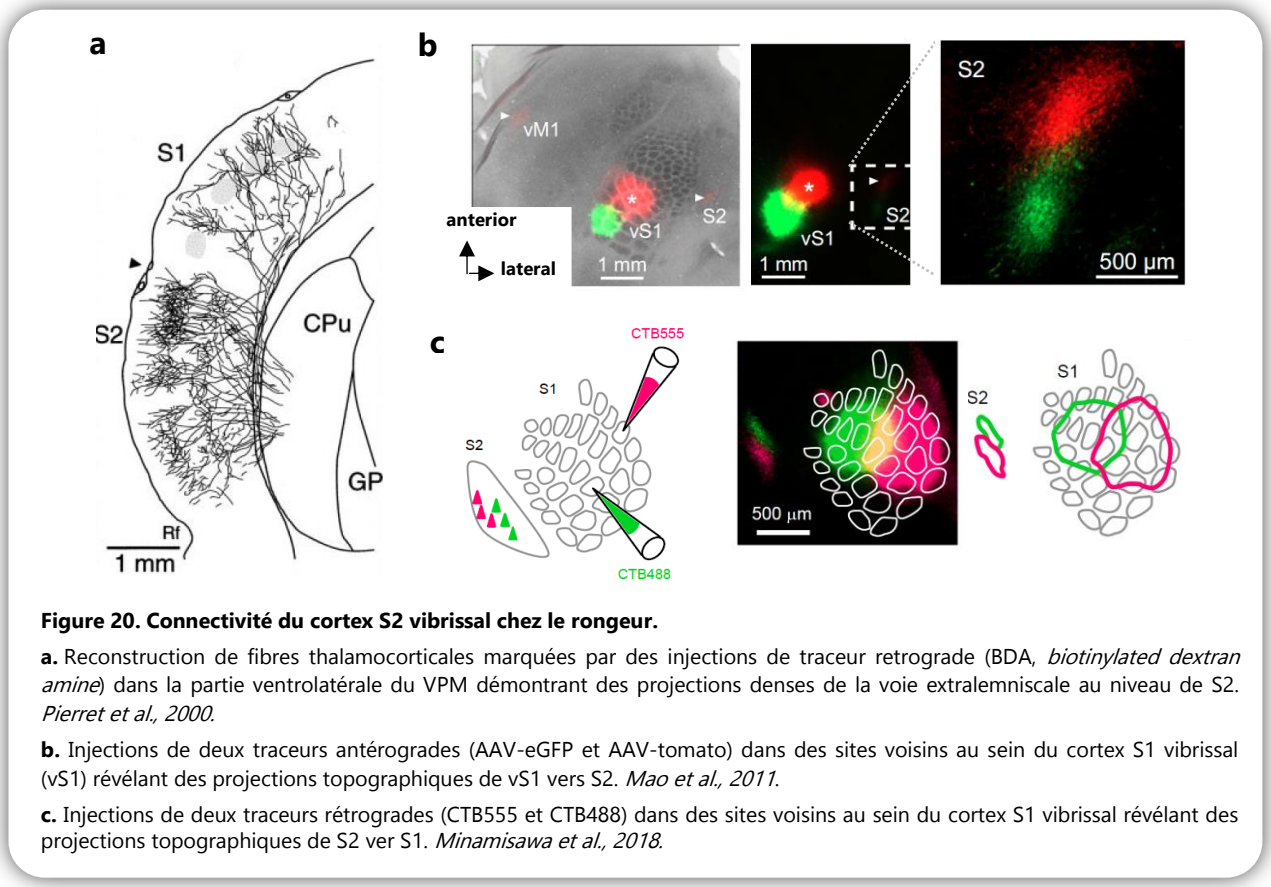

Figure 20. Connectivité du cortex S2 vibrissal chez le rongeur.

a. Reconstruction de fibres thalamocorticales marquées par des injections de traceur retrograde (BDA, *biotinylated dextran amine*) dans la partie ventrolatérale du VPM démontrant des projections denses de la voie extralemniscale au niveau de S2. *Pierret et al., 2000.*

b. Injections de deux traceurs antérogrades (AAV-eGFP et AAV-tomato) dans des sites voisins au sein du cortex S1 vibrissal (vS1) révélant des projections topographiques de vS1 vers S2. *Mao et al., 2011.*

c. Injections de deux traceurs rétrogrades (CTB555 et CTB488) dans des sites voisins au sein du cortex S1 vibrissal révélant des projections topographiques de S2 ver S1. *Minamisawa et al., 2018.*

La rapide activation des neurones de S2 lors de stimulations sensorielles est probablement due au fait qu'ils reçoivent des afférentes provenant directement du noyau VPM du thalamus (**figure 20a**, Pierret et al., 2000, Carvell and Simons, 1987). Le cortex S2 est en outre connecté avec S1 de manière

réciproque et topographique (**figure 20 b,c**, Chakrabarti and Alloway, 2006; Aronoff et al., 2010; Hoffer et al., 2003; Mao et al., 2011; Minamisawa et al., 2018). Les enregistrements électrophysiologiques réalisés dans S2 chez la souris et le rat montrent des champs récepteurs généralement plus larges que dans S1, avec une absence de champs récepteurs monovibrissaux tels qu'ils peuvent être observés dans S1 (Carvell and Simons, 1986; Kwegyir-Afful & Keller, 2004). La question de la topographie de la représentation des vibrisses dans S2 a été explorée sur le plan fonctionnel essentiellement chez le rat à l'aide d'électrodes de surface (**figure 21**, Benison et al., 2007).

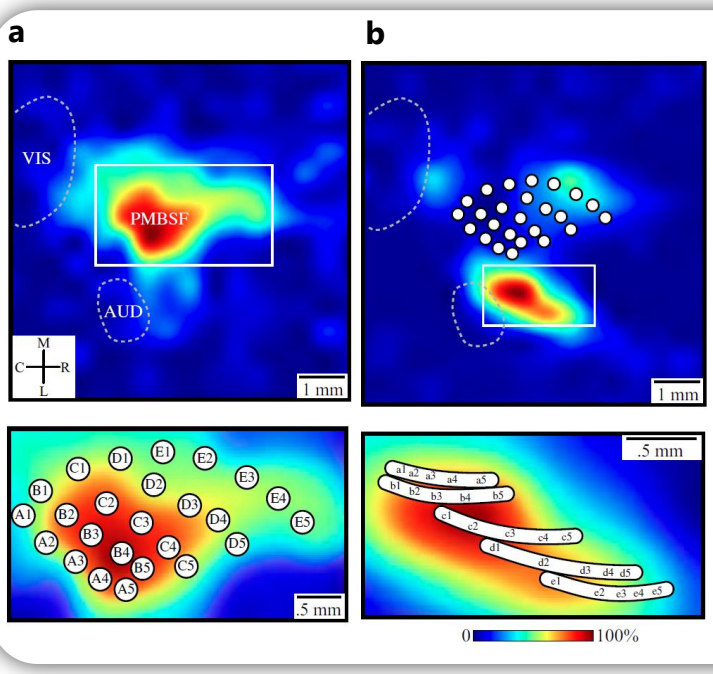

Figure 21. Représentations des vibrisses dans les cortex S1 et S2 chez le rat.

a. Les potentiels évoqués de surface ont été enregistrés chez 6 animaux en réponse aux déflections individuelles de 25 vibrisses. Les cartes d'activité corticale évoquée pour chaque vibrisse ont été normalisées et moyennées pour produire une carte moyenne qui reflète la localisation générale de la représentation des vibrisses (aussi appelée posteromedial barrel subfield PMBSF) par rapport aux aires visuelles (VIS) et auditives (AUD) primaires dans S1 (en haut). Les localisations moyennes des réponses de chaque vibrisse sont représentées au dessous, sur une vue élargie de S1.

b. Carte moyenne de la représentation des vibrisses dans S2 générée de la même manière, à partir des potentiels évoqués de surface qui présentent un pic un peu plus tardif que dans S1. La localisation des réponses individuelles est représentée au-dessous, sur une vue élargie de S2.

Benison et al., 2007.

Cette étude rapporte une organisation topographique de la représentation des vibrisses dans S2 qui semble moins bien définie que dans S1 : il n'est pas toujours possible de distinguer les représentations de deux vibrisses adjacentes. Cependant, la représentation des vibrisses étant moins étendue dans S2 que dans S1, les auteurs se sont sans doute confrontés ici aux limites de la résolution spatiale de la méthode d'enregistrement utilisée. L'ensemble de ces données suggère en tous cas que S2 pourrait traiter les informations sensorielles tactiles de manière parallèle et complémentaire à S1. L'étude de Kwegyir-Afful et al (2004) visant à caractériser les propriétés fonctionnelles de S2 chez le rat, en utilisant des enregistrements extracellulaires, a montré que les neurones de S2 répondaient aux stimuli indépendamment de la couche corticale à laquelle ils appartiennent, ce qui suggère que ses réponses sont principalement dues à des entrées thalamiques plutôt qu'à des connexions cortico-corticales de S1.

Dans ce projet, je souhaite mettre à profit l'excellente résolution spatio-temporelle de l'imagerie sensible au potentiel pour approfondir les connaissances sur le rôle fonctionnel de S2. Etant donné la faible quantité de données dont on dispose sur cette aire corticale, je souhaite débuter par une étude comparative simple visant à enregistrer simultanément les dynamiques neuronales au niveau de S1 et S2 chez la souris anesthésiée. Ainsi il me sera possible d'étudier l'organisation spatiale de la représentation des vibrisses dans S2 (voir données préliminaires présentées **figure 22**), mais aussi de comparer les latences et amplitudes des réponses aux stimulations vibrissales.

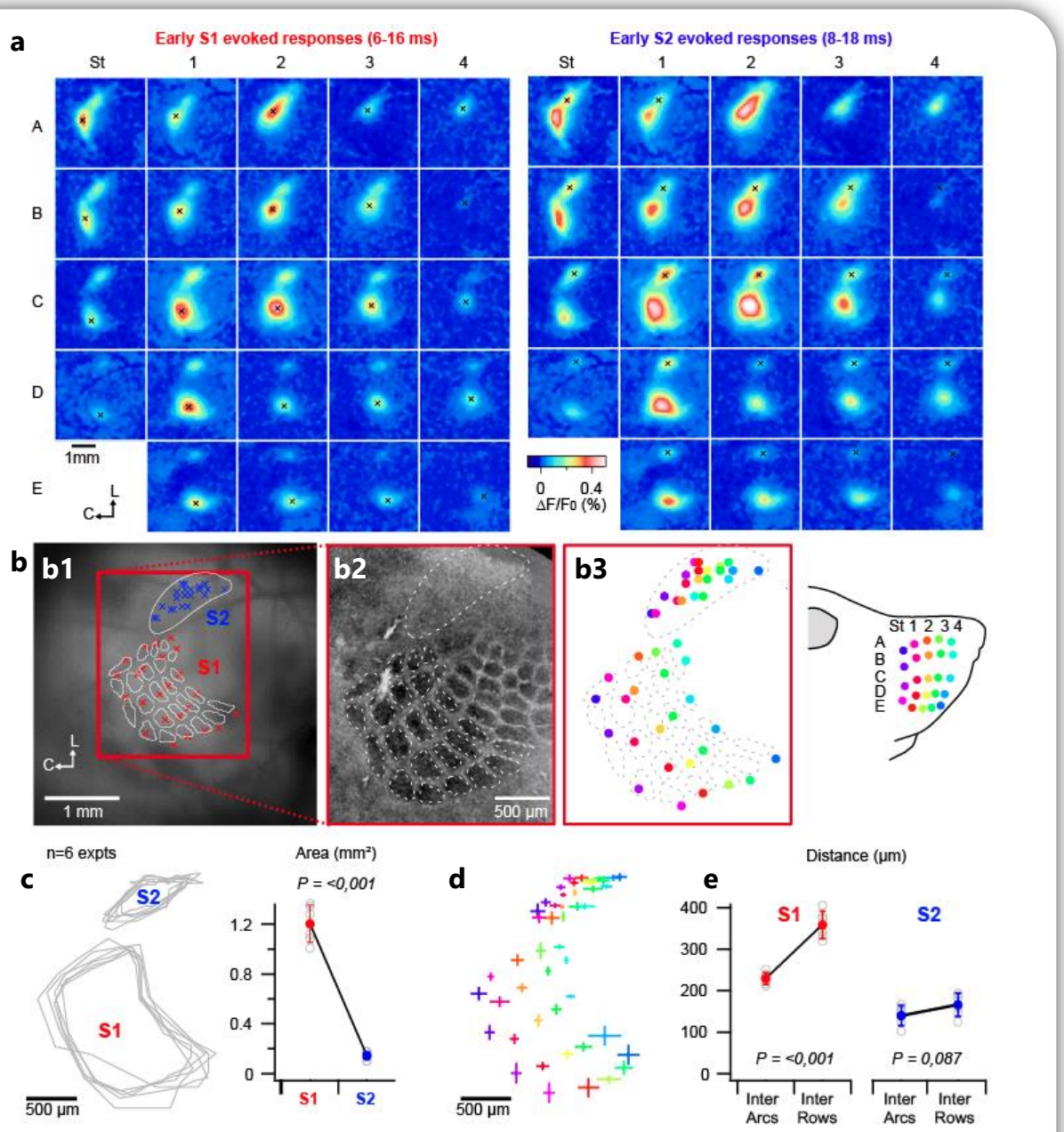

Figure 22. Topographie de la représentation des vibrisses dans le cortex S2 de la souris.

a. Images de l'activation corticale évoquée par la stimulation de 24 vibrisses individuelles, obtenues en moyennant les signaux de fluorescence du colorant sensible au potentiel (RH1691) entre 6 et 16 ms après le début de la stimulation (à gauche) et entre 8 et 18 ms après le début de la stimulation (à droite) utilisées pour localiser la représentation de chaque vibrisse au sein de S1 et S2 (recherche de maxima locaux), respectivement (n = 10 acquisitions par vibrisse).

b1. Image du cortex tel qu'observé avec la caméra d'imagerie fonctionnelle sur laquelle sont indiquées les localisations déterminées en **a**, et les contours des colonnes corticales obtenus après reconstruction de la carte des tonneaux par marquage histologique à la cytochrome oxidase (**b2**). Les mêmes données sont représentées en **b3** avec un code couleur identifiant chaque vibrisse (voir légende sur la droite).

c. Les aires respectives de S1 et S2 ont été calculées pour chaque souris en reliant les représentations des vibrisses situées en périphérie (arcs Str et 4, rangées A et E).

d. Cartes moyennes de S1 et S2 obtenues à partir de 6 expériences réalignées sur les centroïdes de S1 et S2, respectivement (moyennes +/- SD).

e. Si dans S1 les rangées sont plus éloignées que les arcs, ce n'est pas le cas dans S2 où la carte est globalement plus compacte.

Je pourrais enfin vérifier si S2 présente les mêmes propriétés de sélectivité à la direction de stimulation vibrissale que S1, qu'il s'agisse de la direction de déflections des vibrisses individuelles ou de la direction d'un mouvement global impliquant la stimulation de l'ensemble des vibrisses.

Ces données permettront de mieux connaître les propriétés de base de cette aire dite "secondaire" de traitement de l'information tactile, avant d'aller plus loin dans sa caractérisation fonctionnelle au travers d'expériences réalisées chez l'animal vigile, au cours d'une tâche de conditonnement opérant.

2. Etude de l'intégration corticale de stimulations sensorielles tactiles complexes chez la souris en comportement

Projet porté par un financement du DIM NanoK (Neurofib, partenaires : Georges Debregeas, Genevieve Bourg Heckly, Laboratoire Jean Perrin, UMR 8237 – CNRS Sorbonne Université, Cathie Ventalon, IBENS ENS-CNRS UMR8197, Inserm U1024, et moi-même, coordination : Cathie Ventalon), et par l'Initiative de Recherche Stratégique de l'Université Paris Saclay Brainscopes.

- *Projet qui fera l'objet du doctorat de **Timothé Jost-Mousseau** que je vais co-encadrer à partir d'octobre 2018 (Ecole Doctorale Cerveau Cognition Comportement, Sorbonne Université) avec Daniel Shulz.*

Les travaux réalisés dans l'équipe ont démontré, chez l'animal anesthésié, que le cortex en tonneaux des rongeurs est capable d'intégrer les informations multi-vibrissales afin d'extraire les propriétés globales des objets rencontrés. La majorité des neurones de cette aire corticale est en effet sensible à la direction globale d'une stimulation tactile générée par la déflection séquentielle de l'ensemble des vibrisses (Jacob et al., 2008; Vilarchao et al., 2018).

Pour comprendre l'implication de ces mécanismes d'intégration et leur importance perceptive et comportementale, il est essentiel de les étudier chez l'animal éveillé. Nous proposons ici de : 1) lier l'enregistrement des dynamiques corticales avec le comportement de l'animal dans un paradigme expérimental impliquant l'extraction des propriétés globales d'un objet par l'animal; 2) établir des liens causaux entre certaines propriétés de ces dynamiques corticales et la réponse comportementale de l'animal.

De nos jours, les neurophysiologistes abordent généralement ce type de problématique en travaillant avec des souris éveillées dites « tête fixée », c'est-à-dire qui ont été habituées à être maintenues par la tête (à l'aide d'implants fixés au crâne). Il est en effet possible, dans cette configuration, d'entrainer les animaux à effectuer des tâches comportementales simples (Guo et al., 2014). Ces expériences restent cependant fortement contraignantes et limitent le répertoire comportemental qui peut être ainsi étudié.

Nous avons pour objectif de travailler au contraire chez des animaux libres de leurs mouvements en développant un protocole de conditionnement opérant, impliquant l'utilisation des vibrisses par l'animal au sein d'un labyrinthe. Nous nous inspirerons pour ce faire d'un protocole récemment mis au point chez le rat dans l'équipe, par Pauline Kerekes et Valérie Ego-Stengel, qui a permis de démontrer que ces animaux peuvent réaliser une tâche de discrimination tactile sans bouger rythmiquement leurs vibrisses (Kerekes et al., 2017). Nous utiliserons des techniques d'imagerie fonctionnelle fibrée à champ large pour observer à l'échelle mésoscopique, au niveau de S1 (ou de S2 par la suite), les dynamiques évoquées lors de la récolte d'informations tactiles (Ferezou et al., 2006). Dans un second temps, le couplage d'une matrice de micro-miroirs au faisceau de fibres permettra

de perturber ces dynamiques corticales par photo-inhibition ciblée (Abbasi et al., 2018; Ronzitti et al., 2017) au cours de la tâche. Nous tenterons ainsi d'établir des liens de causalité entre les dynamiques observées en imagerie et les capacités de discrimination des objets présentés.

2.1. Tâche comportementale

Afin d'étudier les dynamiques corticales lors de la discrimination motivée des propriétés d'orientation d'un objet par les souris, nous utiliserons un labyrinthe circulaire à allée centrale automatisé par un microcontrôleur inspiré du labyrinthe développé pour les rats (Kerekes et al., 2017). Ce labyrinthe (**figure 23**), déjà partiellement fonctionnel au sein du laboratoire (*prototype développé en collaboration avec l'équipe de Brice Bathellier*), présentera de part et d'autre de l'allée centrale un objet constitué de barres régulièrement espacées.

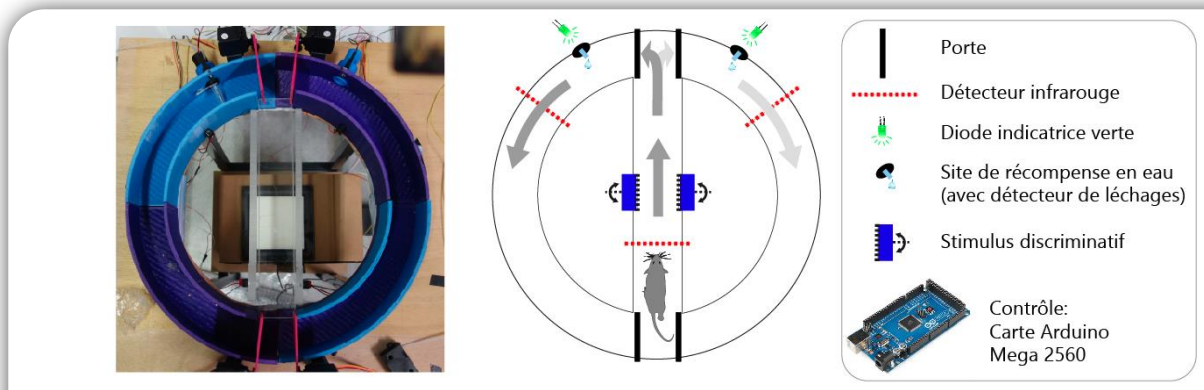

Figure 23. Labyrinthe de comportement.

A chaque essai la souris doit courir dans l'allée centrale, passer deux stimuli tactiles composés de séries de barres d'orientation distinctes disposées de manière aléatoire. A la fin de l'allée, la souris doit tourner du côté de l'orientation cible afin de recevoir une récompense en eau.

L'orientation des objets sera modulable à l'aide d'un moteur pas à pas. Selon l'orientation de l'objet, la souris qui suivra un protocole de restriction hydrique, devra emprunter le bras de droite ou de gauche pour y recevoir, après léchage du tube de récompense, 5 µl d'eau. Des portes automatisées couplées à des détecteurs infrarouges permettent de forcer la rotation au sein du labyrinthe dans un seul sens. Le comportement de la souris dans le labyrinthe sera quantifié à l'aide des détecteurs de léchages et de passages, mais aussi filmé à l'aide de deux caméras infrarouges. Une première caméra filmera à 500 Hz (850 nm) le passage de la souris sur l'allée centrale entre les stimuli discriminatifs. Elle permettra de déterminer précisément les mouvements de vibrisses et les contacts vibrisses-objets. Une seconde caméra filmera à 100 Hz l'ensemble du labyrinthe. Elle permettra de surveiller en temps réel le bon déroulement de la tâche sans perturber les animaux (en dehors des illuminateurs infrarouges, l'ensemble du labyrinthe étant plongé dans l'obcurité).

2.2. Fibroscopie à champ large pour l'enregistrement des dynamiques corticales à l'échelle mésoscopique

Afin d'enregistrer les dynamiques corticales évoquées par les contacts multivibrissaux avec l'objet présenté, nous utiliserons l'imagerie sensible au potentiel qui bénéficie d'une excellente résolution temporelle (500 Hz). Nous imagerons typiquement une zone de 2.5 x 2.5 mm couvrant la totalité du cortex somatosensoriel primaire tout en conservant une résolution spatiale de ~25 µ, inférieure à la

taille d'une colonne corticale. Afin de laisser aux animaux la capacité de se mouvoir nécessaire à la réalisation des tâches de discrimination, nous aurons recours à un faisceau de fibres optiques (assemblage de fibres de 10 µm) pour transmettre les signaux lumineux sous forme d'image depuis et vers le crâne des souris (Ferezou et al., 2006). Enfin, nous évaluerons également la qualité des signaux obtenus en conditions similaires avec des senseurs calciques encodés génétiquement. Ces outils, qui offrent une autre lecture de l'activité du réseau cortical, permettraient en effet d'imager les souris de manière chronique tout au long de l'apprentissage, ce qui n'est pas possible lorsque l'on utilise des colorants synthétiques.

2.3. Photo-activation / inhibition ciblée par matrice de micro-miroirs

La perturbation des dynamiques corticales qui interviendra dans un second temps sera mise en place grâce à une matrice de micro-miroirs digitale (DMD, Abbasi et al., 2018; Ronzitti et al., 2017), par l'intermédiaire de la même interface fibrée. La perturbation corticale sera induite par photo-inhibition ciblée des neurones pyramidaux exprimant une opsine inhibitrice, ou par photo-stimulation les interneurones GABA-ergiques du cortex exprimant une opsine excitatrice. L'avantage de l'utilisation d'une telle matrice couplée avec le faisceau de fibres tel que présenté précédemment est de pouvoir inhiber le cortex suivant un ou des patrons spatiotemporels particuliers. Il est à noter qu'un système de photoactivation ciblée a déjà été développé dans l'équipe avec succès (Abbasi et al., 2018). Le choix de l'agencement de ces motifs de stimulation dépendra des dynamiques observées en imagerie fibrée. Nous perturberons partiellement ou totalement une combinaison de colonnes corticales dont nous avons observé la dynamique spatiotemporelle particulière lors de la présentation d'un objet avec une orientation donnée. La performance de l'animal à choisir le bras du labyrinthe récompensant la reconnaissance de cette orientation de l'objet nous permettra d'évaluer la nécessité de certains patrons corticaux évoqués dans le fonctionnement de l'intégration sensorielle.

La réalisation de ce projet permettra ainsi de mieux comprendre comment le réseau cortical peut contribuer à la genèse d'un percept global sur la base d'une séquence complexe de stimuli en périphérie.

3. Exploration multi-échelles de la prédiction de stimuli tactiles dans les cortex somatosensoriels

Projet porté par l'ANR Expect (2018-2022, partenaires : Laurent Bourdieu, Clément Léna et moi-même, coordination : Laurent Bourdieu), il fait donc l'objet d'une collaboration avec ces deux équipes de (IBENS ENS-CNRS UMR8197, Inserm U1024).

- *Dans le cadre de ce projet, je co-encadre avec Laurent Bourdieu (équipe Dynamique corticale et mécanismes de codage, IBENS ENS-CNRS UMR8197, Inserm U1024) le doctorat de **Sophie Hubatz** qui a débuté en octobre 2017.*

Lorsqu'elles explorent un objet, les souris bougent leurs vibrisses dans un mouvement rythmique de "whisking" quantifiable avec précision. En contactant ainsi plusieurs fois un objet, elles peuvent localiser leur position avec une précision submillimétrique (O'Connor et al., 2010). Suite à ces contacts répétés, une prédiction de la position de l'objet est générée : les vibrisses sont précisément déplacées à la position attendue de l'objet. Un déplacement inopiné de l'objet crée donc un décalage entre cette position prédite de l'objet et l'événement en cours. L'apparition de signaux d'erreur dans les

circuits sensorimoteurs centraux participe vraisemblablement au calcul des commandes motrices correctives générées pour s'adapter à la nouvelle position. Nous proposons d'étudier ici les bases neuronales de cette anticipation sensorimotrice, en explorant comment les signaux d'attente sensorimoteurs sont comparés et modifiés avec l'intégration de nouvelles entrées sensorielles.

Des études récentes suggèrent qu'une représentation mentale de l'objet pourrait émerger au travers d'une activité coordonnée entre S1 et S2 (Kwon et al., 2016; Yamashita and Petersen, 2016; Zuo et al., 2015). Nous formulons ici l'hypothèse que S1 et S2 sont capables de maintenir une représentation des informations somatosensorielles prédites et que les écarts aux signaux d'attente sont calculés au sein d'un réseau impliquant ces deux structures en interaction avec le cortex moteur primaire (M1).

3.1. Tâche sensorimotrice pour générer une attente d'entrées tactiles

Pour étudier la formation de signaux de prédiction, nous allons d'abord entraîner des souris à contacter plusieurs fois un objet avec une vibrisse unique, en échange d'une récompense en eau. Une seule vibrisse sera en effet conservée afin de faciliter la quantification du mouvement vibrissal au cours de la tâche (**Figure 24a**).

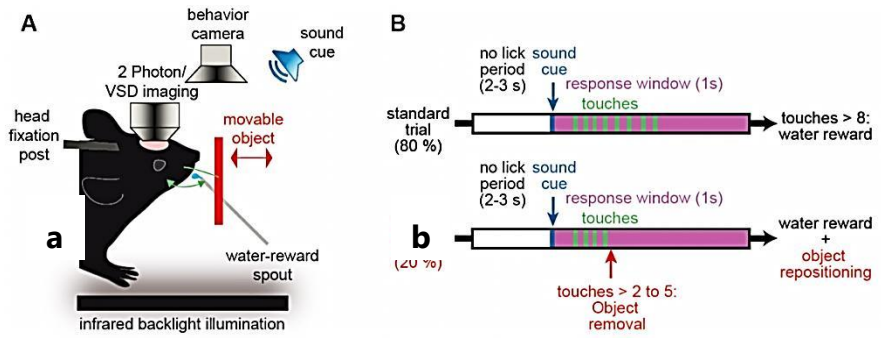

Figure 24. Tâche comportementale générant une prédiction de la position d'un objet par une souris fixée par la tête.

a. Description générale du dispositif expérimental. Les souris seront maintenues éveillées "tête-fixée" dans le noir. Une caméra infra-rouge filmera le mouvement de la vibrisse au cours de la tâche comportementale (500 images/s).

b. Diagramme décrivant le déroulement des événements de la tâche. Des essais standards (~80%) seront initiés après des périodes de 3 secondes au cours desquelles la souris devra s'abstenir de lécher l'embout de récompense. Un signal sonore indiquera le début de l'essai durant lequel la souris apprendra à "whisker" au minimum 8 fois contre l'objet pour être récompensée par une goutte d'eau. Le temps entre les essais sera randomisé. L'objet sera retiré aléatoirement pendant que la souris effectue la tâche, après 3 à 5 contacts avec l'objet (essais tests, ~20% des essais totaux).

Après apprentissage, des essais seront aléatoirement incorporés au protocole, au cours desquels l'objet sera retiré après quelques contacts (**Figure 24b**). Une quantification précise de la position de la vibrisse à l'aide d'une caméra à haute cadence permettra de quantifier l'ajustement de la commande motrice se produisant après la détection de l'événement discordant. Les détails du protocole d'entraînement seront validés au cours d'une première phase du projet dont les grands principes sont illustrés sur la **figure 24**.

3.2. Comment les signaux de prédiction sont-ils distribués au sein du réseau S1-S2-M1?

A l'aide de la technique d'imagerie sensible au potentiel, nous suivrons les dynamiques corticales au sein d'une large portion du cortex cérébral couvrant à la fois S1, S2 et M1 au cours de la tâche, nous pourrons analyser comment et quand ces aires corticales sont activées lorsque des signaux de

prédiction, puis d'erreur sont générés. Nous étudierons également comment ces signaux sont liés à l'ajustement de la commande motrice.

Dans S1, les réponses de neurones uniques, enregistrées alors qu'un animal contacte activement un objet avec une vibrisse ont montré des propriétés d'adaptation différentes en fonction de leurs cibles postsynaptiques (S2 vs. M1). Sachant que l'adaptation spécifique des réponses à un stimulus donné est connue pour jouer un rôle dans l'émergence de signaux d'erreur, la capacité d'analyser simultanément l'activité neuronale de ces trois aires corticales au cours de la tâche constitue un atout déterminant pour ce projet.

3.3. Implication des différents sous-types neuronaux

Le calcul de la différence entre le signal prédit et le retour sensoriel réel repose vraisemblablement sur les réseaux inhibiteurs. Ces dernières années, une classification des neurones inhibiteurs en 3 classes principales génétiquement distinctes a été proposée (Rudy et al., 2011; Tremblay et al., 2016). En parallèle, les circuits élémentaires d'inhibition et de désinhibition ont été caractérisés et impliqués dans différentes tâches comportementales (Fu et al., 2014; Jiang et al., 2013; Letzkus et al., 2011; Pakan et al., 2016; Pi et al., 2013). Un exemple intéressant de réseau désinhibiteur est celui impliquant les projections des neurones excitateurs de M1 sur les interneurones exprimant le peptide vasoactif intestinal (VIP)+ de S1, connectant les interneurones à somatostatine et levant ainsi l'action inhibitrice de ces derniers sur leurs projections au niveau des dendrites distales des neurones pyramidaux de S1 (Lee et al., 2013). Notre projet vise à définir un circuit responsable de la prédiction sensorimotrice et à résoudre les dynamiques neuronales sous-jacentes, révélant comment le cerveau compare continuellement l'information sensorielle lui parvenant avec sa représentation interne du monde, processus essentiel à l'extraction de signaux pertinents et au guidage des comportements moteurs.

3.4. Quels sont les acteurs neuronaux capables de générer de la prédiction au sein du réseau S1-S2-M1 ?

Au cours du même protocole comportemental, nous analyserons par imagerie à deux photons, les sous-types neuronaux impliqués dans la génération des signaux de prédiction, dans le cadre d'une collaboration avec l'équipe de Laurent Bourdieu à l'IBENS. Nous étudierons d'abord le recrutement spécifique de différents types d'interneurones durant la tâche comportementale, en utilisant des lignées de souris exprimant de façon inductible la sonde calcique GCamp6f dans 3 classes d'interneurones inhibiteurs exprimant respectivement : la Parvalbumine, la Somatostatine ou le VIP. L'identification et l'étude des cellules pyramidales se fera en fonction de leurs projections spécifiques à l'aide de traceurs rétrogrades (sous-unité B de la toxine cholérique (CTB) 488 ou 647) injectés au niveau de S1, S2 et M1. L'activité des différentes couches cellulaires ainsi marquées sera enregistrée simultanément à l'aide d'un microscope à deux photons (TPM) créé au sein de l'IBENS par l'équipe de Laurent Bourdieu (en collaboration avec l'équipe de Stéphane Dieudonné), permettant l'enregistrement de signaux fonctionnels en 3 dimensions, à une vitesse et avec un ratio signal/bruit inédits. Pour évaluer la contribution respective de chaque type cellulaire aux différents événements de la tâche quantifiés par la caméra (léchages, contacts attendus, absences de contact attendu,…), nous analyserons les données à l'aide d'un modèle linéaire généralisé. Ce dernier est particulièrement adapté à l'exploration rapide de la dépendance entre de nombreux paramètres à partir de traces calciques (Pinto and Dan, 2015). Ces résultats, en combinaison avec la connectivité connue des

différents types cellulaires du cortex, seront utilisés pour décrire les paramètres principaux des signaux de prédiction sensorimoteurs au sein de S1, S2 et M1, et en déduire les mécanismes possibles sous-tendant leur formation.

4. Conclusion

Depuis mon arrivée à l'UNIC en 2011, j'ai pu financer et monter deux postes d'imagerie fonctionnelle qui m'ont permis d'acquérir une précieuse autonomie sur le plan pratique, mais aussi scientifique. Je bénéficie d'un environnement extrêmement stimulant, au sein d'une équipe soudée, dirigée avec beaucoup de bienveillance par Daniel Shulz dont l'expertise dans notre domaine de recherche est incontestable.

Ainsi, j'ai eu la chance de pouvoir former et co-encadrer, dans un contexte très favorable, des stagiaires et étudiants de différents niveaux. Les années passant, cette activité d'encadrement s'impose comme une part essentielle et incontournable de mon activité de recherche. Ayant pu réunir les moyens financiers nécessaires à la réalisation de plusieurs projets ambitieux, il me tient particulièrement à cœur aujourd'hui de les voir portés par des doctorants afin de transmettre mon intérêt pour les questions scientifiques abordées tout en veillant à leur épanouissement scientifique et personnel. Telle est la principale motivation qui me pousse aujourd'hui à vouloir acquérir mon habilitation à diriger des recherches. Celle-ci me permettra en outre d'intensifier mes interactions scientifiques avec d'autres équipes de recherche au travers de participations à des comités et jurys de thèses. Si elle représente une étape importante dans mon parcours personnel, elle participera également je l'espère à renforcer le dynamisme et la visibilité de l'équipe.

Références bibliographiques

Abbasi, A., Goueytes, D., Shulz, D.E., Ego-Stengel, V., and Estebanez, L. (2018). A fast intracortical brain–machine interface with patterned optogenetic feedback. J. Neural Eng. *15*, 046011.

Agmon, A., and Connors, B.W. (1991). Thalamocortical responses of mouse somatosensory (barrel) cortex in vitro. Neuroscience *41*, 365–379.

Ahissar, E., and Assa, E. (2016). Perception as a closed-loop convergence process. Elife *5*, 1–26.

Arieli, A., Sterkin, A., Grinvald, A., and Aertsen, A. (1996). Dynamics of ongoing activity: explanation of the large variability in evoked cortical responses. Science *273*, 1868–1871.

Armstrong-James, M., Fox, K., and Das-Gupta, a (1992). Flow of excitation within rat barrel cortex on striking a single vibrissa. J. Neurophysiol. *68*, 1345–1358.

Arnold, P.B., Li, C.X., and Waters, R.S. (2001). Thalamocortical arbors extend beyond single cortical barrels: an in vivo intracellular tracing study in rat. Exp. Brain Res. *136*, 152–168.

Aronoff, R., Matyas, F., Mateo, C., Ciron, C., Schneider, B., and Petersen, C.C.H. (2010). Long-range connectivity of mouse primary somatosensory barrel cortex. Eur. J. Neurosci. *31*, 2221–2233.

Ascoli, G. a, Alonso-Nanclares, L., Anderson, S. a, Barrionuevo, G., Benavides-Piccione, R., Burkhalter, A., Buzsáki, G., Cauli, B., Defelipe, J., Fairén, A., et al. (2008). Petilla terminology: nomenclature of features of GABAergic interneurons of the cerebral cortex. Nat. Rev. Neurosci. *9*, 557–568.

Battaglia, D., Karagiannis, A., Gallopin, T., Gutch, H.W., and Cauli, B. (2013). Beyond the frontiers of neuronal types. Front. Neural Circuits *7*, 13.

Benison, A.M., Rector, D.M., and Barth, D.S. (2007). Hemispheric mapping of secondary somatosensory cortex in the rat. J. Neurophysiol. *97*, 200–207.

Blasdel, G.G., and Salama, G. (1986). Voltage-sensitive dyes reveal a modular organization in monkey striate cortex. Nature *321*, 579–585.

Bokor, H., Acsády, L., and Deschênes, M. (2008). Behavioral/Systems/Cognitive Vibrissal Responses of Thalamic Cells That Project to the Septal Columns of the Barrel Cortex and to the Second Somatosensory Area. *28*, 5169–5177.

Borgdorff, A.J., Poulet, J.F.A., and Petersen, C.C.H. (2007). Facilitating Sensory Responses in Developing Mouse Somatosensory Barrel Cortex. J. Neurophysiol. *97*, 2992–3003.

Bosman, L.W.J., Houweling, A.R., Owens, C.B., Tanke, N., Shevchouk, O.T., Rahmati, N., Teunissen, W.H.T., Ju, C., Gong, W., Koekkoek, S.K.E., et al. (2011). Anatomical Pathways Involved in Generating and Sensing Rhythmic Whisker Movements. Front. Integr. Neurosci. *5*, 53.

Boubenec, Y., Shulz, D.E., and Debrégeas, G. (2012). Whisker encoding of mechanical events during active tactile exploration. Front Behav Neurosci *6*, 74.

Boubenec, Y., Claverie, L.N., Shulz, D.E., and Debrégeas, G. (2014). An Amplitude Modulation/Demodulation Scheme for Whisker-Based Texture Perception. J Neurosci *34*, 10832–10843.

Bourassa, J., Deschênes, M., and Bourassa, J; Deschenes, M. (1995). Corticothalamic projections from the primary visual cortex in rats: a single-fiber study using biocytin as an anterograde tracer. Neuroscience *66*, 253–263.

Brecht, M., and Sakmann, B. (2002a). Dynamic representation of whisker deflection by synaptic potentials in spiny stellate and pyramidal cells in the barrels and septa of layer 4 rat somatosensory cortex. J. Physiol. *543*, 49–70.

Brecht, M., and Sakmann, B. (2002b). Whisker maps of neuronal subclasses of the rat ventral posterior medial thalamus, identified by whole-cell voltage recording and morphological reconstruction. J. Physiol. *538*, 495–515.

Brecht, M., Roth, A., and Sakmann, B. (2003). Dynamic Receptive Fields of Reconstructed Pyramidal Cells in Layers 3 and 2 of Rat Somatosensory Barrel Cortex. J. Physiol. *553*, 243–265.

Brioni, J.D., O'Neill, A.B., Kim, D.J., and Decker, M.W. (1993). Nicotinic receptor agonists exhibit anxiolytic-like effects on the elevated plus-maze test. Eur. J. Pharmacol. *238*, 1–8.

Brumberg, J.C., Pinto, D.J., and Simons, D.J. (1996). Spatial gradients and inhibitory summation in the rat whisker barrel system. J. Neurophysiol. *76*, 130–140.

Bullock, T.H., Karamürsel, S., Achimowicz, J.Z., McClune, M.C., and Başar-Eroglu, C. (1994). Dynamic properties of human visual evoked and omitted stimulus potentials. Electroencephalogr. Clin. Neurophysiol. *91*, 42–53.

Bureau, I., Von Paul, F. Saint, and Svoboda, K. (2006). Interdigitated paralemniscal and lemniscal pathways in the mouse barrel cortex. PLoS Biol. *4*, 2361–2371.

Campagner, D., Evans, M.H., Loft, M.S.E., and Petersen, R.S. (2018). What the Whiskers Tell the Brain. Neuroscience *368*, 95–108.

Carvell, G.E., and Simons, D.J. (1986). Somatotopic organization of the second somatosensory area (SII) in the cerebral cortex of the mouse. Somatosens. Res. *3*, 213–237.

Carvell, G.E., and Simons, D.J. (1987). Thalamic and corticocortical connections of the second somatic sensory area of the mouse. J. Comp. Neurol. *265*, 409–427.

Carvell, G.E., and Simons, D.J. (1990). Biometric analyses of vibrissal tactile discrimination in the rat. J. Neurosci. *10*, 2638–2648.

Cauli, B., Audinat, E., Lambolez, B., Angulo, M.C., Ropert, N., Tsuzuki, K., Hestrin, S., and Rossier, J. (1997). Molecular and physiological diversity of cortical nonpyramidal cells. J. Neurosci. *17*, 3894–3906.

Cauli, B., Porter, J.T., Tsuzuki, K., Lambolez, B., Rossier, J., Quenet, B., and Audinat, E. (2000). Classification of fusiform neocortical interneurons based on unsupervised clustering. Proc. Natl. Acad. Sci. U. S. A. *97*, 6144–6149.

Chakrabarti, S., and Alloway, K.D. (2006). Differential Origin of Projections from SI Barrel Cortex to the Whisker Representations in SII and MI. J. Comp. Neurol. *498*, 624:636.

Chemla, S., and Chavane, F. (2010). A biophysical cortical column model to study the multi-component origin of the VSDI signal. Neuroimage *53*, 420–438.

Chemla, S., Muller, L., Reynaud, A., Takerkart, S., Destexhe, A., and Chavane, F. (2017). Improving voltage-sensitive dye imaging: with a little help from computational approaches. Neurophotonics *4*, 031215.

Chen, I.-W., Helmchen, F., and Lutcke, H. (2015). Specific Early and Late Oddball-Evoked Responses in Excitatory and Inhibitory Neurons of Mouse Auditory Cortex. J. Neurosci. *35*, 12560–12573.

Chen, J.L., Carta, S., Soldado-Magraner, J., Schneider, B.L., and Helmchen, F. (2013). Behaviour-dependent recruitment of long-range projection neurons in somatosensory cortex. Nature *499*, 336–340.

Chen, J.L., Voigt, F.F., Javadzadeh, M., Krueppel, R., and Helmchen, F. (2016). Long-range population dynamics of anatomically defined neocortical networks. Elife *5*, 1–26.

Costall, B., Naylor, R.J., and Tyers, M.B. (1990). The psychopharmacology of 5-HT3 receptors. Pharmacol. Ther. *47*, 181–202.

Cruikshank, S.J., Urabe, H., Nurmikko, A. V., and Connors, B.W. (2010). Pathway-Specific Feedforward Circuits between Thalamus and Neocortex Revealed by Selective Optical Stimulation of Axons. Neuron *65*, 230–245.

DeFelipe, J. (1993). Neocortical neuronal diversity: chemical heterogeneity revealed by colocalization studies of classic neurotransmitters, neuropeptides, calcium-binding proteins, and cell surface molecules. Cereb. Cortex *3*, 273–289.

DeFelipe, J. (2002). Cortical interneurons: from Cajal to 2001. Prog. Brain Res. *136*, 215–238.

DeFelipe, J., and Fariñas, I. (1992). The pyramidal neuron of the cerebral cortex: morphological and chemical characteristics of the synaptic inputs. Prog. Neurobiol. *39*, 563–607.

DeFelipe, J., López-Cruz, P.L., Benavides-Piccione, R., Bielza, C., Larrañaga, P., Anderson, S., Burkhalter, A., Cauli, B., Fairén, A., Feldmeyer, D., et al. (2013). New insights into the classification and nomenclature of cortical GABAergic interneurons. Nat. Rev. Neurosci. *14*, 202–216.

Deisseroth, K. (2015). Optogenetics: 10 years of microbial opsins in neuroscience. Nat. Neurosci. *18*, 1213–1225.

Deschenes, M., and Urbain, N. (2009). Vibrissal afferents from trigeminus to cortices. In Scholarpedia, (Paris: Atlantis Press), p. 7454.

Deschênes, M., Veinante, P., and Zhang, Z.W. (1998). The organization of corticothalamic projections: Reciprocity versus parity. Brain Res. Rev. *28*, 286–308.

Deschênes, M., Takatoh, J., Kurnikova, A., Moore, J.D., Demers, M., Elbaz, M., Furuta, T., Wang, F., and Kleinfeld, D. (2016). Inhibition, Not Excitation, Drives Rhythmic Whisking. Neuron *90*, 374–387.

Diamond, M.E., Von Heimendahl, M., and Arabzadeh, E. (2008). Whisker-mediated texture discrimination. PLoS Biol. *6*, 1627–1630.

Douglas, R.J., and Martin, K.A.C. (2004). Neuronal circuits of the neocortex. Annu. Rev. Neurosci. *27*, 419–451.

Ebbesen, C.L., and Brecht, M. (2017). Motor cortex —

to act or not to act? Nat. Rev. Neurosci. *18*, 694–705.

Ebbesen, C.L., Doron, G., Lenschow, C., and Brecht, M. (2017). Vibrissa motor cortex activity suppresses contralateral whisking behavior. Nat. Neurosci. *20*, 82–89.

Ego-Stengel, V., Mello e Souza, T., Jacob, V., and Shulz, D.E. (2005). Spatiotemporal Characteristics of Neuronal Sensory Integration in the Barrel Cortex of the Rat. J. Neurophysiol. *93*, 1450–1467.

Ego-Stengel, V., Le Cam, J., and Shulz, D.E. (2012). Coding of apparent motion in the thalamic nucleus of the rat vibrissal somatosensory system. J Neurosci *32*, 3339–3351.

Engel, A.K., Fries, P., and Singer, W. (2001). Dynamic predictions: oscillations and synchrony in top-down processing. Nat. Rev. Neurosci. *2*, 704–716.

Estebanez, L., Boustani, S. El, Destexhe, A., Shulz, D.E., De, N., Scientifique, R., Terrasse, D., Médicale, R., National, C., and Recherche, D. Supplementary Information for Correlated input reveals coexisting coding schemes. 1–14.

Estebanez, L., Boustani, S. El, Destexhe, A., and Shulz, D.E. (2012). Correlated input reveals coexisting coding schemes in a sensory cortex. Nat Neurosci *15*, 1691–1699.

Estebanez, L., Bertherat, J., Shulz, D.E., Bourdieu, L., and Léger, J.-F. (2016). A radial map of multi-whisker correlation selectivity in the rat barrel cortex. Nat. Commun. *7*, 13528.

Estebanez, L., Férézou, I., Ego-Stengel, V., and Shulz, D.E. (2018). Representation of tactile scenes in the rodent barrel cortex. Neuroscience *368*, 81–94.

Estes, M.L., and McAllister, A.K. (2016). Maternal immune activation: Implications for neuropsychiatric disorders. Science *353*, 772–777.

Feldmeyer, D. (2012). Excitatory neuronal connectivity in the barrel cortex. Front. Neuroanat. *6*, 24.

Feldmeyer, D., Lübke, J., and Sakmann, B. (2006). Efficacy and connectivity of intracolumnar pairs of layer 2/3 pyramidal cells in the barrel cortex of juvenile rats. J. Physiol. *575*, 583–602.

Feldmeyer, D., Brecht, M., Helmchen, F., Petersen, C.C.H., Poulet, J.F.A., Staiger, J.F., Luhmann, H.J., and Schwarz, C. (2013). Barrel cortex function. Prog. Neurobiol. *103*, 3–27.

Feldmeyer, D., Qi, G., Emmenegger, V., and Staiger, J.F. (2018). Inhibitory Interneurons and their Circuit Motifs in the Many Layers of the Barrel Cortex. Neuroscience *368*, 132–151.

Ferezou, I., and Deneux, T. (2017). Review: How do spontaneous and sensory-evoked activities interact? Neurophotonics *4*.

Ferezou, I., Bolea, S., and Petersen, C.C.H. (2006). Visualizing the Cortical Representation of Whisker Touch: Voltage-Sensitive Dye Imaging in Freely Moving Mice. Neuron *50*, 617–629.

Ferezou, I., Haiss, F., Gentet, L.J., Aronoff, R., Weber, B., and Petersen, C.C.H. (2007). Spatiotemporal Dynamics of Cortical Sensorimotor Integration in Behaving Mice. Neuron *56*, 907–923.

Férézou, I., Cauli, B., Hill, E.L., Rossier, J., Hamel, E., and Lambolez, B. (2002). 5-HT3 receptors mediate serotonergic fast synaptic excitation of neocortical vasoactive intestinal peptide/cholecystokinin interneurons. J. Neurosci. *22*, 7389–7397.

Férézou, I., Hill, E.L., Cauli, B., Gibelin, N., Kaneko, T., Rossier, J., and Lambolez, B. (2007). Extensive overlap of mu-opioid and nicotinic sensitivity in cortical interneurons. Cereb. Cortex *17*, 1948–1957.

Frostig, R.D., and Petersen, C.C.H. (2017). Special Section Guest Editorial: Pioneers in Neurophotonics: Special Section Honoring Professor Amiram Grinvald. Neurophotonics *4*, 1.

Fu, M., and Zuo, Y. (2011). Experience-dependent structural plasticity in the cortex. Trends Neurosci. *34*, 177–187.

Fu, Y., Tucciarone, J.M., Espinosa, J.S., Sheng, N., Darcy, D.P., Nicoll, R.A., Huang, Z.J., and Stryker, M.P. (2014). A cortical circuit for gain control by behavioral state. Cell *156*, 1139–1152.

Furuta, T., Timofeeva, E., Nakamura, K., Okamoto-Furuta, K., Togo, M., Kaneko, T., and Deschênes, M. (2008). Inhibitory gating of vibrissal inputs in the brainstem. J. Neurosci. *28*, 1789–1797.

Furuta, T., Kaneko, T., and Deschenes, M. (2009). Septal Neurons in Barrel Cortex Derive Their Receptive Field Input from the Lemniscal Pathway. J. Neurosci. *29*, 4089–4095.

Gabernet, L., Jadhav, S.P., Feldman, D.E., Carandini, M., and Scanziani, M. (2005). Somatosensory integration controlled by dynamic thalamocortical feed-forward inhibition. Neuron *48*, 315–327.

Gavornik, J.P., and Bear, M.F. (2014). Learned spatiotemporal sequence recognition and prediction in primary visual cortex. Nat. Neurosci. *17*, 732–737.

Gilad, A., Gallero-Salas, Y., Groos, D., and Helmchen, F. (2018). Behavioral Strategy Determines Frontal or Posterior Location of Short-Term Memory in Neocortex. Neuron.

Goldin, M.A., Harrell, E.R., Estebanez, L., and Shulz, D.E. (2018). Rich spatio-temporal stimulus dynamics

unveil sensory specialization in cortical area S2. Nat. Commun. *9*, 4053.

Goldreich, D., Peterson, B.E., and Merzenich, M.M. (1998). Optical imaging and electrophysiology of rat barrel cortex. II. Responses to paired-vibrissa deflections. Cereb. Cortex *8*, 184–192.

Gong, Z., Liu, J., Guo, C., Zhou, Y., Teng, Y., and Liu, L. (2006). Supporting Online Material. 1–7.

Grinvald, A., and Hildesheim, R. (2004). VSDI: a new era in functional imaging of cortical dynamics. Nat. Rev. Neurosci. *5*, 874–885.

Grinvald, A., Anglister, L., Freeman, J.A., Hildesheim, R., and Manker, A. (1984). Real-time optical imaging of naturally evoked electrical activity in intact frog brain. Nature *308*, 848–850.

Guo, Z. V., Hires, S.A., Li, N., O'Connor, D.H., Komiyama, T., Ophir, E., Huber, D., Bonardi, C., Morandell, K., Gutnisky, D., et al. (2014). Procedures for behavioral experiments in head-fixed mice. PLoS One *9*.

Gupta, A., Wang, Y., and Markram, H. (2000). Organizing principles for a diversity of GABAergic interneurons and synapses in the neocortex. Science *287*, 273–278.

Haidarliu, S. (2008). Lemniscal and extralemniscal compartments in the VPM of the rat. Front. Neuroanat. *2*, 4.

Harms, L., Michie, P.T., and Näätänen, R. (2016). Criteria for determining whether mismatch responses exist in animal models: Focus on rodents. Biol. Psychol. *116*, 28–35.

Harris, K.D., and Thiele, A. (2011). Cortical state and attention. Nat Rev Neurosci *12*, 509–523.

He, M., Tucciarone, J., Lee, S., Nigro, M.J., Kim, Y., Levine, J.M., Kelly, S.M., Krugikov, I., Wu, P., Chen, Y., et al. (2016). Strategies and Tools for Combinatorial Targeting of GABAergic Neurons in Mouse Cerebral Cortex. Neuron *91*, 1228–1243.

Helmstaedter, M., de Kock, C.P.J., Feldmeyer, D., Bruno, R.M., and Sakmann, B. (2007). Reconstruction of an average cortical column in silico. Brain Res. Rev. *55*, 193–203.

Hestrin, S., and Armstrong, W.E. (1996). Morphology and physiology of cortical neurons in layer I. J. Neurosci. *16*, 5290–5300.

Higley, M.J., and Contreras, D. (2003). Nonlinear integration of sensory responses in the rat barrel cortex: an intracellular study in vivo. J. Neurosci. *23*, 10190–10200.

Hoffer, Z.S., Hoover, J.E., and Alloway, K.D. (2003). Sensorimotor corticocortical projections from Rat Barrel Cortex Have an Anisotropic Organization That Facilitates Integration of Inputs from Whiskers in the Same Row. J Comp Neurol. *544*, 525–544.

Ibrahim, L., and Wright, E.A. (1975). The growth of rats and mice vibrissae under normal and some abnormal conditions. J Embryol Exp Morphol *33*, 831–844.

Inagaki, S., and Nagai, T. (2016). Current progress in genetically encoded voltage indicators for neural activity recording. Curr. Opin. Chem. Biol. *33*, 95–100.

Irvine, E.E., Cheeta, S., Marshall, M., and File, S.E. (2001). Different treatment regimens and the development of tolerance to nicotine's anxiogenic effects. Pharmacol. Biochem. Behav. *68*, 769–776.

Jacob, V., Le Cam, J., Ego-Stengel, V., and Shulz, D.E. (2008). Emergent Properties of Tactile Scenes Selectively Activate Barrel Cortex Neurons. Neuron *60*, 1112–1125.

Jacob, V., Estebanez, L., Le Cam, J., Tiercelin, J.-Y.Y., Parra, P., Par??sys, G., Shulz, D.E., Parésys, G., and Shulz, D.E. (2010). The Matrix: A new tool for probing the whisker-to-barrel system with natural stimuli. J. Neurosci. Methods *189*, 65–74.

Jacquin, M.F., Chiaia, N.L., Haring, J.H., and Rhoades, R.W. (1990). Intersubnuclear connections within the rat trigeminal brainstem complex. Somat. Mot Res *7*, 399–420.

Jensen, K.F., and Killackey, H.P. (1987). Terminal arbors of axons projecting to the somatosensory cortex of the adult rat. II. The altered morphology of thalamocortical afferents following neonatal infraorbital nerve cut. J. Neurosci. *7*, 3544–3553.

Jiang, X., Wang, G., Lee, A.J., Stornetta, R.L., and Zhu, J.J. (2013). The organization of two new cortical interneuronal circuits. Nat. Neurosci. *16*, 210–218.

Jiang, X., Shen, S., Cadwell, C.R., Berens, P., Sinz, F., Ecker, A.S., Patel, S., and Tolias, A.S. (2015). Principles of connectivity among morphologically defined cell types in adult neocortex. Science (80-.). *350*, aac9462-aac9462.

Jin, T.-E. (2004). Fiber Types of the Intrinsic Whisker Muscle and Whisking Behavior. J. Neurosci. *24*, 3386–3393.

Jones, B.J., Costall, B., Domeney, A.M., Kelly, M.E., Naylor, R.J., Oakley, N.R., and Tyers, M.B. (1988). The potential anxiolytic activity of GR38032F, a 5-HT3-receptor antagonist. Br. J. Pharmacol. *93*, 985–993.

Kapfer, C., Glickfeld, L.L., Atallah, B. V, and Scanziani, M. (2007). Supralinear increase of recurrent inhibition during sparse activity in the somatosensory cortex. Nat. Neurosci. *10*, 743–753.

Kawaguchi, Y. (1995). Physiological subgroups of nonpyramidal cells with specific morphological characteristics in layer II/III of rat frontal cortex. J. Neurosci. *15*, 2638–2655.

Kerekes, P., Daret, A., Shulz, D.E., and Ego-Stengel, V. (2017). Bilateral Discrimination of Tactile Patterns without Whisking in Freely Running Rats. J. Neurosci. *37*, 7567–7579.

Kleinfeld, D., and Delaney, K.R. (1996). Distributed representation of vibrissa movement in the upper layers of somatosensory cortex revealed with voltage-sensitive dyes. J. Comp. Neurol. *375*, 89–108.

Kleinfeld, D., and Desch??nes, M. (2011). Neuronal basis for object location in the vibrissa scanning sensorimotor system. Neuron *72*, 455–468.

Kleinfeld, D., Ahissar, E., and Diamond, M.E. (2006). Active sensation: insights from the rodent vibrissa sensorimotor system. Curr. Opin. Neurobiol. *16*, 435–444.

Koralek, K.A., Jensen, K.F., and Killackey, H.P. (1988). Evidence for two complementary patterns of thalamic input to the rat somatosensory cortex. Brain Res. *463*, 346–351.

Kwegyir-Afful, E.E., and Keller, A. (2004). Response Properties of Whisker-Related Neurons in Rat Second Somatosensory Cortex. J. Neurophysiol. *92*, 2083–2092.

Kwon, S.E., Yang, H., Minamisawa, G., and O'Connor, D.H. (2016). Sensory and decision-related activity propagate in a cortical feedback loop during touch perception. Nat. Neurosci. *19*, 1243–1249.

Lambolez, B., Audinat, E., Bochet, P., Crépel, F., and Rossier, J. (1992). AMPA receptor subunits expressed by single Purkinje cells. Neuron *9*, 247–258.

Land, P.W., Buffer, S.A., and Yaskosky, J.D. (1995). Barreloids in adult rat thalamus: three-dimensional architecture and relationship to somatosensory cortical barrels. J. Comp. Neurol. *355*, 573–588.

Lee, S., Hjerling-Leffler, J., Zagha, E., Fishell, G., and Rudy, B. (2010). The largest group of superficial neocortical GABAergic interneurons expresses ionotropic serotonin receptors. J Neurosci *30*, 16796–16808.

Lee, S., Kruglikov, I., Huang, Z.J., Fishell, G., and Rudy, B. (2013). A disinhibitory circuit mediates motor integration in the somatosensory cortex. Nat. Neurosci. *16*, 1662–1670.

Lefort, S., Tomm, C., Floyd Sarria, J.-C.C., and Petersen, C.C.H.H. (2009). The Excitatory Neuronal Network of the C2 Barrel Column in Mouse Primary Somatosensory Cortex. Neuron *61*, 301–316.

Letzkus, J.J., Wolff, S.B.E., Meyer, E.M.M., Tovote, P., Courtin, J., Herry, C., and Lüthi, A. (2011). A disinhibitory microcircuit for associative fear learning in the auditory cortex. Nature *480*, 331–335.

Lin, M.Z., and Schnitzer, M.J. (2016). Genetically encoded indicators of neuronal activity. Nat. Neurosci. *19*, 1142–1153.

Madisen, L., Mao, T., Koch, H., Zhuo, J., Berenyi, A., Fujisawa, S., Hsu, Y.-W.A., Garcia, A.J., Gu, X., Zanella, S., et al. (2012). A toolbox of Cre-dependent optogenetic transgenic mice for light-induced activation and silencing. Nat. Neurosci. *15*, 793–802.

Magnain, C., Castel, A., Boucneau, T., Simonutti, M., Ferezou, I., Rancillac, A., Vitalis, T., Sahel, J.A., Paques, M., and Atlan, M. (2014). Holographic laser Doppler imaging of microvascular blood flow. *31*.

Manns, I.D., Sakmann, B., and Brecht, M. (2004). Sub- and suprathreshold receptive field properties of pyramidal neurones in layers 5A and 5B of rat somatosensory barrel cortex. J. Physiol. *556*, 601–622.

Mao, T., Kusefoglu, D., Hooks, B.M.M., Huber, D., Petreanu, L., and Svoboda, K. (2011). Long-Range Neuronal Circuits Underlying the Interaction between Sensory and Motor Cortex. Neuron *72*, 111–123.

Markram, H., Toledo-Rodriguez, M., Wang, Y., Gupta, A., Silberberg, G., and Wu, C. (2004). Interneurons of the neocortical inhibitory system. Nat. Rev. Neurosci. *5*, 793–807.

Le Merre, P., Esmaeili, V., Charrière, E., Galan, K., Salin, P.-A., Petersen, C.C.H., and Crochet, S. (2018). Reward-Based Learning Drives Rapid Sensory Signals in Medial Prefrontal Cortex and Dorsal Hippocampus Necessary for Goal-Directed Behavior. Neuron *97*, 83–91.e5.

Meyer, H.S., Schwarz, D., Wimmer, V.C., Schmitt, A.C., Kerr, J.N.D., Sakmann, B., and Helmstaedter, M. (2011). Inhibitory interneurons in a cortical column form hot zones of inhibition in layers 2 and 5A. Proc. Natl. Acad. Sci. U. S. A. *108*, 16807–16812.

Meyer, H.S., Egger, R., Guest, J.M., Foerster, R., Reissl, S., and Oberlaender, M. (2013). Cellular organization of cortical barrel columns is whisker-specific. Proc. Natl. Acad. Sci. *110*, 19113–19118.

Milani, H., Steiner, H., and Huston, J.P. (1989). Analysis of recovery from behavioral asymmetries induced by unilateral removal of vibrissae in the rat. Behav. Neurosci. *103*, 1067–1074.

Minamisawa, G., Kwon, S.E., Chevée, M., Brown, S.P., O'Connor, D.H., and O'Connor, D.H. (2018). A Non-

canonical Feedback Circuit for Rapid Interactions between Somatosensory Cortices. Cell Rep. *23*, 2718–2731.e6.

Minnery, B.S. (2003). Response Properties of Whisker-Associated Trigeminothalamic Neurons in Rat Nucleus Principalis. J. Neurophysiol. *89*, 40–56.

Mohajerani, M.H., Chan, A.W., Mohsenvand, M., LeDue, J., Liu, R., McVea, D.A., Boyd, J.D., Wang, Y.T., Reimers, M., and Murphy, T.H. (2013). Spontaneous cortical activity alternates between motifs defined by regional axonal projections. Nat. Neurosci. *16*, 1426–1435.

Moore, C.I., and Nelson, S.B. (1998). Spatio-temporal subthreshold receptive fields in the vibrissa representation of rat primary somatosensory cortex. J. Neurophysiol. *80*, 2882–2892.

Moore, J.D., Deschênes, M., Furuta, T., Huber, D., Smear, M.C., Demers, M., and Kleinfeld, D. (2013). Hierarchy of orofacial rhythms revealed through whisking and breathing. Nature *497*, 205–210.

Mountcastle, V.B. (1997). The columnar organization of the neocortex. Brain 701–722.

MOUNTCASTLE, V.B. (1957). Modality and topographic properties of single neurons of cat's somatic sensory cortex. J. Neurophysiol. *20*, 408–434.

Narayanan, R.T., Egger, R., Johnson, A.S., Mansvelder, H.D., Sakmann, B., de Kock, C.P.J., and Oberlaender, M. (2015). Beyond Columnar Organization: Cell Type- and Target Layer-Specific Principles of Horizontal Axon Projection Patterns in Rat Vibrissal Cortex. Cereb. Cortex *25*, 4450–4468.

Narayanan, R.T., Udvary, D., and Oberlaender, M. (2017). Cell Type-Specific Structural Organization of the Six Layers in Rat Barrel Cortex. Front. Neuroanat. *11*, 91.

Narboux-Nême, N., Evrard, A., Ferezou, I., Erzurumlu, R.S.S., Kaeser, P.S.S., Lainé, J., Rossier, J., Ropert, N., Südhof, T.C., Gaspar, P., et al. (2012). Neurotransmitter Release at the Thalamocortical Synapse Instructs Barrel Formation But Not Axon Patterning in the Somatosensory Cortex. J. Neurosci. *32*, 6183–6196.

O'Connor, D.H., Clack, N.G., Huber, D., Komiyama, T., Myers, E.W., and Svoboda, K. (2010). Vibrissa-Based Object Localization in Head-Fixed Mice. J. Neurosci. *30*, 1947–1967.

Orbach, H.S., Cohen, L.B., and Grinvald, A. (1985). Optical mapping of electrical activity in rat somatosensory and visual cortex. J. Neurosci. *5*, 1886–1895.

Pakan, J.M.P., Lowe, S.C., Dylda, E., Keemink, S.W., Currie, S.P., Coutts, C.A., and Rochefort, N.L. (2016). Behavioral-state modulation of inhibition is context-dependent and cell type specific in mouse visual cortex. Elife *5*, 1–18.

Perronnet, L., Vilarchao, M.E., Hucher, G., Shulz, D.E., Peyré, G., and Ferezou, I. (2016). An automated workflow for the anatomo-functional mapping of the barrel cortex. J. Neurosci. Methods *263*, 145–154.

Petersen, C.H. (2007). The functional organization of the barrel cortex. Neuron *56*, 339–355.

Pi, H.-J., Hangya, B., Kvitsiani, D., Sanders, J.I., Huang, Z.J., and Kepecs, A. (2013). Cortical interneurons that specialize in disinhibitory control. Nature *503*, 521–524.

Pierret, T., Lavallée, P., and Deschênes, M. (2000). Parallel streams for the relay of vibrissal information through thalamic barreloids. J. Neurosci. *20*, 7455–7462.

Pinto, L., and Dan, Y. (2015). Cell-Type-Specific Activity in Prefrontal Cortex during Goal-Directed Behavior. Neuron *87*, 437–451.

Polley, D.B., Rickert, J.L., and Frostig, R.D. (2005). Whisker-based discrimination of object orientation determined with a rapid training paradigm. Neurobiol. Learn. Mem. *83*, 134–142.

Porter, J.T., Johnson, C.K., and Agmon, A. (2001). Diverse types of interneurons generate thalamus-evoked feedforward inhibition in the mouse barrel cortex. J. Neurosci. *21*, 2699–2710.

Prigg, T., Goldreich, D., Carvell, G.E., and Simons, D.J. (2002). Texture discrimination and unit recordings in the rat whisker/barrel system. Physiol. Behav. *77*, 671–675.

Ragnauth, A., Schuller, A., Morgan, M., Chan, J., Ogawa, S., Pintar, J., Bodnar, R.J., and Pfaff, D.W. (2001). Female preproenkephalin-knockout mice display altered emotional responses. Proc. Natl. Acad. Sci. U. S. A. *98*, 1958–1963.

Ramirez, A., Pnevmatikakis, E.A., Merel, J., Paninski, L., Miller, K.D., and Bruno, R.M. (2014). Spatiotemporal receptive fields of barrel cortex revealed by reverse correlation of synaptic input. Nat Neurosci *17*, 866–875.

Ronzitti, E., Ventalon, C., Canepari, M., Forget, B.C., Papagiakoumou, E., and Emiliani, V. (2017). Recent advances in patterned photostimulation for optogenetics. J. Opt. *19*, 113001.

Roychoudhury, M., and Kulkarni, S.K. (1997). Antianxiety profile of ondansetron, a selective 5-HT3 antagonist, in a novel animal model. Methods Find. Exp. Clin. Pharmacol. *19*, 107–111.

Rudy, B., Fishell, G., Lee, S., and Hjerling-Leffler, J. (2011). Three groups of interneurons account for nearly 100% of neocortical GABAergic neurons. Dev. Neurobiol. *71*, 45–61.

Sakmann, B. (2017). From single cells and single columns to cortical networks: dendritic excitability, coincidence detection and synaptic transmission in brain slices and brains. Exp. Physiol. *102*, 489–521.

Schubert, D., K??tter, R., and Staiger, J.F. (2007). Mapping functional connectivity in barrel-related columns reveals layer- and cell type-specific microcircuits. Brain Struct. Funct. *212*, 107–119.

Shimegi, S., Ichikawa, T., Akasaki, T., and Sato, H. (1999). Temporal characteristics of response integration evoked by multiple whisker stimulations in the barrel cortex of rats. J. Neurosci. *19*, 10164–10175.

Shimegi, S., Akasaki, T., Ichikawa, T., and Sato, H. (2000). Physiological and anatomical organization of multiwhisker response interactions in the barrel cortex of rats. J. Neurosci. *20*, 6241–6248.

Shoham, D., Glaser, D.E., Arieli, A., Kenet, T., Wijnbergen, C., Toledo, Y., Hildesheim, R., and Grinvald, A. (1999). Imaging cortical dynamics at high spatial and temporal resolution with novel blue voltage-sensitive dyes. Neuron *24*, 791–802.

Simon, P., Dupuis, R., and Costentin, J. (1994). Thigmotaxis as an index of anxiety in mice. Influence of dopaminergic transmissions. Behav. Brain Res. *61*, 59–64.

Simons, D.J. (1978). Response properties of vibrissa units in rat SI somatosensory neocortex. J. Neurophysiol. *41*, 798–820.

Simons, D.J. (1985). Temporal and spatial integration in the rat SI vibrissa cortex. J Neurophysiol *54*, 615–635.

Simons, D.J., and Carvell, G.E. (1989). Thalamocortical response transformation in the rat vibrissa/barrel system. J. Neurophysiol. *61*, 311–330.

Squarzoni, P., Oller, G., Hoeffel, G., Pont-Lezica, L., Rostaing, P., Low, D., Bessis, A., Ginhoux, F., and Garel, S. (2014). Microglia Modulate Wiring of the Embryonic Forebrain. Cell Rep. *8*, 1271–1279.

Squarzoni, P., Thion, M.S., and Garel, S. (2015). Neuronal and microglial regulators of cortical wiring: usual and novel guideposts. Front. Neurosci. *9*, 248.

Sreenivasan, V., Esmaeili, V., Kiritani, T., Galan, K., Crochet, S., and Petersen, C.C.H. (2016). Movement Initiation Signals in Mouse Whisker Motor Cortex. Neuron *92*, 1368–1382.

Sun, Q.-Q., Huguenard, J.R., and Prince, D.A. (2006). Barrel cortex microcircuits: thalamocortical feedforward inhibition in spiny stellate cells is mediated by a small number of fast-spiking interneurons. J. Neurosci. *26*, 1219–1230.

Tan, Z., Hu, H., Huang, Z.J., and Agmon, A. (2008). Robust but delayed thalamocortical activation of dendritic-targeting inhibitory interneurons. Proc. Natl. Acad. Sci. U. S. A. *105*, 2187–2192.

Taniguchi, H., He, M., Wu, P., Kim, S., Paik, R., Sugino, K., Kvitsani, D., Fu, Y., Lu, J., Lin, Y., et al. (2011). A Resource of Cre Driver Lines for Genetic Targeting of GABAergic Neurons in Cerebral Cortex. Neuron *71*, 995–1013.

Tasic, B., Menon, V., Nguyen, T.N., Kim, T.K., Jarsky, T., Yao, Z., Levi, B., Gray, L.T., Sorensen, S.A., Dolbeare, T., et al. (2016). Adult Mouse Cortical Cell Taxonomy by Single Cell Transcriptomics. Nat. Neurosci. *19*, 335.

Thibault, K., Rivière, S., Lenkei, Z., Férézou, I., and Pezet, S. (2016). Orofacial neuropathic pain leads to a hyporesponsive barrel cortex with enhanced structural synaptic plasticity. PLoS One.

Tremblay, R., Lee, S., and Rudy, B. (2016). GABAergic Interneurons in the Neocortex: From Cellular Properties to Circuits. Neuron *91*, 260–292.

Tsodyks, M., Kenet, T., Grinvald, A., and Arieli, A. (1999). Linking spontaneous activity of single cortical neurons and the underlying functional architecture. Science *286*, 1943–1946.

Urbain, N., and Deschenes, M. (2007). A New Thalamic Pathway of Vibrissal Information Modulated by the Motor Cortex. J. Neurosci. *27*, 12407–12412.

Veinante, P., and Deschênes, M. (1999). Single- and multi-whisker channels in the ascending projections from the principal trigeminal nucleus in the rat. J. Neurosci. *19*, 5085–5095.

Veinante, P., Jacquin, M.F., and Deschenes, M. (2000a). Thalamic Projections From the Whisker- Sensitive Regions of the Spinal Trigeminal Complex in the Rat 1. J. Comp. Neurol. *243*, 233–243.

Veinante, P., Lavallée, P., and Deschênes, M. (2000b). Corticothalamic projections from layer 5 of the vibrissal barrel cortex in the rat. J. Comp. Neurol. *424*, 197–204.

Vilarchao, M.E., Estebanez, L., Shulz, D.E., and Férézou, I. (2018). Supra-barrel Distribution of Directional Tuning for Global Motion in the Mouse Somatosensory Cortex. Cell Rep. *22*, 3534–3547.

Vitalis, T., and Rossier, J. (2011). New insights into cortical interneurons development and classification: Contribution of developmental studies. Dev. Neurobiol. *71*, 34–44.

Voigts, J., Herman, D.H., and Celikel, T. (2015). Tactile object localization by anticipatory whisker motion. J. Neurophysiol. *113*, 620–632.

Voisin, D.L., Doméjean-Orliaguet, S., Chalus, M., Dallel, R., and Woda, A. (2002). Ascending connections from the caudal part to the oral part of the spinal trigeminal nucleus in the rat. Neuroscience *109*, 183–193.

Vucurovic, K., Gallopin, T., Ferezou, I., Rancillac, A., Chameau, P., Van Hooft, J.A., Geoffroy, H., Monyer, H., Rossier, J., and Vitalis, T. (2010). Serotonin 3A receptor subtype as an early and protracted marker of cortical interneuron subpopulations. Cereb. Cortex *20*, 2333–2347.

Welker, E., Hoogland, P. V, and Van der Loos, H. (1988). Organization of feedback and feedforward projections of the barrel cortex: a PHA-L study in the mouse. Exp. Brain Res. *73*, 411–435.

Whishaw, I.Q., and Kolb, B. (2005). The behavior of the laboratory rat : a handbook with tests (Oxford University Press).

Wonders, C.P., and Anderson, S.A. (2006). The origin and specification of cortical interneurons. Nat. Rev. Neurosci. *7*, 687–696.

Woolsey, T.A., and Van der Loos, H. (1970). The structural organization of layer IV in the somatosensory region (SI) of mouse cerebral cortex. The description of a cortical field composed of discrete cytoarchitectonic units. Brain Res. *17*, 205–242.

Xu, Y., Zou, P., and Cohen, A.E. (2017). Voltage imaging with genetically encoded indicators. Curr. Opin. Chem. Biol. *39*, 1–10.

Yamashita, T., and Petersen, C.C.H. (2016). Target-specific membrane potential dynamics of neocortical projection neurons during goal-directed behavior. Elife *5*.

Yamashita, T., Pala, A., Pedrido, L., Kremer, Y., Welker, E., and Petersen, C.C.H. (2013). Membrane potential dynamics of neocortical projection neurons driving target-specific signals. Neuron *80*, 1477–1490.

Yu, C., Derdikman, D., Haidarliu, S., and Ahissar, E. (2006). Parallel Thalamic Pathways for Whisking and Touch Signals in the Rat. PLoS Biol. *4*.

Zeisel, A., Manchado, A.B.M., Codeluppi, S., Lonnerberg, P., La Manno, G., Jureus, A., Marques, S., Munguba, H., He, L., Betsholtz, C., et al. (2015). Cell types in the mouse cortex and hippocampus revealed by single-cell RNA-seq. Science (80-.). *347*, 1138–1142.

Zhang, Y., Bonnan, A., Bony, G., Ferezou, I., Pietropaolo, S., Ginger, M., Sans, N., Rossier, J., Oostra, B., LeMasson, G., et al. (2014). Dendritic channelopathies contribute to neocortical and sensory hyperexcitability in Fmr1−/y mice. Nat. Neurosci. *17*, 1701–1709.

Zhu, J.J., and Connors, B.W. (1999). Intrinsic Firing Patterns and Whisker-Evoked Synaptic Responses of Neurons in the Rat Barrel Cortex. J. Neurophysiol. *81*, 1171–1183.

Zuo, Y., Safaai, H., Notaro, G., Mazzoni, A., Panzeri, S., and Diamond, M.E. (2015). Complementary contributions of spike timing and spike rate to perceptual decisions in rat S1 and S2 cortex. Curr. Biol. *25*, 357–363.

Troisième partie : Curriculum Vitae

Née le : 5 février 1978 à Palaiseau (91) - Nationalité française – Pacsée, deux enfants.

Adresse personnelle :
1 impasse de l'Aleu
91 440 Bures sur Yvette
Tél. : 06 75 41 68 25

Adresse professionnelle :
Unité de Neurosciences Information et Complexité (UNIC CNRS FRE 3693). Bât 32/33.
1 avenue de la Terrasse, 91198 Gif sur Yvette.
Tél. : 01 69 82 34 02 / Fax. : 01 69 82 34 27
email : isabelle.ferezou@unic.cnrs-gif.fr
https://www.unic.cnrs-gif.fr

1. Situation actuelle

Chargée de Recherche (CRCN CNRS) – Equipe Traitement sensoriel, neuromodulation et plasticité neuronale Dirigée par **Daniel Shulz** au sein de l'Unité de Neurosciences Information et Complexité (UNIC CNRS FRE 3693) dirigée par **Daniel Shulz**, Gif-sur-Yvette, France.

2. Parcours au sein du CNRS

2017 - Changement de grade : CR1 vers CRCN.

2013 - Changement de section : passage de la section 26 à la section 25 : Neurobiologie moléculaire et cellulaire, neurophysiologie.

2012 - Changement de grade : CR2 vers CR1.

2011 - **Mobilité** - affectation à l'Unité de Neurosciences Information et Complexité (UNIC), CNRS UPR 3293 (Gif-sur-Yvette) dirigée par le Pr. Yves Fregnac (au sein de l'équipe : « Traitement sensoriel, neuromodulation et plasticité neuronale » dirigée par le Dr. Daniel Shulz) et rattachement à la section 26 : Cerveau, cognition et comportement.

2009 - **Titularisation** (Laboratoire de Neurobiologie de l'ESPCI ParisTech, CNRS UMR 7637, Paris, dirigé par le Dr. Serge Birman) au sein de l'équipe « Physiologie des Interneurones du Néocortex» dirigée par le Pr. Jean Rossier.

2008 - **Recrutement** en tant que Chargée de Recherche 2ème Classe (CR2) au sein du CNRS (classée première en section 25 et deuxième en section 24) – Rattachement à la section 24 : Interactions cellulaires et affectation au Laboratoire de Neurobiologie et Diversité Cellulaire de l'Ecole Supérieure de Physique et de Chimie Industrielles de la ville de Paris (ESPCI ParisTech), CNRS UMR 7637 (Paris) dirigé par le Pr. Jean Rossier (au sein de l'équipe « Physiologie des Interneurones du Néocortex» dirigée par le Pr. Jean Rossier).

3. Post-doctorat

2004-2007- Post-doctorat : *Étude du traitement cortical de l'information sensorielle par imagerie sensible au potentiel chez l'animal éveillé.* Laboratory of Sensory Processing, Brain Mind Institute, École Polytechnique Fédérale de Lausanne, Suisse. Direction : Pr. Carl Petersen.

4. Formations complémentaires

2014 - Formation proposée par la délégation Ile de France Sud du CNRS : **Accompagner et encadrer un projet doctoral** (2 journées + 1 journée de retour sur expérience).

2009 - Formation pour la qualification des personnels appelés à pratiquer la **chirurgie** sur animaux vivants (rongeurs) de laboratoire (agrément n° I-63IUTCIFd-Chir-07).

2008 - Stage de formation spéciale à **l'expérimentation animale** pour les cadres biologistes de Niveau 1 (enregistrée sous le numéro : R-45GRETA-F1-04).

2005 - Cours de formation à **l'expérimentation animale**, Centre Hospitalier Universitaire Vaudois, Lausanne, Suisse.

5. Titres Universitaires

2003 - Thèse de Doctorat en Neurosciences (mention très honorable), Université Paris VI : *Étude des propriétés fonctionnelles d'une population d'interneurones GABAergiques inhibiteurs du néocortex*. Laboratoire de Neurobiologie et Diversité Cellulaire (CNRS UMR 7637), École Supérieure de Physique et de Chimie Industrielles, Paris. Direction : Pr. Jean Rossier et Dr. Bertrand Lambolez.

2000 - DEA de Neurosciences (obtention d'une allocation de recherche MENRT), Université Paris VI : *Enzymes du métabolisme du monoxyde d'azote dans le cortex cérébelleux de rat : localisation cellulaire et données nouvelles sur la cellule candélabre.* Laboratoire de Neurobiologie du Cervelet, Université Paris VI. Direction : Dr. Herbert Axelrad.

1999 - Maîtrise de Biochimie, option Physiologie Animale (mention bien), Université Paris XI.

1998 - Licence de Biochimie (mention bien), Université Paris XI.

1997 - DEUG de Sciences de la Vie (mention assez bien), Université Paris XI.

1995 - Baccalauréat série S, spécialité Physique-Chimie (mention assez bien), Orsay (91).

6. Activités d'enseignement

2015 – 20.. - Cours de Master 2 : ImaLiS - ENS Paris - UE "Optical microscopy: principles and applications to Neuroscience" - 1,5 heures/an. Signalisation Cellulaire ; Neurosciences – UPsud – UE "Perception"– 3 heures/an.

2014 – 2017 - Cours de Master 1 : Master Biologie Intégrative et Physiologie – UPMC – UE 4B019 "Neurophysiologie Intégrative" – 3 heures/an.

2013 - 20.. - **TD de Master 1** : "Biologie et Santé", spécialité "Signalisation cellulaire - UPsud - Neurosciences" - UE : "Neuroscience Intégrative" – 1 à 3 heures/an.

2009-2014 - **Préceptorats** de Physiologie pour les élèves de deuxième année de l'École Supérieure de Physique et de Chimie Industrielles de Paris (ESPCI ParisTech) – 12 heures/an.

2008-2013 - **Cours de Master 2** : Master Biologie Intégrative et Physiologie – UPMC – UE NB045 "Réseaux neuronaux : "Traitement et représentation de l'information" – 3 heures/an.

2009-2010 – **Cours de Master 2** : Master Signalisation Cellulaire ; Neurosciences – UPsud – UE "Perception"– **2 heures/an**.

2008 - Cours : L3 Biologie ENS Paris. 3 heures.

2007-2008 - **Préceptorats** de Biologie pour les élèves de première année de l'ESPCI ParisTech – 16 heures/an.

2006 - Encadrement de 6 participants au : « Programme of European Neuroscience Schools Training Center: Imaging Brain Function: From Molecules to Mind » au cours des deux semaines de projet expérimental.

2004 - **Préceptorat** de Physiologie pour les élèves de deuxième année de l'ESPCI ParisTech – 10 heures/an.

2002 – **Travaux Pratiques de Maîtrise** de Biologie Cellulaire et Physiologie de l'Université Paris XII dans le cadre du certificat de Physiologie Moléculaire (80 heures).

7. Activités liées à l'administration

- Membre du **comité opérationnel de l'animalerie** de Gif sur Yvette (2012-2014). Ce comité s'inscrivait comme une structure de soutien au fonctionnement de l'animalerie. Son but était de faciliter la prise en charge quotidienne de l'animalerie dans la gestion du personnel, les demandes de financement, l'organisation du travail. Il a aidé à la mise en place des mesures nécessaires au respect de la nouvelle réglementation issue de la transposition de la directive européenne 2010/63/UE relative à la protection des animaux utilisés à des fins scientifiques.

- Participation à des **groupes de travail** «analyse fonctionnelle» (groupe animalerie et biochimie/biologie moléculaire) et «analyse systèmes» (groupe animalerie) dans le cadre de la réalisation du cahier des charges fonctionnel du futur bâtiment de Neurosciences à Saclay (2012).

- Participation à un **comité de sélection** de l'Université Pierre et Marie Curie (2010) pour un poste de Maître de Conférences.

- Participation au **conseil scientifique** de l'UMR 7637 Laboratoire de Neurobiologie de l'ESPCI ParisTech (2009-2011) en tant que co-représentante élue de l'équipe « Physiologie des Interneurones du Néocortex ».

8. Activités liées à la recherche

- Participation, en tant qu'examinatrice, aux **Jurys de thèse** de Pierre Le Merre (Université Claude Bernard Lyon 1 - 16/12/2016), d'Alexandre Moreau (Université Paris Sud, 11/12/2009) et de Julie Le Cam-Erraud (Université Pierre et Marie Curie) – 23/09/2010.

- Participation à des **comités de lecture** pour les revues internationales suivantes : Nature, Scientific Reports, Journal of Neurophysiology, Cerebral Cortex, European Journal of Neuroscience, Journal of

Neuroscience Research, Plos One, Neuroscience Letters, Learning & Memory, Journal of Physiology (Paris).

- Implication dans des **contrats de recherche** :

- Partenaire d'un contrat **ANR Projet de recherche collaboratif 2017**: EXPECT à hauteur de **228 k€**. *Computation corticale de l'attente de stimuli tactiles hautement prédictibles.*
- Partenaire d'une labellisation "Equipe FRM" 2017: Interface cerveau-machine à boucle fermée: intégration d'un retour sensoriel biomimétique à une neuroprothèse motrice. Financement total : **390 k€**.
- Partenaire d'une Initiative de Recherche Stratégique 2016: **BRAINSCOPES** Multiscale dissection of the structure and function of the nervous system through novel imaging techniques, à hauteur de **100k€**. *Fibroscopy for large scale imaging of cortical interactions during active sensing.*
- Partenaire d'un Projet « Mi lourds » Région Ile de France (DIM Nano-K), à hauteur de **45 k€**: **NEUROFIB** Microscopie bi-photonique fibrée pour l'optogénétique et l'endoscopie : des neurosciences à l'imagerie médicale.
- Coordination d'un contrat **ANR Programme Jeunes Chercheuses Jeunes Chercheurs** (JCJC) 2011: **SENSORY PROCESSING** - (Projet ANR 11-JSV4-004-1, 01/01/2012 - 31/12/2014 208 k€). *Modulation cholinergique du traitement cortical de l'information sensorielle tactile : couplage de l'imagerie fonctionnelle à l'optogénétique.*

9. Activités d'encadrement

2018 - ... - Co-Encadrement (95 %) du **doctorat** de Timothé Jost-Mousseau (ED n°158, "Cerveau-Cognition-Comportement", Sorbonne Université) avec Daniel Shulz (UNIC). Projet : *Etude de l'intégration corticale de stimulations sensorielles tactiles complexes chez la souris en comportement.*

2017 - ... - Co-Encadrement (50 %) du **doctorat** de Sophie Hubatz (ED 474 "Frontières du Vivant", Paris Sciences et Lettres) avec Laurent Bourdieu (IBENS). Projet : *Bases neuronales de l'attente de stimuli tactiles prédictibles, étude par imagerie optique du cortex cérébral et inférence de la connectivité fonctionnelle.*

2016/2017 - Encadrement d'une étudiante de **Master 2** – Sophie Hubatz (Master BioMedical Engineering, Paris). Titre du mémoire: Functional role of the secondary somatosensory cortex in the processing of complex tactile scenes: A voltage sensitive dye imaging study.

2011-2015 – Co-Encadrement (95 %) du **doctorat** d'Eugenia Vilarchao (ED 474 Frontières du Vivant, Université Paris Descartes) avec Daniel Shulz (UNIC). Titre de la thèse : Spatiotemporal properties of sensory integration in the mouse barrel cortex.

Publications associées : *Perronnet L*, Vilarchao ME*, Hucher G, Shulz DE, Peyré G, Ferezou I. An automated workflow for the anatomo-functional mapping of the barrel cortex. J Neurosci Methods. 2016 263:145-54. Vilarchao ME, Estebanez L, Shulz DE*, Ferezou I*. Supra-barrel distribution of directional tuning for global motion in the mouse somatosensory cortex. Cell Rep. 2018 Mar 27;22(13):3534-3547. *contrubion égale au travail.*

2015 – Encadrement d'une étudiante de **Master 2** – Juliette Blondy (Master Biologie Intégrative et Physiologie de l'Université Paris VI). Titre du mémoire : *Modulation cholinergique du traitement cortical de l'information sensorielle tactile : couplage de l'imagerie fonctionnelle à l'optogénétique*.

2014 - Encadrement d'un étudiant de **Master 2** – Matthias Billaud (Master Biologie Intégrative et Physiologie de l'Université Paris VI). Titre du mémoire : *Réactivation de patterns d'activité corticale induits par des stimuli tactiles complexes, investigation par imagerie sensible au potentiel chez la souris*.

2013 - Co−encadrement (50 %) d'une étudiante en **Master 2** - Lorraine Perronnet (Master Mathématiques, vision, apprentissage (MVA) de l'Ecole Normale Supérieure de Cachan) avec Gabriel Peyré (ENS). Titre du mémoire : *Reconstruction of the mouse barrel cortex from histological sections.*

Publication associée : Perronnet, Vilarchao et al., 2015 (voir plus haut).

2012 - Encadrement d'une étudiante en **Master 1** - Pauline Kerekes (Magistère de Biologie et Biotechnologie de l'Université Paris XI). Titre du mémoire : *Développement d'une approche optogénétique pour l'étude de la modulation cholinergique du traitement cortical de l'information sensorielle tactile*.

2010-2011 - Co−encadrement (50 %) d'un étudiant de **Master 2** - Sébastien Rivière (Master Biologie Intégrative et Physiologie de l'Université Paris VI) avec Sophie Pezet.

Publication associée : Un article en « co-dernier auteur » en cours de préparation : *Molecular and functional cortical plasticity in a model of orofacial neuropathic pain in mice*.

2010 - Encadrement d'une élève de l'ESPCI ParisTech - Alice Gaudin (pour son stage obligatoire de 3ème année). Titre du mémoire : La sonde VSFP2.3 : *Mise au point d'une technique d'injection et validation par imagerie fonctionnelle de son fonctionnement chez la souris WT et la souris PV-CRE*.

2010 - Encadrement de deux élèves de troisième année de l'ESPCI ParisTech - Romain Dubreuil et Victor Delattre - pour la réalisation d'un projet dans le cadre du module : « Echelles d'Espace et de Temps ».

2010 - Encadrement d'une élève de première année de l'ESPCI ParisTech – Célia Amabile – pour un stage optionnel d'un mois en fin de première année.

10. Liste des productions scientifiques

10.1. Publications dans des revues internationales à comité de lecture

1. Vilarchao ME, Estebanez L, Shulz DE, **Férézou I**.
   Supra-barrel Distribution of Directional Tuning for Global Motion in the Mouse Somatosensory Cortex.
   Cell Rep. 2018 Mar 27;22(13):3534-3547.
2. Estebanez L, **Férézou I**, Ego-Stengel V, Shulz DE. Representation of tactile scenes in the rodent barrel cortex.
   Neuroscience. 2018, 368:81-94.
3. **Ferezou I**, Deneux T.
   Review: How do spontaneous and sensory-evoked activities interact?
   Neurophotonics. 2017,4(3):031221.

4. Raguet H, Monier C, Foubert L, **Ferezou I**, Fregnac Y, Peyré G.
Spatially Structured Sparse Morphological Component Separation for voltage-sensitive dye optical imaging.
J Neurosci Methods. 2016, 257:76-96.
5. Perronnet L*, Vilarchao ME*, Hucher G, Shulz DE, Peyré G, **Ferezou I**.
*Ces auteurs ont contribué de manière égale à ce travail.
An automated workflow for the anatomo-functional mapping of the barrel cortex.
J Neurosci Methods. 2016, 263:145-54
6. Thibault K, Rivière S, Lenkei Z, **Férézou I***, Pezet S*.

*Ces auteurs ont contribué de manière égale à ce travail.

Orofacial Neuropathic Pain Leads to a Hyporesponsive Barrel Cortex with Enhanced Structural Synaptic Plasticity.

PLoS One. 2016, 11(8):e0160786.
7. Magnain C, Castel A, Boucneau T, Simonutti M, **Ferezou I**, Rancillac A, Vitalis T, Sahel JA, Paques M, Atlan M.
Holographic laser Doppler imaging of microvascular blood flow.
J Opt Soc Am A Opt Image Sci Vis. 2014, 31(12):2723-35.
8. Zhang Y, Bonnan A, Bony G, **Ferezou I**, Pietropaolo S, Ginger M, Sans N, Rossier J, Oostra B, LeMasson G, Frick A.
Dendritic channelopathies contribute to neocortical and sensory hyperexcitability in Fmr1(-/y) mice.
Nat Neurosci. 2014, 17(12):1701-9.
9. Narboux-Nême N, Evrard A, **Ferezou I**, Erzurumlu RS, Kaeser PS, Lainé J, Rossier J, Ropert N, Südhof TC, Gaspar P.

Neurotransmitter release at the thalamocortical synapse instructs barrel formation but not axon patterning in the somatosensory cortex.

J Neurosci. 2012, 32(18):6183-96.
10. Perrenoud Q, Rossier J, **Férézou I**, Geoffroy H, Gallopin T, Vitalis T, Rancillac A.

Activation of cortical 5-HT(3) receptor-expressing interneurons induces NO mediated vasodilatations and NPY mediated vasoconstrictions.

Front Neural Circuits. 2012; 6:50.
11. Vucurovic K*, Gallopin T*, **Ferezou I***, Rancillac A, Chameau P, van Hooft JA, Geoffroy H, Monyer H, Rossier J, Vitalis T.

Serotonin 3A receptor subtype as an early and protracted marker of cortical interneuron subpopulations.

Cereb Cortex. 2010, 20(10):2333-47.

* Ces auteurs ont contribué de manière égale à ce travail.
12. Rancillac A, Lainé J, Perrenoud Q, Geoffroy H, **Ferezou I**, Vitalis T, Rossier J.

Degenerative abnormalities in transgenic neocortical neuropeptide Y interneurons expressing tau-green fluorescent protein.

J Neurosci Res. 2010, 88(3):487-99.
13. Lebeuf R, **Férézou I**, Rossier J, Arseniyadis S, Cossy J.

Straightforward synthesis of the near-infrared fluorescent voltage-sensitive dye RH1691 and analogues thereof.

Org Lett. 2009 Nov 5;11(21):4822-5.

14. **Ferezou I**, Haiss F, Gentet L, Aronoff R, Weber B, Petersen CCH.

    Spatiotemporal dynamics of cortical sensorimotor integration in behaving mice.

    Neuron. 2007, 56(5):907-923.

    Cet article a fait l'objet d'un commentaire dans Neuron (Kleinfeld D, Waters J. Wilder Penfield in the Age of YouTube: Visualizing the Sequential Activation of Sensorimotor Areas across Neocortex. Neuron. 2007 56(5):760-2).

15. **Ferezou I**, Hill EL, Cauli B, Gibelin N, Kaneko T, Rossier J, Lambolez B.

    Extensive Overlap of μ-Opioid and Nicotinic Sensitivity in Cortical Interneurons.

    Cereb Cortex. 2007, 17(8):1948-57.

16. Berger T, Borgdorff A, Crochet S, Neubauer FB, Lefort S, Fauvet B, **Ferezou I**, Carleton A, Lüscher HR, Petersen CCH.

    Combined voltage and calcium epifluorescence imaging in vitro and in vivo reveals subthreshold and suprathreshold dynamics of mouse barrel cortex.

    J Neurophysiol. 2007, 97(5):3751-62.

17. Hill EL, Gallopin T, **Ferezou I**, Cauli B, Rossier J, Schweitzer P, Lambolez B.

    Functional CB1 receptors are broadly expressed in neocortical GABAergic and glutamatergic neurons.

    J Neurophysiol. 2007, 97(4):2580-9.

18. **Ferezou I**, Bolea S, Petersen CCH.

    Visualising the cortical representation of whisker touch: voltage-sensitive dye imaging in freely moving mice.

    Neuron. 2006, 50(4):617-29.

    Cet article a fait l'objet d'un Commentaire dans Neuron (Curtis JC, Kleinfeld D. Seeing what the mouse sees with its vibrissae: a matter of behavioral state. Neuron. 2006 50(4):524-6) et d'un "Research highlight" dans Nature (A touching story. Nature. 2006 441:552-553).

19. **Ferezou I**, Cauli B, Hill E, Rossier J, Hamel E, Lambolez B.

    5-HT3 receptors mediate serotonergic fast synaptic excitation of neocortical VIP/CCK interneurons.

    J Neurosci. 2002, 22(17):7389–7397.

10.2. Autres publications

Article de conférence

Puyo L, **Ferezou I**, Rancillac A, Simonutti M, Paques M, Sahel JA, Fink M, and Atlan M. (2015) Pulsatile microvascular blood flow imaging by short-time Fourier transform analysis of ultrafast laser holographic interferometry. BMEiCON 2015 – 8th Biomedical Engineering International Conference.

Publication invitée

Férézou I. Combien de neurones pour une sensation ? *Médecine/Sciences (Paris)*. 2008, 24(10):802-4.

10.3. Chapitres d'Ouvrage

1. Crochet S, **Ferezou I**, Petersen CCH.
   Spontaneous activity in the rodent primary somatosensory cortex. Dans : "Mechanisms of spontaneous active states in the neocortex". Editions : Research Signpost (Kerala, India). Editeur en Chef: Igor Timofeev. ISBN 81-308-0175-2.
2. **Ferezou I**, Matyas F, Petersen CCH.
   Imaging the brain in action - real-time voltage-sensitive dye imaging of sensorimotor cortex of awake behaving mice. Dans : "In vivo optical imaging of brain function" édité par Ron Frostig. Editions : CRC Press (Boca Raton, USA), 2009.

10.4. Communications orales dans le cadre de congrès internationaux

1. Global tactile information processing in the mouse somatosensory cortex at the mesoscopic scale. NeuroFrance (Bordeaux 2017).
2. Real time voltage sensitive dye imaging of cortical spatiotemporal dynamics evoked by tactile sensory inputs in mice. International Workshop: Network dynamics at mesoscopic scales (Marseille, 2015).
3. Visualising the cortical representation of whisker touch: voltage-sensitive dye imaging in freely moving mice. 2nd Swiss Meeting on Cellular & Molecular Neurobiology of Mental Diseases (Giessbach, Suisse, 2006).
4. Visualising the cortical representation of touch: voltage-sensitive dye imaging of barrel cortex spatiotemporal dynamics in freely moving mice. EMBO Workshop: The Assembly and Function of Neuronal Circuits (Ascona, Suisse, 2005).
5. Extensive overlap of nicotinic and μ-opioid signaling in cortical interneurons. International Narcotics Research Conference, Abstr O VIII-3 (Perpignan, France, 2003).

10.5. Communications orales dans le cadre de congrès nationaux

1. Voltage-sensitive dye imaging of cortical dynamics in awake mice. 9e Colloque de la Société des Neurosciences (Bordeaux, France, 2009).
2. Le traitement cortical de l'information sensorielle tactile, visualisation en temps réel par imagerie sensible au potentiel chez la souris éveillée. Congrès de Physiologie de Pharmacologie et de Thérapeutique (Marseille, France, 2009).

10.6. Séminaires invités

1. Voltage-sensitive dye imaging of cortical dynamics in mice. Séminaire donné sur invitation au laboratoire de Physiologie intégrée du système d'éveil INSERM/UCBL-U628 (Lyon, France, 2010).
2. Voltage-sensitive dye imaging of cortical dynamics in awake mice. Séminaire donné dans le cadre du "Cercle des imageurs" de l'Ecole Normale Supérieure (Paris, France, 2007), et sur invitation à l'Institut de Biologie Animale Intégrative et Cellulaire de l'Université Paris Sud (Orsay, France, 2007) et à l'Institut du Fer à Moulin (Paris, France, 2007).
3. Neocortical interneurons integrate multiple neurotransmission pathways. Séminaire donné sur invitation à l'Institut de Physiologie de l'Université de Marburg (Marburg, Allemagne 2003), à l'École Polytechnique Fédérale de Lausanne (Lausanne, Suisse, 2003) et au Collège Universitaire de Londres (UCL, Londres, 2003).

4. Intégration des voies sérotoninergique, cholinergique et opioïdergique par les interneurones néocorticaux. Journée de l'IFR de Biologie Intégrative (IFR83, Paris, France, 2003).

10.7. Communications affichées dans le cadre de congrès internationaux

1. Vilarchao ME, Shulz DE, **Ferezou I**. Direction selectivity in the mouse barrel cortex, a voltage sensitive dye (VSD) imaging study. Barrels XXVI (La Jolla, CA, USA, 2013).
2. Vilarchao ME, Shulz DE, **Ferezou I**. Direction selectivity in the mouse barrel cortex, a voltage sensitive dye (VSD) imaging study. Society for Neuroscience, Abstr. 465.10 (San Diego, CA, USA, 2013).
3. **Ferezou I**, Bolea S, Petersen CCH. Voltage-sensitive dye imaging of cortical dynamics in awake mice. Barrels XIX (Atlanta GA, USA, 2006).
4. **Ferezou I**, Bolea S, Crochet S, Petersen CCH. Voltage-sensitive dye imaging of cortical dynamics in awake mice. Society for Neuroscience, Abstr. 53.9 (Atlanta GA, USA, 2006).
5. **Ferezou I**, Bolea S, Petersen CCH. Visualizing the cortical representation of touch: voltage-sensitive dye imaging of barrel cortex spatiotemporal dynamics in freely moving mice. Cold Spring Harbor Meeting: Imaging Neurons & Neural Activity: new methods, new results (Cold Spring Harbor NY, USA, 2005).
6. **Ferezou I**, Bolea S, Petersen CCH. Voltage-sensitive dye imaging of cortical spatiotemporal dynamics in freely moving mice. USGEB-SSN-SSBP Meeting (Zurich, Suisse, 2005).
7. **Ferezou I**, Hill E, Cauli B, Gibelin N, Rossier J, Lambolez B. A cellular mechanism for the involvement of μ-opioid receptor in nicotine addiction. Society for Neuroscience, Abstr. 890.1 (New Orleans, USA, 2003).
8. **Ferezou I**, Cauli B, Hill E, Rossier J, Hamel E, Lambolez B. 5-HT3 Receptors mediate serotonergic fast synaptic excitation of neocortical VIP/CCK interneurons. Society for Neuroscience, Abstr. 38.2 (Orlando, USA, 2002).
9. Hill E, Cepeda C, **Ferezou I**, Cauli B, Rossier J, Lambolez B. Two subtypes of cortical excitatory neurons express the vesicular glutamate transporter VGLUT1. Society for Neuroscience, Abstr. 343.3 (Orlando, USA, 2002).
10. **Ferezou I**, Cauli B, Hill E, Rossier J, Hamel E, Lambolez B. Serotonergic synaptic excitation of neocortical VIP/CCK interneurons mediated by 5–HT3 receptors. Federation of European Neuroscience Societies, Abstr. 015.15 (Paris, France, 2002).
11. Cauli B, **Ferezou I**, Hill E, Rossier J, Lambolez B. D-Ala2,N-MePhe4,Gly5-ol-enkephalin (DAMGO), a μ-opioid receptor agonist, selectively inhibits a subset of neocortical interneurons expressing vasoactive intestinal peptide (VIP). Federation of European Neuroscience Societies, Abstr. 178.2 (Paris, France, 2002).
12. Hill E, Cepeda C, **Ferezou I**, Cauli B, Rossier J, Lambolez B. Two subtypes of cortical excitatory neurons express the vesicular glutamate transporter VGLUT1. Federation of European Neuroscience Societies, Abstr. 217.12 (Paris, France, 2002).
13. **Ferezou I**, Cauli B, Rossier J, Lambolez B. D-Ala2,N-MePhe4,Gly5-ol-enkephalin (DAMGO), a μ-opioid receptor agonist, selectively inhibits a subset of neocortical interneurons. Society for Neuroscience, Abstr. 37.2 (San-Diego, USA, 2001).
14. Cauli B, **Ferezou I**, Rossier J, Lambolez B. Selective excitation by 5–HT3 receptors of subtypes of interneurons in the rat neocortex. Society for Neuroscience, Abstr. 459.7 (San-Diego, USA 2001).

10.8. Communications affichées dans le cadre de congrès nationaux

1. Vilarchao ME, Sulz DE**, Ferezou I**. Representation of global motion in the mouse barrel cortex. Société des Neurosciences (Montpellier, France, 2015).
2. Shulz DE, Vilarchao E, **Ferezou I**. Direction selectivity in the mouse barrel cortex, a voltage sensitive dye (VSD) imaging study. Société des Neurosciences (Lyon-Grenoble, France, 2013).
3. **Ferezou I**, Hill E, Cauli B, Gibelin N, Rossier J, Lambolez B. Expression sélective des récepteurs opioïdes de type μ au sein d'une population d'interneurones GABAergiques néocorticaux, mise en évidence et conséquences fonctionnelles. Société des Neurosciences (Rouen, France, 2003).
4. **Ferezou I**, Axelrad H, Lainé J, Marc M.E, O'Brien W.E, Wiesinger H. Localisation cellulaire de l'argininosuccinate synthétase (ASS) dans le cortex cérébelleux de rat. Société des Neurosciences (Toulouse, France, 2000).

Annexes

1. Sélection de 10 publications (revues à comité de lecture)

2. Résumés des autres publications (revues à comité de lecture)

Article

Cell Reports

Supra-barrel Distribution of Directional Tuning for Global Motion in the Mouse Somatosensory Cortex

Graphical Abstract

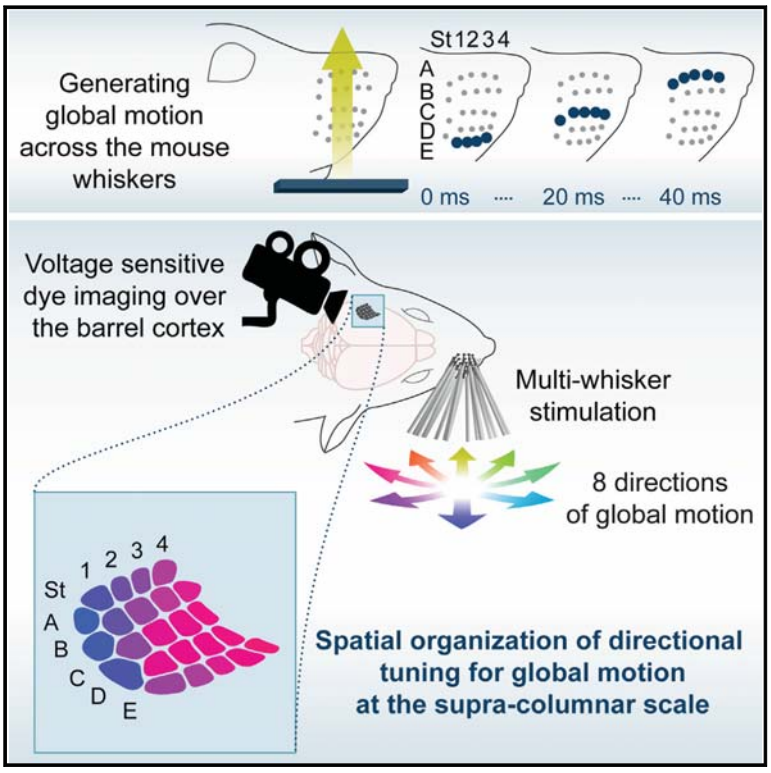

Highlights

- Multi-whisker stimuli generating global motions activate the entire barrel cortex
- Responses are sublinear and depend upon the direction of the global motion
- Overall, the barrel cortex responds preferentially to caudo-ventral global motions
- Directional tuning for global motion varies gradually over the barrel map

Authors

María Eugenia Vilarchao, Luc Estebanez, Daniel E. Shulz, Isabelle Férézou

Correspondence

daniel.shulz@unic.cnrs-gif.fr (D.E.S.), isabelle.ferezou@unic.cnrs-gif.fr (I.F.)

In Brief

Using voltage-sensitive dye imaging of the mouse barrel cortex, Vilarchao et al. demonstrate the presence of direction selectivity to global motion generated by multi-whisker stimuli. Selectivity to global motion is spatially organized at the supra-columnar scale with an overrepresentation of selectivity to caudo-ventral directions.

Vilarchao et al., 2018, Cell Reports *22*, 3534–3547
March 27, 2018
https://doi.org/10.1016/j.celrep.2018.03.006

CellPress

OPEN ACCESS
CellPress

Cell Reports
Article

Supra-barrel Distribution of Directional Tuning for Global Motion in the Mouse Somatosensory Cortex

María Eugenia Vilarchao,[1,2] Luc Estebanez,[1] Daniel E. Shulz,[1,*] and Isabelle Férézou[1,3,*]
[1]Unité de Neurosciences, Information et Complexité, Centre National de la Recherche Scientifique, FRE 3693, 91198 Gif-sur-Yvette, France
[2]Present address: Laboratory for Perception and Memory, Institut Pasteur and Centre National de la Recherche Scientifique, UMR 3571, 75015 Paris, France
[3]Lead Contact
*Correspondence: daniel.shulz@unic.cnrs-gif.fr (D.E.S.), isabelle.ferezou@unic.cnrs-gif.fr (I.F.)
https://doi.org/10.1016/j.celrep.2018.03.006

SUMMARY

Rodents explore their environment with an array of whiskers, inducing complex patterns of whisker deflections. Cortical neuronal networks can extract global properties of tactile scenes. In the primary somatosensory cortex, the information relative to the global direction of a spatiotemporal sequence of whisker deflections can be extracted at the single neuron level. To further understand how the cortical network integrates multi-whisker inputs, we imaged and recorded the mouse barrel cortex activity evoked by sequences of multi-whisker deflections generating global motions in different directions. A majority of barrel-related cortical columns show a direction preference for global motions with an overall preference for caudo-ventral directions. Responses to global motions being highly sublinear, the identity of the first deflected whiskers is highly salient but does not seem to determine the global direction preference. Our results further demonstrate that the global direction preference is spatially organized throughout the barrel cortex at a supra-columnar scale.

INTRODUCTION

Layer 4 of the rodent primary somatosensory cortex contains anatomical structures named "barrels" topologically organized as the whiskers on the animal's snout. Since their description by Woolsey and Van der Loos (1970), the barrels are considered as the prototypical morphological manifestation of the functional columnar organization of the cerebral cortex. Each neuronal column associated with a barrel processes primarily the information coming from its corresponding whisker (Feldmeyer et al., 2013; Petersen, 2003, 2007). However, when rodents explore their environment, they contact objects with the whole array of whiskers, inducing complex sequences of multi-whisker deflections. Although the topographic organization of the whisker-to-barrel cortex pathway suggests a parallel processing of the inputs originating from distinct whiskers, it also contains the neural bases for the integration of more complex interwhisker information (Armstrong-James and Callahan, 1991; Arnold et al., 2001; Ego-Stengel et al., 2005; Narayanan et al., 2015).

The principal candidates for integrating complex spatiotemporal sequences of tactile inputs are neurons with multi-whisker receptive fields (RFs). It has been shown that, in the supra- and infragranular layers of the barrel cortex, single neurons receive inputs from their principal whisker (PW) and from several surrounding whiskers (Brecht and Sakmann, 2002; Brecht et al., 2003; Manns et al., 2004; Moore and Nelson, 1998; Zhu and Connors, 1999). The structure of these multi-whisker RFs is stimulus dependent. They differ according to the direction of the whisker deflection (Le Cam et al., 2011). In addition to multi-whisker thalamic input, the cortico-cortical connections have profound effects on the RFs and the spread of subthreshold activity. For example, intracortical circuitry shows anisotropy toward within-row connectivity (Kim and Ebner, 1999; Petersen and Sakmann, 2001; Simons, 1978). A morphometric study revealed a much higher degree of horizontal connectivity than originally reported in the rat barrel cortex, with a majority of excitatory neurons projecting their axon far beyond their cortical column (Narayanan et al., 2015). Altogether, these observations suggest that complex interactions are likely to take place in the barrel cortex and might be essential for the integration of multi-whisker contacts.

Understanding how the barrel cortex can extract the emergent properties of such complex tactile inputs requires the use of multi-whisker stimuli that are locally invariant but differ by their global coherent properties. This is the case of "global motion" stimuli (Jacob et al., 2008), which consist in sequences of 24 whisker deflections presented in spatio-temporal orders mimicking front edges crossing the whisker pad in eight different directions. Single-unit recordings from the C2 barrel-related column in rat barrel cortex have shown that a majority of neurons are able to extract directional information from global motions independently of the local direction of deflections of individual whiskers. Preferred direction for global motions in regular spiking units presented a bias for caudo-ventral directions in the C2 barrel-related column (Jacob et al., 2008).

Whereas the spatial mapping of stimulus features, like the direction of a local stimulation, has been documented in the

visual and somatosensory cortices (Hubel and Wiesel, 1963; Andermann and Moore, 2006; Kremer et al., 2011), there is no experimental evidence for a spatial organization of global properties of stimulation at a larger spatial scale. Here, we hypothesized that directional tuning for global motion could be spatially distributed over the entire barrel cortex. Indeed, different dimensions of a stimulus can be mapped over the same cortical area. For instance, in cat visual cortex, the retinotopic, the ocular dominance, and the orientation selectivity maps are overlaid in the same cortical area (Hübener et al., 1997; Rothschild and Mizrahi, 2015). Evidence that multiple features of a stimulus can be represented within the same cortical area has been reported in the rat barrel cortex, where the somatotopic map coexists with a subcolumnar spatial mapping of direction preference for the individual deflection of the PW (Andermann and Moore, 2006; Kremer et al., 2011; Wilson et al., 2010).

Here, we assessed the spatial organization for the direction selectivity to global motions by means of voltage-sensitive dye (VSD) imaging and extracellular electrophysiological recordings of the cortical spatiotemporal dynamics evoked by multi-whisker stimuli.

RESULTS

VSD Imaging of Depolarizing Responses Evoked by Multi-whisker Stimuli

A mechanical multi-whisker stimulator (Jacob et al., 2010) was used to deflect the 24 macrovibrissae on the right side of the snout while recording the spatiotemporal dynamics of activity of the left barrel cortex by means of VSD imaging (Figure 1A). Multi-whisker stimuli were locally invariant—caudal or rostral whisker deflections—and globally coherent (Figure 1B), mimicking a bar moving in eight different directions, henceforth, "global directions." The whisker local deflection consisted of a 2.7° displacement with a 2-ms rising ramp, 2-ms plateau, and 2-ms fall (Figure 1C). The anatomical map of the layer 4 barrels was reconstructed post hoc (Perronnet et al., 2016; Supplemental Experimental Procedures) and superimposed to the functional VSD images using the surface blood vessels as anatomical landmarks.

A rostral global motion evoked a cortical activation that was initiated in the cortical columns corresponding to the first stimulated whiskers and then rapidly spread to cover the entire barrel cortex (Figure 1D). The cortical columns corresponding to the subsequently stimulated whiskers were activated even before the actual deflection of their corresponding whiskers. Measuring the signal from a region of interest (ROI) corresponding to the central C2 column indeed reveals that, at time 0, which corresponds to the actual deflection of the C2 whisker, a high level of activity is already present (46.83% of the peak response amplitude in this case). The response reaches its maximum 10 ms after the deflection of the arc 2 whiskers and slowly goes back to the baseline level. In addition to the activation of the whole barrel subfield, the global motion evoked the activation of a lateral area corresponding to the location of the secondary somatosensory cortex (Carvell and Simons, 1986).

The Evoked Responses Depend upon the Global Direction of the Multi-whisker Stimulation

Different global directions of stimulation elicited different patterns of responses. Figure 2A shows, for the same case as in Figure 1, the averaged response to eight global directions at different times relative to the stimulation of the central C2 whisker. For each direction, the early response occurred at regions representing the first stimulated whiskers. Subsequently, the activation spread across the barrel field according to the direction of the global motion. Finally, the late dynamics of the evoked cortical activity shared similar spatial properties.

For the eight global directions, the whiskers were always deflected in the same direction (either rostral or caudal); only the spatiotemporal sequence of the whisker deflections varied. If the cortex could extract global information about this spatiotemporal sequence, we could obtain, for a given cortical column, different responses to different global directions. To address this question, we first focused on the C2 column because of the central position of the C2 whisker in the stimulation matrix. The profiles of fluorescence computed from a ROI delimited by the anatomical C2 barrel are shown in Figure 2B, color coded for the eight directions of stimulation (same case as in Figures 1 and 2A). For all the global directions, the evoked activity reaches the C2 column before the whisker C2 was actually deflected (dashed line).

To quantify the degree of activity at the time of stimulation of the C2 whisker (T_0), we computed the level of activation relative to the maximum of the response for the eight directions and eight independent experiments (Figure 2C, top). All global directions showed an activation of the C2 barrel column around 50% at T_0 (52.55% ± 8.00%), except the global directions 45° and 90°, which showed lower activation (18.08% ± 0.24%). This fast lateral spread of activity is likely to impact the cortical activation induced by the C2 whisker deflection.

This suggests that, for most directions, the feedforward activity corresponding to the C2 whisker deflection contributes to only about half of the total amplitude of the response in the C2 column.

When measuring the responses latency in the C2 column, similar results were observed (Figure 2C, middle). For almost all directions, the latencies were negative, suggesting that the lateral spread of activity in the barrel cortex is faster than the moving bar stimulation on the receptive surface. As a consequence, if an adjacent row/arc was deflected 10 ms earlier, afferent signals coming from the thalamus might encounter neurons that were already activated by cortico-cortical connections, significantly impacting their responses. The shortest latencies correspond to the global motion of 315°, a direction that showed the smallest response (Figure 2C, bottom), suggesting that, within this global direction, the intracortical lateral connections might have a more prominent impact on the feedforward responses to the C2 whisker deflection.

The velocity of the cortical propagation of the early activation evoked by global motions was further quantified by focusing on the 4 cardinal directions (0°, 90°, 180°, and 270°), where the initial front edge of the stimulus similarly involves the synchronous

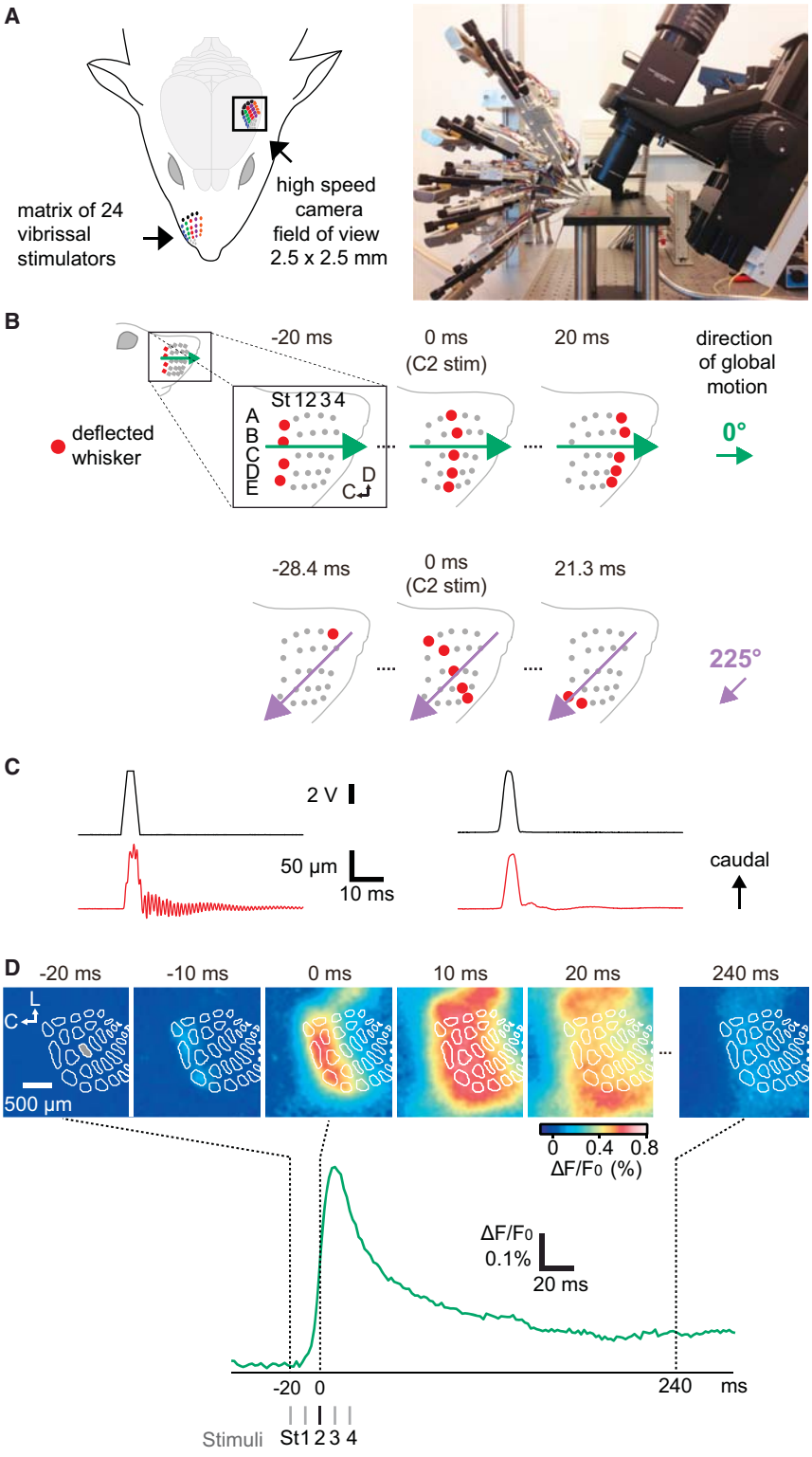

Figure 1. VSD Imaging of Cortical Responses to Multi-whisker Stimulation

(A) Scheme and photograph of the experimental setup. The left barrel cortex is imaged using a high-speed imaging system while the whiskers on the right side of the snout are stimulated with a 24-whisker stimulator.

(B) Global motion protocol. On the whisker pad, rows are named with letters and arcs with numbers, except the more caudal arc that corresponds to the four straddlers (St). Caudal (C) is left; dorsal (D) is up. These conventions apply to all figures. Three steps corresponding to two directions of the global motion protocol (0° and 225°) are illustrated. Red dots indicate the whiskers that are deflected at the time indicated on top.

(C) Voltage command (black trace) sent to a whisker stimulator and the resulting deflection measured with a laser telemeter at the tip of a stimulator (red trace), before (left) and after (right) correction of the command to prevent mechanical ringing.

(D) Snapshots of the averaged fluorescence signal (n = 30 trials) for a representative case at six different timings relative to the time of deflection of the central C2 whisker for the rostral global direction (0°). The barrel map reconstructed from a post hoc cytochrome oxidase staining and overlaid onto the VSD signals is shown as white outlines. The profile of fluorescence measured from the C2 barrel-related column (the ROI of the column C2 is shown as a gray area on the −20 ms snapshot) is shown below. The dotted lines indicate the time of deflection of the first arc of whiskers (−20 ms), the central Arc 2 stimulation time (0 ms), and a later time, tens of milliseconds following the stimulation (+240 ms), corresponding to the last snapshot.

deflection of all whiskers from one arc or row (Figure S1). On average, the speed of the spread was 95.2 ± 19.3 µm/ms, about twice as fast as it would be if it were relying primarily on the sequential feedforward activation of the cortical columns, a value that could be estimated around ~27–38 µm/ms, from the interwhisker interval of the stimulus (10 ms) and the distance between cortical barrel-related columns (~270 µm inter-arc and 380 µm inter-row averaged distances from Knutsen et al., 2016). Comparing the 4 directions of global motion revealed a slightly lower velocity for dorsal (90°) compared to ventral (270°) global motions, which corroborates the longer latency of the response observed in the C2 column for the dorsal motion. The early spread velocity, however, did not differ significantly between the caudal and rostral directions.

Depending upon the direction of the global motion, cortical activation of the central C2 column differed both in amplitude and temporal dynamics (Figure 2C, bottom), suggesting that information about the global direction could be extracted at the level of a single column (C2 in this case).

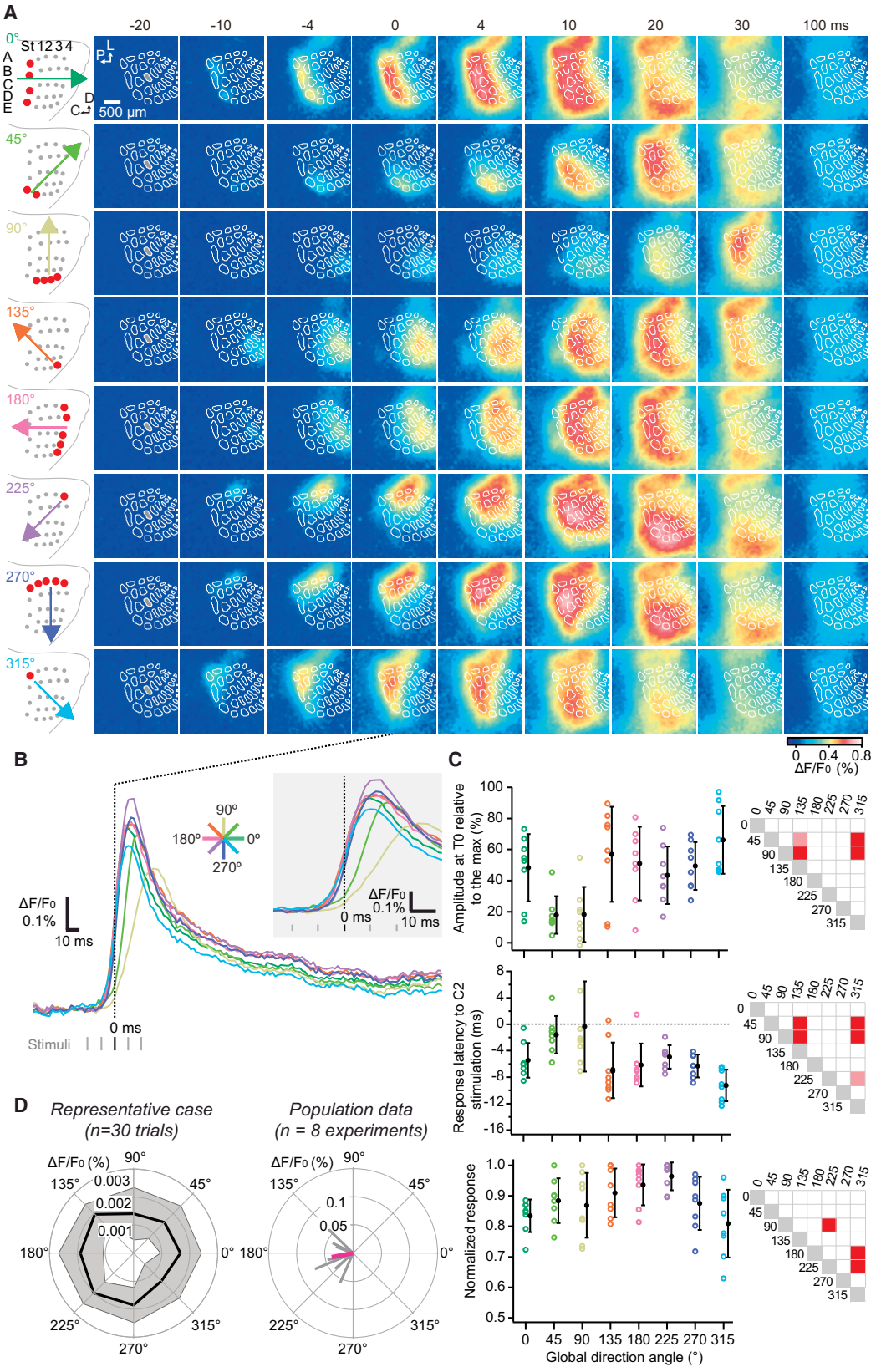

(legend on next page)

The C2 Barrel Column Shows Global Direction Selectivity Biased toward Caudo-ventral Directions

For the case illustrated in Figures 1, 2A, and 2B, the averaged responses were quantified over the C2 barrel-related column over a large time window (−20–240 ms) and represented on a polar plot (Figure 2D, left). The preferred direction was calculated (Experimental Procedures) and is shown as the thick vector whose length represents the vector summation. A bias toward caudo-ventral global direction can be observed in this case and in all the experiments (n = 8; Figure 2D, right) for the C2 barrel-related column (Rayleigh test; $p = 0.0015$).

These results suggest that neurons belonging to the C2 column in the mouse barrel cortex are tuned preferentially to caudo-ventral directions of global motions, consistent with observations in the rat barrel cortex (Jacob et al., 2008).

A Supra-barrel Distribution of Direction Selectivity to Global Motions Superimposed to the Somatotopic Map

To investigate the spatial organization of the direction selectivity to global motions for other barrel-related columns than C2, we computed the preferred direction and direction index for each column by aligning the profiles of VSD activity to the time of stimulation of its corresponding whisker (Experimental Procedures). The resulting direction selectivity and direction index maps for a representative case (same as illustrated in Figures 1 and 2) revealed that barrel-related columns corresponding to rostral whiskers show a significant anisotropic distribution of the direction selectivity with a bias toward caudo-ventral global motions (Rayleigh test; $p < 0.05$; dotted yellow outlines, Figure 3A). This distribution was more uniform in the columns corresponding to more caudal whiskers (Rayleigh test; $p > 0.05$). However, the direction selectivity for global motions is organized along a continuum, with the rostral columns presenting a direction preference with a strong caudal bias, the most lateral columns showing a caudo-ventral preference whereas the most caudal columns prefer ventral directions.

This spatial distribution of the direction preference for global motion was confirmed by analyzing 8 independent experiments (Figures 3B and 3C). For every barrel-related column, we computed a "similarity" value by comparing the preferred directions obtained for the eight experiments (Experimental Procedures). The similarity map confirmed a stronger directional preference for the more rostral columns. Direction selectivity was significant for the columns corresponding to the rostral whiskers (arcs 2–4; Rayleigh test; $p < 0.05$) and also for the alpha-whisker-related column (StA), which showed a significant selectivity toward the ventral direction (Rayleigh test; $p = 0.026$). Although the distribution of the direction index calculated for each experiment and each column reveals relatively small values, it is not centered at zero, which would be the case in the absence of direction selectivity for global motions.

The angular distribution of preferred directions for the eight individual experiments highlights the gradual spatial organization of direction selectivity to global motions across the barrel cortex (Figure 3C). It indeed illustrates the ventral bias for the caudal barrel-related columns, which is significant for the column corresponding to the dorsal alpha whisker (StA), but not for the columns corresponding to more ventral whiskers, such as gamma (StC). The angular distribution of preferred directions for global motions gradually becomes more anisotropic for the columns corresponding to rostral whiskers (as for C2 and C4 barrel-related columns in Figure 3C). The resulting directional bias gradually becomes strongly caudal for the most rostral columns (see the C4-related column in Figure 3C).

Additional VSD experiments were performed to test whether the selectivity to global motion depends on the direction of individual whisker deflections. Previous work suggested that it is not the case in the rat barrel cortex (Jacob et al., 2008). Whiskers were individually deflected in one of the 4 cardinal directions (caudal, ventral, rostral, or dorsal) within spatiotemporal sequences generating global motions in 8 different directions (n = 6 mice). Our results (Figures S2 and S3) show that congruent stimuli (similar direction of individual whisker deflections and global motion) do not systematically induce higher evoked responses when compared to non-congruent stimuli and that direction selectivity for global motions is not biased toward the direction of the individual whisker deflection.

The impact of the apparent speed of the global motions on the global direction selectivity was also tested in three additional experiments (Figure S4). Global motions were presented either like in the original protocol with an inter-whisker interval (IWI) of 10 ms or with a shortened IWI of 1 ms. In this second configuration, feedforward activity is likely to activate the consecutive columns faster than the cortico-cortical spread of activity. The spatial

Figure 2. Local Cortical Activation Depends on the Spatio-temporal Sequence of Multi-whisker Deflections

(A) Snapshots of the averaged fluorescence signals (same case as in Figure 1C) for the eight global directions (shown on the left) at different timings relative to the central C2 whisker deflection (0 ms). The barrel map is shown as white outlines.

(B) Fluorescent profiles measured from the C2 barrel-related column (gray area indicated on the −20 ms snapshots) for the eight directions of global motion. Global directions are color coded. The dotted line indicates the time of whisker C2 deflection. The inset shows the initial activation with an expanded timescale.

(C) (Top) Percentage of the response at the time of C2 whisker deflection. (Middle) Latencies were quantified by calculating a linear regression from 20% to 80% of the peak of the response for each global direction. Latency 0 ms corresponds to the time of C2 whisker deflection. (Bottom) The integral of each profile was calculated within a time window of −20–240 ms and normalized, for each individual experiment, to the higher response. Open circles represent the individual experiments, and filled black circles represent the averages (n = 8 experiments). Error bars correspond to the SD. Statistical tests are shown on the right: Friedman repeated-measures ANOVA on ranks followed by a Tukey test for multiple comparisons for the upper two and one-way ANOVA for repeated measures followed by the Holm-Sidak method for the lower one. Pale red, $p < 0.05$; red, $p < 0.01$.

(D) (Left) Polar plot of the averaged responses quantified over the C2 column for the representative case, integrated along a time window of −20–240 ms. The thick vector shows the preferred angle (color coded), and the length of the vector shows the vector sum of the responses (direction index: 0.074). The gray shadow corresponds to the SD (n = 30 repetitions). (Right) The distribution of global direction vectors for eight experiments (gray vectors) and the average (colored vector), calculated for the C2 column, are shown.

See also Figure S1.

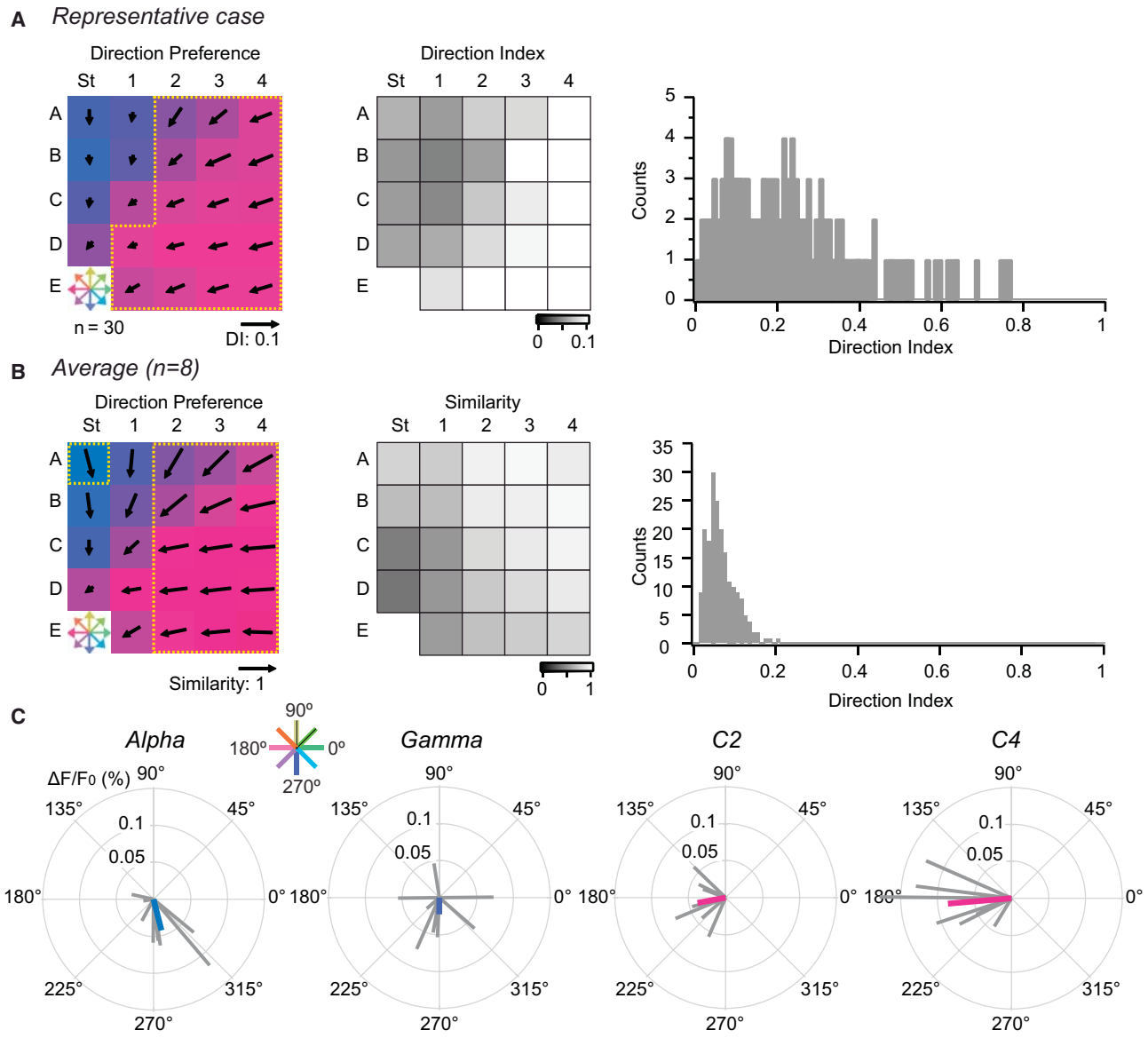

Figure 3. Spatial Distribution of Direction Selectivity to Global Motion

(A) 24-whisker map of direction preferences obtained for a representative case (left). For each barrel, the direction preference is color coded and represented by the angle of the arrow; the length of the arrow represents the direction index. The anisotropy of the direction preference distribution was evaluated with a Rayleigh test (over the 30 repetitions), and its significance ($p < 0.05$) is indicated by the dotted yellow contour. In the middle is represented a 24-whisker map of direction indexes. The histogram on the right shows the direction index values calculated individually for the 30 repetitions of the protocol and for the 24 barrel-related columns (n = 720 values; bin size: 0.01).

(B) Averaged 24-whisker map of direction preferences (n = 8 mice, left). The direction preference is color coded and represented by the angle of the arrows; the length of the arrow represents the similarity index between experiments and the significant anisotropic barrels (Rayleigh test; $p < 0.05$) are indicated by dotted yellow contours. In the middle is represented a 24-whisker map of similarity indexes. The histogram on the right shows the distribution of the direction indexes computed for all experiments and each barrel column (n = 192 values; bin size: 0.01).

(C) Representative angular distributions of preferred directions for global motion for each experiment (gray vectors) shown for the barrel columns that correspond to the whiskers alpha (StA), gamma (StC), C2, and C4. Vector sums for the 8 experiments, shown as colored vectors, indicate the averaged direction preferences. See also Figures S2, S3, and S4.

organization of direction selectivity for global motion was not affected with short IWI, although we observed a decrease in selectivity in this condition. Thus, as in the rat barrel cortex (Jacob et al., 2008), global direction selectivity can be revealed for a range of interstimulus intervals, but there is a limited dependence of the tuning strength on the apparent speed of the stimulus.

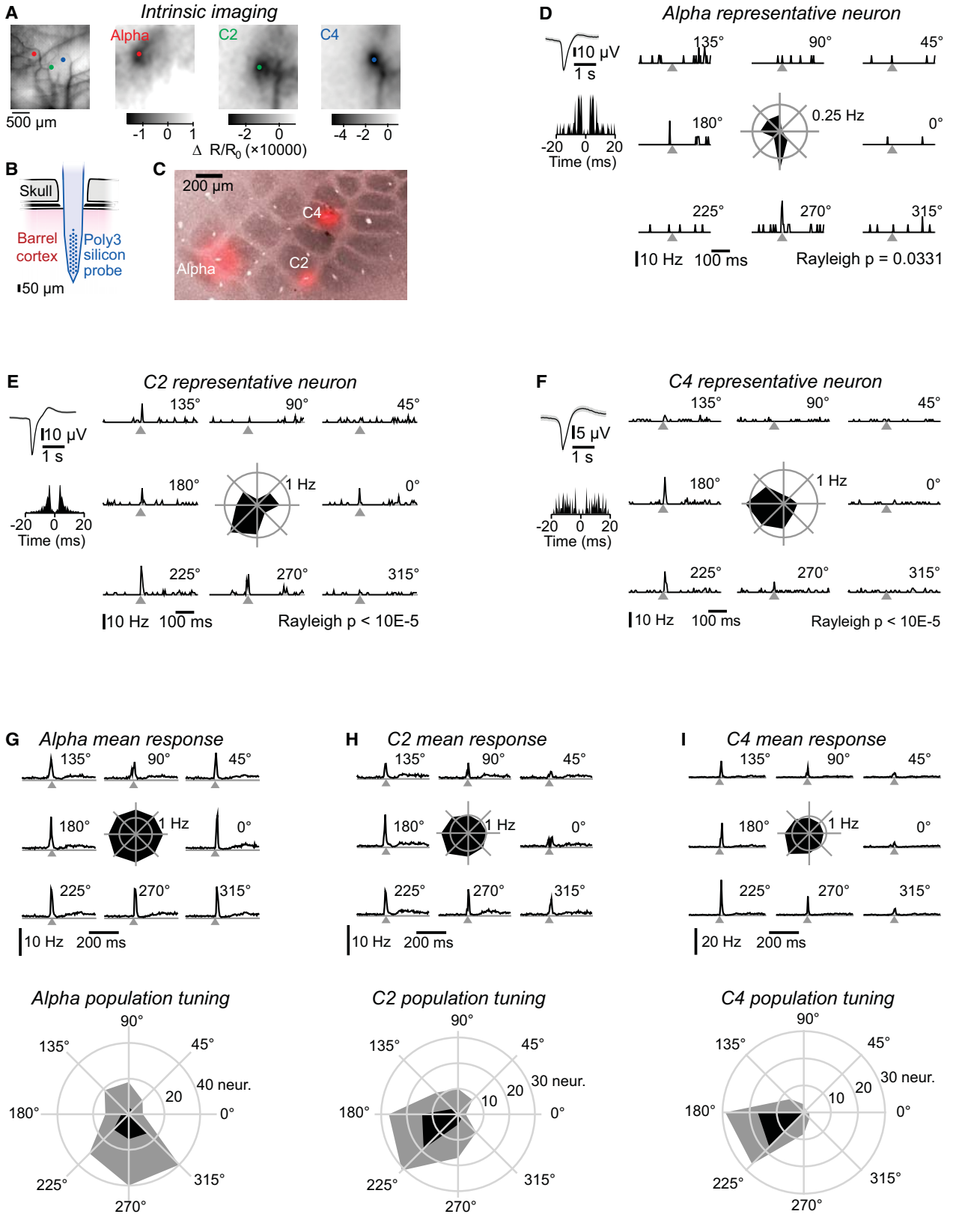

(legend on next page)

Electrophysiological Recordings Confirm the Spatial Organization of Direction Selectivity to Global Motions

To firm up the observation of a supra-barrel gradient of directional tuning, we performed extracellular recordings in 5 additional mice (Supplemental Experimental Procedures). We first used intrinsic imaging to functionally locate three barrels, corresponding to the straddler alpha (StA), the C2, and the C4 whiskers (Figure 4A). At these locations, we performed a craniotomy and inserted a Poly3 silicon probe into the cortex at depths ranging from 200 to 600 μm below the cortical surface (Figure 4B). We recorded extracellular spiking activity in the barrels while applying the same multi-whisker stimulation protocol that was performed during VSD experiments. After recordings were done, cytochrome oxidase staining of tangential sections of the barrel cortex combined with DiI marks left by the electrode validated the positioning of the electrode with respect to layer 4 barrels (Figure 4C).

For each target whisker (StA, C2, and C4), we grouped units that were recorded at most ½ barrel away from the target barrel, according to the histology. Consistent with the VSD-based findings, units near StA were often tuned to ventral global motion (case study in Figure 4D), whereas C2 units preferred ventro-rostral motion (Figure 4E), and for C4 units, caudal motion was predominant (Figure 4F). These findings were confirmed at a population level by looking both at population average firing rate and the distribution of the preferred global motion direction of the neurons (Figures 4G–4I). Overall, in the three points of the barrel map that we have explored, the distribution of the neurons' tuning was consistent with the VSD results described in Figure 3, both for neurons with a significant direction preference (Rayleigh $p < 0.05$) and when looking at the direction preference of all recorded neurons (Figures 4G–4I).

Cortical Responses to Global Motions Are Highly Sublinear

To further understand the mechanisms for global direction selectivity and its distribution over the barrel field of the somatosensory cortex, we first hypothesized that the direction selectivity to global motions might be determined by the suppressive interactions that have been reported when adjacent whiskers are sequentially deflected (Brumberg et al., 1996; Civillico and Contreras, 2006; Ego-Stengel et al., 2005; Higley and Contreras, 2005; Jacob et al., 2008; Kleinfeld and Delaney, 1996; Simons, 1985; Simons and Carvell, 1989). To test this hypothesis, we designed a protocol in which we randomly alternated two types of stimulations: global motions in four cardinal directions (moving bars, Figure 5A) and the stimulation of individual rows or arcs (static bars, Figure 5B). By linearly adding up the responses to the static bars, we constructed linear predictions of the responses to the moving bars (Figure 5C). A representative example of the rostral global motion (0°) is illustrated in Figure 5, with snapshots of the activity over the barrel cortex at the time of stimulation of the indicated whiskers.

By comparing the evoked responses to global motions (moving bars, blue lines) with the corresponding linear predictions (green lines), we observed that the linear summations reached much higher levels of activation (Figure 6A). This indicates that suppressive mechanisms are involved in shaping the cortical responses to global motions. We next quantified these sublinearities and tested whether they depend upon the direction of the global stimulation. For five independent experiments, we calculated the integral of responses (moving bars and linear summations) from a ROI corresponding to the C2 barrel-related column (Figure 6B) within a time window of −20–240 ms and for the four cardinal directions. The ratio of moving bar responses over linearly predicted responses is overall 0.30 ± 0.03 ($n = 5$ experiments). This ratio does not differ according to the direction of stimulation (one-way ANOVA for repeated measures; $p = 0.1$).

To assess whether the sublinearities could nevertheless be determinant to encode the direction of the global motion, we computed the direction selectivity map that would result from the linear predictions of the responses to moving bars. The direction selectivity map obtained from the linear predictions ($n = 5$ experiments) is qualitatively different from the one obtained from the responses to moving bars (Figure 6C). Only some columns—located mainly on the borders of the barrel field—showed a significant preferred direction (Rayleigh test; $p < 0.05$; dotted yellow outlines), with angles distributed in an inversed pinwheel, pointing toward the borders of the field. This inversed pinwheel is expected given that the linear prediction responses are obtained by sequentially adding the responses to the static bars. The border columns are expected

Figure 4. Extracellular Recordings Confirm the Spatial Organization of Direction Selectivity

(A) (Left) Blood vessel pattern at barrel cortex surface visualized through the intact skull under green illumination. (Right) Intrinsic optical signals imaged through the bone in response to the stimulation (100 Hz; 1 s) of whiskers alpha, C2, and C4 are shown.

(B) Insertion of Poly3 silicon probe in a localized craniotomy.

(C) DiI mark left by probe insertion in the three recording sites, shown in a tangential slice of the barrel cortex. Barrels are highlighted using post hoc cytochrome oxidase staining.

(D) Global motion direction tuning of a representative unit recorded in the alpha barrel. (Left margin, top) Largest spike shape recorded across the channels is shown (Light background: SEM). (Left margin, bottom) Autocorrelogram. (Right) Peristimulus time histogram (PSTH) for the 8 directions of global motion stimuli, and at the center, a polar plot of the mean firing rate in a window (−20–240 ms) aligned on alpha whisker stimulations (gray arrowhead) across the 8 bar directions is shown.

(E) Same as (D) for a C2 representative unit.

(F) Same as (D) for a C4 representative unit.

(G) (Top) Averaged PSTHs and polar plot of the mean firing rate around stimulus for the 58 units with a significant tuning to the global motion stimulus direction (Rayleigh $p < 0.05$), recorded close to the alpha barrel in 3 mice. (Bottom) Population histogram of the preferred global direction for significantly tuned units (black) and for all units recorded close to the alpha barrel (187 units, gray).

(H) Same as (G) for 45 significantly direction-tuned units recorded in 5 mice and for a total of 126 units recorded close to the C2 barrel.

(I) Same as (G) for 35 significantly direction-tuned units recorded in 2 mice and for a total of 81 units recorded close to the C4 barrel.

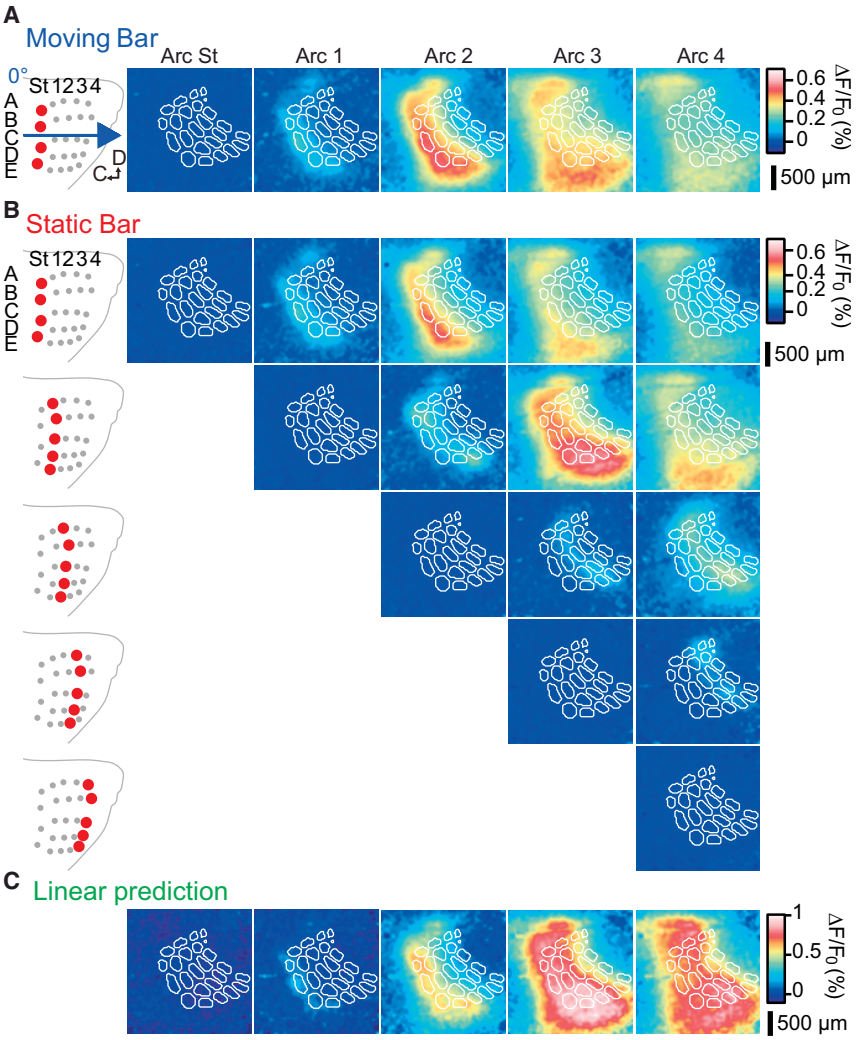

Figure 5. Moving/Static Bar Protocols and Linear Prediction

(A) Illustration of the moving bar stimulus for 0° direction with snapshots of the cortical response observed for a representative case, at the time of deflection of each arc (n = 30 repetitions).

(B) Examples of static bar stimuli. Snapshots of cortical activity evoked by the stimulation of the arc indicated on the left (averaged over 30 repetitions) are shown for the same case as in (A) at the time of deflection of each arc and subsequently every 10 ms.

(C) Linear prediction of cortical activity evoked by a moving bar stimulus for 0° direction computed as the sum of the responses to static bar stimuli at times that match the moving bar. Snapshots of the summed cortical activity (n = 30 repetitions) for the same case as in (A) and (B) are shown, computed at the time of deflection of each arc.

to show a larger response for the direction that activates first the columns of the opposite side of the barrel field. The distribution of the corresponding direction index for all the columns (n = 24) and all the experiments (n = 5; Figure 6C, bottom left) shows most values close to zero in the case of the linear prediction model, confirming that the majority of the columns do not present significant direction selectivity under the linear assumption.

To quantify the differences between the two maps, we computed for each barrel-related column the angular difference between the direction preference obtained from the linear prediction and the one obtained from responses to the moving bars (Figure 6D). This angular difference (in average of 127° ± 59°) was large for most of the columns, especially in the barrel columns corresponding to the more rostral and dorsal whiskers, which are the ones that show significant direction selectivity with the moving bar protocol.

These results therefore indicate that the observed spatial organization of direction selectivity for global motions emerges from sublinear interactions.

Direction Selectivity to Global Motion Does Not Only Rely on the Identity of the First Stimulated Whiskers

Images of the early cortical activation evoked by a moving bar look very similar to the ones obtained in response to a static bar, where only the first row or arc at the border of the barrel field (arc St, arc 4, row A, or row E) is stimulated (henceforth "front static bar"). To quantitatively compare these cortical responses, we integrated them along a time window of −20–240 ms and over a ROI corresponding to the C2 column (Figure 7A). We found that responses for the front static and moving bars did not differ significantly (one-way ANOVA for repeated measures; p = 0.077). The ratio of the responses to the front static bar over the moving bar was overall 0.58 ± 0.12 and did not differ significantly according to the direction (Figure 7B; n = 5 experiments).

To further assess whether the spatial distribution of selectivity to the direction of global motion could result from the salience of the starting position of the moving bar, we computed a direction selectivity map using the responses to the front static bars: arc St; arc 4; row A; and row E (n = 5 experiments). This map shows a pinwheel-like distribution of the preferred directions, with the center close to the column D3 (Figure 7C, left). Both the direction selectivity maps and the direction index distributions differed between front static bar and moving bar conditions (Figure 7C, right). By computing the angular difference between the two direction selectivity maps, we observed that only few columns among the ones corresponding to the most dorsal and rostral whiskers share comparable direction preference in both conditions (Figure 7D). The preferred directions differed on average from 83° ± 46° between the two conditions.

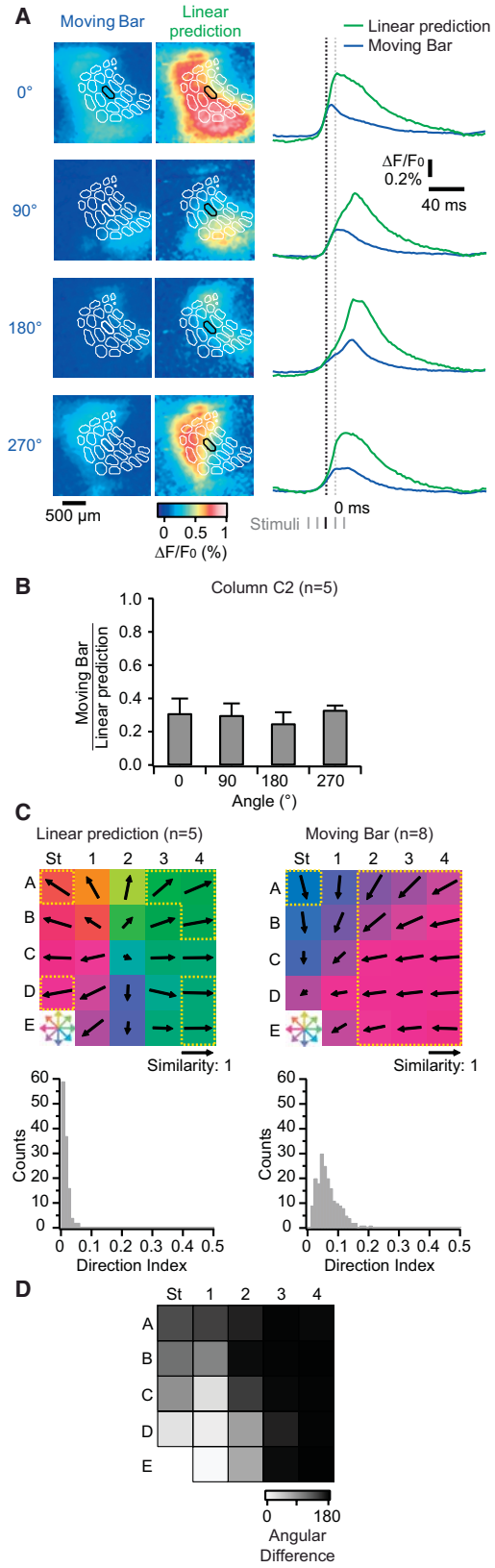

Figure 6. Cortical Responses to a Moving Bar Are Highly Sublinear

(A) Comparison of the cortical activity evoked by moving bars and their corresponding linear prediction. (Left) Snapshots of the responses at 30 ms following the beginning of the stimulation for four global directions (0°, 90°, 180°, and 270°) of the moving bar (n = 30 trials) and their corresponding linear prediction from static bar responses summation (same fluorescence scale) are shown. (Right) Profiles of activity calculated from the C2 barrel-related column for the moving bar and linearly predicted responses are shown. The vertical bars below indicate the time of stimulation of arcs/rows, the time of deflection of the Arc 2 being in black and indicated by the long black dotted line. The gray dotted line indicates the time +30 ms of the snapshots shown on the left.

(B) Population ratios (n = 5 experiments) of responses to the moving bar and the linear prediction computed from the C2 column over a time window of −20–240 ms for the different directions. Error bars correspond to the SD.

(C) (Left) Averaged 24-whisker map of direction preference (n = 5 experiments) for the linear prediction and histogram of the corresponding direction indexes (n = 120 values; bin size: 0.01). (Right) Moving bar map and histogram (as in Figure 3B) are shown.

(D) Angular difference map between the preferred angles of the linear prediction and the moving bar responses.

These results suggest that, although the salience of the starting position of the moving bar might participate in part to the emergence of the spatial distribution of the global direction selectivity, other mechanisms that build up when the bar is moving across the whisker pad are also required.

DISCUSSION

Emergence of Direction Selectivity to Global Motion

Is direction selectivity to global motion emerging in the cortex or in subcortical structures? Direction selectivity to global motion is already present at the level of the ventral posterior medial nucleus of the thalamus (VPM) in the rat (Ego-Stengel et al., 2012), but it is amplified in the cortex. Indeed, VPM selectivity decreased under cortical inactivation. Moreover, stimulating the closest adjacent whiskers or including the more distant ones from the principal whisker does not change selectivity in VPM, whereas it increases selectivity in the cortex.

In 2010, Wilson and collaborators proposed a computational model to explain the emergence of local direction selectivity maps in L2/3 of the rat barrel cortex (Wilson et al., 2010). This model generates predictions about the spatial organization of local direction selectivity (i.e., the preference for a given direction of deflection of the principal whisker), not only within single columns but also at the scale of the entire barrel field. The level of correlation between the individual whisker deflections and the global stimulus during the training of the network strongly influences the supra-columnar spatial distribution of local direction selectivity. It is therefore likely that the input statistics can also shape the supra-columnar organization of direction selectivity for global motion in an experience-dependent manner.

Both in barrel cortex and VPM, the responses recorded extracellularly to global motion protocols and to only one whisker deflection were similar (Ego-Stengel et al., 2012; Jacob et al., 2008). The nonlinearities involved in the generation of the global direction selectivity are therefore likely to be suppressive rather than facilitatory, such as the ones involved in cross-whisker suppressive interactions in VPM and cortex (Brumberg et al., 1996; Civillico and Contreras, 2006; Ego-Stengel et al., 2005; Higley

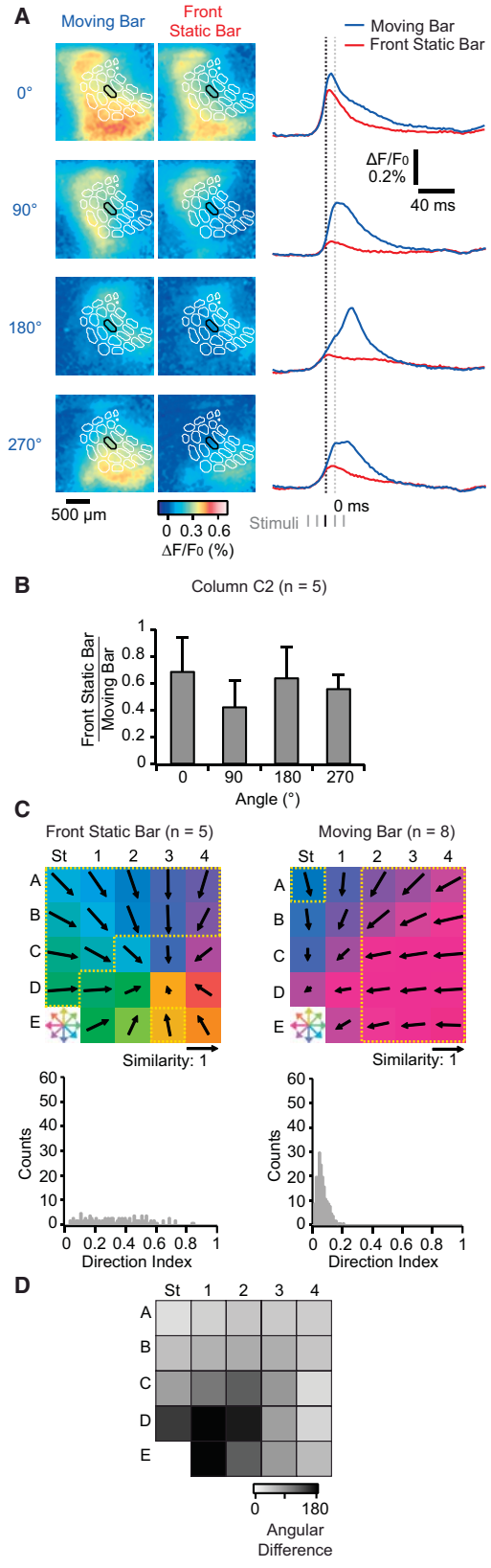

Figure 7. Global Direction Selectivity Does Not Only Rely on the Starting Position of the Moving Bar

(A) Comparison of the cortical activity evoked by moving bars and their corresponding front static bars where only the first row or arc of whiskers is stimulated. (Left) Snapshots of the responses at 30 ms following the beginning of the stimulation for four global directions (0°, 90°, 180°, and 270°) of the moving bar (n = 30 trials) and their corresponding front static bars (same fluorescence scale) are shown. (Right) Profiles of activity calculated from the C2 barrel-related column for moving bar and front static bar responses are shown. Same conventions as in Figure 5A for the vertical bars below and the dotted lines are shown.

(B) Population ratios (n = 5 experiments) of responses to the static bar and the moving bar computed from the C2 column over a time window of −20–240 ms for the different directions. Error bars correspond to the SD.

(C) (Left) Averaged 24-whisker map of direction preference (n = 5 experiments) for the front static bar and histogram of the corresponding direction indexes (n = 120 values; bin size: 0.01). (Right) Moving bar map and histogram are shown (as shown in Figure 3B).

(D) Angular difference map between the preferred angles of the front static bar and the moving bar responses.

and Contreras, 2003, 2005; Kleinfeld and Delaney, 1996; Shimegi et al., 1999, 2000; Simons, 1985; Simons and Carvell, 1989).

At the single-neuron level, linear summation of the responses to single-whisker deflections failed to explain the selectivity to global motion (Jacob et al., 2008). Here, we constructed a linear prediction of the response to global motion by sequentially adding the responses to the stimulation of individual arcs or rows. Linear summation of the responses to a group of whiskers (arcs or rows) also failed to explain the global direction selectivity. Cortical activation induced by such sequential stimuli is highly sublinear.

Importance of Cortical Nonlinearities

The starting point of a front edge crossing the whiskers has a strong impact on cortical responses (Drew and Feldman, 2007). Thus, the spatial distribution of the global direction selectivity could be influenced by the starting position of the moving bar. To test this hypothesis, we compared the direction selectivity maps obtained with the moving bar protocol and with the deflection of the first arcs or rows (front static bar protocol). The two maps differed significantly, with rostral and dorsal directions more represented using the front static bar protocol and a bias toward the caudal direction for the moving bar protocol. The direction preferences observed with the front static bar protocol are likely to result from functional asymmetries of the barrel cortex, with stronger responses to the deflection of the large caudal whiskers (straddlers) than to the small rostral whiskers (belonging to arc 4) and, similarly, larger responses to row A than row E.

The differences between the two maps suggest that the global direction selectivity emerges when sequentially deflecting all the whiskers. These results are in agreement with previous recordings of neuronal responses to proximal (stimulating only 9 whiskers) and global stimuli (24 whiskers), which revealed that all the whiskers need to be deflected to observe a significant global direction selectivity in the rat barrel cortex (Jacob et al., 2008). Drew and Feldman (2007) deflected only 9–12 whiskers, which might explain the lack of direction selectivity reported in their

study. This long range integration is originating in the cortex because applying the protocol to only 9 whiskers had little influence on the selectivity of VPM neurons (Ego-Stengel et al., 2012).

Selectivity to Natural Statistics of the Stimulus

Our results showed a caudo-ventral bias for preferred directions of global motions, consistent with our previous results (Jacob et al., 2008) for the C2 barrel-related column in the rat. This bias is also spatially distributed: rostral columns preferred caudal global directions whereas dorsal columns tend to prefer ventral global directions.

Why do caudal and ventral global directions of stimulation elicit the largest responses in the majority of the barrel-related columns? We recorded the profile of a running mouse and observed that the rows of whiskers are not horizontal but oriented about 40° downward (data not shown). With such head position, the global direction of deflection of the whiskers during classical thigmotactic behavior is in the caudo-ventral axis. A higher cortical representation of global caudo-ventral stimuli could reflect experience-dependent, adaptive mechanisms leading to higher sensitivity to the most frequent stimuli. Indeed, given that the rat intrabarrel direction selectivity maps emerge late in development and are likely to be shaped by experience-dependent plasticity (Kremer et al., 2011, Wilson et al., 2010), we can hypothesize that the same might happen to global direction selectivity maps. Further studies of the statistics of the mouse natural tactile inputs should be conducted to understand the emergence of direction selectivity to global motion.

To conclude, here, we showed that the mouse barrel cortex is able to extract the global direction of a multi-whisker moving stimulus. This form of direction selectivity emerges from nonlinear interactions and is spatially distributed over the topographic arrangement of barrels in a supra-barrel manner. How this distribution is exploited by the cerebral cortex to construct a global percept of a moving object is still unknown. A supra-barrel organization could be computationally advantageous in conveying stimulus information into higher brain areas (Thivierge and Marcus, 2007). It could be used to discriminate stimulus features, such as orientation of object movements (Polley et al., 2005) or self-movement. Higher order areas, such as the secondary somatosensory cortex, which likely integrates tactile sensory information over larger time and spatial scales, might play a role in the functional readout. Future studies focusing on the integration of multi-whisker inputs within this cortical area are needed to further understand the cortical processing of complex tactile scenes.

EXPERIMENTAL PROCEDURES

Animals and Surgery

Experiments were performed in conformity with French and European (2010/63/UE) legislations on animal experimentation (authorization number: 2012-0068 delivered by the local ethical committee no. 59). VSD imaging was performed on male or female 6- to 10-week-old C57BL6J mice under urethane (1.7 mg/g) or isoflurane (induction 3%–4%; maintenance 1%–1.5%) anesthesia. Paw withdrawal, whisker movement, and eye-blink reflexes were suppressed by the anesthesia. Body temperature was maintained at 37°C. Respiration was monitored with a piezoelectric device. Brain state was monitored by using epidural electrodes above the barrel cortex and the frontal cortex ipsilateral to the stimulated whiskers. A metallic post was solidly glued on the occipital bone. A 3 × 3 mm craniotomy centered on the stereotaxic location of the C2 barrel column (1.5 mm caudal and 3.3 mm lateral) was made to expose the barrel cortex. Care was taken not to damage the cortex during the removal of the dura.

Voltage-Sensitive Dye Imaging

The voltage-sensitive dye RH1691 (Optical Imaging, Israel) was dissolved at 1 mg/mL in Ringer's solution containing (in mM) 135 NaCl, 5 KCl, 5 HEPES, 1.8 CaCl2, and 1 MgCl2. It was topically applied to the exposed cortex and allowed to diffuse 1 hr into the cortex. After removal of the unbound dye, the cortex was covered with agarose (0.5%–1% in Ringer's) and a coverslip. Cortical imaging was performed through a tandem-lens fluorescence microscope (SciMedia, USA) equipped with one Leica PlanApo 5× (objective side) and one Leica PlanApo 1× (condensing side), a 100-W halogen lamp gated with an electronic shutter, a 630-nm excitation filter, a 650-nm dichroic mirror, and a long-pass 665-nm emission filter. Images were acquired with a high-speed MiCam Ultima camera (SciMedia, USA) at 500 Hz with a field of view of 2.5 × 2.5 mm, resulting in a pixel resolution of 25 × 25 μm. The illumination of the cortical surface started 500 ms before each image acquisition to avoid acquiring signal in the steeper phase of the fluorescence bleaching. Recordings were of 1 s duration with 200 ms baseline and 800 ms post-stimulation. Variations of the light intensity were initially recorded as variations over the resting light intensity (first acquired frame).

VSD Imaging Analysis

Acquisition and data preprocessing were done using in-house software (Elphy, G. Sadoc, UNIC-CNRS). Further analyses were with IgorPro (WaveMetrics, USA). For each experiment, all the blank trials were averaged together and subtracted pixel by pixel from each trial to correct for bleaching-related artifact.

Variations of the fluorescence signal are expressed as ΔF/F0, the averaged signal over three frames just preceding the stimulus being used as a reference (F0).

Profiles of fluorescence were computed from ROIs corresponding to the layer 4 barrels delineated from the post hoc barrel map reconstruction. Variations of fluorescence from all the pixels included in a barrel were averaged.

Whisker Stimulation

Deflections of the right 24 posterior macrovibrissae of the mice were performed using a multi-whisker stimulator (Jacob et al., 2010). The experimental imaging setup is shown in Figure 1A. Whiskers on the right side were cut to a length of 10 mm and inserted, keeping their natural angle in 27G stainless steel tubes attached to the piezoelectric benders (Noliac, Denmark), leaving 2 mm between the tip of the tube and the whisker base. Each whisker deflection consisted of a 95-μm displacement (measured at the tip of the tube), a 2-ms rising time, a 2-ms plateau, and a 2-ms fall. The deflection amplitude of each actuator was calibrated using a laser telemeter (Micro-Epsilon, France), and specific filters were applied to the voltage commands to prevent mechanical ringing of the stimulators (Figure 1C). The resulting initial deflection velocity was of 1,270°/s.

Multi-whisker Global Motion Protocol

The 24 whiskers were stimulated either in the caudal or rostral direction within spatiotemporal sequences generating global motions in eight different directions (Jacob et al., 2008). The sweep duration in the horizontal and vertical axes was 46 ms (interval between two consecutive stimulated arcs or rows or IWI: 10 ms); the whisker C2 was deflected 20 ms after the beginning of the sweep. For oblique directions, a sweep lasted 62.57 ms (IWI: $10/\sqrt{2}$ = 7.1 ms), and the whisker C2 was stimulated 28.3 ms after the beginning of the protocol.

During VSD imaging experiments, the eight global motion stimuli together with an extra blank trial (no stimulation) were presented 30 times in a pseudo-randomized way. Two consecutive sequences were separated by a 15-s interval. For electrophysiological recordings, the interval between two consecutive global motion stimuli was shortened to 2 s. Continuous

recordings were made during about 1 hr, resulting in more than 1,500 trials per direction of global motion.

Multi-whisker Moving/Static Bar Protocols

All the whiskers were deflected as described above, in the caudal direction (Figure 1C). For the moving bar condition, the 24 macrovibrissae were stimulated with spatiotemporal sequences generating global motions as described above but only in the four cardinal directions (IWI: 10 ms). The static bar sequences consisted of deflecting the 5 arcs and the 5 rows of whiskers independently of each other. In total, four moving bar and ten static bar stimuli, together with two blank trials, were repeated 30 times in a pseudo-randomized way. An interval of 15 s was applied between two consecutive sequences.

Direction Selectivity

The response magnitude (Ri) to each direction (θi) of stimulation was defined as the integral of the fluorescence profiles (for VSD imaging) or mean firing rate (for extracellular recordings) on a large time window (−20–240 ms relative to the time of stimulation of the corresponding whisker). The preferred direction (Dpref) was defined as the circular mean (Fisher, 1995):

$$Dpref = \arctan\left[\sum Risin(\theta i) \Big/ \sum Ricos(\theta i)\right].$$

To quantify the Dpref, the direction index (DI) was defined as

$$DI = \sqrt{\left[\sum Risin(\theta i)\right]^2 + \left[\sum Ricos(\theta i)\right]^2} \Big/ \sum Ri.$$

The DI takes values from 0 (equal responses to all directions) to 1 (complete selectivity to one direction).

Likewise, we quantified the similarity between the Dprefs for barrel across the different experiments, defining the similarity index (SI) as

$$SI = \sqrt{\left[\sum Disin(Dpref)\right]^2 + \left[\sum Dicos(Dpref)\right]^2} \Big/ \sum Di.$$

The SI takes values from 0 (different Dpref between experiments) to 1 (equal Dpref).

Statistical Tests

Rayleigh test of circular uniformity was used to test the significance of the direction selectivity, analyzing the distribution of the preferred direction angles for the different experiments in each barrel.

Other quantifications were analyzed using the SigmaStat software (Systat, USA) by one-way ANOVA for repeated measures followed by the Holm-Sidak method for multiple comparisons or, if the normality test failed, by Friedman repeated-measures ANOVA on ranks followed by a Tukey test for multiple comparisons.

SUPPLEMENTAL INFORMATION

Supplemental Information includes Supplemental Experimental Procedures and four figures and can be found with this article online at https://doi.org/10.1016/j.celrep.2018.03.006.

ACKNOWLEDGMENTS

This work was supported by the Centre National de la Recherche Scientifique (France), the European Union Seventh Framework Programme BrainScaleS (FP7-ICT-2009-6 and N 269921), the Agence Nationale pour la Recherche (SensoryProcessing, Transtact), the Region Ile de France (DIM Nano-K, ML02 Neurofib), and the Lidex Neuro-Saclay. We thank Gérard Sadoc, Guillaume Hucher, and Aurélie Daret for technical and experimental assistance.

AUTHOR CONTRIBUTIONS

Conceptualization, D.E.S. and I.F.; Methodology, M.E.V., L.E., D.E.S., and I.F.; Software, M.E.V., L.E., and I.F.; Investigation, M.E.V., L.E., and I.F.; Formal Analysis, M.E.V., L.E., and I.F.; Writing – Original Draft, M.E.V.; Writing – Review & Editing, L.E., D.E.S., and I.F.; Funding Acquisition, D.E.S. and I.F.; Supervision, D.E.S. and I.F.

DECLARATION OF INTERESTS

The authors declare no competing interests.

Received: March 21, 2017
Revised: January 17, 2018
Accepted: February 28, 2018
Published: March 27, 2018

REFERENCES

Andermann, M.L., and Moore, C.I. (2006). A somatotopic map of vibrissa motion direction within a barrel column. Nat. Neurosci. *9*, 543–551.

Armstrong-James, M., and Callahan, C.A. (1991). Thalamo-cortical processing of vibrissal information in the rat. II. spatiotemporal convergence in the thalamic ventroposterior medial nucleus (VPm) and its relevance to generation of receptive fields of S1 cortical "barrel" neurones. J. Comp. Neurol. *303*, 211–224.

Arnold, P.B., Li, C.X., and Waters, R.S. (2001). Thalamocortical arbors extend beyond single cortical barrels: an in vivo intracellular tracing study in rat. Exp. Brain Res. *136*, 152–168.

Brecht, M., and Sakmann, B. (2002). Dynamic representation of whisker deflection by synaptic potentials in spiny stellate and pyramidal cells in the barrels and septa of layer 4 rat somatosensory cortex. J. Physiol. *543*, 49–70.

Brecht, M., Roth, A., and Sakmann, B. (2003). Dynamic receptive fields of reconstructed pyramidal cells in layers 3 and 2 of rat somatosensory barrel cortex. J. Physiol. *553*, 243–265.

Brumberg, J.C., Pinto, D.J., and Simons, D.J. (1996). Spatial gradients and inhibitory summation in the rat whisker barrel system. J. Neurophysiol. *76*, 130–140.

Carvell, G.E., and Simons, D.J. (1986). Somatotopic organization of the second somatosensory area (SII) in the cerebral cortex of the mouse. Somatosens. Res. *3*, 213–237.

Civillico, E.F., and Contreras, D. (2006). Integration of evoked responses in supragranular cortex studied with optical recordings in vivo. J. Neurophysiol. *96*, 336–351.

Drew, P.J., and Feldman, D.E. (2007). Representation of moving wavefronts of whisker deflection in rat somatosensory cortex. J. Neurophysiol. *98*, 1566–1580.

Ego-Stengel, V., Mello e Souza, T., Jacob, V., and Shulz, D.E. (2005). Spatiotemporal characteristics of neuronal sensory integration in the barrel cortex of the rat. J. Neurophysiol. *93*, 1450–1467.

Ego-Stengel, V., Le Cam, J., and Shulz, D.E. (2012). Coding of apparent motion in the thalamic nucleus of the rat vibrissal somatosensory system. J. Neurosci. *32*, 3339–3351.

Feldmeyer, D., Brecht, M., Helmchen, F., Petersen, C.C.H., Poulet, J.F.A., Staiger, J.F., Luhmann, H.J., and Schwarz, C. (2013). Barrel cortex function. Prog. Neurobiol. *103*, 3–27.

Fisher, N.I. (1995). Statistical Analysis of Circular Data (Cambridge University Press).

Higley, M.J., and Contreras, D. (2003). Nonlinear integration of sensory responses in the rat barrel cortex: an intracellular study in vivo. J. Neurosci. *23*, 10190–10200.

Higley, M.J., and Contreras, D. (2005). Integration of synaptic responses to neighboring whiskers in rat barrel cortex in vivo. J. Neurophysiol. *93*, 1920–1934.

Hubel, D.H., and Wiesel, T.N. (1963). Shape and arrangement of columns in cat's striate cortex. J. Physiol. *165*, 559–568.

Hübener, M., Shoham, D., Grinvald, A., and Bonhoeffer, T. (1997). Spatial relationships among three columnar systems in cat area 17. J. Neurosci. *17*, 9270–9284.

Jacob, V., Le Cam, J., Ego-Stengel, V., and Shulz, D.E. (2008). Emergent properties of tactile scenes selectively activate barrel cortex neurons. Neuron *60*, 1112–1125.

Jacob, V., Estebanez, L., Le Cam, J., Tiercelin, J.-Y., Parra, P., Parésys, G., and Shulz, D.E. (2010). The Matrix: a new tool for probing the whisker-to-barrel system with natural stimuli. J. Neurosci. Methods *189*, 65–74.

Kim, U., and Ebner, F.F. (1999). Barrels and septa: separate circuits in rat barrels field cortex. J. Comp. Neurol. *408*, 489–505.

Kleinfeld, D., and Delaney, K.R. (1996). Distributed representation of vibrissa movement in the upper layers of somatosensory cortex revealed with voltage-sensitive dyes. J. Comp. Neurol. *375*, 89–108.

Knutsen, P.M., Mateo, C., and Kleinfeld, D. (2016). Precision mapping of the vibrissa representation within murine primary somatosensory cortex. Philos. Trans. R. Soc. Lond. B Biol. Sci. *371*, 20150351.

Kremer, Y., Léger, J.-F., Goodman, D., Brette, R., and Bourdieu, L. (2011). Late emergence of the vibrissa direction selectivity map in the rat barrel cortex. J. Neurosci. *31*, 10689–10700.

Le Cam, J., Estebanez, L., Jacob, V., and Shulz, D.E. (2011). Spatial structure of multiwhisker receptive fields in the barrel cortex is stimulus dependent. J. Neurophysiol. *106*, 986–998.

Manns, I.D., Sakmann, B., and Brecht, M. (2004). Sub- and suprathreshold receptive field properties of pyramidal neurones in layers 5A and 5B of rat somatosensory barrel cortex. J. Physiol. *556*, 601–622.

Moore, C.I., and Nelson, S.B. (1998). Spatio-temporal subthreshold receptive fields in the vibrissa representation of rat primary somatosensory cortex. J. Neurophysiol. *80*, 2882–2892.

Narayanan, R.T., Egger, R., Johnson, A.S., Mansvelder, H.D., Sakmann, B., de Kock, C.P.J., and Oberlaender, M. (2015). Beyond Columnar Organization: Cell Type- and Target Layer-Specific Principles of Horizontal Axon Projection Patterns in Rat Vibrissal Cortex. Cereb. Cortex *25*, 4450–4468.

Perronnet, L., Vilarchao, M.E., Hucher, G., Shulz, D.E., Peyré, G., and Ferezou, I. (2016). An automated workflow for the anatomo-functional mapping of the barrel cortex. J. Neurosci. Methods *263*, 145–154.

Petersen, C.C.H. (2003). The barrel cortex–integrating molecular, cellular and systems physiology. Pflugers Arch. *447*, 126–134.

Petersen, C.C. (2007). The functional organization of the barrel cortex. Neuron *56*, 339–355.

Petersen, C.C.H., and Sakmann, B. (2001). Functionally independent columns of rat somatosensory barrel cortex revealed with voltage-sensitive dye imaging. J. Neurosci. *21*, 8435–8446.

Polley, D.B., Rickert, J.L., and Frostig, R.D. (2005). Whisker-based discrimination of object orientation determined with a rapid training paradigm. Neurobiol. Learn. Mem. *83*, 134–142.

Rothschild, G., and Mizrahi, A. (2015). Global order and local disorder in brain maps. Annu. Rev. Neurosci. *38*, 247–268.

Shimegi, S., Ichikawa, T., Akasaki, T., and Sato, H. (1999). Temporal characteristics of response integration evoked by multiple whisker stimulations in the barrel cortex of rats. J. Neurosci. *19*, 10164–10175.

Shimegi, S., Akasaki, T., Ichikawa, T., and Sato, H. (2000). Physiological and anatomical organization of multiwhisker response interactions in the barrel cortex of rats. J. Neurosci. *20*, 6241–6248.

Simons, D.J. (1978). Response properties of vibrissa units in rat SI somatosensory neocortex. J. Neurophysiol. *41*, 798–820.

Simons, D.J. (1985). Temporal and spatial integration in the rat SI vibrissa cortex. J. Neurophysiol. *54*, 615–635.

Simons, D.J., and Carvell, G.E. (1989). Thalamocortical response transformation in the rat vibrissa/barrel system. J. Neurophysiol. *61*, 311–330.

Thivierge, J.-P., and Marcus, G.F. (2007). The topographic brain: from neural connectivity to cognition. Trends Neurosci. *30*, 251–259.

Wilson, S.P., Law, J.S., Mitchinson, B., Prescott, T.J., and Bednar, J.A. (2010). Modeling the emergence of whisker direction maps in rat barrel cortex. PLoS ONE *5*, e8778.

Woolsey, T.A., and Van der Loos, H. (1970). The structural organization of layer IV in the somatosensory region (SI) of mouse cerebral cortex. The description of a cortical field composed of discrete cytoarchitectonic units. Brain Res. *17*, 205–242.

Zhu, J.J., and Connors, B.W. (1999). Intrinsic firing patterns and whisker-evoked synaptic responses of neurons in the rat barrel cortex. J. Neurophysiol. *81*, 1171–1183.

NEUROSCIENCE

REVIEW

L. Estebanez et al. / Neuroscience 368 (2018) 81–94

Representation of Tactile Scenes in the Rodent Barrel Cortex

Luc Estebanez, Isabelle Férézou, Valérie Ego-Stengel and Daniel E. Shulz *

Unité de Neuroscience, Information et Complexité (UNIC), Centre National de la Recherche Scientifique, FRE 3693, 91198 Gif-sur-Yvette, France

Abstract—After half a century of research, the sensory features coded by neurons of the rodent barrel cortex remain poorly understood. Still, views of the sensory representation of whisker information are increasingly shifting from a labeled line representation of single-whisker deflections to a selectivity for specific elements of the complex statistics of the multi-whisker deflection patterns that take place during spontaneous rodent behavior – so called natural tactile scenes. Here we review the current knowledge regarding the coding of patterns of whisker stimuli by barrel cortex neurons, from responses to single-whisker deflections to the representation of complex tactile scenes. A number of multi-whisker tunings have already been identified, including center-surround feature extraction, angular tuning during edge-like multi-whisker deflections, and even tuning to specific statistical properties of the tactile scene such as the level of correlation across whiskers. However, a more general model of the representation of multi-whisker information in the barrel cortex is still missing. This is in part because of the lack of a human intuition regarding the perception emerging from a whisker system, but also because in contrast to other primary sensory cortices such as the visual cortex, the spatial feature selectivity of barrel cortex neurons rests on highly nonlinear interactions that remained hidden to classical receptive field approaches.

This article is part of a Special Issue entitled: Barrel Cortex.

Key words: barrel cortex, whisker stimulation, naturalistic stimulus, sensory responses, neural coding.

INTRODUCTION

In this Review, we describe the wide repertoire of whisker movement features that are coded by barrel cortex neurons in the anesthetized rodent preparation. We start from the low-dimensional properties described with simple single-whisker deflections that can be combined into a linear model of barrel cortex neurons. We then discuss the impact of several elements of the sensory context, such as the stimulation density and the effect of an immediately preceding stimulus, which both affect neuronal responses in ways not predicted by the linear model. These observations reveal the existence of numerous intrinsic nonlinearities of cortical neurons.

Neuronal selectivity for global tactile properties of the surfaces contacted by multiple whiskers cannot be available from any single-whisker contact alone. We describe recent efforts to understand how neurons in the vibrissal system analyze simultaneous whisker deflections and how the barrel cortex extracts collective properties of complex stimuli.

*Corresponding author.
E-mail address: daniel.shulz@unic.cnrs-gif.fr (D. E. Shulz).

https://doi.org/10.1016/j.neuroscience.2017.08.039

A RECEPTIVE FIELD ANALYSIS OF BARREL CORTEX NEURONS FUNCTION

To identify the functional properties of neurons, the traditional approach in sensory physiology has been to explore the sensory periphery and find the limits of the area of the periphery that triggers a neuronal response. Delineating this area – the so called receptive field (Hartline, 1938) – has been a dominant research strategy in the study of the barrel cortex, inspired by the earlier studies of the visual system (Hubel, 1959; Hubel and Wiesel, 1962) that were highly informative of visual functional properties. In the whisker system, the relevant stimulus space includes not only the identity of the stimulated whiskers (Welker, 1971), but also a number of additional parameters of the whisker deflection – including the direction and amplitude of the whisker stimulation – that are encoded by the highly specialized tactile sensors in whisker follicles (Rice, 1993; Rice et al., 1993; Mosconi et al., 1993).

Multiple tunings to specific whisker deflection properties

With the advent of the first controlled single-whisker stimulators, several studies have demonstrated that barrel cortex neurons encode specific properties of

whisker deflections. These features include the amplitude of the peripheral movement, either in position, speed or acceleration (Simons, 1978; Simons, 1983; Arabzadeh et al., 2003), the frequency of an oscillatory input (Simons, 1978; Arabzadeh et al., 2003; Andermann et al., 2004; Ewert et al., 2008), the interval between repetitive stimulations (Simons, 1985; Ahissar et al., 2001; Webber and Stanley, 2004) and the direction of deflection (Simons, 1978; Bruno and Simons, 2002; Wilent and Contreras, 2005). These studies have mostly focused on responses to movements of the principal whisker (PW), which is classically defined based on the latency and/or strength of the neuronal response to a standard ramp-and-hold whisker deflection. Similar response properties are observed for stimulation of the surround whiskers that elicit a response, albeit with reduced amplitude and dynamical characteristics.

Among these tuning properties, direction selectivity has been one of the most thoroughly studied, perhaps because it represents the most obvious feature of the input space that can be parameterized and is also a prominent feature of barrel cortex neuronal responses. For example, Fig. 1A shows intracellular recordings of a layer 4 neuron in the anesthetized rat in response to deflection of its principal whisker in eight randomly interleaved directions (Wilent and Contreras, 2005). Robust synaptic responses were observed, occasionally leading to one or two spikes. The selectivity to the direction was larger for the spike output than for the synaptic potentials, highlighting the contribution of intracellular mechanisms and spike thresholding to information processing.

Most natural whisker deflections occur at very high speed and acceleration (Ritt et al., 2008), and particularly during discrete stick then slip events (Wolfe et al., 2008) that occur when a whisker is rubbed against a surface. Neuronal recordings have been performed during such events (Jadhav et al., 2009). In a 20-ms time window following slip events, particularly those with high acceleration, the firing rate of the neuron recorded in an awake head-fixed rat is increased (Fig. 1B). Even more systematic and reliable spiking (approximately 1 action potential per event) was observed in the first-order mechanosensory neurons in the trigeminal ganglion of the anesthetized rat (Lottem and Azouz, 2009). These results suggest that a few profiles of whisker motion can trigger the response of a sensory neuron to its principal whisker. Like in the visual system, the signal processing filters through which each neuron analyzes its input can be viewed as elemental neuronal computations.

Recently, several studies have systematically measured the temporal filters of barrel cortex neurons, that is the optimal whisker deflection shape to trigger spikes (Maravall et al., 2007; Estebanez et al., 2012). This has been done by delivering white noise (randomized deflections) to the peripheral inputs while recording the spiking output of a neuron (Fig. 1C1). Significant temporal filters are then extracted using reverse correlation techniques such as the spike-triggered average or the spike-triggered covariance, in particular for the principal whisker (Fig. 1C2). In the barrel cortex, principal component analysis of significant linear filters obtained from neurons in layers 4 to 6 showed that most individual filters could be described as a linear combination of two 30-ms deflection profiles, called the common filters of the system. These filters are 90° dephased versions of each other (Fig. 1C3). These filters are a combination of pure speed and pure acceleration filters, and suggest that barrel cortex neurons may focus on stimulation events that maximize these components such as stick and slip shapes (that turn out to have time profiles that can be directly compared to the filters shapes, Lottem and Azouz, 2009). This speed/acceleration also triggers spiking in layer 2/3 of the barrel cortex (Estebanez et al., 2016; Martini et al., 2017). A full review of the buildup of temporal filters across the different stages of the whisker system can be found in the same volume (Bale and Maravall, 2017).

The relevance of the features identified in anesthetized rodents is confirmed by behavioral studies showing that trained head-fixed animals can accurately decode these parameters in the absence of self-generated whisker movements, including the presence of "slip-like" events (Waiblinger et al., 2015) or the frequency and speed of an oscillatory pattern (Stüttgen et al., 2006; Mayrhofer et al., 2013). Recent results obtained in freely running rats further demonstrate that extraction of tactile information from the environment does not necessarily rely on active rhythmic whisker motion (Kerekes et al., 2017).

In the behaving rodent, these fine-scale touch inputs may be often dominated by large-scale whisking (Welker, 1964), which can activate Merkel mechanoreceptors in the whisker follicles (Severson et al., 2017) and get relayed up to the trigeminal ganglion neurons (Campagner et al., 2016). However, inhibitory neurons located in the layer 4 of the barrel-cortex seem capable to filter out the inputs related to the whisker active movements, allowing the transmission of mostly touch-related inputs to layer 4 excitatory neurons (Yu et al., 2016). Therefore, the stimulus space that is tested in the anesthetized rodent preparation is likely to match the inputs that are actually processed in the barrel cortex of awake behaving animals.

The receptive field, a collection of single-whisker filters

The discovery, half a century ago, of the discrete anatomy of the barrel cortex (Woolsey and Van der Loos, 1970), and of the precise point-to-point projections at many levels across the pathway from follicles to the cortex, have initially emphasized a fundamentally parallel view of the whisker system (Welker, 1971). At first sight, this sensory-processing system could thus seem like a coexistence of labeled lines, each whisker sending information to a given barrelette, barreloid and barrel. However, very early on, functional studies have reported that the firing rate of neurons is increased following movements of more than one whisker (Simons, 1978; Ito, 1981; Armstrong-James and Fox, 1987; Ghazanfar and Nicolelis, 1999).

Fig. 2A shows the spatial extent of the receptive field of a neuron in layer 4 of barrel C2 of an anesthetized rat

(Le Cam et al., 2011). In addition to the principal whisker, the deflection of neighboring whiskers evokes spiking significantly above the baseline level. Spiking receptive fields can encompass more than 10 whiskers, especially in layer 5b, and tend to be elongated along rows (Simons, 1978; Armstrong-James and Fox, 1987). Intracellular recordings have confirmed these results and extended them to a detailed description of the subthreshold postsynaptic potentials evoked by stimulation of the principal and neighboring whiskers (Moore and Nelson, 1998; Zhu and Connors, 1999; Brecht and Sakmann, 2002a; Brecht et al., 2003; Manns et al., 2004). In particular, subthreshold membrane potential studies have revealed the existence of "silent" cells in layer 3, which fire very few spikes but receive inputs from whiskers two to three rows away from the PW (Fig. 2B, Erchova & Shulz, unpublished results; Brecht et al., 2003). Another interesting property gathered from these intracellular recordings is the relative paucity of inhibitory or suppressive zones in barrel cortex receptive fields. This differs from the thalamic stage, in which both inhibitory potentials and suppression of activity can be demonstrated for deflection of surround whiskers (Brecht and Sakmann, 2002b; Ego-Stengel et al., 2012). The dominance of excitatory responses in S1 is also contrasting with typical receptive fields in the visual system, and could originate in the very fast arrival of excitatory and inhibitory signals in S1 (< 10 ms), those signals being tightly synchronized and correlated in amplitude (Okun and Lampl, 2008).

This neuron-centered view of barrel cortex function can be complemented with a whisker-centered view, using techniques which allow the measure of activity across the surface of the cortex. Indeed, single-whisker evoked activity extends over at least 10 cortical barrels (Fig. 2C) as shown by exploring responses across the surface of the cortex (Axelrad et al., 1976), and in later works by recording with electrode arrays the spread of spiking activity in response to the deflection of a single whisker, (Petersen and Diamond, 2000). This finding was confirmed using Voltage-Sensitive Dye Imaging (VSDI), which reveals subthreshold responses (Berger et al., 2007): a single-whisker deflection triggered a large wave of activity originating in the corresponding barrel column, and rapidly spreading throughout the whole-barrel cortex and beyond (Fig. 2D) (Ferezou et al., 2006, 2007). These results confirm that functional connections allow barrel cortex neurons to gather information from

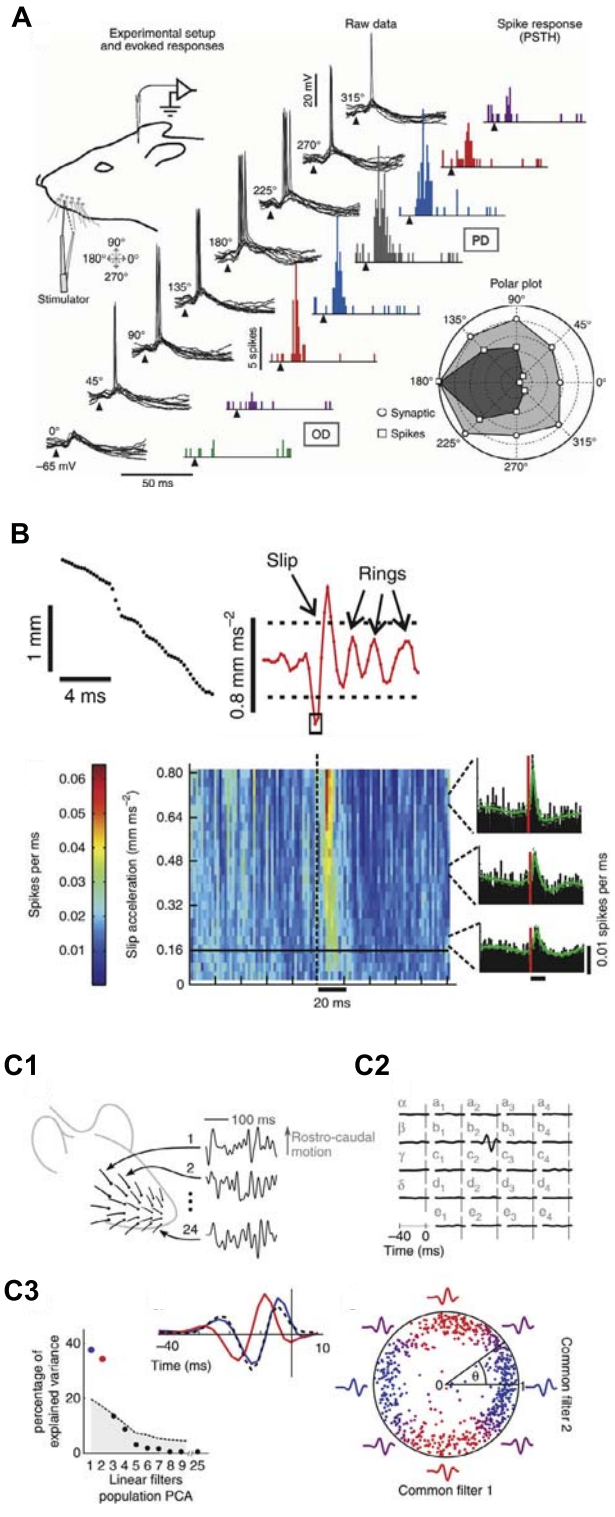

Fig. 1. Response properties of barrel cortex neurons to movement features of the principal whisker. (A) Direction selectivity in a layer 4 neuron recorded intracellularly in an anesthetized rat, while its principal whisker was deflected in eight different directions. The membrane potential and spike histograms are shown for 8 trials for each direction (PD: preferred direction, OD: opposite direction). The average responses are plotted in polar coordinates, revealing a significant directionality, larger for the spike output than for the synaptic response (from Wilent and Contreras, 2005). (B) Spiking response to slip-stick events in a barrel cortex neuron recorded in the awake rat. Top, Example of whisker motion on a coarse sandpaper (left, position; right, acceleration) revealing a high-acceleration slip event. Bottom, Time course of the response as a function of peak whisker acceleration, revealing strong tuning of the neuron to the slip events (from Jadhav et al., 2009). (C) Neuronal filters revealed by probing rat barrel cortex neurons with white noise as the input (C1). Spike-triggered covariance analysis for this neuron reveals the recurrence of a specific deflection profile on whisker B2 before each spike (C2). Population principal component analysis (PCA) showed that neuronal filters are surprisingly similar, and can be described as linear combinations of two generic filters (red and blue traces, C3) (from Estebanez et al., 2012).

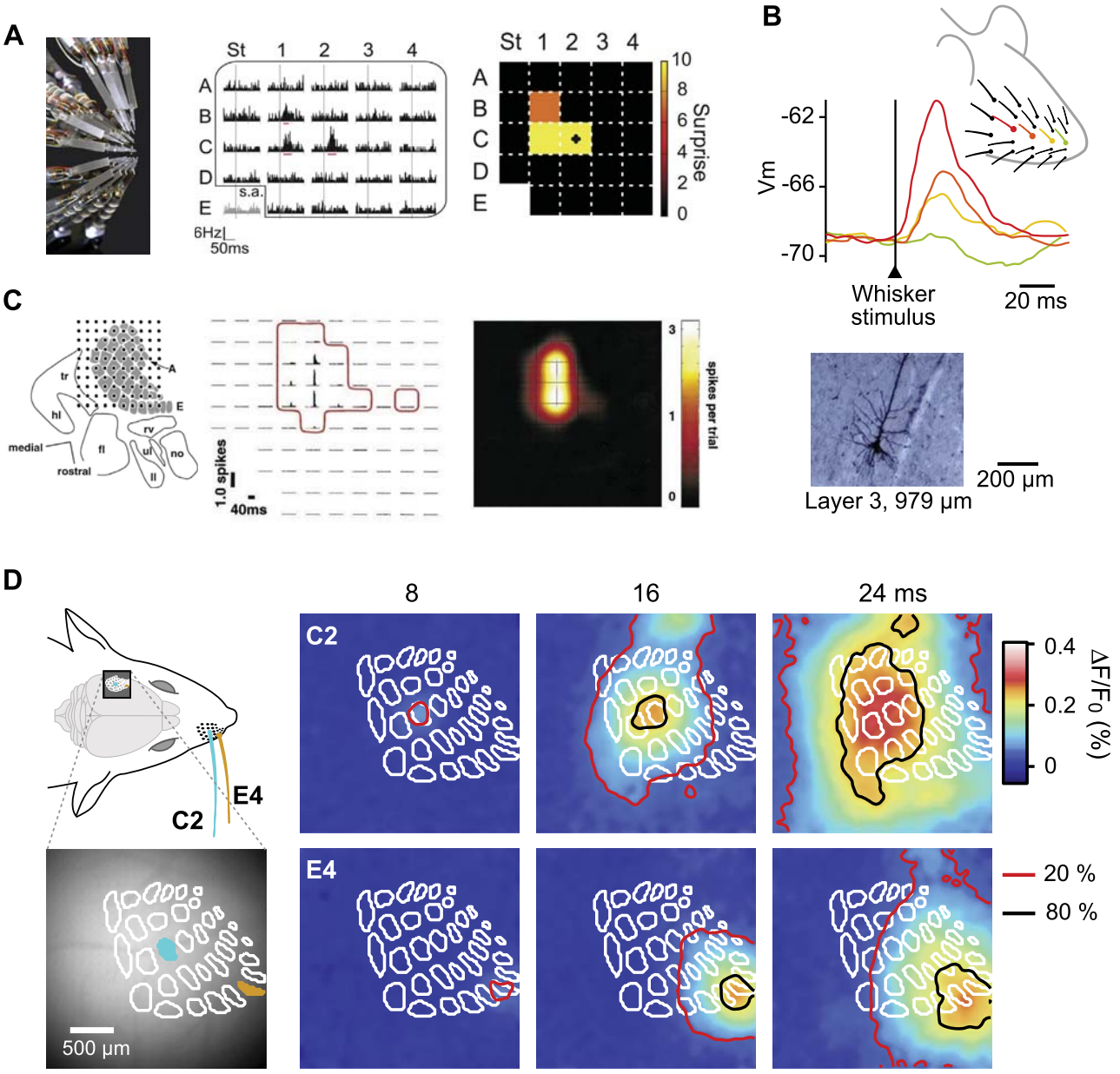

Fig. 2. Spatial extent of barrel cortex receptive fields tested with single-whisker stimuli. (A) Receptive field of a neuron recorded in layer 4 of the C2 barrel in an anesthetized rat. Left, multi-whisker stimulator controlling independently 24 whiskers. Middle, peri-stimulus time histograms of spikes recorded during sparse noise stimulation (deflection of one whisker every 50 ms; s.a.: spontaneous activity). Right, surprise value (a significance measure) for the response to each whisker (from Le Cam et al., 2011). (B) Subthreshold receptive field of a neuron recorded intracellularly in layer 3 of the C1 barrel in an anesthetized rat (C1 whisker in red). Top, averaged membrane potential in response to the deflection of the C1 whisker (principal whisker, red), C2 (orange), C3 (yellow) and C4 whisker (green). Bottom, microphotograph of the same pyramidal neuron filled with biocytin (Erchova et al., 2006). (C) Cortical spread of spiking activity in response to a single-whisker deflection. Left, 10×10 electrode array placement relative to the barrel map. Middle, peri-stimulus time histograms of spikes recorded during stimulation of whisker C1 in an anesthetized rat. Significant responses are indicated by the red line. Right, Response map in average number of spikes per trial (from Petersen and Diamond, 2000). (D) Subthreshold spread of cortical activity in response to single-whisker deflections. Left, schematic and picture of the field imaged over the barrel cortex on the anesthetized mouse brain, while individual whiskers C2 and E4 are successively deflected on the contralateral side. Right, Three snapshots of the Voltage-Sensitive Dye signal, 8, 16 and 24 ms after a deflection of C2 (top) and E4 (bottom) whiskers, showing a spreading wave of activity starting in the appropriate whisker column and invading progressively the whole imaged area (from Ferezou et al., unpublished data).

way more than a single whisker and are a possible substrate for the integration of information from multiple whiskers.

Overall, in contrast to the sharp feature selectivity observed at the single-whisker level, the spatial organization of barrel cortex receptive fields reveals little consistent structure in their spatial extent and mostly consists of a number (0–10) of adjacent whiskers in addition to the principal one. Therefore, in contrast to other primary sensory areas such as the primary visual cortex (Hubel and Wiesel, 1962), the first-order structure of the whisker receptive fields suggests that the dominant

computation may be a simple averaging of the whisker stimulations occurring over a patch of 1 to 10 nearby whiskers.

BEYOND THE LINEAR RECEPTIVE FIELD

Compared to the visual and auditory primary sensory cortices, the lack of a sharp spatial structuring of barrel cortex linear receptive fields is perplexing. They generally follow a blob-like shape (Brecht and Sakmann, 2002b; Moore and Nelson, 1998; Zhu and Connors, 1999; Brecht et al., 2003; Manns et al., 2004) and there is little indication that such receptive fields may support a complex spatial feature extraction mechanism such as ON/OFF fields (Le Cam et al., 2011). This observation suggests either that barrel cortex neurons only perform simple averaging of the stimulus intensity observed across nearby whiskers, or that more complex spatial computations are performed in the barrel cortex but can only be unveiled by looking beyond the classical linear receptive field.

Rats and mice rarely, if ever, have their whiskers deflected individually during behavior. Rather, during active exploration, animals control the acquisition of sensory information by moving their head and their whisker arrays in a goal-directed manner to collect relevant information (Mitchinson et al., 2007; Grant et al., 2009). Because of these strategies of information collection, animals encountering objects or running past surfaces have many of their whiskers on one or both sides deflected simultaneously. Some components of these deflections are strongly synchronized across the pad, while others are independent. Moreover, the inputs on each whisker follow complex time courses distributed over many frequencies, often looking like ‘‘noise”, and never repeating in exactly the same way upon repetitive scanning of the same surface (Boubenec et al., 2014). One direction of research consists in characterizing common elements and statistics of these highly complex spatiotemporal patterns of contact. For example, this approach has revealed the dominant temporal sequences of whiskers ordered by their first touch during exploration of a flat surface (Hobbs et al., 2015).

In the visual system, the principles of organization of visual receptive fields have been successfully reconstituted from the knowledge of the natural stimulation statistics (Atick, 1992; Olshausen and Field, 1996). This approach could potentially lead to similar insights into the whisker system. However, we have learned from decades of investigations in the visual system that such an approach is challenging and presents many obstacles to overcome (Rust and Movshon, 2005).

This difficulty is particularly true for the whisker system. Even if multi-whisker natural stimuli are likely to constitute a relevant subset of all possible stimuli, the task of characterizing quantitatively natural tactile scenes in the context of the rodent vibrissal system is far from trivial and is in itself the object of intensive research efforts (Hartmann, 2011). In addition, in contrast to the visual system, cortical tactile responses are highly nonlinear and dependent on the statistics of the stimulation, and call for a tight control of the sensory context in which sensory responses are probed (Maravall et al., 2007; Estebanez et al., 2012; Ramirez et al., 2014). This tight control is best obtained when using artificial whisker stimulation sequences. Therefore, even if ultimately the goal is to understand the responses to natural tactile scenes, synthetic multi-whisker stimulation paradigms built from artificial single-whisker deflections have been largely predominant in the study of the barrel cortex.

In the following sections, we first describe the means to apply independent deflections on multiple whiskers simultaneously – a prerequisite to study multi-whisker integration. We then review a large body of studies that have characterized several simple spatial and temporal nonlinearities revealed with carefully designed stimulation patterns, based on the features observed during spontaneous behavior.

Generating complex tactile stimuli for a thorough exploration of the rodent whisker system

Deflecting identified whiskers by hand is the most immediate way to generate sensory stimulations in the whisker system of the anesthetized animal (Welker, 1971), and is thus a practice still in use today to estimate the receptive field of a neuron in preparation for further investigations (Whitmire et al., 2017). Similarly, applying air puffs on the whisker pad is a straightforward way to obtain multi-whisker stimulations (Hutson and Masterton, 1986; Núñez et al., 1994; Brecht and Sakmann, 2002a; Jouhanneau et al., 2015). However, the accuracy and the constancy of this global stimulation are not well controlled. In contrast, the systematic deflection of each whisker in a controlled way has required the development of specific tools exclusively for this goal, since whisker stimulation requires large and fast movements that are not attainable with conventional mechanical actuators. Early technologies for whisker stimulation included galvanometric actuators (Simons, 1978) that allowed precise movements but at the expense of sufficient accelerations (Ito, 1981), although recent galvanometer-based actuators have largely solved this issue (Van der Bourg et al., 2016). Another choice is loudspeaker-derived whisker deflectors (Fig. 3A) that met many requirements but were unable to produce accurate positioning of the whiskers beyond the two end-stops of the solenoid (Chapin, 1986; Ghazanfar and Nicolelis, 1999; Krupa et al., 2001). More recently, most of the community has settled on using piezoelectric ‘‘benders” (Simons, 1983). These actuators are made of two sheets of piezoelectric material that perform a differential sheering action under an electric field. These devices can produce angular deflections up to 1500 degrees per second (Simons and Carvell, 1989) and up to a few degrees of whisker deflection range. More importantly, this technology allows broadband and micrometer-accurate playback of naturally occurring whisker deflection sequences (Jacob et al., 2010), and can be extended from a 1D to 2D deflection space (Fig. 3B, C; Simons, 1983; Andermann and Moore, 2006; Jacob et al., 2010; Ramirez et al., 2014; Estebanez et al., 2016).

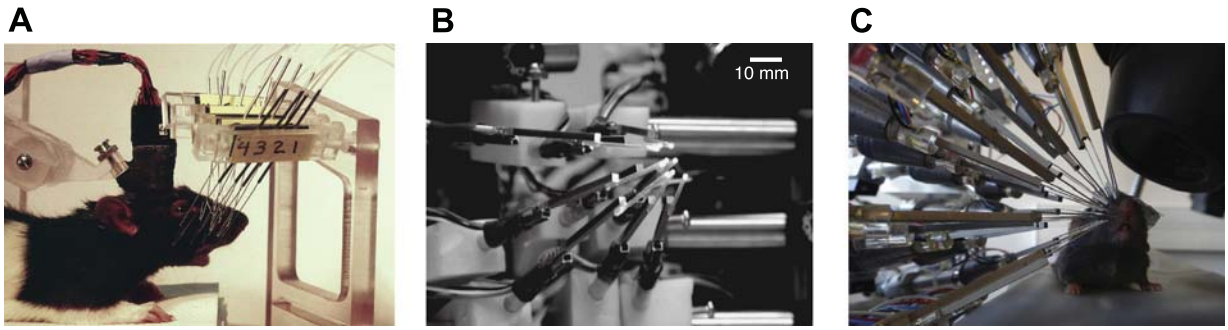

Fig. 3. Multi-whisker stimulation devices to generate complex multi-whisker tactile scenes. (A) The first documented rat multi-whisker stimulation system addressing most macrovibrissae (with 16 independent actuators) was based on solenoids pulling whiskers through stainless steel wirings (from Krupa et al., 2001). (B) The first rat multi-whisker stimulator based on piezoelectric multidirectional actuators allowed the application of controlled deflections to 9 whiskers within the rostro-caudal/ventro-dorsal plane (from Andermann and Moore, 2006). (C) Dense, 24-whisker multidirectional stimulations can be efficiently applied on the mouse whisker pad (VSD imaging experiment in the anesthetized mouse, from Ferezou, Vilarchao and Shulz, unpublished).

Beyond single-whisker stimulation, neurophysiologists have attempted early on to control separately the deflection of multiple whiskers, in order to study how the cortical activation recorded during single-whisker deflections combine during parallel deflections of multiple whiskers.

The development of the required multi-whisker stimulators has been a demanding task because of the complex geometry of the whisker pad (Brecht et al., 1997; Jacob et al., 2010; Towal et al., 2011). This implies the need to assemble a set of independent stimulators converging into the approximate 1 cm^2 of the rat whisker pad. Still, multi-whisker stimulators have been progressively developed that allow the independent stimulation of 5 whiskers (Simons, 1985; Brumberg et al., 1996; Rodgers et al., 2006), 9 whiskers (Andermann and Moore, 2006; Drew and Feldman, 2007; Ramirez et al., 2014) and finally 16 to 24 whiskers (meaning that most of the macrovibrissae are stimulated, Krupa et al., 2001; Jacob et al., 2010; Fig. 3A).

In our laboratory, we have designed a flexible and compact piezoelectric holder which can be packed in a 5×5 matrix arrangement (Jacob et al., 2008). We have developed a software solution to allow the delivery of deflection signals up to 1000 Hz with minimal ringing artifacts (less than 5% of the total amplitude) (Jacob et al., 2010). With this new generation of multi-whisker device, we can thus deliver complex spatiotemporal patterns of whisker deflections in all directions with high-frequency content, even on the very compact whisker pad of the mouse, and therefore combine complex tactile input with an easy access to modern genetic tools (Fig. 3C).

Nonlinear integration of simple deflection sequences

Nonlinearities in the cortical processing of tactile inputs were first observed in the seminal work of Simons (1978). During sinusoidal oscillatory single-whisker deflections in anesthetized rats, Simons observed that most regular spiking units responded mainly to the onset of the stimulation and progressively decreased their response to subsequent stimulation. This phenomenon of rapid sensory adaptation to repetitive whisker stimuli (Fig. 4A) has been further characterized by many studies (for review see Whitmire and Stanley, 2016; Lampl and Katz, 2017). Interestingly, its appearance seems to coincide developmentally with the acquisition of exploratory whisking (Borgdorff et al., 2007; Grant et al., 2012; Arakawa and Erzurumlu, 2015).

Rapid sensory adaptation can be observed both in the trigeminal nuclei (Mohar et al., 2013, 2015) and in the thalamus (Ahissar et al., 2000; Sosnik et al., 2001; Ganmor et al., 2010). Nonetheless, the depression of thalamocortical synaptic transmission is likely to be a major determinant of this sensory adaptation. Indeed, simultaneous recordings from the VPM and the barrel cortex during repetitive stimulation of the principal whisker revealed modest adaptation in the thalamus, but a rapid and strong suppression of both subthreshold and suprathreshold responses at the cortical level (Fig. 4A, Chung et al., 2002). The same study also showed that responses to cortical microstimulation were not affected by adaptation to the repetitive principal whisker deflection, suggesting that adaptation does not rely on a change in the efficacy of intracortical synapses. Within the cortical layer 4, classically seen as the major thalamo-recipient compartment, sensory adaptation has been shown to vary according to the recorded cell type (Brecht and Sakmann, 2002; Khatri et al., 2004; Gabernet et al., 2005), indicating that the thalamo-cortical synaptic transmission is target-specific as reported in other cortical connections (Reyes et al., 1998; Rozov et al., 2001).

The brain state, and more specifically the thalamic firing mode, strongly impacts sensory adaptation, which cannot therefore be considered as a fixed property of the bottom-up flow of information (Castro-Alamancos, 2004; Whitmire et al., 2016, 2017). Sensory adaptation leads to a shrinkage of the receptive field, as revealed by repetitive stimulation not only of the principal whisker but also of adjacent whiskers (Fig. 4B, Katz et al., 2006). This observation is indeed consistent with the reduced spatial extent of adapted cortical responses (Kleinfeld and Delaney, 1996; Sheth et al., 1998; Ollerenshaw et al., 2014). Such sharpening of cortical responses (Fig. 4C) suggests that the adapted state could improve the ability to discriminate finer features of the tactile scenes (Ollerenshaw et al., 2014; Musall et al., 2014). Furthermore, this rapid stimulus-specific sensory adap-

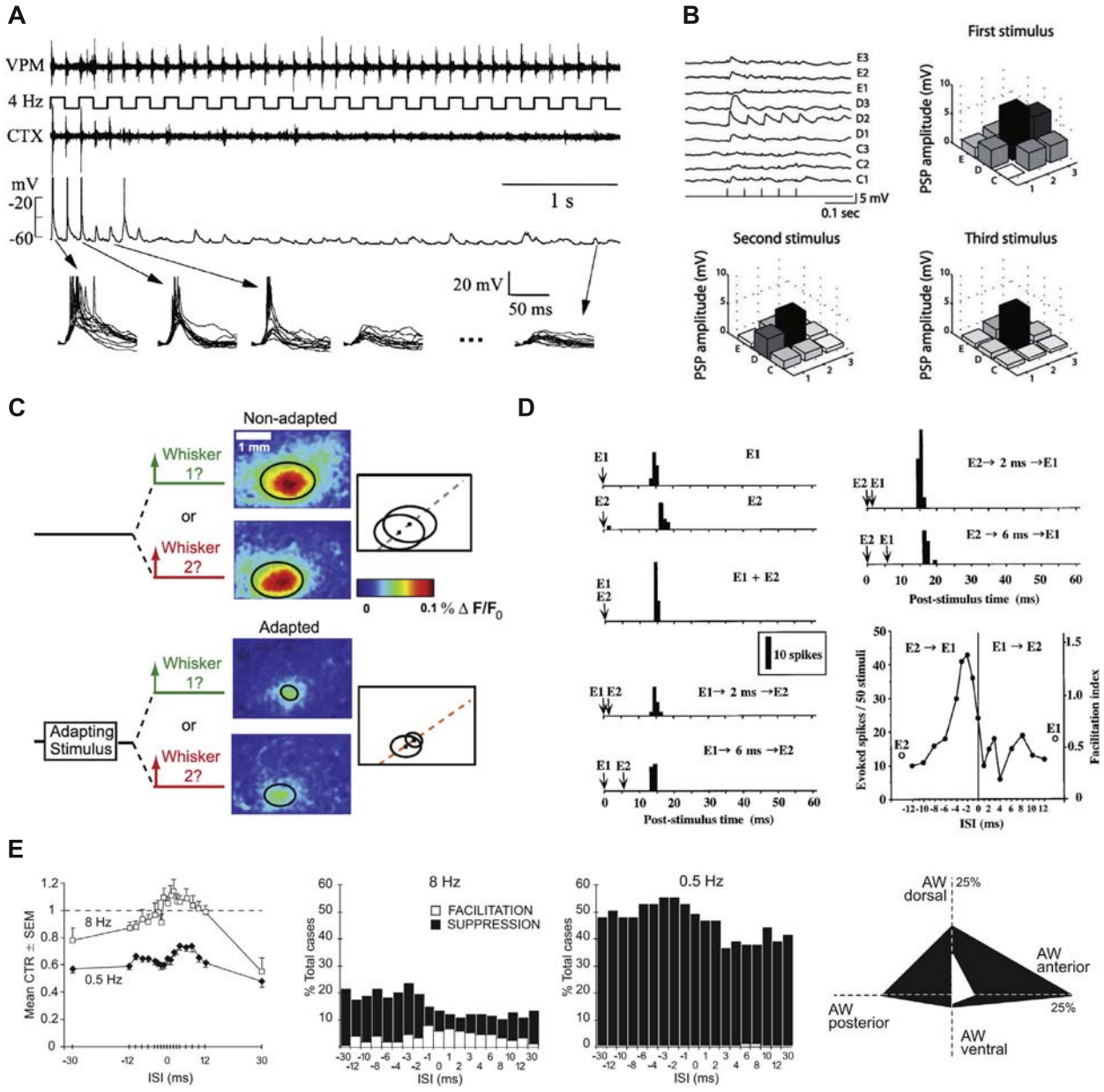

Fig. 4. Nonlinear processing of successive stimulations. (A) Rapid adaptation of whisker responses. Top: simultaneous extracellular multiunit recordings from the rat thalamus (VPM, upper trace) and barrel cortex (CTX, 390 μm depth, middle trace) during 4-Hz stimulation of the principal whisker (B1). Bottom: Responses of a cortical neuron in the C1 barrel (470 μm depth) to a 4 Hz stimulation of the principal whisker (single trial). Multiple repetitions (n = 12) of the first four and the last onset responses in the train are shown below at expanded time scale (from Chung et al., 2002). (B) The subthreshold receptive field shrinks during adaptation. Average response of a layer 4 cell to repetitive stimulation at 18 Hz of nine different whiskers (top left,) in an anesthetized rat. Note that the response to the PW (D2) shows less adaptation than that of the other whiskers. Histograms show the receptive field of the same cell constructed from the peak amplitude of the first, second and third responses to a train of stimuli (from Katz et al., 2006). (C) Adaptation spatially constrains the cortical response. Top: the cortical responses to a single-whisker stimulation in the absence of preceding stimuli. Whisker 1 (W1) and whisker 2 (W2) were adjacent to each other on the rat snout and stimulated separately. Images were averaged over 50 trials. The black ellipses on the images are half-height contours of the two-dimensional Gaussian fits to the images. On the right is the superposition of the Gaussian contours. Bottom: In contrast, when a 10-Hz adapting stimulus was preceding the whisker stimulation, the cortical response was significantly reduced in magnitude and in area (from Ollerenshaw et al., 2014). (D) Facilitation of response for specific two-whisker stimulation patterns. PSTHs of activity of a layer 2/3 neuron for deflections of E1 (principal whisker), E2 (an adjacent whisker), and simultaneous or successive deflections of E1 and E2 in an anesthetized rat. The latency difference of stimulation of individual whiskers was 3ms. Note that response facilitation peaked when E2 stimulation preceded E1 stimulation by a few milliseconds, when evoked potentials are expected to coincide in the cell (from Shimegi et al., 1999). (E) Facilitatory and suppressive interactions depend on the frequency of stimulation. Left: mean facilitation index (condition-test ratio, CTR) as a function of interstimulus intervals (ISI) averaged for all tests at 8 Hz (white symbols) and 0.5 Hz (black symbols) (86 and 42 multi-units, respectively). Note that sublinear and supralinear summations resulted in ratios < 1 and > 1, respectively. Middle graphs: The percentage of cases for which a significant facilitatory (white bars) or suppressive (black bars) effect was found as a function of ISI (1 neuron may contribute multiple times to the histogram) are depicted for whisker stimulation at 8 Hz and 0.5 Hz. Right: Average percentages depicted as polar plots, as a function of the location of the adjacent whisker relative to the principal whisker on the rat snout (from Ego-Stengel et al., 2005).

tion (Katz et al., 2006; Musall et al., 2014, 2017) might be fundamental to extract behaviorally important information from a background of constantly varying sensory inputs (Whitmire and Stanley, 2016).

Interactions between spatially separate components of the receptive fields have been studied in other sensory modalities (Heggelund, 1981; Sillito et al., 1995; Lampl et al., 2004) in order to identify nonlinearities of spatial integration. In the barrel cortex, the discrete whisker grid defines a natural way to split spatially the receptive field. It is thus particularly straightforward to compare the responses to separate whiskers versus the response to a stimulation that combines the selected whiskers. When recording the neuronal responses to deflections of pairs of whiskers with varying delays, mainly suppressive interactions have been reported (Simons, 1985; Carvell and Simons, 1988; Simons and Carvell, 1989; Kleinfeld and Delaney, 1996; Goldreich et al., 1998; Mirabella et al., 2001; Higley and Contreras, 2005; Erchova et al., 2006). Both sub-cortical and intracortical processes are thought to contribute to such sublinear integration of multi-whisker input. However, at odds with these observations, some supralinear interactions have also been reported in supra (Fig. 4D) and infra granular layers of the barrel cortex (Ghazanfar and Nicolelis, 1997; Shimegi et al., 1999, 2000). Such facilitation occurs for short inter-stimuli intervals and specific combinations of whisker stimuli, and could therefore serve as a detection mechanism for coincidences of behaviorally relevant multi-whisker input.

We have extended these results by demonstrating that pairwise whisker interactions are reshaped when delivering stimulations at a frequency corresponding to behaviorally active states, that is, the frequency of exploratory whisking (Ego-Stengel et al., 2005). Paired whisker stimuli delivered at 8 Hz, where rapid sensory adaptation is engaged, indeed favored supralinear responses. Moreover we found that the facilitation was enhanced when the adjacent whisker was located anterior or dorsal to the principal whisker (Fig. 4E, Ego-Stengel et al., 2005). This observation that adaptation tends to facilitate multi-whisker integration has been subsequently confirmed and demonstrated functionally by more recent studies (Higley and Contreras, 2007; Ollerenshaw et al., 2014), suggesting that specific spatiotemporal patterns of two-whisker deflections can be detected by subsets of neurons.

Overall, these results reveal that nonlinear processing is carried out by barrel cortex neurons even with simulation sequences involving simple pulse-like deflections of only one or two whiskers at a time. Nonetheless, single-whisker deflections are seldom encountered in a natural settings and more complex sensory context strongly influences the spatiotemporal dynamics of cortical responses in the barrel cortex.

Impact of the sensory context on the linear receptive field properties

We refer here as sensory context to the collection of tactile stimuli taking place in an extended window in time and space, which can modulate the responses of a neuron to the stimuli present in the center of the receptive field.

Similar to the visual system (Fournier et al., 2011), increasing the spatiotemporal density of tactile inputs to ranges that are more relevant behaviorally has been shown to affect the integrative properties of barrel cortex neurons. Maravall and collaborators have shown that in the barrel cortex, changes in stimulus statistics induced strong spike rate adaptation (Fig. 5A, Maravall et al., 2007) and a corresponding change in the coding space used by the neurons. To do so they applied continuously changing, randomized deflections to several whiskers, and they switched back and forth between two set values of Gaussian variance in position and velocity. Spike-triggered covariance analysis of single units revealed that adapting neurons rescaled their input–output tuning function according to the stimulus distribution. By means of such adaptive gain rescaling, the information transmission about stimulus features was maintained despite the change in sensory context. This feature of neuronal integration in the barrel cortex might be essential to enhance stimulus discriminability across behavioral contexts.

Increasing the dimensionality of the stimulus space can thus help revealing important principles of neuronal processing. In this line of research, Ramirez and collaborators (2014) used a nine-whisker multi-directional stimulator to compare the barrel cortex activity during sparse, non-overlapping stimuli (‘‘simple”) versus dense (‘‘complex”), overlapping random stimulations of 9 whiskers in 8 directions (Fig. 5B, C). Reverse correlation analysis of the neurons membrane potential was used to identify the spatiotemporal receptive fields obtained in the two conditions. The complex stimulation protocol revealed markedly sharpened receptive fields compared to the ones obtained with sparse whisker stimulation. For example, layer 5 thick-tufted pyramidal neurons, which responded equally to most whiskers when mapped with conventional single-whisker stimuli, became highly focused on the principal whisker during complex stimuli. This switch in coding, most likely due to adaptation mechanisms, is particularly marked in layer 5 neurons. Once again, the sensory context and the level of adaptation (both being highly modulated in natural conditions of whisker tactile explorations) appear to strongly impact the integration of tactile inputs. This stresses the importance of exploring a stimulus space with high dimensionality to obtain a more comprehensive description of cortical input/output relationships.

CODING BEYOND MULTIPLE SINGLE-WHISKER STIMULATIONS

The nonlinearity of the response to combinations of deflections of two whiskers indicates that beyond the shape of the linear receptive field, spatial features of the tactile stimuli are indeed coded in the barrel cortex in the form of higher order interactions between whisker stimulations.

This nonlinearity results in a major experimental difficulty as there is no simple way to estimate the

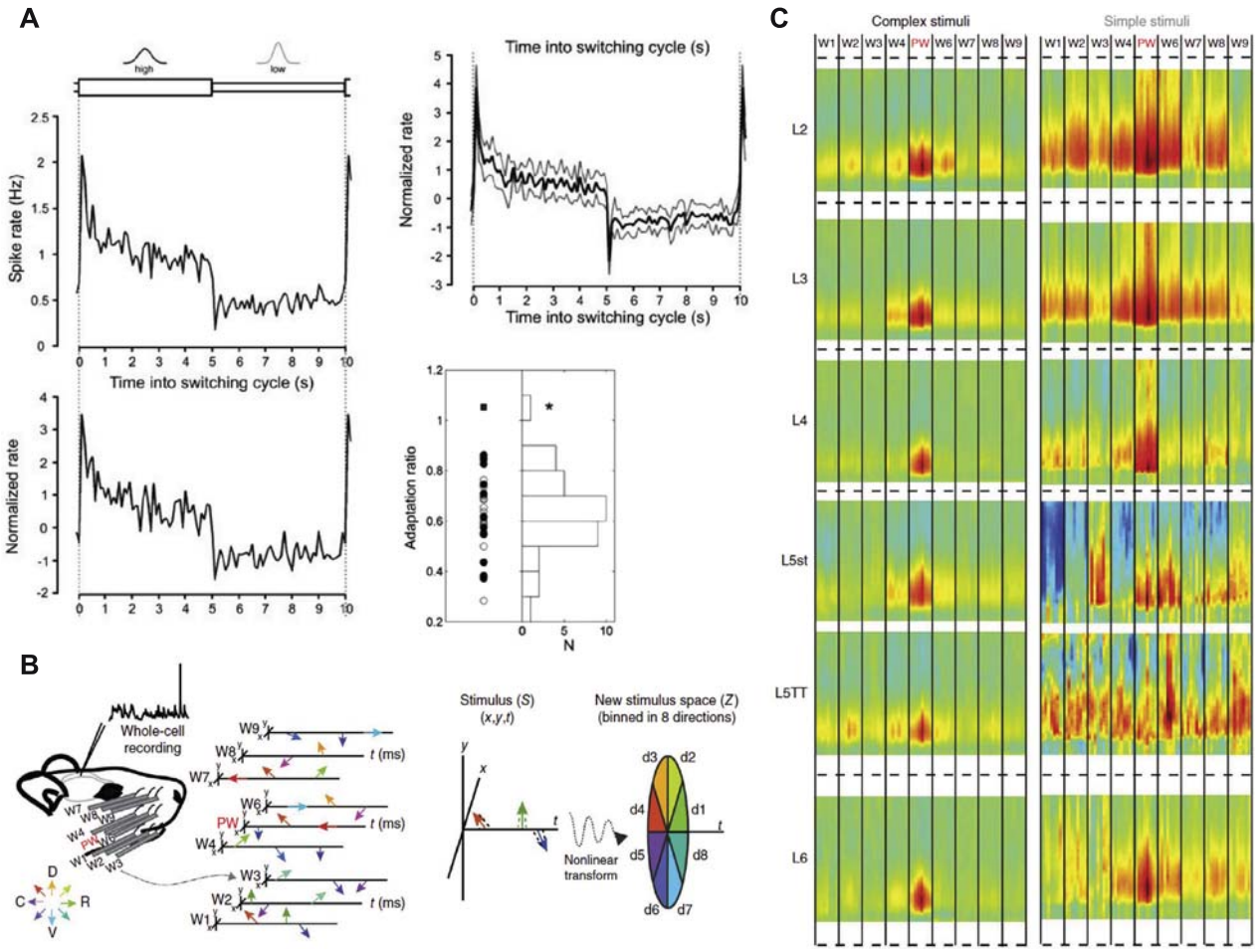

Fig. 5. Impact of tactile input density on neuronal dynamics in the barrel cortex. (A) Adaptive responses to switching variance of noise stimuli. The principal whisker together with its adjacent whiskers was deflected in one dimension with a random sequence of positions in an anesthetized rat. Instantaneous positions were distributed according to a Gaussian distribution whose variance was switched every 5 s. Top left: Absolute spike rate of a single unit averaged over switching cycles (1 080 repetitions, bin size, 100 ms). Below is normalized rate modulation. Top right: rate modulation pooled over all adapting single neurons (n = 9, average ± standard deviation). Rate modulation was robust and occurred over a similar timescale across the population. Bottom right: adaptation ratios. The firing rate at steady state (binned 4–5 s after each upward switch in stimulus variance) was divided by the rate immediately after switching to high variance (binned 0–100 ms after the switch). Left: data points. Filled gray square, non-adapting neuron (n = 1); filled black circles, adapting single neurons (n = 13); open circles, adapting multi-neuron clusters (n = 20). Right: histogram of adaptation ratios for all recordings shown on the left side. Only a single-cortical neuron showed non-adapting behavior. The asterisk denotes that this neuron's adaptation ratio was significantly different from that of the rest of the population (p = 0.001) (from Maravall et al., 2007). (B) Spatiotemporal receptive fields of barrel cortex neurons revealed by reverse correlation of synaptic inputs. Left, schematic of the experimental setup. Rat barrel cortex neurons were recorded intracellularly during simple or complex stimulation of nine whiskers (W1–W9) delivered by means of multi-directional piezoelectric stimulators. Simple stimulations consisted in the ramp-and-hold deflection of one whisker selected randomly among the nine, and moved in one of the eight cardinal directions every 1.5 s while other whiskers did not move. The complex stimulation protocol where the nine whiskers are moved simultaneously and continuously is illustrated. Each arrow represents an independent deflection of one whisker. Deflections occurred stochastically in time (frequency of ~9.1 Hz) and direction (among 8 possible, C: caudal, R: rostral, D: dorsal, V: ventral). Nonlinear stimulus representation where whisker movements are represented in an eight angle–binned space instead of Cartesian space is shown on the right panel (from Ramirez et al., 2014). (C) Complex stimuli reveal markedly sharpened receptive fields relative to conventional stimuli. Population-averaged spatiotemporal receptive fields were calculated for neurons of the same cell type based on complex multi-whisker stimuli (left) or simple single-whisker stimuli (right) (from Ramirez et al., 2014).

meaningful spatial features of the whisker stimulation scenes that are extracted by the barrel cortex neurons. This is in contrast to the ON and OFF subfields that can be identified during simple receptive field mappings in the cat V1 cortical area and which are structured in the shape of a Gabor filter (Marcelja, 1980). In addition, the lack of a direct equivalent of the whisker system in humans (although relationship with the human hand touch system have be drawn, Ahissar and Assa, 2016) limits the possibility of an introspection strategy that may provide an experimenter with critical insight in the sensory system (as well as a substantial bias). Overall, very few cues are available to guide a neurophysiologist in the identification of relevant spatial features of multi-whisker stimulations.

To explore this question nonetheless, one strategy is to start from the observation, already reviewed above, that changes in the sensory context of whisker

stimulations can have a strong impact on the barrel cortex functional responses. The so called "context" was initially a change in the density of whisker stimulations outside of the receptive field of the neurons (Brumberg et al., 1996; Ramirez et al., 2014). But this concept could be extended to whisker pad-wide homogeneous changes in cross-whisker correlation patterns, thereby defining a spatial structure in statistical terms. This hypothesis was tested by comparing the functional responses obtained during independent dense white noise stimulation on 24 whiskers (in which each whisker receives a different input), versus a correlated dense noise stimulation in which the same deflection is applied to all 24 whiskers simultaneously. Both inputs share the same stimulus density, but one is uncorrelated and the other fully correlated. In this study, we described two separate populations of neurons, one triggered specifically by the correlated stimulus, while a second population of neurons is mostly responsive during uncorrelated stimulations (Estebanez et al., 2012, 2016). Interestingly, these two populations of neurons are spatially segregated in the superficial layers of the cortex, which suggests that they may be part of separate processing circuits and/or project to separate downstream areas (Estebanez et al., 2016).

Beyond whisker pad-wide homogeneous stimulus statistics, whiskers are often subject to heterogeneous touch scenes where dynamic subsets of whiskers contact a surface (Hobbs et al., 2016). These changes in the configuration of stimulated whiskers may be coded by barrel cortex neurons. Again, based on current knowledge, it is difficult to come up with spatial motifs of whisker stimulations that would be relevant to the whisker system. Based

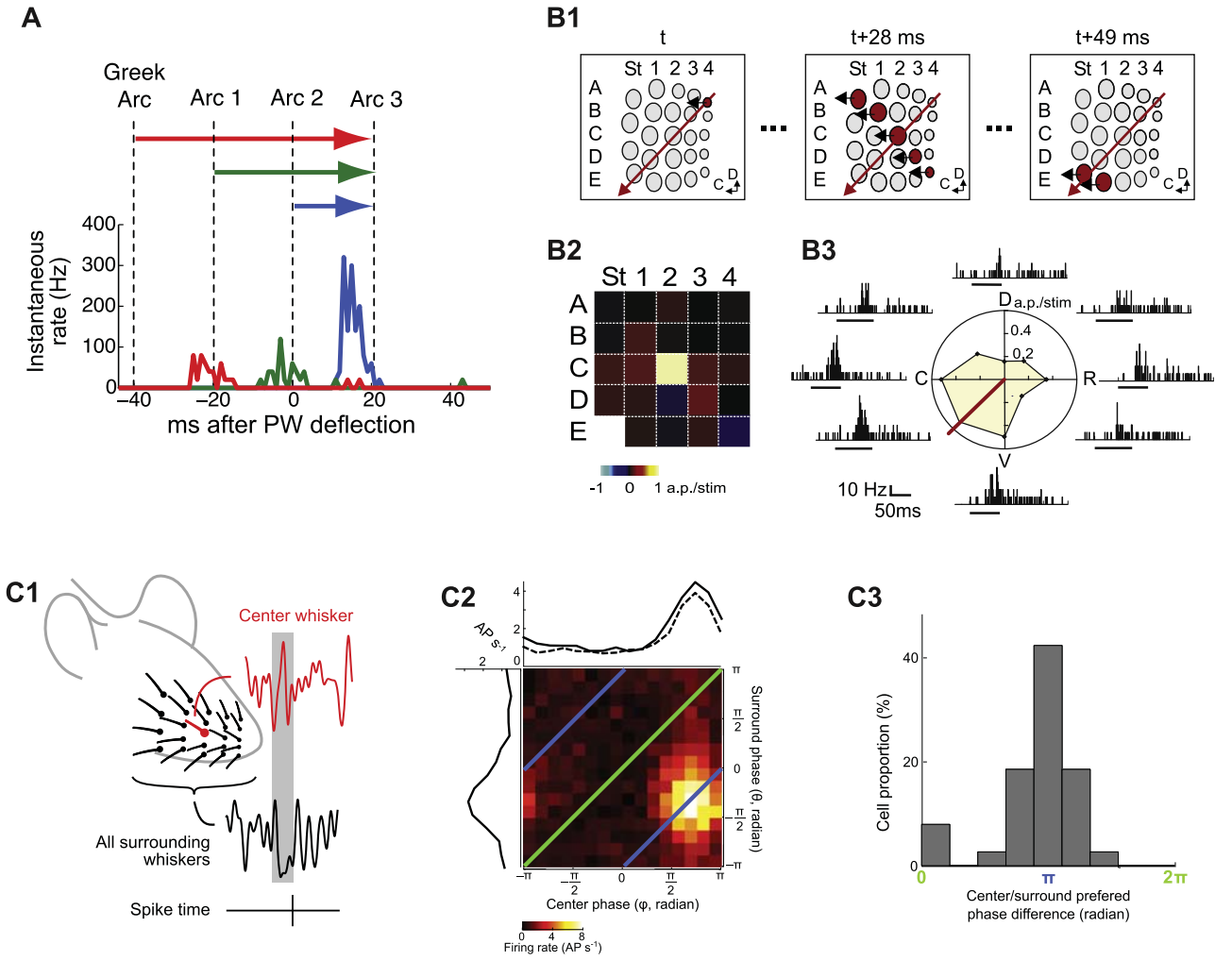

Fig. 6. Coding a spatially structured multi-whisker features. (A) Recording of a neuron in the D2 column of the barrel cortex during a sweeping bar stimulus across the whisker pad, starting from the Straddlers arc (red), arc 1 (green) or arc 2 (blue), in an anesthetized rat (PW: principal whisker). Responses to whiskers stimulated downstream from the stimulus onset location are suppressed (adapted from Drew and Feldman, 2007). (B1) Bar stimulus sweeping the whisker pad in one of eight directions. Note that although the bar is advancing in an oblique direction, the local whisker deflections are backward. (B2) Receptive field of a neuron centered on C2 in the rat barrel cortex. B3, Tuning of the same neuron to the direction of the bar sweeping movement (C: caudal, D: dorsal, R: rostral, V: ventral), (from Jacob et al., 2008). (C1) White noise applied to the principal whisker (red) and 23 adjacent whiskers at the periphery (black), in an anesthetized rat. (C2) Interaction between the principal and adjacent whiskers in the phase space (see Fig. 2C3) showing that anti-phased stimuli (blue line) are optimal for this neuron. (C3) Population analysis of the optimal phase relationship between principal whisker and surround, showing that in most neurons with responses enhanced by out of phase surround stimuli, antiphased stimuli are optimal (adapted from Estebanez et al., 2012).

on a simple physical intuition of the contact on an object, researchers have hypothesized that the sweeping of a deflection front edge across the whisker pad is a relevant stimulus feature for barrel cortex neurons, similar to the coding by V1 neurons of oriented edges in visual scenes.

To test this hypothesis, ad-hoc whisker stimulation devices have been developed, including a rolling drum holding an actual bar stimulus (Benison et al., 2006) and a stimulator that can deflect columns of whiskers separately (Drew and Feldman, 2007). Using these devices, extracellular recordings of single units (Drew and Feldman, 2007) as well as evoked field potentials (Benison et al., 2006) showed that after a strong increase in activity to the first stimulated whiskers, the functional response is strongly suppressed during the rest of the sweeping stimulus (Fig. 6A). This strong suppression is likely to be related to the sublinear summation during the simultaneous stimulation of large counts of whiskers (Hirata and Castro-Alamancos, 2008; Chen-Bee et al., 2012).

However, the exploration of the parameter space of the bar stimulus using a more generic multi-whisker stimulator (Jacob et al., 2010) shows that emergent parameters of the bar stimulus are actually coded in the whisker system (Jacob et al., 2008). In particular, barrel cortex neurons appear to be sharply tuned to the direction of the movement of the bar stimulus, independently of the direction of the deflection of the individual whiskers (Fig. 6B).

More recently, the study of the coding of bar-like stimulus has been extended to awake behaving mice. In a head-fixed behavioral task, barrel cortex neurons turned out to be tuned for the rostro-caudal position of a pole that was advanced along the whisker array (Pluta et al., 2017). Interestingly, neurons coding for different pole positions are organized following a smooth map at the surface of the cortex. This further suggests that bar-like stimuli may be – like in the visual cortex – a key building block of the barrel cortex functional responses to complex tactile scenes.

Similarly, another hypothesis inspired from previous findings in the visual system, particularly in the thalamus, is that the organization of spatial receptive fields follows a center-surround structure. Applying contrasting whisker deflections between the principal whisker and 23 surrounding whiskers revealed a strong enhancement of the response in a subset of barrel cortex neurons, thereby suggesting that these neurons are detectors of local whisker contrasts (Estebanez et al., 2012; Fig. 6C).

CONCLUSION

Increasingly, the functional properties identified in the rodent barrel cortex can be compared to the ability of the primary visual cortex of cats and monkeys to capture spatial features in a complex visual scene. Not only do barrel cortex neurons carry low-level feature selectivities including whisker direction and phase sensitivity, but also higher order multi-whisker selectivities including center-surround and edge detection. However, in stark contrast with the primary visual cortex, there is currently no overarching model of the barrel cortex spatial feature selectivity, in part because the description of the barrel cortex spatial tuning features remains incomplete.

To move toward a more complete model of the representations of tactile scenes in the barrel cortex, the combination of several experimental approaches will be required, including the observation of spontaneous and operantly conditioned rodent behavior, the comparison of the functional properties across whisker-specialist mammal species (Dehnhardt et al., 1998; Anjum et al., 2006), awake behaving studies of the whisker system sensorimotor loop (Jadhav et al., 2009), but also the more classical anesthetized rodent preparation which is the backbone of most of the findings reported in this review. Anesthesia has a clear impact on the functional properties of neurons in the whisker system (Simons et al., 1992; Friedberg et al., 1999; Malina et al., 2016) and alternatives have been proposed including the transection of the facial nerves (Sachidhanandam et al., 2013), but they have not yet been fully characterized and come with their unique drawbacks. We therefore argue that so far, the anesthetized rodent preparation remains the most tractable model available to explore complex multi-whisker feature integration in the rodent barrel cortex.

Acknowledgments—Funding: This work was supported by CNRS and by the ANR Neurowhisk.

REFERENCES

Ahissar E, Assa E (2016) Perception as a closed-loop convergence process. eLife 5.

Ahissar E, Sosnik R, Bagdasarian K, Haidarliu S (2001) Temporal frequency of whisker movement. II. Laminar organization of cortical representations. J Neurophysiol 86:354–367.

Ahissar E, Sosnik R, Haidarliu S (2000) Transformation from temporal to rate coding in a somatosensory thalamocortical pathway. Nature 406(6793):302.

Andermann ML, Moore CI (2006) A somatotopic map of vibrissa motion direction within a barrel column. Nat Neurosci 9:543–551.

Andermann ML, Ritt J, Neimark MA, Moore CI (2004) Neural correlates of vibrissa resonance; band-pass and somatotopic representation of high-frequency stimuli. Neuron 42:451–463.

Anjum F, Turni H, Mulder PGH, van der Burg J, Brecht M (2006) Tactile guidance of prey capture in Etruscan shrews. Proc Natl Acad Sci U S A 103:16544–16549.

Arabzadeh E, Petersen RS, Diamond ME (2003) Encoding of whisker vibration by rat barrel cortex neurons: implications for texture discrimination. J Neurosci 23:9146–9154.

Arakawa H, Erzurumlu RS (2015) Role of whiskers in sensorimotor development of C57BL/6 mice. Behav Brain Res 287:146–155.

Armstrong-James M, Fox K (1987) Spatiotemporal convergence and divergence in the rat S1 "barrel" cortex. J Comp Neurol 263:265–281.

Atick J (1992) Could information theory provide an ecological theory of sensory processing? Network: Computation in Neural Systems 3:213–251.

Axelrad H, Verley R, Farkas E (1976) Responses evoked in mouse and rat SI cortex by vibrissa stimulation. Neurosci Lett 3:265–274.

Bale MR, Maravall M (2017) Organization of sensory feature selectivity in the whisker system. Neuroscience. same volume.

Benison AM, Ard TD, Crosby AM, Barth DS (2006) Temporal patterns of field potentials in vibrissa/barrel cortex reveal stimulus orientation and shape. J Neurophysiol 95:2242–2251.

Berger T, Borgdorff A, Crochet S, Neubauer FB, Lefort S, Fauvet B, Ferezou I, Carleton A, Lüscher H-R, Petersen CCH (2007) Combined voltage and calcium epifluorescence imaging in vitro and in vivo reveals subthreshold and suprathreshold dynamics of mouse barrel cortex. J Neurophysiol 97:3751–3762.
Borgdorff AJ, Poulet JFA, Petersen CCH (2007) Facilitating sensory responses in developing mouse somatosensory barrel cortex. J Neurophysiol 97:2992–3003.
Boubenec Y, Claverie LN, Shulz DE, Debrégeas G (2014) An amplitude modulation/demodulation scheme for whisker-based texture perception. J Neurosci 34:10832–10843.
Brecht M, Preilowski B, Merzenich MM (1997) Functional architecture of the mystacial vibrissae. Behav Brain Res 84:81–97.
Brecht M, Roth A, Sakmann B (2003) Dynamic receptive fields of reconstructed pyramidal cells in layers 3 and 2 of rat somatosensory barrel cortex. J Physiol 553:243–265.
Brecht M, Sakmann B (2002) Dynamic representation of whisker deflection by synaptic potentials in spiny stellate and pyramidal cells in the barrels and septa of layer 4 rat somatosensory cortex. J Physiol 543:49–70.
Brecht M, Sakmann B (2002) Whisker maps of neuronal subclasses of the rat ventral posterior medial thalamus, identified by whole-cell voltage recording and morphological reconstruction. J Physiol 538:495–515.
Brumberg JC, Pinto DJ, Simons DJ (1996) Spatial gradients and inhibitory summation in the rat whisker barrel system. J Neurophysiol 76:130–140.
Bruno RM, Simons DJ (2002) Feedforward mechanisms of excitatory and inhibitory cortical receptive fields. J Neurosci 22:10966–10975.
Campagner D, Evans MH, Bale MR, Erskine A, Petersen RS (2016) Prediction of primary somatosensory neuron activity during active tactile exploration. eLife 5.
Carvell GE, Simons DJ (1988) Membrane potential changes in rat SmI cortical neurons evoked by controlled stimulation of mystacial vibrissae. Brain Res 448:186–191.
Castro-Alamancos MA (2004) Absence of rapid sensory adaptation in neocortex during information processing states. Neuron 41:455–464.
Chapin JK (1986) Laminar differences in sizes, shapes, and response profiles of cutaneous receptive fields in the rat SI cortex. Exp Brain Res 62:549–559.
Chen-Bee CH, Zhou Y, Jacobs NS, Lim B, Frostig RD (2012) Whisker array functional representation in rat barrel cortex: transcendence of one-to-one topography and its underlying mechanism. Front Neural Circuits 6:93.
Chung S, Li X, Nelson SB (2002) Short-term depression at thalamocortical synapses contributes to rapid adaptation of cortical sensory responses in vivo. Neuron 34:437–446.
Dehnhardt G, Mauck B, Hyvärinen H (1998) Ambient temperature does not affect the tactile sensitivity of mystacial vibrissae in harbour seals. J Exp Biol 201:3023–3029.
Drew PJ, Feldman DE (2007) Representation of moving wavefronts of whisker deflection in rat somatosensory cortex. J Neurophysiol 98:1566–1580.
Ego-Stengel V, Le Cam J, Shulz DE (2012) Coding of apparent motion in the thalamic nucleus of the rat vibrissal somatosensory system. J Neurosci 32:3339–3351.
Ego-Stengel V, Mello e Souza T, Jacob V, Shulz DE (2005) Spatiotemporal characteristics of neuronal sensory integration in the barrel cortex of the rat. J Neurophysiol 93:1450–1467.
Erchova I, Jacob V, Ego-Stengel V, Destexhe A, Shulz DE (2006) Multiwhisker suppressive interactions in the rat barrel cortex described by a MAX operator. Soc Neurosci Abstr 144:17.
Estebanez L, Bertherat J, Shulz DE, Bourdieu L, Léger J-F (2016) A radial map of multi-whisker correlation selectivity in the rat barrel cortex. Nature Commun 7:13528.
Estebanez L, Boustani SE, Destexhe A, Shulz DE (2012) Correlated input reveals coexisting coding schemes in a sensory cortex. Nat Neurosci 15:1691–1699.
Ewert TA, Vahle-Hinz C, Engel AK (2008) High-frequency whisker vibration is encoded by phase-locked responses of neurons in the rat's barrel cortex. J Neurosci 28(20):5359–5368.
Ferezou I, Bolea S, Petersen CC (2006) Visualizing the cortical representation of whisker touch: voltage-sensitive dye imaging in freely moving mice. Neuron 50:617–629.
Ferezou I, Haiss F, Gentet LJ, Aronoff R, Weber B, Petersen CC (2007) Spatiotemporal dynamics of cortical sensorimotor integration in behaving mice. Neuron 56(5):907–923.
Fournier J, Monier C, Pananceau M, Frégnac Y (2011) Adaptation of the simple or complex nature of V1 receptive fields to visual statistics. Nat Neurosci 14:1053–1060.
Friedberg MH, Lee SM, Ebner FF (1999) Modulation of receptive field properties of thalamic somatosensory neurons by the depth of anesthesia. J Neurophysiol 81(5):2243–2252.
Gabernet L, Jadhav SP, Feldman DE, Carandini M, Scanziani M (2005) Somatosensory integration controlled by dynamic thalamocortical feed-forward inhibition. Neuron 48:315–327.
Ganmor E, Katz Y, Lampl I (2010) Intensity-dependent adaptation of cortical and thalamic neurons is controlled by brainstem circuits of the sensory pathway. Neuron 66(2):273–286.
Ghazanfar AA, Nicolelis MA (1997) Nonlinear processing of tactile information in the thalamocortical loop. J Neurophysiol 78:506–510.
Ghazanfar AA, Nicolelis MA (1999) Spatiotemporal properties of layer V neurons of the rat primary somatosensory cortex. Cereb Cortex 9:348–361.
Goldreich D, Peterson B, Merzenich M (1998) Optical imaging and electrophysiology of rat barrel cortex. II. Responses to paired-vibrissa deflections. Cereb Cortex 8:184–192.
Grant RA, Mitchinson B, Fox CW, Prescott TJ (2009) Active touch sensing in the rat: anticipatory and regulatory control of whisker movements during surface exploration. J Neurophysiol 101:862–874.
Grant RA, Sperber AL, Prescott TJ (2012) The role of orienting in vibrissal touch sensing. Front Behav Neurosci 6:39.
Hartline HK (1938) The responses of single optic nerve fibers of the vertebrate eye to illumination of the retina. Amer J Physiol 121:400–415.
Hartmann MJZ (2011) A night in the life of a rat: vibrissal mechanics and tactile exploration. Ann N Y Acad Sci 1225:110–118.
Heggelund P (1981) Receptive field organization of simple cells in cat striatecortex. Exp Brain Res 42:89–98.
Higley MJ, Contreras D (2005) Integration of synaptic responses to neighboring whiskers in rat barrel cortex in vivo. J Neurophysiol 93:1920–1934.
Higley MJ, Contreras D (2007) Frequency adaptation modulates spatial integration of sensory responses in the rat whisker system. J Neurophysiol 97:3819–3824.
Hirata A, Castro-Alamancos MA (2008) Cortical transformation of wide-field (multiwhisker) sensory responses. J Neurophysiol 100:358–370.
Hobbs JA, Towal RB, Hartmann MJZ (2015) Spatiotemporal patterns of contact across the rat vibrissal array during exploratory behavior. Front Behav Neurosci 9:356.
Hobbs JA, Towal RB, Hartmann MJZ (2016) Evidence for functional groupings of vibrissae across the rodent mystacial pad. PLoS Comput Biol 12:e1004109.
Hubel DH (1959) Single unit activity in striate cortex of unrestrained cats. J Physiol 147:226–238.
Hubel DH, Wiesel TN (1962) Receptive fields, binocular interaction and functional architecture in the cat's visual cortex. J Physiol 160:106–154.
Hutson KA, Masterton RB (1986) The sensory contribution of a single vibrissa's cortical barrel. J Neurophysiol 56:1196–1223.
Ito M (1981) Some quantitative aspects of vibrissa-driven neuronal responses in rat neocortex. J Neurophysiol 46:705–715.
Jacob V, Estebanez L, Le Cam J, Tiercelin J-Y, Parra P, Parésys G, Shulz DE (2010) The Matrix: a new tool for probing the whisker-to-barrel system with natural stimuli. J Neurosci Methods 189:65–74.

Jacob V, Le Cam J, Ego-Stengel V, Shulz DE (2008) Emergent properties of tactile scenes selectively activate barrel cortex neurons. Neuron 60:1112–1125.
Jadhav SP, Wolfe J, Feldman DE (2009) Sparse temporal coding of elementary tactile features during active whisker sensation. Nat Neurosci 12:792–800.
Jouhanneau J-S, Kremkow J, Dorrn AL, Poulet JFA (2015) In vivo monosynaptic excitatory transmission between layer 2 cortical pyramidal neurons. Cell Rep 13:2098–2106.
Katz Y, Heiss JE, Lampl I (2006) Cross-whisker adaptation of neurons in the rat barrel cortex. J Neurosci 26:13363–13372.
Kerekes P, Daret A, Shulz DE, Ego-Stengel V (2017) Bilateral discrimination of tactile patterns without whisking in freely-running rats. J Neurosci 37:7567–7579.
Khatri V, Hartings JA, Simons DJ (2004) Adaptation in thalamic barreloid and cortical barrel neurons to periodic whisker deflections varying in frequency and velocity. J Neurophysiol 92:3244–3254.
Kleinfeld D, Delaney KR (1996) Distributed representation of vibrissa movement in the upper layers of somatosensory cortex revealed with voltage-sensitive dyes. J Comp Neurol 375:89–108.
Krupa DJ, Brisben AJ, Nicolelis MA (2001) A multi-channel whisker stimulator for producing spatiotemporally complex tactile stimuli. J Neurosci Methods 104:199–208.
Lampl I, Ferster D, Poggio T, Riesenhuber M (2004) Intracellular measurements of spatial integration and the MAX operation in complex cells of the cat primary visual cortex. J Neurophysiol 92:2704–2713.
Lampl I, Katz Y (2017) Neuronal adaptation in the somatosensory system of rodents. Neuroscience 343:66–76.
Le Cam J, Estebanez L, Jacob V, Shulz DE (2011) Spatial structure of multiwhisker receptive fields in the barrel cortex is stimulus dependent. J Neurophysiol 106:986–998.
Lottem E, Azouz R (2009) Mechanisms of tactile information transmission through Whisker vibrations. J Neurosci 29:11686–11697.
Malina KCK, Mohar B, Rappaport AN, Lampl I (2016) Local and thalamic origins of correlated ongoing and sensory-evoked cortical activities. Nat Commun 7.
Manns ID, Sakmann B, Brecht M (2004) Sub- and suprathreshold receptive field properties of pyramidal neurones in layers 5A and 5B of rat somatosensory barrel cortex. J Physiol 556:601–622.
Maravall M, Petersen RS, Fairhall AL, Arabzadeh E, Diamond ME (2007) Shifts in coding properties and maintenance of information transmission during adaptation in barrel cortex. PLoS Biol 5:e19.
Marĉelja S (1980) Mathematical description of the responses of simple cortical cells. JOSA 70(11):1297–1300.
Martini FJ, Molano-Mazón M, Maravall M (2017) Interspersed distribution of selectivity to kinematic stimulus features in supragranular layers of mouse barrel cortex. Cereb Cortex:1–8.
Mayrhofer JM, Skreb V, von der Behrens W, Musall S, Weber B, Haiss F (2013) Novel two-alternative forced choice paradigm for bilateral vibrotactile whisker frequency discrimination in head-fixed mice and rats. J Neurophysiol 109:273–284.
Mirabella G, Battiston S, Diamond ME (2001) Integration of multiple-whisker inputs in rat somatosensory cortex. Cereb Cortex 11:164–170.
Mitchinson B, Martin CJ, Grant RA, Prescott TJ (2007) Feedback control in active sensing: rat exploratory whisking is modulated by environmental contact. Proc Biol Sci 274:1035–1041.
Mohar B, Katz Y, Lampl I (2013) Opposite adaptive processing of stimulus intensity in two major nuclei of the somatosensory brainstem. J Neurosci 33(39):15394–15400.
Mohar B, Ganmor E, Lampl I (2015) Faithful representation of tactile intensity under different contexts emerges from the distinct adaptive properties of the first somatosensory relay stations. J Neurosci 35(18):6997–7002.
Moore CI, Nelson SB (1998) Spatio-temporal subthreshold receptive fields in the vibrissa representation of rat primary somatosensory cortex. J Neurophysiol 80:2882–2892.
Mosconi TM, Rice FL, Song MJ (1993) Sensory innervation in the inner conical body of the vibrissal follicle-sinus complex of the rat. J Comp Neurol. 328(2):232–251.
Musall S, von der Behrens W, Mayrhofer JM, Weber B, Helmchen F, Haiss F (2014) Tactile frequency discrimination is enhanced by circumventing neocortical adaptation. Nat Neurosci 17:1567–1573.
Musall S, Haiss F, Weber B, von der Behrens W (2017) Deviant processing in the primary somatosensory cortex. Cereb Cortex 27:863–876.
Núñez A, Barrenechea C, Avendaño C (1994) Spontaneous activity and responses to sensory stimulation in ventrobasal thalamic neurons in the rat: an in vivo intracellular recording and staining study. Somatosens Mot Res 11:89–98.
Okun M, Lampl I (2008) Instantaneous correlation of excitation and inhibition during ongoing and sensory-evoked activities. Nat Neurosci 11:535–537.
Ollerenshaw DR, Zheng HJV, Millard DC, Wang Q, Stanley GB (2014) The adaptive trade-off between detection and discrimination in cortical representations and behavior. Neuron 81:1152–1164.
Olshausen BA, Field DJ (1996) Emergence of simple-cell receptive field properties by learning a sparse code for natural images. Nature 381:607–609.
Petersen RS, Diamond ME (2000) Spatial-temporal distribution of whisker-evoked activity in rat somatosensory cortex and the coding of stimulus location. J Neurosci 20:6135–6143.
Pluta SR, Lyall EH, Telian GI, Ryapolova-Webb E, Adesnik H (2017) Surround integration organizes a spatial map during active sensation. Neuron 94:1220–1233.
Ramirez A, Pnevmatikakis EA, Merel J, Paninski L, Miller KD, Bruno RM (2014) Spatiotemporal receptive fields of barrel cortex revealed by reverse correlation of synaptic input. Nat Neurosci 17:866–875.
Reyes A, Lujan R, Rozov A, Burnashev N, Somogyi P, Sakmann B (1998) Target-cell-specific facilitation and depression in neocortical circuits. Nat Neurosci 1:279–285.
Rice FL (1993) Structure, vascularization, and innervation of the mystacial pad of the rat as revealed by the lectin Griffonia simplicifolia. J Comp Neurol 337(3):386–399.
Rice FL, Kinnman E, Aldskogius H, Johansson O, Arvidsson J (1993) The innervation of the mystacial pad of the rat as revealed by PGP 9.5 immunofluorescence. J Comp Neurol 337 (3):366–385.
Ritt JT, Andermann ML, Moore CI (2008) Embodied information processing: vibrissa mechanics and texture features shape micromotions in actively sensing rats. Neuron 57:599–613.
Rodgers KM, Benison AM, Barth DS (2006) Two-dimensional coincidence detection in the vibrissa/barrel field. J Neurophysiol 96:1981–1990.
Rozov A, Jerecic J, Sakmann B, Burnashev N (2001) AMPA receptor channels with long-lasting desensitization in bipolar interneurons contribute to synaptic depression in a novel feedback circuit in layer 2/3 of rat neocortex. J Neurosci 21:8062–8071.
Rust NC, Movshon JA (2005) In praise of artifice. Nat Neurosci 8:1647–1650.
Sachidhanandam S, Sreenivasan V, Kyriakatos A, Kremer Y, Petersen CCH (2013) Membrane potential correlates of sensory perception in mouse barrel cortex. Nat Neurosci 16:1671–1677.
Severson KS, Xu D, Van de Loo M, Bai L, Ginty DD, O'Connor DH (2017) Active touch and self-motion encoding by merkel cell-associated afferents. Neuron 94:666–676.
Sheth BR, Moore CI, Sur M (1998) Temporal modulation of spatial borders in rat barrel cortex. J Neurophysiol 79:464–470.
Shimegi S, Akasaki T, Ichikawa T, Sato H (2000) Physiological and anatomical organization of multiwhisker response interactions in the barrel cortex of rats. J Neurosci 20:6241–6248.
Shimegi S, Ichikawa T, Akasaki T, Sato H (1999) Temporal characteristics of response integration evoked by multiple whisker stimulations in the barrel cortex of rats. J Neurosci 19:10164–10175.

Sillito AM, Grieve KL, Jones HE, Cudeiro J, Davis J (1995) Visual cortical mechanisms detecting focal orientation discontinuities. Nature 378:492–496.
Simons DJ (1978) Response properties of vibrissa units in rat SI somatosensory neocortex. J Neurophysiol 41:798–820.
Simons DJ (1983) Multi-whisker stimulation and its effects on vibrissa units in rat SmI barrel cortex. Brain Res 276:178–182.
Simons DJ (1985) Temporal and spatial integration in the rat SI vibrissa cortex. J Neurophysiol 54:615–635.
Simons DJ, Carvell GE (1989) Thalamocortical response transformation in the rat vibrissa/barrel system. J Neurophysiol 61:311–330.
Simons DJ, Carvell GE, Hershey AE, Bryant DP (1992) Responses of barrel cortex neurons in awake rats and effects of urethane anesthesia. Exp Brain Res 91(2):259–272.
Sosnik R, Haidarliu S, Ahissar E (2001) Temporal frequency of whisker movement. I. Representations in brain stem and thalamus. J Neurophysiol 86(1):339–353.
Stüttgen MC, Rüter J, Schwarz C (2006) Two psychophysical channels of whisker deflection in rats align with two neuronal classes of primary afferents. J Neurosci 26:7933–7941.
Towal RB, Quist BW, Gopal V, Solomon JH, Hartmann MJZ (2011) The morphology of the rat vibrissal array: a model for quantifying spatiotemporal patterns of whisker-object contact. PLoS Comput Biol 7:e1001120.
Van der Bourg A, Yang JW, Reyes-Puerta V, Laurenczy B, Wieckhorst M, Stüttgen MC, Luhmann HJ, Helmchen F (2016) Layer-specific refinement of sensory coding in developing mouse barrel cortex. Cereb Cortex:1–16.
Waiblinger C, Brugger D, Whitmire CJ, Stanley GB, Schwarz C (2015) Support for the slip hypothesis from whisker-related tactile perception of rats in a noisy environment. Front Integr Neurosci 9:53.
Webber RM, Stanley GB (2004) Nonlinear encoding of tactile patterns in the barrel cortex. J Neurophysiol 91(5):2010–2022.
Welker WI (1964) Analysis of sniffing of the albino rat. Behaviour 22 (3/4):223–244.
Welker C (1971) Microelectrode delineation of fine grain somatotopic organization of (SmI) cerebral neocortex in albino rat. Brain Res 26:259–275.
Whitmire CJ, Millard DC, Stanley GB (2017) Thalamic state control of cortical paired-pulse dynamics. J Neurophysiol 117:163–177.
Whitmire CJ, Stanley GB (2016) Rapid sensory adaptation redux: a circuit perspective. Neuron 92:298–315.
Wilent WB, Contreras D (2005) Dynamics of excitation and inhibition underlying stimulus selectivity in rat somatosensory cortex. Nat Neurosci 8:1364–1370.
Wolfe J, Hill DN, Pahlavan S, Drew PJ, Kleinfeld D, Feldman DE (2008) Texture coding in the rat whisker system: slip-stick versus differential resonance. PLoS Biol 6:e215.
Woolsey TA, Van der Loos H (1970) The structural organization of layer IV in the somatosensory region (SI) of mouse cerebral cortex. The description of a cortical field composed of discrete cytoarchitectonic units. Brain Res 17:205–242.
Yu J, Gutnisky DA, Hires SA, Svoboda K (2016) Layer 4 fast-spiking interneurons filter thalamocortical signals during active somatosensation. Nat Neurosci 19:1647–1657.
Zhu JJ, Connors BW (1999) Intrinsic firing patterns and whisker-evoked synaptic responses of neurons in the rat barrel cortex. J Neurophysiol 81:1171–1183.

(Received 8 June 2017, Accepted 21 August 2017)
(Available online 23 August 2017)

Neurophotonics

Neurophotonics.SPIEDigitalLibrary.org

Review: How do spontaneous and sensory-evoked activities interact?

Isabelle Ferezou
Thomas Deneux

SPIE.

Isabelle Ferezou, Thomas Deneux, "Review: How do spontaneous and sensory-evoked activities interact?," *Neurophoton.* **4**(3), 031221 (2017), doi: 10.1117/1.NPh.4.3.031221.

Neurophotonics 4(3), 031221 (Jul–Sep 2017)

REVIEW

Review: How do spontaneous and sensory-evoked activities interact?

Isabelle Ferezou and Thomas Deneux*
Unité de Neurosciences, Information et Complexité, Centre National de la Recherche Scientifique, Gif-sur-Yvette, France

Abstract. Twenty years ago, the seminal work of Grinvald et al. revolutionized the view cast on spontaneous cortical activity by showing how, instead of being a mere measure of noise, it profoundly impacts cortical responses to a sensory input and therefore could play a role in sensory processing. This paved the way for a number of studies on the interactions between spontaneous and sensory-evoked activities. Spontaneous activity has subsequently been found to be highly structured and to participate in high cognitive functions, such as influencing conscious perception in humans. However, its functional role remains poorly understood, and only a few speculations exist, from the maintenance of the cortical network to the internal representation of an *a priori* knowledge of the environment. Furthermore, elucidation of this functional role could stem from studying the opposite relationship between spontaneous and sensory-evoked activities, namely, how a sensory input influences subsequent internal activities. Indeed, this question has remained largely unexplored, but a recent study by the Grinvald laboratory shows that a brief sensory input largely dampens spontaneous rhythms, suggesting a more sophisticated view where some spontaneous rhythms might relate to sensory processing and some others not. [DOI: 10.1117/1.NPh.4.3.031221]

Keywords: spontaneous activity; sensory processing; cerebral cortex; brain states.

Paper 17010SSVR received Jan. 17, 2017; accepted for publication May 16, 2017; published online Jun. 13, 2017.

1 Spontaneous Activity Influences Evoked Responses

Investigating the features detected by individual neurons or by neuronal assemblies has been one of the most successful approaches to understanding brain organization and function. This approach requires measuring the neuronal responses to a set of different sensory inputs; as a consequence, the variability of these responses between different presentations of the same stimulus has long been considered a disturbance that needed to be overcome by trigger-averaging over a number of presentations. This unfortunately led to the disregard of this variability in evoked responses—as well as the large activity fluctuations observed in the absence of stimulation—and rather consider them as noise.

Twenty years ago, however, Arieli et al.[1] focused their interest on these response variabilities and spontaneous ongoing activity, using single-neuron electrical recordings coupled with voltage-sensitive dyes (VSDs) to measure coherent activities in the visual cortex of anesthetized cats. They observed, in particular, that ongoing fluctuations and response variabilities had amplitudes as large as the evoked responses, were highly correlated between neurons as far as 6-mm apart, and showed structure in both space and time. This led them to emphasize the importance of studying these activities as they speculated that the "ongoing electrical activity and its specific interactions with the activity evoked by the stimulus may be one neuronal expression of context." This speculation was greatly confirmed by their next report[2] where they showed that the variability in response patterns evoked by individual stimulus presentations could be well accounted for by the ongoing patterns that immediately preceded the stimulation [Fig. 1(a)]. This evidence for integration of a deterministic response to the sensory input with the ongoing network dynamics reinforced their argument that ongoing activity "may provide the neural substrate for the dependence of sensory information processing on context and on behavioral and conscious states."

They succeeded in triggering a new consideration for ongoing dynamics, and a large number of studies that followed investigated how spontaneous activity patterns influence the responses to specific stimulations.[4–23] It is noteworthy that the positive correlation that they reported between ongoing activity and sensory-evoked responses was soon contradicted and that a wider range of interactions was subsequently reported. Indeed, Petersen et al.[7] observed, in the barrel cortex of anesthetized rats, that sensory-evoked responses were much stronger when ongoing activity was low compared to when it was high. More precisely, the ongoing activity in this preparation showed characteristic up and down states,[24] where the whole network activity in a local neighborhood alternates between periods of tonic activity (up), possibly propagating as waves, and silence (down). During such synchronized cortical states, which can also be observed during quiet wakefulness,[6,7,14] responses evoked by tactile or tone stimuli are typically of large amplitude and are inversely correlated to the prestimulus membrane potential.[7,15,23] The sensory-evoked cortical responses are further suppressed when the cortex switches from slow wave activity to a more desynchronized state, typical of active wakefulness.[6,14] Such suppression of evoked cortical activity occurring during behaviorally active states has been reported both in the primary somatosensory (see also Refs. 25 and 26) and primary auditory cortex.[27–29] However, several recent studies indicate that the interaction

*Address all correspondence to: Thomas Deneux, E-mail: thomas.deneux@unic.cnrs-gif.fr

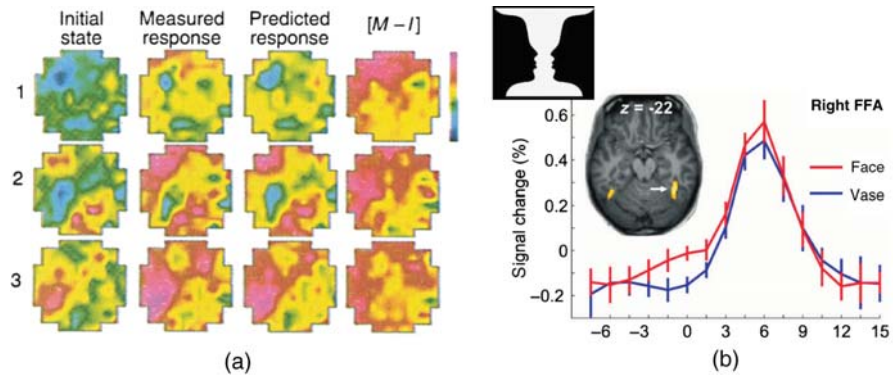

Fig. 1 Spontaneous activity influences evoked responses: (a) three consecutive single-trial responses (rows) to the same visual stimulus, showing the initial state, the measured response 28 ms later, and the predicted response obtained by simple summation of initial state and the average response to all trials. Subtracting the initial state from the measured response yielded the net pattern ($M - I$). Reproduced from Ref. 2 with permission. (b) Peristimulus fMRI signal time courses from right FFA in response to an ambiguous face–vase image (inset), averaged across subjects, after sorting trials according to whether they reported a face or vase perception: face perception was associated with a higher prestimulus activation level. Adapted from Ref. 3 with permission.

between behavioral activity, cortical state, and sensory-evoked responses is opposite in the primary visual cortex.[4,22,30–35] The interplay between ongoing cortical dynamics and sensory inputs, therefore, does not seem to follow common rules across sensory modalities. Furthermore, by recording the membrane potential of mice engaged in a tactile detection task, a recent study from Petersen lab[36] revealed that, although the ongoing cortical state impacts the evoked sensory response, it has no effect on the performance of the animal.

In the human neuroscience community, the study of ongoing dynamics has met a great interest[3,37–42] (see Ref. 38 for a review). This stems from the interest for high cognitive functions in humans, such as imagination or consciousness, of which ongoing activity could be a hallmark [see also later our mention to the "default mode network (DMN)"]. The influence of ongoing cortical dynamics on the processing of sensory inputs was also established. As an example, Hesselmann et al.[3] found using fMRI that the perception of a flashed ambiguous face–vase stimulus depended of prestimulation activity level in the fusiform face area (FFA) and an extrastriate visual region specialized for face processing as well as in some other brain areas [Fig. 1(b)]. It thus appears that even conscious perception cannot be considered independently of the "initial state of the system," to take the author's words, and that the measured spontaneous activity signals, even though their functional meaning remain unfathomed, constitute at least a fingerprint of this initial state.

2 Structure of Spontaneous Activity Reflects Functional Organization and is Influenced by Experience

The Grinvald laboratory made other keystone contributions to the study of spontaneous activity by taking advantage of the exquisite topographical organization of the cat visual cortex, on the one hand, and of VSDs on the other hand, to capture this organization. Functional structures usually revealed by sensory stimulation were also found in the spontaneous dynamics: at the level of a single-neuron functional connectivity,[43] where population activity maps trigger-averaged on a single-neuron spikes appeared to be near-identical in the resting or stimulation conditions; and at the level of the population representations,[44] where spontaneous activity patterns were observed, which highly resembled evoked orientation maps [Fig. 2(a)].

That the spontaneous activity reflects the functional organization of the cortical network on which it is riding is not a surprise and has been confirmed at the scale of the whole dorsal surface of cortical hemispheres in mice by VSD imaging.[47]

However, the spectacular aspect of spontaneously emerging orientation maps raised a new question: can the spontaneous cortical states play an active role in sensory processing, as the authors suggested that they might "reflect expectations about the sensory input?"

An additional relationship between sensory-evoked and spontaneous activities lies in the plasticity of the latter, in the sense that sensory-evoked activity can reshape the structure of subsequent spontaneous patterns through learning. This was shown in particular by Dan group[45,48] who, after training rats with visual stimuli to evoke wave patterns in their primary visual cortex, observed recalls of these specific patterns in the spontaneous activity during the resting period that followed [Fig. 2(b)]. Such recalls or replays are in fact a phenomenon that is well-known and abundantly studied, in particular, in hippocampal structures.[49–54]

The similarities in structure between spontaneous and sensory-evoked activities might, therefore, be learned through experience rather than innately. In this light, Berkes et al.[46] emphasized changes that occur during development, whereby an initial mismatch between the statistics of spontaneous and sensory-evoked (using natural visual stimuli) activities in young ferrets disappears in adult animals [Fig. 2(c)]. There again it is suggested that spontaneous activity reflects prior expectations of "an internal model (of the natural environment) that is adapted gradually during development."

Moreover, spontaneous activity is known to play an active role during development, in particular, in the early stages of development where propagating waves of activity are known to shape and consolidate the developing networks (see reviews in Refs. 29 and 55, as well as the review from Luhmann[56] in this issue of *Neurophotonics*). This is a whole field of investigation

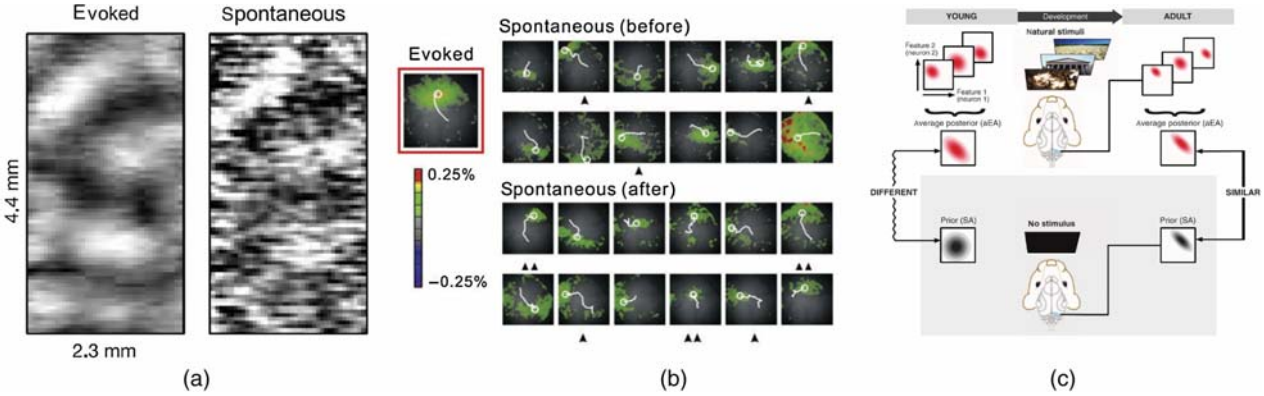

Fig. 2 The structure of spontaneous activity reflects functional organization and is influenced by experience: (a) an activation pattern obtained from a single frame from spontaneous activity VSD recording (right) matches the orientation map obtained by averaging responses to full-field gratings of vertical orientation (left), in the visual cortex of an anesthetized cat. Adapted from Ref. 43 with permission. (b) Spontaneous waves recorded using VSD in an anesthetized rat barrel cortex, immediately before and after training with a flashing sequence that evoked the wave template represented on the left. Waves are represented by their first frame and the trajectory of their center over ~160 ms. Spontaneous waves well matched to the template are indicated by a single arrowhead [correlation coefficient (CC) > 0.6] or by double arrowheads (CC > 0.7) and are more frequent after training. Adapted from Ref. 45 with permission. (c) Multiunit activity recorded in V1 of awake, freely viewing ferrets either receiving no stimulus (bottom) or viewing natural (top) or artificial stimuli (not shown in this adapted figure) is used to construct neural activity distributions in young and adult animals. Distributions of evoked activities averaged over different stimuli are compared with the distribution of spontaneous activities, assumed to represent the prior expectations about visual features. The internal model of young animals (left) is expected to show little adaptation to the natural environment and thus show a mismatch between spontaneous and evoked distributions. On the contrary, adult animals (right) are expected to be adapted to natural scenes and thus to exhibit a high degree of similarity. Adapted from Ref. 46 with permission.

in itself, and it is not obvious how these spontaneous activities during early development relate to those observed in adults.

Plasticity in the spontaneous activity structure has also been shown in humans. Lewis et al.[57] found that a stimulated part of the visual cortex modified its resting-state connectivity after training as compared to the untrained part. A few studies have investigated changes in the resting-state network induced by preceding task periods involving memorization or emotional content (see Ref. 38 for review).

Whereas we started this retrospective review with the influence of spontaneous activity on sensory-evoked responses,[2] we have now discussed influences in the opposite direction through learning. However, another important question has been raised: does the spontaneous activity really embed a representation of "expectations" in such a way that it plays an active role during sensory processing? To address this question, a new level of interaction is envisioned: how are spontaneous dynamics affected by a sensory inflow?

3 Sensory Input Switches the Brain Internal Dynamics

3.1 *Brain Dynamics during a Sensory Input*

"Stimulus onset quenches neural variability: a widespread cortical phenomenon,"[58] under this title, a number of well-known neuroscientists gathered 14 different electrophysiology datasets recorded in cats and monkeys, which all showed that intertrial variability decreased in sensory-evoked responses as compared to the preceding period of spontaneous activity [Fig. 3(a)], fluctuations present in the spontaneous activity [Fig. 3(a), top] systematically decreased in amplitude during stimulation, even in instances where this stimulation was not eliciting an "average response" [Fig. 3(a), middle] (Note that, even though it is artificial to split the signals after stimulus onset between an "average response" and "remaining fluctuations," we chose to call these fluctuations "internal" or "internally generated" activity, as obviously it cannot be called a "spontaneous activity"). This phenomenon actually was already known from intracellular studies[61] that showed how a sensory input resulted in very reproducible driving of a neuron membrane potential as compared to the spontaneous fluctuations and identified shunting inhibition as a mechanism for the rescaling of the cell excitability.

Even though it appears intuitive that a sensory drive might "clamp" the firing dynamics to fixed patterns and therefore reduce the variability due to random fluctuations generated by the network itself, neural simulations revealed interesting properties of this general effect. For example, the work of Abbott group[62,63] showed not only that variability reduction was an intrinsic property of interconnected networks shifting from chaotic to driven dynamics when exposed to an input but also that complex nonlinear interactions occurred between intrinsic and sensory-driven dynamics. These included the preference for some input frequency without any resonance effect, the drive at harmonic frequencies initially not present in the input, and the curving of the spatial patterns of the input toward those of the intrinsic dynamics. Some of these effects were later confirmed experimentally.[64] On the other hand, other computational neuroscientists have advocated that the reduction of variability corresponds to a very peculiar structural property of the brain network, such that its activity spans a highly multidimensional space "at the edge" of multiple bifurcations, leading to multiple

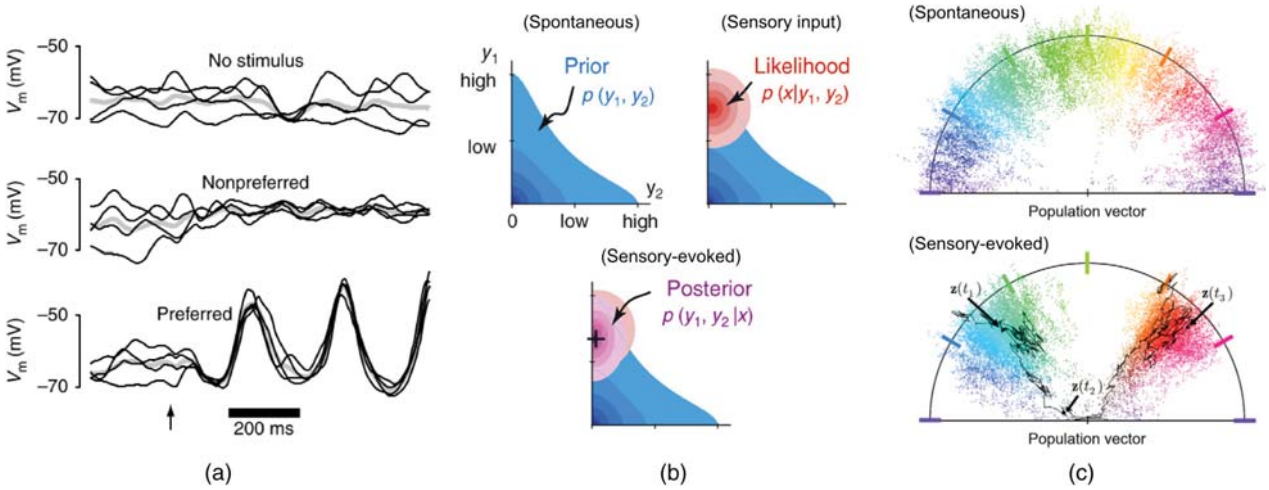

Fig. 3 Brain dynamics during a sensory input: (a) example intracellular recordings from a neuron in cat V1. Intertrial variability decreases in stimulated recordings for both nonpreferred (middle) and preferred (bottom) orientations and frequencies of the sine-wave gratings as compared to unstimulated recordings (top). Reproduced from Ref. 58 with permission. (b) Schematic illustration of probabilistic inference in sensory processing. The information brought by *a priori* knowledge about the environment and by the sensory input are represented, respectively, as *a prior* and likelihood probability distributions (top). These two types of information are optimally combined by Bayes' theorem, forming a posterior probability distribution that displays less uncertainty (is narrower) than the two previous distributions (bottom). Adapted from Ref. 59 with permission. (c) Simulations of a small population of neurons inferring the orientation of a grating by implementing a sampling of the above-mentioned distributions. Individual neurons in these simulations are tuned to different orientations and are preferentially connected to neurons with similar preferences. Individual points in the graphs represent the activity of the full population at different time points, their color and angular position encoding the orientation of the most active neurons, and their radius of the population coherence. In the spontaneous activity, the population activity wanders throughout all orientations, representing the prior distribution (top), whereas, in presence of an ambiguous input, its wandering is restricted to the possible orientations as constrained by the input, representing the posterior distribution (bottom). Adapted from Ref. 60 with permission.

"ghost attractors."[65,66] In the absence of a sensory input, the spontaneous activity can visit a large repertoire of states; however, even a weak external input can lead it to fall into one of the attractors, which decreases variability.

In addition to this modeling effort, a functional role in sensory processing was proposed:[59,60,67] the spontaneous activity, by sampling a large ensemble of states, maintains an internal representation of all possible external environments and thereby implements an "expectation" or, in Bayesian terms, a "prior." Once combined with the information brought by a sensory input about the actual state of the external world, this prior is reshaped into a "posterior," which by essence embeds less uncertainty and therefore restricts the number of sampled states [Figs. 3(b) and 3(c)].

According to this theory, the spontaneous activity is viewed as playing an active role in sensory processing, the network being permanently in an attempt to make inferences about the environment, even under resting condition or sleep where it explores all possibilities learned from accumulated experience. Because sensory-evoked activity is then viewed as a combination of the information entailed in the internal dynamics, on the one hand, and in the sensory input, on the other hand, it gives a functional significance to the above-mentioned patterns of integration between spontaneous fluctuations and sensory-evoked activities, as well as the reshaping of spontaneous activity by experience. This view, however, appears quite restrictive in regard to some stereotypic and widespread spontaneous rhythms, which are unlikely to achieve a "sampling of internal representations," such as the up and down fluctuations.[24]

3.2 *Brain Dynamics after a Sensory Input*

To further investigate the interactions between spontaneous and evoked activities, Deneux and Grinvald[68] explored how the internal dynamics would be modified "after" a brief sensory input. In the barrel cortex of anesthetized rats, with a preparation that displays the stereotypical up and down states, the authors observed that even after a brief single whisker stimulation, this rhythm was significantly perturbed for several seconds, with up events failing to occur, in particular, in the stimulated barrel-related column [Fig. 4(a)]. As a result, the interaction between internal (recurrent, top-down) and feedforward activities did not appear any more as the smooth integration of two complementary activities, but on the contrary as a competition between orthogonal activities. The authors indeed suggested that "at the onset of a sensory input, some internal messages are silenced to prevent overloading of the processing of relevant incoming sensory information." In addition, this switch in the internal dynamics was also characterized by a transient burst of activity at around 15 Hz (identified as a thalamo-cortical oscillation)[70,71] and a transient activity increase of a small fraction of the neurons [both visible in Fig. 4(a); the ~15-Hz activity is marked with gray arrows]. These two patterns occur identically as well after the onset of a longer, sustained stimulation (not visible

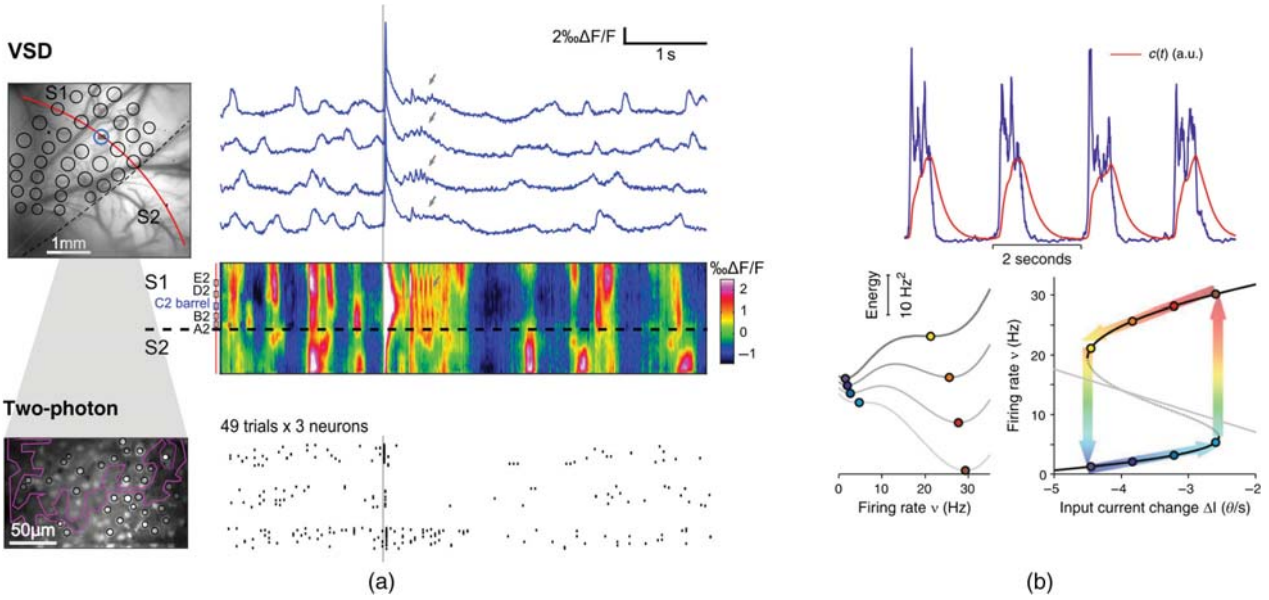

Fig. 4 Brain dynamics after a sensory input: (a) spontaneous dynamics, response evoked by a brief somatosensory stimulation and poststimulation dynamics, recorded in anesthetized rat barrel cortex using both VSD imaging of population activity and two-photon microscopy of individual neurons spiking activity. VSD signals display four example trials and are extracted from the stimulated barrel location (blue circle in the barrel map on the left); in addition, a spatiotemporal display allows visualizing activity throughout a line (marked in red in the barrel map) crossing both the primary and secondary somatosensory cortices (S1 and S2). Raster plot of spikes extracted from the two-photon recordings displays 49 trials for three different neurons. The main effect of the sensory input on the subsequent dynamics is a decrease or even interruption of the up states appearances for a few seconds (see text for more details). Adapted from Ref. 68 with permission. (b) A model of up and down states generation that involves a fatigue mechanism. (top) Example multiunit activity trace from experiment (blue) and reconstructed fatigue variable $c(t)$. (bottom left): energy landscapes for different levels of activity-dependent adaptation/fatigue; when fatigue is high (top trace), the minimum energy point is an absence of activity. (bottom right): stable (solid branches) and unstable (dotted branch) asymptotic states of firing rate at different fatigue levels here represented as effective changes in the input current to the neurons in the network; colored arrows and circles depict the orbit in the phase plane followed by the network under the relaxation oscillator regime. Adapted from Ref. 69 with permission.

in the figure, see Ref. 68 for details) and thus appear as a stereotyped sequence of events that take place in the presence of a new sensory stream. Finally, the internal activity decrease showed some spatial organization as it was maximal in the stimulated barrel location [visible in Fig. 4(a)], indicating that local mechanisms might be at work.

In this report, emphasis is put on a rupture between pre- and poststimulus onset activities, with the notion that specific switching occurs, affecting subsequent dynamics at the temporal scale of seconds. To this respect, the authors of this review also present in this issue of *Neurophotonics* a research article of particular interest as it reproduces in an awake monkey V4 area the variability "quenching" reported by Churchland et al.[58] (yet adding the precision that the activity that is suppressed is a specific global and low-frequency fluctuation). It further shows that this suppression already occurs with maximal strength from the lowest contrast, suggesting that a specific switch occurs rather than a continuous integration.

The notion that an input may cause a switch in the dynamics of a network activity is already present in computational models of the brain[65] and has been reported in *in-vitro* studies[72–74] where microstimulations remarkably induced transitions between up and down, or between synchronized and desynchronized states, as well as *in vivo*, using nonphysiological stimuli.[75] Also, it has been known for a long time in the human neuroscience community that sensory inputs alter synchronized rhythms, with the most famous effect being the decrease in alpha rhythms,[76–78] and that resting-state activity in the DMN decreases upon stimulation.[39,42,79]

It is in fact expected that a new sensory input might cause major changes in the global brain state, switching it, for example, from quiet to active or from asleep to conscious. Studying the details and mechanisms of these switches in addition to the mechanisms of specific rhythms taken in isolation will probably provide new insights on these complex properties of the brain network. As an example, checking how existing models of generation of the up and down fluctuations[69,80,81] [Fig. 4(b)] would predict not only the evoked responses[18,82] but also subsequent internal activity changes is warranted.

3.3 *Global Network Changes*

The changes in cortical dynamics induced by the presence of a sensory input occur also at the scale of the full brain, indicative of a change of the subject global state. This is the topic of functional connectivity studies in humans, for which the imaging techniques (EEG, MEG, fMRI, PET), characterized by coarse spatial resolution but access to the whole brain at once, are

particularly adapted. A set of structurally and functionally connected brain regions specifically deactivated during tasks that demand attention to external stimuli and innovative events has been collectively named the "DMN." Although the understanding of its role in brain function still remains largely elusive, the implication of the DMN in internal modes of cognition (autobiographical memory, self-referential thought, and mind-wandering) as well as its alterations in neuropsychiatric disorders is the subject of intense research efforts.[42,79] The ongoing DMN activity has been reported to be negatively correlated with stimulus-induced responses and perception in humans;[83,84] however, positive correlation has been also observed,[85] suggesting that the experimental context and the behavioral paradigm strongly impact the link between DMN activity and sensory processing.

4 Not One but Many Spontaneous Activities

Altogether, it appears that, despite considerable efforts aimed at studying the spontaneous activity, its functional role remains elusive and might range from low-level maintenance and consolidation of the network[86,87] to high-level signature of consciousness.[39,42,79] In particular, even though it is undisputable that ongoing states interfere with sensory processing and are reshaped by learning, direct experimental testing of whether they take an active role in sensory processing remains difficult.

Obviously, it is a pitfall anyway to consider spontaneous activity as a homogeneous phenomenon, as it entails all neural processes, unconscious and conscious, that are not directly (or at least not easily) accessible to probing by identified stimulations or tasks. Even the apparent same rhythms in different contexts can in fact display important structural differences, as was shown with slow frequency activity that appeared to be more local during slow wave sleep compared to during quiet wakefulness.[88,89]

However, the impressive development of *in vivo* optical methods, pioneered in particular by Grinvald, which allow probing cortical spatiotemporal dynamics at the single-trial level in both anesthetized and awake preparations, will undoubtedly keep on bringing precious keys to further unravel the functional interplay between internal dynamics and sensory inputs in cortical networks.

Disclosure

No conflicts of interest, financial or otherwise, are declared by the authors.

Acknowledgments

The authors are funded by the Centre National de la Recherche Scientifique, France.

References

1. A. Arieli et al., "Coherent spatiotemporal patterns of ongoing activity revealed by real-time optical imaging coupled with single-unit recording in the cat visual cortex," *J. Neurophysiol.* **73**(5), 2072–2093 (1995).
2. A. Arieli et al., "Dynamics of ongoing activity: explanation of the large variability in evoked cortical responses," *Science* **273**(5283), 1868–1871 (1996).
3. G. Hesselmann et al., "Spontaneous local variations in ongoing neural activity bias perceptual decisions," *Proc. Natl. Acad. Sci. U. S. A.* **105**(31), 10984–10989 (2008).
4. C. Bennett, S. Arroyo, and S. Hestrin, "Subthreshold mechanisms underlying state-dependent modulation of visual responses," *Neuron* **80**(2), 350–357 (2013).
5. M. L. Schölvinck et al., "Cortical state determines global variability and correlations in visual cortex," *J. Neurosci.* **35**(1), 170–178 (2015).
6. S. Crochet and C. C. H. Petersen, "Correlating whisker behavior with membrane potential in barrel cortex of awake mice," *Nat. Neurosci.* **9**(5), 608–610 (2006).
7. C. C. H. Petersen et al., "Interaction of sensory responses with spontaneous depolarization in layer 2/3 barrel cortex," *Proc. Natl. Acad. Sci. U. S. A.* **100**(23), 13638–13643 (2003).
8. E. F. Civillico and D. Contreras, "Spatiotemporal properties of sensory responses in vivo are strongly dependent on network context," *Front. Syst. Neurosci.* **6**, 25 (2012).
9. M. Zhou et al., "Scaling down of balanced excitation and inhibition by active behavioral states in auditory cortex," *Nat. Neurosci.* **17**(6), 841–850 (2014).
10. A. Hasenstaub, R. N. S. Sachdev, and D. A. McCormick, "State changes rapidly modulate cortical neuronal responsiveness," *J. Neurosci.* **27**(36), 9607–9622 (2007).
11. S. A. Romano et al., "Spontaneous neuronal network dynamics reveal circuit's functional adaptations for behavior," *Neuron* **85**(5), 1070–1085 (2015).
12. B. Haider et al., "Enhancement of visual responsiveness by spontaneous local network activity in vivo," *J. Neurophysiol.* **97**(6), 4186–4202 (2007).
13. K. D. Harris and A. Thiele, "Cortical state and attention," *Nat. Rev. Neurosci.* **12**(9), 509–523 (2011).
14. I. Ferezou, S. Bolea, and C. C. H. Petersen, "Visualizing the cortical representation of whisker touch: voltage-sensitive dye imaging in freely moving mice," *Neuron* **50**(4), 617–629 (2006).
15. R. N. S. Sachdev, "Effect of subthreshold up and down states on the whisker-evoked response in somatosensory cortex," *J. Neurophysiol.* **92**(6), 3511–3521 (2004).
16. I. Nauhaus et al., "Stimulus contrast modulates functional connectivity in visual cortex," *Nat. Neurosci.* **12**(1), 70–76 (2008).
17. T. Altwegg-Boussac et al., "Excitability and responsiveness of rat barrel cortex neurons in the presence and absence of spontaneous synaptic activity in vivo," *J. Physiol.* **592**(16), 3577–3595 (2014).
18. R. Reig et al., "Gain modulation of synaptic inputs by network state in auditory cortex in vivo," *J. Neurosci.* **35**(6), 2689–2702 (2015).
19. M. Pachitariu et al., "State-dependent population coding in primary auditory cortex," *J. Neurosci.* **35**(5), 2058–2073 (2015).
20. I. Timofeev, D. Contreras, and M. Steriade, "Synaptic responsiveness of cortical and thalamic neurones during various phases of slow sleep oscillation in cat," *J. Physiol.* **494**(Pt. 1), 265–278 (1996).
21. R. Azouz and C. M. Gray, "Cellular mechanisms contributing to response variability of cortical neurons in vivo," *J. Neurosci.* **19**(6), 2209–2223 (1999).
22. P.-O. Polack, J. Friedman, and P. Golshani, "Cellular mechanisms of brain state-dependent gain modulation in visual cortex," *Nat. Neurosci.* **16**(9), 1331–1339 (2013).
23. M. R. Deweese and A. M. Zador, "Shared and private variability in the auditory cortex," *J. Neurophysiol.* **92**(3), 1840–1855 (2004).
24. M. Steriade, D. McCormick, and T. Sejnowski, "Thalamocortical oscillations in the sleeping and aroused brain," *Science* **262**(5134), 679–685 (1993).
25. E. E. Fanselow and M. A. Nicolelis, "Behavioral modulation of tactile responses in the rat somatosensory system," *J. Neurosci.* **19**(17), 7603–7616 (1999).
26. H. Hentschke, F. Haiss, and C. Schwarz, "Central signals rapidly switch tactile processing in rat barrel cortex during whisker movements," *Cereb. Cortex* **16**(8), 1142–1156 (2005).
27. G. H. Otazu et al., "Engaging in an auditory task suppresses responses in auditory cortex," *Nat. Neurosci.* **12**(5), 646–654 (2009).
28. D. M. Schneider, A. Nelson, and R. Mooney, "A synaptic and circuit basis for corollary discharge in the auditory cortex," *Nature* **513**(7517), 189–194 (2014).
29. A. V. Egorov and A. Draguhn, "Development of coherent neuronal activity patterns in mammalian cortical networks: common principles and local hetereogeneity," *Mech. Dev.* **130**(6–8), 412–423 (2013).
30. M. L. Andermann et al., "Functional specialization of mouse higher visual cortical areas," *Neuron* **72**(6), 1025–1039 (2011).
31. Y. Fu et al., "A cortical circuit for gain control by behavioral state," *Cell* **156**(6), 1139–1152 (2014).

32. C. M. Niell and M. P. Stryker, "Modulation of visual responses by behavioral state in mouse visual cortex," *Neuron* **65**(4), 472–479 (2010).
33. G. B. Keller, T. Bonhoeffer, and M. Hübener, "Sensorimotor mismatch signals in primary visual cortex of the behaving mouse," *Neuron* **74**(5), 809–815 (2012).
34. J. Reimer et al., "Pupil fluctuations track fast switching of cortical states during quiet wakefulness," *Neuron* **84**(2), 355–362 (2014).
35. A. M. Lee et al., "Identification of a brainstem circuit regulating visual cortical state in parallel with locomotion," *Neuron* **83**(2), 455–466 (2014).
36. S. Sachidhanandam et al., "Membrane potential correlates of sensory perception in mouse barrel cortex," *Nat. Neurosci.* **16**(11), 1671–1677 (2013).
37. M. D. Fox et al., "Coherent spontaneous activity accounts for trial-to-trial variability in human evoked brain responses," *Nat. Neurosci.* **9**(1), 23–25 (2006).
38. G. Northoff, P. Qin, and T. Nakao, "Rest-stimulus interaction in the brain: a review," *Trends Neurosci.* **33**(6), 277–284 (2010).
39. M. E. Raichle, "Two views of brain function," *Trends Cognit. Sci.* **14**(4), 180–190 (2010).
40. S. Dehaene and J.-P. Changeux, "Experimental and theoretical approaches to conscious processing," *Neuron* **70**(2), 200–227 (2011).
41. S. Dehaene and J.-P. Changeux, "Ongoing spontaneous activity controls access to consciousness: a neuronal model for inattentional blindness," *PLoS Biol.* **3**(5), e141 (2005).
42. M. E. Raichle, "The restless brain: how intrinsic activity organizes brain function," *Philos. Trans. R. Soc. London B, Biol. Sci.* **370**(1668), 20140172 (2015).
43. M. Tsodyks et al., "Linking spontaneous activity of single cortical neurons and the underlying functional architecture," *Science* **286**(5446), 1943–1946 (1999).
44. T. Kenet et al., "Spontaneously emerging cortical representations of visual attributes," *Nature* **425**(6961), 954–956 (2003).
45. F. Han, N. Caporale, and Y. Dan, "Reverberation of recent visual experience in spontaneous cortical waves," *Neuron* **60**(2), 321–327 (2008).
46. P. Berkes et al., "Spontaneous cortical activity reveals hallmarks of an optimal internal model of the environment," *Science* **331**(6013), 83–87 (2011).
47. M. H. Mohajerani et al., "Spontaneous cortical activity alternates between motifs defined by regional axonal projections," *Nat. Neurosci.* **16**(10), 1426–1435 (2013).
48. S. Xu et al., "Activity recall in a visual cortical ensemble," *Nat. Neurosci.* **15**(3), 449–455 (2012).
49. D. R. Euston, M. Tatsuno, and B. L. McNaughton, "Fast-forward playback of recent memory sequences in prefrontal cortex during sleep," *Science* **318**(5853), 1147–1150 (2007).
50. E. J. B. Contreras et al., "Formation and reverberation of sequential neural activity patterns evoked by sensory stimulation are enhanced during cortical desynchronization," *Neuron* **79**(3), 555–566 (2013).
51. D. Ji and M. A. Wilson, "Coordinated memory replay in the visual cortex and hippocampus during sleep," *Nat. Neurosci.* **10**(1), 100–107 (2007).
52. M. A. Wilson and B. L. McNaughton, "Reactivation of hippocampal ensemble memories during sleep," *Science* **265**(5172), 676–679 (1994).
53. W. E. Skaggs and B. L. McNaughton, "Replay of neuronal firing sequences in rat hippocampus during sleep following spatial experience," *Science* **271**(5257), 1870–1873 (1996).
54. G. R. Sutherland and B. McNaughton, "Memory trace reactivation in hippocampal and neocortical neuronal ensembles," *Curr. Opin. Neurobiol.* **10**(2), 180–186 (2001).
55. A. G. Blankenship and M. B. Feller, "Mechanisms underlying spontaneous patterned activity in developing neural circuits," *Nat. Rev. Neurosci.* **11**(1), 18–29 (2009).
56. H. J. Luhmann, "Review of imaging network activities in developing rodent cerebral cortex in vivo," *Neurophotonics* **4**(3), 031202 (2016).
57. C. M. Lewis et al., "Learning sculpts the spontaneous activity of the resting human brain," *Proc. Natl. Acad. Sci. U. S. A.* **106**(41), 17558–17563 (2009).
58. M. M. Churchland et al., "Stimulus onset quenches neural variability: a widespread cortical phenomenon," *Nat. Neurosci.* **13**(3), 369–378 (2010).
59. J. Fiser et al., "Statistically optimal perception and learning: from behavior to neural representations," *Trends Cognit. Sci.* **14**(3), 119–130 (2010).
60. L. Buesing et al., "Neural dynamics as sampling: a model for stochastic computation in recurrent networks of spiking neurons," *PLoS Comput. Biol.* **7**(11), e1002211 (2011).
61. L. J. Borg-Graham, C. Monier, and Y. Fregnac, "Visual input evokes transient and strong shunting inhibition in visual cortical neurons," *Nature* **393**(6683), 369–373 (1998).
62. K. Rajan, L. F. Abbott, and H. Sompolinsky, "Stimulus-dependent suppression of chaos in recurrent neural networks," *Phys. Rev. E* **82**(Pt. 1), 011903 (2010).
63. L. F. Abbott, K. Rajan, and H. Sompolinsky, "Interactions between intrinsic and stimulus-dependent activity in recurrent neural networks," in *The Dynamic Brain: An Exploration of Neuronal Variability and Its Functional Significance*, M. Ding and D. Glanzman, Eds., pp. 65–82, Oxford University Press, New York (2011).
64. B. White, L. F. Abbott, and J. Fiser, "Suppression of cortical neural variability is stimulus- and state-dependent," *J. Neurophysiol.* **108**(9), 2383–2392 (2012).
65. G. Deco and V. K. Jirsa, "Ongoing cortical activity at rest: criticality, multistability, and ghost attractors," *J. Neurosci.* **32**(10), 3366–3375 (2012).
66. A. Ponce-Alvarez et al., "Task-driven activity reduces the cortical activity space of the brain: experiment and whole-brain modeling," *PLoS Comput. Biol.* **11**(8), e1004445 (2015).
67. D. L. Ringach, "Spontaneous and driven cortical activity: implications for computation," *Curr. Opin. Neurobiol.* **19**(4), 439–444 (2009).
68. T. Deneux and A. Grinvald, "Milliseconds of sensory input abruptly modulate the dynamics of cortical states for seconds," *Cereb. Cortex* 1–15 (2016).
69. M. Mattia, "Exploring the spectrum of dynamical regimes and timescales in spontaneous cortical activity," *Cognit. Neurodyn.* **6**(3), 239–250 (2012).
70. D. Derdikman et al., "Imaging spatiotemporal dynamics of surround inhibition in the barrels somatosensory cortex," *J. Neurosci.* **23**(8), 3100–3105 (2003).
71. M. M. Halassa et al., "Selective optical drive of thalamic reticular nucleus generates thalamic bursts and cortical spindles," *Nat. Neurosci.* **14**(9), 1118–1120 (2011).
72. Y. Shu, A. Hasenstaub, and D. A. McCormick, "Turning on and off recurrent balanced cortical activity," *Nature* **423**(6937), 288–293 (2003).
73. J. N. MacLean et al., "Internal dynamics determine the cortical response to thalamic stimulation," *Neuron* **48**(5), 811–823 (2005).
74. S. Fujisawa, N. Matsuki, and Y. Ikegaya, "Single neurons can induce phase transitions of cortical recurrent networks with multiple internal States," *Cereb. Cortex* **16**(5), 639–654 (2006).
75. F. Kasanetz, L. A. Riquelme, and M. G. Murer, "Disruption of the two-state membrane potential of striatal neurones during cortical desynchronisation in anaesthetised rats," *J. Physiol.* **543**(Pt. 2), 577–589 (2002).
76. E. Callaway and R. S. Layne, "Interaction between the visual evoked response and two spontaneous biological rhythms: the EEG alpha cycle and the cardiac arousal cycle," *Ann. N. Y. Acad. Sci.* **112**, 421–431 (1964).
77. G. Pfurtscheller and W. Klimesch, "Functional topography during a visuoverbal judgment task studied with event-related desynchronization mapping," *J. Clin. Neurophysiol.* **9**(1), 120–131 (1992).
78. M. Siegel, T. H. Donner, and A. K. Engel, "Spectral fingerprints of large-scale neuronal interactions," *Nat. Rev. Neurosci.* **13**(2), 121–134 (2012).
79. R. L. Buckner, J. R. Andrews-Hanna, and D. L. Schacter, "The brain's default network: anatomy, function, and relevance to disease," *Ann. N. Y. Acad. Sci.* **1124**(1), 1–38 (2008).
80. K. E. Poskanzer and R. Yuste, "Astrocytes regulate cortical state switching in vivo," *Proc. Natl. Acad. Sci. U. S. A.* **113**(19), E2675–E2684 (2016).
81. R. Yuste et al., "The cortex as a central pattern generator," *Nat. Rev. Neurosci.* **6**(6), 477–483 (2005).
82. C. Curto et al., "A simple model of cortical dynamics explains variability and state dependence of sensory responses in urethane-anesthetized auditory cortex," *J. Neurosci.* **29**(34), 10600–10612 (2009).

83. M. D. Greicius and V. Menon, "Default-mode activity during a passive sensory task: uncoupled from deactivation but impacting activation," *J. Cognit. Neurosci.* **16**(9), 1484–1492 (2004).
84. M. Boly et al., "Baseline brain activity fluctuations predict somatosensory perception in humans," *Proc. Natl. Acad. Sci. U. S. A.* **104**(29), 12187–12192 (2007).
85. S. Sadaghiani, G. Hesselmann, and A. Kleinschmidt, "Distributed and antagonistic contributions of ongoing activity fluctuations to auditory stimulus detection," *J. Neurosci.* **29**(42), 13410–13417 (2009).
86. L. Marshall et al., "Boosting slow oscillations during sleep potentiates memory," *Nature* **444**(7119), 610–613 (2006).
87. M. V. Sanchez-Vives and M. Mattia, "Slow wave activity as the default mode of the cerebral cortex," *Arch. Ital. Biol.* **152**(2–3), 147–155 (2015).
88. U. Olcese et al., "Spike-based functional connectivity in cerebral cortex and hippocampus: loss of global connectivity is coupled to preservation of local connectivity during non-REM sleep," *J. Neurosci.* **36**(29), 7676–7692 (2016).
89. L. M. J. Fernandez et al., "Highly dynamic spatiotemporal organization of low-frequency activities during behavioral states in the mouse cerebral cortex," *Cereb. Cortex* 1–19 (2016).

Isabelle Ferezou studies the processing of tactile sensory information in the mouse cortex using voltage-sensitive dye (VSD) imaging in Daniel Shulz Lab, Unité de Neurosciences Information et Complexité (UNIC), Centre National de la Recherche Scientifique (CNRS), France. During her PhD supervised by Bertrand Lambolez at ESPCI, Paris, France, she studied GABAergic interneurons using single-cell RT-PCR after patch-clamp *in vitro*. She was then trained in *in vivo* VSD imaging and electrophysiology in the laboratory of Professor Carl Petersen at EPFL, Switzerland.

Thomas Deneux develops data analysis methods for high-throughput recordings of neural activity at UNIC, CNRS, France. His PhD supervised by Olivier Faugeras at the Institut National de Recherche en Informatique et Automatique, Paris, France, focused on human brain data analysis, whereas he studied spontaneous activity and multisensory integration using VSD and two-photon microscopy during his postdoctoral trainings supervised by Amiram Grinvald at the Weizmann Institute, Rehovot, Israel, Ivo Vanzetta at Institut de Neurosciences de la Timone, Marseille, France, and Brice Bathellier at CNRS-UNIC, Paris, France.

Journal of Neuroscience Methods 263 (2016) 145–154

Contents lists available at ScienceDirect

Journal of Neuroscience Methods

journal homepage: www.elsevier.com/locate/jneumeth

Basic Neuroscience

An automated workflow for the anatomo-functional mapping of the barrel cortex

Lorraine Perronnet[a,b,1,2], María Eugenia Vilarchao[b,2], Guillaume Hucher[b], Daniel E. Shulz[b], Gabriel Peyré[a], Isabelle Ferezou[b,*]

[a] CNRS and Ceremade, Université Paris-Dauphine, Place du Maréchal De Lattre De Tassigny, 75775, Paris Cedex 16, France
[b] Unité de Neurosciences, Information et Complexité, CNRS FRE 3693, 91198 Gif-sur-Yvette Cedex, France

HIGHLIGHTS

- Here is a new tool to map functional data onto the barrel cortex structure.
- It realigns histological slices and reconstructs the barrel map in 2-D.
- Slice realignment by rigid transformations is computed using detected blood vessels.
- Barrel map reconstruction is obtained by gradient fusion.
- Its application is exemplified for voltage sensitive dye imaging experiments.

ARTICLE INFO

Article history:
Received 17 November 2014
Received in revised form 4 September 2015
Accepted 7 September 2015
Available online 15 September 2015

Keywords:
Barrel cortex
Histological sections
Blood vessels
Registration
Robust iterative closest point
Gradient domain fusion
Voltage sensitive dye imaging

ABSTRACT

Background: The rodent barrel cortex is a widely used model to study the cortical processing of tactile sensory information. It is notable by the cytoarchitecture of its layer IV, which contains distinguishable structural units called barrels that can be considered as anatomical landmarks of the functional columnar organization of the cerebral cortex. To study sensory integration in the barrel cortex it is therefore essential to map recorded functional data onto the underlying barrel topography, which can be reconstructed from the post hoc alignment of tangential brain slices stained for cytochrome oxidase.
New method: This article presents an automated workflow to perform the registration of histological slices of the barrel cortex followed by the 2-D reconstruction of the barrel map from the registered slices. The registration of two successive slices is obtained by computing a rigid transformation to align sets of detected blood vessel cross-sections. This is achieved by using a robust variant of the classical iterative closest point method. A single fused image of the barrel field is then generated by computing a nonlinear merging of the gradients from the registered images.
Comparison with existing methods: This novel anatomo-functional mapping tool leads to a substantial gain in time and precision compared to conventional manual methods. It provides a flexible interface for the user with only a few parameters to tune.
Conclusions: We demonstrate here the usefulness of the method for voltage sensitive dye imaging of the mouse barrel cortex. The method could also benefit other experimental approaches and model species.

1. Introduction

The rodent primary somatosensory cortex is a very convenient model for studying the cortical processing of sensory information because of its well defined structural and functional layout that is invariant from animal to animal (Welker and Van der Loos, 1986; Meyer et al., 2013; Egger et al., 2012). In its layer IV, neurons are gathered into clusters called barrels that respect the same topology as the whiskers on the snout of the animal (Woosley and Loos, 1970). Each barrel is dedicated primarily to the processing of the input coming from its corresponding whisker (Fig. 1A,B). When

* Corresponding author at: Unité de Neurosciences Information et Complexité (UNIC), CNRS FRE 3693, 1 Avenue de la Terrasse, Bât. 32/33, 91198 Gif-sur-Yvette Cedex, France. Tel.: +33 01 69 82 34 02; fax: +33 01 69 82 34 27.
E-mail address: isabelle.ferezou@unic.cnrs-gif.fr (I. Ferezou).
[1] Present address: VISAGES, INRIA, INSERM U746, Université de Rennes 1, CNRS UMR6074, IRISA, campus de Beaulieu, F-35042 Rennes, France.
[2] These authors contributed equally to the work.

http://dx.doi.org/10.1016/j.jneumeth.2015.09.008
0165-0270/

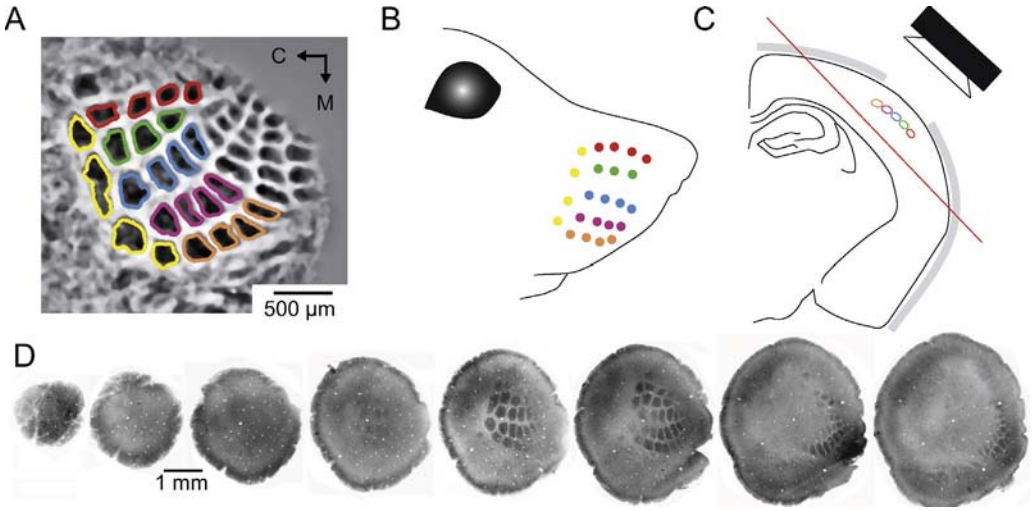

Fig. 1. Cytochrome oxidase staining of tangential sections from the mouse primary somatosensory cortex reveals the structural organization of layer 4 barrels that mirrors the arrangement of the vibrissae on the snout. (A) Following the registration of tangential histological slices and the reconstruction of the barrel map, one can see that the spatial organization of the layer 4 barrels matches the layout of the vibrissae on the snout of the animal (B). (C) Drawing of a coronal section of the left hemisphere of the mouse brain illustrating the position of layer 4 barrels within the primary somatosensory area of the cortex. After in vivo imaging of barrel cortex activity, sections are cut tangentially to reconstruct the layer 4 barrel map (cutting plane indicated by the red line). (D) A series of tangential histological slices stained for cytochrome oxidase. On the first slice one can see superficial blood vessels. On the other slices, one can see white circular to elliptic spots that correspond to sections of plunging blood vessels. Depending on the exact axis of the cut, barrels can be spread over several slices.

studying sensory processing in the barrel cortex either with electrophysiological or imaging methods, it is therefore of great interest to superimpose the recorded activity onto the underlying barrel topography, which can be reconstructed from the post hoc alignment of tangential brain slices stained for cytochrome oxidase. In order to optimize this anatomo-functional mapping, which is usually accomplished manually, we developed an automated workflow for the registration of the histological slices of the barrel cortex and the 2-D barrel map reconstruction.

Here we focus our attention on voltage sensitive dye imaging (VSDI) of the mouse barrel cortex to illustrate the usefulness of the approach. However, the method can be extended to the study of the rat barrel cortex and applied to other techniques such as 2-photon calcium imaging.

The traditional first step to recover the map of the barrel cortex after imaging experiments is: brain fixation by perfusing the animal with a solution of paraformaldehyde, followed by the cutting of tangential slices (~100 μm thick, with or without previous flattening of the cortex), which are subsequently stained for cytochrome oxidase using classical histological procedures that reveal the barrel arrangement in layer IV (Fig. 1C and D (Land and Simons, 1985)).

Next, using digital microphotographs of the slices, it is necessary to:

1. register the slices;
2. fuse the registered slices to define a reconstructed barrel image.

In this article we provide an automated solution for these two steps which are the most time-consuming tasks of the workflow when using conventional manual methods. After completing these steps, it is then relatively simple to define the barrel map by segmenting the reconstructed barrel cortex image. The superimposition of the map with the functional data can be finally achieved by using the superficial blood vessels as anatomical landmarks (Fig. 2). The proposed anatomo-functional mapping tool significantly speeds up the overall process and provides more accurate anatomo-functional mapping.

1.1. Registration of histological slices

A typical example of a series of images obtained after the histological process is shown in Fig. 1D. Depending on their depth, the histological sections present different properties: in the first

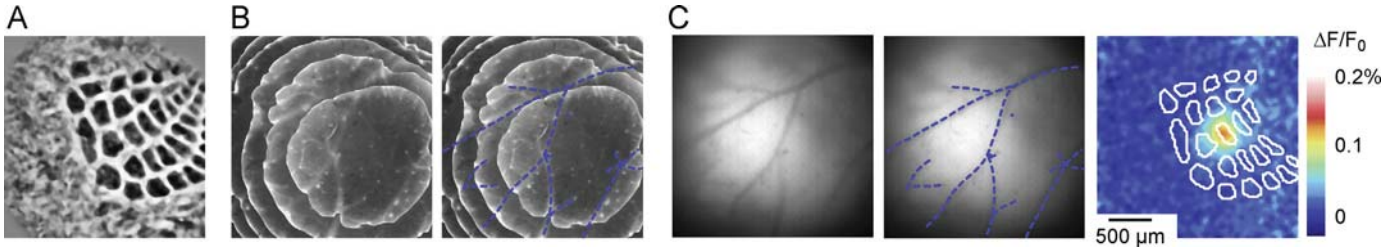

Fig. 2. Alignment of the barrel map with VSDI data using the superficial blood vessels as blueprints. (A) Barrel map reconstructed from the histological slices shown in Fig. 1D, using our anatomo-functional mapping method. (B) Superimposition of the registered histological slices, allowing the delineation of the superficial blood vessels (in blue). (C) The superficial blood vessels also appear in vivo on the fluorescent images taken during the VSDI session. The VSDI data can therefore be aligned with the underlying structural map of the barrel cortex using the blood vessels as anatomical landmarks. On the right, the cortical activity is shown imaged at 10 ms following a single C2 whisker deflection with the voltage sensitive dye RH1691 under urethane anesthesia. The barrels outlined from the reconstruction in A are superimposed on the image as white lines.

section, which corresponds to the surface of the cortex, some large superficial blood vessels are visible together with plunging blood vessels. This section is crucial for the whole process since it contains most of the superficial blood vessels that will be used for the final alignment of the histological data with the VSDI data (Fig. 2). The intermediate sections usually contain orthogonal blood vessels (white dots on the slices shown in Fig. 1D) that can be used to align subsequent sections. Barrels start appearing on Section 3 or 4 and can be visualized on up to 5 sections.

We do not use the deeper sections from subgranular layers as they do not contain any useful information for the reconstruction.

Image registration is a classical problem and its solutions find many applications in medical image analysis. Depending on the imaging modality and the specific prior knowledge of the object to register, a wide variety of methods have been considered in the literature (for an overview see (Glocker et al., 2011; Sotiras et al., 2013)). Only a few previous studies explicitly deal with the problem of registering rodent brain histological sections, usually in order to reconstruct a whole brain in 3-D (Ourselin et al., 2001; Ju et al., 2006).

In order to exploit the microscopic-scale information of the histological data, these applications require the precise registration of a large number of histological slices from the whole brain with a method that accounts for global but also local nonlinear deformations due to tissue shrinkage and tearing after histological preparation. Ourselin et al. presented in Ourselin et al. (2001) a block matching strategy to compute local similarities and then estimate the rigid transformation that matches the maximum of similar regions in a robust way. Alternatively (Ju et al., 2006) used a method based on pairwise elastic imaging warps, with the specificity to compute the deformation of each section by considering not only two neighbors for each section, but an extended neighborhood including a group of images.

The specific problem of registering histological sections of the rodent barrel cortex has been rarely addressed in the literature. Egger et al. (2012) proposed a tool for the 3-D reconstruction and standardization of the rat barrel cortex for the precise registration of single neuron morphology. Seventy micrometer thick tangential sections of rat barrel cortex are aligned pairwise by finding the rotation and translation that best superimpose blood vessels of two adjacent sections either manually or automatically, using a tool originally developed for the reconstruction of neuronal processes (Dercksen et al., 2009). Finally the barrels are segmented by using a semi-automated method.

Here we developed a tool to compute the rigid transformations to align sets of detected blood vessels (Fig. 3A), and we decided to focus on a 2-D image fusion using an automated method. The usual approach to perform point cloud registration is the iterative closest point (ICP) algorithm introduced by Besl and McKay (1992). While the initial formulation is not robust to outliers, several approaches explicitly deal with this issue (Chetverikov et al., 2005; Nishino and Ikeuchi, 2008; Stewart et al., 2003; Kaneko et al., 2003; Ma et al., 1999). These approaches are related to reweighting least squares methods and we propose in Appendix B a unifying presentation and convergence analysis of a robust ICP method.

1.2. Fusion of histological slices

In our framework, the 2-D reconstruction of the barrel maps amounts to perform a fusion of the registered sections (Fig. 3B). The goal is to reconstruct the edges of the barrels that are spread over the slices. Image fusion is classically addressed in the field of image processing and computer vision, to perform for instance image editing and stitching. To reconstruct sharp edges, it is necessary to use

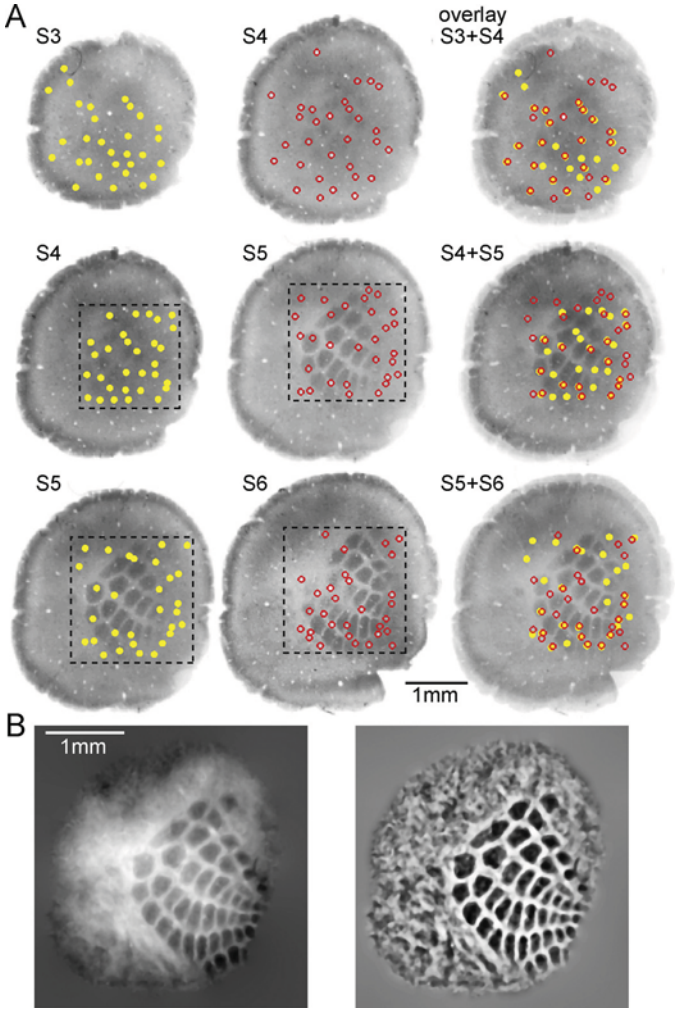

Fig. 3. Registration of histological slices and subsequent barrel map reconstruction. (A) Snapshots extracted from the GUI illustrating the results of the automated detection of blood vessel cross sections on consecutive histological slices (yellow filled circles and red open circles, respectively – S_3–S_6 previously shown in Fig. 1D). The result of the registration obtained by robust ICP applied on the detected blood vessels is illustrated on the right for each pair of slices. Note that the user can delimit manually a region of interest (black dashed lines) in order to restrict blood vessel detection to the barrel field region. (B) Images from the same experiment obtained by using our automated barrel map reconstruction tool before (left) or after (right) post-processing steps.

non-linear methods, the most popular one being based on gradient-domain blending (Pérez et al., 2003; Raskar et al., 2004). The goal is to generate a novel image by locally keeping the content of the image having the highest local frequency. In this article, we focus on the use of gradient-domain methods, which have the advantage of being simpler and can be easily tuned for the purpose of barrel map fusion.

1.3. Contributions

Our main contribution is a comprehensive pipeline for the 2-D reconstruction of the barrel cortex from tangential histological sections. This pipeline is composed of 2 successive modules that respectively perform: histological section registration and barrel image reconstruction using image fusion. As a side contribution, we propose to recast the registration problem using a robust ICP optimization method, and we show that a Majorize-Minimize framework can be applied to provably ensure the convergence of the method. These contributions originate from specific needs

Table 1
Notations used in the paper.

Notation		See
$m \in \{1, \ldots, Q\}$	Index of a slice	Section 2.2
$\{S_1, \ldots, S_Q\}$	Input slices	Section 2.2
NCC	Norm. cross correlation	Appendix A
$\mathcal{X}_m$	Set of detected vessels	Section 2.2.2
$\mathcal{M}$	Slices containing barrels	Section 2.3.2
$\mathcal{T}_m$	Registration map	Eq. (5)
$\{\tilde{S}_1, \ldots, \tilde{S}_Q\}$	Registered slices	Eq. (5)
$\{\bar{S}_1, \ldots, \bar{S}_Q\}$	Inpainted slices	Section 2.3.1
S	Fused image	Section 2.3.2
$\bar{S}$	Drift-corrected result	Eq. (6)

Table 2
Parameters used in the paper.

Param.		See	Default
τ	NCC threshold	Section 2.2.2	0.75
N	Max. number of vessels	Section 2.2.2	30
$\sigma_{\max}$	Maximum vessel radius	Section 2.2.2	4.5
ϵ	ICP robustness parameter	Eq. (2)	–
$\sigma^\star$	Width of debiasing kernel	Eq. (6)	10

raised by studies of sensory integration in the barrel cortex, however the histological section registration tool proposed here might be helpful to reconstruct any anatomical tissue in which blood vessels penetrate predominantly orthogonally to the cutting plane of the histological slices.

2. Material and methods

2.1. Overview of the proposed framework

This section details each step of the proposed method. The corresponding Matlab code to reproduce the figures of this article is available online[3]. This code is packaged as a graphical user interface (GUI) that is helpful to guide the user through the various processing steps, from image loading to the final reconstructed barrel map.

Table 1 reviews the notation introduced in the paper. Table 2 lists the parameters of the method, together with the default values used in our numerical simulations.

The successive steps of the algorithms are:

- Segment the foreground to obtain the input section images $\{S_1, \ldots, S_Q\}$ (Section 2.2.1).
- For each $m \in \{1, \ldots, Q\}$, compute the list of detected vessel positions $\mathcal{X}_m$ (Section 2.2.2).
- For each $m \in \{1, \ldots, Q-1\}$, compute the optimal transform T_m to register S_m with S_{m+1} (Section 2.2.3).
- Apply the transforms to obtain the registered images $\{\tilde{S}_1, \ldots, \tilde{S}_Q\}$ (Eq. (5)).
- For each m, inpaint the detected vessel and denoise the resulting images to obtain $\{\bar{S}_1, \ldots, \bar{S}_Q\}$ (Section 2.3.1).
- Fuse the relevant maps $\{\bar{S}_m\}_{m \in \mathcal{M}}$ (where $\mathcal{M} \subset \{1, \ldots, Q\}$ indexes the maps containing apparent barrels) to obtain the fused map S (Section 2.3.2).
- Remove the low frequency drift to obtain $\bar{S}$ (Section 2.3.3).

[3] https://github.com/gpeyre/2014-NeuroMeth-barrels.

2.2. Step 1: pairwise registration of histological sections

The input of the algorithm is Q raw images which are digital images with range normalized in $[0, 1]$ (0 being black and 1 white). Fig. 1D shows examples of such images.

2.2.1. Pre-processing

Depending on the configuration of the microscope used to acquire the images, the input images contain 2 or 3 regions:

- In the center of the image, a gray region corresponding to the histological section of the cortex. This is the foreground region.
- A circular white region corresponding to the lens/plate of the microscope and that surrounds the cortex region. It is considered as background.
- In some cases, a black region can also surround the two other regions. It is also considered as background.

We extract the background using a K-means algorithm with $K = 3$ regions. The background is then replaced by the value 0 and the resulting images (the so-called "slices" in the following) are denoted $\{S_1, \ldots, S_Q\}$.

2.2.2. Vessel detection

Blood vessels which are approximately orthogonal to the cutting plane look like slightly elliptic spots that can be approximated by small Gaussians. To be invariant to local contrast fluctuations, we detect these orthogonal vessels using normalized cross correlations with Gaussian templates of varying standard deviations, assumed to be smaller than $\sigma_{\max}$.

For each slice S_m, for $m \in \{1, \ldots, Q\}$, we compute its associated normalized cross correlation $\mathrm{NCC}(S_m)$ against the set of Gaussian templates, as detailed in Appendix A. Given a threshold $\tau \in [0, 1]$ and a maximum number N of detected vessels, we define the detected vessel centers $\mathcal{X}_m$ to be the set of pixels x satisfying both $\mathrm{NCC}(S_m)(x) > \tau$ and $\mathrm{NCC}(S_m)(x)$ is among the N largest values of $\mathrm{NCC}(S_m)$.

2.2.3. Slice registration by robust ICP

For each m, we now register the slice S_m with the slice S_{m+1} (see Fig. 3A). Registration is obtained by computing an optimal transformation T_m which maps pixels in slice S_{m+1} to pixels in image S_m. We restrict here the computation to rigid transformations, i.e. of the form $T(x) = R(x) + t$ where R is a planar rotation and $t \in \mathbb{R}^2$ is a translation vector.

Variational registration. This optimal deformation is obtained by exploiting the fact that detected orthogonal vessels should have approximately the same position in two consecutive frames. We denote $\mathcal{X}_{m+1} = \{x_i\}_{i \in I}$ and $\mathcal{X}_m = \{y_j\}_{j \in J}$ the two sets of vessel positions. We cast this problem as the optimization of a non-convex functional measure of the goodness of fit between the transformation $T(x_i)$ of each detected vessel x_i in S_m and its closest neighbor y_j in S_{m+1}. T_m is obtained by computing a local minimizer of

$$\min_T \sum_{i \in I} \min_{j \in J} \rho(||T(x_i) - y_j||). \tag{1}$$

Here $\rho : \mathbb{R}^+ \to \mathbb{R}^+$ is a penalty function. The most common choice is a quadratic loss $\rho(r) = r^2$, which assumes some sort of Gaussian distribution of the fitting errors. This choice poorly handles outliers in the detected vessels, which are likely to be present in our datasets. We choose here to use the following robust loss function

$$\rho(r) = \log(\varepsilon^2 + r^2), \tag{2}$$

which gives less weight to outliers (large values of r) than a quadratic loss. Small values of ε are used to cope with many outliers. Note that setting $\varepsilon \to +\infty$ recovers the quadratic loss r^2 which assumes no outliers. Note also that other loss functions could be used as well, as long as they satisfy the hypotheses exposed in Appendix B.

ICP iterations. A classical algorithm to minimize (1) is the iterative closest point (ICP), introduced by Besl and McKay (1992) for the quadratic loss $\rho(r) = r^2$. This algorithm has been extended by several authors to cope with robust loss (see Section 1.1 for more details). We use a similar approach here, and provide more details in Appendix B.

The ICP algorithm iterates between two steps. In the first step, T is known and assumed to be fixed, and one computes a nearest neighbor $z_i = y_j$ for each vessel x_i, where the index j minimizes

$$\min_{j \in J} \quad \rho(||T(x_i) - y_j||). \tag{3}$$

In the second step, the optimal T is updated by solving

$$\min_{T} \quad \sum_{i \in I} \rho(||T(x_i) - z_i||). \tag{4}$$

For the quadratic loss $\rho(r) = r^2$, this second step is solved in closed form as detailed in Appendix B.2. For a generic loss ρ, there is no such closed form. We detail in Appendix B.1 a Majorize–Minimize (MM) method to compute a local minimizer. To the best of our knowledge, this presentation, and the corresponding convergence analysis, is new.

Initialization. A major difficulty to solve (2) is that it is highly non-convex, and the ICP algorithm is likely to converge to a local minimizer T. To improve the quality of the result, it is important to test several initializations to obtain a good registration.

Registered images. Once the registration transforms $\{T_1, \ldots, T_{Q-1}\}$ have been computed, they can be cascaded to warp the input slice images to obtain the sequence $\{\tilde{S}_1, \ldots, \tilde{S}_Q\}$ of sections, all registered with respect to the initial one $S_1 = \tilde{S}_1$ as follow

$$\tilde{S}_m(x) = S_m(\mathcal{T}_m(x)) \quad \text{where} \quad \mathcal{T}_m = T_1 \circ \ldots \circ T_{m-2} \circ T_{m-1}. \tag{5}$$

2.3. Step 2: reconstruction of the barrel image

We now have a set $\{\tilde{S}_1, \ldots, \tilde{S}_Q\}$ of registered slices. We fuse them in a single image S, which gathers the edge information of the relevant images to reconstruct the barrel map.

2.3.1. Pre-processing

In order to avoid the amplification of artifacts during the gradient fusion process detailed next, we inpaint (i.e. remove) the orthogonal vessel traces and denoise the resulting image. The inpainting method is detailed in Appendix C. The output of the inpainting is then denoised using a median filter on 3×3 patches. We use this non-linear filter to reduce salt-and-pepper noise instead of a convolution, as it removes noise while preserving edges. We denote the output of this pre-processing $\bar{S}_m$.

2.3.2. Slice gradient fusion

We denote $m \in \mathcal{M}$ the set of relevant slices containing partial barrel information. To reconstruct a sharp image, we fuse together the gradient of the input slices $\{\bar{S}_m\}_{m \in \mathcal{M}}$ by keeping at each pixel the gradient with the largest magnitude. This method is partly inspired by some recent works in computational photography, such as Pérez et al. (2003), Raskar et al. (2004). The details of this method are given in Appendix D. We denote S the output of the fusion process.

2.3.3. Drift removal

The histological sections often present variations in intensity across the barrel cortex that might be due to anatomical reasons. Usually, the anterior lateral barrel subfield (small barrels corresponding to small vibrissae) appears darker than the posterior medial barrel subfield (large barrels corresponding to large vibrissae). This drift is enhanced by the gradient fusion operation that is applied on each pair. As a consequence, the merged image S obtained by the procedure explained above exhibits a strong drift in intensity. We thus filter the merged image with a high-pass filter to remove this low frequency component

$$\bar{S} = S - S \star h_{\sigma\star} \tag{6}$$

where $h_{\sigma\star}$ is a low-frequency gaussian filter of standard deviation $\sigma\star$, and $\star$ is the discrete 2-D convolution.

2.4. In vivo VSDI and DiI staining

Animal preparation and VSDI setup. Experiments were performed in conformity with the French (authorization number: 2012-0068) and European (2010/63/UE) legislations relative to the protection of animals used for experimental and other scientific purposes. VSDI of the cortical activity evoked by single whisker deflections was performed on 6–12 week-old C57Bl6 mice under urethane anesthesia (1.7 mg/g), essentially as previously described in Ferezou et al. (2006). Briefly, the left barrel cortex was exposed and stained for 1 h with the VSD RH1691 (1 mg/ml, in Ringer's solution containing [in mM]: 135 NaCl, 5 KCl, 5 HEPES, 1.8 $CaCl_2$, 1 $MgCl_2$). After removal of the unbound dye, the cortex was covered with agarose (0.5–1% in Ringer's) and a coverslip. Cortical imaging was performed through a tandem-lens fluorescence microscope (SciMedia), equipped with one Leica PlanApo 5× (objective side) and one Leica PlanApo 1× (condensing side), a 630 nm excitation filter, a 650 nm dichroic mirror, and a long pass 665 nm emission filter. The field of view was 2.5×2.5 mm, resulting in a pixel resolution of 25×25 μm.

Whisker stimulation. Individual deflections of the right 24 posterior macrovibrissae of the mice were performed using a custom built multi-whisker stimulator based on a matrix of 24 multidirectional piezoelectric benders (Jacob et al., 2010). The whiskers were inserted in 27G stainless steel tubes attached to the benders, leaving 2 mm between the tip of the tube and the whisker base. The 24 whiskers were stimulated individually, in the 4 cardinal directions, at 0.1 Hz within pseudo randomized sequences containing extra blank trials (each stimulation being repeated 10 times). Each whisker deflection consisted of a 100 μm displacement (measured at the tip of the tube), with a 2 ms rising time, a 2 ms plateau and a 2 ms fall (specific filters were used to correct for the mechanical ringing of the stimulators).

Image analysis. Acquisition and data preprocessing were done using in-house software (Elphy, G. Sadoc, UNIC-CNRS), further analyses were made using custom written routines in IgorPro (Wavemetrics). Subtraction of the averaged unstimulated blank trials was used to correct for bleaching artifacts. For each whisker, data corresponding to the 4 directions of deflection were averaged.

DiI in vivo staining. DiI stain (Molecular Probes, LifeTechnologies) was deposited on the shanks of silicon electrodes (DiCarlo et al., 1996) that were inserted in the barrel cortex perpendicularly with a microcontroller (Luigs & Neumann).

2.5. Histological procedures

Following the experiments and the administration of an overdose of urethane, mice were perfused with saline followed by paraformaldehyde (4% in 0.1 M phosphate buffer). After an overnight post-fixation in paraformaldehyde, the brains were cut

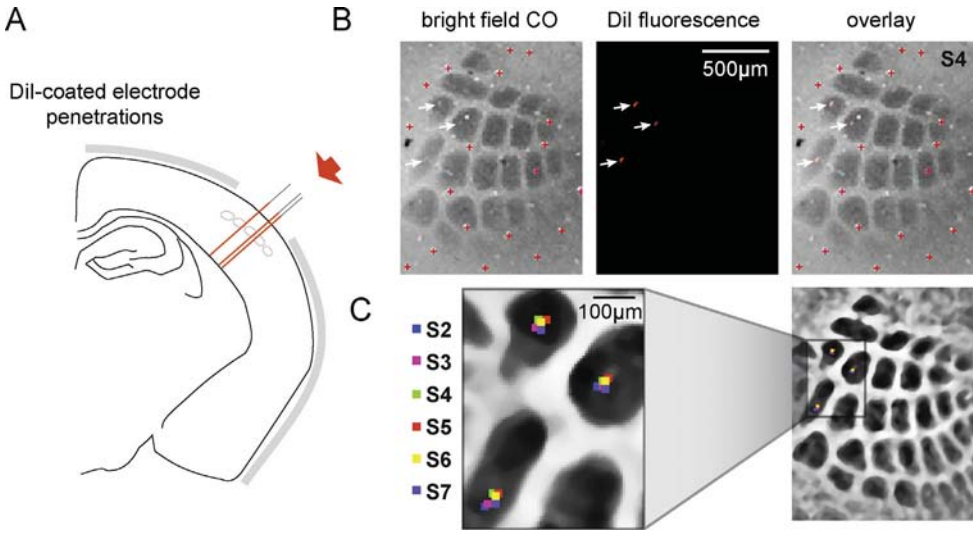

Fig. 4. Histological validation of the registration method. (A) Drawing of a coronal section of the left hemisphere of the mouse brain illustrating the penetration sites of DiI-coated electrodes. (B) The DiI fluorescent staining (middle image) does not interfere with the process of blood vessel detection used on bright field images (left), as shown by the absence of detected spots on the DiI stain (right), arrowheads indicate the DiI stained spots corresponding to electrode tracks. (C) Following the registration of the slices 2–7, we observe a good overlap of DiI spots, indicative of the accuracy of our registration method.

in 100 μm thick tangential sections and stained for cytochrome oxidase.

3. Results

Starting from tangential slices stained for cytochrome oxidase, the reconstructed 2-D barrel map can be obtained in a few clicks by using the provided GUI. The whole procedure takes 7–9 min including 3–5 min of computation that do not require the intervention of the user. The same process using traditional manual methods (with the help of a raster graphics editor such as Adobe Photoshop) takes, for a well-trained person, 16–28 min. Most importantly, our automated approach prevents user dependent variability in the obtained barrel map. In order to assess the accuracy of our registration method, we first carried out histological control experiments, and then used VSD imaging to functionally evaluate the precision of the barrel map obtained following the full reconstruction procedure.

3.1. Histological validation of the registration method

In order to assess the efficiency of our registration method based on automated blood vessel detection and robust ICP, we perpendicularly inserted DiI coated electrodes in the barrel cortex of urethane anesthetized mice ($n = 5$ experiments, 3–6 electrode penetrations per experiments), before processing the brain for histological staining of the cytochrome oxidase following our standard procedures. The electrodes being flat, they did not leave any round or elliptic white marks in the tissue and therefore did not interfere with our registration method (Fig. 4). Because the penetration of DiI coated electrodes was perpendicular to the cortical surface, the DiI staining should appear aligned on consecutive cortical sections following proper registration of the slices. In order to control this alignment, the location of DiI spots was reported for each slice on the final fused barrel map image for each section (Fig. 4C). The calculated mean distance between DiI spots from the same electrode penetration (34.41 ± 18.93 μm, mean ± SD, $n = 5$) revealed the subcolumnar resolution of our registration method. These control experiments were further used to evaluate the eventual shrinkage of the cortical tissue due to brain fixation and histological procedures. The distances of 250 μm and 500 μm separating the electrode penetration sites in vivo, were compared to the distances measured between DiI spots on the slices following histological procedures. Over our 5 control experiments, the observed tissue shrinkage within the $x - y$ plane was minimal (<1.5%).

3.2. Assessment of the barrel map reconstruction tool using VSDI of cortical responses to individual whisker deflections

To finally validate our 2-D barrel map reconstruction method, we confronted its resulting map with the functional organization of the barrel cortex established in vivo by real time imaging of cortical responses to individual whisker deflections under urethane anesthesia ($n = 4$ experiments). Using a mechanical multi-whisker stimulator (Jacob et al., 2010), we deflected independently the 24 principal whiskers in a pseudo random order, and imaged the evoked cortical responses in the contralateral barrel cortex using the VSD RH1691. Fig. 5 illustrates the results obtained from one experiment. As previously reported in similar conditions (Ferezou et al., 2006), the earliest responses to whisker deflections were localized to the corresponding barrel-related columns (Fig. 5A). When reporting the 90% contours of the early cortical responses onto the aligned barrel map, we observe a good anatomo-functional match (Fig. 5B). To quantify this match, the distance between the centroid of the anatomically defined barrels and the centroid of the early VSD response (area above a 90% threshold) was measured (Fig. 5C). The mean centroid-centroid distance over the 4 control experiments for all the barrels is 60.5 ± 21.2 μm (34.8–116.5 μm range across the barrel field). We observed slightly higher values for the columns located at the border of the map which might result from the curvature of the cortex, the maxima of cortical responses were located within the corresponding barrel area in the majority of cases (86.55%), attesting to the accuracy of the method.

4. Discussion

We have designed a comprehensive pipeline for the reconstruction of the 2-D barrel map from histological sections. This tool enables a fast reconstruction of a precise barrel map, thus saving a significant amount of time for the experimentalist. Indeed, most of the studies based on optical imaging which required a post-hoc anatomo-functional mapping of the barrel cortex relied

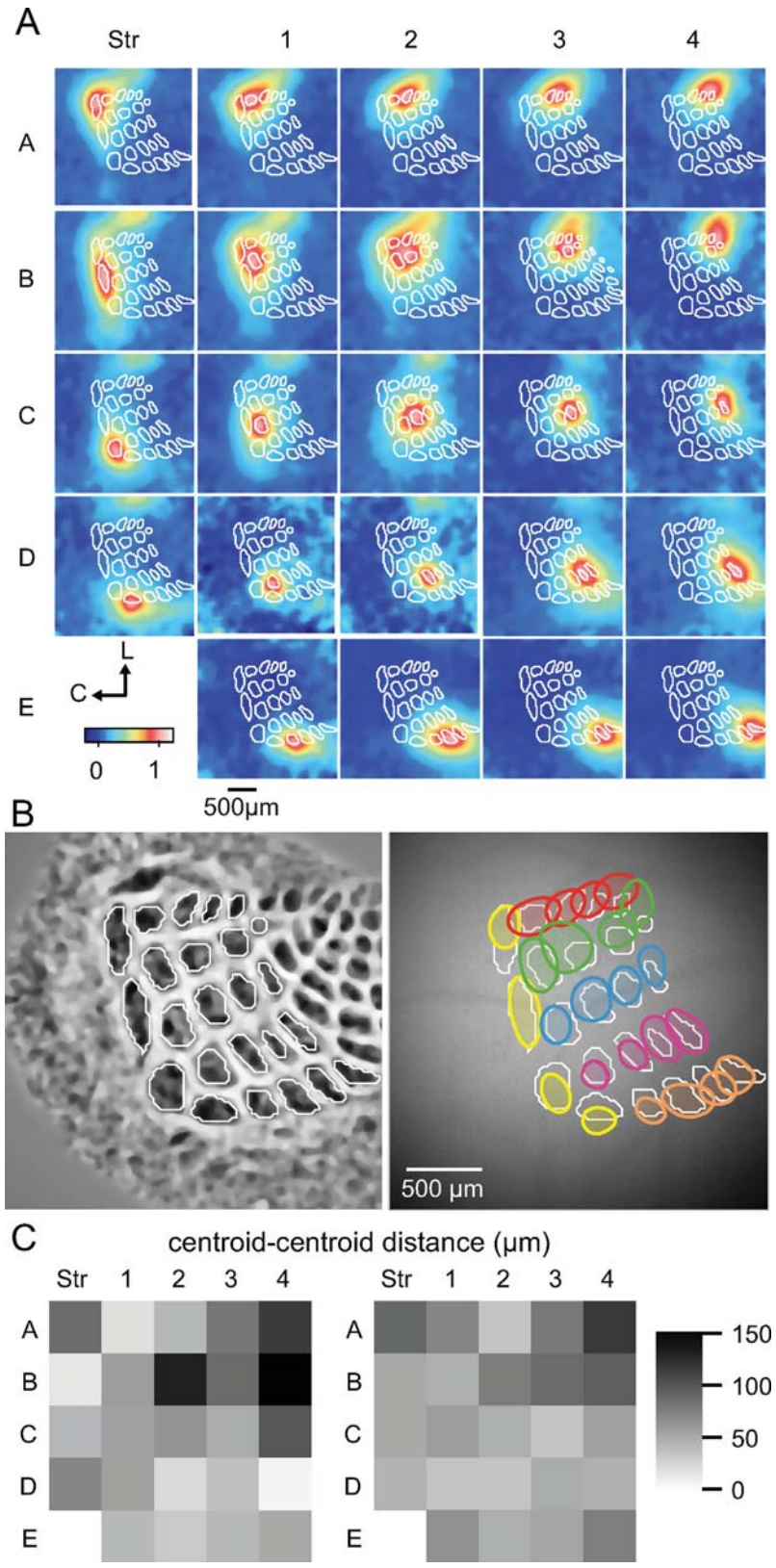

Fig. 5. Functional validation of the registration method. (A) Cortical responses evoked by individual deflections of the 24 principal vibrissae in a urethane anesthetized mouse were imaged using the VSD RH1691. For each whisker, the early cortical response is shown (data averaged from 4 to 18 ms post stimulation time and 40 trials, Gaussian filtered (5×5 pxls), and normalized), together with the aligned barrel map obtained from our reconstruction method (white lines). (B) The barrel map was extracted from the fused barrel field image (left) and overlaid on the VSD reference image (right) together with the early response locations (90% contours of the early responses (in A) are shown in colors) obtained for each whisker. (C) The distance between the centroid of the barrel area and the centroid of the early cortical response (as illustrated in B) was computed, column by column, for the experiment illustrated in A and B (left), and in average for all the control experiments ($n = 4$, right).

on manual reconstruction and alignment of the barrel map with the functional images (Kleinfeld and Delaney, 1996; Takashima and Kajiwara, 2001; Ferezou et al., 2006; Kerr et al., 2007; Tsytsarev et al., 2010; Lustig et al., 2013; Harris et al., 2013). Other studies (Berwick et al., 2004, 2008; Devonshire et al., 2010) used a method based on a warping algorithm described by Zheng et al. (2001). However, the manual detection of the fiducial markers required with this approach remains time-consuming in comparison to the automatic detection of blood vessel cross sections proposed here.

In a recent article, Guy et al. (2014) used a warping algorithm in order to align the layer IV barrel map, reconstructed manually from histological slices of flattened cortex, with the in vivo functional images using sets of fiducial points. Although the algorithm is not described in detail and probably involves manual selection of the fiducial points, it might be an interesting complement to our approach when working with flattened barrel cortex slices, since it allows a compensation for the curvature of the brain and distortion of the tissue. Finally, instead of using the superficial blood vessels as anatomical landmarks to align the barrel map on the functional images, an alternative approach is to use the images of early cortical responses to single whisker deflections as landmarks (Wallace and Sakmann, 2008; Wang et al., 2012; Yang et al., 2013). Using such a method as a standard requires the acquisition of several additional single whisker responses, which might be difficult to implement for instance when working with awake head fixed animals. Note that the tool we propose here to reconstruct the barrel map is valuable whatever solution is chosen in the end to realign the barrel map with the functional images.

On the methodological and mathematical sides, we mainly re-use a set of already existing tools (cross-correlation, ICP and gradient fusion). Our main contribution is to put them together in a coherent processing pipeline. A result of independent interest, that seems to be new, is to show how a family of robust ICP algorithms can be recasted as majorization-minimization algorithms. This in turn allows us to analyze the convergence of these methods.

Obviously the efficacy of the proposed anatomo-functional mapping tool depends upon the quality of the histological slices. Although the preparation of these slices relies on standard protocols which often belong to the daily routines of neurophysiology laboratories, two aspects are essential for the accuracy of the outcome: the quality of the perfusion, and the right thickness of the first (most superficial) slice. Indeed, on the one hand blood vessels have to appear as white circular or elliptical spots on the images to allow the proper registration of consecutive slices and, on the other hand, the superficial blood vessels should be intact to allow the final overlay of the obtained barrel map with the in vivo recordings. When cutting the brain, it is therefore important to set the zero position of the blade with care to ensure a 100 μm thickness to the first slice and thus preserve the integrity of the superficial blood vessels. Finally, although one could deplore that this overlay is a crucial step of the analysis that remains to be achieved manually, we propose here a solution that automatises the most time-consuming phases of the overall process and thus represents a substantial gain in time and precision. Although its use has been demonstrated successfully for VSDI of the adult mouse barrel cortex, it could be expanded to other experimental model species or to the developing brain. Furthermore, the histological section registration method described here might be helpful to reconstruct any tissue in which a majority of blood vessels are orthogonal to the cutting plane of the slices.

Acknowledgments

We thank Gérard Sadoc for technical expertise, and Aurélie Daret for her exprimental assistance. This work was supported by the Centre National de la Recherche Scientifique (France), the European Research Council (ERC project SIGMA-Vision), the European Union Seventh Framework Programme BrainScaleS (FP7-ICT-2009-6, N 269921), the Agence Nationale pour la Recherche (SensoryProcessing, Transtact).

Appendix A. Feature detection with normalized cross-correlation

We consider a set of Gaussian templates $\{g_k\}_{k\in\mathcal{K}}$,

$$g_k(x) = \frac{1}{Z_k}\exp\left(-\frac{||x||^2}{2\sigma_k^2}\right)$$

where Z_k is a constant ensuring a normalization $\sum_x g_k(x)^2 = 1$. The standard deviations σ_k are chosen equally spaced in the range $[0, \sigma_{\max}]$ (note that $\sigma_k = 0$ corresponds to a Dirac, supported on a single pixel).

Given a template g_k, we denote its support as

$$I_k = \left\{x \;;\; g_k(x) > \eta\right\}$$

where $\eta = 10^{-3}$ is a small tolerance threshold. The normalized cross correlation of a section S with the template g_k is then defined as

$$\mathrm{NCC}_k(S)(x) = \frac{\sum_{y\in I_k} S(x+y)g_k(y)}{\left(\sum_{y\in I_k} S(x+y)^2\right)^{1/2}}.$$

The normalized cross correlation with the whole set of filters is the maximum of all the correlations

$$\mathrm{NCC}(S)(x) = \max_{k\in\mathcal{K}} \mathrm{NCC}_k(S)(x). \tag{A.1}$$

A large value of $\mathrm{NCC}(S)(x)$ indicates that a vessel is likely to be present at pixel x. In this case, the value $k = k(x)$ of the maximum appearing in (A.1), i.e. such that $\mathrm{NCC}(S)(x) = \mathrm{NCC}_k(S)(x)$, indicates that the radius of this vessel is approximately σ_k.

Appendix B. Robust iterative closet point

B.1. ICP Step 1 with Majorize–Minimize (MM) iterations

We give here the details of an iterative algorithm to compute a local minimizer (in fact a stationary point) of (3), which reads

$$\min_T \; \mathcal{E}(T) = \sum_{i\in I} \rho(||T(x_i) - z_i||). \tag{B.1}$$

This method is similar to re-weighting ℓ^2 methods often used for robust ICP (see for instance (Bouaziz et al., 2013)), but we integrate it into a Majorize–Minimize framework, which ensures its convergence.

Starting from an initial transform $R^{(0)}$, we compute the iterations as

$$T^{(\ell+1)} \in \operatorname*{argmin}_T \; \tilde{\mathcal{E}}(T, T^{(\ell)}) \tag{B.2}$$

where $\tilde{\mathcal{E}}$ is a so-called surrogate function, which should satisfy

(H_1) $\tilde{\mathcal{E}}(T, T') - \mathcal{E}(T)$ is a smooth function of T (of class C^1);
(H_2) for all (T, T'), $\tilde{\mathcal{E}}(T, T') \geqslant \mathcal{E}(T)$;
(H_3) for all T, $\tilde{\mathcal{E}}(T, T) = \mathcal{E}(T)$.

Under these conditions, it can be shown that the iterations enjoy some good convergence properties. The sequence $\mathcal{E}(T^{(\ell)})$ is decaying and converges to some value $\mathcal{E}^\star$. If $\mathcal{E}$ is smooth (which is the case here), $||\nabla\mathcal{E}(T^{(\ell)})|| \to 0$. Since in our case, the energy $\mathcal{E}$ is coercive, the sequence $T^{(\ell)}$ is bounded, and all its cluster points $T^\star$ are stationary (i.e. $\nabla\mathcal{E}(T^\star) = 0$) with same energy $\mathcal{E}(T^\star) = \mathcal{E}^\star$.

The main difficulty in general is to devise a "good" surrogate function $\tilde{\mathcal{E}}$, i.e. such that one can compute the iteration (B.2) in closed form. The following proposition shows that one can actually design such a surrogate function using a quadratic loss.

Proposition 1. *If ρ is $C^1(\mathbb{R})$ and $w(r) = \frac{\rho'(r)}{2r}$ is decreasing, there exists a constant $C(T')$ independent of T so that the functional*

$$\tilde{\mathcal{E}}(T, T') = C(T') + \sum_{i \in I} w_i ||T(x_i) - z_i||^2 \tag{B.3}$$

$$\text{where} \quad w_i = w(||T'(x_i) - z_i||)$$

is a majorizing functional for (B.1) and thus satisfies properties (H_1, H_2, H_3).

Proof. We rewrite $\tilde{\mathcal{E}}$ as

$$\tilde{\mathcal{E}}(T, T') = \sum_{i \in I} \tilde{\rho}(||T(x_i) - z_i||, ||T'(x_i) - z_i||),$$

where we defined

$$\tilde{\rho}(r, r') = c(r') + w(r')r^2 \quad \text{where} \quad c(r') = \rho(r') - \frac{\rho'(r')}{2} r'.$$

Thanks to the separability $\tilde{\mathcal{E}}$ (it is a summation over i of functions involving independent variables) and the change of variables $r = ||T(x_i) - z_i||$, it thus suffices to prove that $\tilde{\rho}$ is a surrogate functional for ρ on $\mathbb{R}^+$. Hypothesis (H_1) holds because ρ is C^1, and one verifies that $\tilde{\rho}(r', r') = \rho(r')$ so that (H_3) holds. For any $r' \geqslant 0$, we consider

$$h(r) = \rho(r, r') - \rho(r) = \rho(r) - \rho(r') + \frac{\rho'(r')}{2r'} r^2 - \frac{\rho'(r')}{2} r'.$$

It satisfies $h(r') = h'(r') = 0$ and $h'(r) = 2r(w(r') - w(r))$. Since w is decaying, r' is the only point where h' is vanishing on $\mathbb{R}^+$. This implies that $h \geqslant 0$, hence (H_2).

The hypothesis that w is decreasing should be interpreted as the condition that ρ should penalize less than a quadratic loss, which makes sense for a robust penalization. Note that the loss (2) that we use in our method satisfies this condition, and that the weighting function satisfies

$$w(r) = \frac{1}{\varepsilon^2 + r^2}.$$

B.2. ICP Step 2 with weighted quadratic loss

We consider the problem of solving

$$\min_T \sum_{i \in I} w_i ||T(x_i) - z_i||^2 \quad \text{where} \quad T(x) = R(x) + t$$

where R is a rotation and $t \in \mathbb{R}^2$. This minimization appears in the MM iteration (B.2) when using the majorizing function (B.3). This problem has a closed form solution, as detailed for instance in Maurer et al. (1996). For the sake of completeness, we recall the steps of the method. One first centers the points, for $i \in I$

$$\tilde{x}_i = x_i - \frac{\sum_{k \in I} w_k x_k}{\sum_{k \in I} w_k} \quad \text{and} \quad \tilde{z}_i = z_i - \frac{\sum_{k \in I} w_k z_k}{\sum_{k \in I} w_k}.$$

The optimal rotation is obtained as $R = VU^T$ where (U, V) are the eigenvectors of the correlation matrix

$$\sum_{i \in I} w_i \tilde{x}_i \tilde{y}_i^T = U \Lambda V^T \tag{B.4}$$

(here Λ is the diagonal matrix of eigenvalues). The optimal translation is then computed as

$$t = \frac{\sum_{i \in I} w_i (\tilde{z}_i - R\tilde{x}_i)}{\sum_{i \in I} w_i}.$$

Appendix C. Inpainting

We consider a registered slice $\tilde{S}_m$ and its associated vessel locations $\mathcal{X}_m = \{x_i\}_{i \in I}$. We denote $\tilde{x}_i = \mathcal{T}_m(x_i)$ the registered vessel locations, where the cumulative transform $\mathcal{T}_m$ is defined in (5). We recall that the cross-correlation minimization (as detailed in Appendix A) outputs at each pixel x the index $k(x)$ of the optimal Gaussian template at this location, which has a radius $\sigma_{k(x)}$.

We define a mask Φ, which is the set of pixels that are at distance smaller than $\sigma_{k(x_i)}$ from the point $\tilde{x}_i$. It is thus a union of disks. Pixels in Φ should be discarded and inpainted. This is achieved using a quadratic minimization that seeks a smooth interpolation of missing data

$$\min_S \sum_x ||\nabla S(x)||^2 \text{subject} \quad \text{to} \forall y \notin \Phi, \quad S(x) = S_m(x), \tag{C.1}$$

where ∇S is a finite difference approximation of the gradient of the image S. The solution of (C.1) corresponds to solving a Poisson equation $\Delta S = 0$ on Φ with Dirichlet boundary conditions given by the constraints. This can be solved using a conjugate gradient method.

Appendix D. Gradient domain image fusion

We consider a set $\{\bar{S}_m\}_{m \in \mathcal{M}}$ of input images to fuse. At each pixel x, we denote the index of largest gradient magnitude as

$$m(x) = \operatorname*{argmin}_{m \in \mathcal{M}} \quad ||\nabla \bar{S}_m(x)||$$

where ∇ is a finite differences approximation of the gradient operator.

We design a fused vector field as

$$u(x) = \nabla \bar{S}_{m(x)}(x) \in \mathbb{R}^2.$$

Since the vector field u is obtained by gluing together gradients from several different images, it is in general not anymore the gradient of an image. We thus reconstruct a valid fused image S using the minimal norm pseudo-inverse, i.e. by computing an image S whose gradient is as close as possible to u

$$\min_S \quad ||u - \nabla S||^2 = \sum_x ||u(x) - \nabla S(x)||^2.$$

The solution is obtained by solving a Poisson equation

$$\Delta S = \operatorname{div}(u) \tag{D.1}$$

with adequate boundary conditions, where $\Delta = \operatorname{div} \circ \nabla$ is the Laplacian operator and $\operatorname{div} = -\nabla^*$ is the divergence. When using periodic boundary conditions (which can be used in our case), one solves (D.1) in $O(N \log(N))$ operations (where N is the number of pixels) using an FFT Poisson solver.

References

Berwick J, Redgrave P, Jones M, Hewson-Stoate N, Martindale J, Johnston D, et al. Integration of neural responses originating from different regions of the cortical somatosensory map. Brain Res 2004;1030(2):284–93.

Berwick J, Johnston D, Jones M, Martindale J, Martin C, Kennerley AJ, et al. Fine detail of neurovascular coupling revealed by spatiotemporal analysis of the hemodynamic response to single whisker stimulation in rat barrel cortex. J Neurophysiol 2008;99:787–98.

Besl PJ, McKay ND. A method for registration of 3-D shapes. IEEE Trans Pattern Anal Mach Intell 1992;14(2):239–56.

Bouaziz S, Tagliasacchi A, Pauly M. Sparse iterative closest point. Comput Graph Forum 2013;32(5):113–23.

Chetverikov D, Stepanov D, Krsek P. Robust euclidean alignment of 3D point sets: the trimmed iterative closest point algorithm. Image Vis Comput 2005;23(3):299–309.
Dercksen VJ, Weber B, Güenther D, Oberlaender M, Prohaska S, Hege HC. Automatic alignment of stacks of filament data. In: Proc. IEEE int. symp. on biomedical imaging: from nano to macro (ISBI); 2009. p. 971–4.
Devonshire IM, Grandy TH, Dommett EJ, Greenfield SA. Effects of urethane anaesthesia on sensory processing in the rat barrel cortex revealed by combined optical imaging and electrophysiology. Eur J Neurosci 2010;32(5):786–97.
DiCarlo JJ, Lane JW, Hsiao SS, Johnson KO. Marking microelectrode penetrations with fluorescent dyes. J Neurosci Methods 1996;64(1):75–81.
Egger R, Narayanan RT, Helmstaedter M, de Kock CPJ, Oberlaender M. 3D reconstruction and standardization of the rat vibrissal cortex for precise registration of single neuron morphology. PLoS Comput Biol 2012;8(12).
Ferezou I, Bolea S, Petersen CCH. Visualizing the Cortical Representation of Whisker Touch: Voltage-Sensitive Dye Imaging in Freely Moving Mice. Neuron 2006;50(4):617–29.
Glocker B, Sotiras A, Komodakis N, Paragios N. Deformable medical image registration: setting the state of the art with discrete methods. Annu Rev Biomed Eng 2011;13:219–44.
Guy J, Wagener RJ, Mock M, Staiger JF. Persistence of functional sensory maps in the absence of cortical layers in the somsatosensory cortex of reeler mice. Cereb Cortex 2014, pii:bhu052.
Harris S, Bruyns-Haylett M, Kennerley A, Boorman L, Overton PG, Ma H, et al. The effects of focal epileptic activity on regional sensory-evoked neurovascular coupling and postictal modulation of bilateral sensory processing. J Cereb Blood Flow Metab 2013;33(10):1595–604.
Jacob V, Estebanez L, Cam JL, Tiercelin J-Y, Parra P, Parésys G, et al. The matrix: a new tool for probing the whisker-to-barrel system with natural stimuli. J Neurosci Methods 2010;189(1):65–74.
Ju T, Warren J, Carson J, Bello M, Kakadiaris I, Chiu W, et al. 3d volume reconstruction of a mouse brain from histological sections using warp filtering. J Neurosci Methods 2006;156(1–2):84–100.
Kaneko S, Kondo T, Miyamoto A. Robust matching of 3D contours using iterative closest point algorithm improved by m-estimation. Pattern Recogn 2003;36(9):2041–7.
Kerr JN, de Kock CP, Greenberg DS, Bruno RM, Sakmann B, Helmchen F. Spatial organization of neuronal population responses in layer 2/3 of rat barrel cortex. J Neurosci 2007;27(48):13316–28.
Kleinfeld D, Delaney KR. Distributed representation of vibrissa movement in the upper layers of somatosensory cortex revealed with voltage-sensitive dyes. J Comp Neurol 1996;375(1):89–108.
Land P, Simons D. Cytochrome oxidase staining in the rat smi barrel cortex. J Comp Neurol 1985;238(2):225–35.
Lustig BR, Friedman RM, Winberry JE, Ebner FF, Roe AW. Voltage-sensitive dye imaging reveals shifting spatiotemporal spread of whisker-induced activity in rat barrel cortex. J Neurophysiol 2013;109(9):2382–92.
Ma B, Ellis RE, Fleet DJ. Spotlights: a robust method for surface-based registration in orthopedic surgery. In: MICCAI; 1999. p. 936–44.
Maurer CR, Aboutanos GB, Dawant BM, Maciunas RJ, Fitzpatrick JM. Registration of 3-d images using weighted geometrical features. IEEE Trans Med Imaging 1996;15(6):836–49.
Meyer H, Egger R, Guest J, Foerster R, Reissl S, Oberlaender M. Cellular organization of cortical barrel columns is whisker-specific. Proc Natl Acad Sci U S A 2013;110(47):19113–8.
Nishino K, Ikeuchi K. Robust simultaneous registration of multiple range images. In: Digitally Archiving Cultural Objects. Springer US; 2008. p. 71–88.
Ourselin S, Roche A, Subsol G, Pennec X, Ayache N. Reconstructing a 3D structure from serial histological sections. Image Vis Comput 2001;19(1–2):25–31.
Pérez P, Gangnet M, Blake A. Poisson image editing. In: ACM SIGGRAPH 2003 Papers; 2003. p. 313–8.
Raskar R, Ilie A, Yu J. Image fusion for context enhancement and video surrealism. In: Proc. NPAR 2004; 2004. p. 85–152.
Sotiras A, Davatzikos C, Paragios N. Deformable medical image registration: a survey. IEEE Trans Med Imaging 2013;32(7):1153–90.
Stewart CV, Tsai C, Roysam B. The dual-bootstrap iterative closest point algorithm with application to retinal image registration. IEEE Trans Med Imaging 2003;22(11):1379–94.
Takashima IT, Kajiwara R I. Voltage-sensitive dye versus intrinsic signal optical imaging: comparison of optically determined functional maps from rat barrel cortex. Neuroreport 2001;12(13):2889–94.
Tsytsarev V, Pope D, Pumbo E, Yablonskii A, Hofmann M. Study of the cortical representation of whisker directional deflection using voltage-sensitive dye optical imaging. Neuroimage 2010;53(1):233–8.
Wallace DJ, Sakmann B. Plasticity of representational maps in somatosensory cortex observed by in vivo voltage-sensitive dye imaging. Cereb Cortex 2008;18(6):1361–73.
Wang Q, Millard DC, Zheng HJ, Stanley GB. Voltage-sensitive dye imaging reveals improved topographic activation of cortex in response to manipulation of thalamic microstimulation parameters. J Neural Eng 2012;9(2):026008.
Welker E, Van der Loos H. Quantitative correlation between barrel-field size and the sensory innervation of the whiskerpad: a comparative study in six strains of mice bred for different patterns of mystacial vibrissae. J Neurosci 1986;6(11):3355–73.
Woosley T, Loos HVD. The structural organization of layer IV in the somatosensory region (SI) of mouse cerebral cortex: the description of a cortical field composed of discrete cytoarchitectonic units. Brain Res 1970;17(2):205–38.
Yang JW, An S, Sun JJ, Reyes-Puerta V, Kindler J, Berger T, et al. Thalamic network oscillations synchronize ontogenetic columns in the newborn rat barrel cortex. Cereb Cortex 2013;23(6):1299–316.
Zheng Y, Johnston D, Berwick J, Mayhew J. Signal source separation in the analysis of neural activity in brain. Neuroimage 2001;13(3):447–58.

PLOS ONE

RESEARCH ARTICLE

Orofacial Neuropathic Pain Leads to a Hyporesponsive Barrel Cortex with Enhanced Structural Synaptic Plasticity

Karine Thibault[1,2], Sébastien Rivière[1,2¤a], Zsolt Lenkei[1,2], Isabelle Férézou[1,2☯¤b], Sophie Pezet[1,2☯]*

1 Brain Plasticity Unit, ESPCI, PSL Research University, 10 rue Vauquelin, 75005, Paris, France, **2** Centre National de la Recherche Scientifique, UMR 8249, 75005, Paris, France

☯ These authors contributed equally to this work.
¤a Current address: Centre des Sciences du Goût et de l'Alimentation, UMR 6265 CNRS—Université de Bourgogne—UMR 1324 INRA, 9E boulevard Jeanne D'Arc, 21000, Dijon, France
¤b Current address: Unit of Neuroscience Information and Complexity, Centre National de la Recherche Scientifique FRE 3693, Gif sur Yvette, France.
* sophie.pezet@espci.fr

Citation: Thibault K, Rivière S, Lenkei Z, Férézou I, Pezet S (2016) Orofacial Neuropathic Pain Leads to a Hyporesponsive Barrel Cortex with Enhanced Structural Synaptic Plasticity. PLoS ONE 11(8): e0160786. doi:10.1371/journal.pone.0160786

Editor: Simon Beggs, University of Toronto, CANADA

Received: November 30, 2015

Accepted: July 25, 2016

Published: August 22, 2016

Data Availability Statement: All relevant data are within the paper and its Supporting Information files.

Funding: This work was supported by the Centre National pour la Recherche Scientifique (CNRS) and the Ecole Supérieure de Physique et Chimie Industrielles de la mairie de Paris, ParisTech. The funders had no role in study design, data collection and analysis, decision to publish, or preparation of the manuscript.

Competing Interests: The authors have declared that no competing interests exist.

Abstract

Chronic pain is a long-lasting debilitating condition that is particularly difficult to treat due to the lack of identified underlying mechanisms. Although several key contributing processes have been described at the level of the spinal cord, very few studies have investigated the supraspinal mechanisms underlying chronic pain. Using a combination of approaches (cortical intrinsic imaging, immunohistochemical and behavioural analysis), our study aimed to decipher the nature of functional and structural changes in a mouse model of orofacial neuropathic pain, focusing on cortical areas involved in various pain components. Our results show that chronic neuropathic orofacial pain is associated with decreased haemodynamic responsiveness to whisker stimulation in the barrel field cortex. This reduced functional activation is likely due to the increased basal neuronal activity (measured indirectly using cFos and phospho-ERK immunoreactivity) observed in several cortical areas, including the contralateral barrel field, motor and cingulate cortices. In the same animals, immunohistochemical analysis of markers for active pre- or postsynaptic elements (Piccolo and phospho-Cofilin, respectively) revealed an increased immunofluorescence in deep cortical layers of the contralateral barrel field, motor and cingulate cortices. These results suggest that long-lasting orofacial neuropathic pain is associated with exacerbated neuronal activity and synaptic plasticity at the cortical level.

Introduction

Trigeminal neuralgia is the most common orofacial neuropathic pain disorder [1,2]. This debilitating disorder is often manifested with thermal and mechanical allodynia and hyperalgesia [1]. Chronic orofacial pain disorders, among various other conditions (*e.g.* temporomandibular

disorders), can be difficult to treat due to a maladaptive plasticity that is not well understood [3]. Fundamental research has revealed several key mechanisms underlying neuropathic pain at the level of the spinal cord, such as decreased inhibition [4], glial activation through a BDNF-dependent mechanism [5], enhanced release of cytokines and chemokines [6] and increased receptor activation [3][7,8]. By contrast, far less is known about the supraspinal changes underlying neuropathic pain. Clinical studies have reported strong cortical rearrangements in the primary somatosensory cortex in several neuropathic pain conditions including phantom limb pain [9], chronic back pain [10], fibromyalgia [11], complex regional pain syndrome (CRPS) [12,13][14], unilateral chronic pain [15] and chronic back pain [16](see [17] for review). Strikingly, two separate teams have shown that different chronic pain diseases (*e.g.* chronic back pain, CRPS and knee osteoarthritis [18]) exhibit unique anatomical 'brain signatures' [18,19], *i.e.* these specific anatomical brain reorganizations may reflect a unique maladaptive physiology in these different types of chronic pain. Interestingly, this cortical plasticity is reversed by treatment coincident with clinical improvement [14]. Maladaptive changes in the primary and secondary somatosensory cortices have also been demonstrated in chronic orofacial pain syndromes, including trigeminal neuropathic pain and temporomandibular joint disorder pain [20] (and see [19] for a meta-analysis of both syndromes). Other brain areas comprising the anterior cingulate/mid-cingulate cortex and prefrontal cortex (such as the thalamus or cortical areas involved in the emotional aspects of pain) also display modified activation patterns [19]. Global structural changes, including modifications in grey matter volume [21,22], white matter density [23,24] and fractional anisotropy [22,23] have also been reported. Furthermore, subtle anatomical changes in the prefrontal cortex of patients with chronic orofacial pain can induce changes in their personalities [25,26]. However, while these studies suggest important structural plasticity of cortical regions in chronic pain patients, the underlying molecular and functional changes are still poorly understood. Notably the link between the cortical responsiveness to stimulus application and the concomitant level of neuronal activity and structural synaptic changes in these brain areas is unclear.

To study orofacial neuropathic pain, a model of the chronic constriction injury (CCI) model initially developed by Bennett and Xie in rats at the level of the sciatic nerve [27] has been modified [28]. This approach exploits the rodent trigeminal nervous system, which is anatomically composed of four nuclei (the mesencephalic trigeminal nucleus, motor trigeminal nucleus, principal trigeminal nucleus, and spinal trigeminal nucleus) and the trigeminal ganglion (TG). The spinal trigeminal nucleus caudalis (Sp5C) is a critical relay site for processing nociceptive afferent input from the orofacial area, and for modulating neuroplastic changes [29]. The infraorbital nerve (ION), which is solely composed of sensory fibres, nearly forms the entire maxillary division of the trigeminal nerve in rats. CCI of the ION (CCI-ION) therefore provides a relevant experimental rat model of trigeminal neuropathic pain [28,30,31].

The aim of this study was to determine the possible functional and molecular mechanisms taking place in several cortical areas in neuropathic pain, using a mouse model of ION ligation. Functional intrinsic imaging of the primary sensory cortex barrel field (S1BF) has allowed us to demonstrate a decreased evoked response to whisker stimulation that is due to an enhanced baseline neuronal activity. Immunohistochemical analysis revealed that the primary sensory, motor and cingulate cortices are all subject to strong pre- and postsynaptic changes. These results provide a basis for a better understanding and possible new therapeutical strategies of orofacial neuropathic pain.

Materials and Methods

Animals

30 male C57/BL6 mice (Janvier, France) were used in this study (n = 12 mice, including n = 6 mice with ligation of the infraorbitrary nerve (ION) and n = 6 sham operated mice, for the longitudinal behavioural, imaging and immunohistochemical study, and n = 18 additional mice for the c-fos experiment, see below). Mice were 4 weeks old at the beginning of the experiments. All experiments were performed in agreement with the European Community Council Directive of September 22nd, 2010 (010/63/UE) and the local ethics committee (*Comité d'éthique en matière d'expérimentation animale n°59, C2EA –59, 'Paris Centre et Sud'*). The project was accepted by this ethics committee under the reference #A-1722. The guidelines for investigating experimental pain in animals published by the International Association for the Study of Pain (IASP) were followed. Great care was taken, particularly regarding housing conditions, to avoid or minimize discomfort of the animals. Mice were housed in a solid-floor cage with food and water available *ad libitum* and a deep layer of sawdust to accommodate excess urine. The cages were changed twice a week and kept at a constant temperature (22 ± 1°C) with a 12-hour alternating light/dark cycle.

Surgical implants

Thirty days before the infraorbital nerve (ION) ligation, 12 mice were implanted with a head-fixation post and an imaging chamber to allow subsequent repeated imaging sessions. The animals were anesthetized with a mixture of medetomidine hydrochloride (0.8 mg/kg) and ketamine (60 mg/kg) and maintained at 37°C with a heating blanket. Several minutes after a subcutaneous injection of lidocaine (10 mg/ml) to the head of the animal, the skin covering the interparietal and right parietal bones of the skull was excised. Following a careful cleaning, the exposed intact skull was protected with a layer of cyanoacrylate glue. A metal head-fixation post was then glued on to the interparietal bone and a circular plastic chamber (~6 mm in diameter and 1 mm thick) was glued on to the right parietal bone (the centre of the chamber was located at 1.5 mm posterior to the bregma, and 3.3 mm to the right of the midline). The head post and chamber fixations were secured with dental cement. The anaesthesia was reversed at the end of the implantation procedure by a subcutaneous injection of atipamezole (50 μg).

Habituation to the orofacial stimulation test

After at least 5 days of recovery, the animals (n = 12) were subjected to a habituation period (S1 Table). Mice were first habituated to the room, the experimenter, and then to the orofacial stimulation test (mechanical orofacial test; Ugo Basile, Italy). The orofacial stimulation test measures hypersensitivity to mechanical stimulation of the trigeminal area. Mice were allowed to voluntarily contact a mechanical stimulator (consisting of metal hairs attached to a mounting plate) with their vibrissal pad in order to access a sweet water reward (S1 Table). Drinking duration was measured by detecting the interruption of an infrared beam traversing the opening to the reward. There was no mechanical stimulation at the beginning of the habituation period, and the mice could access the sweetened water just by inserting their noses into the reward opening.

Mice were water-deprived for the subsequent habituation sessions (*i.e.* the water dispenser was removed from the cages 12 hours before the behaviour session) and the mechanical stimulation was progressively added by increasing the number of metallic hairs attached to the mounting plate (from 12 to 18).

During the first week of habituation, the mice were habituated (without being water-deprived) 3 at a time, twice a week in the apparatus, without any metal hair. During the second week of habituation (« -3 » in S1 Table), the mice were water-deprived and habituated 3 at a time, twice a week in the apparatus, without any metal hair. We had to habituate them by 3 initially because we experienced previously that some mice learn slowly to get the sweet water from the drinking port. By habituating initially the mice by groups of three, we did not observe as much "slow learners", probably since they could watch the other mice drinking.

The third week of habituation, the mice were habituated individually in the apparatus, one session without hair, then one session with 12 hairs and finally three sessions with 18 hairs (i.e. 5 sessions in the week). The fourth week of habituation, the mice went through one last individual session with 18 hairs.

Behavioural test: Assessment of mechanical sensitivity

The orofacial stimulation test was used to measure the sensitivity threshold of the 12 mice. Mechanical sensitivity was defined as a significant decrease in drinking duration. Mice were tested after 12 hours of water deprivation using a mechanical stimulator consisting of 18 metallic wires. The baseline was measured one week before the ION ligation (S1 Table). The baseline drinking duration percentage was calculated using individual values as follows: (W/BL)X100 where *W* corresponds to the week of interest: 1W, 2W, 3W, 4W and 5W. Results are expressed as the baseline percentage ± SEM. Animals that were not engaged in drinking at the end of the baseline session were excluded from the study (see S1 Table). Although we began with n = 6 animals per experimental group, the final number of animals included per group was n = 4 (see S1 Table).

Ligation of the infraorbital nerve (ION)

Mice were anesthetized with a mixture of medetomidine hydrochloride (0.8 mg/kg) and ketamine (60 mg/kg) and maintained at 37°C with a heating blanket. Unilateral ligation to the left ION was performed as previously described [29]. An incision was made along the left cheek to expose the ION where it emerges from the infraorbital fissure [30]. After local administration of lidocaine (10 mg/ml), the ION was gently isolated using forceps. Two tight ligations of the nerve (~1 mm from each other) were made with 5.0 diameter catgut sutures (Chromic gut, 5–0; ref. 1248, Angiotech Pharmaceuticals; Canada), which constricted the nerve to approximately 1/3 to 1/2 of its initial diameter [24]. The incision was closed using silk sutures. A subcutaneaous injection of Metacam (1 mg/kg) was performed in order to prevent postsurgical pain. For the sham-operated mice, the ION was exposed on the left side using the same procedure, although the nerve was not ligated.

Optical imaging of intrinsic signals: Assessment of cortical responses to tactile stimuli

For each imaging session, implanted animals were anesthetised with a mixture of medetomidine hydrochloride (0.8 mg/kg) and ketamine (60 mg/kg) and maintained at 37°C with a heating blanket. The cortex was illuminated at 570 nm, through the exposed intact bone within the implanted imaging chamber. The reflected light was collected at 20 Hz through a tandem lens microscope onto a CMOS camera (MiCAM Ultima, SciMedia; Japan). The camera's 10,000-pixel sensor covered a 10 x 10 mm field of view, providing a resolution of 100 μm per pixel. Relative variation of the reflected light was measured in response to left single whisker deflections (100 Hz for 1 s) and averaged over 100 trials. This intrinsic imaging protocol was run successively for each mouse at each imaging session, using two different whiskers (typically

A1 and C1, although B1 and C1 were used for one mouse that lacked A1). These imaging sessions were performed weekly for each animal, starting before the ION ligation (BL) and running until 4 weeks after BL. Results are expressed as $(R-R_0)/R_0$, with R representing the averaged reflected light measured over 1 s immediately after the stimulus presentation and R_0 being the average reflected light measured over 1 s before the stimulus presentation Images obtained from such computation indeed show the spatial extent of the haemodynamic response evoked by the whisker stimulation. Spatial profiles of reflected light were computed from these images along the rostro-caudal axis. Minimal values of these profiles were used to quantify the response amplitude for each condition.

The results from several mice had to be discarded, as they lost some of their whiskers during the 4 weeks of longitudinal follow-up. Consequently, the final number of animals included in each experimental group was n = 3 instead of the initially planned n = 6. A table presented in S1 Table is showing the time points at which animals were excluded and why. Nevertheless, two whiskers were tested independently for each mouse on each run and these results were considered as independent, yielding n = 6 tests of cortical functional activation induced by whisker stimulation per experimental group.

Design of the cFos experiment

In order to investigate if the S1BF of ION mice was subjected to an increased neuronal activity that would unable the possible induction of further neuronal activation following whisker stimulation, we quantified the number of c-fos positive profiles in the S1BF submitted (or not) to sustained whisker activation in freely moving animals. To do so, we used a classical approach that involves the clipping of all whiskers except one or one raw [32,33]. The animal is placed for two hours in a dark environment where it can explore various objects, leading to a sustained sensory activation. In details: eighteen animals were used in total, randomised in 4 experimental groups: two ION groups of animals with ION ligations (n = 9), and two sham groups of control animals (n = 9). Mice from the first ION (n = 5) and sham (n = 4) groups were anesthetized with isoflurane (induction: 3–4%, sustaining: 1.5%) and all but one row of whiskers (row C) on the left side were clipped close to the skin. The whiskers on the right side were left intact. Animals were placed by pairs (when possible) in a stimulating box that was furnished with various objects in order to provide a tactile-enriched environment for two hours in the dark. After the exploration period, animals were anesthetized with urethane (1.75 g/kg i.p.) and perfused. The remaining ION (n = 4) and sham (n = 5) groups were removed from their home cages and immediately anesthetized and perfused for use as controls to obtain a basal level of cFos expression.

Immunohistochemistry

A day after the end of the last imaging session, animals were deeply anaesthetized *via* urethane injection (1.75 g/kg i.p) and transcardially perfused with 10 ml of 0.9% NaCl, followed by 50 ml of 4% paraformaldehyde (PFA) plus 15% picric acid in 0.2 M phosphate buffer (PB), pH 7.4. Urethane was used here for the perfusion, according to a previously described procedure for the immunostaining of p-Erk in pain pathways [34]. TGs and the brain were dissected out and post-fixed in 4% PFA plus 15% picric acid for 2 hours at room temperature or overnight at 4°C, respectively. The TG and the brain were then cryoprotected in 30% sucrose in 0.2 M PB (pH 7.4) overnight at 4°C, and were subsequently cut into a series of 14-μm longitudinal (TG) or 20-μm coronal (brain) serial sections with a cryostat (HM550, Microm Microtech).

ATF3 immunostaining in the TG

In order to assess that all animals had the same level of nerve injury, we quantified the percentage of ATF3 positive cells in the DRG. Indeed, ATF3 has been previously shown to be overexpressed in lesioned DRG neurons [35]. Non-lesioned neurons do not express this transcription factor [35]. Serial sections from the ipsilateral and contralateral TGs were incubated overnight at room temperature with a mixture of the antibodies ATF3 (1:500 rabbit anti-ATF3 (C19); ref. sc-188, Santa Cruz Biotechnology; USA) and βIII tubulin, a neuronal marker, (1:2000 mouse anti-βIII Tubulin; ref. G7121, Promega; San Luis Obispo, CA, USA) diluted in PBS-T-azide (0.02M saline PB containing 0.3% Triton X-100 and 0.02% sodium azide). TG sections were then washed in PBS and subsequently incubated for 2 h at room temperature in 1:1000 Alexa Fluor® 488 anti-rabbit IgG and Alexa Fluor® 350 anti-mouse IgG (Invitrogen; California, USA). Sections were finally washed in PBS and mounted in Vectashield medium (Vector; Burlingame, USA).

Quantification of ATF3- and βIII tubulin-positive neurons in the TG

The proportion of ATF3- and βIII tubulin-expressing TG cells was quantified by counting the number of positive cells with visible nuclei in images acquired using a 40x objective. All acquisitions were performed using the same settings. To determine the total number of neuronal cells, βIII tubulin staining was used as a neuronal marker to manually count the cells with visible nuclei. At least 200 cells (across four or five sections) were counted per TG. Results are expressed as the percentage of ATF3-positive cells out of the total number of cells in the TG.

cFos and p-Erk immunostainings in the brain

Serial sections from the brain were immunostained for cFos according to the avidin-biotin-peroxidase method and followed by DAB revelation. Tissue sections were incubated overnight at room temperature in primary antiserum (diluted in PBS-T-azide) directed against either the cFos protein (1:5000 rabbit anti-cFos; ref. sc-52, Santa Cruz Biotechnology; USA) or against the p-Erk protein (1:1000 rabbit anti-phospho p44/42 MAPK; ref. 4370L, Cell Signaling). Incubated sections were washed in three successive baths of PBS and subsequently incubated in 1:300 biotinylated goat anti-rabbit IgG (Vector; Burlingame, USA) in PBS-T for 1 h at room temperature. Sections were then washed three times in PBS and incubated for 1 h in avidin-biotin-peroxidase complex (Vectastain, Vector Laboratories) diluted 1:500 in PBS. Finally, after 3 washes in PBS, staining was revealed with a peroxidase substrate kit (Vector Laboratories, SK-4100) according to the manufacturer's protocol. The reaction proceeded at 20°C under the visual control of a light microscope, and was stopped 5 min later by washing in distilled water. Sections were sequentially dehydrated through an alcohol series (70%, 90%, 95% and absolute alcohol), air-dried, xylene treated, and cover-slipped with DPX mounting medium for histology (Sigma). Brain sections of mice from all experimental groups were simultaneously immunostained to accommodate quantification of the number of immunoreactive neurons and to correct for immunochemistry variation between experiments.

Quantification of cFos-positive neurons

Tissue sections were first examined using dark-field microscopy to determine structures of interest. To quantify cFos staining in both groups of animals, black and white images with 256 grey levels were acquired with a 5x objective on a Zeiss microscope. All acquisitions were performed with the same acquisition settings. We quantified cFos positive neurons in the S1BF cortex contralateral to the ION ligation. To count the number of nuclei, we performed a

particle analysis using the ImageJ software (USA). Briefly, a threshold is set and pixels with values within this range are converted to black; pixels with values outside of this range are converted to white. The threshold was determined to obtain clear objects representing cFos-labelled nuclei. The same threshold was applied to each image for all animal groups. Only objects with an area superior to 25 μm^2 were counted.

Quantification of p-Erk-positive cells

Tissue sections were first examined using dark-field microscopy to determine structures of interest. Three specific regions were defined (the S1BF cortex, the motor cortex including primary and secondary motor cortices, and the cingulate cortex) and the number of p-Erk-positive cells in each area was counted. All p-Erk immunoreactive cells were counted regardless of staining intensity. The investigator responsible for counting p-Erk-positive cells was blind to the animal's treatment.

Piccolo and p-Cofilin immunostainings in the brain

Serial sections from the brain were incubated with either anti-Piccolo (1:100; rabbit, ref. 20664, Abcam; Cambridge, UK) or anti-p-Cofilin protein (1:300; rabbit, ref. 47281, Abcam; Cambridge, UK) as primary antibodies in PBS-T-azide overnight at room temperature. After washings in PBS, the sections were incubated in Alexa Fluor® 488 anti-rabbit IgG (1:1000; Invitrogen; California, USA) in PBS-T for 2 h at room temperature. Following PBS washes, the sections were mounted in Vectashield medium (Vector Laboratories; Burlingame, USA).

p-Cofilin/NeuN double staining in the brain

Serial brain sections were incubated overnight at room temperature with a mixture of the antibodies anti-p-Cofilin (1:300; rabbit, ref. 47281, Abcam; Cambridge, UK) and the neuronal marker anti-NeuN (1:1000 mouse anti-NeuN; ref. VMA 377, Abcys) diluted in PBS-T-azide. Following washes, sections were incubated 2 h in Alexa Fluor® 568 anti-rabbit IgG and Alexa Fluor® 488 anti-mouse IgG (Invitrogen; California, USA) diluted 1:1000 in PBS-T. Sections were washed and mounted in Vectashield medium.

Quantification of Piccolo staining

Analysis was performed on the contralateral side of the brain relative to the ION ligation. To quantify Piccolo staining in both groups of animals, black and white images with 256 grey levels were acquired with a 20x objective on a Zeiss microscope. All acquisitions were performed with the same acquisition settings. To quantify the staining, we performed an area fraction analysis using the ImageJ software (USA). Briefly, a threshold is set and pixels with values within this range are converted to black; pixels with values outside of this range are converted to white. The threshold was determined to obtain a clear area representing Piccolo labelling. This analysis measured the area of labelling in the previously described regions of interest (the S1BF, motor and cingulate cortices). Area fraction, representing the percentage of pixels in the selection that were highlighted in black, was compared between sham and ION-ligatured animals. Quantification was performed on 4 sections for each animal using the following bregma coordinates: 0.36 mm, -0.46 mm, -1.22 mm and -1.94 mm. For each cortical region, quantification was performed within two regions of interest (325 x 440 μm): one located on the superficial laminae (II-IV) and the other located on the deep laminae (V and VI).

Quantification of p-Cofilin staining

The contralateral side of the brain relative to the ION ligation was analysed. To quantify p-Cofilin staining in both groups of animals, black and white images with 256 grey levels were acquired with a 20x objective on a Zeiss microscope. All acquisitions were performed with the same acquisition settings. We focused our quantification on the number of neurons displaying at least 5 punctate labellings in their cell bodies. A double labelling with anti-NeuN was used to facilitate quantification. The number of p-Cofilin-positive neurons was counted for each specific cortical area. Quantification was performed in the same coordinates as those used for Piccolo staining quantification, and in the same regions of interest (325 x 440 μm). The investigator responsible for the counting of p-Cofilin-positive neurons was blind to the animal's treatment.

Data analysis

Behavioural experiments. Mechanical sensitivity results were analysed by two-way analysis of variance (ANOVA) followed by a Student-Newman-Keuls post-hoc test for multiple comparisons using the SigmaStat software. ANOVA results are reported as the value of the Fisher distribution Fx,y obtained from the data, where x is the degrees of freedom for groups and y is the total degrees of freedom of the distribution.

Imaging experiments. Responses to tactile stimuli were compared between the experimental groups throughout the imaging sessions, using two-way analysis of variance (ANOVA) followed by a Student-Newman-Keuls post-hoc test (SigmaStat).

Immunohistochemistry experiments. Quantification of ATF3+ neurons was evaluated by two-way analysis of variance (ANOVA), using the treatment (sham or ION) and the side analysed (ipsilateral or contralateral) as the two variables. Two-way ANOVA was performed to analyse the cFos experiments using the treatment (sham or ION) and the stimulations (after stimulations or no stimulation) as the two variables. Two-way ANOVA was performed to quantify p-Erk+ cells using the treatment (sham or ION) and the cortical area analysed (barrel, motor or cingulate cortex) as the two variables. Two-way ANOVA tests were followed by a Student-Newman-Keuls post-hoc test for multiple comparisons (SigmaStat). Finally, three-way ANOVA tests were performed to quantify Piccolo and p-Cofilin staining, using the treatment (sham or ION), the cortical area analysed (S1BF, motor cortex or cingulate cortex) and the analysed cortical depth (superficial or deep) as variables. The three-way ANOVA was followed by a Student-Newman-Keuls post-hoc test for multiple comparisons. ANOVA results are reported as the value of the Fisher distribution Fx,y obtained from the data, where x is the degrees of freedom for groups and y is the total degrees of freedom of the distribution. Data were expressed as means ± standard error of the mean (SEM), with the following levels of significance: $^{*}p<0.05$, $^{**}p<0.01$, and $^{***}p<0.001$. For all quantifications of the immunostainings, coordinates and delinations of the brain areas were taken from [36,37]. Quantifications performed at the level of the cingulate cortex were taken in the anterior cingulate cortex; more precisely in both the Cg2 and Cg1 also, denominated 24b and 24a, respectively by Vogt and Paxinos [37]. Note that a mini dataset (S1 Dataset) is providing individual results.

Results

Changes in sensitivity and cortical activity in the primary somatosensory cortex following unilateral ION ligation

We focused on the possible functional and molecular mechanisms following peripheral nerve injury. ATF3 has previously been used as a marker for injured neurons in the dorsal root

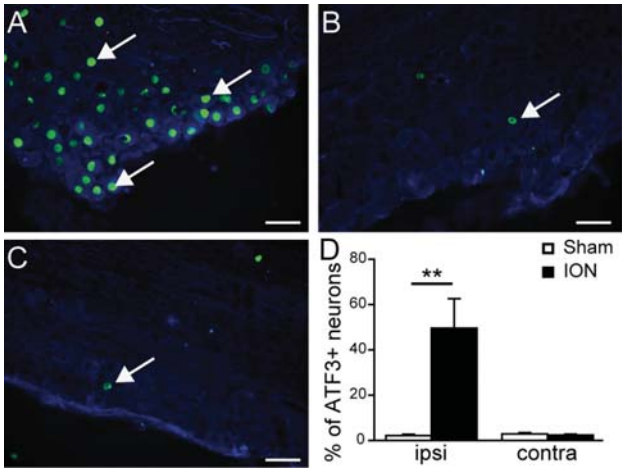

Fig 1. Upregulation of ATF3 in sensory neurons of the trigeminal ganglion after ION ligation. A-C: Double immunostaining showing ATF3 (green)/βIII tubulin (blue) positive neurons in the ipsilateral (A) and contralateral TG (B) of a representative ION animal, and the ipsilateral TG of a sham animal (C). D: Quantification of the percentage of ATF3-positive neurons in sham and ION (animals that received a ligation of the Infraorbitrary nerve) mice, 5 weeks after surgery, in the ipsilateral (ipsi) and contralateral (contra) sides of the lesion. Nerve ligation induced a statistically significant upregulation of ATF3 in the ipsilateral TG of ION animals ($F_{1,21}$ = 15.927; p<0.001). Scale bars = 50μm. ** p<0.01 ION *vs*. sham animals (n = 6 sham, n = 5 ION). Data are expressed as means ± SEM.

doi:10.1371/journal.pone.0160786.g001

ganglion after peripheral nerve injury [35]. Here, in order to verify that all the animals included in this study that underwent ION ligation had the same extent of nerve lesion, we analyzed ATF3 expression in the TGs. Five weeks after the surgery, we observed a significant increase in ATF3 expression specifically in the ipsilateral TG of ligated mice (Fig 1A and 1D; p<0.001). In contrast, no significant ATF3 expression was found in the contralateral TG of ION mice (Fig 1B and 1D) or in the ipsilateral TG of sham-operated mice (Fig 1C and 1D).

In order to measure the changes in orofacial sensitivity evoked by the unilateral ION ligation, we used an operant test in which a mildly water-deprived mouse will voluntarily approach and drink a sweet water reward by introducing its snout in an apparatus that provides mechanical stimulations to the whisker pad (Fig 2). This paradigm involves a conflict between the willingness to drink and the perceived discomfort/pain due to this mechanical stimulation. The time spent drinking was quantified by using an infrared beam. ION-ligated mice displayed a significant decrease in drinking duration as compared to the sham-operated animals, as early as 1 week after the surgery (Fig 2C; p<0.05). This decrease continued for 5 weeks (Fig 2C; p<0.001), suggesting the persistence of mechanical orofacial allodynia.

In order to decipher the link between the alteration of functional plasticity of the barrel field of the primary sensory cortex and mechanical allodynia in this model, we carried out a longitudinal study of the haemodynamic responses induced by whisker stimulations in the S1BF cortex under anaesthesia.

Indeed, focal cortical activation is known to induce a local increase of cerebral blood flow and volume (so called haemodynamic response), in addition to changes in haemoglobin concentration and oxygenation (metabolic response). Optical imaging of intrinsic signals consists in monitoring changes in light reflectance of the cortical surface resulting from these local physiological correlates of neuronal activity. When using light at 570 nm, which corresponds to an isosbestic point at which oxyhaemoglobin and deoxyhaemoglobin share the same absorption properties, the variations of light absorption by the cortical surface reflect changes in

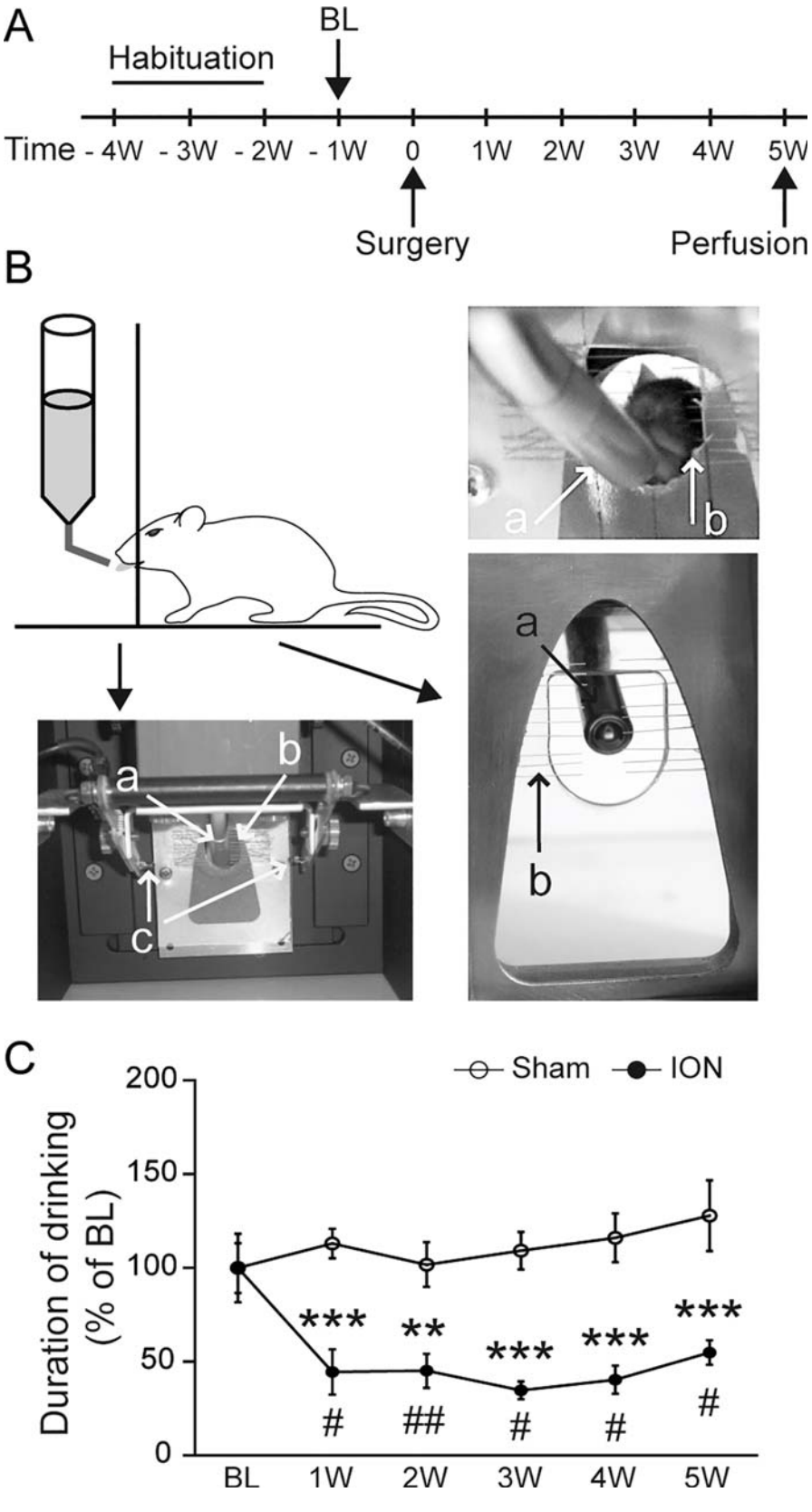
A
BL
Habituation
Time - 4W - 3W - 2W - 1W 0 1W 2W 3W 4W 5W
Surgery
Perfusion
B
a
b
a
b
a
b
c
C
Sham
ION
Duration of drinking (% of BL)
200
150
100
50
0
***
**
***
***
***
#
##
#
#
#
BL
1W
2W
3W
4W
5W

Fig 2. ION ligation induces mechanical hyperalgesia. A: Schematic representation of the experimental paradigm. Habituation to the test lasted 3 weeks, and the baseline (BL) values were measured 1 week before the surgery (-1W). Subsequently, mice were tested once per week. B: The orofacial stimulation test. In this paradigm, mice were allowed to voluntarily contact a mechanical stimulator (b) in order to access a sweet water reward (a). Automatic quantification of the drinking duration was performed using an infrared beam traversing the opening to the reward (c). C: ION ligation induced mechanical hyperalgesia ($F_{1,44} = 63.249$; $p<0.001$). The drinking duration decreased during the first week after surgery (1W) as compared to the BL, and persisted for 5 weeks. **p<0.01 and ***p<0.001 *vs*. sham mice; #p<0.05 and ##p<0.01 *vs*. BL (n = 4 sham, n = 4 ION). All data are expressed as means ± SEM.

doi:10.1371/journal.pone.0160786.g002

blood volume [38]. It has been shown in the rat barrel cortex that this measure of light reflectance at 570 nm is an efficient way to visualise the cortical activation evoked by a single whisker deflection [39]. Indeed, the observed decrease in reflected light following tactile stimulation is linearly correlated with the integrated measure of extracellular field potentials [39,40].

We chose to use this intrinsic imaging approach to study the functional cortical plasticity since it can be performed through the intact skull in mice, keeping the brain's entire integrity [39]. We were indeed able to repeatedly image cortical activations evoked by repeated whisker deflections (Fig 3), with the same groups of mice (ION n = 6 datasets, sham n = 6 datasets, see Materials and Methods section). Although the evoked optical signals measured in sham-operated animals were stable over time, we observed a rapid decrease in the cortical responses imaged in the ION-ligated mice, which was statistically significant as early as one week after the surgery (Fig 3C).

We were initially surprised to observe this decreased sensory response concomitant with the appearance of mechanical hyperalgesia in the ION model (Fig 2C), since an increased local neuronal responsiveness to hindpaw stimulation was previously observed in the rat primary sensory cortex in models of sciatic nerve lesion, both with voltage-sensitive dye imaging [41] and indirectly by fMRI [42]. One possible explanation is that the measured decrease in responses could partially result from an increase in the basal level of neuronal activity, since intrinsic imaging measures the relative changes in cerebral blood volume during the whisker stimulation over the initial basal level (before stimulation).

Therefore, in order to investigate whether the S1BF cortex of ION animals was subjected to enhanced neuronal activity, we examined the number of cells that were immunopositive for the proto-oncogene cFos in both sham and ION animals in two conditions: without any prior sensory stimulation (basal levels); and following sustained whisker stimulation for two hours (stimulated). In the absence of any stimulation, we observed an increase in the number of c-Fos-positive neurons in ION-ligated mice in the contralateral side of the S1BF cortex as compared to sham animals (Fig 4A–4C–4E), although this observation was not statistically significant ($p = 0.064$). As expected [35] after two hours of exploration in a stimulus-rich environment, the number of cFos-positive neurons increased significantly in the barrel field cortex of sham animals, compared to the basal condition (Fig 4A and 4B–4E; $p<0.05$). Interestingly, no difference between basal condition and stimulus-rich environment was observed in the ION-ligated group (Fig 4B–D and 4E), suggesting that the basal level of neuronal activity is increased in the S1BF of ION mice and can hardly be further increased by sensory (whisker) stimulation. These results suggest that there is an increased basal level of neuronal activity in S1BF cortical activity following sensory stimulation.

ION ligation induces plasticity in different cortical areas

To investigate the cortical pathophysiological changes occurring in our model, we next examined fluctuations in Erk phosphorylation as a marker of neuronal activity [43]. Acute and chronic pains have multiple components and numerous studies have described networks of

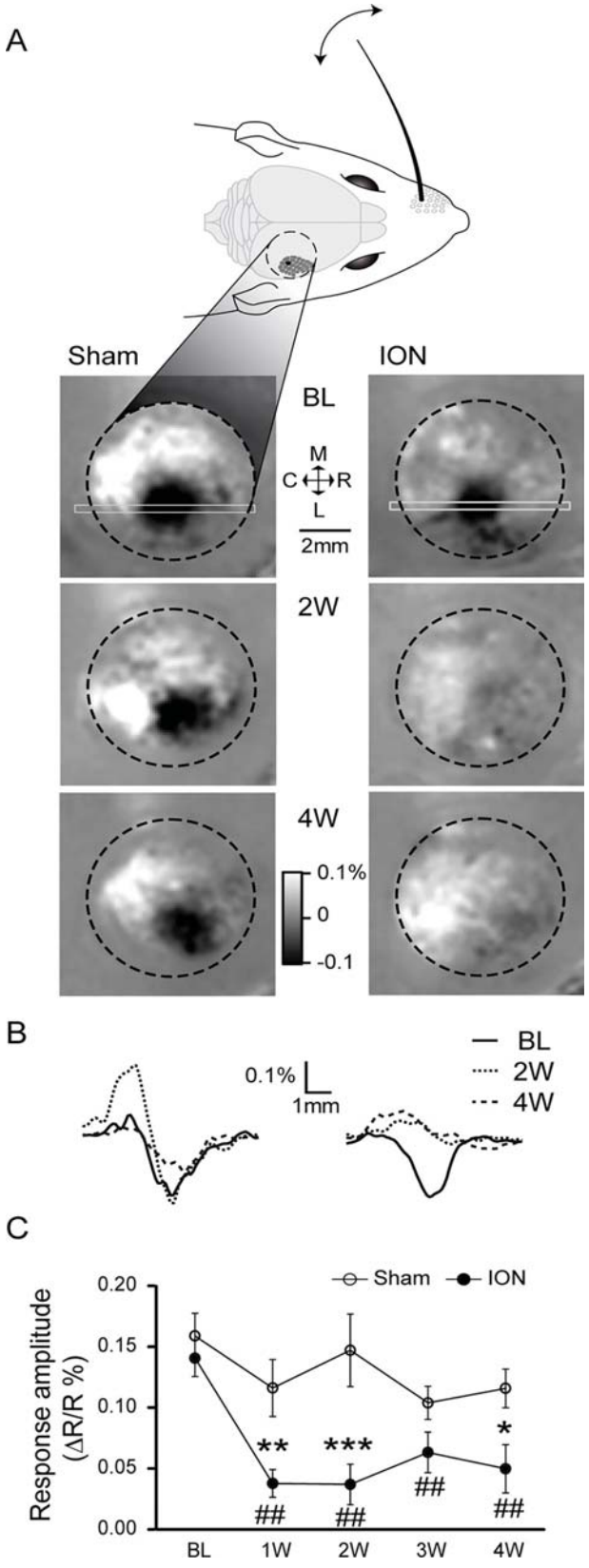
A
Sham
ION
BL
M
C
R
L
2mm
2W
4W
0.1%
0
-0.1
B
BL
2W
4W
0.1%
1mm
C
Sham
ION
Response amplitude (ΔR/R %)
0.20
0.15
0.10
0.05
0.00
**
***
*
##
##
##
##
BL
1W
2W
3W
4W

Fig 3. Intrinsic optical imaging reveals a decrease in sensory-evoked signals in the contralateral somatosensory cortex after ION ligation. A: Intrinsic optical signals were recorded through the intact skull, on the right posteromedial barrel subfield of the primary omatosensory cortex (S1BF; the black dotted line designates the borders of the imaging chamber). Variation in the reflected light (at 570 nm) induced by repetitive C1 whisker deflections (1 s at 100 Hz) is shown for a sham-operated (left) and an ION-ligated mouse (right). The results obtained before surgery (Baseline: BL, upper images) or 2 and 4 weeks after the surgery (2W and 4W, respectively, lower images) are expressed as $R\text{-}R_0/R_0$, with R representing the averaged reflected light measured over 1 s immediately after the stimulus presentation and R_0 representing the reflected light averaged over 1 s before the stimulus presentation. B: Spatial profiles of the reflected light measured along the rostro-caudal axis, using the region of interest indicated in A by the light grey rectangle. Note the absence of signal variation for the ION-ligated mouse at 2W and 4W. C: Quantification of the evoked signals was performed by looking for the minimal values of the spatial profiles (with examples shown in B). The ION ligation resulted in a significant decrease in evoked signals that persisted from the first week after the surgery through the following weeks. *p<0.05 and **p<0.01 ***p<0.001 *vs*. sham mice; #p<0.05 and ##p<0.01 *vs*. BL (n = 6 sham, n = 6 ION). All data are expressed as means ± SEM.

doi:10.1371/journal.pone.0160786.g003

brain areas activated by experimental pain. While some brain areas are rather involved in the sensory discriminative aspect of pain (lateral thalamus, S1 and motor cortex), others such as the cingulate and anterior insulate are rather involved in the affective-emotional aspect of pain [44–47]. We and others have also shown important changes in the anterior cingulate cortex associated with chronic inflammatory or neuropathic pain [48]. Consequently, our quantitative analysis of the number of p-Erk-positive cells was performed in the S1BF, motor and cingulate

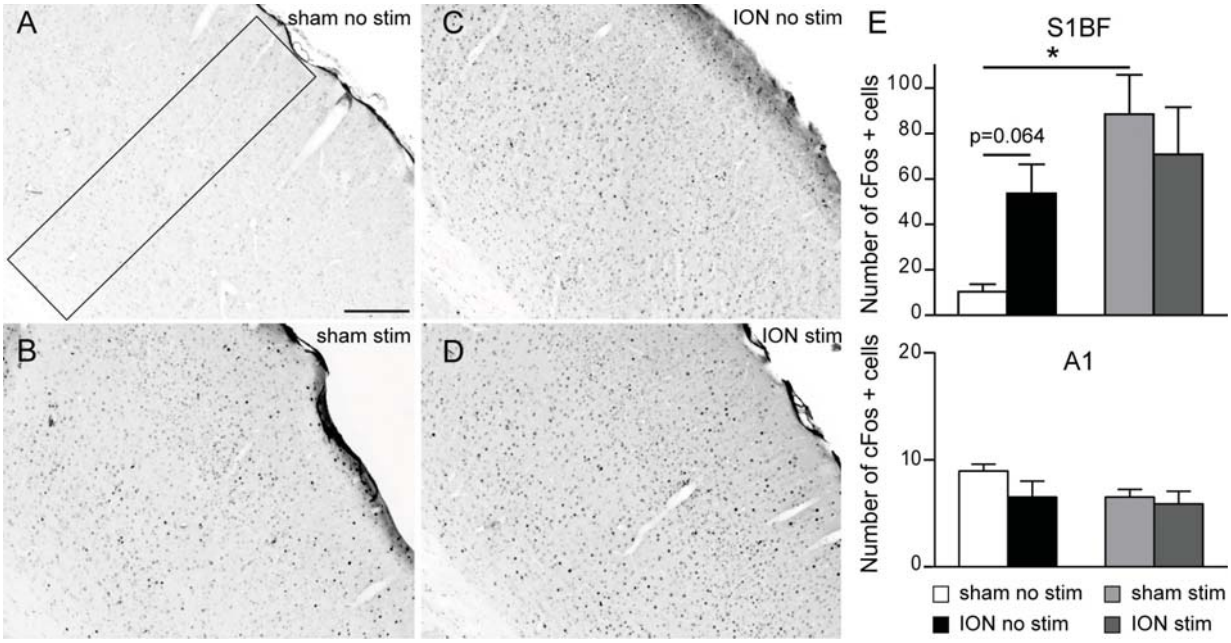

Fig 4. The absence of apparent cFos activation in response to sustained vibrissal stimulation in the cortex of ION constricted animals relies on an increased basal level of cFos in the S1BF cortex. Animals had all whiskers except one raw clipped and were left for two hours to explore an enriched environment. Following perfusion, the number of cFos positive profiles was analysed in the S1BF and primary auditory (A1) cortices. A-D: Representative examples of cFos staining observed in the contralateral side of the S1BF in non-stimulated sham (A), stimulated sham (B), non-stimulated ION (C) and stimulated ION (D) mice. Scale bar = 200 μm. E: Quantification of cFos-positive cells in the S1BF (top) and A1cortex in sham and ION mice 1 week post-surgery, after no stimulation or following 2 hours of natural vibrissal stimulation. Stimulation (Stim) induced a statistically significant upregulation of cFos in sham animals (p = 0.003) in the S1BF, although there was no difference in ION animals (p = 0.44). However, nerve ligation induced the upregulation of cFos in the S1BF of ION animals after no stimulation (p = 0.064). There was no change in the number of cFos positive cells in the A1 between all animals groups (bottom panel). Scale bars = 200 μm (n = 5 sham after no stimulation, n = 4 ION after no stimulation, n = 4 sham after stimulation, n = 5 ION after stimulation). Data are expressed as means ± SEM.

doi:10.1371/journal.pone.0160786.g004

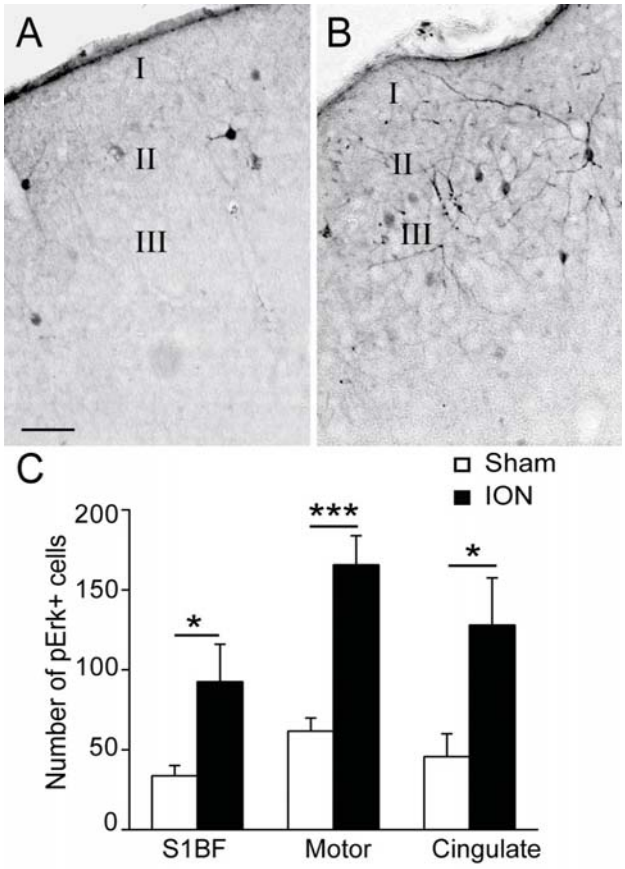

Fig 5. ION ligation induces the upregulation of p-Erk in different cortical areas. A-B: Representative examples of p-Erk staining in the barrel field cortex (S1BF) in sham (A) and ION (B) mice 5 weeks after the lesion/sham operation. Scale bars = 50μm. C: Quantification of the numbers of p-Erk-labelled cells in the S1BF, motor and cingulate cortices. ION ligation induced the upregulation of p-Erk+ cells. ($F_{1,26} = 29.571$; $p<0.001$, n = 6 sham, n = 5 ION)

doi:10.1371/journal.pone.0160786.g005

cortices 5 weeks post-injury. As previously observed by other teams, p-Erk cells are mostly located in pyramidal neurons in laminae II-III and laminae V and VI [49]. These results indicate that the number of p-Erk-positive cells was significantly increased in ION mice (Fig 5B) as compared to the sham group (Fig 5A) in the 3 structures (Fig 5C; $p<0.05$, $p<0.001$ and $p<0.05$ in the S1BF, motor and cingulate cortices, respectively).

Based on these results, we focused on how this exacerbated cortical activity could be linked to neuronal plasticity mechanisms. Global changes of activity in neuronal networks are likely to induce homeostatic adaptations of synaptic strengths, which involve functional remodelling of both presynaptic and postsynaptic sites [49]. To measure presynaptic adaptations, we studied the expression of the Piccolo protein (Fig 6A and 6B), which is a component of the presynaptic cytoskeletal matrix assembled at the active zone of neurotransmitter release [50]and has been shown to be regulated upon homeostatic adaptation to network activity [51][52].

Piccolo expression was quantified by measuring the fluorescence staining area in the S1BF, motor and cingulate cortices (Fig 6F). We separated the analysis into two parts: the superficial layers including layers II through IV, and the deep layers including layers V and VI. Compared to the sham mice, the mean fluorescent staining area was significantly increased in the deep

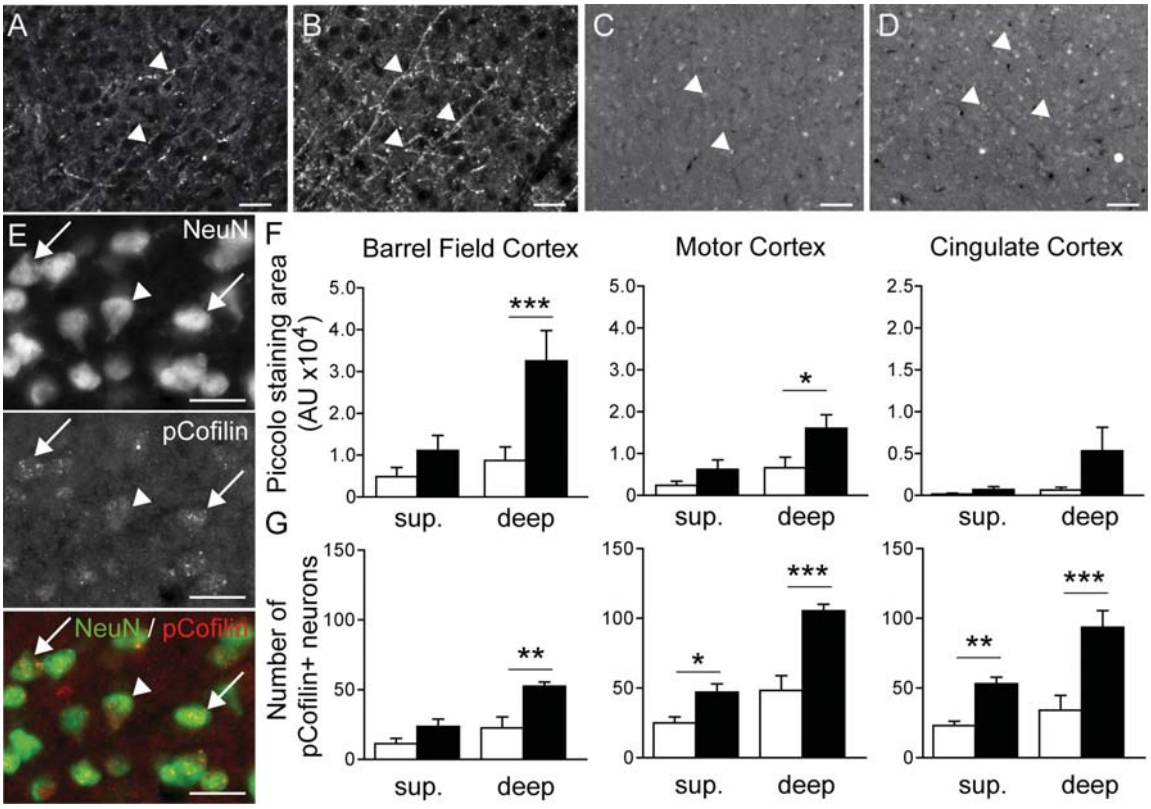

Fig 6. ION ligation induces synaptic plasticity in the S1BF, motor and cingulate cortices. A-B: Representative examples of Piccolo staining (arrow heads) in the deep laminae of the S1BF cortex in sham (A) and ION (B) mice 5 weeks after surgery. Scale bar = 50μm. C-D: Representative examples of p-Cofilin staining (arrow heads) in the deep laminae of the S1BF cortex in sham (C) and ION (D) mice. Scale bar = 50μm. E: Double immunostaining showing NeuN (green)/p-Cofilin (red) positive neurons in the S1BF (arrows). The arrow head point at a NeuN positive neuron negative for pcofilin. Scale bar = 25μm. F: Quantification of Piccolo staining in the S1BF, motor and cingulate cortices in deep and superficial laminae. ION ligation induced the upregulation of Piccolo staining in deep laminae in the S1BF and the motor cortex. Data are expressed as means ± SEM. *p<0.05 and **p<0.01 ***p<0.001 *vs*. sham mice, (n = 5 sham, n = 5 ION).

doi:10.1371/journal.pone.0160786.g006

layers of the barrel field and motor cortices in ION mice (Fig 6F; $p<0.001$ and $p<0.05$, respectively). We also observed a non-significant increase in the mean fluorescent staining area in the deep layers of the cingulate cortex (Fig 6F).

Postsynaptic modifications were examined by measuring p-Cofilin expression (Fig 6C and 6D). Cofilin is a protein expressed in the postsynaptic compartment that increases the turnover of F-actin by severing its filaments, and it has also been shown to regulate immature spine structure [53][54]. The number of p-Cofilin–positive neurons was significantly increased in the deep layers of the barrel field, motor and cingulate cortices in ION mice (Fig 6G; $p<0.01$ and $p<0.001$). The ION mice also showed an increased number of p-Cofilin-positive neurons in the superficial layers of the motor and cingulate cortices (Fig 6G; $p<0.05$ and $p<0.01$, respectively).

Discussion

We combined experimental approaches ranging from immunohistochemistry to *in vivo* functional imaging in order to study the neuronal correlates of orofacial neuropathic pain in the mouse cerebral cortex. Our results show that the motor, cingulate and barrel field cortices are

the sites of p-ERK over-expression, a surrogate marker of neuronal activation, and over-expression of markers of active pre- and post-synaptic elements, suggesting an enhanced synaptic plasticity. These results provide a unique opportunity to increase our understanding of the molecular mechanisms underlying long-lasting cortical plasticity associated with persistent neuropathic pain.

Ligation of the infraorbitral nerve induces long-lasting mechanical hyperalgesia

Traditionally, assessing trigeminal nerve-mediated nociceptive responses has been performed using methods that quantify brain stem-dependent behaviours (*e.g.* withdrawal responses or grooming) [55][28,56,57], in which the unlearned behaviours are elicited by mechanical stimulations using von Frey filaments [28] or thermal stimulation [30]. Such non-operant assessments may be relatively easy to execute; however, they evaluate innate behaviours that do not reveal cerebral processing of nociception. In this study we sought a more suitable approach, and used an orofacial operant test system. These types of pain tests employ a conflict paradigm that allows animals to make a choice between receiving a positive reward and escaping an aversive stimulus. For this reason, operant behavioural responses are not simple reflexive responses; rather, they should be considered as better indicators of pain in comparison to classical behavioural tests. Although operant behavioural responses are time-consuming (since they require several weeks of habituation), they are a better measure of spontaneous pain and their analysis can be fully automatized (therefore making them experimenter-independent). Orofacial operant tests have been used to characterize thermal (either cold [58,59] or hot temperatures [58,60–62]) and mechanical orofacial hypersensitivity [59,61]. Here, we have convincingly shown that mice experience long-lasting mechanical hyperalgesia following ION ligation, as previously reported in rat models [28].

ION ligation exacerbates cortical activity

As previously described, ION ligation induced upregulation of ATF3, a marker of nerve injury [35,63–65] in TG neurons. This type of nerve injury is known to affect excitability in the sensory cortex [66]. Using *in vivo* intrinsic imaging, we observed that ION ligation induced a decreased haemodynamic response to vibrissae stimulation in the S1BF cortex. This result is consistent with a reduced haemodynamic responsiveness of the primary sensory cortex previously reported in a model of chronic stress and triggered by enhanced iNOS and decreased nNOS and HO-2 expression [67]. However our result was unexpected, since a previous voltage-sensitive dye imaging study had described an increased neuronal response in the primary somatosensory cortex of sciatic nerve-ligated rats, with an enlarged area of activation following electrical stimulation of the hind paw [41,68]. An increase in S1 responsiveness to cold stimuli (acetone applications) has also been observed in sciatic nerve-ligated rats by fMRI [42].

We further investigated this result by using cFos as a marker of neuronal activity. It was previously demonstrated that the increased neuronal expression of cFos is linked to higher neuronal activity in many neuronal networks, including the nociceptive pathways [69]. We observed that peripheral neuropathy induced by ION ligation is associated with an increase in cFos expression in the S1BF cortex under control conditions (although not significantly). Most strikingly, whisker stimulation *via* exposure to an enriched environment was not associated with increased cFos immunoreactivity in ION-ligated mice, in contrast to the sham-operated animals.

These results suggest that ION ligation may be at the origin of an enhanced and sustained activity in the trigeminal fibres [70,71] and/or an enhanced activation of thalamo-cortical

connections, resulting in a postsynaptic enhanced neuronal activation of barrel field neurons. This increase in basal neuronal activity seems to preclude normal responses to tactile sensory input. Previous studies on sciatic nerve-ligated rats have reported a similar increase in cortical basal activity by monitoring either metabolic or vascular correlates of neuronal activity [71,72]. This hyperactivity was observed not only in the primary somatosensory cortex but also in other brain regions (*e.g.* the amygdala, the habenular complex, many thalamic nuclei, and the cingulate and retrosplenial cortices).

ION ligation induces long-term cortical plasticity

We observed enhanced p-Erk immunoreactivity in cortical areas after ION ligation, confirming the hypothesized increase in basal cortical activity. Erk phosphorylation is considered to be a marker of spinal neuronal activation after application of a noxious stimulation [73,74], and previous studies have shown that Erk may contribute to rapid synaptic potentiation and the regulation of neuronal excitability [75]. Furthermore, Erk phosphorylation could result from changes in the strength of synapses. We therefore decided to study long-term adaptations of cortical synapses after ION ligation.

Synaptic adaptations are observed by modulating both presynaptic and postsynaptic functions. Modifications to the probability of neurotransmitter release and synapse size have both been reported at the presynaptic level [76,77], whereas receptor abundance and composition can be modified at the postsynaptic level, as reported for AMPA receptors [78–80]. Any of these parameters could participate in the cortical hyperactivity observed in our model. Neuropathic pain and memory processes exhibit adaptive mechanisms including long-term potentiation and central sensitization [3,81], and these mechanisms depend upon synaptic plasticity.

Prolonged activity depletion induces a significant downregulation in the cellular expression levels of presynaptic scaffolding proteins including Bassoon, RIM, synapsin and Piccolo [52]. The ADF/Cofilin complex may regulate synaptic strength at the postsynaptic compartment. Indeed, ADF/Cofilin phosphorylation and dephosphorylation have been associated with spine growth and shrinkage during LTP and LTD, respectively [82]. Moreover, the number of p-Cofilin-positive puncta is dependent on excitatory transmission [83,84] and use of lentiviral vectors and optogenetically labelled cofilin1 knocked-down-neurons showed that cofilin-1 mediated actin dynamics regulates functional cortical map plasticity in an input-specific mechanism [85]. These data, combined with the upregulation of Piccolo and p-Cofilin observed in our model, suggest the presence of functional and structural plasticity induced by the neuropathic state in diverse cortical areas. The upregulated number of synapses and/or the strength of these synapses may participate in the long-lasting sensory changes in neuropathic mice observed concomitantly with mechanical hyperalgesia. Kim and Nabekura reported a rapid synaptic remodelling following peripheral nerve injury, accompanied by the formation of new spines in the early phase of neuropathic pain [86]. Our results suggest that this remodelling persists into the late phase of neuropathic pain, as revealed by the increased expression of both pre- and postsynaptic markers.

ION ligation-induced cortical plasticity is layer-specific

Our results revealed significant synaptic modifications within cortical deep layers, particularly in the S1BF cortex, where we observed the upregulation of Piccolo and p-Cofilin within layers V and VI. We principally observed the upregulation of p-Cofilin in the deep layers of the motor and cingulate cortices, but also in the superficial layers. One previous report has shown, in the S1 cortical representation of the hind limb in naive rats, that neurons exclusively driven by noxious stimulation are located preferentially in laminae Va, Vb, VIa and VIb, *i.e.* in the

deeper laminae [66]. Similarly, a recent study based on cFos immunoreactivity reported that noxious stimuli in naive mice seem to preferentially activate the subgranular layer Va [33]. Single-unit extracellular recordings in ION rats have revealed reduced background activity of whisker neurons (compared to naive rats) in laminae II-III and IV, accompanied by strongly increased activity in lamina VIa [33,68]. Altogether, these results suggest that the subgranular layers might be particularly involved in the processing of noxious stimuli. In light of our observations, they also appear to be involved in synaptic plasticity mechanisms accompanying trigeminal neuropathic pain.

As in the sensory cortices, where layer VI appears to influence the activity of thalamic neurons that relay sensory information [87,88], the upregulation of active synapses after nerve ligation in deep layers suggests that neuropathic pain may be associated with reorganization at the thalamo-cortical level. Previous studies have demonstrated that neuropathic pain conditions are associated with changes in thalamic anatomy and biochemistry [21,89,90], suggesting that firing patterns within thalamo-cortical loops are altered in the neuropathic pain state.

These results suggest a novel conceptual framework for the comprehension of chronic-pain induced cortical plasticity, by showing that long-lasting orofacial neuropathic pain is associated with exacerbated neuronal activity and synaptic plasticity. The resulting over-enhanced synaptic strength, putatively upregulated from it's physiological optimum, may explain both exacerbated sensitivity (allodynia) and loss of performance in fine-textured sensory discrimination tasks, both reported in chronic pain patients [44]. Consequently, controlled therapeutic regulation of structural synaptic plasticity in chronic pain may represent a novel and original clinical target, to be validated in future pre-clinical studies.

Supporting Information

S1 Dataset. Mini dataset presenting in different tabs individual results from Sham and ION treated animals. Each tab shows the results for the following items: ATF3 positive DRG neurons (Fig 1), behaviour (time spent drinking, which provides an indirect measure of mechanical hyperalgesia, Fig 2), intrinsic optical imaging (Fig 3), c-fos expression in the S1BF (Fig 4), and immunostainings quantifications in different cortical areas: p-ERK (Fig 5), Piccolo and p-Cofilin (Fig 6).
(XLSX)

S1 Table. Table reporting the number of animals included in the initial experimental design, and the reasons for the exclusion of some of them during the course of the study. For instance, some animals were excluded from the imaging experiments when they lost some of their whiskers, or from the behavioural analysis if they were not drinking during the habituation sessions. Additionally, one mouse died from unknown reasons. The three bottom lines indicate the number ("N") of animals included for each one of the following approaches (Behaviour, Imaging and Immnohistochemistry ("Immuno")) at the different time points during of these experiments.
(XLSX)

Acknowledgments

This work has been supported by the Centre National pour la Recherche Scientifique (CNRS) and the Ecole Supérieure de Physique et Chimie Industrielles de la mairie de Paris, ParisTech. The authors thank Mr. Marcel Leopoldie for animal husbandry and Brandon Loveall of Improvence for English proofreading of the manuscript.

Author Contributions

Conceived and designed the experiments: KT IF SP.

Performed the experiments: KT SR IF SP.

Analyzed the data: KT SR IF SP.

Contributed reagents/materials/analysis tools: ZL.

Wrote the paper: KT IF SP ZL.

References

1. Bennetto L, Patel NK, Fuller G. Trigeminal neuralgia and its management. BMJ. 2007; 334: 201–5. doi: 10.1136/bmj.39085.614792.BE PMID: 17255614
2. Zakrzewska JM, McMillan R. Trigeminal neuralgia: the diagnosis and management of this excruciating and poorly understood facial pain. Postgrad Med J. 2011; 87: 410–6. doi: 10.1136/pgmj.2009.080473 PMID: 21493636
3. Costigan M, Scholz J, Woolf CJ. Neuropathic pain: a maladaptive response of the nervous system to damage. Annu Rev Neurosci. 2009; 32: 1–32. doi: 10.1146/annurev.neuro.051508.135531 PMID: 19400724
4. Guo D, Hu J. Spinal presynaptic inhibition in pain control. Neuroscience. 2014. pp. 95–106. doi: 10.1016/j.neuroscience.2014.09.032
5. Pirttimaki TM, Hall SD, Parri HR. Sustained neuronal activity generated by glial plasticity. J Neurosci. 2011; 31: 7637–47. doi: 10.1523/JNEUROSCI.5783-10.2011 PMID: 21613477
6. Abbadie C, Bhangoo S, De Koninck Y, Malcangio M, Melik-Parsadaniantz S, White FA. Chemokines and pain mechanisms. Brain Research Reviews. 2009. pp. 125–134. doi: 10.1016/j.brainresrev.2008.12.002 PMID: 19146875
7. Scholz J, Woolf CJ. The neuropathic pain triad: neurons, immune cells and glia. Nat Neurosci. 2007; 10: 1361–1368. doi: 10.1038/nn1992 PMID: 17965656
8. Marchand F, Perretti M, McMahon SB. Role of the immune system in chronic pain. Nat Rev Neurosci. 2005; 6: 521–32. doi: 10.1038/nrn1700 PMID: 15995723
9. Flor H, Elbert T, Knecht S, Wienbruch C, Pantev C, Birbaumer N, et al. Phantom-limb pain as a perceptual correlate of cortical reorganization following arm amputation. Nature. 1995; 375: 482–484. doi: 10.1038/375482a0 PMID: 7777055
10. Flor H, Braun C, Elbert T, Birbaumer N, Knecht S, Wienbruch C, et al. Extensive reorganization of primary somatosensory cortex in chronic back pain patients\rPhantom-limb pain as a perceptual correlate of cortical reorganization following arm amputation. Neurosci Lett. 1997. pp. 5–8.
11. Gracely RH, Geisser ME, Giesecke T, Grant MAB, Petzke F, Williams DA, et al. Pain catastrophizing and neural responses to pain among persons with fibromyalgia. Brain. 2004; 127: 835–843. doi: 10.1093/brain/awh098 PMID: 14960499
12. Juottonen K, Gockel M, Sil??n T, Hurri H, Hari R, Forss N. Altered central sensorimotor processing in patients with complex regional pain syndrome. Pain. 2002; 98: 315–323. doi: 10.1016/S0304-3959(02)00119-7 PMID: 12127033
13. Pleger B, Ragert P, Schwenkreis P, Förster AF, Wilimzig C, Dinse H, et al. Patterns of cortical reorganization parallel impaired tactile discrimination and pain intensity in complex regional pain syndrome. Neuroimage. 2006; 32: 503–510. doi: 10.1016/j.neuroimage.2006.03.045 PMID: 16753306
14. Maihofner C, Handwerker HO, Neundorfer B, Birklein F. Cortical reorganization during recovery from complex regional pain syndrome. Neurology. 2004; 63: 693–701. doi: 10.1212/01.WNL.0000134661.46658.B0 PMID: 15326245
15. Vartiainen N, Kirveskari E, Kallio-Laine K, Kalso E, Forss N. Cortical reorganization in primary somatosensory cortex in patients with unilateral chronic pain. J Pain. 2009; 10: 854–859. doi: 10.1016/j.jpain.2009.02.006 PMID: 19638329
16. Apkarian a V, Sosa Y, Sonty S, Levy RM, Harden RN, Parrish TB, et al. Chronic back pain is associated with decreased prefrontal and thalamic gray matter density. J Neurosci. 2004; 24: 10410–10415. doi: 10.1523/JNEUROSCI.2541-04.2004 PMID: 15548656

17. (Karin) Swart C.M.A. CMA, Stins JF, Beek PJ. Cortical changes in complex regional pain syndrome (CRPS). European Journal of Pain. 2009. pp. 902–907. doi: 10.1016/j.ejpain.2008.11.010 PMID: 19101181

18. Baliki MN, Schnitzer TJ, Bauer WR, Apkarian AV. Brain morphological signatures for chronic pain. PLoS One. 2011; 6. doi: 10.1371/journal.pone.0026010

19. Lin CS. Brain signature of chronic orofacial pain: A systematic review and meta-analysis on neuroimaging research of trigeminal neuropathic pain and temporomandibular joint disorders. PLoS ONE. 2014. doi: 10.1371/journal.pone.0094300

20. Becerra L, Morris S, Bazes S, Gostic R, Sherman S, Gostic J, et al. Trigeminal neuropathic pain alters responses in CNS circuits to mechanical (brush) and thermal (cold and heat) stimuli. J Neurosci. 2006; 26: 10646–10657. doi: 10.1523/JNEUROSCI.2305-06.2006 PMID: 17050704

21. Gustin SM, Peck CC, Wilcox SL, Nash PG, Murray GM, Henderson LA. Different pain, different brain: thalamic anatomy in neuropathic and non-neuropathic chronic pain syndromes. J Neurosci. 2011; 31: 5956–5964. doi: 10.1523/JNEUROSCI.5980-10.2011 PMID: 21508220

22. Desouza DD, Hodaie M, Davis KD. Abnormal trigeminal nerve microstructure and brain white matter in idiopathic trigeminal neuralgia. Pain. 2014; 155: 37–44. doi: 10.1016/j.pain.2013.08.029 PMID: 23999058

23. Gustin SM, Peck CC, Cheney LB, Macey PM, Murray GM, Henderson LA. Pain and plasticity: is chronic pain always associated with somatosensory cortex activity and reorganization? J Neurosci. 2012; 32: 14874–14884. 32/43/14874 [pii]\r doi: 10.1523/JNEUROSCI.1733-12.2012 PMID: 23100410

24. DaSilva AF, Becerra L, Pendse G, Chizh B, Tully S, Borsook D. Colocalized structural and functional changes in the cortex of patients with trigeminal neuropathic pain. PLoS One. 2008; 3. doi: 10.1371/journal.pone.0003396

25. Gustin SM, Peck CC, Macey PM, Murray GM, Henderson LA. Unraveling the effects of plasticity and pain on personality. J Pain. 2013; 14: 1642–1652. doi: 10.1016/j.jpain.2013.08.005 PMID: 24290444

26. Gustin SM, McKay JG, Petersen ET, Peck CC, Murray GM, Henderson LA. Subtle alterations in brain anatomy may change an Individual's personality in chronic pain. PLoS One. 2014; 9. doi: 10.1371/journal.pone.0109664

27. Bennett GJ, Xie YK. A peripheral mononeuropathy in rat that produces disorders of pain sensation like those seen in man. Pain. 1988; 33: 87–107. doi: 10.1016/0304-3959(88)90209-6 PMID: 2837713

28. Vos BP, Strassman AM, Maciewicz RJ. Behavioral evidence of trigeminal neuropathic pain following chronic constriction injury to the rat's infraorbital nerve. J Neurosci. 1994; 14: 2708–2723. Available: http://f1000.com/pubmed/ref/8182437. PMID: 8182437

29. Lam DK, Sessle BJ, Cairns BE, Hu JW. Neural mechanisms of temporomandibular joint and masticatory muscle pain: a possible role for peripheral glutamate receptor mechanisms. Pain Res Manag. 2005; 10: 145–52. Available: http://www.ncbi.nlm.nih.gov/pubmed/16175250. PMID: 16175250

30. Imamura Y, Kawamoto H, Nakanishi O. Characterization of heat-hyperalgesia in an experimental trigeminal neuropathy in rats. Exp Brain Res. 1997; 116: 97–103. doi: 10.1007/PL00005748 PMID: 9305818

31. Kitagawa J, Takeda M, Suzuki I, Kadoi J, Tsuboi Y, Honda K, et al. Mechanisms involved in modulation of trigeminal primary afferent activity in rats with peripheral mononeuropathy. Eur J Neurosci. 2006; 24: 1976–1986. doi: 10.1111/j.1460-9568.2006.05065.x PMID: 17040479

32. Staiger JF, Bisler S, Schleicher A, Gass P, Stehle JH, Zilles K. Exploration of a novel environment leads to the expression of inducible transcription factors in barrel-related columns. Neuroscience. 2000; 99: 7–16. doi: 10.1016/S0306-4522(00)00166-4 PMID: 10924947

33. Frangeul L, Porrero C, Garcia-Amado M, Maimone B, Maniglier M, Clasc?? F, et al. Specific activation of the paralemniscal pathway during nociception. Eur J Neurosci. 2014; 39: 1455–1464. doi: 10.1111/ejn.12524 PMID: 24580836

34. Pezet S. Noxious Stimulation Induces Trk Receptor and Downstream ERK Phosphorylation in Spinal Dorsal Horn. Mol Cell Neurosci. 2002; 21: 684–695. doi: 10.1006/mcne.2002.1205 PMID: 12504600

35. Tsujino H, Kondo E, Fukuoka T, Dai Y, Tokunaga a, Miki K, et al. Activating transcription factor 3 (ATF3) induction by axotomy in sensory and motoneurons: A novel neuronal marker of nerve injury. Mol Cell Neurosci. 2000; 15: 170–182. doi: 10.1006/mcne.1999.0814 PMID: 10673325

36. Paxinos G and Franklin KBJ. Paxinos and Franklin's the Mouse Brain in Stereotaxic Coordinates [Internet]. São Paulo, Academic Press. 2012. Available: https://www.elsevier.com/books/paxinos-and-franklins-the-mouse-brain-in-stereotaxic-coordinates/paxinos/978-0-12-391057-8.

37. Vogt BA, Paxinos G. Cytoarchitecture of mouse and rat cingulate cortex with human homologies. doi: 10.1007/s00429-012-0493-3

38. Frostig RD, Lieke EE, Ts'o DY, Grinvald a. Cortical functional architecture and local coupling between neuronal activity and the microcirculation revealed by in vivo high-resolution optical imaging of intrinsic signals. Proc Natl Acad Sci U S A. 1990; 87: 6082–6086. doi: 10.1073/pnas.87.16.6082 PMID: 2117272

39. Sheth S, Nemoto M, Guiou M, Walker M, Pouratian N, Toga AW. Evaluation of coupling between optical intrinsic signals and neuronal activity in rat somatosensory cortex. Neuroimage. 2003; 19: 884–894. doi: 10.1016/S1053-8119(03)00086-7 PMID: 12880817

40. Nemoto M, Sheth S, Guiou M, Pouratian N, Chen J. Functional Signal-and Paradigm-Dependent Linear Relationships between Synaptic Activity and . . .. J Neurosci. 2004; Available: http://www.ncbi.nlm.nih.gov/entrez/query.fcgi?db=pubmed&cmd=Retrieve&dopt=AbstractPlus&list_uids=4082963686573044763related:G3QBKdeZqTgJ\npapers3://publication/uuid/3C68B265-0A9A-4B65-BED1-D5D96692A8FA.

41. Cha MH, Kim DS, Cho ZH, Sohn JH, Chung MA, Lee HJ, et al. Modification of cortical excitability in neuropathic rats: A voltage-sensitive dye study. Neurosci Lett. 2009; 464: 117–121. doi: 10.1016/j.neulet.2009.08.024 PMID: 19682547

42. Hubbard CS, Khan SA, Xu S, Cha M, Masri R, Seminowicz DA. Behavioral, metabolic and functional brain changes in a rat model of chronic neuropathic pain: A longitudinal MRI study. Neuroimage. 2015; 107: 333–344. doi: 10.1016/j.neuroimage.2014.12.024 PMID: 25524649

43. Ji RR, Baba H, Brenner GJ, Woolf CJ. Nociceptive-specific activation of ERK in spinal neurons contributes to pain hypersensitivity. Nat Neurosci. 1999; 2: 1114–1119. doi: 10.1038/16040 PMID: 10570489

44. Treede RD, Kenshalo DR, Gracely RH, Jones AK. The cortical representation of pain. Pain. 1999; 79: 105–11. Available: http://www.ncbi.nlm.nih.gov/pubmed/10068155. PMID: 10068155

45. Tracey I. Nociceptive processing in the human brain. Curr Opin Neurobiol. 2005; 15: 478–87. doi: 10.1016/j.conb.2005.06.010 PMID: 16019203

46. Hayes DJ, Northoff G. Common brain activations for painful and non-painful aversive stimuli. BMC Neurosci. 2012; 13: 60. doi: 10.1186/1471-2202-13-60 PMID: 22676259

47. Apkarian AV, Bushnell MC, Treede R-D, Zubieta J-K. Human brain mechanisms of pain perception and regulation in health and disease. Eur J Pain. 2005; 9: 463–84. doi: 10.1016/j.ejpain.2004.11.001 PMID: 15979027

48. Thibault K, Lin WK, Rancillac A, Fan M, Snollaerts T, Sordoillet V, et al. BDNF-Dependent Plasticity Induced by Peripheral Inflammation in the Primary Sensory and the Cingulate Cortex Triggers Cold Allodynia and Reveals a Major Role for Endogenous BDNF As a Tuner of the Affective Aspect of Pain. J Neurosci. 2014; 34: 14739–14751. doi: 10.1523/JNEUROSCI.0860-14.2014 PMID: 25355226

49. Kawai HD, La M, Kang HA, Hashimoto Y, Liang K, Lazar R, et al. Convergence of nicotine-induced and auditory-evoked neural activity activates ERK in auditory cortex. Synapse. 2013; 67: 455–468. doi: 10.1002/syn.21647 PMID: 23401204

50. Pozo K, Goda Y. Unraveling mechanisms of homeostatic synaptic plasticity. Neuron. 2010. pp. 337–351. doi: 10.1016/j.neuron.2010.04.028 PMID: 20471348

51. Fenster SD, Chung WJ, Zhai R, Cases-Langhoff C, Voss B, Garner a M, et al. Piccolo, a presynaptic zinc finger protein structurally related to bassoon. Neuron. 2000; 25: 203–214. doi: 10.1016/S0896-6273(00)80883-1 PMID: 10707984

52. Lazarevic V, Schöne C, Heine M, Gundelfinger ED, Fejtova A. Extensive Remodeling of the Presynaptic Cytomatrix upon Homeostatic Adaptation to Network Activity Silencing. J Neurosci. 2011; 31: 10189–10200. doi: 10.1523/JNEUROSCI.2088-11.2011 PMID: 21752995

53. Pontrello CG, Sun M-Y, Lin A, Fiacco TA, DeFea KA, Ethell IM. Cofilin under control of β-arrestin-2 in NMDA-dependent dendritic spine plasticity, long-term depression (LTD), and learning. Proc Natl Acad Sci U S A. 2012; 109: E442–51. doi: 10.1073/pnas.1118803109 PMID: 22308427

54. Bamburg JR, McGough A, Ono S. Putting a new twist on actin: ADF/cofilins modulate actin dynamics. Trends in Cell Biology. 1999. pp. 364–370. doi: 10.1016/S0962-8924(99)01619-0 PMID: 10461190

55. Clavelou P, Dallel R, Orliaguet T, Woda a, Raboisson P. The orofacial formalin test in rats: effects of different formalin concentrations. Pain. 1995; 62: 295–301. 030439599400273H [pii]. PMID: 8657429

56. Krzyzanowska A, Pittolo S, Cabrerizo M, S??nchez-L??pez J, Krishnasamy S, Venero C, et al. Assessing nociceptive sensitivity in mouse models of inflammatory and neuropathic trigeminal pain. J Neurosci Methods. 2011; 201: 46–54. doi: 10.1016/j.jneumeth.2011.07.006 PMID: 21782847

57. Pelissier T, Pajot J, Dallel R. The orofacial capsaicin test in rats: Effects of different capsaicin concentrations and morphine. Pain. 2002; 96: 81–87. doi: 10.1016/S0304-3959(01)00432-8 PMID: 11932064

58. Rossi HL, Jenkins AC, Kaufman J, Bhattacharyya I, Caudle RM, Neubert JK. Characterization of bilateral trigeminal constriction injury using an operant facial pain assay. Neuroscience. 2012; 224: 294–306. doi: 10.1016/j.neuroscience.2012.08.015 PMID: 22909425

59. Cha M, Kohan KJ, Zuo X, Ling JX, Gu JG. Assessment of chronic trigeminal neuropathic pain by the orofacial operant test in rats. Behav Brain Res. 2012; 234: 82–90. doi: 10.1016/j.bbr.2012.06.020 PMID: 22743005

60. Neubert JK, Widmer CG, Malphurs W, Rossi HL, Vierck CJ, Caudle RM. Use of a novel thermal operant behavioral assay for characterization of orofacial pain sensitivity. Pain. 2005; 116: 386–395. doi: 10.1016/j.pain.2005.05.011 PMID: 15982812

61. Nolan TA, Hester J, Bokrand-Donatelli Y, Caudle RM, Neubert JK. Adaptation of a novel operant orofacial testing system to characterize both mechanical and thermal pain. Behav Brain Res. 2011; 217: 477–480. doi: 10.1016/j.bbr.2010.10.022 PMID: 20974188

62. Anderson EM, Mills R, Nolan T a, Jenkins AC, Mustafa G, Lloyd C, et al. Use of the Operant Orofacial Pain Assessment Device (OPAD) to Measure Changes in Nociceptive Behavior. J Vis Exp. 2013; 76: 1–6. doi: 10.3791/50336

63. Braz JM, Basbaum AI. Differential ATF3 expression in dorsal root ganglion neurons reveals the profile of primary afferents engaged by diverse noxious chemical stimuli. Pain. 2010; 150: 290–301. doi: 10.1016/j.pain.2010.05.005 PMID: 20605331

64. Xu M, Aita M, Chavkin C. Partial Infraorbital Nerve Ligation as a Model of Trigeminal Nerve Injury in the Mouse: Behavioral, Neural, and Glial Reactions. J Pain. 2008; 9: 1036–1048. doi: 10.1016/j.jpain.2008.06.006 PMID: 18708302

65. Ma F, Zhang L, Lyons D, Westlund KN. Orofacial neuropathic pain mouse model induced by Trigeminal Inflammatory Compression (TIC) of the infraorbital nerve. Mol Brain. 2012; 5: 44. doi: 10.1186/1756-6606-5-44 PMID: 23270529

66. Lamour Y, Guilbaud G, J.C. W. Rat somatosensory cortex II-Laminar and columnar organisation of noxious and non noxious inputs. Exp Brain Res. 1983; 49: 46–54. PMID: 6861936

67. Lee S, Kang B-M, Shin M-K, Min J, Heo C, Lee Y, et al. Chronic Stress Decreases Cerebrovascular Responses During Rat Hindlimb Electrical Stimulation. Front Neurosci. 2015; 9: 462. doi: 10.3389/fnins.2015.00462 PMID: 26778944

68. Benoist JM, Gautron M, Guilbaud G. Experimental model of trigeminal pain in the rat by constriction of one infraorbital nerve: Changes in neuronal activities in the somatosensory cortices corresponding to the infraorbital nerve. Exp Brain Res. 1999; 126: 383–398. doi: 10.1007/s002210050745 PMID: 10382623

69. Abbadie C, Besson JM. c-fos Expression in rat lumbar spinal cord during the development of adjuvant-induced arthritis. Neuroscience. 1992; 48: 985–993. doi: 10.1016/0306-4522(92)90287-C PMID: 1630632

70. Kajander KC, Bennett GJ. Onset of a painful peripheral neuropathy in rat: a partial and differential deafferentation and spontaneous discharge in A beta and A delta primary afferent neurons. J Neurophysiol. 1992; 68: 734–744. Available: http://eutils.ncbi.nlm.nih.gov/entrez/eutils/elink.fcgi?dbfrom=pubmed&id=1331353&retmode=ref&cmd=prlinks\npapers2://publication/uuid/D505610D-8C89-49D5-B353-83AE5AAD11E8. PMID: 1331353

71. Mao J, Mayer DJ, Price DD. Patterns of increased brain activity indicative of pain in a rat model of peripheral mononeuropathy. J Neurosci. 1993; 13: 2689–702. Available: http://www.ncbi.nlm.nih.gov/pubmed/8388924. PMID: 8388924

72. Paulson PE, Casey KL, Morrow TJ. Long-term changes in behavior and regional cerebral blood flow associated with painful peripheral mononeuropathy in the rat. Pain. 2002; 95: 31–40. doi: 10.1016/S0304-3959(01)00370-0 PMID: 11790465

73. Karim F, Wang CC, Gereau RW. Metabotropic glutamate receptor subtypes 1 and 5 are activators of extracellular signal-regulated kinase signaling required for inflammatory pain in mice. J Neurosci. 2001; 21: 3771–3779. 21/11/3771 [pii]. PMID: 11356865

74. Pezet S. Noxious Stimulation Induces Trk Receptor and Downstream ERK Phosphorylation in Spinal Dorsal Horn. Mol Cell Neurosci. 2002; 21: 684–695. Available: http://www.sciencedirect.com/science/article/pii/S1044743102912054. PMID: 12504600

75. Hu H-J, Alter BJ, Carrasquillo Y, Qiu C-S, Gereau RWI V. Metabotropic Glutamate Receptor 5 Modulates Nociceptive Plasticity via Extracellular Signal-Regulated Kinase Kv4.2 Signaling in Spinal Cord Dorsal Horn Neurons. J Neurosci. 2007; 27: 13181–13191. doi: 10.1523/jneurosci.0269-07.2007 PMID: 18045912

76. Moulder KL, Meeks JP, Shute AA, Hamilton CK, De Erausquin G, Mennerick S. Plastic elimination of functional glutamate release sites by depolarization. Neuron. 2004; 42: 423–435. doi: 10.1016/S0896-6273(04)00184-9 PMID: 15134639

77. De Gois S, Schafer MK, Defamie N, Chen C, Ricci A, Weihe E, et al. Homeostatic scaling of vesicular glutamate and GABA transporter expression in rat neocortical circuits. J Neurosci. 2005; 25: 7121–7133. doi: 10.1523/JNEUROSCI.5221-04.2005 PMID: 16079394

78. O'Brien RJ, Kamboj S, Ehlers MD, Rosen KR, Fischbach GD, Huganir RL. Activity-dependent modulation of synaptic AMPA receptor accumulation. Neuron. 1998; 21: 1067–1078. doi: 10.1016/S0896-6273(00)80624-8 PMID: 9856462

79. Thiagarajan TC, Lindskog M, Tsien RW. Adaptation to synaptic inactivity in hippocampal neurons. Neuron. 2005; 47: 725–737. doi: 10.1016/j.neuron.2005.06.037 PMID: 16129401

80. Wierenga CJ, Ibata K, Turrigiano GG. Postsynaptic expression of homeostatic plasticity at neocortical synapses. J Neurosci. 2005; 25: 2895–2905. doi: 10.1523/JNEUROSCI.5217-04.2005 PMID: 15772349

81. Ji RR, Kohno T, Moore KA, Woolf CJ. Central sensitization and LTP. Trends Neurosci. 2003; 26: 696–705. PMID: 14624855

82. Gu J, Lee CW, Fan Y, Komlos D, Tang X, Sun C, et al. ADF/cofilin-mediated actin dynamics regulate AMPA receptor trafficking during synaptic plasticity. Nat Neurosci. 2010; 13: 1208–1215. doi: 10.1038/nn.2634 PMID: 20835250

83. Chen LY, Rex CS, Casale MS, Gall CM, Lynch G. Changes in synaptic morphology accompany actin signaling during LTP. J Neurosci. 2007; 27: 5363–5372. doi: 10.1523/JNEUROSCI.0164-07.2007 PMID: 17507558

84. Rex CS, Lin C-Y, Kramar EA, Chen LY, Gall CM, Lynch G. Brain-Derived Neurotrophic Factor Promotes Long-Term Potentiation-Related Cytoskeletal Changes in Adult Hippocampus. J Neurosci. 2007; 27: 3017–3029. doi: 10.1523/jneurosci.4037-06.2007 PMID: 17360925

85. Tsubota T, Okubo-suzuki R, Ohashi Y, Tamura K, Ogata K. Cofilin1 Controls Transcolumnar Plasticity in Dendritic Spines in Adult Barrel Cortex. 2015; 1–29. doi: 10.1371/journal.pbio.1002070

86. Kim S, Nabekura J. Rapid synaptic remodeling in the adult somatosensory cortex following peripheral nerve injury and its association with neuropathic pain. J Neurosci. 2011; 31: 5477–5482. doi: 10.1523/JNEUROSCI.0328-11.2011 PMID: 21471384

87. Zhang ZW, Deschênes M. Intracortical axonal projections of lamina VI cells of the primary somatosensory cortex in the rat: a single-cell labeling study. J Neurosci. 1997; 17: 6365–6379. PMID: 9236245

88. Jones EG. Synchrony in the interconnected circuitry of the thalamus and cerebral cortex. Ann N Y Acad Sci. 2009; 1157: 10–23. doi: 10.1111/j.1749-6632.2009.04534.x PMID: 19351352

89. Gustin RM, Bichell TJ, Bubser M, Daily J, Filonova I, Mrelashvili D, et al. Tissue-specific variation of Ube3a protein expression in rodents and in a mouse model of Angelman syndrome. Neurobiol Dis. 2010; 39: 283–291. doi: 10.1016/j.nbd.2010.04.012 PMID: 20423730

90. Pattany PM, Yezierski RP, Widerstrom-Noga EG, Bowen BC, Martinez-Arizala A, Garcia BR, et al. Proton Magnetic Resonance Spectroscopy of the Thalamus in Patients with Chronic Neuropathic Pain after Spinal Cord Injury. AJNR Am J Neuroradiol. 2002; 23: 901–905. Available: http://www.ajnr.org/content/23/6/901.short. PMID: 12063213

Cerebral Cortex October 2010;20:2333–2347
doi:10.1093/cercor/bhp310
Advance Access publication January 18, 2010

Serotonin 3A Receptor Subtype as an Early and Protracted Marker of Cortical Interneuron Subpopulations

Ksenija Vucurovic[1,2], Thierry Gallopin[1], Isabelle Ferezou[1], Armelle Rancillac[1], Pascal Chameau[3], Johannes A. van Hooft[3], Hélène Geoffroy[1], Hannah Monyer[4], Jean Rossier[1] and Tania Vitalis[1,2]

[1]CNRS-UMR 7637, Laboratoire de Neurobiologie, ESPCI ParisTech, 75005 Paris, France, [2]INSERM U616, Développement Normal et Pathologique du Cerveau, Hôpital de la Salpétrière, 75013 Paris, France, [3]University of Amsterdam, Swammerdam Institute for Life Sciences, Section Neurobiology, Center for Neuroscience, NL-1090 GB Amsterdam, The Netherlands and [4]Department of Clinical Neurobiology, Interdisziplinaeres Zentrum fuer Neurowissenschaften, University of Heidelberg, Heidelberg, Germany

Ksenija Vucurovic, Thierry Gallopin, and Isabelle Ferezou contributed equally.

Address correspondence to Tania Vitalis, CNRS-UMR 7637, Laboratoire de Neurobiologie, ESPCI ParisTech, 10 rue Vauquelin, 75005 Paris, France. Email: tania.vitalis@espci.fr.

To identify neocortical neurons expressing the type 3 serotonergic receptor, here we used transgenic mice expressing the enhanced green fluorescent protein (GFP) under the control of the 5-HT_{3A} promoter (5-HT_{3A}:GFP mice). By means of whole-cell patch-clamp recordings, biocytin labeling, and single-cell reversed-transcriptase polymerase chain reaction on acute brain slices of 5-HT_{3A}:GFP mice, we identified 2 populations of 5-HT_{3A}-expressing interneurons within the somatosensory cortex. The first population was characterized by the frequent expression of the vasoactive intestinal peptide and a typical bipolar/bitufted morphology, whereas the second population expressed predominantly the neuropeptide Y and exhibited more complex dendritic arborizations. Most interneurons of this second group appeared very similar to neurogliaform cells according to their electrophysiological, molecular, and morphological properties. The combination of 5-bromo-2-deoxyuridine injections with 5-HT_{3A} mRNA detection showed that cortical 5-HT_{3A} interneurons are generated around embryonic day 14.5. Although at this stage the 5-HT_{3A} receptor subunit is expressed in both the caudal ganglionic eminence and the entopeduncular area, homochronic in utero grafts experiments revealed that cortical 5-HT_{3A} interneurons are mainly generated in the caudal ganglionic eminence. This protracted expression of the 5-HT_{3A} subunit allowed us to study specific cortical interneuron populations from their birth to their final functional phenotype.

Keywords: development, GABA, 5-HT_{3A}, NPY, VIP

Introduction

The cerebral cortex is the main integrative center of higher-order cognitive functions. It processes information through a complex neuronal network comprising efferent excitatory pyramidal cells and GABAergic inhibitory interneurons. Although they represent a minority of cells in the cortex, interneurons are key coordinators of intercellular communications and serve a crucial role in modulating neuronal output via the release of γ-aminobutyric acid (GABA) and neuropeptides (Baraban and Tallent 2004). The intrinsic properties of these neurons are highly diverse, suggesting the existence of distinct classes of interneurons exerting specific functions within the cortical network. Indeed, cortical interneurons are typically described and classified according to their morphological, physiological, and molecular characteristics, and to their connectivity (DeFelipe 1993; Cauli et al. 1997; Gupta et al. 2000; Kawaguchi and Kondo 2002; Ascoli et al. 2008). Interestingly, the diversity of cortical interneurons appears to rely on differential developmental ontogeny that is becoming another obvious criterion of their classification and could help to understand their functional specificity.

In rodents, unlike in humans or primates (Letinic et al. 2002), telencephalic interneurons mainly derive from the anlagen of the basal telencephalon (Corbin et al. 2001; Marín and Rubenstein 2001). In vitro studies of cortical interneurons migration (Lavdas et al. 1999; Wichterle et al. 1999) and fate-mapping experiments (Xu et al. 2003) have shown that the ganglionic eminences (lateral [LGE], medial [MGE], and caudal [CGE]) are the principal sources of cortical interneurons (Nery et al. 2002; Xu et al. 2003). Previous reports have also indicated the contribution of several other regions such as the entopeduncular area (AEP, Anderson et al. 2001) and the preoptic area (Gelman et al. 2009), albeit little is known about their potential to generate distinct telencephalic interneurons. Compelling evidence is suggesting that the commitment of 1 interneuron subtype is linked to its birth date and location within a particular region of the basal telencephalon. Indeed, in vivo fate-mapping experiments suggest that cortical parvalbumin (Parv)- and somatostatin (SOM)-expressing subtypes of interneurons arise mainly from the MGE/AEP, whereas a large proportion of interneurons containing vasoactive intestinal peptide (VIP) and/or calretinin (CR) are predominantly generated in the CGE (Nery et al. 2002; Butt et al. 2005).

In the telencephalon, like in the spinal cord, unique combinations of transcription factors expressed by progenitor cells specify the identity of each class of interneurons that derive from individual progenitor domains (Jessell 2000; Schuurmans and Guillemot 2002). Most transcription factors are turned off in part or entirely at postnatal stages (such as Lhx6 or Nkx2.1) when interneurons are mature and express neurochemical markers generally used for their classification (Cobos et al. 2006). So far, only few molecular markers have been identified as continuously expressed by a distinct subtype of interneurons from the embryonic period to adulthood. By using bacterial artificial chromosome (BAC) transgenic mice expressing enhanced green fluorescent protein (GFP) under the control of the 5-HT_{3A} promoter (5-HT_{3A}) and homochronic in utero grafts of 5-HT_{3A}:GFP+ cells, we provide evidence that the 5-HT_{3A} receptor is protractedly expressed from early postmitotic stages by 2 subtypes of cortical interneurons exhibiting distinctive morphological, molecular, and physiological properties.

Materials and Methods

Animals

Animal procedures were conducted in strict compliance with approved institutional protocols and in accordance with the provisions for animal care and use described in the European Communities Council directive of 24 November 1986 (86-16-09/EEC). The day of vaginal plug detection was counted as embryonic day (E) E 0.5. Two transgenic mouse lines expressing the enhanced GFP under the control of the 5-HT_{3A} (5-HT_{3A}:GFP) obtained by using modified BACs were used: The first one has been generated in H. Monyer's laboratory (Inta et al. 2008), was maintained under the C57/Bl6 background, and was mainly used to assess the feasibility of the project. The second transgenic mouse line Tg(Htr3a-GFP)1Gsat was provided by the GENSAT Consortium (Rockeffeler University-GENSAT Consortium; Heintz 2004) and was maintained under the Swiss background. Both strains gave identical expression patterns in cortical areas and match mRNAs expression. Genitors were polymerase chain reaction (PCR) genotyped for GFP insertion using the primers (from 5′ to 3′): ATGGTGAGCAAGGGC-GAGGAGCT and GCCGAGAGTGATCCCGGCGGCGGT. Embryos were phenotyped by macroscopic observation under fluorescent optics. Characterization of juvenile 5-HT_{3A}-expressing interneurons was performed using the Tg(Htr3a-GFP) mouse line provided by GENSAT. Both the GENSAT and Hannah Monyer's mouse lines were used for analysis of embryonic GFP expression and grafting experiments and gave similar results.

Radioactive In Situ Hybridization

5-HT_{3A} cRNA probe corresponded to the full-length domain of the protein. The plasmid was linearized with *Bam*H1 for antisense RNA synthesis by T7 polymerase and with *Eco*RI for sense RNA synthesis by T3 polymerase. The *Dlx2* cRNA probe (*Hin*d3 linearization, T7 polymerization) was also used. The transcription was carried out using the Promega kit, and probes were labeled with ^{35}S-UTP (>1000 Ci/mmol; Amersham). Hybridization was performed on fresh frozen brain sections (15 μm thick) as previously described (Fontaine and Changeux 1989). Slides were dipped in photographic emulsion (NTB2, Kodak) and exposed for about 5–10 days. Emulsions were then developed, and sections were Nissl counterstained (0.25 % thionin solution).

The laminar density of cells expressing the 5-HT_{3A} mRNA was estimated at P25. Quantifications of 5-HT_{3A}+ cells were performed at the level of the primary somatosensory cortex, in 500-μm-wide cortical strips (data are expressed as percentage). Three adjacent sections of at least 5 independent preparations were used.

Immunohistochemistry

Neuronal populations expressing 5-HT_{3A}:GFP were analyzed at embryonic (E13/E13.5 [n = 8], E14.5 [n = 12], E15.5 [n = 8], E16.5 [n = 12], E17.5 [n = 10], and E18.5 [n = 10]), and postnatal stages (P0 [n = 14], P1 [n = 8], P3 [n = 10], P5 [n = 6], P15–P16 [n = 10], and P25 [n = 14]). Embryos collected by cesarean section after cervical dislocation of the dam were placed overnight in 4% paraformaldehyde in 0.1 M phosphate buffer (PB), pH 7.4 (PFA). Embryos were cryoprotected, embedded into gelatine (7%)–sucrose (10%), frozen into isopentane (−40°C) and sectioned coronally (20 μm) with a cryostat. Postnatal animals were deeply anesthetized with an intraperitoneal (IP) injection of pentobarbital (150 mg/kg body weight) and perfused transcardially with 4% PFA. Postnatal brains were cryoprotected in 30% sucrose and cut on a freezing microtome (35 μm). For immunofluorescence, sections were incubated overnight at 4 °C with the following antibodies diluted in saline PB (PBS): rabbit anti-CR (1:8000, Swant), rabbit anti-Parv (1:1000; Swant), rabbit anti-SOM (1:500; a kind gift of Dr Epelbaum), rabbit anti-NPY (neuropeptide Y) (1:500, Amersham), rabbit anti-VIP (1:800, Incstar), rabbit anti-Nr2F2 (1:200; Acris GmbH), rabbit anti-GABA (1:5000; Sigma), rabbit anti-GFP (1:1000, Molecular Probes), mouse anti-tuj1 (1:2000, Babco), or mouse anti-Parv (1:200, Sigma). After washing in PBS, sections were incubated with Cy3-conjugated goat antirabbit or/and antimouse antibodies (1:200; Jackson Laboratory). Sections were rinsed in PB, mounted in Vectashield (Vector) containing 4′,6′-diamidino-2-phénylindole (Dapi) and were observed with a fluorescent microscope (Leica, DMR). Images were acquired with a Coolsnap camera (Photometrics, Tucson, AZ) and analyzed with the Metamorph software (Molecular Devices, Foster City, CA).

The laminar density of cells expressing GFP was estimated at P25. Quantifications of GFP:5-HT_{3A}+ cells were performed at the level of the primary somatosensory cortex, in 500-μm-wide cortical strips (data are expressed as percentage). Three adjacent sections of at least 5 independent preparations were used.

The proportion of green fluorescent cells labeled for GABA at E14.5 (n = 9) in the low intermediate zone (LIZ) was estimated at 2 different levels, 1 rostral including MGE and 1 caudal including CGE. For each case, data obtained from 3 adjacent sections were averaged.

Preparation of Juvenile Brain Slices and Electrophysiological Recordings of 5-HT_{3A}-Expressing Cells

5-HT_{3A}:GFP transgenic mice (postnatal days 14–18) were decapitated, brains were quickly removed and placed into cold (~4 °C) artificial cerebrospinal fluid (ACSF) containing (in mM): 110 choline chloride, 11.6 Na-ascorbate, 7 $MgCl_2$, 2.5 KCl, 1.25 NaH_2PO_4, and 0.5 $CaCl_2$, continuously bubbled with 95%O_2–5%CO_2. Coronal brain slices (300 μm thick) containing the somatosensory cortex were cut with a vibratome (VT1200S; Leica, Nussloch, Germany), and transferred to a holding chamber containing ACSF (in mM): 126 NaCl, 2.5 KCl, 1.25 NaH_2PO_4, 2 $CaCl_2$, 1 $MgCl_2$, 26 $NaHCO_3$, 20 glucose, and 1 kynurenic acid (nonspecific glutamate receptor antagonist, Sigma), constantly oxygenated (95% O_2/5% CO_2) and held at room temperature.

Individual slices were placed in a submerged recording chamber and perfused (1–2 mL/min) with oxygenated ACSF (in the absence of kynurenic acid). Patch micropipettes pulled from borosilicate glass capillaries (3–5 MΩ) were filled with 8 μL of autoclaved reverse transcription polymerase chain reaction (RT-PCR) internal solution (in mM): 144 K-gluconate, 3 $MgCl_2$, 0.5 ethylene glycol tetraacetic acid, 10 4-(2-hydroxyethyl)-1-piperazineethanesulfonic acid (pH 7.2, 285/295 mOsm), and 3 mg/mL biocytin for intracellular labeling. Neurons were visualized in the slice using infrared transmitted light with Dodt gradient contrast optics or epifluorescence illumination, using a Zeiss (Axioskop 2FS) microscope equipped with a ×40 water-immersion objective. Images were captured with CoolSnap HQ2 CCD camera (Photometrics) controlled by Image-Pro 5.1 software (Media Cybernetics Inc., San Diego, CA). Just before breaking the seal, GFP expression in the targeted cell was rechecked by fluorescence detection. Whole-cell recordings in current-clamp mode were performed at room temperature using a patch-clamp amplifier (Multiclamp 200B, Molecular Devices). Data were filtered at 5 kHz and digitized at 50 kHz using an acquisition board (Digidata 1322A, Molecular Devices) attached to a computer running pCLAMP 9.2 software package (Molecular Devices). All membrane potentials were not corrected for liquid junction potential.

For each recorded neuron, 28 electrophysiological parameters were quantified using custom written routines running within IgorPro (Wavemetrics). The detailed procedures are described in the Supplementary Methods S1.

Single-Cell Reverse Transcription Polymerase Chain Reaction (scRT-PCR)

At the end of the recording, the cell's cytoplasm was aspirated into the recording pipette while maintaining the tight seal. Then, the pipette was removed delicately to allow outside-out patch formation. Next the content of the pipette was expelled into a test tube, and reverse transcription (RT) was performed in a final volume of 10 μL as described previously (Lambolez et al. 1992). The scRT-PCR protocol was designed to detect simultaneously the expression of the 2 isoforms of glutamic acid decarboxylase (*GAD65* and *GAD67*), 3 genes encoding for calcium-binding proteins: calbindin D28k (CB), CR, and Parv, 3 neuropeptides NPY, SOM, and VIP, 2 transcription factors (Lhx6 and Nr2F2), and the protein reelin implicated in neuronal migration and morphology (Chameau et al. 2009). The next 2 steps of PCR were performed essentially as described previously (Ruano et al. 1995). The cDNAs present in 10 μL of the RT reaction were first simultaneously amplified by using all of the primer pairs described in Supplementary Table S1 (for

each primer pair, the sense and antisense primers were positioned on 2 different exons). GoTaq polymerase (2.5 U; Promega, Madison, United States) and 20 pmol of each primer were added to the buffer supplied by the manufacturer (final volume, 100 μL), and 21 cycles (94 °C for 30 s, 60 °C for 30 s, and 72 °C for 35 s) of PCR were run. Second rounds of amplification were performed using 2 μL of the first PCR product as template. In this second round, each cDNA was amplified individually with a second primer pair internal to the pair used in the first PCR, excepted for *Nr2F2* (nested primers, see Supplementary Table S1). Thirty-five PCR cycles were performed as described earlier (Cauli et al. 1997). Then, 10 μL of each individual PCR product were run on a 2% agarose gel using 100-bp ladders (Promega) as molecular weight marker and stained with ethidium bromide. All the transcripts were detected from 500 pg of neocortical RNA using this protocol (data not shown). The sizes of the PCR-generated fragments were as predicted by the mRNA sequences (see Supplementary Table S1).

Intracellular Labeling and Morphological Reconstructions

Slices containing recorded neurons filled with biocytin were fixed overnight at 4 °C in 4% PFA. The morphology of the recorded neurons was investigated by histochemical labeling of intracellular biocytin with diaminobenzidine (DAB) by using the ABC elite kit (Vector Laboratories, Burlingame, CA). After blocking endogenous peroxidase with 0.3% H_2O_2 in PB 0,1 M for 15–30 min, slices were rinsed in PB (4× 10 min), permeabilized in 2% Triton X-100 in PBS for 1 h, and incubated in AB diluted 1:200 in PBS and 1% Triton X-100 for 2 h. Slices were then washed in PBS (6× 10 min). For the visualization of the stain, the sections were incubated with the DAB reagent for ABC (elite kit, Vector) containing 0.05% DAB and 0.01% H_2O_2 in PBS. The reaction was monitored under a dissecting microscope and stopped by rinsing in PBS (4× 10 min) when the cell body and dendritic processes were clearly visible. The slices were then mounted in 50%PBS–50%glycerol, coverslipped, and sealed with nail polish. Biocytin-filled neurons were visualized, traced, and digitally reconstructed using the Neurolucida software (MicroBrightField, Bioscience Europe, Magdeburg, Germany) with a ×100 oil-immersion objective (Leica). The morphological parameters, quantified as mean ± standard deviation (SD) were compared for significance using Student's test. The average tortuosity of the neurons was calculated as the ratio between the distance along a process over the straight line distance, the smallest tortuosity possible being 1 for a straight path. The spatial distribution of the dendritic processes from the centroid of the cell body was studied using Wedge analysis. For this purpose, the *xy* plane was divided into 12 equiangular wedges. The total dendritic length in each wedge was then quantified (taking into account the *z* information) and displayed as a round directional histogram. The total length over all wedges corresponds to the total length of the neuronal dendritic arborization. Finally, in order to quantify the orientation of the analyzed neurons, the total dendritic length contained in the 4 most horizontally oriented wedges was divided by the length enclosed in the 4 most vertically oriented wedges. This ratio, called here "equipolarity," would be equal to 1 for a perfectly radially oriented dendritic arbor and decreases with more vertically oriented processes.

Electrophysiological Statistical Analysis

All data are presented as mean ± SD unless otherwise stated. Mann–Whitney *U* test was employed to compare electrophysiological properties between cell types. *P* values of $\leqslant 0.05$ were considered statistically significant. To classify 5-HT_{3A}-expressing neocortical neurons sampled without a priori knowledge, unsupervised clustering was performed using 28 electrophysiological parameters (see Supplementary Methods S1) and the laminar location determined by infrared videomicroscopy. For neurons located at the border of layers I–II and II–III, the laminar location was digitized by 1.5 and 2.5, respectively. After standardizing the data, cluster analysis was performed using squared Euclidean distances and Ward's method linkage rules (Ward 1963). Ward's clustering method has been used successfully by previous studies to define neuronal classes based on multiple electrophysiological, molecular, and/or morphological features (Tamas et al. 1997; Cauli et al. 2000; Karube et al. 2004; Dumitriu et al. 2006; Gallopin et al. 2006; Halabisky et al. 2006; Dávid et al. 2007; Andjelic et al. 2008; Helmstaedter et al. 2009; Karagiannis et al. 2009). Thorndike analysis of the critical threshold was conducted to suggest the likely number of different clusters in the data set (Thorndike 1953). Descriptive statistics and cluster analysis were calculated with Statistica v 6.0 (Statsoft, Tulsa, OK).

Birth Dating In Vivo

Pregnant females of the Swiss genetic background received a single 5-bromo-2-deoxyuridine (BrdU) injection (IP, 50 mg/kg; in 0.9% NaCl) at gestational days E11.5, E12.5, E13.5, E14.5, E15.5, or E16.5. Animals, aged P25, were anesthetized as described above and perfused transcardially with 4% PFA. Cryosections (17 μm thick) were first processed for in situ hybridization to reveal 5-HT_{3A} mRNA transcripts and then processed for immunocytochemistry to detect BrdU. Nonradioactive in situ hybridization was performed as described in Schaeren-Wiemers and Gerfin-Moser (1993) (products were purchased from Roche Diagnostics). Sense probes were used as control and did not show any labeling. Subsequently, sections were treated with 2 N HCl for 45 min, rinsed in 0.1 M PBS, pH 7.4, incubated during 1 h in PBS supplemented by normal goat serum (10%) and incubated overnight with anti-BrdU (1:100, Progen, GmbH, Germany) in PBS. After washing, sections were incubated 2 h in Alexa Fluor 488 goat antimouse antibody (1:200, Invitrogen) and were mounted in Vectashield containing Dapi. To estimate the number of BrdU-labeled cells among the 5-HT_{3A}-expressing population, a least 3 litters were analyzed per time point, and at least 2 animals per litter were processed for histology. For each anatomical area selected, 5 adjacent sections were analyzed per case. On each section, the number of 5-HT_{3A}+ neurons heavily labeled for BrdU (defined as having >50% of the nucleus immunolabeled; Gillies and Price 1993) was estimated using a ×40 objective. The number of double-labeled cells was expressed as percentage of cells double labeled over the 5-HT_{3A}+ population. In the primary somatosensory cortex, the total number of cells per radial sector of (700-μm width) was pulled to produce the graphs.

In Utero Cells Transplantation

Homochronic transplantations were performed using E13/E13.5 and E14/E14.5 donor and host embryos. Donor embryos were collected into cold PBS following cervical dislocation of the pregnant mouse. Embryonic heads were dissected into cold L15 medium and embedded in 3% low-melting-point agarose (Sigma) in L15 medium. From these blocks, 270–300-μm-thick coronal sections were obtained using a Leica vibroslicer (Leica VTS1000) and were collected into cold L15 medium. CGE and AEP/preoptic (AEP/Po) explants were dissected out of the sections, collected into L15 medium, and kept on ice until transplantation. CGE or AEP/Po were mechanically dissociated prior transplantation. In addition, some experiments were performed using 5-HT_{3A}:GFP+ cells sorted by flow cytometry (see Supplementary Method S2). For transplantation, time mate pregnant OF1 mice (Charles River) were anaesthetized with Xylazine–Ketamine (1 mg/kg/IP; 10 mg/kg/IP, in sterile saline solution). Uterine horns were exposed, and each embryo was manipulated under the uterine wall until position of the lateral ventricle was discernable. A glass micropipette (50 μm) containing an average of 5×10^4–10^5 cells in L15 stained with blue trypan (in 1 μL of solution) was introduced through the placenta in the ventricle (lateral or third) of each embryo. Cell transfer was achieved using mouth-control tubing attached to the pipette. The procedure was repeated for each embryo except for the most proximal and distal embryos. Injections were performed using E13/E13.5 5-HT_{3A}:GFP (CGE: $n = 6$ litters, $n = 18$ hosts; AEP/Po: $n = 5$ litters, $n = 20$ hosts) or using E14/E14.5 5-HT_{3A}:GFP donors (for cell suspension: CGE: $n = 10$ litters, $n = 43$ hosts; AEP $n = 12$ litters, $n = 40$ hosts, and for FACsorted cells: $n = 2$ litters, $n = 5$ hosts). After surgical recovery, animals were returned to their cages, and pups were reared until postnatal days 16–25 (P16–P25). Animals were processed as described above.

The distribution of 5-HT_{3A}:GFP+ grafted cells was determined on coronal sections counterstained with bis-benzimide. Quantification of GFP+ cells in the somatosensory cortex was carried out under a fluorescent microscope (Leica, DMR) using a 250 000-μm^2 area under a ×20 objective lens or a 66 000-μm^2 area under a ×40 objective lens. The laminar distribution of GFP+ cells was quantified at the level of the primary somatosensory area, in 500-μm-wide cortical strips (data obtained from 3 adjacent sections of at least 7 animals and expressed as

mean ± standard error of the mean). The proportion of GFP+ grafted cells labeled for Parv, SOM, CR, VIP, or NPY was estimated in a cortical strip (700-μm width) in the primary somatosensory area and was expressed as percentage of double-labeled cells over the GFP+ population (data obtained from 3 adjacent sections of at least 12 animals from 5 different experiments).

Results

Distribution and Neurochemical Phenotype of Telencephalic 5-HT$_{3A}$-Expressing Neurons in Adult Wild-Type and Transgenic 5-HT$_{3A}$:GFP Mice

The 5-HT$_{3A}$ receptor expression pattern in the adult wild-type mice telencephalon was first studied by in situ hybridization (Fig. 1*A–C*). The distribution of 5-HT$_{3A}$ mRNA transcripts closely mirrored that previously reported in the rat (Tecott et al. 1993; Morales and Bloom 1997). The 5-HT$_{3A}$ mRNA was detected in the cortex, olfactory bulb, hippocampal formation, amygdaloid complex, septum, and hypothalamus. Within the neocortex, 5-HT$_{3A}$ mRNA-expressing cells were preferentially located in supragranular layers I–III and to a lesser extent in infragranular layers V–VI (Fig. 1*A–C*). This pattern of expression was observed from the frontal to the occipital regions of the neocortex. The detailed laminar distribution of 5-HT$_{3A}$-expressing cells within the primary somatosensory cortex is illustrated in Figure 1*B*.

To further study 5-HT$_{3A}$-expressing neurons, we decided to use BAC transgenic mice where the 5-HT$_{3A}$ expression is accurately reported by GFP (Heintz 2001). Two 5-HT$_{3A}$:GFP BAC mouse lines were tested of which 1 was generated in H.

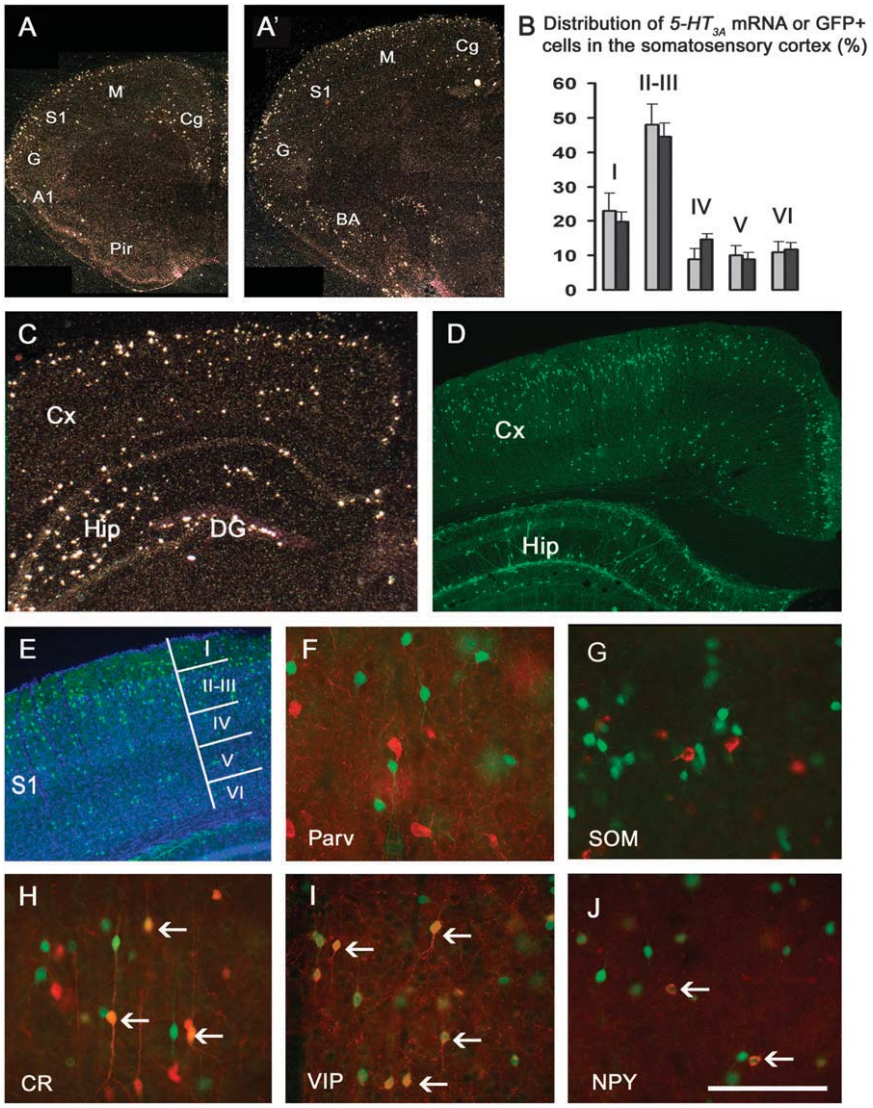

Figure 1. Expression of 5-HT3A in the adult telencephalon. (*A*, *A′*, *C*) Coronal sections from an adult wild-type mouse showing the distribution of 5-HT$_{3A}$ transcripts. (*B*) Graph showing the density of both 5-HT$_{3A}$ mRNA-expressing cells from adult wild-type animals (gray bars) and 5-HT$_{3A}$:GFP+ cells from transgenic 5-HT$_{3A}$:GFP mice (black bars) in the different layers of the somatosensory cortex. Data are means ± standard error of the mean (SEM). (*C*,*D*) Sections from identical stereotaxic levels showing "a similar location of both 5-HT$_{3A}$ mRNA-expressing cells from a wild type" mouse (*C*) and GFP fluorescent cells from a 5-HT$_{3A}$:GFP mouse (*D*). (*E*) Coronal section of a 5-HT$_{3A}$:GFP mouse counterstained with Dapi (blue) showing the preferential location of 5-HT$_{3A}$-expressing cells in supragranular layers. Cortical layers are indicated. (*F–J*) Expression of 5-HT$_{3A}$:GFP (green) is restricted to subpopulations of interneurons (red). (*F*,*G*) Overlays showing the lack of Parv (*F*) or SOM (*G*) expression in GFP+ cells. (*H–J*) Overlays showing the colocalization of GFP with CR (*H*), VIP (*I*), or NPY (*J*). A1, agranular insular cortex; BA, basolateral amygdaloid nucleus; Cg, cingulate cortex area; Ctx, cerebral cortex; G, gustatory cortex area; Hip, hippocampus; M, motor cortex area; Pir, piriform cortex; S1, somatosensory cortex area; Scale bar: (*A–A′*) 1 mm; (*C*,*D*) 700 μm; (*E*) 500 μm; and (*F–J*) 100 μm.

Monyer's laboratory (Inta et al. 2008) and the other was provided by GENSAT (see animals in the Materials and Methods section). Both mouse lines showed a similar distribution of cortical 5-HT_{3A}:GFP+ neurons, which also mirrored the expression pattern of 5-HT_{3A} transcripts observed in wild-type animals (Fig. 1*C–E*). The laminar density of both GFP immunoreactive cells from 5-HT_{3A}:GFP transgenic mice and 5-HT_{3A} mRNA-expressing cells from wild-type animals, quantified within the primary somatosensory cortex indeed revealed similar distribution profiles (Fig. 1*B*). In situ hybridization performed on 5-HT_{3A}:GFP+ animals confirmed the expression of 5-HT_{3A} mRNA in GFP immunoreactive cells (Supplementary Fig. S1) and Western blot analysis showed that GFP expression does not alter 5-HT_{3A} protein synthesis (Supplementary Fig. S2).

The observation of 5-HT_{3A}:GFP+ cells clearly revealed a nonpyramidal morphology, suggesting that the 5-HT_{3A} receptor is expressed by a subpopulation of GABAergic INs in the mouse neocortex, similarly to what has been observed in the rat (Morales and Bloom 1997; Ferezou et al. 2002; see also Jakab and Goldman-Rakic 2000 for comparison with primate cerebral cortex). Hence, we next performed immunohistochemical analyses to assess the expression of neurochemical markers usually used to classify INs subtypes such as CR, VIP, Parv, SOM, and NPY (Kawaguchi and Kondo 2002). We found that in all telencephalic regions, 5-HT_{3A}:GFP+ INs did not express Parv or SOM (Fig. 1*F,G*) whereas CR, VIP, and NPY were frequently detected (Fig. 1*H–J*). Within the primary somatosensory cortex, the proportion of cells in which GFP colocalized with 1 of the 3 markers was layer dependent (see Supplementary Table S2). Indeed, VIP/GFP+ and CR/GFP+ INs were preferentially located in layers II–III whereas NPY/GFP+ INs were distributed in all cortical layers.

These results therefore indicate that the 5-HT_{3A} expression is likely to characterize specific subtypes of cortical interneurons.

Characterization and Classification of Cortical 5-HT_{3A}-Expressing Interneurons in the Juvenile Somatosensory Cortex

To further describe the electrophysiological, molecular, and morphological properties of 5-HT_{3A}-expressing cortical interneurons, a sample of GFP-positive cells from layer I ($n = 12$) and II–III ($n = 41$) was analyzed by combining patch-clamp recordings, scRT-PCR and biocytin labeling on somatosensory cortex slices from 5-HT_{3A}:GFP mice (P14–P17).

The scRT-PCR protocol was designed to detect mRNAs encoding for 8 molecular markers commonly used to define subpopulations of cortical neurons: GAD65, GAD67, CB, Parv, CR, NPY, VIP, and SOM. In addition, we assessed the expression of 3 developmental markers known to be involved in the maturation of neocortical neurons: Reelin (Chameau et al. 2009), Lhx6 (Liodis et al. 2007), and Nr2F2 (Kanatani et al. 2008). In this report, cells positive for GAD65 and/or GAD67 are denoted as GAD positive. Only cells expressing *GAD* and at least 1 gene encoding for 1 neuropeptide or 1 calcium-binding protein were analyzed.

Neurons expressing 5-HT_{3A} were classified using unsupervised cluster analyses based on their laminar location and 28 electrophysiological parameters (see Supplementary Methods S1) adopting Petilla terminology (Ascoli et al. 2008; Karagiannis et al. 2009). On the basis of the Thorndike threshold, this multifactorial analysis segregated 5-HT_{3A}-expressing neurons into 2 clusters of cells corresponding to branches a and b in the tree diagram (Fig. 2). The molecular profile of these clusters has been established by plotting the percentage of neurons expressing given molecular markers for each group. Each cluster was then named according to its prominent characteristics: the high NPY expression level for cluster a (NPY-cluster, $n = 31$) and the large occurrence of VIP expression in cluster b (VIP-cluster, $n = 22$). Expression of *Lhx6* was almost never detected on both VIP- and NPY-cluster (0% and 6%, respectively). Indeed, *Lhx6* is known to be associated with other subtypes of interneurons expressing Parv or SOM (Liodis et al. 2007).

The laminar distribution of these interneurons appears to be different between the 2 clusters because all the cells recorded in the layer I ($n = 12$) belong to the NPY-cluster (in addition to 19 layers II–III NPY neurons), whereas all the VIP-cluster neurons were located in the layers II–III ($n = 22$). As expected by the targeting of our recordings toward GFP fluorescent neurons,

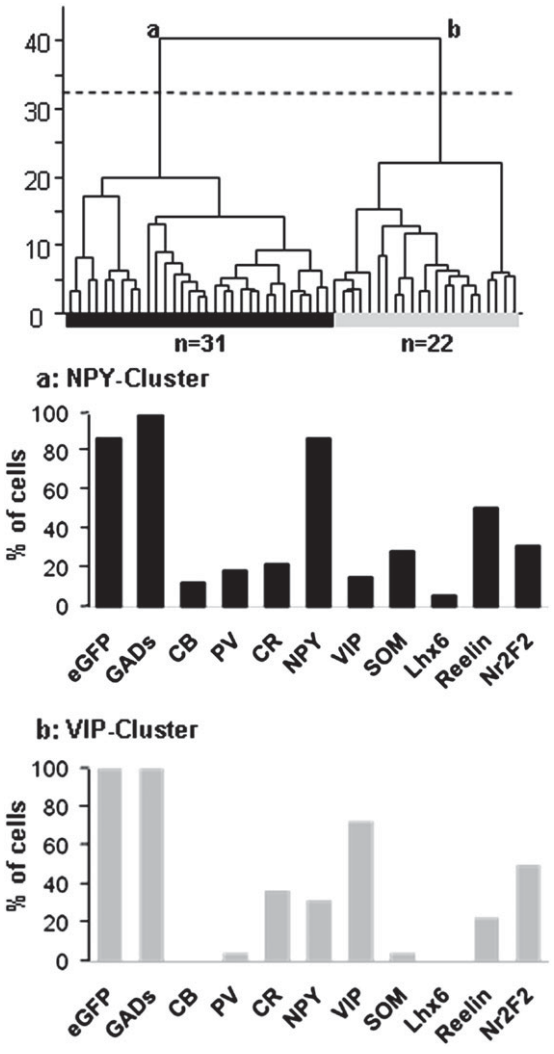

Figure 2. Unsupervised cluster analysis applied to GFP-positive neocortical neurons. The *x* axis represents individual cells, and the *y* axis represents the average within-cluster linkage distance. Distances were calculated on the basis of the laminar location of the cells, in addition to 28 electrophysiological parameters (see Supplementary Methods S1). On the basis of the Thorndike threshold (dotted line), this analysis disclosed 2 groups of cells (corresponding to branches a and b): the NPY-cluster (black) and the VIP-cluster (gray). Histograms show the distribution of molecular markers within each cluster.

eGFP mRNA was detected in a large majority of the cells (in 100% of the VIP-cluster cells and in 87% of the NPY-cluster cells). Representative examples of interneurons from each cluster are presented in Figure 3 and Supplementary Fig. S3.

The NPY-cluster of 5-HT$_{3A}$ Interneurons

The major molecular characteristics of neurons in the NPY-cluster were the high occurrence of *NPY* (n = 27/31, 87%), *reelin* (52%), and *Nr2F2* (32%). These neurons expressed to a lower extent mRNAs for *SOM* and *CR* (29% and 23%, respectively). mRNAs for *Parv*, *VIP*, and *CB* were slightly present in this group (19%, 16%, and 13%, respectively). Neurons of the NPY-cluster were characterized by distinctive electrophysiological properties (see Supplementary Methods S1), in particular when depolarized just above the threshold of action potential generation (see example illustrated in Fig. 3*A*1). Indeed, the main electrophysiological hallmarks of this group of cells were a high rheobase, a long latency of action

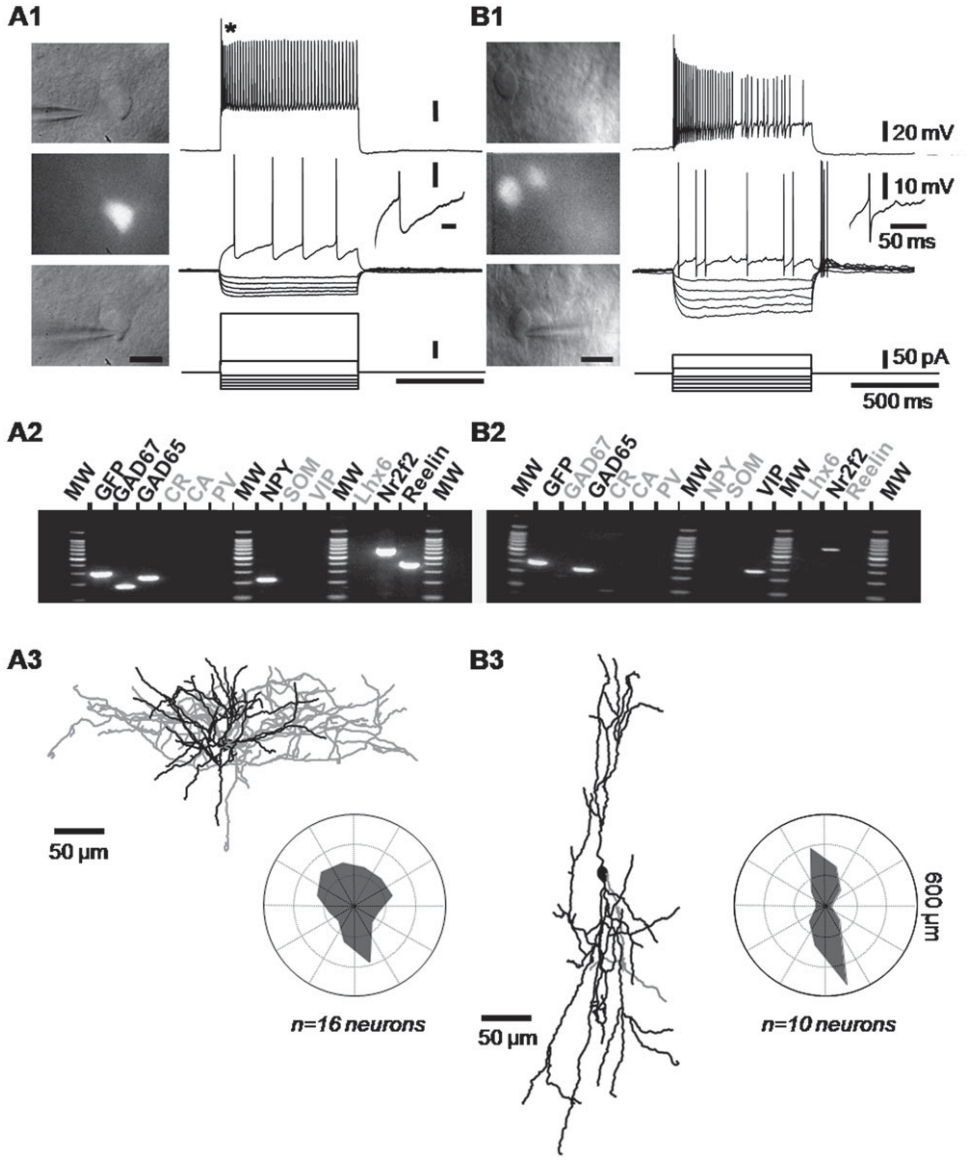

Figure 3. Electrophysiological, molecular and morphological properties of 5-HT$_{3A}$-expressing interneurons of the NPY-cluster and VIP-cluster. (*A*1) The electrophysiological behavior of a neuron belonging to the NPY-cluster was recorded using whole-cell patch-clamp recording in current-clamp mode, in response to current pulses injections (lower traces). Suprathreshold and just above the threshold responses are illustrated in the upper and medium traces, respectively. Just above threshold current induced the delayed firing of action potentials. Application of a larger depolarizing current induced a marked frequency adaptation with pronounced amplitude accommodation (upper trace, asterisk). The right inset shows the repolarization phase of the first action potential. Note the monophasic aspect of the after hyperpolarization. The Infrared and epifluorescence images of the same neuron have been taken just before the recording (top and middle panels) and during the recording (bottom panel) (scale bar 10 µm). (*A*2) Agarose gel showing the expression of *GFP*, *GAD67*, *GAD65*, *NPY*, *Nr2F2*, and *Reelin*. (*B*1) Voltage traces recorded from a VIP-cluster neuron in response to current pulses (lower traces). The right inset details the complex repolarization phase of the first action potential. On the left panels, the infrared and epifluorescence images of the same cell were taken just before and during the recording (scale bar: 10 µm). (*B*2) Agarose gel showing the expression of *GFP*, *GAD65*, *VIP*, and *Reelin*. (*A*3,*B*3) Neurolucida reconstructions of the neurons shown in (*A*1,*B*1), respectively. Axons are represented in gray, whereas somata and dendrites are illustrated in black. Cells of the NPY-cluster show characteristics of "neurogliaform" neurons: the soma of these cells is rather multipolar with smooth dendrites and the axon is densely distributed within and around the dendritic arborization (*A*3). VIP-positive cells are characterized by their bipolar, vertically oriented main dendrites and axon (*B*3). Polar histograms illustrate the results of the Wedge analysis for each cluster of cells. The dendritic arbors organization around the centroid of the cells bodies was quantified by plotting the averaged dendritic length for each equiangular wedge.

potentials discharge, a weak acceleration of their firing rate, and low minimal frequency (Table 1). These electrophysiological features indicated a slow spiking behavior near threshold. The large majority of neurons belonging to the NPY-cluster (90%) fired action potentials with monophasic after hyperpolarizations (AHPs) resulting in the absence of after depolarizing potential component (ADP). At higher stimulation intensities, these cells displayed a frequency adaptation and a pronounced amplitude accommodation.

Of the 31 recorded neurons belonging to the NPY-cluster, 16 were analyzed for their morphological properties following their histochemical staining and 3D reconstruction (see example in Fig. 3*A*3). Indeed, neurons that were not sufficiently well stained, located too deep into the slice to focus properly, or too superficial, presenting truncated processes, had to be discarded. In many cases, we had difficulties in recover the entire axonal arborisation of the reconstructed neurons. Indeed, high sc-RT-PCR efficiency requires harvesting the cytoplasm of GFP+ cells within 10 min, and this is not optimal for biocytin labeling (Karagiannis et al. 2009). We therefore focus our observations on the neuronal somatodendritic features of the interneurons. Although the NPY-cluster regrouped neurons presenting heterogeneous aspects, the most prominent traits of this group are a relatively high number of primary dendrites emerging from the soma (7.9 ± 4.5), a dendritic arborization radially organized (equipolarity = 0.98 ± 0.10, see Wedge analysis presented in Fig. 3*A*3), and a notable tortuosity of the processes (1.4 ± 0.1). In the following part of this paper, we will refer to them as NPY multipolar/neurogliaforms.

The VIP-cluster of 5-HT$_{3A}$ Interneurons

Unsupervised clustering discriminated another group of cells characterized by a high occurrence of *VIP* mRNA (n = 16/22, 73%). *CR* (36%), *NPY* (32%), and *Nr2F2* (50%) were also frequently expressed in this group whereas *CB*, *Parv*, and *SOM* mRNAs were rarely detected (Fig. 2). Neurons of the VIP-cluster exhibit 2 types of firing behavior, adapting (n = 15/22, 68%) or bursting (n = 7/22, 32%) as described previously (Cauli et al. 1997; Karagiannis et al. 2009). In comparison with the NPY-cluster neurons, neurons of this cluster exhibited more depolarized resting membrane potential and lower rheobase, suggesting that they should be electrically more excitable (Table 1). Cells of the VIP-cluster exhibited the highest input resistance and membrane time constant of our sample. They fired action potentials with larger spike amplitude and shorter spike latency, exhibiting in some cases a biphasic repolarization phase. Indeed, the first 2 action potentials of adapting VIP were followed by a first AHP component, an ADP, and a late AHP component (n = 8/15). However, this repolarization behavior was almost never observed in bursting-VIP cells (n = 2/7).

Of the 22 recorded neurons belonging to the VIP-cluster, 10 were analyzed for their somatodendritic morphological properties (see example in Fig. 3*B*3). These interneurons presented less primary dendrites emerging from the soma than NPY-cluster neurons (4.5 ± 2.1 vs. 7.9 ± 4.5, respectively), although this difference was not significant. The most striking particularity of these cells was the bipolar organization of their dendritic tree (equipolarity = 0.18 ± 0.25, see the wedge diagram in Fig. 3*B*3). Finally, the dendritic processes of the VIP-cluster neurons are less tortuous than those of the NPY-cluster neurons (1.25 ± 0.11 vs. 1.39 ± 0.13, P = 0.01).

Birth-Dating Analysis of Cortical 5-HT$_{3A}$-Expressing Interneurons

Having characterized 2 types of cortical interneurons expressing the 5-HT$_{3A}$ subunit, we next investigated their date of genesis. Although Inta et al. (2008) have reported that

Table 1
Electrophysiological properties of 5-HT$_{3A}$-expressing neocortical interneurons

Electrophysiological parameters	VIP-cluster (n = 22)	NPY-cluster (n = 31)	Electrophysiological parameters	VIP-cluster (n = 22)	NPY-cluster (n = 31)
(1) Resting potential (mV)	−55.98 ± 3.92	−60.5 ± 5.59	(15) First spike amplitude (mV)	83.82 ± 9.8	75.1 ± 9.72
	VIP-cluster << VIP-cluster			NPY-cluster << VIP-cluster	
(2) Input resistance (MΩ)	761.45 ± 306.46	391.92 ± 124.15	(16) Second spike amplitude (mV)	78.80 ± 8.86	70.6 ± 10.6
	NPY-cluster <<< VIP-cluster			NPY-cluster < VIP-cluster	
(3) Time constant (ms)	40.61 ± 19.53	25.65 ± 12.09	(17) First spike duration (ms)	0.95 ± 0.37	1.8 ± 0.53
	NPY-cluster << VIP-cluster			VIP-cluster <<< NPY-cluster	
(4) Membrane capacitance (pF)	56.94 ± 25.39	66.20 ± 25.52	(18) Second spike duration (ms)	0.99 ± 0.38	2.00 ± 0.52
	VIP-cluster — NPY-cluster			VIP-cluster < < < NPY-cluster	
(5) Sag index (%)	12.09 ± 7.83	5.84 ± 6.02	(19) Amplitude reduction (%)	5.78 ± 5.1	5.99 ± 6.98
	NPY-cluster << VIP-cluster			VIP-cluster — NPY-cluster	
(6) Rheobase (pA)	17.72 ± 9.22	64.83 ± 71.36	(20) Duration increase (%)	4.54 ± 2.69	11.43 ± 15.53
	VIP-cluster << NPY-cluster			VIP-cluster << NPY-cluster	
(7) First spike latency (ms)	133.00 ± 147.21	243.01 ± 235.14	(21) First spike, AHP max (mV)	−16.07 ± 4.1	−12.10 ± 3.89
	VIP-cluster — NPY-cluster			VIP-cluster << NPY-cluster	
(8) Adaptation (Hz/s)	−12.12 ± 21.59	4.1 ± 24.28	(22) Second spike, AHP max (mV)	−17.58 ± 3.47	−14.30 ± 3.25
	VIP-cluster << NPY-cluster			VIP-cluster << NPY-cluster	
(9) Minimal steady state frequency (Hz)	14.53 ± 11.21	7.42 ± 5.17	(23) First spike, AHP max latency (ms)	5.82 ± 1.40	15.2 ± 6.88
	NPY-cluster << VIP-cluster			VIP-cluster <<< NPY-cluster	
(10) Amplitude accommodation (mV)	0.88 ± 2.18	3.11 ± 0.83	(24) Second spike, AHP max latency (ms)	10.11 ± 14.63	16.3 ± 6.79
	VIP-cluster << NPY-cluster			NPY-cluster < < < VIP-cluster	
(11) Amplitude of early adaptation (Hz)	57.85 ± 34.81	46.73 ± 27.15	(25) First spike ADP (mV)	1.02 ± 1.72	0.1 ± 0.23
	VIP-cluster — NPY-cluster			VIP-cluster < NPY-cluster	
(12) Time constant of early adaptation (ms)	23.93 ± 9.21	33.92 ± 40.48	(26) Second spike ADP (mV)	0.80 ± 1.28	0.0 ± 0.10
	VIP-cluster — NPY-cluster			VIP-cluster < NPY-cluster	
(13) Late adaptation (Hz/s)	−26.99 ± 18.79	−10.08 ± 17.64	(27) First spike ADP latency (ms)	1.89 ± 2.8	0.2 ± 0.85
	VIP-cluster << NPY-cluster			NPY-cluster < VIP-cluster	
(14) Maximal steady state frequency (Hz)	75.11 ± 21.36	46.76 ± 17.58	(28) Second spike ADP latency (ms)	1.67 ± 2.56	0.1 ± 0.56
	NPY-cluster <<< VIP-cluster			NPY-cluster < VIP-cluster	

telencephalic 5-HT_{3A}:GFP+ cells can be generated as early as embryonic day E12.5, we wanted to determine more specifically the birth date of neocortical 5-HT_{3A}-expressing neurons. With this aim, we used BrdU labeling combined with 5-HT_{3A} mRNA detection. Wild-type mice received a single injection of BrdU at a given stage (between E11.5 and E16.5), a minimum of 3 litters per time point were subsequently analyzed at P25 and at least 2 animals per litter were processed for histology. These experiments revealed that 5-HT_{3A}-expressing neurons are generated at distinct embryonic stages according to their telencephalic region of destination.

A large proportion of 5-HT_{3A}-expressing neurons populating the neocortex were generated over a narrow period, between E13.5 and E14.5 (Fig. 4*A–C,F,H–K*). In contrast, 5-HT_{3A}-expressing neurons of the cingulate and retrosplenial cortices were generated 1 day earlier compared with those located in the neocortex at similar stereotaxic levels (Fig. 4*D,I–K*). Within the hippocampal formation, 5-HT_{3A} interneurons were mainly generated over the E12.5–E13.5 period (Fig. 4*E,G,J,K*), before the genesis of glutamatergic neurons (Soriano et al. 1989). Birth-dating analysis of 5-HT_{3A}-expressing neurons in the piriform cortex was more heterogeneous than in other regions of the hippocampal formation, extending from E12.5 to E16.5 (Fig. 4*I,J*). Finally, 5-HT_{3A} neurons located in the amygdala were generated between E12.5 and E14.5, with a peak of genesis at E13.5 (Fig. 4*J–K*).

The birth of 5-HT_{3A}-expressing neurons therefore occurs within a variety of embryonic time windows according to their destination, with a specific peak of genesis between E13.5 and E14.5 for the 5-HT_{3A} neocortical interneurons.

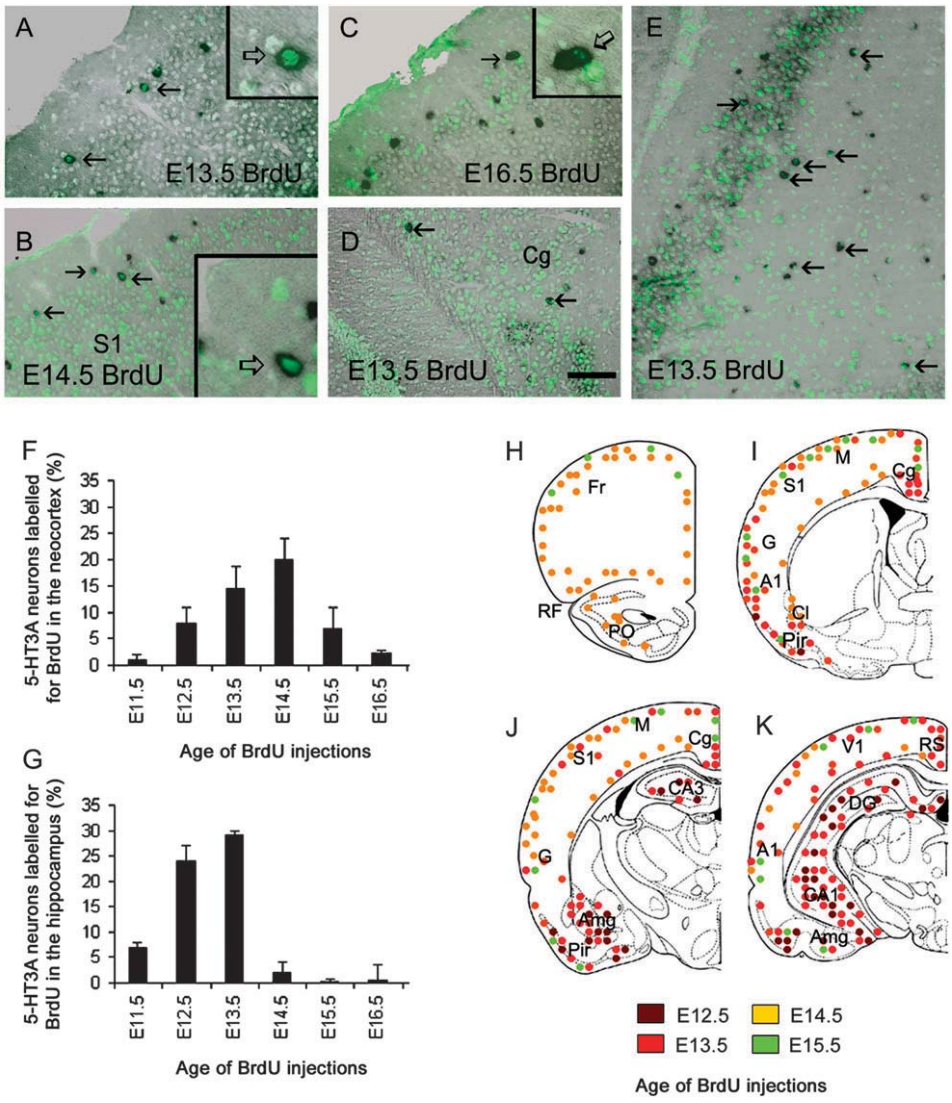

Figure 4. Birth-dating of telencephalic 5-HT3A interneurons. (*A–E*) Simultaneous detection of 5-HT_{3A} transcripts (black) and BrdU (green) in coronal sections at the level of the cerebral cortex (*A–C*), the cingulated cortex (*D*) and the hippocampus (*E*) in P25 wild-type mice. Age of pulse injection is indicated on the images. (*A–C*) Coronal sections taken at the level of the primary somatosensory cortex showing double-labeled cells in the supragranular layers (arrows). (*D*) Coronal section taken at the level of the cingulate cortex. (*F,G*) Histograms showing the percentage of 5-HT3A-expressing cells labeled for BrdU after a pulse injection at a given age, quantified in the neocortex (*F*) and the hippocampus (*G*). Note that the peak of genesis of cortical 5-HT_{3A}-expressing cells takes place around E14.5. Data are represented as mean ± SEM (percentage of double-labeled cells over the 5-HT_{3A}-postive cells). (*H–K*) Drawings showing the location and date of genesis of 5-HT_{3A}-expressing cells. Drawings are presented from rostral (*H*) to caudal (*K*). A1, auditory cortex; Amg, amygdala; CA1-3, field CA1-3 of the hippocampus; Cl, claustrum; Cg, cingulate cortex area; DG, dentate gyrus; Fr, Frontal cortex area G, gustatory cortex area; M, motor cortex area; Pir, piriform cortex; PO, primary olfactory cortex; RF, Rhinal fissure; RS, retrosplenial cortex; S1, somatosensory cortex area; V1, visual cortex area. Scale bar: (*A–D*) 200 μm; (*E*) 250 μm.

Localization of 5-HT$_{3A}$-Expressing Neurons during Mouse Embryogenesis

Johnson and Heinemann (1995) have described a very early expression of 5-HT$_{3A}$ mRNA in the basal telencephalon, a region well known to give rise to cortical interneurons (Marín and Rubenstein 2001). Having determined precisely the peak of genesis of cortical 5-HT$_{3A}$-expressing interneurons, we next analyzed the specific 5-HT$_{3A}$ distribution at this embryonic stage (E13.5–E14.5). In this aim, we used both GFP immunodetection in 5-HT$_{3A}$:GFP mice and 5-HT$_{3A}$ mRNA detection in wild-type animals (Fig. 5).

We found a good correlation between regions of high 5-HT$_{3A}$ mRNA expression (Fig. 5*C*,*G*) and high GFP-immunoreactivity (Fig. 5*D*,*H*). At E13.5, expression was highest in the AEP/Preoptic (AEP/Po) region, whereas discrete labeling was also observed in the CGE (data not shown). At E14.5, 5-HT$_{3A}$ expression was high both in AEP (Fig. 5*A*,*C*–*D*) and CGE (Fig. 5*E*,*G*–*H*) 2 regions included in territories expressing the transcription factor *Dlx1/2* that is required for interneuron specification (Anderson et al. 1999).

Within the CGE, the expression of the differentiation marker class III β-tubulin (tuj-1; Menezes and Luskin 1994) in GFP+ neurons reveals their postmitotic state (Fig. 5*I*–*L*).

Both MGE and LGE contained only scattered GFP+ neurons (Fig. 3*M*), presumably corresponding to interneurons that will populate the olfactory bulb (LGE) and interneurons passing through these structures (Marín and Rubenstein 2001). We observed that all GFP immunoreactive cells (E14.5, n = 9 embryos) migrating tangentially along the intermediate zone were also immunoreactive for GABA (Fig. 5*H*,*N*–*Q*). However, GFP was only found in a subset of GABA immunoreactive cells in the low intermediate zone (LIZ, Fig. 5*N*-*Q*) ~42% (rostral level) and ~67% (caudal level; Fig.5*H*,*N*).

Contribution of CGE and AEP/Po in the Genesis of Cortical 5-HT$_{3A}$-Expressing Interneurons

To determine the relative contribution of AEP/Po and CGE in the genesis of cortical 5-HT$_{3A}$-expressing interneurons homochronic in vivo grafts of AEP/Po- and CGE-derived postmitotic neurons from 5-HT$_{3A}$:GFP embryos into wild-type host embryos were performed at the peak of genesis of cortical 5-HT$_{3A}$ interneurons.

Figure 6*A* shows the territories dissected and used for donor tissues. Subsequently, the positions of 5-HT$_{3A}$:GFP+ grafted cells were analyzed in host mice (P19–P25). In Figure 6*B* schematic drawings of coronal sections of grafted animals indicate the location of 5-HT$_{3A}$:GFP+ grafted cells. Both AEP and CGE contributed to several telencephalic structures; however, only CGE-derived cells populated the neocortex.

Contribution of AEP/Po

In utero grafts of E13/E13.5 AEP/Po-derived cells demonstrated that 5-HT$_{3A}$:GFP+ grafted cells contribute to populate the hippocampal formation as grafted cells were mostly found in the dentate gyrus (Fig. 6*B*). 5-HT$_{3A}$:GFP+ cells grafted from the caudal part of the AEP at E14/E14.5 mainly populated the amygdala (basolateral and lateral nuclei), the endopiriform nucleus and the claustrum. Grafted cells from the rostral part of the AEP gave rise to rare cells located in the deep cortical layers of the retrosplenial and motor cortices (Fig. 6*B*). These results demonstrate that at the peak of genesis of neocortical 5-HT$_{3A}$-expressing interneurons (E14.5, Fig. 4*F*), cells generated in AEP/Po do not contribute to the genesis of cortical 5-HT$_{3A}$ interneurons.

Contribution of CGE

E13/E13.5 and E14/E14.5 CGE-derived cells contribute to populate the neocortex (Figs. 6 and 7), in addition to several limbic structures, including the bed nucleus of the stria terminalis, the hippocampus, and several nuclei of the amygdala (Fig. 6*B*). Within the hippocampal formation, the majority of grafted cells were located in CA3 and CA1, whereas fewer cells were found in the hilus and the dentate gyrus (Fig. 6*B*). Within the amygdaloid complex, grafted cells were found in the basolateral, the lateral and the corticoamygdaloid nuclei (Fig. 6*B*). E14/E14.5 CGE-derived cells were more often found in the neocortex and amygdala compared with E13/E13.5 CGE-derived cells that were mainly populating hippocampal structures (Fig. 6*B*).

Interestingly, homotopic and homochronic in vitro grafts of E14.5 GFP+ donor cells derived from CGE into wild-type slices clearly show that GFP+ cells migrate toward the amygdala and the cortex following several migratory routes, along the marginal zone and along the subventricular zone (Supplementary Fig. S4).

Most fluorescent grafted cells that were observed in the neocortex were located in supragranular layers I–III (Fig. 7*B*–*F*). Note that similar results were obtained in animals receiving 5-HT$_{3A}$:GFP+ cells freshly dissected or sorted by flow cytometry (Fig. 7*C*–*D*). Within the cortical layers II–III, some of these cells displayed characteristic bipolar/double bouquet morphologies and therefore presumably belong to the VIP-cluster of 5-HT$_{3A}$-expressing interneurons (Fig. 7*E*). We also found multipolar/neurogliaform cells presumably belonging to the NPY-cluster. These cells displayed complex morphologies and were distributed throughout the layers I and II–III (Fig. 7*F*). To determine the phenotype of grafted cells, we used several immunohistochemical markers commonly used to discriminate different interneurons classes. In all telencephalic regions, grafted cells displayed the same phenotype as those observed in 5-HT$_{3A}$:GFP animals. Grafted cells never displayed Parv or SOM immunoreactivity, but expressed CR, VIP, and NPY (Fig. 7*G*–*O*,*P*).

Discussion

In this study, we show that 5-HT$_{3A}$ is protractedly expressed from early postmitotic to adult stages by selective subpopulations of mouse neocortical interneurons. Although the functional role of the 5-HT$_{3A}$ subunit during early developmental stages is yet unresolved (but see also Riccio et al. 2008), its protracted expression enabled us to follow the development of neocortical 5-HT$_{3A}$+ interneurons. Various techniques including homochronic in utero grafts performed at the peak of genesis of cortical 5-HT$_{3A}$+ interneurons revealed that these neurons are mainly generated in the CGE. We further demonstrate that grafted interneurons retain their specific neurochemical phenotype, distribution, and functional properties after grafting, as previously described for different subpopulation of neocortical interneurons (Nery et al. 2002; Butt et al. 2005). The characterization of mature neocortical 5-HT$_{3A}$-expressing interneurons from 5-HT$_{3A}$:GFP mice shows that 5-HT$_{3A}$ is expressed by VIP-expressing bipolar/bitufted interneurons and NPY-expressing interneurons displaying more complex dendritic

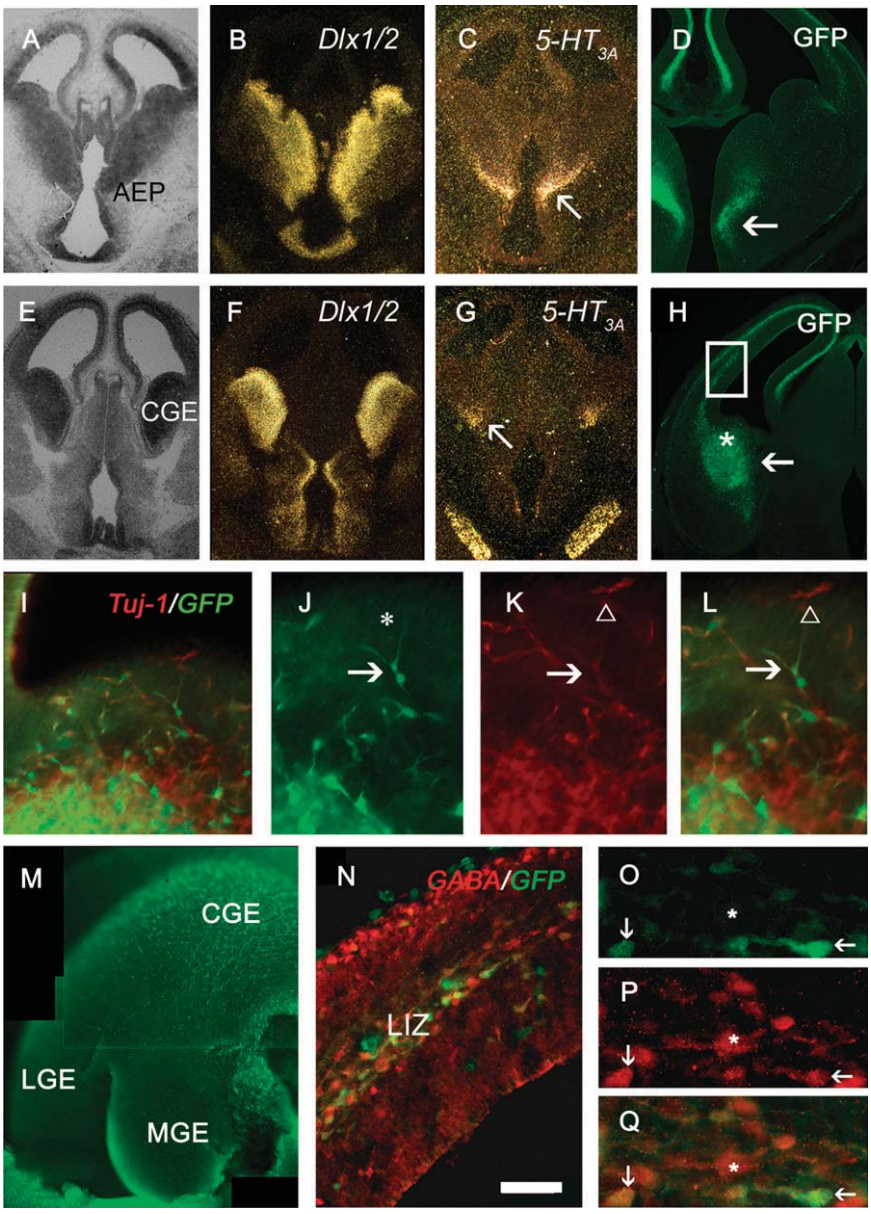

Figure 5. Expression of 5-HT_{3A} in the developing embryo at E14.5. (*A*,*E*): Brightfield coronal views of the entopeduncular area (AEP, *A*) and the caudal ganglionic eminence (CGE, *E*). (*C*,*D*,*G*,*H*): Coronal sections where arrows point to restricted expression of 5-HT_{3A} mRNA in wild-type mouse (*C*,*G*) and GFP immunostaining from a 5-HT_{3A}:GFP transgenic mouse (*D*,*H*). The main sites of 5-HT_{3A} expression where located at the telencephalic–diencephalic junction, in AEP (*A*,*B*,*D*) and in CGE (*E*,*F*,*H*). (*B*–*F*) Alternate sections of the preparations shown in (*A*,*E*) showing *Dlx1/2* expression. (*I*–*L*) Coronal section taken at the level of the CGE indicated by the asterisk in (*H*) showing cells double labeled for GFP (green) and the postmitotic marker tuj-1 (red). (*J*–*L*) Higher magnifications of the region shown in (*I*). Arrow points to a double-labeled cell and the open arrowhead points to a cell expressing only tuj-1. (*M*) Whole-mount preparation of a E14.5 5-HT_{3A}:GFP embryo showing restricted expression of GFP+ cells in the CGE. (*N*) Coronal section of the caudal cortex (boxed in *H*) of a 5-HT_{3A}:GFP embryo stained for GABA (red) showing GABA+ cells in the migratory pathway of interneurons (LIZ). (*O*–*Q*) High-power view of the section shown in (*N*). Note that only a proportion of GABA+ cells express GFP (arrows) and that all GFP+ cells in LIZ express GABA. The asterisk points to a GABA-positive cell that is not expressing GFP. LGE, lateral ganglionic eminence, LIZ, Low intermediate zone, MGE, medial ganglionic eminence. Scale bar: (*A*–*C*,*E*–*G*) 1 mm; (*D*,*H*) 800 μm; (*I*,*N*) 125 μm; (*J*–*L*) 90 μm; (*M*) 500 μm; (*O*–*Q*) 75 μm.

morphologies. Most interneurons of this second class are very similar to neurogliaform cells according to their specific electrophysiological, molecular and morphological properties.

Diversity of Neocortical 5-HT_{3A}-Expressing Interneurons

GABAergic interneurons within the neocortex are typically described and classified on the bases of their physiological, molecular, and morphological features. The large amount of data collected from the rat neocortex led to the distinction of at least 5 subclasses of interneurons according to the Petilla 2005 nomenclature (Ascoli et al. 2008; Karagiannis et al. 2009): Fast spiking (FS) cells expressing Parv, Martinotti cells expressing SOM and CB, Neurogliaform cells expressing NPY, VIP bipolar cells and large CCK basket cells.

The unsupervised clustering performed in the present study disclosed 2 main groups of 5-HT_{3A}-expressing interneurons with distinctive electrophysiological, molecular, and morphological hallmarks that were remarkably similar to those characterizing particular interneuronal subtypes previously described in the rat neocortex (Kubota and Kawaguchi 1994; Cauli et al. 1997; Cauli et al. 2000; Ascoli et al. 2008; Karagiannis et al. 2009).

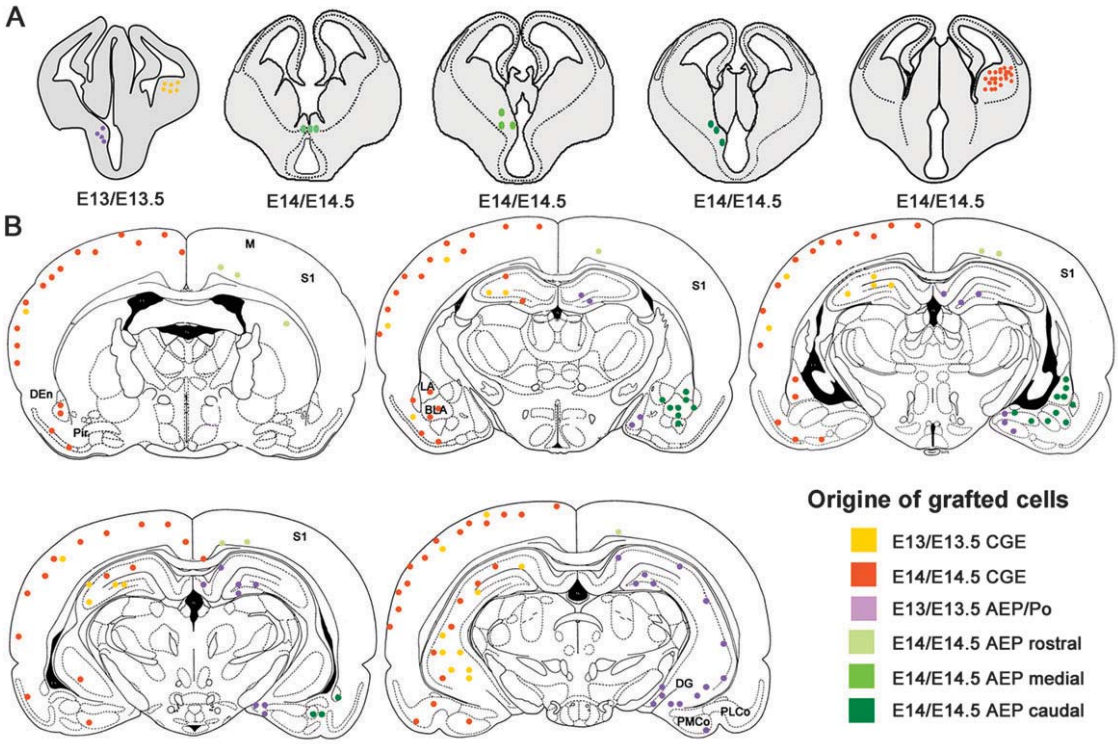

Figure 6. Distribution of 5-HT3A:GFP+ grafted cells derived from the APE/Po and CGE. (*A*) Schematic drawings indicating the regions taken for donor cells dissociation. (*B*) Schematic drawings showing the general distribution of 5-HT_{3A}:GFP+ grafted cells in the host brain (P19–P25). Amg, amygdala; BLA, basolateral amygdaloid nucleus; Cg, cingulate cortex area; DEn, dorsal endopiriform nucleus; DG, dentate gyrus; LA, lateral amygdaloid nucleus; M, motor cortex; Pir, piriform cortex; PlCo, posterolateral cortical amygdaloid nucleus; PMCo, posteromedial cortical amygdaloid nucleus; S1, somatosensory cortex.

GFP-expressing cells segregated in the VIP-cluster were never found in layer I and were characterized by the high occurrence of *VIP* and to a lower extent *CR* but the absence of *CB*, *Parv*, and *SOM*. These molecular properties match those characterizing 5-HT_{3A}-expressing interneurons in the rat neocortex (Morales and Bloom 1997; Ferezou et al. 2002). The adapting or bursting firing behavior of these cells correspond to that of VIP-expressing cells previously characterized in the rat somatosensory cortex (Bayrakter et al. 1997; Cauli et al. 1997; Porter et al. 1998). However, at high stimulation intensity, these cells did not exhibit the typical pronounced amplitude accommodation described in rat VIP-expressing neurons (Cauli et al. 2000). This divergence could be ascribable to species differences between mice and rats. On the other hand, the large majority of cells belonging to the VIP-cluster exhibited bipolar somatodendritic morphology with descending axonal arborization, morphological traits that typically correspond to the descriptions of rat VIP-expressing interneurons (Kawaguchi and Kubota 1996; Bayraktar et al. 1997).

The main characteristic of the second group of cells identified by Ward's clustering was the high expression of *NPY* (87%). Our results revealed that the electrophysiological, morphological, and molecular properties of 5-HT_{3A}-expressing neurons of the NPY-cluster were very similar to those of previously characterized neurogliaform cells (Kawaguchi 1995; Hestrin and Armstrong 1996; Zhou and Hablitz 1996; Cauli et al. 2004). Indeed, the typical physiological features of the neurogliaform interneurons are found in this group such as high rheobase, delayed firing, marked frequency adaptation at high firing rates, and pronounced amplitude accommodation during the action potentials discharge (Kawaguchi 1995; Chu et al. 2003; Simon et al. 2005; Ascoli et al. 2008; Karagiannis et al. 2009). Interestingly, *Reelin* was expressed in 52% of cells in the NPY-cluster, whereas only 23% of cells of the VIP-cluster contained this marker. These results are in agreement with immunohistochemical studies indicating that reelin is preferentially coexpressed with NPY and/or SOM (Alcántara et al. 1998; Pesold et al. 1999). Although our immunohistochemical experiments did not disclose any coexpression of GFP and SOM, the scRT-PCR results revealed the presence of *SOM* mRNA in 29% ($n = 9$ of 31) of cells within the NPY-cluster. This discrepancy could be explained by the different sensitivities of both techniques (Gallopin et al. 2006, Burkhalter 2008). Indeed, it is unlikely that neurons of the NPY-cluster that present *SOM* mRNA detection could belong to the Martinotti subtype because it has been demonstrated that Martinotti cells derive from the MGE (Butt et al. 2005; Miyoshi et al. 2007). Furthermore, this is in agreement with the absence of expression of *Lhx6* mRNAs in the GFP cells recorded and harvested. Indeed, *Lhx6* has been reported to be expressed in Parv-expressing FS interneurons and SOM Martinotti cells at mature stages (Liodis et al. 2007).

Genesis and Specification of Neocortical 5-HT_{3A}+ Interneurons

Our birth-dating experiments show that neocortical 5-HT_{3A} interneurons display a peak of genesis at E14.5 that largely precedes those observed for glutamatergic neurons in the same areas. In particular, in the superficial neocortical layers, 5-HT_{3A} interneurons are generated between E13.5 and E14.5, whereas

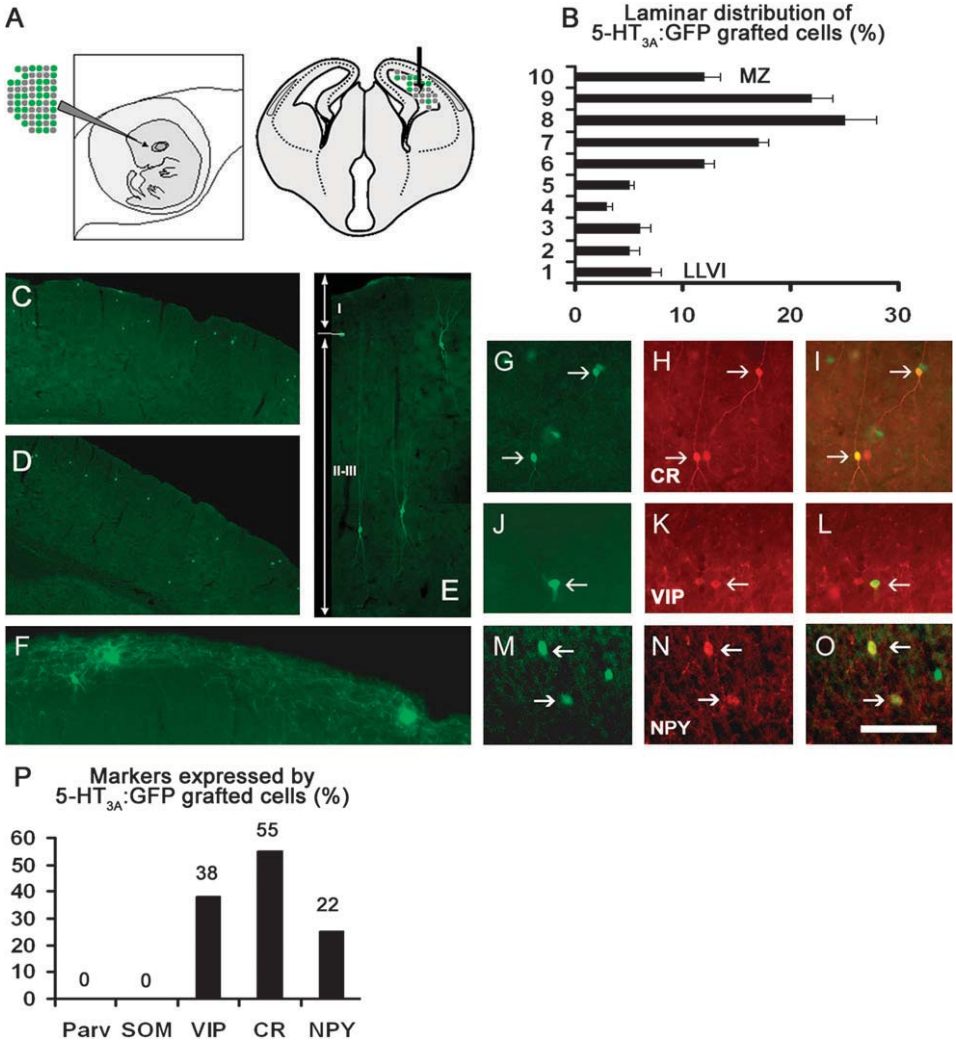

Figure 7. Fate of In utero grafted 5-HT_{3A}:GFP+ cells from the CGE at E14.5. (*A*) Schematic drawing illustrating the in utero grafting technique. (*B*) Histogram (percentage ± SEM) indicating the laminar distribution of 5-HT_{3A}:GFP+ grafted cells ($n = 235$ cells obtained from 7 grafted animals) in the somatosensory cortex. Cortical strips (500 μm width) were longitudinally subdivided into 10 equal bins from the marginal zone (MZ) to the lower part of the layer VI (LLVI). (*C*,*D*) E14 5-HT_{3A}:GFP+ CGE-derived cells give rise to numerous interneurons located in the supragranular layers of the cerebral cortex. Note that the section shown in panel (*C*) was taken from an animal that received 5-HT_{3A}:GFP+ cells that were sorted by flow cytometry. (*E*) Section showing 5-HT_{3A}:GFP+ cells located in the supragranular layers of the cortex and displaying bipolar or double bouquet morphologies. Cortical layers are indicated. (*F*) Section showing multipolar 5-HT_{3A}:GFP+ grafted cells located in cortical layer I displaying complex morphologies. (*G–O*) Neocortical grafted cells labeled for CR (*G–I*; red), VIP (*J–L*; red) or NPY (*M–O*; red) in the supragranular layers II–III. (*P*) Histogram showing the percentage of grafted cells that express different interneuronal markers in the somatosensory cortex. Throughout the cortex, the most commonly expressed markers were CR, VIP and NPY. Scale bar: (*C–D*): 700 μm; (*E*): 80 μm; (*F–O*) 100 μm.

glutamatergic neurons are generated between E15.5 and E17.5 (Bayer and Altman 1991). This is in contrast with the general view that GABAergic neurons tend to integrate the same cortical layer as projection neurons born at the same time (Miller 1986), following their typical inside-out neurogenesis gradient with early generated neurons constituting the deeper cortical layers and subsequently born neurons populating progressively more superficial layers (Angevine and Sidman 1961; Rakic 1971). Such an inside-out neurogenesis gradient has been demonstrated for Parv+ and SOM+ interneurons that account for a large majority of cortical GABAergic interneurons (Cavanagh and Parnavelas 1988; Ang et al. 2003; Rymar and Sadikot 2007), and this has masked for a long time the behavior of specific subpopulation of interneurons. Indeed, exceptions have been noticed such as VIP+ interneurons that do not show a distinct inside-out neurogenesis gradient (Cavanagh and Parnavelas 1989) and NPY+ interneurons that display a scattered neurogenesis pattern (Cavanagh and Parnavelas 1990). Moreover, CR+ interneurons have recently revealed an outside-in neurogenetic gradient (Rymar and Sadikot 2007). Together, these reports suggest that different subpopulations of cortical GABAergic neurons may use different strategies and cues for their layer targeting. Our study confirms and extends this atypical behavior to neocortical interneurons expressing 5-HT_{3A}.

Our grafting experiments demonstrate that neocortical 5-HT_{3A}-expressing interneurons are originating from the CGE. Following their ventricular transplantation into wild-type animals, the E14/E14.5 CGE-derived 5-HT3A:GFP cells adopt neurochemical phenotype, distribution, and functional properties similar to those found in intact 5-HT_{3A}:GFP mice. The fate of these interneurons is therefore determined at early developmental stages, similarly to what have been observed for other subpopulation of interneurons (Nery et al. 2002; Butt et al. 2005).

It is unclear how progenitor cells from the CGE are specified and how their pattern of migration and maturation behavior are regulated. Two nonexcluding mechanisms may account for the areal and laminar specificity of 5-HT_{3A}+ grafted interneurons. One hypothesis would be that interneurons that were not correctly positioned (i.e., inappropriate cortical lamina) would either have failed to fully differentiate or would have undergone apoptosis. In favor of this assumption, it has been shown that, in vitro, the survival of small interneurons expressing VIP/CR critically depends on glutamatergic activity during a restricted time window corresponding to the early postnatal period (de Lima et al. 2004; Vitalis et al. 2007). On the other hand, our favored hypothesis would be that a specific combination of transcription factors and guidance molecules in young postmitotic neurons would be sufficient to target one interneuron to a specific prosencephalic area and more precisely in a specific cortical lamina. Indeed, recent studies suggest that motility (Powell et al. 2001; Polleux et al. 2002; Tripodi et al. 2004) and guidance (Tripodi et al. 2004; Pozas and Ibanez 2005) of interneurons depend on several molecular cues that are at least in part differentially expressed in ganglionic eminences and cortical compartments.

The transcription factor Nr2F2 is preferentially expressed in the CGE (Tripodi et al. 2004; Kanatani et al. 2008) and plays a crucial role in specifying the typical caudal migration of CGE cells (Yozu et al. 2005). In the present study, immunocytochemistry data indicate that Nr2F2 is selectively expressed by a large proportion of migrating 5-HT_{3A}+ interneurons at E16 (Fig. S5). In addition, both our immunocytochemical and scRT-PCR results reveal that Nr2F2 expression persists in these cells at later stages (P21 and P14–18, respectively), when the 5-HT_{3A}+ interneurons have integrated the superficial cortical layers. These observations suggest that Nr2F2 is likely to play a role in the maintenance of this cell population. Hence, although the involvement of Nr2F2 in the migration of GABAergic neurons has been well described (Tripodi et al. 2004; Kanatani et al. 2008), its functional role within the mature neocortex remains to be further studied.

Our work highlights the protracted expression of the 5-HT_{3A} subunit, which is specifically expressed by 2 subtypes of neocortical GABAergic interneurons. Although various studies tend to explore the involvement of 5-HT_3 receptors on the mature neocortical network activity (Ferezou et al. 2002; Puig et al. 2004; Moreau et al. 2009), further investigations would be essential to elucidate the developmental role of these receptors in the migration and maturation behavior of CGE cells specified to give rise to VIP- and NPY-expressing neocortical interneurons. This last point would be of great interest because endogenous serotonin or maternal serotonin is known to be implicated in various aspects of brain development (Gaspar et al. 2003; Vitalis and Parnavelas 2003; Côté et al. 2007; see also Riccio et al. 2008).

Supplementary Material

Supplementary material can be found at: http://www.cercor.oxfordjournals.org/.

Funding

CNRS, INSERM, FRM, ESPCI ParisTech, and the French National Research Agency (ANR-06-NEURO-033-01 grant).

Notes

We warmly thank Dr Marie-Claude Potier for advice and support. We thank Dr Luc Maroteaux, Dr Patricia Gaspar, Dr Bruno Cauli, and Dr Olivier Cases for comments and advice. We thank Chantal Alvarez and Dragos Inta for precious technical help. We thank Dr Epelbaum for providing antisomatostatin antibodies and Dr Emerit for providing specific 5-HT_{3A} plasmid. We thank Dr Philippe Vielh for allowing us to carry out the flow cytometry purification in his laboratory and Dr Zofia Maciorowski for advice on cytometry. We thank Marie Fan and Christophe Varin, students at ESPCI, for their precious help in the project. The Tg(Htr3a-GFP)1Gsat was provided by the GENSAT Consortium (Rockeffeler University-GENSAT Consortium). *Conflict of Interest*: None declared.

References

Alcántara S, Ruiz M, D'Arcangelo G, Ezan F, de Lecea L, Curran T, Sotelo C, Soriano E. 1998. Regional and cellular patterns of reelin mRNA expression in the forebrain of the developing and adult mouse. J Neurosci. 18:7779–7799.

Anderson S, Mione M, Yun K, Rubenstein JL. 1999. Differential origins of neocortical projection and local circuit neurons: roles of Dlx genes in neocortical interneurogenesis. Cereb Cortex. 9:646–654.

Anderson SA, Marín O, Horn C, Jennings K, Rubenstein JL. 2001. Distinct cortical migrations from the medial and lateral ganglionic eminences. Development. 128:353–363.

Andjelic S, Gallopin T, Cauli B, Hill EL, Roux L, Badr S, Hu E, Tamas G, Lambolez B. 2008. Glutamatergic non-pyramidal neurons from neocortical layer VI and their comparison with pyramidal and spiny stellate neurons. J Neurophysiol. 101:641–654.

Ang ES, Jr., Haydar TF, Glucnic V, Rakic P. 2003. Four-dimensional migratory coordinates of GABAergic interneurons in the developing mouse cortex. J Neurosci. 23:5805–5815.

Angevine JB, Jr., Sidman RL. 1961. Autoradiographic study of cell migration during histogenesis of cerebral cortex in the mouse. Nature. 192:766–768.

Ascoli GA, Alonso-Nanclares L, Anderson SA, Barrionuevo G, Benavides-Piccione R, Burkhalter A, Buzsáki G, Cauli B, Defelipe J, Fairén A, et al. 2008. Petilla terminology: nomenclature of features of GABAergic interneurons of the cerebral cortex. Nat Rev Neurosci. 9:557–568.

Baraban SC, Tallent MK. 2004. Interneuron diversity series: interneuronal neuropeptides–endogenous regulators of neuronal excitability. Trends Neurosci. 27:135–142.

Bayer S, Altman J. 1991. Neocortical development. New York: Raven Press.

Bayraktar T, Staiger JF, Acsady L, Cozzari C, Freund TF, Zilles K. 1997. Co-localization of vasoactive intestinal polypeptide, gamma- aminobutyric acid and choline acetyltransferase in neocortical interneurons of the adult rat. Brain Res. 757:209–217.

Burkhalter A. 2008. Many specialists for suppressing cortical excitation. Front Neurosci. 2:155–167.

Butt SJ, Fucillo M, Nery S, Noctor S, Kriegstein A, Corbin JG, Fishell G. 2005. The temporal and spatial origins of cortical interneurons predict their physiological subtype. Neuron. 48:591–604.

Cauli B, Audinat E, Lambolez B, Angulo MC, Ropert N, Tsuzuki K, Hestrin S, Rossier J. 1997. Molecular and physiological diversity of cortical nonpyramidal cells. J Neurosci. 17:3894–3906.

Cauli B, Porter JT, Tsuzuki K, Lambolez B, Rossier J, Quenet B, Audinat E. 2000. Classification of fusiform neocortical interneurons based on unsupervised clustering. Proc Natl Acad Sci U S A. 97:6144–6149.

Cauli B, Tong XK, Rancillac A, Serluca N, Lambolez B, Rossier J, Hamel E. 2004. Cortical GABA interneurons in neurovascular coupling: relays for subcortical vasoactive pathways. J Neurosci. 24:8940–8949.

Cavanagh ME, Parnavelas JG. 1988. Development of somatostatine immunoreactive neurons in the rat occipital cortex: a combined immunocytochemical-autoradiographic study. J Comp Neurol. 268:1–12.

Cavanagh ME, Parnavelas JG. 1989. Development of vasoactive-intestinal-polypeptide-immunoreactive neurons in the rat occipital cortex: a combined immunocytochemical-autoradiographic study. J Comp Neurol. 284:637–645.
Cavanagh ME, Parnavelas JG. 1990. Development of neuropeptide Y (NPY) immunoreactive neurons in the rat occipital cortex: a combined immunocytochemical-autoradiographic study. J Comp Neurol. 297:553–563.
Chameau P, Inta D, Vitalis T, Monyer H, Wadman WJ, van Hooft JA. 2009. The N-terminal region of reelin regulates postnatal dendritic maturation of cortical pyramidal neurons. Proc Natl Acad Sci U S A. 106:7227–7232.
Chu Z, Galarreta M, Hestrin S. 2003. Synaptic interactions of late-spiking neocortical neurons in layer 1. J Neurosci. 23:96–102.
Cobos I, Long JE, Thwin MT, Rubenstein JL. 2006. Cellular patterns of transcription factor expression in developing cortical interneurons. Cereb cortex. 16(Suppl. 1):82–88.
Corbin JG, Nery S, Fishell G. 2001. Telencephalic cells take a tangent: non-radial migration in the mammalian forebrain. Nat Neurosci Rev. 4(Suppl.):1177–1182.
Côté F, Fligny C, Bayard E, Launay JM, Gershon MD, Mallet J, Vodjdani G. 2007. Maternal serotonin is crucial for murine embryonic development. Proc Natl Acad Sci U S A. 104:329–334.
Dávid C, Schleicher A, Zuschratter W, Staiger JF. 2007. The innervation of parvalbumin-containing interneurons by VIP-immunopositive interneurons in the primary somatosensory cortex of the adult rat. Eur J Neurosci. 25:2329–2340.
DeFelipe J. 1993. Neocortical neuronal diversity: chemical heterogeneity revealed by colocalization studies of classic neurotransmitters, neuropeptides, calcium-binding proteins, and cell surface molecules. Cereb Cortex. 3:273–289.
de Lima AD, Opitz T, Voigt T. 2004. Irreversible loss of a subpopulation of cortical interneurons in the absence of glutamatergic network activity. Eur J Neurosci. 19:2931–2943.
Dumitriu D, Cossart R, Huang J, Yuste R. 2006. Correlation between axonal morphologies and synaptic input kinetics of interneurons from mouse visual cortex. Cereb Cortex. 17:81–91.
Ferezou I, Cauli B, Hill EL, Rossier J, Hamel E, Lambolez B. 2002. 5-HT3 receptors mediate serotonergic fast synaptic excitation of neocortical vasoactive intestinal peptide/cholecystokinin interneurons. J Neurosci. 22:7389–7397.
Fontaine P, Changeux JP. 1989. Localization of nicotinic acetylcholine receptor alpha-subunit transcripts during myogenesis and motor endplate development in the chick. J Cell Biol. 103:1025–1037.
Gallopin T, Geoffroy H, Rossier J, Lambolez B. 2006. Cortical sources of CRF, NKB, and CCK and their effects on pyramidal cells in the neocortex. Cereb Cortex. 16:1440–1452.
Gaspar P, Cases O, Maroteaux L. 2003. The developmental role of serotonin: news from mouse molecular genetics. Nat Rev Neurosci. 4:1002–1012.
Gelman DM, Martini FJ, Pereira SN, Pierani A, Kessaris N, Marín O. 2009. The Embryonic preoptic area is a novel source of cortical GABAergic interneurons. J Neurosci. 29:9380–9389.
Gillies K, Price DJ. 1993. The fates of cells in the developing cerebral cortex of normal and methylazoxymethanol acetate-lesioned mice. Eur J Neurosci. 5:73–84.
Gupta A, Wang Y, Markram H. 2000. Organizing principles for a diversity of GABAergic interneurons and synapses in the neocortex. Science. 287:273–278.
Halabisky BE, Shen F, Huguenard JR, Prince DA. 2006. Electrophysiological classification of somatostatin-positive interneurons in mouse sensorimotor cortex. J Neurophysiol. 96:834–845.
Heintz N. 2001. BAC to the future: the use of bac transgenic mice for neuroscience research. Nat Rev Neurosci. 2:861–870.
Heintz N. 2004. Gene expression nervous system atlas (GENSAT). Nat Neurosci. 7:483.
Helmstaedter M, Sakmann B, Feldmeyer D. 2009. The relation between dendritic geometry, electrical excitability, and axonal projections of L2/3 interneurons in rat. Barrel Cortex. 19:938–50.
Hestrin S, Armstrong WE. 1996. Morphology and physiology of cortical neurons in layer I. J Neurosci. 16:5290–5300.
Inta D, Alfonso J, von Engelhardt J, Kreuzberg MM, Meyer AH, van Hooft JA, Monyer H. 2008. Neurogenesis and widespread forebrain migration of distinct GABAergic neurons from the postnatal subventricular zone. Proc Natl Acad Sci U S A. 105:20994–20999.
Jakab RL, Goldman-Rakic PS. 2000. Segregation of serotonin 5-HT2A and 5-HT3 receptors in inhibitory circuits of the primate cerebral cortex. J Comp Neurol. 417:337–348.
Jessell TM. 2000. Neuronal specification in the spinal cord: inductive signals and transcriptional codes. Nat Rev Genet. 1:20–29.
Johnson DS, Heinemann S. 1995. Embryonic expression of the 5-HT_{3A} receptor subunit, 5-HT_{3A}R-A, in the rat: an in situ hybridization study. Mol Cell Neurosci. 6:122–138.
Kanatani S, Yozu M, Tabata H, Nakajima K. 2008. COUP-TFII is preferentially expressed in the caudal ganglionic eminence and is involved in the caudal migratory stream. J Neurosci. 28: 13582–13591.
Karagiannis A, Gallopin T, Dávid C, Battaglia D, Geoffroy H, Rossier J, Hillman E, Staiger J, Cauli B. 2009. Classification of NPY-expressing neocortical interneurons. J Neurosci. 29:3642–3659.
Karube F, Kubota Y, Kawaguchi Y. 2004. Axon branching and synaptic bouton phenotypes in GABAergic nonpyramidal cell subtypes. J Neurosci. 24:2853–2865.
Kawaguchi Y. 1995. Physiological subgroups of nonpyramidal cells with specific morphological characteristics in layer II/III of rat frontal cortex. J Neurosci. 15:2638–2655.
Kawaguchi Y, Kondo Y. 2002. Parvalbumin, somatostatin and cholecystokinin as chemical markers for specific GABAergic interneuron types in the rat frontal cortex. J Neurocytol. 31:277–287.
Kawaguchi Y, Kubota Y. 1996. Physiological and morphological identification of somatostatin- or vasoactive intestinal polypeptide-containing cells among GABAergic cell subtypes in rat frontal cortex. J Neurosci. 16:2701–2715.
Kubota Y, Kawaguchi Y. 1994. Three classes of GABAergic interneurons in neocortex and neostriatum. Jpn J Physiol. 44(Suppl. 2): S145–S148.
Lambolez B, Audinat E, Bochet P, Crepel F, Rossier J. 1992. AMPA receptor subunits expressed by single Purkinje cells. Neuron. 9:247–258.
Lavdas AA, Grigoriou M, Pachnis V, Parnavelas JG. 1999. The medial ganglionic eminence gives rise to a population of early neurons in the developing cerebral cortex. J Neurosci. 19:7881–7888.
Letinic K, Zoncu R, Rakic P. 2002. Origin of GABAergic neurons in the human neocortex. Nature. 417:645–649.
Liodis P, Denaxa M, Grigoriou M, Akufo-Addo C, Yanagawa Y, Pachnis V. 2007. Lhx6 activity is required for the normal migration and specification of interneuron subtypes. J Neurosci. 27:3078–3089.
Marín O, Rubenstein JL. 2001. A long, remarkable journey: tangential migration in the telencephalon. Nat Rev Neurosci. 2:780–790.
Menezes JR, Luskin MB. 1994. Expression of neuron-specific tubulin defines a novel population in the proliferative layers of the developing telencephalon. J Neurosci. 14:5399–5416.
Miller MW. 1986. The migration and neurochemical differentiation of gamma-aminobutyric acid (GABA)-immunoreactive neurons in rat visual cortex as demonstrated by a combined immunocytochemical-autoradiographic technique. Brain Res. 393:41–46.
Miyoshi G, Butt SJ, Takebayashi H, Fishell G. 2007. Physiologically distinct temporal cohorts of cortical interneurons arise from telencephalic Olig2-expressing precursors. J Neurosci. 27: 7786–7798.
Morales M, Bloom E. 1997. The 5-HT_{3A} receptor is present in different subpopulations of GABAergic neurons in the rat telencephalon. J Neurosci. 17:3157–3167.
Moreau AW, Amar M, Le Roux N, Morel N, Fossier P. 2009. Serotoninergic fine-tuning of the excitation-inhibition balance in rat visual cortical networks. Cereb Cortex. Jul 8. [Epub ahead of print].
Nery S, Fishell G, Corbin JG. 2002. The caudal ganglionic eminence is a source of distinct cortical and subcortical cell populations. Nat Neurosci. 5:1279–1287.
Pesold C, Liu WS, Guidotti A, Costa E, Caruncho HJ. 1999. Cortical bitufted, horizontal, and Martinotti cells preferentially express and

secrete reelin into perineuronal nets, nonsynaptically modulating gene expression. Proc Natl Acad Sci U S A. 96:3217–3222.
Polleux F, Whitford KL, Dijkhuizen PA, Vitalis T, Ghosh A. 2002. Control of cortical interneuron migration by neurotrophins and PI3-kinase signaling. Development. 129:3147–3160.
Porter JT, Cauli B, Staiger JF, Lambolez B, Rossier J, Audinat E. 1998. Properties of bipolar VIPergic interneurons and their excitation by pyramidal neurons in the rat neocortex. Eur J Neurosci. 10: 3617–3628.
Powell EM, Mars WM, Levitt P. 2001. Hepatocyte growth factor/scatter factor is a motogen for interneurons migrating from the ventral to dorsal telencephalon. Neuron. 30:79–89.
Pozas E, Ibanez CF. 2005. GDNF and GFRalpha1 promote differentiation and tangential migration of cortical GABAergic neurons. Neuron. 45:701–713.
Puig MV, Santana N, Celada P, Mengod G, Artigas F. 2004. In vivo excitation of GABA interneurons in the medial prefrontal cortex through 5-HT3 receptors. Cereb Cortex. 14:1365–1375.
Rakic P. 1971. Guidance of neurons migrating to the fetal monkey neocortex. Brain Res. 33:471–476.
Riccio O, Potter G, Walzer C, Vallet P, Szabo G, Vutskits L, Kiss JZ, Dayer AG. 2008. Excess of serotonin affects embryonic interneuron migration through activation of the serotonin receptor 6. Mol. Psychiatry. 14:280–290.
Ruano D, Lambolez B, Rossier J, Paternain AV, Lerma J. 1995. Kainate receptor subunits expressed in single cultured hippocampal neurons: molecular and functional variants by RNA editing. Neuron. 14:1009–1017.
Rymar VV, Sadikot AF. 2007. Laminar fate of cortical GABAergic interneurons is dependent on both birthdate and phenotype. J Comp Neurol. 501:369–380.
Schaeren-Wiemers N, Gerfin-Moser A. 1993. A single protocol to detect transcripts of various types and expression levels in neural tissue and cultured cells: in situ hybridization using digoxigenin-labelled cRNA probes. Histochemistry. 100:431–440.
Schuurmans C, Guillemot F. 2002. Molecular mechanisms underlying cell fate specification in the developing telencephalon. Curr Opin Neurobiol. 12:26–34.
Simon A, Olah S, Molnar G, Szabadics J, Tamas G. 2005. Gap-junctional coupling between neurogliaform cells and various interneuron types in the neocortex. J Neurosci. 25:6278–6285.
Soriano E, Cobos A, Fairen A. 1989. Neurogenesis of glutamic acid decarboxylase immunoreactive cells in the hippocampus of the mouse. I: region superior and region inferior. J Comp Neurol. 281: 586–602.
Tamas G, Buhl EH, Somogyi P. 1997. Fast IPSPs elicited via multiple synaptic release sites by different types of GABAergic neurone in the cat visual cortex. J Physiol. 500(Pt 3):715–738.
Tecott LH, Maricq AV, Julius D. 1993. Nervous system distribution of the serotonin 5-HT3 receptor mRNA. Proc Natl Acad Sci U S A. 90:1430–1434.
Thorndike RL. 1953. Who belongs in the family? Psychometrika. 18:267–276.
Tripodi M, Filosa A, Armentano M, Studer M. 2004. The COUP-TF nuclear receptors regulate cell migration in the mammalian basal forebrain. Development. 131:6119–6129.
Vitalis T, Cases O, Passemard S, Callebert J, Parnavelas JG. 2007. Embryonic depletion of serotonin affects cortical development. Eur J Neurosci. 26:331–344.
Vitalis T, Parnavelas JG. 2003. The role of serotonin in early cortical development. Dev Neurosci. 25:245–256. Review.
Ward JH. 1963. Hierarchical grouping to optimize an objective function. J Am Stat Assoc. 58:236–244.
Wichterle H, Garcia-Verdugo JM, Herrera DG, Alvarez-Buylla A. 1999. Young neurons from medial ganglionic eminence disperse in adult and embryonic brain. Nat Neurosci. 2:461–466.
Xu Q, de la Cruz E, Anderson SA. 2003. Cortical interneuron fate determination: diverse sources for distinct subtypes? Cereb Cortex. 13:670–676.
Yozu M, Tabata H, Nakajima K. 2005. The caudal migratory stream: a novel migratory stream of interneurons derived from the caudal ganglionic eminence in the developing mouse forebrain. J Neurosci. 25:7268–7277.
Zhou FM, Hablitz JJ. 1996. Morphological properties of intracellularly labeled layer I neurons in rat neocortex. J Comp Neurol. 376: 198–213.

Neuron
Article

Spatiotemporal Dynamics of Cortical Sensorimotor Integration in Behaving Mice

Isabelle Ferezou,[1,3] Florent Haiss,[2] Luc J. Gentet,[1] Rachel Aronoff,[1] Bruno Weber,[2] and Carl C.H. Petersen[1,*]
[1]Laboratory of Sensory Processing, Brain Mind Institute, Ecole Polytechnique Federale de Lausanne (EPFL), Switzerland
[2]Institute of Pharmacology and Toxicology, University of Zurich, Winterthurerstrasse 190, CH-8057 Zurich, Switzerland
[3]Present address: Laboratoire de Neurobiologie et Diversite Cellulaire, Ecole Superieure de Physique et de Chimie Industrielles (ESPCI), Paris, France.
*Correspondence: carl.petersen@epfl.ch
DOI 10.1016/j.neuron.2007.10.007

SUMMARY

Tactile information is actively acquired and processed in the brain through concerted interactions between movement and sensation. Somatosensory input is often the result of self-generated movement during the active touch of objects, and conversely, sensory information is used to refine motor control. There must therefore be important interactions between sensory and motor pathways, which we chose to investigate in the mouse whisker sensorimotor system. Voltage-sensitive dye was applied to the neocortex of mice to directly image the membrane potential dynamics of sensorimotor cortex with subcolumnar spatial resolution and millisecond temporal precision. Single brief whisker deflections evoked highly distributed depolarizing cortical sensory responses, which began in the primary somatosensory barrel cortex and subsequently excited the whisker motor cortex. The spread of sensory information to motor cortex was dynamically regulated by behavior and correlated with the generation of sensory-evoked whisker movement. Sensory processing in motor cortex may therefore contribute significantly to active tactile sensory perception.

INTRODUCTION

Sensory information is actively acquired by animals. This is particularly evident for the sense of touch, where self-generated movements often drive tactile input. To understand somatosensory perception it is therefore important to consider the interactions between sensory and motor systems. The rodent whisker system provides a relatively simple mammalian sensorimotor pathway (recently reviewed by Kleinfeld et al., 2006, and Petersen, 2007). During active sensation, the mystacial vibrissae predominantly move in a forward and backward motion termed "whisking." Such one-dimensional movement has the advantage that it can be easily and accurately quantified. Whisker movements can be evoked by the direct stimulation of neurons in the primary whisker motor cortex (Brecht et al., 2004; Haiss and Schwarz, 2005; Berg et al., 2005). Motor cortex activity can phase lock to whisker movements in rats trained to whisk for rewards (Ahrens and Kleinfeld, 2004) and during epileptiform activity (Castro-Alamancos, 2006). However, other data suggest that action potential firing in motor cortex is not normally phase-locked to the whisking cycle (Carvell et al., 1996). Equally, the frequency of whisking evoked by intracortical microstimulation is different from the frequency of the stimuli delivered to the motor cortex (Haiss and Schwarz, 2005; Cramer and Keller, 2006). From a behavioral perspective, it is clear that whisking occurs even in rodents with lesioned motor cortex (Gao et al., 2003), lesioned neocortex (Welker, 1964; Semba and Komisaruk, 1984), and in decerebrate rats (Lovick, 1972). Finally, a serotonergic input onto the facial nucleus motor neurons is sufficient to evoke whisking (Hattox et al., 2003; Cramer et al., 2007). The major role of the whisker motor cortex is therefore unlikely to be the simple rhythmic control of each whisking cycle.

Anatomical studies have provided evidence for sensory input to motor cortex originating from somatosensory cortex and thalamus (White and DeAmicis, 1977; Porter and White, 1983; Miyashita et al., 1994; Izraeli and Porter, 1995; Deschenes et al., 1998; Hoffer et al., 2003; Alloway et al., 2004). The whisker motor cortex could therefore serve to integrate sensory input with motor commands. In support of such a hypothesis, previous electrophysiological studies have shown that electrical stimulation of trigeminal sensory afferents (Farkas et al., 1999) or repetitive whisker deflections (Kleinfeld et al., 2002) could evoke responses in motor cortex. In this study, we applied voltage-sensitive dye to sensorimotor cortex to directly image the interactions between somatosensory and motor cortex in both anesthetized and awake head-fixed mice during behavior. We find that a single whisker deflection can evoke a highly distributed sensory response, with complex spatiotemporal dynamics, which begins in somatosensory cortex and is then relayed to motor cortex, in a manner dependent upon ongoing behavior. The

sensory-evoked activity in motor cortex in turn correlates with sensory-evoked whisker movement. Our results suggest that the whisker motor cortex is guided by powerful sensory input from the primary somatosensory barrel cortex directing active control of whisker movement during tactile sensory perception.

RESULTS

Voltage-Sensitive Dye Imaging of Sensorimotor Cortex

A large fraction of mouse somatosensory and motor cortex was exposed bilaterally and stained with voltage-sensitive dye (VSD) RH1691 (Figure 1A). Imaging the voltage-dependent fluorescence changes of neocortex stained with RH1691 allows the visualization of the ensemble membrane potential dynamics of the supragranular layers at millisecond temporal resolution and subcolumnar spatial resolution (Shoham et al., 1999; Seidemann et al., 2002; Slovin et al., 2002; Kenet et al., 2003; Petersen et al., 2003a, 2003b; Jancke et al., 2004; Grinvald and Hildesheim, 2004; Civillico and Contreras, 2006; Ferezou et al., 2006; Borgdorff et al., 2007; Berger et al., 2007; Lippert et al., 2007; Benucci et al., 2007; Xu et al., 2007).

A single brief passive deflection of the C2 whisker evoked a stereotypical pattern of cortical activity imaged with VSD in urethane-anesthetized mice (n = 15; Figures 1B–1F and see Movies S1 and S2 in the Supplemental Data available with this article online). The earliest sensory response occurred with a latency of 7.2 ± 0.9 ms following whisker deflection and was highly localized, specifically exciting the C2 barrel column of the contralateral primary somatosensory cortex (S1) (Ferezou et al., 2006). Over the next few milliseconds, the depolarization spread across a large part of the barrel cortex. Supragranular neurons in the surrounding barrel columns therefore become depolarized, in good agreement with electrophysiological membrane potential recordings revealing broad subthreshold receptive fields of L2/3 cortical neurons (Moore and Nelson, 1998; Zhu and Connors, 1999; Brecht et al., 2003). Approximately 8 ms after the earliest response in S1 cortex, a second localized anteromedial cortical region is depolarized, located 1.4 ± 0.2 mm anterior and 1.1 ± 0.2 mm lateral relative to Bregma (n = 15 experiments). This is within the previously identified location of the mouse motor cortex (M1) (Caviness, 1975; Franklin and Paxinos, 1996). The motor cortex depolarization occurred with a latency of 15.3 ± 1.3 ms following whisker deflection and also spread over the following milliseconds. Finally, after ~30 ms following whisker deflection, the sensory-evoked activity propagates to the other hemisphere, although depolarization in the hemisphere ipsilateral to the stimulated whisker is relatively weak (Figure 1C). Deflection of the C2 whisker therefore initiates cortical activity in two clearly separate focal regions, from which propagating waves of depolarization can spread to a large part of the sensorimotor cortex.

VSD Fluorescence Changes Reflect Cortical Synaptic Activity

In previous studies, we found that RH1691 VSD fluorescence changes in somatosensory cortex in vivo were correlated with the local ensemble subthreshold membrane potential changes of layer 2/3 pyramidal neurons (Petersen et al., 2003a, 2003b; Ferezou et al., 2006; Berger et al., 2007). These previous measurements were made in small craniotomies encompassing only part of the barrel cortex. In order to test whether local synaptic drive underlies the VSD signals in the larger craniotomies studied here, we combined local field potential (LFP) recordings with simultaneous VSD imaging (n = 4 mice, an example experiment is shown in Figures 2A–2C). The LFP signal correlated closely with the VSD signal, as reported by Lippert et al. (2007). A single brief deflection of the C2 whisker evoked VSD and LFP signals first in S1 and ~8 ms later in M1 (Figure 2A). The LFP signal, however, has a shorter duration because it primarily reflects the extracellular synaptic currents, whereas the VSD signal reflects membrane potential changes and is therefore prolonged due to the neuronal membrane time constants.

To address concerns that the large craniotomies might damage the cortex, we carried out control experiments applying VSD on two small craniotomies (one centered on S1 and the other in M1) and found a similar sequential activation of S1 and M1 following single C2 whisker deflection (n = 8 experiments, including 5 experiments in anesthetized mice and 3 experiments in awake mice; Figures S1A–S1C). We also observed a similar sensory-evoked LFP response in M1 with a small craniotomy centered on motor cortex leaving the somatosensory cortex untouched (n = 5 experiments, data not shown). Finally, in whole-cell recordings from small M1 craniotomies, we found neurons responding with depolarizing membrane potentials to single brief C2 whisker deflections at similar latencies (21 ± 6 ms, n = 7) to those recorded with VSD and LFP (an example experiment is shown in Figure S1D).

VSD Imaging of Spontaneous Activity in Sensorimotor Cortex

The spatiotemporal dynamics of cortical spontaneous activity can also be imaged using VSD (Arieli et al., 1996; Kenet et al., 2003; Petersen et al., 2003b; Ferezou et al., 2006; Berger et al., 2007). The ability to resolve spontaneous activity is of importance when considering the real-time imaging of cortical function during behavior (see Figures 7 and 8). We found close correlations between spontaneous VSD fluorescence changes and LFP signals in both S1 (Figure 2B) and M1 (Figure 2C) in urethane-anesthetized mice. The images and movie (Movie S3) reveal complex patterns of spontaneous activity across the sensorimotor cortex. Typically activity propagated as waves of depolarization reflecting UP states (Steriade et al., 1993; Cowan and Wilson, 1994; Petersen et al., 2003b; Cossart et al., 2003; Shu et al., 2003; Volgushev et al., 2006) and often very large fractions of sensorimotor cortex were synchronously depolarized. The amplitude of

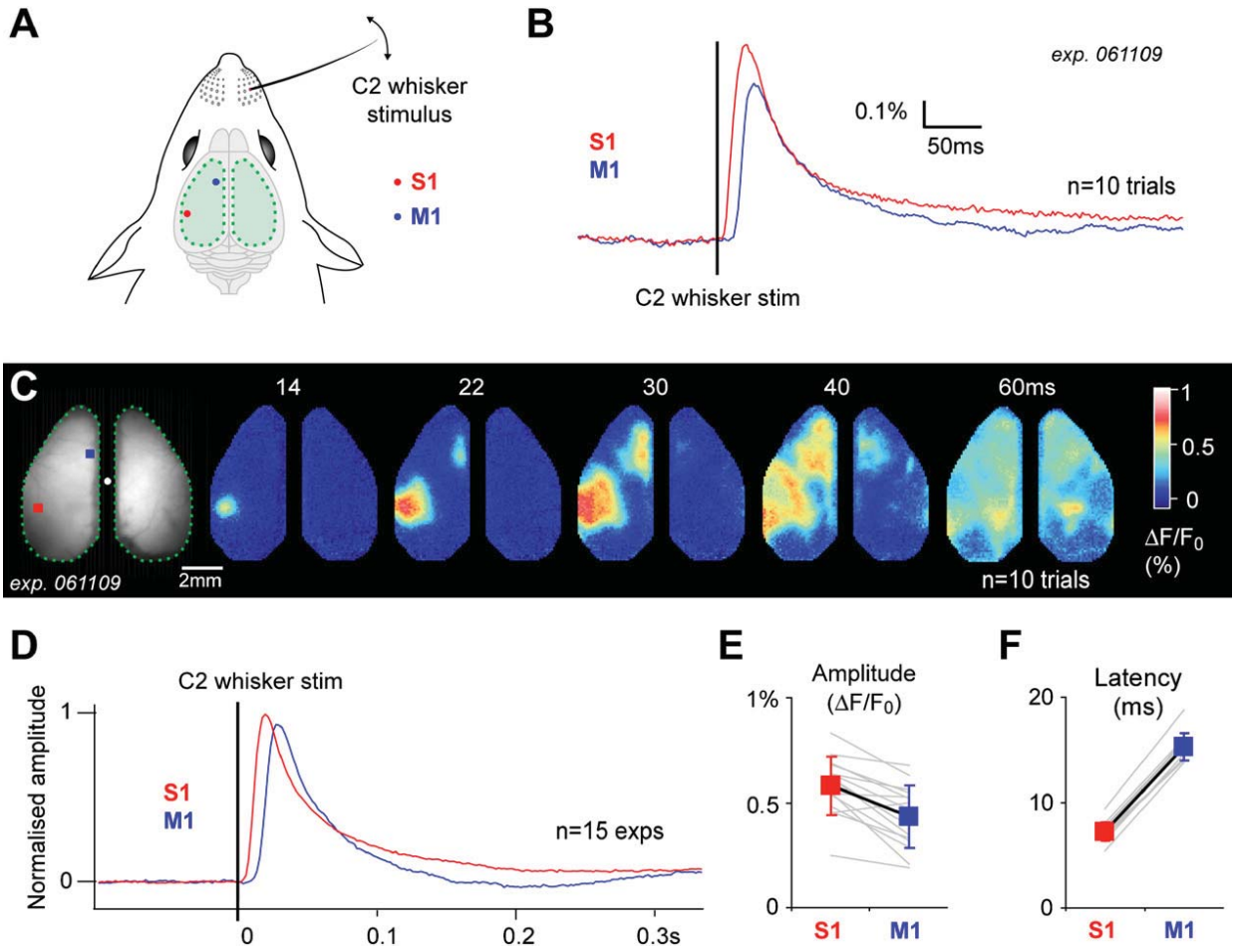

Figure 1. A Brief Deflection of a Single Whisker Evokes a Depolarizing Response in Both Somatosensory and Motor Cortex

(A) The green-shaded region schematically indicates locations of bilateral craniotomies. The craniotomies include a large fraction of somatosensory and motor cortex. The red dot indicates the position of the C2 barrel column of primary somatosensory cortex, and the blue dot is located in motor cortex. A small part of the primary visual cortex may be included in the posterior part of the craniotomies in some experiments.

(B) The craniotomies were stained with VSD RH1691 in a mouse under urethane anesthesia. A single brief deflection of the right C2 whisker evoked a transient increase in VSD fluorescence, first in primary somatosensory barrel cortex (S1, red trace) and then approximately 8 ms later in motor cortex (M1, blue trace). These traces were averaged across ten trials. Images from the same experiment showing the regions of interest from which the traces were computed are shown in (C).

(C) The left image shows resting VSD fluorescence with a white dot indicating the location of Bregma. The red square corresponds to the location of the C2 whisker representation in S1, and the blue square is located in M1. The single brief deflection of the right C2 whisker evoked an early localized response in the contralateral barrel cortex, followed by depolarization of the motor cortex. At later times, the sensory response is highly distributed, even spreading to parts of the ipsilateral cortex.

(D) Similar sequence of cortical activation, first in the somatosensory cortex and followed by motor cortex, was imaged with VSD in the 15 mice tested. Changes of fluorescence induced by a single C2 whisker deflection were quantified from S1 (red) and M1 (blue), normalized to the S1 peak response amplitude and averaged.

(E) Comparison of the peak amplitudes of the sensory responses measured in S1 and M1, for each individual experiment (grey lines) and mean ± SD (red for S1, blue for M1, linked by a black line).

(F) The latency of the sensory-evoked cortical activation was quantified in S1 and M1 by extrapolation of a linear 20%–80% fit of the rising phase of the signal. Data from individual experiments are shown in grey lines. Mean ± SD is indicated in red for S1, blue for M1, and linked by a black line.

spontaneous activity was similar, although usually smaller, to that of evoked activity (Figure S2).

We also imaged spontaneous activity in awake head-fixed mice, finding similarly diverse patterns of dynamic depolarizations propagating across sensorimotor cortex (Figure 2D). The example images show a correlated wave of depolarization spreading synchronously across somatosensory and motor cortex. We simultaneously filmed the whisker-related behavior of the mice at 500 Hz and matched the behavioral movie frame-by-frame to the VSD images of sensorimotor cortex function, allowing precise quantification of whisker movement. In order to quantify whisker-related behavior, the large mystacial vibrissae were trimmed immediately before the recording session,

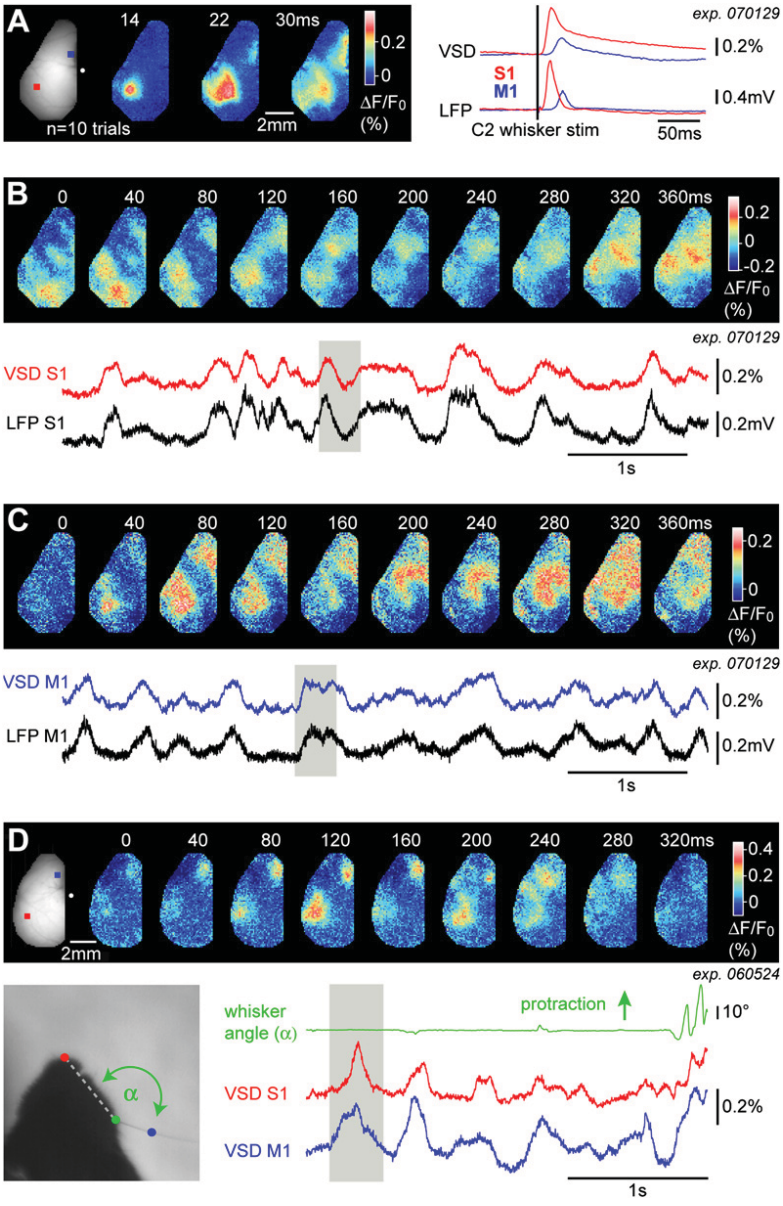

Figure 2. Voltage-Sensitive Dye Imaging and Local Field Potential Recording of Evoked and Spontaneous Activity in Sensorimotor Cortex

(A) The local field potential (LFP) in a urethane-anesthetized mouse was sequentially recorded in S1 and M1 locations corresponding to the regions of interest used to quantify the VSD fluorescence. Recordings of responses to C2 whisker deflection (n = 10 trials for each LFP location) revealed a close correlation between the simultaneously recorded optical and electrophysiological signals. Since the LFP signal relates to extracellular synaptic currents, the LFP response has a shorter duration than the VSD signal, which relates to membrane potential and is therefore slower due to the membrane time constants. The sign of the LFP signal is inverted for ease of comparison with the VSD signal.

(B) The LFP and VSD signals in the same urethane-anesthetized mouse were also correlated in the absence of sensory input, during spontaneous cortical activity. Lower traces show the quantification of the VSD fluorescence and the corresponding LFP recording in S1. The VSD images above illustrate the spontaneous events highlighted in gray.

(C) A different period of spontaneous activity in the same experiment, now with the LFP recording and VSD quantification in M1.

(D) VSD imaging of spontaneous activity in the sensorimotor cortex of an awake head-fixed mouse. The VSD images in this example show a correlated wave of spontaneous activity in motor (blue square) and somatosensory (red square) cortex. The whisker-related behavior was filmed at 500 Hz, and images were matched frame-by-frame to the VSD images (lower left image shows an example frame). The whisker angle was quantified for each frame (green trace) and plotted together with the changes in fluorescence in S1 (red trace) and M1 (blue trace). The period of spontaneous activity shown in the images above is highlighted by gray shading. At the end of the trial, the mouse begins to whisk, which is accompanied by depolarization of both somatosensory and motor cortex.

leaving only the right-hand C2 whisker intact. Under these conditions, we could precisely measure the rostrocaudal whisker movements. Toward the end of the trial, the mouse begins to whisk with concomitant depolarization of both motor and somatosensory cortex. From this trace, it is clear that the supragranular motor cortex can depolarize without whisker movement and, conversely, from other trials (data not shown), we found that whisker movement can be initiated without strong VSD signals in motor cortex. These results, highlighting the complex relationship between motor cortex activity and movement, may not be surprising in view of the fact that whisking can occur in rodents with lesioned motor cortex (Gao et al., 2003), lesioned neocortex (Welker, 1964; Semba and Komisaruk, 1984), and in decerebrate rats (Lovick, 1972). Equally, it is important to stress that the VSD imaging primarily reflects subthreshold depolarizations of layer 2/3, whereas it is the action potential activity of the layer 5/6 pyramidal neurons that is directly involved in the regulation of movement.

Somatotopic Organization of Tactile Responses in Sensorimotor Cortex

Having established the utility of imaging VSD fluorescence in these big craniotomies encompassing a large extent of somatosensory and motor cortex, we next began to functionally map the spatiotemporal dynamics of sensory responses evoked by different tactile stimuli. An example experiment is shown in Figure 3. The earliest responses

in somatosensory cortex were highly localized. The position of these early localized tactile responses changed depending upon the stimulus delivered. Deflection of the left C2 whisker evoked an early response in the right hemisphere (Figure 3A and Movie S2). Deflection of the right C2 whisker evoked an early localized response in the mirror symmetric location on the left hemisphere (Figure 3B and Movie S1). The dynamic patterns of evoked activity are very similar and allow a direct comparison of the bilateral propagation of the sensory signal. Interestingly, the response in the hemisphere ipsilateral to the stimulated whisker was not most prominent in the barrel cortex, but rather in frontal and posteriomedial parts of the dorsal cortex (likely motor cortex and parietal association cortex, respectively). That the spreading VSD signal appears to avoid exciting the ipsilateral barrel field is in good agreement with the lack of sensory responses to ipsilateral whisker deflections in whole-cell recordings of neurons in the supragranular barrel cortex (Brecht et al., 2003).

Single brief deflections of different individual neighboring whiskers evoked early localized sensory responses in accord with the somatotopic map of barrel cortex (Woolsey and Van der Loos, 1970). Responses in S1 to right C2 whisker deflections (Figures 3B and 3F) were mapped to lie between responses to whiskers B2 (Figures 3C and 3F), D2 (Figures 3D and 3F), C1 (Figure 3F), and C3 (Figure 3F). Tactile stimulation of the right forepaw (Figure 3E) evoked a sensory response anteromedial to the whisker responses. Superimposing these early localized responses provides a functional map of the somatosensory cortex (Figure 3F). However, as noted previously, the sensory responses do not remain localized to these cortical columns for more than a few milliseconds. Instead, the sensory information spreads across the supragranular cortex and even single brief whisker deflections can inform a large cortical area (Figure 3G).

The second localized region of activity evoked by whisker deflection occurred in the motor cortex ~8 ms after the initial response in S1. It is evident that the map of the early M1 responses evoked by whisker stimulation is more compact, with a greater overlap of the representation of different whiskers than in the S1 map (Figures 3B–3D, 3G, and 3H). Nonetheless, the early localized whisker responses in M1 were spatially ordered and were found to occur in a mirror symmetric map to the somatosensory cortex (Figure 3H).

Quantitative analysis of the spatial properties of the early S1 and M1 responses after stimulation of C2 and E2 whiskers confirmed this mirror symmetric organization (Figures 3I–3K). The early S1 responses evoked by C2 and E2 whiskers were separated by 894 ± 25 μm (n = 5). The early sensory responses evoked by C2 and E2 whisker deflection in M1 were separated by 387 ± 59 μm (n = 5). The somatotopic map representation of these whiskers in S1 is therefore approximately two times larger than in M1.

We made a further quantitative analysis of the relative somatotopic separations of the whisker representations comparing arcs versus rows of the whisker pattern. Sensory responses were evoked by C1, C2, and C3 whisker deflections for studying the separation of whisker representation along the C-row; and whiskers B2, C2, and D2 were deflected to study arc-2 organization. In S1, adjacent whiskers in the arc-2 were separated by 475 ± 116 μm (n = 4), and in the C-row they were separated by 251 ± 31 μm (n = 4). In M1, arc-2 whiskers were separated by 221 ± 94 μm (n = 4), and the C-row whiskers were separated by 138 ± 22 μm (n = 4). Both in S1 and M1, the whiskers lying in the same row are therefore represented in cortical regions closer to each other than the whiskers lying in the same arc.

Stimulation of the forepaw did not evoke a second localized region of activity (Figure 3E), and we propose that the somatosensory cortex and the motor cortex representations of the forepaw are too close to be distinguished under these experimental conditions.

These data demonstrate a highly dynamic map of sensorimotor processing in the dorsal cortex of mice, and they indicate that a sensory whisker map representation exists in motor cortex.

Whisker Deflection-Evoked Sensory Responses Are Located in the Whisker Motor Cortex

In view of the whisker deflection-evoked sensory responses in motor cortex, we wondered whether these might colocalize with the region of motor cortex involved in controlling whisker movement. We therefore performed intracortical microstimulation in lightly anesthetized mice to functionally map this cortical area (Figure 4). Trains of extracellular electrical current pulses of 100 μA at 60 Hz for 1.5 s were delivered sequentially to different locations in the mouse motor cortex (Figure 4A). Depending on the location of the stimulus, whisker retraction, whisker protraction, jaw movement, or forepaw movement was evoked. Movement of the C2 whisker was quantified with millisecond precision using a laser micrometer (Figure 4B). A consistent functional map of evoked movements was obtained through alignment, relative to Bregma, of data obtained from four mice (Figures 4C and 4D). Electrical stimulation of an anterior region (roughly located between 1–2 mm anterior to Bregma and 1–1.5 mm lateral) reliably evoked whisker retraction. Intracortical microstimulation of an adjacent more medial and posterior region evoked whisker protraction. This region corresponds to the previously identified rhythmic whisking region in rat motor cortex (Haiss and Schwarz, 2005). Clearly, the region of M1 where we imaged C2 whisker deflection evoked sensory responses (located 1.4 ± 0.2 mm anterior and 1.1 ± 0.2 mm lateral relative to Bregma, n = 15) is within the whisker motor cortex (Figure 4C and 4D).

Sensory Processing in M1 Depends on S1

We next began to investigate the pathways involved in directing sensory information to the whisker motor cortex. Given that somatosensory cortex always responded earlier than motor cortex to a brief C2 whisker deflection, we wondered whether activity in somatosensory cortex might in fact drive the sensory response in motor cortex.

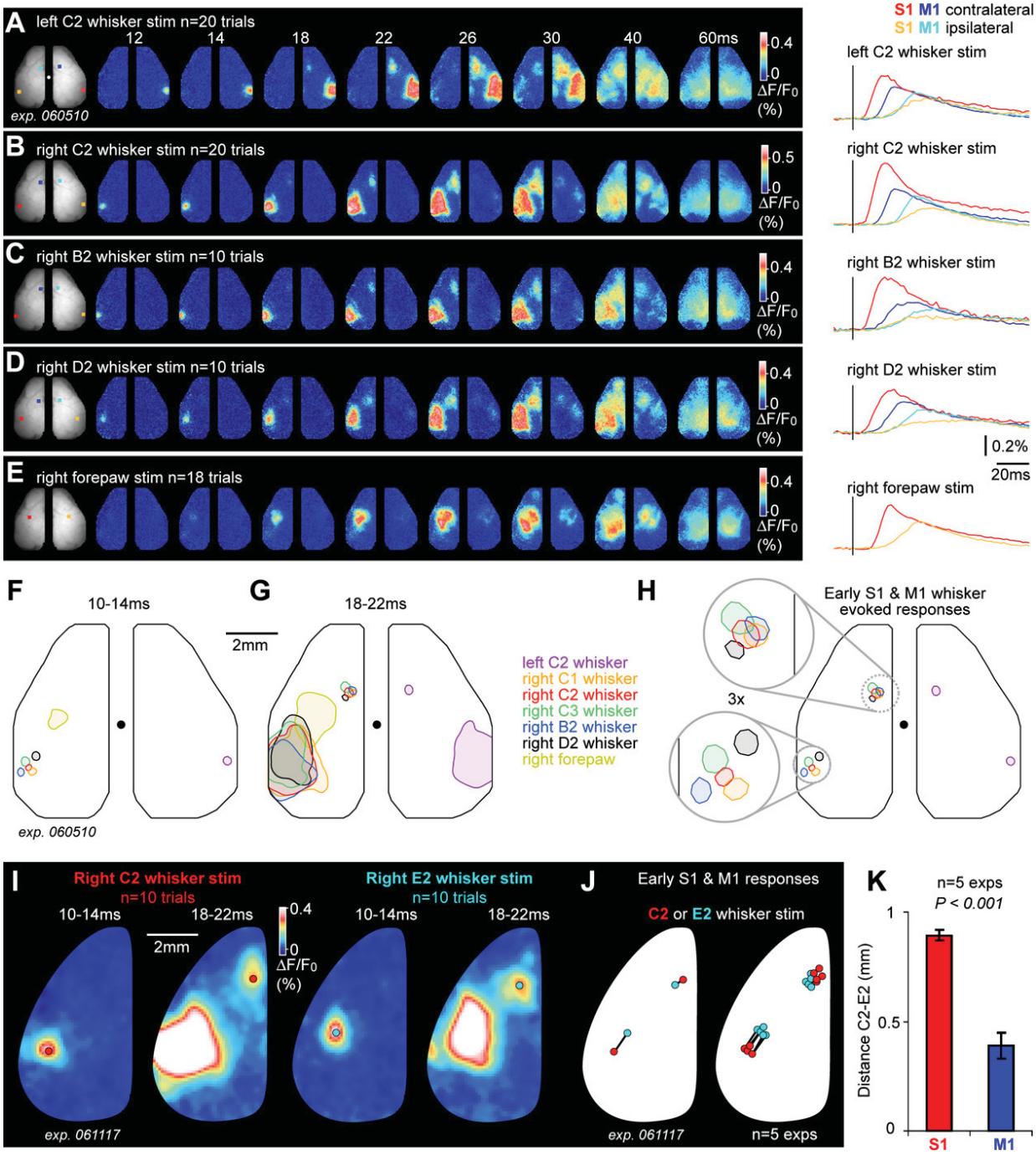

Figure 3. Bilateral VSD Imaging of Sensory Responses to Tactile Stimulation of Different Whiskers and the Forepaw

(A) Image of resting fluorescence of the VSD-stained bilateral craniotomies (far left). Bregma is indicated with a white dot. The red square indicates the location of the earliest response in contralateral somatosensory cortex, and the blue square the location of the first response in contralateral motor cortex. The orange and light-blue squares on the hemisphere ipsilateral to the stimulated whisker correspond respectively to somatosensory and motor areas. Their locations are symmetrical to the red and blue squares on the contralateral hemisphere. The spatiotemporal dynamics of VSD fluorescence changes evoked by a brief deflection of the left C2 whisker is shown in the adjacent panels. The time courses (far right) of responses to the whisker stimulus were measured within the regions of the red square (contralateral S1), blue square (contralateral M1), orange square (ipsilateral S1), and light-blue square (ipsilateral M1).

(B) The same experiment as in (A), but now with stimulation of the right C2 whisker.

(C) Stimulation of the right B2 whisker.

(D) Stimulation of the right D2 whisker.

We carried out two sets of experiments in urethane-anesthetized mice to test this hypothesis.

First, we used intracortical stimulation to directly excite the C2 barrel column (Figure 5A). Single brief current pulses evoked a response with short latency in the C2-related column, which spread across the barrel cortex and later depolarized the motor cortex. The pattern of the activity evoked by intracortical microstimulation is similar to that induced by the single deflection of the C2 whisker, suggesting that local excitation of the C2 column is sufficient to trigger the entire sensorimotor response (n = 3 experiments). These results from intracortical microstimulation are in good agreement with the rapid spread of depolarization observed upon intracortical microstimulation in the frontal eye field area of monkeys (Seidemann et al., 2002), although the late hyperpolarization evoked by the 500 Hz train of stimuli for 24 ms used in the monkey experiments was less prominent in our recordings, perhaps relating to our use of only a single stimulus.

In the second set of experiments, we investigated the effect of locally blocking synaptic activity upon the spreading VSD response (Figure 5B). Local injection of ~20 nl CNQX (250 μM) and APV (1 mM) to block ionotropic glutamate receptors in the C2 barrel column suppressed the entire C2 whisker deflection-evoked sensory response in both somatosensory and motor cortex (in S1 only 6% ± 4% and in M1 only 7% ± 4% of the control response remained, n = 10 experiments) (Farkas et al., 1999). Such local pharmacological blockade had little effect on the responses to deflection of the nearby E2 whisker (Figure S3). We conclude that activity in the C2 barrel column is necessary and sufficient for the depolarization in motor cortex evoked by C2 whisker deflection.

Monosynaptic Pathway from S1 to M1

Previous anatomical work in rats has provided evidence for a direct projection from septal regions of the barrel cortex to motor cortex (Miyashita et al., 1994; Izraeli and Porter, 1995; Hoffer et al., 2003). However, the mouse barrel cortex does not have an equivalent septal organization, with each barrel being tightly apposed to its neighbor. Nonetheless, it is clear that there is a projection from S1 to M1 in mice (White and DeAmicis, 1977; Porter and White, 1983), and here, we specifically investigated whether neurons in the mouse C2 barrel column project to M1 (Figure 6A). Pyramidal neurons located in the C2 barrel column were labeled with GFP expressed from a lentiviral vector driven by the αCaMKII promoter (Dittgen et al., 2004; Aronoff and Petersen, 2006). A strong axonal projection was found targeting motor cortex on the same cortical hemisphere (Figures 6B and 6D–6F). High-density axons with many boutons were found in the same location where sensory-evoked responses were imaged in motor cortex (Figure 6C). Despite strong labeling of the corpus callosum, the density of fibers in the somatosensory cortex of the other hemisphere was low (Figure 6G), in agreement with the weak long-latency ipsilateral VSD signals. The paucity of callosal axons terminating in the barrel cortex of the opposite hemisphere is also in good agreement with recent mouse data showing that only a small very lateral portion of the barrel field is innervated by supragranular callosal axons (Petreanu et al., 2007).

Our anatomical data provide evidence for a strong and direct glutamatergic connection from the C2 column of somatosensory barrel cortex to motor cortex. This monosynaptic pathway could mediate the sensory-evoked response in motor cortex. The ~8 ms latency difference between S1 and M1 activity is consistent with a pyramidal neuron axonal conduction velocity of ~450 μm/ms (Meeks and Mennerick, 2007). For the ~4 mm separation of S1 and M1, this would give an action potential propagation time of ~9 ms, consistent with our functional imaging results. However, we cannot exclude a contribution of other indirect pathways. Indeed, from previous studies, it is known that infragranular S1 neurons project to the posterior medial (POM) thalamic nucleus (Veinante et al., 2000), and POM, in turn, innervates M1 (Deschenes et al., 1998; Miyashita et al., 1994). Interestingly, under anesthesia, POM is inhibited by zona incerta (Lavallee et al., 2005), and activity in POM depends upon S1 cortex (Diamond et al., 1992), but during active whisking this sensory pathway could become important (Trageser et al., 2006).

(E) The same experiment as (A)–(D), but now with deflection of the skin on the right forepaw. In this case, there is not a clear spatial separation of the somatosensory and motor cortex response, which may, in fact, colocalize. Therefore, only two regions of interest are quantified.
(F) Contour plots showing the location of the early S1 responses. The half-maximal S1 response amplitude contours were computed from Gaussian-filtered VSD images at 10-14 ms after the stimulus.
(G) Equivalent half-maximal contour plots of the VSD responses 8 ms later than the previous panel, showing the early M1 responses and the spreading S1 responses.
(H) Superposition of the early S1 and M1 response components. The insets in the circles show three times magnified views of the early responses in S1 and M1. The somatotopic representation in S1 and M1 show a mirror symmetric organization. Thus the D2 whisker representations are closer to each other than the B2 representations.
(I) The VSD signals evoked by C2 and E2 whisker stimulation in a different experiment are shown on an expanded color scale to highlight the small early responses. The central region of the early responses (highlighted by filled circles in red for C2 and in cyan for E2) were quantitatively identified through Gaussian fitting. The primary sensory responses evoked by the C2 and the E2 whiskers are in different locations in both S1 and M1.
(J) Superposition of the primary response locations for the C2 whisker (red) and E2 whisker (cyan) for the example experiment (left) and from all five experiments (right). A line links the data from individual experiments. In S1 there is a large somatotopic shift in the primary representation comparing the C2 and E2 whiskers. In M1 there is also a clear shift observed in each of the five experiments, but the shift is smaller with a mirror symmetric displacement compared to the S1 shift.
(K) Quantification of the somatotopic shift comparing C2 and E2 whisker representations in S1 and M1. The somatotopic map in S1 is approximately twice as large as the M1 map. Bar graph shows mean ± SD.

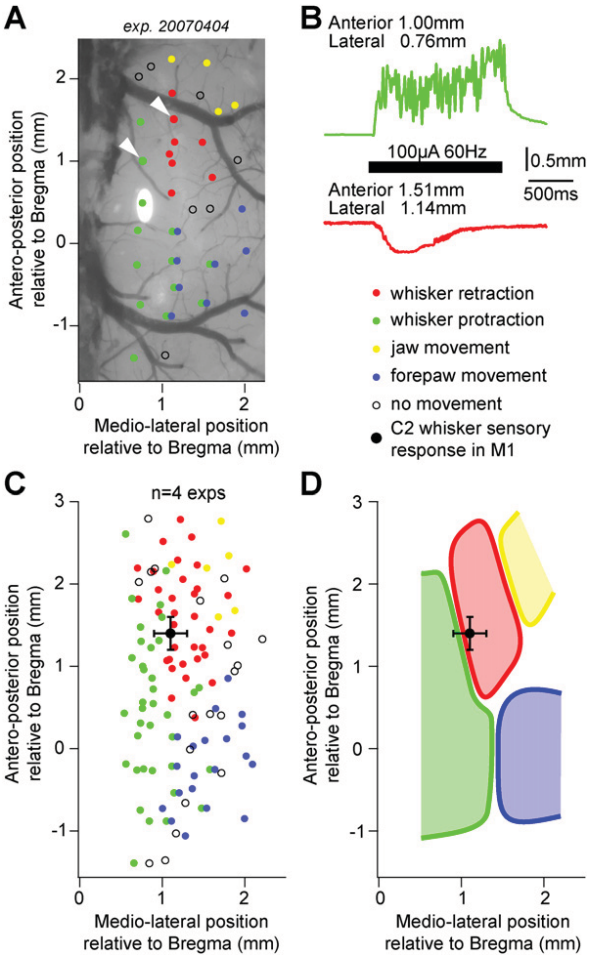

Figure 4. Functional Mapping of Mouse Motor Cortex with Intracortical Microstimulation

(A) Photomicrograph of the cortex with coordinates relative to Bregma. Each color-coded circle corresponds to a motor cortex location where intracortical microstimulation was tested in a lightly anesthetized mouse. Red points correspond to locations where intracortical microstimulation evoked whisker retraction. Green points indicate locations where stimulation evoked protraction. Blue points indicate evoked forepaw movement (in some cases both whisker protraction and forepaw movement were evoked, and in these locations the blue is displaced by ~0.05 mm to the right to allow both blue and green to be visible). The yellow points correspond to locations where stimulation evoked jaw movement. No movement was observed by stimulation at locations indicated by open black circles.

(B) Movements of the C2 whisker evoked by intracortical microstimulation at the locations indicated by white arrowheads in (A).

(C) Functional mouse whisker motor maps from four different mice were aligned at Bregma and superimposed. The location of the earliest sensory-evoked VSD signal (quantified in separate experiments) is superimposed as a black dot together with standard deviation bars (n = 15 experiments).

(D) Schematic drawing of the mouse whisker motor cortex map.

Sensory Responses in Awake Head-Fixed Mice during Behavior

In the above experiments, we investigated sensory processing in anesthetized mice. A critical issue is whether similar sensory-evoked responses occur in awake mice. We therefore trained mice for head fixation and performed VSD imaging experiments while filming whisker-related behavior. In order to deliver reproducible whisker deflections in awake and active mice, we attached a small metal particle to the C2 whisker and evoked whisker movement by generating brief magnetic fields (Crochet and Petersen, 2006; Ferezou et al., 2006). Such brief passive whisker deflections in awake mice (n = 13; Figure 7A) evoked the same stereotypical pattern of activity as observed in anesthetized mice. The highly distributed cortical sensory response to a single whisker deflection involving sequential activity in somatosensory cortex followed by motor cortex is therefore not induced by anesthesia, but appears to be a feature of normal brain function.

Sensory whisker information can also be actively gathered by mice as they move whiskers into contact with objects in their surroundings. We therefore combined VSD imaging of sensorimotor cortex and filming of whisker movements to identify the precise timing of individual whisker-object contacts. We observed the stereotypical sequence of cortical activity of S1 followed by M1 during the active touch of an object with the C2 whisker (Figures 7B and 7C and Movie S4). Although different whisker-object touches evoked variable responses, sequential depolarization of somatosensory cortex followed by motor cortex was observed in the averaged response of all 18 touches in this experiment (Figure 7D). Depolarization of both somatosensory and motor cortex evoked by active touch was observed in all five mice tested. In awake mice and under anesthesia, a single brief whisker deflection, be it active or passive, can therefore evoke depolarizing propagating sensory activity in both somatosensory and motor cortex.

Sensorimotor Processing Correlates with Behavior

The sensory responses in motor cortex could directly contribute to whisker motor control and thus we next analyzed the trial-by-trial correlations between cortical sensorimotor processing and behavior (Figure 8). The C2 whisker of awake head-fixed mice was passively deflected by magnetic pulses, while we simultaneously imaged VSD fluorescence and whisker movement. We distinguished between three different sequences of whisker-related behavior, which we analyzed separately. In the first case, the mice were quiet (without whisker movement) at the time of the stimulus, and following the stimulus, they began whisking (Figure 8A). In the second class of trials, the mice were quiet at the time of the stimulus and remained quiet, without whisker movement, after the stimulus (Figure 8B). In the third class, the mice were actively whisking at the time of the stimulus (Figure 8C), in which case they always continued to whisk after the stimulus. The whisker deflection induced by the magnetic field was oriented in a vertical plane and therefore not apparent on the images or the quantified traces of whisker movement (Figures 8A–8C). Sensory responses evoked by the

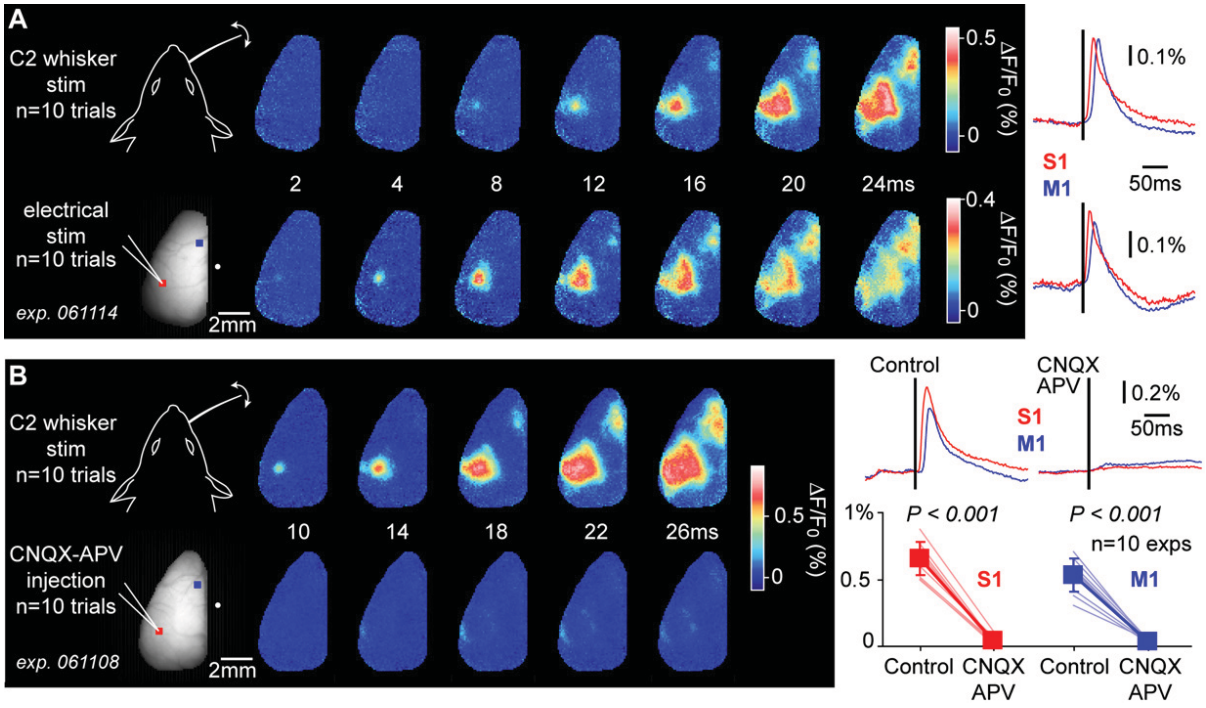

Figure 5. Sensory Processing in M1 Depends upon Activity in S1

(A) Intracortical microstimulation of the C2 barrel column evoked a similar response to that evoked by C2 whisker deflection, including sequential depolarization of S1 followed by M1.

(B) Local injection of ionotropic glutamate receptor antagonists into the C2 barrel column blocked the C2 whisker-evoked response in both S1 and M1. Time course of VSD responses before and after pharmacological blockade for this example experiment are shown in the upper right panel. The lower right panels indicate the effect CNQX and APV in all ten experiments carried out (light-red lines quantify responses in S1 in individual experiments, with bright red indicating the mean ± SD; light-blue lines show the effect in M1, with bright blue indicating the mean ± SD).

same magnetic C2 whisker deflection and imaged with VSD were highly variable, but correlated closely with the three different classes of whisker-related behaviors.

Large-amplitude spreading sensory responses were imaged in S1 and M1 on trials when the stimulus provoked the mouse to begin active whisking, whereas before the stimulus the whisker was not moving (Figures 8A and 8E and Movie S5). However, if the C2 whisker was neither actively moving before nor after the stimulus delivery, then smaller-amplitude localized responses were recorded in S1 with strongly reduced activity in M1 (Figures 8B and 8E). For stimuli that did not provoke whisking, responses were significantly reduced in S1 by 23% ± 42% (mean ± SD, $p = 0.026$) and in M1 by 45% ± 46% ($p = 0.034$), quantified across experiments in nine mice. This effect was significantly stronger in M1 than in S1 ($p = 0.042$, $n = 9$ mice). The stimulus-driven depolarization in M1 therefore correlates with the generation of sensory-evoked whisker movements. A passive whisker stimulus evoking a sensory response in the whisker motor cortex during quiet wakefulness might therefore be an important command signal for the mouse to begin whisking. The underlying mechanism for the variability of the responses evoked during quiet wakefulness is currently unclear. Strong responses were intermixed with weak responses, so it is unlikely to reflect slow changes in behavioral state. At least part of the variability is likely to result from interactions with spontaneous activity (Figure 2D), which could have a strong impact upon sensory processing in the same way that UP and DOWN states play profound roles in regulating sensory processing in the anesthetized rodent whisker sensory pathway (Petersen et al., 2003b; Sachdev et al., 2004). Further experiments in awake mice directly investigating the interactions of spontaneous cortical activity and sensory processing would be of great interest.

When the C2 whisker stimulus occurred during active whisking, smaller-amplitude sensory responses were evoked in somatosensory cortex (Chapin and Woodward, 1982; Fanselow and Nicolelis, 1999; Castro-Alamancos and Oldford, 2002; Hentschke et al., 2006; Ferezou et al., 2006; Crochet and Petersen, 2006). These small-amplitude sensory responses evoked during whisking were spatially restricted to a small part of the S1 barrel cortex, generating only very weak depolarization of motor cortex (Figures 8C and 8F). Across 11 experiments, the response evoked during whisking was decreased by 91% ± 36% in M1, and by 61% ± 18% in S1, relative to stimuli delivered at a time when there was no ongoing whisker movement. The decrease in evoked responses during whisking was significantly greater in M1 compared

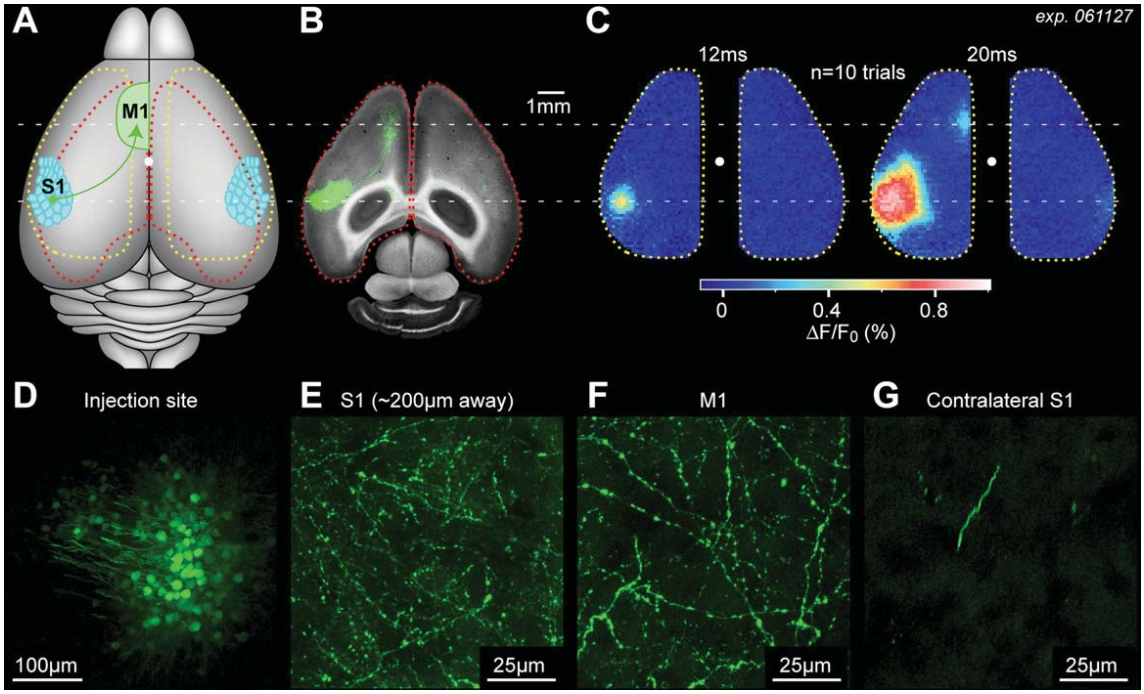

Figure 6. Monosynaptic Input from the Somatosensory Cortex Could Contribute to the Sensory Response in Motor Cortex

(A) Schematic drawing indicating location of the primary somatosensory barrel cortex (S1) and the whisker motor cortex (M1).

(B) Lentivirus encoding GFP under the control of the αCaMKII promoter was injected directly into the C2 barrel column, which had been functionally mapped by intrinsic optical imaging. Three weeks later, the brain was sliced horizontally in 100 μm sections and the GFP fluorescence imaged. The red dashed line (also in panel [A]) outlines a horizontal brain slice with superimposed GFP epifluorescence montage from three mice. A dense axonal projection from the C2 barrel column to motor cortex is evident.

(C) The yellow outline (also in panel [A]) indicates the area imaged by VSD showing early responses to C2 whisker deflection. The sensory evoked activity in the motor cortex colocalizes with the dense axonal projection from the C2 barrel column.

(D) Confocal maximal-intensity projection of the entire thickness of a horizontal brain slice showing the lentiviral injection site.

(E) As above, but for a region ~200 μm anterior to the injection site.

(F) As above, but for a region of the motor cortex.

(G) As above, but for a region of the barrel cortex on the opposite hemisphere symmetrical to the injection site.

to S1 ($p = 0.032$, $n = 11$ mice), demonstrating that sensory processing is more localized during active behavior. Ongoing behavior therefore plays a key role in dynamically gating cortical sensorimotor processing.

DISCUSSION

The data in this study provide the first images of the spatiotemporal dynamics of cortical sensorimotor integration, revealing highly dynamic and distributed processing, which correlates strongly with behavior.

Highly Distributed Processing of a Single Whisker Deflection

A single brief deflection of a single whisker evokes a somatotopically mapped cortical depolarization, which remains localized to its barrel column only for a few milliseconds. Pyramidal neurons then rapidly inform a large part of sensorimotor cortex about the whisker deflection. This dynamic highly distributed cortical depolarization provides a mechanism for the integration of sensory information. The corollary of such a spatially extended single whisker response across sensorimotor cortex is that individual neurons should be sensitive to a very broad range of stimuli, that is they should have broad subthreshold receptive fields. Whole-cell recordings in somatosensory barrel cortex show that supragranular neurons indeed have large receptive fields (Moore and Nelson, 1998; Zhu and Connors, 1999; Brecht et al., 2003) in good agreement with our VSD imaging results, which also relate primarily to subthreshold membrane potential changes in the superficial cortical layers (Ferezou et al., 2006). In fact, it is becoming increasingly clear that stimuli of one sensory modality can even affect processing in primary cortical areas of other sensory modalities (Fu et al., 2003; Wallace et al., 2004; Ghazanfar et al., 2005; Kayser et al., 2005; Martuzzi et al., 2006; Lakatos et al., 2007; reviewed in Schroeder and Foxe, 2005; Ghazanfar and Schroeder, 2006; Bulkin and Groh, 2006; Macaluso, 2006).

Such highly distributed processing of sensory information may be an important feature of the neocortex. Somehow, the brain must correlate tactile sensory input from different body parts. If a whisker has just been deflected by an approaching object or animal, it may well be that

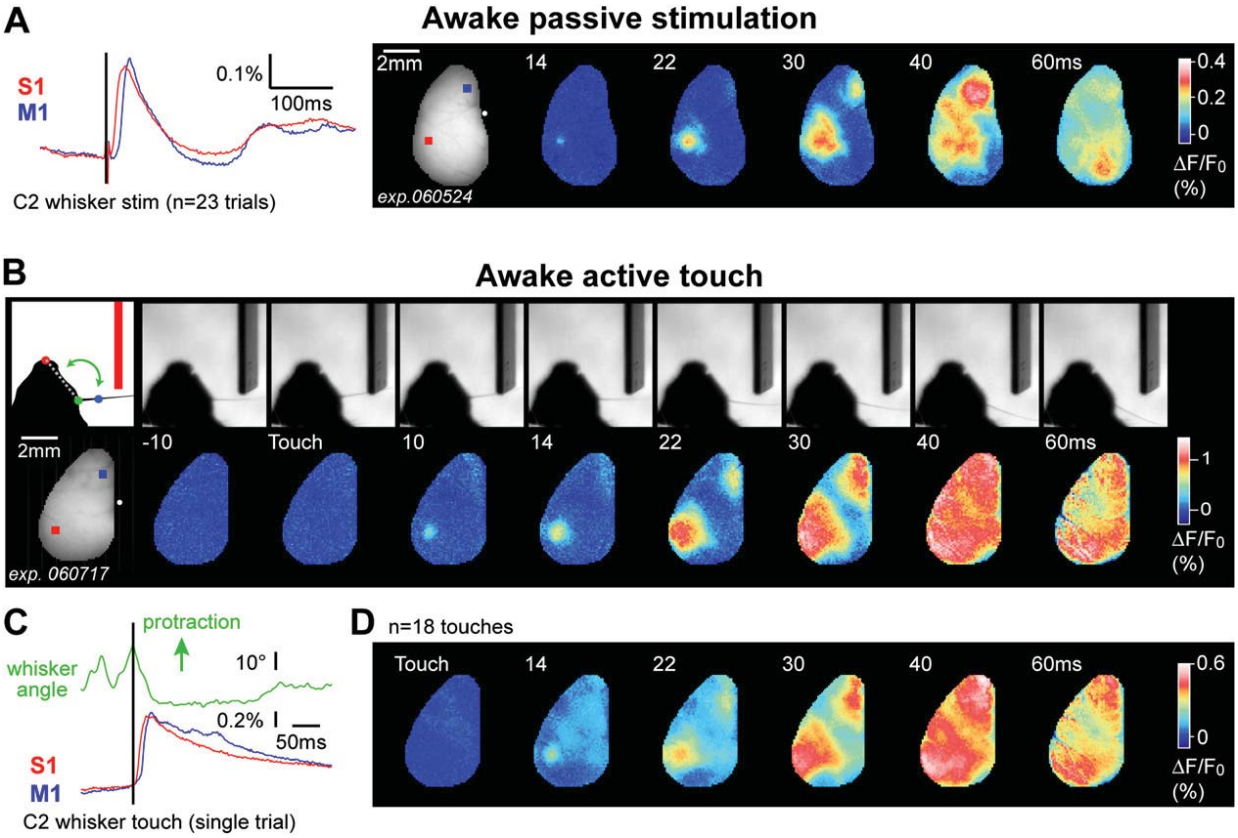

Figure 7. Both Passive and Active Deflections of the C2 Whisker Evoke Activity in Somatosensory and Motor Cortex of Awake Head-Fixed Mice

(A) Passive deflection of the C2 whisker in an awake mouse evoked VSD responses first in the somatosensory cortex followed by motor cortex, as observed in urethane-anesthetized mice.

(B) A single-trial example of active touch, imaged in an awake behaving mouse. The C2 whisker actively touched an object (upper image sequence), evoking a spreading VSD response, first in somatosensory and then in the motor cortex (lower image sequence).

(C) Quantification of whisker movement (green trace) and VSD fluorescence changes in S1 (red) and M1 (blue) from the same single trial.

(D) A similar sequence of sensorimotor cortex depolarization was observed on average across 18 different whisker-object touches in the same experiment.

the cause of the sensory stimulus will very soon affect input at other body locations. That a single whisker deflection can inform a large cortical area allows the modulation of sensory processing in these other regions, in a manner dependent upon the immediate previous sensory experience. In a quiet animal, the activity in the C2 barrel column has spread across sensorimotor cortex within tens of milliseconds, and the sensorimotor system may now be primed to respond to further input. Subsequent tactile stimuli occurring within the next tens or hundreds of milliseconds can therefore very easily become associated with the initial event. Such context-dependent processing of sensory information could be an important feature of the neocortex. Perhaps most importantly, such highly distributed processing is essential for associational plasticity and learning.

It should be noted that VSD imaging corresponds closely to subthreshold membrane potential changes in supragranular neurons, but not necessarily to action potential activity. Depolarization is of course necessary to evoke action potentials, but since neuronal membrane potential is often far from threshold, large depolarizations are possible without evoking action potentials even in awake mice (Crochet and Petersen, 2006). Current evidence in awake rodents would suggest that most of the electrical activity in the neocortex is in fact subthreshold with relatively low action potential firing rates (Crochet and Petersen, 2006; Lee et al., 2006). The VSD imaging technique thus provides information relating to depolarization, but not action potential firing. Indeed, we recently compared the spatiotemporal differences between sensory responses imaged with voltage- and calcium-sensitive dyes (which respectively reflect subthreshold and suprathreshold activity primarily) and found that the suprathreshold calcium signals remained more localized than the spreading VSD responses (Berger et al., 2007). The highly distributed sensory responses evoked by single whisker deflections are therefore likely to reflect subthreshold depolarizations rather than action potential firing.

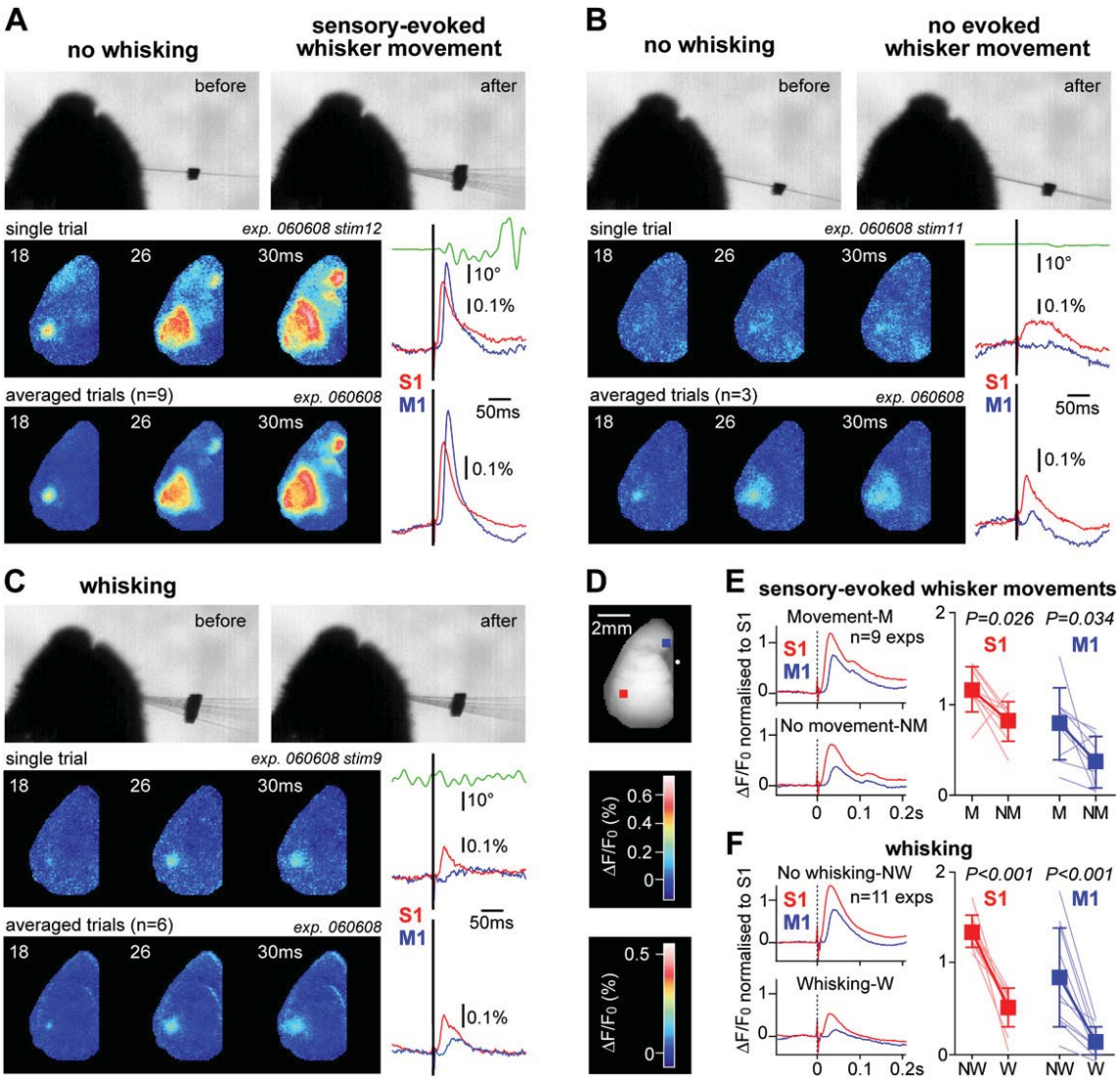

Figure 8. Trial-to-Trial Variability in Sensorimotor Processing Correlates with Behavior

(A) Individual trials were analyzed depending upon the whisker-related behavior. In trials during quiet wakefulness where the C2 whisker deflection drove a sensory-evoked whisker movement, a large spreading sensory response was evoked in both sensory and motor cortices. The upper images show 25 superimposed frames taken over a 100 ms period immediately before (left) and after (right) stimulation of the C2 whisker. The images show that in this trial the C2 whisker stimulus drives a sensory-evoked whisker movement. The middle panel shows VSD images and quantification from the same single trial. There is a large-amplitude spreading VSD signal that evokes a strong response in M1. The lower series of images shows the average of VSD images from all trials in this experiment where the stimulus was delivered during quiet wakefulness and evoked a whisker movement. The green trace (right) indicates whisker position; red and blue traces show the time course of the VSD signal in S1 and M1, respectively.

(B) In other trials from the same experiment, the same whisker stimulus was delivered during quiet periods as in (A), but in this case, the stimulus did not evoke a whisker movement. In these trials, only a small cortical response was observed, which remained localized to the somatosensory cortex.

(C) A small localized somatosensory response was also evoked during trials in the same experiment, when the mouse was spontaneously whisking at the time of the stimulus delivery.

(D) Location of regions of interest and color scales for the previous panels.

(E) Across 9 experiments, stimuli delivered during quiet wakefulness evoked significantly bigger responses in S1 and M1, if they were associated with a sensory-evoked whisker movement. This effect was significantly greater for the M1 response compared to the S1 response. The left panel shows the grand average time courses of the sensory responses with either evoked movement (M) or no movement (NM). The right panel indicates the data from individual experiments shown in light red for S1 and light blue for M1. The dark red and dark blue indicate mean ± SD.

(F) Across 11 experiments, the passively evoked sensory response in S1 and M1 was significantly smaller during active whisking compared to during quiet wakefulness. The smaller response evoked during whisking was more localized to S1, spreading little to M1. The left panel shows the grand average time courses of the evoked responses during no whisking (NW) or during whisking (W). The right panel indicates the data from individual experiments shown in light red for S1 and light blue for M1. The dark red and dark blue indicate mean ± SD.

There are many factors that regulate the spread of the VSD response. We previously demonstrated that very weak and brief whisker deflections can evoke VSD responses that remain localized to a single cortical column (Petersen et al., 2003a; Berger et al., 2007). Spontaneous activity also interacts strongly with sensory processing, with localized small-amplitude VSD responses being evoked during UP states (Petersen et al., 2003b). Equally, during early development, sensory responses to individual whisker deflections do not spread far, but rather remain localized to their specific cortical column (Borgdorff et al., 2007). Sensory experience has also been shown to profoundly regulate the extent of sensory processing (Polley et al., 1999, 2004). Finally, it is clear that sensory processing depends strongly upon ongoing behavior, as further discussed below.

Dynamic Control of Sensorimotor Processing

The large-amplitude sensory responses evoked during quiet wakefulness (Figure 8A), which propagate across sensorimotor cortex, may function as a sensitive detection system alerting the mouse to the presence of an unexpected sensory input. Sensory input to whisker motor cortex, together with lower-level sensorimotor loops (Nguyen and Kleinfeld, 2005), may be an important mechanism for the initiation of whisking—after a passive stimulus is perceived, the mouse can actively explore to uncover further sensory information relating to the stimulus.

On the other hand, small-amplitude localized sensory responses were evoked by passive stimuli during whisking (Figure 8C). Sensory processing is therefore dynamically gated by ongoing behavior (Chapin and Woodward, 1982; Fanselow and Nicolelis, 1999; Castro-Alamancos and Oldford, 2002; Hentschke et al., 2006; Ferezou et al., 2006; Crochet and Petersen, 2006). The barrel cortex during active whisking is in a different state compared to quiet periods without whisking. The slow large-amplitude cortical oscillations that propagate as waves during quiet periods (Ferezou et al., 2006) disappear during active whisking (Crochet and Petersen, 2006). Supragranular barrel cortex neurons depolarize during whisking with slight decrease of input resistance (Crochet and Petersen, 2006). These changes in brain state and in individual neurons likely contribute to the different sensory processing during active whisking compared to quiet wakefulness. Whereas the spreading responses to passive stimuli during quiet wakefulness may function to alert the animal to the presence of an unexpected stimulus, the localized processing of single whisker information in its cortical column may allow more specific sensory processing to occur. The more localized sensory processing during active whisking may be better suited to discriminate and perform fine-grain analyses of sensory stimuli rather than the large-amplitude propagating responses evoked during quiet wakefulness. Localized cortical processing of single-whisker information may be useful for texture discrimination or object location (Harris et al., 1999; Szwed et al., 2003; Arabzadeh et al., 2005; Knutsen et al., 2006; Mehta et al., 2007). Alternatively, the small-amplitude localized processing of the brief passive stimulus that we deliver during active whisking may simply go unnoticed by the mouse, making little impact upon brain or behavior. From this point of view, it is interesting to note that large-amplitude propagating sensory responses can occur during active touch of real objects (Figures 7B–7D; Ferezou et al., 2006; Crochet and Petersen, 2006). Active touch of real objects might be amplified by brain stem sensorimotor loops accelerating the whisker into the object (Nguyen and Kleinfeld, 2005), which would not occur for the brief passive stimuli applied in Figure 8. In order to address the functional roles of the dynamic gating of sensorimotor processing during behavior, future experiments must investigate the psychophysical detection thresholds (Stuttgen et al., 2006) for stimuli delivered during different behaviors.

Sensory Control of Motor Cortex

Sensory responses in M1 were prominent when a passive stimulus was delivered during inactive periods, and might therefore correspond to a "wake-up" call for the sensorimotor cortex (Figure 8A). Movements initiated through the sensory-evoked depolarization of the motor cortex might then be organized to actively gather further information relating to the tactile input. Equally, sensory responses were observed in motor cortex following active touch (Figures 7B–7D). Thus, in a similar way that we change our finger and hand movements during active contact with an object to obtain shape and textural information, the mouse might regulate whisker movements to help extract tactile information. The sensory map in whisker motor cortex (Figure 3) suggests that sensory information relating to individual whiskers is processed in specific regions of the whisker motor cortex. This might allow fine adjustments of individual whisker movements guided by specific sensory feedback related to that same whisker relayed from S1. Interestingly, the independent movement of individual whiskers has already been observed (Sachdev et al., 2002).

The sensory processing that we observe with VSD imaging could be gated in complex manners before resulting in alterations in motor output. The current VSD imaging technique provides information primarily relating to subthreshold membrane potential changes in layer 2/3. One interesting possibility requiring further investigation is that sensory processing in motor cortex might be most prominent in layer 2/3, which could be differentially regulated compared to the action potential firing of layer 5/6 pyramidal neurons that contribute more directly to motor control. It would therefore be of great interest to image the spatiotemporal dynamics of deeper cortical layers, which could potentially be achieved in future studies using dye injections combined with fiber imaging technology.

Future Perspectives

VSD imaging of sensorimotor cortex appears to be a promising technique for observing real-time integration

of information between sensory and motor cortex. Here, we studied processing related to passively and actively evoked whisker sensory input, but future studies should further investigate spontaneous activity (Figures 2B–2D) correlating both the activity patterns between brain areas and with behavior. The dynamic correlations between different cortical areas might provide information relating to the organization of the functional connectivity between cortical areas (Vincent et al., 2007) and how this is regulated by behavior. Equally, by making craniotomies extending further posteriorly, it might well be possible to image visual cortex and perhaps even cerebellar activity simultaneously with sensorimotor cortex. Over the next years, we plan to develop tapered fiber optic image bundles to visualize cortical dynamics in these large craniotomies in freely moving mice (Ferezou et al., 2006). This study, in which we imaged a large fraction of the mouse sensorimotor cortex at millisecond temporal resolution and subcolumnar resolution, is therefore a first step toward high spatiotemporal resolution imaging of the entire dorsal mouse brain during behavior.

EXPERIMENTAL PROCEDURES

Voltage-Sensitive Dye Imaging

All experiments were carried out with C57BL6J mice aged from 1 to 5 months in accordance with authorizations approved by the Swiss Federal Veterinary Office. Surgical and imaging procedures were largely as previously described (Petersen et al., 2003a, 2003b; Ferezou et al., 2006; Berger et al., 2007). Surgery for awake recordings (Figures 2D, 7, and 8) was carried out with isoflurane (1.5%), and a head-fixation post was glued onto the skull. For anesthetized recordings (Figures 1, 2A–2C, 3, 5, and 6), mice were injected with urethane (1.5 mg/g). The bone overlying the area to be imaged was removed. Extreme care was taken at all times not to damage the cortex, especially during removal of the dura. The VSD RH1691 was dissolved at 1 mg/ml in Ringer's solution containing (in mM) 135 NaCl, 5 KCl, 5 HEPES, 1.8 $CaCl_2$, 1 $MgCl_2$. This dye solution was topically applied to the exposed cortex and allowed to diffuse into the cortex for 1 hr. The cortex was subsequently washed to remove unbound dye and covered with agarose before placing a coverslip on top. The VSD was excited with 630 nm light from a 100 W halogen lamp gated by a Uniblitz shutter (Vincent Associates) under computer control via an ITC18 (Instrutech) communicating with custom software running within IgorPro (Wavemetrics). The excitation light was reflected using a 650 nm dichroic and focused onto the cortical surface with a 50 mm SLR camera lens (Nikon). Fluorescence was collected via the same optical pathway, but without reflection of the dichroic, long-pass filtered (>665 nm) and focused onto the sensor of a high-speed MiCam Ultima (Scimedia) camera via a 50 mm video lens (Navitar). This high-speed CMOS camera has a detector with 100 × 100 pixels. The field of view was 10 × 10 mm, and therefore every pixel collects light from a cortical region of 100 × 100 μm. Images were collected with 2 ms temporal resolution and analyzed offline using custom-written routines in IgorPro. Bleaching of fluorescence was corrected by subtraction of a best-fit double-exponential or, in experiments on anesthetized mice, by subtraction of heart-beat synchronized and averaged sweeps recorded without whisker stimulus. Time courses of fluorescence changes were quantified as $\Delta F/F_0$ from regions of interest covering 5 × 5 pixels, indicated by the colored squares in the images (corresponding to 500 × 500μm of cortex). In order to compare VSD signals from different animals, regions of interest were centered on the locations of the earliest responses in S1 and M1. Responses from these functionally identified regions were then compared or averaged across different experiments. Amplitudes of sensory-evoked responses were calculated as the change in the VSD signal ($\Delta F/F_0$) over a fixed time interval for each experiment (baseline time point was immediately before the stimulus; the response time point was chosen to be at the maximum of the averaged response).

Filming and Stimulating the C2 Whisker

In order to quantify whisker-related behavior, the large mystacial vibrissae were trimmed immediately before the recording sessions, leaving only the right-hand C2 whisker intact. The mouse was illuminated from below with infrared light and filmed through a 50 mm video lens (Navitar) with a high-speed MotionPro camera (Redlake). The behavioral images were obtained at 2 ms intervals between frames synchronized to the VSD imaging through TTL pulses. Custom-written routines running within ImageJ were used to automatically track whisker position. For the experiments involving passive whisker deflection in awake mice, reproducible whisker stimuli were evoked by attaching a small metal particle to the C2 whisker and generating brief magnetic pulses (Ferezou et al., 2006; Crochet and Petersen, 2006). For the experiments in anesthetized mice, 2 ms whisker deflections were generated by a computer-controlled piezoelectric bimorph (Ferezou et al., 2006).

Recording Local Field Potentials

The local field potential (LFP) was recorded in urethane-anesthetized mice by inserting a Ringer-filled pipette (~10 MΩ) into the supragranular cortex (~250 μm depth), successively in S1 and M1 locations corresponding to the regions of interest used to quantify the VSD fluorescence. The signal was amplified by a Multiclamp 700 amplifier (Axon Instruments) and filtered from DC to 500 Hz.

Intracortical Microstimulation of S1

A glass micropipette (~10 μm tip diameter) filled with Ringer's solution was introduced into the cortex to a depth of ~400 μm to target layer 4. The horizontal location of the pipette was targeted to the functional location of the C2 barrel column, as identified by precise colocalization of the cortical microstimulation evoked VSD response and the C2 whisker deflection-evoked VSD response. Electrical stimuli of duration 500 μs and amplitude four to eight times the threshold for evoking a VSD response (50–1000 μA) were applied using current injections delivered by a linear stimulus isolator (A395, World Precision Instruments).

Intracortical Microstimulation of M1

Surgery was carried out under 1.5% isoflurane, and anesthesia was subsequently switched to a continuous intravenous injection of ketamine at 3 mg/kg/min. Trains of 60 Hz stimuli with 100 μA bipolar current pulses, each of duration 200 μs, were delivered with glass-coated platinum-tungsten electrodes (80 μm shank diameter; 23 μm diameter of the metal core; free tip length, 8 μm; impedance, >1 MΩ; Thomas Recording). The C2 whisker position was quantitatively recorded using a laser curtain and a linear CCD array (RX 03, Metralight).

Local Pharmacology

A glass micropipette (~10 μm tip diameter) back-filled with mineral oil and tip-filled with the drug dissolved in Ringer's solution was slowly inserted to a depth of ~400 μm directly into the C2 column of the barrel cortex as identified by VSD imaging. By advancing a metal piston into the pipette by a known distance, we could inject a defined quantity of the drug directly into the C2 barrel column (typically ~20 nl, with each calibrated unit denoting 0.2 nl).

Lentiviral-Based Anatomy

Lentiviral vector was produced by transient calcium phosphate transfection of human embryonic kidney 293T cells with the Gag-Pol construct (pCMVΔ8.92), the Rev expression plasmid (pRSV-Rev), the

VSV-G protein envelope construct (pMD2.G), and the pFCK(1.3)GW transfer vector encoding GFP under the control of a 1.3 kb fragment of the αCaMKII promoter (Dittgen et al., 2004). Media was changed ~7 hr post-transfection and viral supernatant was harvested after ~40 hr, clarified by low-speed centrifugation, filtered at a 0.22 μm pore size, concentrated ~1000× by ultracentrifugation and resuspended in phosphate-buffered saline with 0.5% BSA. Lentivirus (~50 nl) was injected into both supragranular and infragranular layers of the C2 barrel column. The location of the C2 barrel column was identified by intrinsic optical imaging (Grinvald et al., 1986; Polley et al., 2004) following previously described procedures (Ferezou et al., 2006; Crochet and Petersen, 2006).

Statistical Tests

Data are expressed as mean ± standard deviation, and they were tested using SigmaStat (Systat Software) for statistical significance using Student's t test (paired when appropriate) or Wilcoxon signed rank test for data without a normal distribution.

Supplemental Data

The Supplemental Data for this article can be found online at http://www.neuron.org/cgi/content/full/56/5/907/DC1/.

ACKNOWLEDGMENTS

This work was supported by grants from the Swiss National Science Foundation and the Leenaards Foundation. We thank Pavel Osten for the plasmid pFCK(1.3)GW. We thank Sylvain Crochet and James Poulet for discussion and comments on a previous version of the manuscript.

Received: June 8, 2007
Revised: September 8, 2007
Accepted: October 2, 2007
Published: December 5, 2007

REFERENCES

Ahrens, K.F., and Kleinfeld, D. (2004). Current flow in vibrissa motor cortex can phase-lock with exploratory rhythmic whisking in rat. J. Neurophysiol. *92*, 1700–1707.

Alloway, K.D., Zhang, M., and Chakrabarti, S. (2004). Septal columns in rodent barrel cortex: functional circuits for modulating whisking behavior. J. Comp. Neurol. *480*, 299–309.

Arabzadeh, E., Zorzin, E., and Diamond, M.E. (2005). Neuronal encoding of texture in the whisker sensory pathway. PLoS Biol. *3*, e17. 10.1371/journal.pbio.0030017.

Arieli, A., Sterkin, A., Grinvald, A., and Aertsen, A. (1996). Dynamics of ongoing activity: explanation of the large variability in evoked cortical responses. Science *273*, 1868–1871.

Aronoff, R., and Petersen, C.C.H. (2006). Controlled and localized genetic manipulation in the brain. J. Cell. Mol. Med. *10*, 333–352.

Benucci, A., Frazor, R.A., and Carandini, M. (2007). Standing waves and traveling waves distinguish two circuits in visual cortex. Neuron *55*, 103–117.

Berg, R.W., Friedman, B., Schroeder, L.F., and Kleinfeld, D. (2005). Activation of nucleus basalis facilitates cortical control of a brain stem motor program. J. Neurophysiol. *94*, 699–711.

Berger, T., Borgdorff, A.J., Crochet, S., Neubauer, F.B., Lefort, S., Fauvet, B., Ferezou, I., Carleton, A., Luscher, H.R., and Petersen, C.C.H. (2007). Combined voltage and calcium epifluorescence imaging in vitro and in vivo reveals subthreshold and suprathreshold dynamics of mouse barrel cortex. J. Neurophysiol. *97*, 3751–3762.

Borgdorff, A.J., Poulet, J.F.A., and Petersen, C.C.H. (2007). Facilitating sensory responses in developing mouse somatosensory barrel cortex. J. Neurophysiol. *97*, 2992–3003.

Brecht, M., Roth, A., and Sakmann, B. (2003). Dynamic receptive fields of reconstructed pyramidal cells in layers 3 and 2 of rat somatosensory barrel cortex. J. Physiol. *553*, 243–265.

Brecht, M., Schneider, M., Sakmann, B., and Margrie, T.W. (2004). Whisker movements evoked by stimulation of single pyramidal cells in rat motor cortex. Nature *427*, 704–710.

Bulkin, D.A., and Groh, J.M. (2006). Seeing sounds: visual and auditory interactions in the brain. Curr. Opin. Neurobiol. *16*, 415–419.

Carvell, G.E., Miller, S.A., and Simons, D.J. (1996). The relationship of vibrissal motor cortex unit activity to whisking in the awake rat. Somatosens. Mot. Res. *13*, 115–127.

Castro-Alamancos, M.A. (2006). Vibrissa myoclonus (rhythmic retractions) driven by resonance of excitatory networks in motor cortex. J. Neurophysiol. *96*, 1691–1698.

Castro-Alamancos, M.A., and Oldford, E. (2002). Cortical sensory suppression during arousal is due to the activity-dependent depression of thalamocortical synapses. J. Physiol. *541*, 319–331.

Caviness, V.S. (1975). Architectonic map of neocortex of the normal mouse. J. Comp. Neurol. *164*, 247–263.

Chapin, J.K., and Woodward, D.J. (1982). Somatic sensory transmission to the cortex during movement: gating of single cell responses to touch. Exp. Neurol. *78*, 654–669.

Civillico, E.F., and Contreras, D. (2006). Integration of evoked responses in supragranular cortex studied with optical recordings in vivo. J. Neurophysiol. *96*, 336–351.

Cossart, R., Aronov, D., and Yuste, R. (2003). Attractor dynamics of network UP states in the neocortex. Nature *423*, 283–288.

Cowan, R.L., and Wilson, C.J. (1994). Spontaneous firing patterns and axonal projections of single corticostriatal neurons in the rat medial agranular cortex. J. Neurophysiol. *71*, 17–32.

Cramer, N.P., and Keller, A. (2006). Cortical control of a whisking central pattern generator. J. Neurophysiol. *96*, 209–217.

Cramer, N.P., Li, Y., and Keller, A. (2007). The whisking rhythm generator: a novel mammalian network for the generation of movement. J. Neurophysiol. *97*, 2148–2158.

Crochet, S., and Petersen, C.C.H. (2006). Correlating whisker behavior with membrane potential in barrel cortex of awake mice. Nat. Neurosci. *9*, 608–610.

Deschenes, M., Veinante, P., and Zhang, Z.-W. (1998). The organization of corticothalamic projections: reciprocity versus parity. Brain Res. Brain Res. Rev. *28*, 286–308.

Diamond, M.E., Armstrong-James, M., Budway, M.J., and Ebner, F.F. (1992). Somatic sensory responses in the rostral sector of the posterior group (POm) and in the ventral posterior medial nucleus (VPM) of the rat thalamus: dependence on the barrel field cortex. J. Comp. Neurol. *319*, 66–84.

Dittgen, T., Nimmerjahn, A., Komai, S., Licznerski, P., Waters, J., Margrie, T.W., Helmchen, F., Denk, W., Brecht, M., and Osten, P. (2004). Lentivirus-based genetic manipulations of cortical neurons and their optical and electrophysiological monitoring in vivo. Proc. Natl. Acad. Sci. USA *101*, 18206–18211.

Fanselow, E.E., and Nicolelis, M.A.L. (1999). Behavioral modulation of tactile responses in the rat somatosensory system. J. Neurosci. *19*, 7603–7616.

Farkas, T., Kis, Z., Toldi, J., and Wolff, J.R. (1999). Activation of the primary motor cortex by somatosensory stimulation in adult rats is mediated mainly by associational connections from the somatosensory cortex. Neuroscience *90*, 353–361.

Ferezou, I., Bolea, S., and Petersen, C.C.H. (2006). Visualizing the cortical representation of whisker touch: voltage-sensitive dye imaging in freely moving mice. Neuron *50*, 617–629.

Franklin, K.B.J., and Paxinos, G. (1996). The Mouse Brain in Stereotaxic Coordinates (San Diego, CA: Academic Press).

Fu, K.M., Johnston, T.A., Shah, A.S., Arnold, L., Smiley, J., Hackett, T.A., Garraghty, P.E., and Schroeder, C.E. (2003). Auditory cortical neurons respond to somatosensory stimulation. J. Neurosci. *23*, 7510–7515.

Gao, P., Hattox, A.M., Jones, L.M., Keller, A., and Zeigler, H.P. (2003). Whisker motor cortex ablation and whisker movement patterns. Somatosens. Mot. Res. *20*, 191–198.

Ghazanfar, A.A., and Schroeder, C.E. (2006). Is neocortex essentially multisensory? Trends Cogn. Sci. *10*, 278–285.

Ghazanfar, A.A., Maier, J.X., Hoffman, K.L., and Logothetis, N.K. (2005). Multisensory integration of dynamic faces and voices in rhesus monkey auditory cortex. J. Neurosci. *25*, 5004–5012.

Grinvald, A., and Hildesheim, R. (2004). VSDI: a new era in functional imaging of cortical dynamics. Nat. Rev. Neurosci. *5*, 874–885.

Grinvald, A., Lieke, E., Frostig, R.D., Gilbert, C.D., and Wiesel, T.N. (1986). Functional architecture of cortex revealed by optical imaging of intrinsic signals. Nature *324*, 361–364.

Haiss, F., and Schwarz, C. (2005). Spatial segregation of different modes of movement control in the whisker representation of rat primary motor cortex. J. Neurosci. *25*, 1579–1587.

Harris, J.A., Petersen, R.S., and Diamond, M.E. (1999). Distribution of tactile learning and its neural basis. Proc. Natl. Acad. Sci. USA *96*, 7587–7591.

Hattox, A., Li, Y., and Keller, A. (2003). Serotonin regulates rhythmic whisking. Neuron *39*, 343–352.

Hentschke, H., Haiss, F., and Schwarz, C. (2006). Central signals rapidly switch tactile processing in rat barrel cortex during whisker movements. Cereb. Cortex *16*, 1142–1156.

Hoffer, Z.S., Hoover, J.E., and Alloway, K.D. (2003). Sensorimotor corticocortical projections from rat barrel cortex have an anisotropic organization that facilitates integration of inputs from whiskers in the same row. J. Comp. Neurol. *466*, 525–544.

Izraeli, R., and Porter, L.L. (1995). Vibrissal motor cortex in the rat: connections with the barrel field. Exp. Brain Res. *104*, 41–54.

Jancke, D., Chavane, F., Naaman, S., and Grinvald, A. (2004). Imaging cortical correlates of illusion in early visual cortex. Nature *428*, 423–426.

Kayser, C., Petkov, C.I., Augath, M., and Logothetis, N.K. (2005). Integration of touch and sound in auditory cortex. Neuron *48*, 373–384.

Kenet, T., Bibitchkov, D., Tsodyks, M., Grinvald, A., and Arieli, A. (2003). Spontaneously emerging cortical representations of visual attributes. Nature *425*, 954–956.

Kleinfeld, D., Sachdev, R.N.S., Merchant, L.M., Jarvis, M.R., and Ebner, F.F. (2002). Adaptive filtering of vibrissa input in motor cortex of rat. Neuron *34*, 1021–1034.

Kleinfeld, D., Ahissar, E., and Diamond, M.E. (2006). Active sensation: insights from the rodent vibrissa sensorimotor system. Curr. Opin. Neurobiol. *16*, 435–444.

Knutsen, P.M., Pietr, M., and Ahissar, E. (2006). Haptic object localization in the vibrissal system: behavior and performance. J. Neurosci. *26*, 8451–8464.

Lakatos, P., Chen, C.M., O'Connell, M.N., Mills, A., and Schroeder, C.E. (2007). Neuronal oscillations and multisensory interaction in primary auditory cortex. Neuron *53*, 279–292.

Lavallee, P., Urbain, N., Dufresne, C., Bokor, H., Acsady, L., and Deschenes, M. (2005). Feedforward inhibitory control of sensory information in higher-order thalamic nuclei. J. Neurosci. *25*, 7489–7498.

Lee, A.K., Manns, I.D., Sakmann, B., and Brecht, M. (2006). Whole-cell recordings in freely moving rats. Neuron *51*, 399–407.

Lippert, M.T., Takagaki, K., Xu, W., Huang, X., and Wu, J.Y. (2007). Methods for voltage-sensitive dye imaging of rat cortical activity with high signal-to-noise ratio. J. Neurophysiol. *98*, 502–512.

Lovick, T.A. (1972). The behavioral repertoire of precollicular decerebrate rats. J. Physiol. *224*, 4P–6P.

Macaluso, E. (2006). Multisensory processing in sensory-specific cortical areas. Neuroscientist *12*, 327–338.

Martuzzi, R., Murray, M.M., Michel, C.M., Thiran, J.P., Maeder, P.P., Clarke, S., and Meuli, R.A. (2006). Multisensory interactions within human primary cortices revealed by BOLD dynamics. Cereb. Cortex *17*, 1672–1679.

Meeks, J.P., and Mennerick, S. (2007). Action potential initiation and propagation in CA3 pyramidal axons. J. Neurophysiol. *97*, 3460–3472.

Mehta, S.B., Whitmer, D., Figueroa, R., Williams, B.A., and Kleinfeld, D. (2007). Active spatial perception in the vibrissa scanning sensorimotor system. PLoS Biol. *5*, e15. 10.1371/journal.pbio.0050015.

Miyashita, E., Keller, A., and Asanuma, H. (1994). Input-output organization of the rat vibrissal motor cortex. Exp. Brain Res. *99*, 223–232.

Moore, C.I., and Nelson, S.B. (1998). Spatio-temporal subthreshold receptive fields in the vibrissa representation of rat primary somatosensory cortex. J. Neurophysiol. *80*, 2882–2892.

Nguyen, Q.T., and Kleinfeld, D. (2005). Positive feedback in a brainstem tactile sensorimotor loop. Neuron *45*, 447–457.

Petersen, C.C.H. (2007). The functional organisation of the barrel cortex. Neuron *56*, 339–355.

Petersen, C.C.H., Grinvald, A., and Sakmann, B. (2003a). Spatiotemporal dynamics of sensory responses in layer 2/3 of rat barrel cortex measured in vivo by voltage-sensitive dye imaging combined with whole-cell voltage recordings and anatomical reconstructions. J. Neurosci. *23*, 1298–1309.

Petersen, C.C.H., Hahn, T.T.G., Mehta, M., Grinvald, A., and Sakmann, B. (2003b). Interaction of sensory responses with spontaneous depolarization in layer 2/3 barrel cortex. Proc. Natl. Acad. Sci. USA *100*, 13638–13643.

Petreanu, L., Huber, D., Sobczyk, A., and Svoboda, K. (2007). Channelrhodopsin-2-assisted circuit mapping of long-range callosal projections. Nat. Neurosci. *10*, 663–668.

Polley, D.B., Chen-Bee, C.H., and Frostig, R.D. (1999). Two directions of plasticity in the sensory-deprived adult cortex. Neuron *24*, 623–637.

Polley, D.B., Kvasnak, E., and Frostig, R.D. (2004). Naturalistic experience transforms sensory maps in the adult cortex of caged animals. Nature *429*, 67–71.

Porter, L.L., and White, E.L. (1983). Afferent and efferent pathways of the vibrissal region of primary motor cortex in the mouse. J. Comp. Neurol. *214*, 279–289.

Sachdev, R.N., Sato, T., and Ebner, F.F. (2002). Divergent movement of adjacent whiskers. J. Neurophysiol. *87*, 1440–1448.

Sachdev, R.N., Ebner, F.F., and Wilson, C.J. (2004). Effect of subthreshold up and down states on the whisker-evoked response in somatosensory cortex. J. Neurophysiol. *92*, 3511–3521.

Schroeder, C.E., and Foxe, J. (2005). Multisensory contributions to low-level, 'unisensory' processing. Curr. Opin. Neurobiol. *15*, 454–458.

Seidemann, E., Arieli, A., Grinvald, A., and Slovin, H. (2002). Dynamics of depolarization and hyperpolarization in the frontal cortex and saccade goal. Science *295*, 862–865.

Semba, K., and Komisaruk, B.R. (1984). Neural substrates of two different rhythmical vibrissal movements in the rat. Neuroscience *12*, 761–774.

Shoham, D., Glaser, D.E., Arieli, A., Kenet, T., Wijnbergen, C., Toledo, Y., Hildesheim, R., and Grinvald, A. (1999). Imaging cortical dynamics at high spatial and temporal resolution with novel blue voltage-sensitive dyes. Neuron *24*, 791–802.

Shu, Y., Hasenstaub, A., and McCormick, D.A. (2003). Turning on and off recurrent balanced cortical activity. Nature *423*, 288–293.

Slovin, H., Arieli, A., Hildesheim, R., and Grinvald, A. (2002). Long-term voltage-sensitive dye imaging reveals cortical dynamics in behaving monkeys. J. Neurophysiol. *88*, 3421–3438.

Steriade, M., Nunez, A., and Amzica, F. (1993). A novel slow (< 1 Hz) oscillation of neocortical neurons in vivo: depolarizing and hyperpolarizing components. J. Neurosci. *13*, 3252–3265.

Stuttgen, M.C., Ruter, J., and Schwarz, C. (2006). Two psychophysical channels of whisker deflection in rats align with two neuronal classes of primary afferents. J. Neurosci. *26*, 7933–7941.

Szwed, M., Bagdasarian, K., and Ahissar, E. (2003). Encoding of vibrissal active touch. Neuron *40*, 621–630.

Trageser, J.C., Burke, K.A., Masri, R., Li, Y., Sellers, L., and Keller, A. (2006). State-dependent gating of sensory inputs by zona incerta. J. Neurophysiol. *96*, 1456–1463.

Veinante, P., Lavallee, P., and Deschenes, M. (2000). Corticothalamic projections from layer 5 of the vibrissal barrel cortex in the rat. J. Comp. Neurol. *424*, 197–204.

Vincent, J.L., Patel, G.H., Fox, M.D., Snyder, A.Z., Baker, J.T., Van Essen, D.C., Zempel, J.M., Snyder, L.H., Corbetta, M., and Raichle, M.E. (2007). Intrinsic functional architecture in the anaesthetized monkey brain. Nature *447*, 83–86.

Volgushev, M., Chauvette, S., Mukovski, M., and Timofeev, I. (2006). Precise long-range synchronization of activity and silence in neocortical neurons during slow-wave oscillations. J. Neurosci. *26*, 5665–5672.

Wallace, M.T., Ramachandran, R., and Stein, B.E. (2004). A revised view of sensory cortical parcellation. Proc. Natl. Acad. Sci. USA *101*, 2167–2172.

Welker, W.I. (1964). Analysis of sniffing of the albino rat. Behaviour *22*, 223–244.

White, E.L., and DeAmicis, R.A. (1977). Afferent and efferent projections of the region of mouse SmI cortex which contains the posteromedial barrel subfield. J. Comp. Neurol. *175*, 455–482.

Woolsey, T.A., and Van der Loos, H. (1970). The structural organisation of layer IV in the somatosensory region (SI) of the mouse cerebral cortex: the description of a cortical field composed of discrete cytoarchitectonic units. Brain Res. *17*, 205–242.

Xu, W., Huang, X., Takagaki, K., and Wu, J.Y. (2007). Compression and reflection of visually evoked cortical waves. Neuron *55*, 119–129.

Zhu, J.J., and Connors, B.W. (1999). Intrinsic firing patterns and whiskers-evoked synaptic responses of neurons in the rat barrel cortex. J. Neurophysiol. *81*, 1171–1183.

Neuron 50, 617–629, May 18, 2006 ©2006 Elsevier Inc. DOI 10.1016/j.neuron.2006.03.043

Visualizing the Cortical Representation of Whisker Touch: Voltage-Sensitive Dye Imaging in Freely Moving Mice

Isabelle Ferezou,[1] Sonia Bolea,[1] and Carl C.H. Petersen[1,*]
[1] Laboratory of Sensory Processing
Brain Mind Institute
SV-BMI-LSENS AAB 105
Station 15
Ecole Polytechnique Federale de Lausanne
CH-1015 Lausanne
Switzerland

Summary

Voltage-sensitive dye imaging resolves the spatiotemporal dynamics of supragranular subthreshold cortical activity with millisecond temporal resolution and subcolumnar spatial resolution. We used a flexible fiber optic image bundle to visualize voltage-sensitive dye dynamics in the barrel cortex of freely moving mice while simultaneously filming whisker-related behavior to generate two movies matched frame-by-frame with a temporal resolution of up to 2 ms. Sensory responses evoked by passive whisker stimulation lasted longer and spread further across the barrel cortex in awake mice compared to anesthetized mice. Passively evoked sensory responses were large during behaviorally quiet periods and small during active whisking. However, as an exploring mouse approached an object while whisking, large-amplitude, propagating cortical sensory activity was evoked by active whisker-touch. These experiments demonstrate that fiber optics can be used to image cortical sensory activity with high resolution in freely moving animals. The results demonstrate differential processing of sensory input depending upon behavior.

Introduction

Sensory information is processed in a highly distributed manner in the mammalian brain. Neocortical sensory processing can be imaged using voltage-sensitive dye (VSD), providing millisecond temporal resolution and subcolumnar spatial resolution (Grinvald et al., 1984; Orbach et al., 1985; Arieli et al., 1996; Kleinfeld and Delaney, 1996). Recent advances in imaging technology and new voltage-sensitive dyes (Shoham et al., 1999; Grinvald and Hildesheim, 2004) have allowed routine measurement of the spatiotemporal dynamics of sensory processing in head-fixed animals (Spors and Grinvald, 2002; Seidemann et al., 2002; Slovin et al., 2002; Petersen et al., 2003a, 2003b; Derdikman et al., 2003). Since the brain state and behavior likely affect sensory processing, it would clearly be important to be able to image cortical function in awake, freely moving animals, allowing a direct comparison of behavior, sensory input, and cortical activity. We therefore developed a technique for imaging cortical spatiotemporal dynamics in awake, freely moving mice using fiber optic image bundles. We focus on the processing of sensory input from the mystacial vibrissae which are represented in the primary somatosensory barrel cortex (Woolsey and Van der Loos, 1970). Using this technique, we analyzed differences in sensory responses between anesthetized and awake animals and during different behaviors in awake animals. We furthermore imaged the cortical representation of touch in real time as a mouse approached an object and made vibrissa contact.

*Correspondence: carl.petersen@epfl.ch

Results

Our goal was to develop a system for imaging both the whisker-related behavior and the spatiotemporal dynamics of barrel cortex in freely moving mice (Figure 1). Image transfer from the mouse to the epifluorescent imaging optics was achieved through the use of a fiber optic image bundle. The fiber was sufficiently light and flexible to allow the mice to move freely within a behavioral chamber. The flexibility of the fiber bundle derives from the assembly process, in which the fibers are only fused at the ends and left loose in the middle section. This allows the animal freedom to move and to turn around (see Movie S1 in the Supplemental Data).

Imaging Fluorescence with Fiber Optic Arrays

The fiber (Figures 2A–2C) was custom manufactured by Schott Fiber Optics based on their wound image bundle technology. The fibers were 50 cm long and had 8 μm cores with a numerical aperture of 0.6. The wound image bundle was prepared in a two-step process. Fibers were first assembled to form a multifiber array composed of 6 × 6 fibers (the multifibers can be seen in Figure 2A) and were then arranged into a 3 × 3 mm array containing 300 × 300 fibers (Figure 2B), forming a well-ordered array for coherent image transfer. The tip was enclosed in a nonmagnetic metal with a diameter of approximately 5 mm for mechanical stability (Figure 2C). This fiber tip was placed in direct contact with the cortical surface to achieve a high efficiency for emitting and collecting photons. The spatial resolution is limited by light scattering in the brain tissue.

Excitation light for fluorescence imaging can be brought to the cortical surface via the same fibers that detect the emission by using standard epifluorescence optics at the camera end of the fiber (Figure 1). To analyze how the excitation light penetrates into the cortex, we placed a single multifiber in direct contact with an in vitro brain slice of the mouse primary somatosensory cortex (Figure 2D). The end of the fiber nearer to the camera was illuminated with light of 630 nm. We imaged the brain slice using an Olympus 20× 0.95NA objective, mounted on a BX51WI microscope with a CoolSNAP HQ camera (Figure 2E). The penetration of the light into the brain slice was quantified from the photomicrograph by calculating contours of the normalized light intensity (Figure 2F). This excitation light penetrates the cortical layers 1, 2, and 3, with little reaching layer 4 or the infragranular layers. These measurements were made in

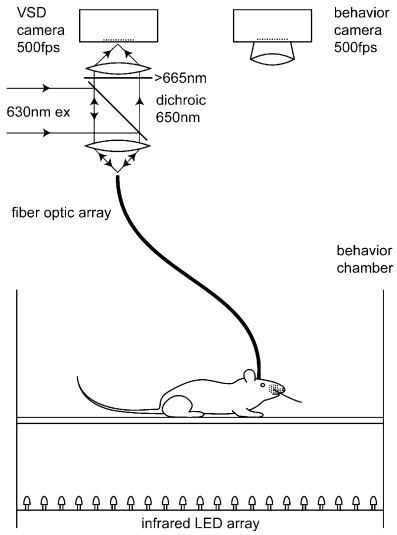

Figure 1. Voltage-Sensitive Dye Imaging and Filming of Behavior in Freely Moving Mice

The excitation light (630 nm) for fluorescence imaging was reflected using a dichroic mirror (650 nm) and focused onto the end of the fiber optic array with a 25 mm lens. The flexible fibers transferred the excitation light to the mouse cortex stained with voltage-sensitive dye RH1691. The emitted fluorescence was collected via the same optical pathway, long-pass filtered (>665 nm) and focused onto the high-speed camera sensor via a 135 mm lens. The fiber array was sufficiently light and flexible to allow the mouse to move freely within a behavior chamber. During the experiments, the chamber was illuminated from below by infrared LEDs. The silhouette of the mouse and its whiskers was filmed using another high-speed camera.

brain slices, which are largely exsanguinated. In vivo it is likely that the light penetration is further reduced through the light absorption of blood. The fiber imaging will therefore relate primarily to fluorescence in the supragranular layers. The light remained surprisingly confined laterally, suggesting that a reasonable horizontal spatial resolution might be achieved.

To analyze the lateral resolution of this fiber imaging technique, the tail vein was injected with ~100 μl of 1 mg/ml voltage-sensitive dye RH1691, and the fluorescence of the blood vessels was visualized via both standard optics (Figure 2H) and the fiber optic image bundle (Figure 2I). Both fluorescent images of the cortical surface blood vessels were very similar to the image of the blood vessels obtained with standard optics under green light illumination (Figure 2G). Even small surface vessels were clearly visible with the fiber fluorescence imaging. The horizontal spatial resolution of fluorescence deeper in the brain will, of course, be lower, but this is also true for conventional epifluorescence imaging. It is therefore important to know the depth of the fluorescence to be imaged.

The Voltage-Sensitive Dye RH1691 Preferentially Stains Layer 2/3

In this study we aimed to image the spatiotemporal dynamics of sensory processing using the voltage-sensitive dye RH1691. The dye can be topically applied to the craniotomy after removal of the dura. After staining for 1 hr, the cortical surface is extensively washed to remove unbound dye and then imaging can begin. In order to measure the penetration of RH1691 into the cortex, we fixed the brains of four mice with paraformaldehyde after imaging sessions and prepared 100 μm thick parasagittal slices (Figures 2J–2L). In four additional mice, we flash-froze the brain and prepared 20 μm thick cryosections to prevent any dye diffusion following the imaging experiment (Kleinfeld and Delaney, 1996). The dye penetration was not different when comparing the frozen cryosections and the paraformaldehyde-fixed slices (Figure 2L). Confocal imaging showed that RH1691 fluorescence was preferentially located in neocortical layer 2/3 (Figure 2J, individual experiment; Figure 2L, data from eight animals). The dye was excluded from intracellular compartments, leaving dark holes where neuronal cell bodies and large dendrites were located (Figure 2K). This is consistent with the dye staining and remaining on the outer plasma membrane of the cells in the brain tissue. Taken together with the data from Figures 2D–2I, it appeared likely that the fiber would image voltage-sensitive dye fluorescence in the supragranular layers with subcolumnar resolution. We therefore began functional VSD imaging using the fiber technology.

Fiber Imaging of Sensory Responses under Anesthesia Using Voltage-Sensitive Dye

To better understand the fluorescence signals imaged with the fiber, we compared the conventional epifluorescence tandem lens optics with the fiber optics. We imaged the whisker-evoked voltage-sensitive dye signals in the urethane anesthetized mouse barrel cortex using conventional optics and fiber optics in the same animal, using otherwise identical experimental conditions (Figure 3). In order to gain greater consistency from animal to animal, all our experiments were conducted on the signaling pathway that begins with one defined whisker. We chose to study the right C2 whisker, and all other whiskers on both sides were trimmed immediately before the experiment to a length of approximately 1 mm. Deflection of the C2 whisker excites sensory neurons of the trigeminal nerve, which signal primarily to the homologous region of the C2 barrel column of the somatosensory cortex via the brain stem and thalamus. To locate the C2 barrel column, we performed intrinsic optical imaging (Grinvald et al., 1986) through the intact skull (Figure 3A, left). A craniotomy centered on the C2 barrel column was then performed using the blood vessel pattern (Figure 3A, middle) for anatomical landmarks relative to the intrinsic signal. The blood vessels (aligned in serial tangential brain slices as they penetrate into the cortex) were also used in the post hoc alignment of cytochrome oxidase-stained tangential brain slices (Figure 3A, right), allowing the overlay of the barrel map (Figure 3D) on the functional images. RH1691 was applied to the craniotomy for an hour to evenly stain the cortex. A glass coverslip was placed in direct contact with the cortex to seal the craniotomy, which allowed the fiber to be repeatedly attached and removed from the animal in an easily reversible manner. The C2 whisker was deflected for 2 ms by a piezoelectric bimorph under computer control and the sensory response was observed in the barrel cortex after ~10 ms latency (Petersen et al. 2003a, Derdikman et al. 2003). The earliest sensory response was localized to the C2 barrel column, which was confirmed in three animals by cytochrome

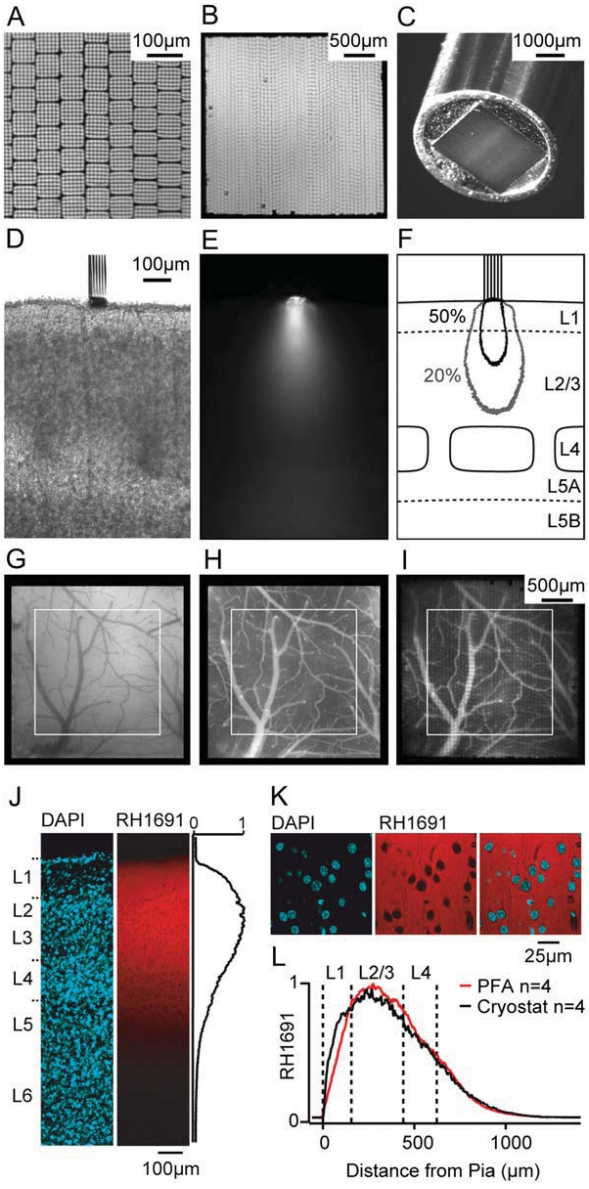

Figure 2. The Fiber Bundle Images Fluorescence in the Supragranular Cortex at Subcolumnar Resolution

(A) High-magnification micrograph of the end of the fiber optic image bundle showing the arrangement of individual fibers (8 μm cores; numerical aperture: 0.6). Multifibers containing 6 × 6 individual fibers were assembled together in a larger bundle.

(B) Micrograph showing the 3 × 3 mm final bundle containing 300 × 300 individual fibers.

(C) The tip of the fiber optic array was enclosed in a nonmagnetic metal (diameter: ~5 mm). The end of the fiber was placed in direct contact with the cortical surface.

(D) A single multifiber (composed of 6 × 6 individual fibers) was placed in direct contact with an in vitro brain slice of the mouse primary somatosensory barrel cortex.

(E) Excitation light (630 nm) was guided through the multifiber to analyze the penetration of light into the brain slice.

(F) Excitation light penetrated cortical layers 1, 2, and 3 with little reaching layer 4 or infragranular layers.

(G) Cortical surface blood vessels visualized with standard optics under green light (530 nm) illumination.

(H) Same cortical area imaged with standard epifluorescence optics after injection of the tail vein with ~100 μl of 1 mg/ml voltage-sensitive dye RH1691.

(I) Fluorescence of the blood vessels imaged via the fiber optic image bundle. Comparison of (G), (H), and (I) reveals that even small surface vessels were clearly visible with the fiber fluorescence imaging, attesting to a good horizontal spatial resolution. There is a slight reduction in image quality at the periphery of the fiber. All functional VSD imaging was therefore made within the central 2 × 2 mm region of the fiber indicated by the white square (also in [G] and [H]).

(J) After a functional VSD imaging session, the mouse brain was fixed with paraformaldehyde and cut in 100 μm thick parasagittal slices, which were counterstained with DAPI. Confocal images of these slices show that the RH1691 fluorescence was preferentially located in neocortical layer 2/3.

(K) Higher-magnification micrographs reveal that the dye was excluded from intracellular compartments.

(L) Average depth penetration of RH1691 measured from four mice with paraformaldehyde-fixed brains (PFA, red trace) and four mice with flash-frozen brains (cryostat, black trace) showing preferential labeling of layer 2/3.

oxidase staining of the layer 4 barrels followed by computer-aided alignment with the blood vessels. The response subsequently spread over the entire barrel cortex over the next 20 ms. Resonance vibrations of the piezoelectric bimorph wafers did not make a significant impact upon the cortical sensory responses, which were dominated by the brief high velocity onset whisker deflection (Figure S1). This pattern of sensory-evoked activity was imaged by both the conventional epifluorescence optics and the fiber optics (Figures 3B and 3C; Movie S2). We repeatedly switched back and forth between fiber and conventional optics three times in each experiment, and in all cases we observed similar spatiotemporal dynamics when comparing fiber and conventional optics. Quantification of the VSD signals showed that time course and amplitude of the signals recorded were almost identical between fiber and conventional optics (Figures 3E and 3F). This comparison was repeated in nine mice, and across these experiments we found that there was no difference between fiber and conventional optics in regards to the peak amplitude ($p = 0.94$), the duration (half-width, $p = 0.21$), or the spatial extent (the area responding with over half the peak amplitude, $p = 0.27$) of the sensory response (Figure 3G).

Voltage-Sensitive Dye Signals Correlate with Changes in Membrane Potential of Layer 2/3 Neurons

The fiber and the conventional optics report the same functional signals relating to voltage-sensitive dye RH1691, which is preferentially located in layer 2/3 (Figures 2J–2L). It is thus likely that the VSD signals would relate to membrane potential changes in layer 2/3. To directly test this, we performed whole-cell recordings from layer 2/3 neurons of the C2 cortical column while imaging VSD fluorescence under conventional optics in urethane anesthetized mice ($n = 10$ animals). As illustrated in Figures 4A–4C, the VSD signal quantified from the C2 column location was closely correlated with the spontaneous subthreshold membrane potential changes. However, when we observed action potentials (APs) in the whole-cell recording, these were not correlated with large VSD signals (Figure 4A). Closer analysis averaging many APs shows that action potentials observed in single cells make no impact on the VSD signal (Figure 4D). The temporal kinetics of RH1691 are sufficiently fast to record action potentials (T. Berger, A. Borgdorff, S. Crochet, S. Lefort, H-R. Lüscher, and C. Petersen, unpublished data), and if action potentials occurred with

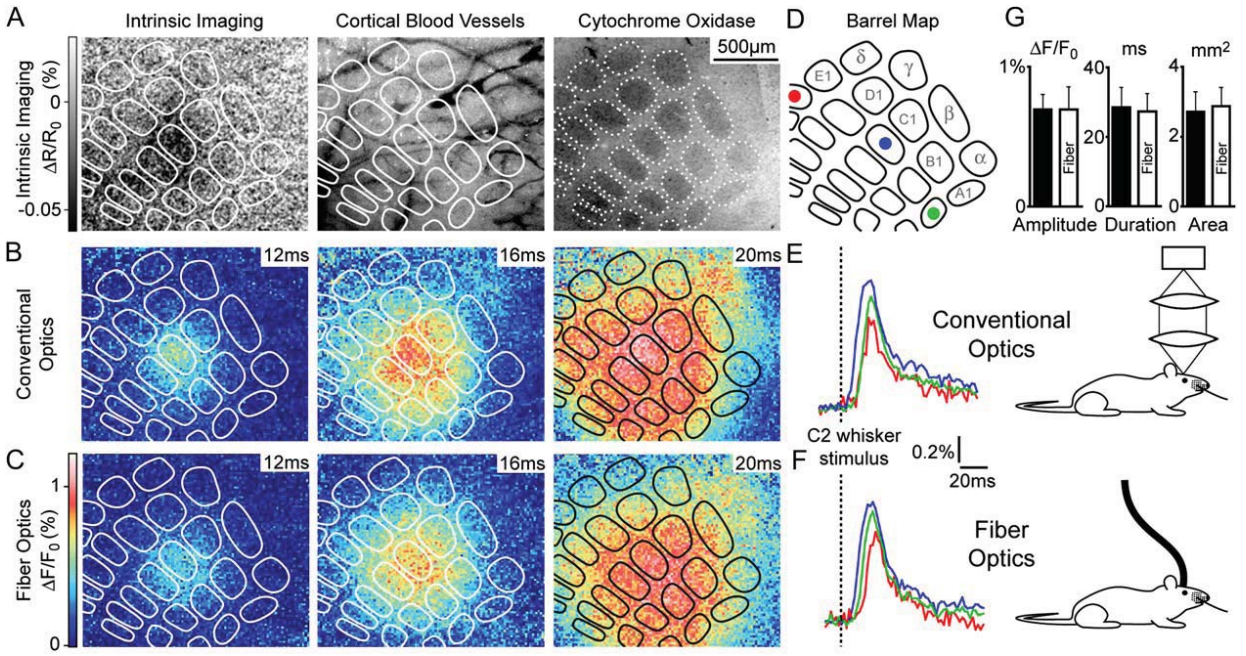

Figure 3. Fiber Optics and Conventional Optics Image Similar Voltage-Sensitive Dye Sensory Responses Evoked by Whisker Stimuli in Anesthetized Mice

(A) (Left) Intrinsic optical signal in response to repetitive C2 whisker stimulation (10 Hz, 4 s) imaged through the intact skull. This functionally identified location of the C2 whisker column was mapped onto the blood vessel pattern to guide surgery for the craniotomy. (Middle) Surface blood vessels visualized through the bone using 530 nm illumination. (Right) Cytochrome oxidase staining of layer 4 barrels. The VSD signals were aligned with the barrel map using the blood vessels.

(B) Voltage sensitive dye (RH1691) imaging of responses to single C2 whisker deflections (2 ms) observed using conventional epifluorescence optics (data averaged from n = 10 sweeps). The earliest response to the C2 whisker stimulation was localized to the C2 barrel column. Over the next tens of milliseconds depolarization spread to cover the entire barrel cortex.

(C) Imaging of responses to single C2 whisker deflections observed using the fiber optic image bundle (data averaged from n = 10 sweeps). The spatiotemporal dynamics of the sensory response recorded by the fiber bundle is similar to that observed with conventional optics.

(D–F) Quantification of VSD signals from ~100 × 100 μm areas centered on the E2 (red), C2 (blue), and A2 (green) barrel columns. Both time course and amplitude of the VSD signals were almost identical between fiber and conventional optics.

(G) Quantification of VSD signals imaged in response to C2 whisker stimulation with conventional optics and fiber optics across nine experiments. Response amplitude, duration (half-width), and spatial extent (area excited over half-maximal amplitude) showed no significant difference between conventional and fiber optics (p = 0.940, 0.205, and 0.274, respectively).

millisecond synchronization in a large fraction of the neuronal population, they would be observed in the VSD signal. The data thus suggest that spontaneous APs do not occur simultaneously in a large fraction of neurons. We therefore removed APs from the membrane potential traces by median filtering before computing the correlation of subthreshold membrane potential and VSD fluorescence. Across the ten experiments with simultaneous imaging and whole-cell recording, we obtained a Pearson's correlation coefficient of r = 0.68 ± 0.18 ($p < 0.001$) for spontaneous activity. The spontaneous depolarizations observed in whole-cell recordings corresponded to propagating waves of excitation as illustrated in Figure 4C. In each of these experiments, we also recorded VSD fluorescence and membrane potential changes evoked by C2 whisker deflections (Figures 4E–4G). The time course of the membrane potential changes during the cortical sensory response was very similar to the time course of the VSD signal. Plotting the VSD signal amplitude as a function of membrane potential also revealed a close to linear relationship between these two signals during evoked responses (Pearson's correlation coefficient r = 0.81 ± 0.18, n = 10, $p < 0.001$). Heartbeat-related artifacts were an order of magnitude smaller than the amplitude of the spontaneous waves, and there were no measurable breathing-related artifacts (Figure S2).

The VSD signals measured by conventional optics therefore correlate closely with the membrane potential changes of layer 2/3 neurons in the mouse barrel cortex (as observed in rat barrel cortex, Petersen et al., 2003a, 2003b). Since the VSD signals recorded by conventional optics match the signals recorded by the fiber optics, we can conclude that the fiber optics also image the membrane potential changes in layer 2/3.

Comparing Sensory Responses in Anesthetized and Awake Mice

We next asked how layer 2/3 cortical sensory responses might differ between anesthetized and awake animals. To investigate this we used isoflurane anesthesia, which offers both rapid induction and wake up, and in all experiments we repeatedly went in and out of anesthesia several times to validate the robustness of experimental findings. Reproducible whisker deflections in an awake, freely moving mouse were evoked by attaching a small metal particle to the C2 whisker and generating brief magnetic pulses (Figures 5A and 5B). Each single magnetic pulse reliably evoked a brief whisker movement as measured by an optical displacement sensor (Figure 5B).

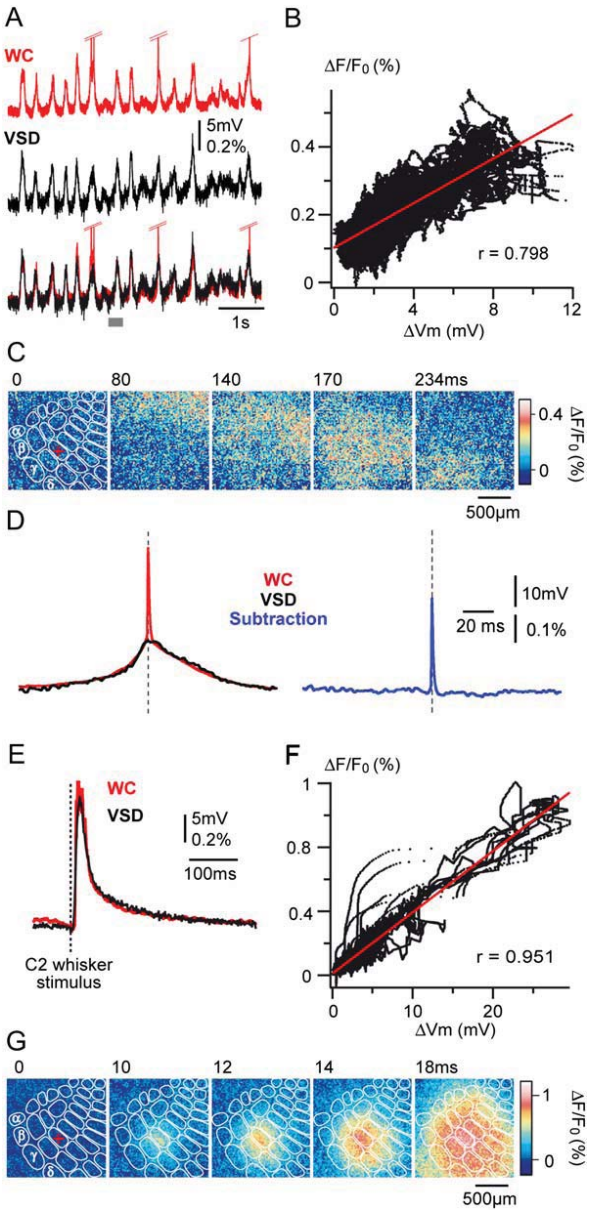

Figure 4. VSD Signals Correlate with the Membrane Potential of Layer 2/3 Neurons

(A) Whole-cell (WC) recording of a layer 2/3 neuron of the C2 cortical barrel column was performed simultaneously with measurement of VSD fluorescence under conventional optics in a urethane anesthetized mouse. Typical traces showing the WC recording (with truncated APs, red) and the VSD florescence (black) quantified from the C2 column location during spontaneous activity. The overlay of WC and VSD traces reveals a close correlation between the spontaneous subthreshold membrane potential and the VSD fluorescence changes. However, spontaneous APs were not correlated with large deflections of the VSD signal.

(B) The VSD signal plotted as a function of change in subthreshold membrane potential (Vm; APs were removed with a median filter) demonstrates a close to linear relationship.

(C) VSD images corresponding to a spontaneous depolarization recorded in WC (indicated by a gray bar in panel [A]). The red cross on the first image indicates the center of the region used to quantify the VSD fluorescence and the targeted location for the WC recording. These images show that the spontaneous depolarization recorded in WC corresponded to a propagating wave of excitation which crossed the entire barrel cortex.

(D) The VSD signal was aligned to APs recorded in the WC configuration and averaged across many APs (n = 29, from eight experiments). The subthreshold depolarization is nearly identical between the WC membrane potential recording and the VSD signal. However, the action potential is observed exclusively in the WC trace. The subtraction of the appropriately scaled traces (right) shows that the action potential is specifically missing from the VSD traces. This suggests that APs do not occur with millisecond synchronization in a large fraction of cortical neurons.

(E) For the same neuron, Vm changes in response to C2 whisker deflection were recorded while imaging VSD fluorescence. The averaged WC recording (red) and VSD signal measured from the C2 column location (black) are superimposed (n = 6 sweeps). The time course of the Vm changes during the cortical response to C2 whisker deflection was similar to the VSD signal.

(F) The VSD signal is plotted as a function of change in membrane potential for each individual sweep (APs were removed from Vm trace by a median filter). The two signals were linearly correlated.

(G) Image sequence corresponding to the average cortical responses shown in panel (E).

Fiber imaging of voltage-sensitive dye signals revealed that these stimuli evoked robust sensory responses in the barrel cortex of both anesthetized and awake mice (Figures 5C and 5D). Qualitatively, many aspects of the sensory responses were similar between anesthetized and awake conditions (as also suggested by Chapin and Lin, 1984). The magnetic deflection of the C2 whisker evoked a sensory response that began in the C2 barrel column and spread over a large area of the barrel cortex. The duration of the sensory response was significantly longer in awake animals (half-width: 86 ± 69 ms), than in animals under isoflurane (37 ± 8 ms, $p = 0.016$), likely reflecting more complex processing of the sensory signals (Krupa et al., 2004) in an awake mouse (Figures 5C–5E). The area responding with over half the peak amplitude of the sensory response also increased significantly in awake animals (2.87 ± 0.51 mm^2) compared to anesthetized mice (1.66 ± 0.81 mm^2; $p < 0.001$). This suggests that the surprisingly large area of cortex that can be excited by a single whisker stimulus is not an artifact of anesthesia, but is an important integrative property of sensory processing also occurring in awake animals. Quantitatively, the peak amplitude of the sensory response in awake animals (0.33% ± 0.20%) on average was larger than that of animals under isoflurane anesthesia (0.26% ± 0.11%), although not significantly ($p = 0.35$). The lack of significance likely reflects the very high variability of the sensory response during the awake recordings (Figure 5E). When we quantified whisker-related behavior, we found that a large part of this response variability can be accounted for by differences in ongoing behavior at the time of stimulus delivery.

Sensory Responses during Quiet and Active Whisker Behavior

We combined the functional VSD imaging of somatosensory barrel cortex with high-speed filming of the mouse behavior with particular attention paid to obtaining high-contrast images of the C2 whisker. The behavioral platform was illuminated from below with infrared light from a custom-made LED array. The silhouette of the mouse and its whiskers were filmed using a high speed camera allowing up to 2 ms temporal resolution and a spatial resolution of 0.2 mm with a field of view of 20 × 20 cm. We tracked the position of the head, the head direction and the C2 whisker angle (Figure S3; Movie S3) for each frame of the recorded movies, either

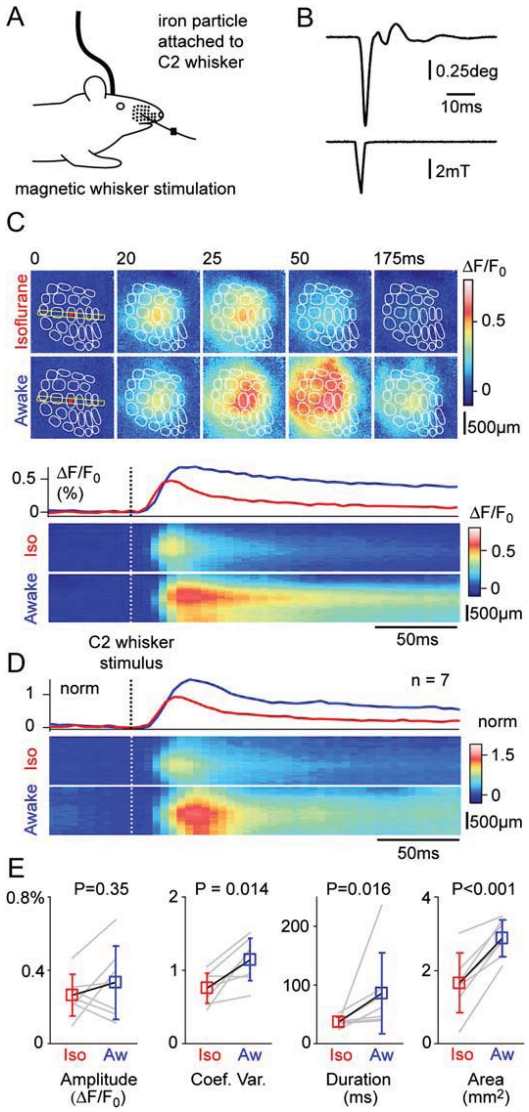

Figure 5. Evoked Sensory Responses Last Longer and Spread Further in Awake Compared to Anesthetized Mice

(A) To evoke reproducible whisker stimuli in freely moving mice, a small metal particle was attached to the C2 whisker and brief magnetic pulses (1–5 ms) were delivered through an electromagnetic coil.

(B) The whisker displacement induced by the magnetic pulse was measured with an optical displacement sensor (upper trace). The magnetic field was also measured (lower trace) and we verified that each single magnetic pulse reliably evoked whisker displacement. The magnetic field was uniform across the entire xy plane of the behavior platform that was placed in the center of the magnetic coil.

(C) Comparison of cortical responses to C2 whisker deflections imaged by VSD in a mouse while it was either under isoflurane anesthesia or awake. Averaged data from 30 sweeps are shown for each condition. The time course of the VSD signal quantified from the C2 barrel column (region shown in red on the first image of the image sequences) reveals that the duration of the response was much longer when the mouse was awake (middle panel). Linescan plot (time on x axis and space on y axis) of the VSD signal from a region crossing the barrel cortex (yellow rectangle on the first image of the image sequences) is shown in the lower panel.

(D) VSD responses to C2 whisker deflection were compared between isoflurane anesthesia and wakefulness in seven animals. Responses were normalized to the amplitude evoked during isoflurane anesthesia and averaged.

(E) The peak amplitude of the sensory response in awake animals on average was larger than under isoflurane anesthesia (although not significantly). The coefficient of variation, the duration and the spread of the sensory response were significantly larger in awake animals.

by hand or by automated image analysis (L. Segapelli, S. Crochet, I.F., C.P., D. Sage, and M. Unser, unpublished data). We then studied how sensory responses evoked by delivering magnetic whisker-stimuli in freely moving animals differed during active whisking compared to periods when the animal was quiet. In addition to this detailed behavioral analysis, we also measured the EEG in three additional mice, finding consistent changes in the power spectrum differentiating between isoflurane anesthesia, sleep, quiet wakefulness, and whisking (Figure S4). When the mouse was still and not whisking, passive magnetic deflection of the C2 whisker could evoke large sensory responses, which propagated across the barrel cortex. The sequence of events in the experiment shown in Figures 6A and 6B and in Movie S4 is particularly interesting. At the beginning of the sequence the animal is quiet and the whiskers are not moving. The magnetic stimulus evokes a small whisker deflection in the z direction, which is normal to the plane of the behavioral imaging and therefore not recorded on the plot of whisker position. The sensory response begins ~10 ms after whisker deflection in a localized region of the C2 barrel column and then spreads across the barrel field. Approximately 70 ms after the peak of the sensory response, the mouse makes an active whisker movement, protracting its whisker a long way forward. We think this active whisker movement resulted from the mouse perceiving the applied sensory stimulus and then proceeding to actively investigate the cause of the whisker deflection. Equally, one can speculate that the wave of excitation that we observed propagating across the barrel cortex is only the beginning of a more complex wave of excitation encompassing larger brain areas and perhaps exciting the motor cortex to drive whisker movement. The very next stimulus in this experiment was delivered some minutes later when the animal was actively whisking (Figures 6C and 6D; Movie S5). In this case, only a small sensory response evoked by the passive magnetic stimulus was observed in the barrel cortex during whisking, and there were no obvious alterations in behavior (Figures 6C and 6D; Movie S5). This reduction in the amplitude of the passively evoked sensory response during active whisking was extremely robust and accounted for a large part of the variability of the sensory responses in awake mice. The peak amplitude of sensory responses in the C2 barrel column was quantified for each individual sweep and categorized according to the whisker-related behavior at the time of the stimulus. The mean amplitude of the sensory response during active whisking was reduced to 26.3% ± 16.8% (n = 6 mice, $p < 0.001$) of the quiet response. The enhanced responses during quiet behavior were observed in all six mice of this experimental series (Figures 6E and 6F).

Imaging Spontaneous Waves during Quiet Behavior

In addition to the large sensory responses observed during quiet behavioral periods, we also observed spontaneous waves of activity, which propagated across the imaged area of the barrel cortex in freely moving mice when they were not actively exploring their environment (Figure 7; Movie S6). The direction of the waves was

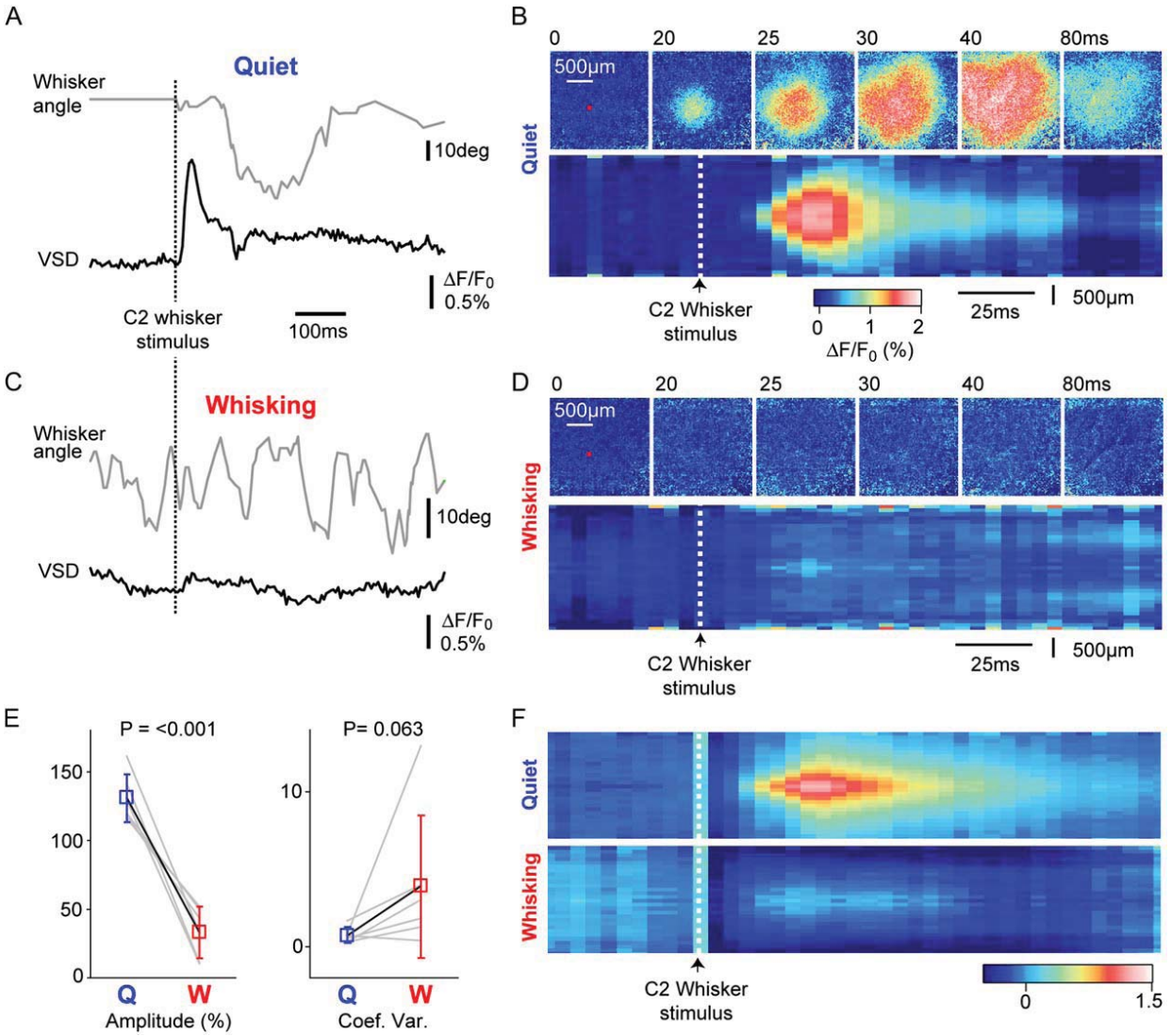

Figure 6. The Evoked Sensory Response in Freely Moving Mice Depends Strongly on Behavior

(A) Example of a sensory response to C2 whisker deflection imaged with VSD while the mouse was sitting still and not whisking (as indicated by the prestimulus whisker angle, gray trace). As the displacement of the whisker induced by the magnetic pulse was in the vertical direction, it does not appear on the whisker angle trace, which plots only the horizontal whisker position. The VSD signal (black trace) quantified from the center of the C2 column (red square on the first image in [B]) showed a large amplitude response following the stimulus. Note that approximately 70 ms after this cortical response, the mouse protracted its whisker as if to investigate what caused the whisker deflection.

(B) Image sequence corresponding to the cortical response shown in (A) (upper panel). The response was first restricted to a localized region and then spread across the barrel cortex. The outward radial spread of the VSD signal from the center of the response is shown in the lower panel (time is plotted on the x axis and space on the y axis).

(C) During the next sweep in the same experiment, the C2 whisker deflection occurred while the same mouse was actively whisking. Only a very small sensory response was observed in the VSD images.

(D) Image sequence and quantification of the VSD signal from the response shown in (C).

(E) The peak amplitude of sensory responses in the C2 barrel column was quantified for each individual sweep and categorized according to the whisker-related behavior at the time of the stimulus (quiet or whisking). VSD response amplitudes were normalized to the average evoked response for each experiment (n = 6). During quiet behavior the response amplitude was larger than average, whereas it was strongly reduced during whisking. Evoked responses may also be more variable during whisking than during quiet behavior, as suggested by the coefficients of variation.

(F) The outward radial spread of the VSD signals from the C2 barrel column compared between quiet and whisking behavior normalized across all six experiments.

different from one spontaneous event to the next. The velocity of the propagating wave-front was measured (Figures 7E and 7F) at the half-maximal amplitude and found to be highly variable. Interestingly, both the amplitude and velocity of the spontaneous waves were the same during quiet wakefulness as observed during urethane anesthesia (Figure 7F). The waves observed during urethane anesthesia correlate with UP and DOWN states (Petersen et al., 2003b), and their appearance during quiet wakefulness suggests that UP and DOWN states may also be a feature of some awake states in mice.

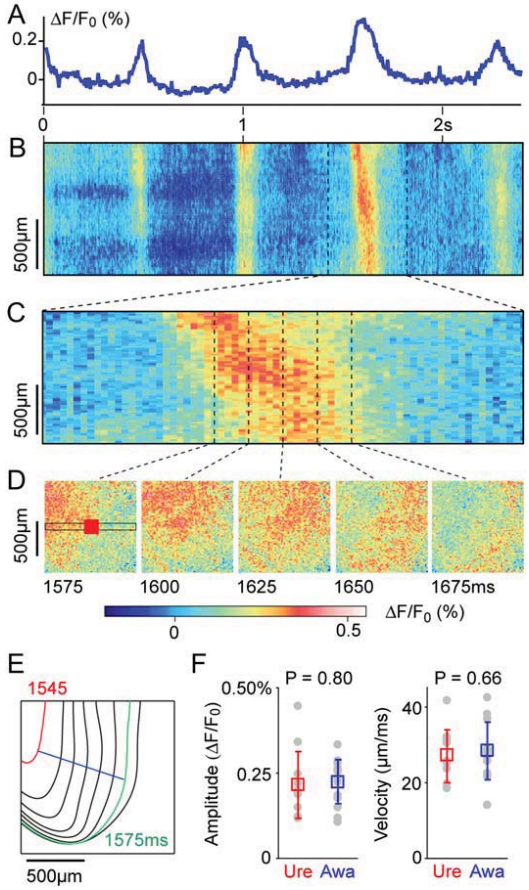

Figure 7. Spontaneous Waves of Cortical Activity Occur during Quiet Wakefulness

(A) VSD signal (quantified from the region indicated by the red square in panel [D]) reveals slow spontaneous depolarizations during quiet behavior.

(B) Linescan plot (time on x axis and space on y axis) of the VSD signal from a region crossing the barrel cortex (black rectangle in panel [D]) shows that these slow depolarizations crossed the entire barrel cortex.

(C) Temporal zoom of the plot in panel (B) showing that these slow depolarizations can occur as propagating waves of excitation.

(D) A time series of VSD images showing the propagating wave highlighted in panel (C).

(E) Wave-fronts corresponding to half-maximal amplitudes were computed from Gaussian-filtered VSD image sequences, in order to calculate the propagation velocity of the spontaneous events. Each contour is therefore derived from a different image occurring at a different time during the wave propagation. The velocity was taken as the maximal distance propagated by the half-maximal wave-front during a 30 ms interval (indicated by the blue line connecting two contours 30 ms apart).

(F) The amplitude and velocity of the spontaneous waves were computed from the awake mice and compared to spontaneous events recorded under urethane anesthesia. The quantitation revealed that these properties were remarkably similar between quiet wakefulness (n = 14 waves from three mice) and anesthesia (n = 11 waves from three mice).

We furthermore investigated whether we could observe patterns of activity in the primary somatosensory cortex that correlated with active whisking. Even after averaging many whisking cycles, only small-amplitude signals were detected, suggesting weak correlation between the ensemble average supragranular membrane potential and whisker movement. This surprisingly weak correlation may result from the activity of different individual neurons being tuned to different phases of the whisker cycle (Fee et al., 1997; Crochet and Petersen, 2006). The correlation would likely increase if the mice were trained to perform goal-directed whisking (Ganguly and Kleinfeld, 2004).

Imaging the Cortical Representation of Active Whisker Touch

We were concerned by the data suggesting that whisker stimuli evoked small sensory responses during active whisking. This is odd since it is thought that this is when the animal is actively gathering whisker-related information. It therefore seems that this should be the period in which whisker input should be particularly important for the mouse, and naively, one might then have expected larger sensory responses. We therefore performed experiments to investigate if there was sensory activity in the primary somatosensory barrel cortex when a mouse was actively exploring its environment and touched an object with its C2 whisker. We imaged mouse behavior and barrel cortex activity with the fiber optics as before, but now instead of applying passive stimuli to the whiskers with the magnetic stimuli, we allowed the mouse to touch objects placed in the behavioral chamber (Figure 8; Movie S7). We analyzed 11 whisker contacts which evoked VSD signals in three different animals. Whisker contact with an object was visualized with the high-speed camera and defined to occur at the first frame where the whisker was bent by the object contact (Figure 8). Although the amplitudes of cortical responses were highly variable (Figures 8C and 8E), the spatiotemporal dynamics of the recorded signals induced by active touches shared similar properties. The earliest cortical activity imaged immediately after C2 whisker contact occurred in a small localized region, from which it spread over a large part of the barrel cortex (Figure 8A). The location of the early response to active touch was found to be identical to the location of the early response evoked by passive whisker stimulation of the C2 whisker during anesthesia (Figure 8D). The sensory response during active touch with the C2 whisker therefore initiates in the C2 barrel column and the sensory information is distributed rapidly across the barrel cortex, allowing integration with multiwhisker input.

These images of active sensory processing in an awake, freely moving animal show that some aspects of the sensory processing of active touch appear similar to the sensory responses evoked by a passive stimulus (Figure 8B). The early signals are localized to the C2 whisker barrel column and spread over large cortical areas. The large cortical area excited by single whisker touch suggests that a single whisker can inform a large area of the brain under physiological conditions of recording in an awake, freely moving mouse.

Discussion

Whisker Sensation

Processing of single whisker-related information occurs through a similar spatiotemporal dynamic in anesthetized and awake animals. The earliest cortical supragranular responses occurred ~10 ms after whisker deflection and were localized to the isomorphic whisker barrel

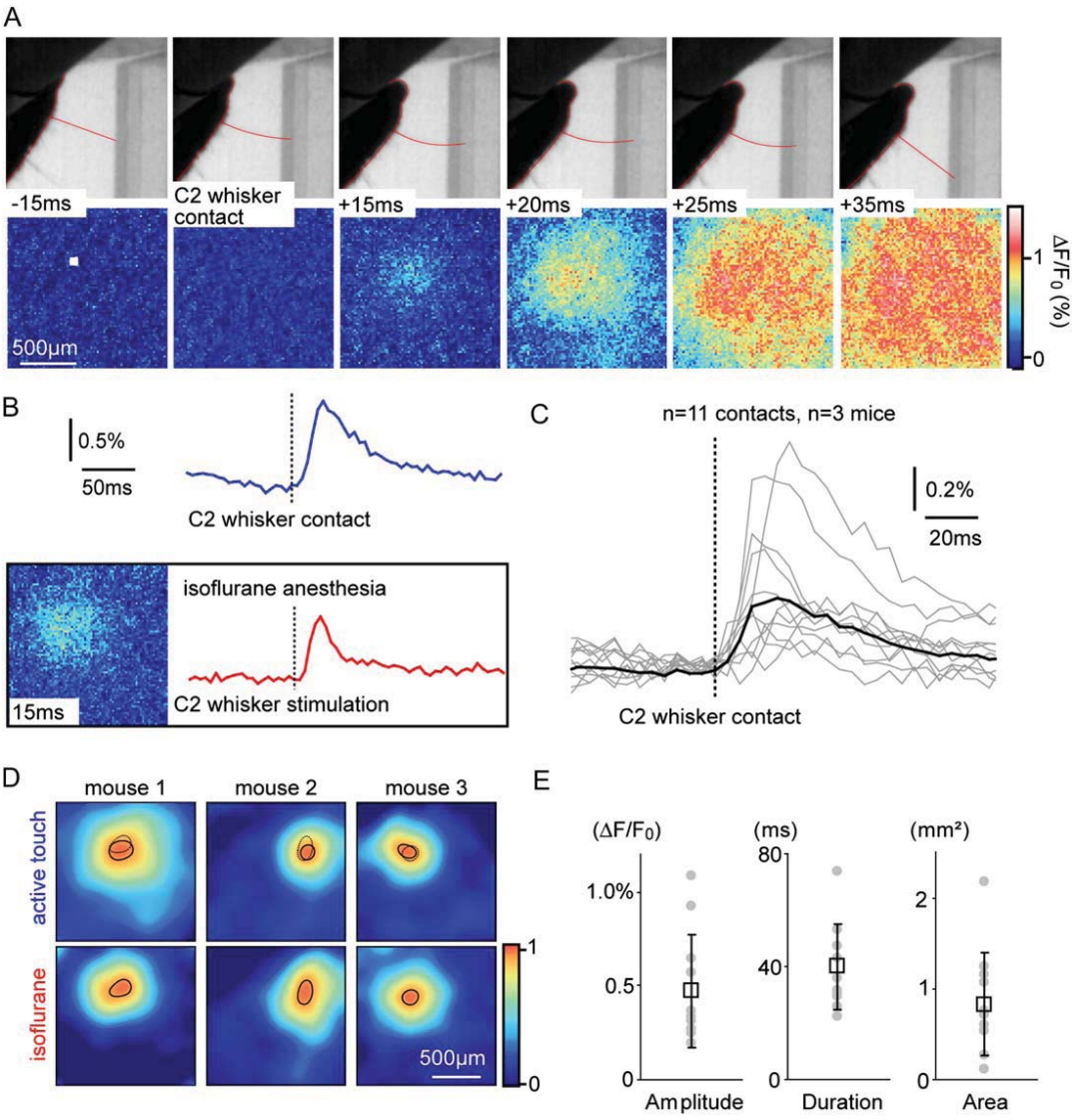

Figure 8. Imaging the Cortical Representation of Active Whisker Touch

(A) Images of the mouse behavior (upper panel) and the VSD signals from its somatosensory barrel cortex (lower panel) recorded as the mouse was approaching and actively touching an object with its C2 whisker. Active whisker touch evoked an initially localized sensory response, which over the next 20 ms propagated across the barrel cortex.

(B) VSD signal quantified from the region indicated by the white square in (A). The C2 whisker contact is followed by a large amplitude response. The image and trace in the box below show the VSD response to a passive C2 whisker deflection recorded while the mouse was under isoflurane anesthesia.

(C) VSD responses to 11 whisker contacts recorded in three mice. In each case the active whisker contact with an object evoked a brief propagating sensory response.

(D) The location of the early sensory response evoked by active touch is compared to the location of the early sensory response evoked by a piezo whisker stimulus under isoflurane anesthesia. The solid contour indicates the 95% contour of the evoked VSD response in each condition. In the active touch condition, the dotted contour indicates the location of the early sensory response evoked during isoflurane. There is excellent agreement of the location of the early sensory response in each of the three mice.

(E) The amplitude, duration (half-width), and spatial extent (area at half-maximal amplitude) were computed for each active contact.

column. The brain may compute which whisker was deflected by this early localized response (Petersen et al., 2001). Over the next tens of milliseconds depolarization propagated to cover the entire barrel cortex. This later spreading sensory response informs the neighboring cortical columns of the single whisker deflection and may underlie sensory integration of multiwhisker inputs. The distributed coding of single whisker deflection in layer 2/3 across the barrel cortex, which we visualized with voltage-sensitive dye, is also reflected in broad subthreshold receptive fields (Zhu and Connors, 1999; Moore and Nelson, 1998; Brecht et al., 2003). Interestingly, the subthreshold supragranular cortical dynamics of active touch (Figure 8) do not appear to be qualitatively different from passively evoked sensory responses. Indeed, responses to active touches consisted of early localized excitations that subsequently propagated across the barrel cortex. This spreading sensory response is likely to be mediated at least in part through the extensive lateral axonal arborizations of layer 2/3 pyramidal

neurons, which have been characterized previously (Keller and Carlson, 1999; Petersen et al., 2003a). The propagating sensory response is therefore a physiological signature of single whisker deflection, but during natural tactile processing animals use the entire array of whiskers. During object palpation many whiskers would near-simultaneously make contact, and it is therefore important to note that previous observations have highlighted profound roles for suppression of principal whisker responses by neighboring whiskers (Simons, 1985; Kelly et al., 1999; Higley and Contreras, 2005). In addition, sensory experience plays a profound role in regulating the receptive-field properties of barrel cortex neurons (recently reviewed by Feldman and Brecht, 2005), resulting in changes in the map representation of individual whiskers (Polley et al., 1999, 2004). It will therefore be of great interest in future studies to image cortical sensory processing during active touch of objects with the complete array of whiskers in mice, with different histories of sensory experience and during learning.

It seems counterintuitive that smaller sensory responses to passive magnetic whisker stimulation are evoked during active whisking behavior, since this is when one might expect whisker-related sensory processing to be most relevant for the animal. However, the suppression of sensory responses during active behavior (an issue first raised by Chapin and Woodward, 1982) has also been observed in whole-cell recordings (Crochet and Petersen, 2006), extracellular unit activity (Fanselow and Nicolelis, 1999; Hentschke et al., 2005), and field potential recordings (Castro-Alamancos, 2004; Hentschke et al., 2005). In our experiments, the magnetic field, and hence the force applied to the whisker, was consistent between quiet and active periods, but we do not know if the same activity was evoked in the trigeminal nerve. However, previous studies found that sensory responses evoked by direct stimulation of the sensory nerve were also suppressed during whisking (Fanselow and Nicolelis, 1999; Castro-Alamancos, 2004; Hentschke et al., 2005). The suppression of the sensory response during whisking is therefore, at least in part, mediated by processes downstream of the whisker follicle. One possible contribution to the suppression is that thalamic synapses may be weakened during whisking by short-term synaptic depression induced by increased thalamic "background" firing rates (Chung et al., 2002; Castro-Alamancos and Oldford, 2002). Another likely contribution to sensory response suppression is that the cortical brain state is different between quiet and whisking behavior (for example, spontaneous waves of activity were only observed during quiet periods and the EEG spectra are different), and this could affect how synaptic inputs are integrated in the context of ongoing spontaneous activity.

Having found strongly depressed sensory responses during active whisking, it is then a surprise that we were able to record sensory responses during active touch. The trigeminal sensory neurons may be engaged in a different manner during active touch as compared to passive stimuli (Szwed et al., 2003). During active whisking, vibrissae may be actively accelerated into objects by a recently described early feedback motor loop in the brainstem (Nguyen and Kleinfeld, 2005). Sensory activity in the trigeminal neurons generated by an initial object contact would be amplified as the whisker was accelerated into the object, driving increasing deflection of the whisker. However, if the sensory stimulus is not attributed to a physical object, then the whisker acceleration will only pass through air and it will thus have less consequence. This positive feedback loop would therefore specifically amplify activity in sensory neurons when the whisker contacted a real object.

In addition, there may be "top-down" influences on the sensory activity of the barrel cortex. As the mouse explores its environment, it is likely to construct a mental image of its environment. Because it moves the whisker through a given region of space many times, it may interpret our passive magnetic stimulus as just noise—it has already had the whisker through that region of space and on previous whisks it did not contact an object. It may be that our passive whisker stimulus is then actively filtered out as noise.

The variability of the cortical processing of whisker sensation that we have observed may correlate with different perceptual thresholds. To investigate this, we are now beginning to train mice to perform sensory discrimination linked with specific motor output to inform us of the mouse percept. It will then be interesting to see if the smaller sensory responses evoked during whisking correlate with reduced perception.

Applications and Technological Outlook

A major advantage of the current fiber-based imaging technique that we describe here is that it is relatively simple and easy to use, in contrast to the advanced technology of the head-mounted, scanning, two-photon fiber imaging system that has been recently developed (Helmchen et al., 2001). It should therefore be easy to transfer the technique to make measurements of other sensory areas. Of particular interest to us would be the simultaneous imaging of both primary and secondary somatosensory cortices. Equally, it should be straightforward to apply the current fiber-based imaging technique for measurements of visual cortex, motor cortex, and the olfactory bulb in freely moving animals. Ideally, one might be able to image simultaneously from the entire dorsal aspect of the neocortex; this could be achieved by shaping the fiber end so that it envelopes the whole cortex.

We think the most important technical advances that need to be made for this fiber imaging technology will be those that allow repeated imaging from trained animals. Repeated voltage-sensitive dye imaging has been achieved in monkeys (Slovin et al., 2002) through the development of artificial dura. For rodents, implanted canula to deliver the dye within a sealed imaging window over a craniotomy (Holtmaat et al., 2005) are likely to offer the best possibilities. Recent advances in developing genetically encoded fluorescing membrane potential sensors (Siegel and Isacoff, 1997; Cacciatore et al., 1999; Sakai et al., 2001; Ataka and Pieribone, 2002) may help long-term chronic imaging and in addition could offer cell type-specific labeling.

In conclusion, there are many further applications and future developments to be made based on fiber imaging. Here, we have demonstrated that fiber bundle-based, voltage-sensitive dye imaging is useful for analyzing the dynamics of cortical function in freely moving mice,

allowing a correlation of brain function and behavior on a millisecond timescale with subcolumnar resolution.

Experimental Procedures

Animals and Surgery

All experiments were carried out in accordance with authorizations approved by the Swiss Federal Veterinary Office. C57BL6J mice aged 1 to 5 months were anesthetized with either urethane (1.5 mg/g) or isoflurane (1.5%). Paw withdrawal, whisker movement, and eyeblink reflexes were largely suppressed. A heating blanket maintained the rectally measured body temperature at 37ºC. The head of the mouse was fixed by a nose clamp. The skin overlying the somatosensory cortex was removed and the bone gently cleaned.

Intrinsic Optical Imaging

The cortical surface was visualized through the intact bone covered with Ringer's solution and sealed with a glass coverslip. The surface blood vessels were visualized using light of 530 nm to enhance contrast. The illumination was switched to 630 nm for functional imaging. The reflected light was imaged using a Qicam CCD camera (Q-imaging) coupled to a Leica MZ9.5 microscope. Image acquisition via FireWire and stimulus control via an ITC-18 (Instrutech) was governed by custom routines running in IgorPro (Wavemetrics). Alternating sweeps were imaged with or without piezo stimuli delivered to the C2 whisker. Stimuli were applied at 10 Hz for 4 s and the intrinsic signal was quantified as the difference in the reflected light upon stimulus compared to immediately before. The intrinsic imaging gave a localized signal centered on the C2 barrel column. This functionally identified location of the C2 barrel column was mapped onto the blood vessel pattern to guide surgery for the craniotomy.

Voltage-Sensitive Dye Imaging

A 2 × 2 mm craniotomy was made, centered on the location of the C2 barrel column as determined by the intrinsic optical imaging. Extreme care was taken at all times not to damage the cortex, especially during the removal of the dura. Voltage-sensitive dye RH1691 was dissolved at 1 mg/ml in Ringer's solution containing the following (in mM): 135 NaCl, 5 KCl, 5 HEPES, 1.8 $CaCl_2$, and 1 $MgCl_2$. This dye solution was topically applied to the exposed cortex and allowed to diffuse into the cortex over 1 hr. The cortex was subsequently washed to remove unbound dye.

In experiments where conventional epifluorescence imaging was compared to fiber imaging, the cortex was then sealed by gluing on a glass coverslip which was in direct contact with the cortical surface. In experiments combined with electrophysiology, the cortex was covered with agarose and a coverslip placed on top in a manner that allowed access for recording pipettes. In all experiments performed with urethane anesthetized mice, electrocardiogram (ECG) electrodes were inserted under the skin of the forearms.

In the fiber imaging experiments, a U-shaped aluminum fiber holder was first implanted, centered on the location of the C2 barrel column, before performing the craniotomy and dye staining. The fiber holder was designed to allow reproducible placement and orientation of the fiber. During epifluorescent visualization, the fiber tip was placed in direct contact with the cortical surface, and fixed in place to the fiber holder using dental cement.

The voltage-sensitive dye was excited with 630 nm light from a 100 W halogen lamp gated by a Uniblitz shutter (Vincent Associates) under computer control via an ITC-18 (Instrutech) communicating with custom software running within IgorPro (Wavemetrics). The excitation light was reflected using a 650 nm dichroic and focused onto the cortical surface or the proximal fiber end with a 25 mm video lens (Navitar). Fluorescence was collected via the same optical pathway, but without reflection of the dichroic, long-pass filtered 665 nm, and focused onto the sensor of a high-speed MiCam Ultima (Scimedia) camera via a 135 mm camera lens (Nikon).

Fiber Optics

The fiber optics were custom made by Schott Fiber Optics based on their wound image bundle technology (http://www.schott.com/fiberoptics).

Whole-Cell Recordings

Pipettes were slowly advanced into the cortex under high positive pressure (~200 mbar) and targeted to the functionally mapped C2 barrel column. Positive pressure was reduced (~25 mbar) and the pipette was advanced in 2 μm steps until the pipette resistance increased, and then suction was applied to establish a gigaseal followed by the whole-cell configuration. Whole-cell pipettes had resistances of ~5 MΩ filled with a solution containing the following (in mM): 135 potassium gluconate, 4 KCl, 10 HEPES, 10 phosphocreatine, 4 MgATP, 0.3 Na_3GTP (adjusted to pH 7.2 with KOH), and 2 mg/ml biocytin. Whole-cell electrophysiological measurements were made with a Multiclamp 700 amplifier (Axon Instruments). The membrane potential was filtered at 10 kHz and digitized at 20 kHz in a sweep-based manner by an ITC-18 (Instrutech Corporation) under the control of IgorPro (Wavemetrics).

Whisker Stimuli

For the experiments performed with anesthetized mice, 2 ms C2 whisker deflections were generated by using a computer-controlled piezoelectric bimorph. For the experiments performed with awake, freely moving mice, reproducible whisker deflections were evoked by attaching a small metal particle to the C2 whisker and generating brief magnetic pulses. Magnetic pulses were generated by a copper wire coil with 1500 windings totaling 50 cm height in the z direction and 20 cm diameter in the xy plane. Single brief current pulses (1–5 ms) were driven through the coil by discharge from a capacitor gated by a solid-state relay under computer control. The magnetic field was measured at different positions within the coil and was found to be uniform across the entire xy plane in the central 20 cm of the z direction. The behavioral platform, where the mouse was placed, was therefore mounted in this central z location.

Filming and Quantifying Whisker Behavior

The behavioral area was illuminated from below with infrared light and filmed through a 50 mm video lens (Navitar) with a high-speed MotionPro camera (Redlake). This transillumination gave a high contrast silhouette of the mouse body and sufficient contrast to visualize the mouse whiskers. The field of view was 20 × 20 cm, giving a single pixel resolution of 0.2 mm. The behavioral images were obtained at either 2 ms or 5 ms intervals between frames and imaging was synchronized to the voltage-sensitive dye imaging through TTL pulses. Custom-written routines running within ImageJ were used to automatically track head and whisker position (L. Segapelli, S. Crochet, I.F., C.P., D. Sage, and M. Unser, unpublished data).

Analysis of Voltage-Sensitive Dye Images

VSD image sequences acquired with the high-speed MiCam Ultima camera were analyzed using custom-written routines in IgorPro (Wavemetrics).

In all experiments performed with urethane anesthetized mice, alternating sweeps triggered on a fixed phase of the ECG were imaged with or without stimuli delivered to the C2 whisker. Subtraction of the averaged unstimulated sweeps was then used to correct both bleaching and heartbeat-related artifacts. In experiments combined with electrophysiology, image sequences of spontaneous cortical activity were corrected for bleaching by subtracting the exponential fit of the average fluorescence decrease over the time. For all the experiments performed with awake, freely moving mice, the ECG was not monitored. Therefore, VSD signals were not corrected for heartbeat artifacts, but bleaching was corrected for by linear fits to the average fluorescence decay. In experiments where sensory responses in anesthetized mice were compared to responses in awake mice, alternating sweeps with or without stimuli delivered to the C2 whisker were recorded. Subtraction of the averaged unstimulated sweeps was then used to correct for bleaching.

Recordings of VSD signals presented surprisingly small heartbeat-related artifacts (Figure S2). However, large movements of the mice, such as jumping or running into the wall of the behavioral chamber, were accompanied with movement-related artifacts. These movement-related artifacts could be clearly differentiated from VSD signals reflecting neuronal activity since (1) they were correlated across the entire imaged area, (2) they occurred in cortical areas not stained with VSD, and (3) the movement artifacts were highlighted at the border of the craniotomy.

VSD signals were quantified as the mean pixel value within square regions of interest. Linescan plots were calculated by averaging pixel values along short segments in the normal direction to a defined line crossing the barrel cortex. Outward radial spread plots were calculated by averaging pixel values from circular regions of interest (rings) of increasing diameter around a given center location.

Histology

After completion of the physiological measurements, mice were deeply anesthetized with urethane and perfused with PBS followed by 4% paraformaldehyde. After fixation, 100 μm thick brain slices were cut. Most brains were sectioned tangentially, stained for cytochrome oxidase revealing the layer 4 barrel map, and the VSD signals aligned using the blood vessels. Other brains were sectioned parasagitally to analyze the penetration and staining of voltage-sensitive dye RH1691 by confocal microscopy (Leica SP2). In four additional experiments, the mouse brain was rapidly frozen in isopentane chilled by dry ice, transferred to a cryostat (Leica CM3050S), and sectioned in 20 μm thick parasagital slices.

Statistical Tests

Data are expressed as mean ± standard deviation, and they were tested using SigmaStat (Systat Software) for statistical significance using Student's t test (paired when appropriate) or Wilcoxon signed rank test (for data without a normal distribution).

Supplemental Data

The Supplemental Data for this article can be found online at http://www.neuron.org/cgi/content/full/50/4/617/DC1/.

Acknowledgments

The authors are grateful for the generous support of the Swiss National Science Foundation and the Leenaards Foundation. We thank Amiram Grinvald and Bert Sakmann for help and advice concerning voltage-sensitive dye imaging. We thank Mathew Diamond and Ehud Ahissar for help and advice on how to obtain high-contrast filming of whiskers. We thank Rolf Rödel (MPI Heidelberg) and Cedric Nicolas (EPFL) for electronic design and construction of the magnetic whisker stimulators. We thank Sylvain Crochet and James Poulet for discussion and critical reading of the manuscript.

Received: September 26, 2005
Revised: February 10, 2006
Accepted: March 28, 2006
Published: May 17, 2006

References

Arieli, A., Sterkin, A., Grinvald, A., and Aertsen, A. (1996). Dynamics of ongoing activity: explanation of the large variability in evoked cortical responses. Science *273*, 1868–1871.

Ataka, K., and Pieribone, V.A. (2002). A genetically targetable fluorescent probe of channel gating with rapid kinetics. Biophys. J. *82*, 509–516.

Brecht, M., Roth, A., and Sakmann, B. (2003). Dynamic receptive fields of reconstructed pyramidal cells in layers 3 and 2 of rat somatosensory barrel cortex. J. Physiol. *553*, 243–265.

Cacciatore, T.W., Brodfuehrer, P.D., Gonzalez, J.E., Jiang, T., Adams, S.R., Tsien, R.Y., Kristan, W.B., and Kleinfeld, D. (1999). Identification of neural circuits by imaging coherent electrical activity with FRET-based dyes. Neuron *23*, 449–459.

Castro-Alamancos, M.A., and Oldford, E. (2002). Cortical sensory suppression during arousal is due to the activity-dependent depression of thalamocortical synapses. J. Physiol. *541*, 319–331.

Castro-Alamancos, M.A. (2004). Absence of rapid sensory adaptation in neocortex during information processing states. Neuron *41*, 455–464.

Chapin, J.K., and Woodward, D.J. (1982). Somatic sensory transmission to the cortex during movement: gating of single cell responses to touch. Exp. Neurol. *78*, 654–669.

Chapin, J.K., and Lin, C.S. (1984). Mapping the body representation in the SI cortex of anesthetized and awake rats. J. Comp. Neurol. *229*, 199–213.

Chung, S., Li, X., and Nelson, S.B. (2002). Short-term depression at thalamocortical synapses contributes to rapid adaptation of cortical sensory responses in vivo. Neuron *34*, 437–446.

Crochet, S., and Petersen, C.C.H. (2006). Correlating whisker behavior with membrane potential in barrel cortex of awake mice. Nat. Neurosci. *9*, 608–610.

Derdikman, D., Hildesheim, R., Ahissar, E., Arieli, A., and Grinvald, A. (2003). Imaging spatiotemporal dynamics of surround inhibition in the barrels somatosensory cortex. J. Neurosci. *23*, 3100–3105.

Fanselow, E.E., and Nicolelis, M.A.L. (1999). Behavioral modulation of tactile responses in the rat somatosensory system. J. Neurosci. *19*, 7603–7616.

Fee, M.S., Mitra, P.P., and Kleinfeld, D. (1997). Central versus peripheral determinants of patterned spike activity in rat vibrissa cortex during whisking. J. Neurophysiol. *78*, 1144–1149.

Feldman, D.E., and Brecht, M. (2005). Map plasticity in the somatosensory cortex. Science *310*, 810–815.

Ganguly, K., and Kleinfeld, D. (2004). Goal-directed whisking increases phase-locking between vibrissa movement and electrical activity in primary sensory cortex in rat. Proc. Natl. Acad. Sci. USA *101*, 12348–12353.

Grinvald, A., and Hildesheim, R. (2004). VSDI: a new era in functional imaging of cortical dynamics. Nat. Rev. Neurosci. *5*, 874–885.

Grinvald, A., Anglister, L., Freeman, J.A., Hildesheim, R., and Manker, A. (1984). Real-time optical imaging of naturally evoked electrical activity in intact frog brain. Nature *308*, 848–850.

Grinvald, A., Lieke, E., Frostig, R.D., Gilbert, C.D., and Wiesel, T.N. (1986). Functional architecture of cortex revealed by optical imaging of intrinsic signals. Nature *324*, 361–364.

Helmchen, F., Fee, M.S., Tank, D.W., and Denk, W. (2001). A miniature head-mounted two-photon microscope: high resolution brain imaging in freely moving animals. Neuron *31*, 903–912.

Hentschke, H., Haiss, F., and Schwarz, C. (2005). Central signals rapidly switch tactile processing in rat barrel cortex during whisker movements. Cereb. Cortex, in press. Published online October 12, 2005. 10.1093/cercor/bhj056.

Higley, M.J., and Contreras, D. (2005). Integration of synaptic responses to neighboring whiskers in rat barrel cortex in vivo. J. Neurophysiol. *93*, 1920–1934.

Holtmaat, A.J., Trachtenberg, J.T., Wilbrecht, L., Shepherd, G.M., Zhang, X., Knott, G.W., and Svoboda, K. (2005). Transient and persistent dendritic spines in the neocortex in vivo. Neuron *45*, 279–291.

Keller, A., and Carlson, G.C. (1999). Neonatal whisker clipping alters intracortical, but not thalamocortical projections, in rat barrel cortex. J. Comp. Neurol. *412*, 83–94.

Kelly, M.K., Carvell, G.E., Kodger, J.M., and Simons, D.J. (1999). Sensory loss by selected whisker removal produces immediate disinhibition in the somatosensory cortex of behaving rats. J. Neurosci. *19*, 9117–9125.

Kleinfeld, D., and Delaney, K.R. (1996). Distributed representation of vibrissa movement in the upper layers of somatosensory cortex revealed with voltage-sensitive dyes. J. Comp. Neurol. *375*, 89–108.

Krupa, D.J., Wiest, M.C., Shuler, M.G., Laubach, M., and Nicolelis, M.A.L. (2004). Layer-specific somatosensory cortical activation during active tactile discrimination. Science *304*, 1989–1992.

Moore, C.I., and Nelson, S.B. (1998). Spatio-temporal subthreshold receptive fields in the vibrissa representation of rat primary somatosensory cortex. J. Neurophysiol. *80*, 2882–2892.

Nguyen, Q.T., and Kleinfeld, D. (2005). Positive feedback in a brainstem tactile sensorimotor loop. Neuron *45*, 447–457.

Orbach, H.S., Cohen, L.B., and Grinvald, A. (1985). Optical mapping of electrical activity in rat somatosensory and visual cortex. J. Neurosci. *5*, 1886–1895.

Petersen, C.C.H., Grinvald, A., and Sakmann, B. (2003a). Spatiotemporal dynamics of sensory responses in layer 2/3 of rat barrel cortex measured in vivo by voltage-sensitive dye imaging combined with

whole-cell voltage recordings and anatomical reconstructions. J. Neurosci. *23*, 1298–1309.

Petersen, C.C.H., Hahn, T.T.G., Mehta, M., Grinvald, A., and Sakmann, B. (2003b). Interaction of sensory responses with spontaneous depolarization in layer 2/3 barrel cortex. Proc. Natl. Acad. Sci. USA *100*, 13638–13643.

Petersen, R.S., Panzeri, S., and Diamond, M.E. (2001). Population coding of stimulus location in rat somatosensory cortex. Neuron *32*, 503–514.

Polley, D.B., Chen-Bee, C.H., and Frostig, R.D. (1999). Two directions of plasticity in the sensory-deprived adult cortex. Neuron *24*, 623–637.

Polley, D.B., Kvasnak, E., and Frostig, R.D. (2004). Naturalistic experience transforms sensory maps in the adult cortex of caged animals. Nature *429*, 67–71.

Sakai, R., Repunte-Canonigo, V., Raj, C.D., and Knopfel, T. (2001). Design and characterization of a DNA-encoded, voltage-sensitive fluorescent protein. Eur. J. Neurosci. *13*, 2314–2318.

Seidemann, E., Arieli, A., Grinvald, A., and Slovin, H. (2002). Dynamics of depolarization and hyperpolarization in the frontal cortex and saccade goal. Science *295*, 862–865.

Shoham, D., Glaser, D.E., Arieli, A., Kenet, T., Wijnbergen, C., Toledo, Y., Hildesheim, R., and Grinvald, A. (1999). Imaging cortical dynamics at high spatial and temporal resolution with novel blue voltage-sensitive dyes. Neuron *24*, 791–802.

Siegel, M.S., and Isacoff, E.Y. (1997). A genetically encoded optical probe of membrane voltage. Neuron *19*, 735–741.

Simons, D.J. (1985). Temporal and spatial integration in the rat SI vibrissa cortex. J. Neurophysiol. *54*, 615–635.

Slovin, H., Arieli, A., Hildesheim, R., and Grinvald, A. (2002). Long-term voltage-sensitive dye imaging reveals cortical dynamics in behaving monkeys. J. Neurophysiol. *88*, 3421–3438.

Spors, H., and Grinvald, A. (2002). Spatio-temporal dynamics of odor representations in the mammalian olfactory bulb. Neuron *34*, 301–315.

Szwed, M., Bagdasarian, K., and Ahissar, E. (2003). Encoding of vibrissal active touch. Neuron *40*, 621–630.

Woolsey, T.A., and Van der Loos, H. (1970). The structural organisation of layer IV in the somatosensory region (SI) of the mouse cerebral cortex: the description of a cortical field composed of discrete cytoarchitectonic units. Brain Res. *17*, 205–242.

Zhu, J.J., and Connors, B.W. (1999). Intrinsic firing patterns and whisker-evoked synaptic responses of neurons in the rat barrel cortex. J. Neurophysiol. *81*, 1171–1183.

Cerebral Cortex August 2007;17:1948-1957
doi:10.1093/cercor/bhl104
Advance Access publication October 26, 2006

Extensive Overlap of Mu-Opioid and Nicotinic Sensitivity in Cortical Interneurons

Isabelle Férézou[1], Elisa L. Hill[1], Bruno Cauli[1], Nathalie Gibelin[1], Takeshi Kaneko[2], Jean Rossier[1] and Bertrand Lambolez[1]

[1]Laboratoire de Neurobiologie et Diversité Cellulaire, CNRS UMR 7637, École Supérieure de Physique et de Chimie Industrielles, 75005 Paris, France and [2]Department of Morphological Brain Science, Graduate School of Medicine, Kyoto University, Kyoto 606-8501, Japan

We studied μ-opioid transmission in acute slices of rat neocortex using whole-cell recordings and single-cell reverse transcription–polymerase chain reaction. The μ-opioid receptor (MOR) was found in γ-aminobutyric acidergic (GABAergic) interneurons that were either layer I cells frequently expressing neuropeptide Y or layers II–V cells expressing vasoactive intestinal peptide and enkephalin (Enk). We found that μ-opioid agonists inhibit these interneurons that are selectively excited by nicotinic agonists. The extensive overlap of μ-opioid and nicotinic responsiveness allowed μ-opioid agonists to inhibit nicotinic excitation of responsive interneurons and of their GABAergic output onto pyramidal cells. Finally, nicotinic stimulation resulted in a dynamic sequence where GABAergic transmission was first enhanced and then depressed below its baseline. This latter disinhibitory effect was prevented by a μ-opioid antagonist, indicating that excitation of nicotinic-responsive interneurons induced the release of endogenous Enk, which in turn led to MOR activation. Our results suggest that neocortical μ-opioid transmission acts as an inhibitory feedback onto nicotinic-responsive interneurons, which may change network excitability and inhibition patterns during cholinergic excitation.

Keywords: enkephalin, GABAergic interneuron, μ-opioid receptor, neocortex, nicotinic receptor

Introduction

The neocortical network integrates afferent inputs through a heterogeneous neuronal population comprising excitatory pyramidal cells and interneurons (Peters and Jones 1984; Connors and Gutnick 1990; Thomson and Deuchars 1994; Somogyi et al. 1998; Dantzker and Callaway 2000). These interneurons transmute incoming excitatory signals into local γ-aminobutyric acidergic (GABAergic) inhibition. They also constitute a rich source of neuropeptides whose explicit contributions to neocortical integration are largely undefined (Papadopoulos et al. 1987; DeFelipe 1993; Kubota et al. 1994; Cauli et al. 1997; Kaneko et al. 1998; Gallopin et al. 2005; Toledo-Rodriguez et al. 2005).

μ-Opioid agonists have wide behavioral implications, and it is established that in the hippocampus, they reduce GABAergic transmission by inhibiting interneurons (Zieglgansberger et al. 1979; Madison and Nicoll 1988; Capogna et al. 1993), thereby increasing network excitability (disinhibition). However, little is known about their function in the neocortex. It is well documented that enkephalin (Enk) is the only endogenous μ-opioid agonist in the neocortex (Rossier et al. 1977; Gee et al. 1983; Giraud et al. 1983). In this structure, the immunocytochemical distributions of Enk and of the μ-opioid receptor (MOR) largely overlap and are restricted to GABAergic interneurons (Taki et al. 2000). The coexpression of Enk and MOR suggests that μ-opioid transmission acts as an inhibitory feedback loop onto interneurons to disinhibit the neocortical network.

A functional link between μ-opioid and cholinergic transmission is suggested by behavioral evidence of interactions between nicotine and opioids (Pomerleau 1998; Malin 2001; Mathieu-Kia et al. 2002) and by the reduction of nicotine effects in mice lacking MOR or Enk (Berrendero et al. 2002, 2005). In the neocortex, multiple neuronal types mediate the effects of acetylcholine (McCormick and Prince 1985; Kawaguchi 1997; Xiang et al. 1998; Porter et al. 1999; Christophe et al. 2002). Among these cell types, interneurons expressing vasoactive intestinal peptide (VIP) constitute a major target of nicotinic agonists and express receptor channels with high affinity for nicotine (Porter et al. 1999). The observation that the majority of MOR-expressing interneurons also expresses VIP (Taki et al. 2000) suggests that μ-opioid transmission might contribute to the neocortical integration of cholinergic nicotinic signals.

In the present study, we combined patch-clamp recordings and single-cell reverse transcription–polymerase chain reaction (scPCR; Lambolez et al. 1992) in rat neocortical slices to identify and characterize MOR- and Enk-expressing neurons. The results show that in the neocortex, μ-opioid transmission selectively inhibits interneuron populations that respond to nicotinic agonists and controls the GABAergic contribution of these interneurons to the network.

Materials and Methods

Slice Preparation

All experiments were carried out in accordance with the guidelines published in the European Communities Council Directive of 24 November 1986 (86/609/EEC). Young Wistar rats (14–21 postnatal days old) were decapitated, the brains were quickly removed, and 300-μm-thick parasagittal sections of cerebral cortex were prepared as described (Cauli et al. 1997). The slices were incubated at room temperature (20–25 °C) in artificial cerebrospinal fluid (ACSF) containing (in mM) NaCl, 126; KCl, 5; NaH_2PO_4, 1.25; $CaCl_2$, 2; $MgCl_2$, 1; $NaHCO_3$, 26; Glucose, 20; and pyruvate 5 that was bubbled with a mixture of 95% O_2 and 5% CO_2.

Whole-Cell Recordings

Slices were transferred to a chamber and perfused at 1.5 mL/min with ACSF at room temperature. Patch pipettes (5–7 MΩ) pulled from borosilicate glass were filled with 8 μL of internal solution containing (in mM) K-gluconate, 144; $MgCl_2$, 3; ethyleneglycol-bis(2-aminoethylether)-*N*,*N*,*N*′,*N*′-tetraacetic acid, 0.5; 4-(2-hydroxyethyl)-1-piperazineethanesulfonic acid, 10; and biocytin, 2 mg/mL. The pH was adjusted to 7.2 and osmolarity to 285/295 mosm. Whole-cell patch-clamp recordings were made from neocortical neurons identified under infrared videomicroscopy with Nomarski optics (Stuart et al. 1993) and using a patch-clamp amplifier (Axopatch 200A, Axon Instruments,

Foster City, CA). All membrane potentials were corrected for junction potential (−11 mV). Resting membrane potential was measured just after passing into whole-cell configuration, and only cells with a resting membrane potential more hyperpolarized than −50 mV were selected. After characterization of the recorded neurons according to their firing behavior, effects of different drugs were investigated using current-clamp or voltage-clamp methods (VH, −71 mV). The series resistances were not compensated but were monitored throughout the experiments. The signals were filtered at 5 kHz, digitized at 10 kHz, saved to a PC, and analyzed off-line with pCLAMP8 software (Axon Instruments).

Drugs and chemicals were obtained from Sigma (Saint Louis, MO) except tetrodotoxin (TTX) that was purchased from Latoxan (Valence, France). All drugs were applied in the bath perfusion. The nicotinic receptor agonist 1-1-dimethyl-4-phenyl-piperazinium iodide (DMPP) was applied in the presence of the muscarinic receptor antagonist atropine (5 μM). Reproducible responses to DMPP- and to the MOR-selective agonist [D-Ala2,*N*-Me-Phe4,Gly5-ol]-enkephalin (DAMGO) were obtained with 6- and 13-min intervals between applications, respectively. Somatodendritic responses to drug applications are presented as mean ± standard deviation.

To record inhibitory postsynaptic currents (IPSCs), 27 mM of K-gluconate was replaced by KCl in the internal solution, resulting in a theoretical chloride reversal potential of −40.4 mV. IPSCs were thus recorded as inward currents in our conditions. Recordings were performed in the presence of (±)-2-amino-5-phosphonovaleric acid (AP-5, 20 μM) and 6-cyano-7-nitroquinoxaline-2,3-dione (CNQX, 10 μM) to prevent glutamatergic transmission. In this set of experiments, DMPP was bath applied in the presence of atropine (5 μM) and the selective antagonist for the α7 subtype of nicotinic receptors, methyllycaconitine (10 nM). The GABAergic nature of the DMPP-induced postsynaptic events in pyramidal neurons was confirmed by applying DMPP in the absence of glutamate receptor antagonists and in the presence of bicuculline (10 μM), using an internal solution containing lidocaine *N*-ethyl bromide (QX-314, 5 mM). In these conditions, DMPP did not induce any change in postsynaptic event amplitude or frequency ($n = 3$).

Postsynaptic currents were analyzed off-line using Mini Analysis software (Synaptosoft, Decatur, GA). Signals <7 pA were excluded from the measurements. Average DMPP effects on IPSCs amplitude and frequency in different conditions are presented as mean ± standard error of mean.

Single-Cell Reverse Transcription-PCR

Cytoplasm harvesting of the recorded neurons and reverse transcription were performed as described (Lambolez et al. 1992). At the end of the recording, as much as possible of the cell's content was aspirated into the recording pipette by application of a gentle negative pressure while maintaining the tight seal. The pipette was then delicately removed to allow outside-out patch formation. Next, the content of the pipette was expelled into a test tube and reverse transcription was performed in a final volume of 10 μL. Two steps of multiplex polymerase chain reaction (PCR) were performed essentially as described (Cauli et al. 1997). The cDNAs present in the 10 μL reverse transcription reaction were first amplified simultaneously using all the primer pairs described in Table 1 (for each primer pair, the sense and antisense primers were positioned on 2 different exons). Taq polymerase (2.5 units, Qiagen GmbH, Hilden, Germany) and 20 pmole of each primer were added to the buffer supplied by the manufacturer (final volume 100 μL), and 20 cycles (94 °C, 30 s; 60 °C, 30 s; 72 °C, 35 s) of PCR were run. Second rounds of PCR were then performed using 2 μL of the first PCR product as template. In this second round, each cDNA was individually amplified using its specific primer pair by performing 35 PCR cycles (as described above). Ten microliters of each individual PCR reaction were then run on a 2% agarose gel using ϕ × 174 digested by Hae III as molecular weight marker and stained with ethidium bromide. MOR scPCR was initially performed with sense and antisense primers A (see Table 1) located in exons 1 and 2, respectively. Primer pair B (exons 2 and 3) was used subsequently due to the existence of exon 1 alternative splicing in mouse (Pan et al. 2001). Both primer pairs were equally effective in detecting MOR expression in single cells, suggesting that exon 1 is present in a significant proportion of rat neocortical MOR mRNAs.

Table 1
PCR primers and FRET probes

	Size	PCR primers	FRET probes
MOR # NM_013071	236	Sense A, 75: ACCTGGCTCCTGGCTCAACT Antisense A, 290: TGGTGGCAGTCTTCATTTTGG Sense B, 486: CGTGGACCGCTACATTGCTG Antisense B, 711: CGGCATGATGAAAGCGAAGATA	3′ FITC, 340: AACGACAGCCTGTGCCCTCA 5′ R705, 361: ACCGGCAGCCCTTCCATG Nested sense, 498: CATTGCTGTCTGCCACCCA Nested antisense, 687: AAGACACAGATTTTGAGCAGGTTC
δ-opioid R # NM_012617	508	Sense, 33: GCAGTTTTCGCTCCTCGC Antisense, 520: CCCAACACCTGAAGCCAAGAC	3′ FITC, 307: CCCTTCCAGAGCGCCAAGT 5′ R705, 327: CCTGATGGAAACGTGGCCG
κ-opioid R # NM_017167	326	Sense, 590: GAGGCACCAAAGTCAGGGAA Antisense, 898: GCTGTGGGAGGTGCTGCC	3′ FITC, 733: TGCTACACCCTGATGATCCTGC 5′ R705, 756: CTTGAAGAGTGTCCGGCTCCTC
Enk # M28263	345	Sense, 451: GCCAACTCCTCCGACCTGCT Antisense, 772: GCCTCCGTATCTTTTTTCCATCTC	3′ FITC, 588: TGAAGACAGCACGAGCAAGAGGT 5′ R705, 612: TGGGGGCTTCATGAGAGGC
Dynorphin # NM_019374	286	Sense, 65: ACTGCCTGTCCTTGTGTTCCCT Antisense, 329: GAGACGCTGGTAAGGAGTTGGC	3′ FITC, 113: CCCATCCCATCAACCCCCT 5′ R705, 133: ATTTGCTCCCTGGAGTGCCAG
POMC # K01878	217	Sense, 105: GGACCTCACCACGGAAAGCA Antisense, 304: CCGTCTCTTCCTCCGCAC	mRNA not detected in this study
Gad65 # M72422	391	Sense[a], 713: TCTTTTCTCCTGGTGGTGCC Antisense[a], 1085: CCCCAAGCAGCATCCACAT	3′ FITC[c] 848: TTTCTCTCAAGAAGGGAGCTGCA 5′ R705[c] 872: CCTTGGGGATCGGAACAGACA
Gad67 # M76177	600	Sense[2], 713: TACGGGGTTCGCACAGGTC Antisense[b], 1294: same as GAD65	3′ FITC[c] 930: CCTGGGGGAGCCATATCCAA 5′ R705[c] 951: ATGTACAGCATCATGGCGGCTC
CB # M27839	432	Sense[b], 134: AGGCACGAAAGAAGGCTGGAT Antisense[b], 544: TCCCACACATTTTGATTCCCTG	3′ FITC[c] 263: TCCTGCTGCTCTTTCGATGCC 5′ R705[c] 285: GCAACTGAAGTCCTGCGAGGAA
CR # X66974	309	Sense[b], 142: CTGGAGAAGGCAAGGAAAGGT Antisense[b], 429: AGGTTCATCATAGGGACGGTTG	3′ FITC[c] 248: TTGAGATGGCAGAGCTGGCG 5′ R705[c] 269: AGATCCTGCCAACCGAAGAGAAT
NPY # M15880	359	Sense[b], −45: GCCCAGAGCAGAGCACCC Antisense[b], 292: CAAGTTTCATTTCCCATCACCA	3′ FITC[c] 17: AACGAATGGGGCTGTGTGGA 5′ R705[c] 38: TGACCCTCGCTCTATCCCTGC
SOM # K02248	209	Sense[b], 43: ATCGTCCTGGCTTTGGGC Antisense[b], 231: GCCTCATCTCGTCCTGCTCA	3′ FITC[c] 105: GCAGAAGTCTCTGGCGGCTG 5′ R705[c] 126: CACCGGGAAACAGGAACTGGC
VIP # X02341	286	Sense[b], 167: TGCCTTAGCGGAGAATGACA Antisense[b], 434: CCTCACTGCTCCTCTTCCCA	3′ FITC[c] 199: TGTGTCCAGAAATGCCAGGCA 5′ R705[c] 221: GCTGATGGAGTTTTCACCAGCG
CCK # K01259	216	Sense[b], 174: CGCACTGCTAGCCCGATACA Antisense[b], 373: TTTCTCATTCCGCCTCCTCC	3′ FITC[c] 198: CCAGCAGGTCCGCAAAGCT 5′ R705[c], 218: CCTCTGGCCGCATGTCCG

Position 1: First base of the start codon.
[a]Bochet et al. (1994).
[b]Cauli et al. (1997).
[c]Ferezou et al. (2002).

Identification of the PCR Products and Test of the scPCR Protocol

PCR-generated fragments obtained from each cell were analyzed by fluorescence resonance energy transfer (FRET) between 2 adjacent oligoprobes (Table 1, purchased from Proligo, Paris, France) internal to the amplified sequence. The upstream probe was fluorescein isothiocyanate labeled at the 3′ end (donor, excitation 470 nm) and the downstream probe Red705 labeled at the 5′ end (acceptor, emission, 710 nm). FRET between the 2 fluorophores, which can only occur when both probes are hybridized to their cognate PCR fragment, was measured with a LightCycler instrument (Roche Diagnostics GmbH, Mannheim, Germany) as described (Ferezou et al. 2002). The identity of PCR fragments obtained with MOR primer pair B was confirmed using a nested PCR with primers described in Table 1. The reverse transcription-PCR protocol was tested on 500 pg of total RNA purified from rat neocortex (Chomczynski and Sacchi 1987). All the transcripts were detected from 500 pg of neocortical RNA except for the pro-opiomelanocortin (POMC) mRNA, which was detected from 4 ng of whole brain RNA. The sizes of the PCR-generated fragments were as predicted by the mRNA sequences (see Table 1), and their identity was confirmed by FRET between adjacent oligoprobes (as described above).

Intracellular Labeling

Identification of the recorded neurons was regularly confirmed by histochemical revelation of intracellular biocytin, performed using the ABC elite kit (Vector Laboratories, Burlingame, CA).

Results

Characterization of MOR-Expressing Neurons

With the aim of characterizing MOR-expressing neurons, 360 neurons from cortical layers I–V were electrophysiologically characterized and analyzed by scPCR. Pyramidal cells (n = 98) and interneurons (n = 262) were selected according to the shape of their soma and proximal dendrites as seen with infrared videomicroscopy. Cells were classified as regular spiking nonpyramidal (RSNP, n = 174), irregular spiking (IS, n = 39), fast spiking (n = 38), or pyramidal neurons according to their action potential firing behavior upon application of depolarizing current pulses (McCormick et al. 1985; Kawaguchi 1993, 1995; Cauli et al. 1997). The scPCR protocol was designed to probe for the expression of mRNAs encoding MOR and its endogenous agonist Enk, in addition to 8 interneuron markers (GABA synthesizing enzymes: GAD65, GAD67; calcium binding proteins: calretinin [CR] and calbindin [CB]; and neuropeptides: neuropeptide Y [NPY], somatostatin [SOM], cholecystokinin [CCK], and VIP). MOR mRNA was detected in a small subset of neocortical neurons (n = 60 of 360), which all expressed GAD65 and/or GAD67 mRNAs and exhibited IS or RSNP firing patterns. This confirms that MOR expression is restricted to inhibitory GABAergic interneurons in the neocortex (Taki et al. 2000). Within neocortical layers II–V, MOR-expressing IS (n = 15) and RSNP (n = 40) interneurons exhibited similar molecular profiles (Fig. 1*a*,*b*). Indeed, they frequently expressed VIP (IS: 100%, RSNP: 78%), CCK (IS: 67%, RSNP: 58%), Enk (IS: 73%, RSNP: 55%), and CR (IS: 67%, RSNP: 43%) and showed a low occurrence of CB (IS: 13%, RSNP: 18%), SOM (IS: 7%, RSNP: 28%), and NPY (IS: 7%, RSNP: 15%). It has been shown previously that VIP-expressing IS and RSNP interneurons form a relatively homogenous cell population despite their different firing patterns (Porter et al. 1999; Cauli et al. 2000; Ferezou et al. 2002). The present data indicate that MOR and Enk expression is another shared property of VIP-expressing interneurons and are consistent with a previous immunocytochemical report showing that most MOR-positive cells coexpress VIP (Taki et al. 2000).

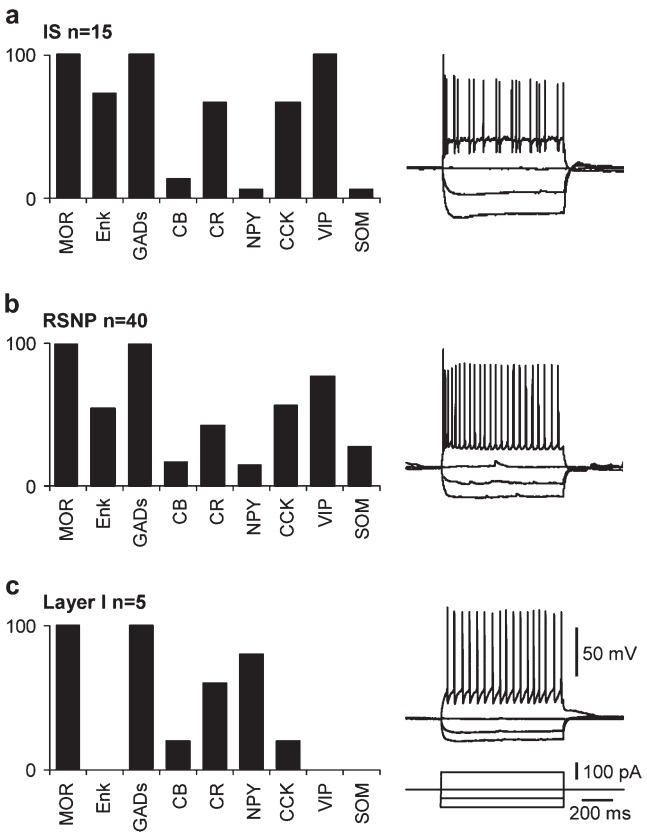

Figure 1. MOR-expressing neurons. The scPCR analyses of 360 neocortical neurons, including 98 pyramidal cells and 262 GABAergic interneurons, revealed MOR expression in 60 neurons including 15 IS (*a*), 40 RSNP (*b*), and 5 layer I interneurons (*c*). All MOR-positive neurons expressed GAD67 and/or GAD65 (GADs). MOR-expressing IS and RSNP interneurons exhibited similar molecular profiles characterized by a high expression level of VIP, CCK, Enk, and CR and a low expression level of CB, NPY, and SOM (*a*–*b*). MOR-expressing layer I interneurons presented a high expression level of NPY and CR, a low expression level of CB and CCK, and did not express Enk, VIP, and SOM (*c*). The current-clamp recordings shown on the right of each panel illustrate the voltage responses exhibited by an IS (*a*), a RSNP (*b*), and a layer I (*c*) MOR-expressing interneurons induced by hyperpolarizing and depolarizing current injections.

In contrast, MOR-expressing interneurons from layer I (n = 5 RSNP cells) expressed neither Enk nor VIP (Fig. 1*c*) and showed a low occurrence of CCK (20%) and a high occurrence of NPY (80%). The occurrences of CR, CB, and SOM (60, 20, and 0%, respectively) in layer I MOR-expressing interneurons were similar to those of layers II–V (P > 0.56, z-test). These properties were shared by all layer I neurons analyzed (n = 11, including the 5 MOR-positive neurons), for which Enk, VIP, CCK, and NPY expression levels (0, 0, 18, and 55%, respectively, data not shown) were significantly different from those of MOR-expressing neurons from layer II to V ($P \leq 0.05$, z-test). Altogether, these results disclose striking similarities between the distribution of MOR expression and the reported sensitivity to nicotinic agonists, mainly found in VIP-expressing (Porter et al. 1999) and layer I (Christophe et al. 2002) neocortical interneurons. This indicates that μ-opioid and nicotinic agonists may share the same neuronal targets in the neocortex.

The distribution of the Enk mRNA was broader than expected from immunocytochemical detection of this neuropeptide,

essentially observed in MOR-positive neurons (Taki et al. 2000). Indeed, the Enk mRNA was detected in all MOR-negative layer II–V neuronal populations, including in 32% of pyramidal neurons, albeit at lower levels than in VIP-expressing neurons (60%).

A subset of 166 neurons was additionally tested for the expression of the δ- and κ-opioid receptors (DOR and KOR, respectively) and the endogenous opioid peptides POMC and dynorphin (data not shown). Within MOR-expressing interneurons (n = 28), the KOR mRNA was detected in 3 cells, whereas the DOR, POMC, and dynorphin mRNAs were not detected. Within MOR-negative neurons (n = 138), DOR and KOR mRNAs were detected in 2 and 6 GABAergic interneurons, respectively. The dynorphin mRNA was detected in 16 GABAergic interneurons characterized by a high occurrence of SOM (94%). The POMC mRNA was never detected, confirming that Enk is the only μ-opioid endogenous agonist in the neocortex, as previously established (Rossier et al. 1977; Gee et al. 1983; Giraud et al. 1983).

MOR Is Coupled with Potassium Channels in Neocortical Interneurons

The functional effect of MOR activation was investigated by applying the MOR-selective agonist DAMGO (2.5 μM) on 169 neocortical neurons recorded in voltage-clamp or current-clamp conditions. The presence of the MOR mRNA was tested in a subset of these neurons by scPCR. DAMGO responses, observed in 86 interneurons, consisted of a slow hyperpolarization (–9.3 ± 3.4 mV, n = 17) due to the activation of an outward current (15.5 ± 6.2 pA, n = 69) associated with a significant decrease in membrane resistance (–187.6 ± 145.8 MΩ, n = 86; P < 0.001, Wilcoxon signed rank test). The DAMGO-induced current persisted in the presence of TTX (1 μM, n = 10) and was prevented by the selective MOR antagonist D-Pen-Cys-Tys-D-Trp-Orn-Thr-Pen-Thr-NH_2: (CTOP, n = 4, not shown). The MOR mRNA was detected in 20 out of 32 DAMGO-responsive neurons. Conversely, all MOR-positive neurons responded to DAMGO application, indicating that the occurrence of the MOR mRNA was underestimated by scPCR. Indeed, although we detected the MOR mRNA in 5 out of 11 layer I interneurons, we observed that all layer I interneurons tested responded to DAMGO application (n = 10). An example of a MOR-positive neuron is illustrated in Figure 2*a*. The expression of VIP was observed in 21 out of 22 DAMGO-responsive neurons found in layers II–V, confirming the frequent coexpression of VIP and MOR observed by scPCR.

Altogether, these data confirmed that DAMGO responses were due to the activation of somatodendritic MORs in neocortical interneurons. DAMGO responses were not observed in pyramidal cells (n = 19), consistent with the absence of the MOR mRNA in these neurons. To further characterize DAMGO responses, we determined current–voltage relationships in the presence of TTX (1 μM), before and during DAMGO application (Fig. 2*b*). Voltage steps (2 s) were applied to responsive neurons in control condition and at the peak of the DAMGO response. The DAMGO-induced current reversed at –84.2 ± 1.6 mV (n = 4), close to the equilibrium potential of potassium in our experimental conditions (–85 mV). These results indicate that neocortical MOR activation leads to the opening of a potassium conductance, as described in other structures (Williams et al. 2001).

Nicotinic and μ-Opioid Responsiveness Extensively Overlap in the Neocortex

In order to establish whether nicotinic receptors and MOR are expressed by the same neuronal population, we sequentially applied the nicotinic agonist DMPP (100 μM) and the MOR-selective agonist DAMGO (2.5 μM) on 61 neocortical interneurons visually identified from layers I to V. As exemplified in Figure 3*a*, the majority of responsive neurons (36 out of 39) responded to both DMPP and DAMGO applications, whereas 2 neurons responded only to DMPP and 1 responded only to DAMGO. All

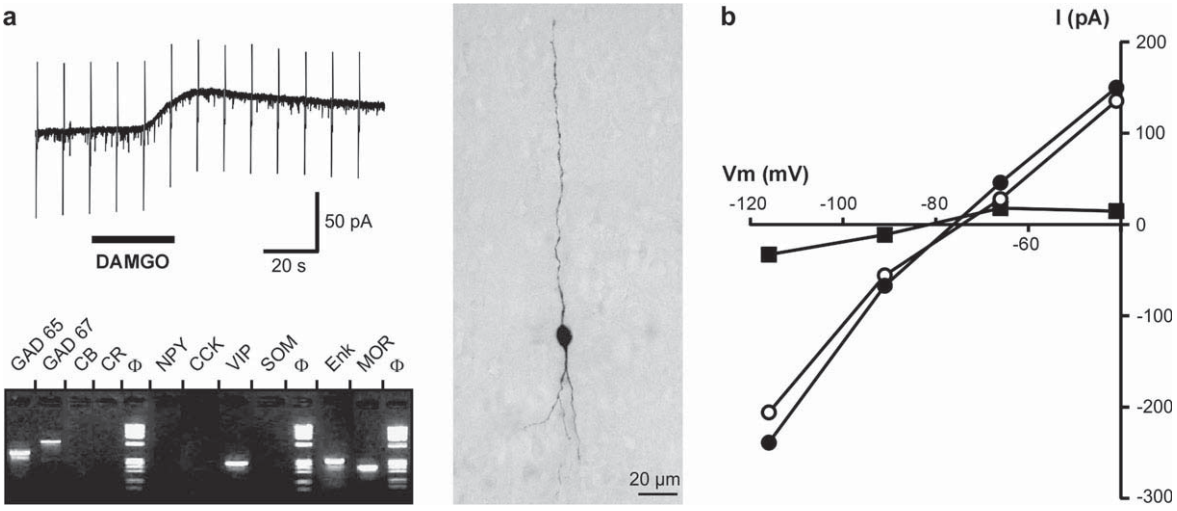

Figure 2. MOR activation opens a potassium conductance. (*a*) DAMGO (2.5 μM) induced a slow outward current with a peak amplitude of 32 pA (upper left panel, steps of −5 mV were applied every 10 s) in a neuron recorded in voltage-clamp mode. Molecular analysis of this DAMGO-responsive neuron showed the expression of MOR together with GAD65, GAD67, VIP, and Enk (lower left panel, ϕ: molecular weight marker). Intracellular labeling of the same neuron by biocytin (right panel) revealed a bipolar/bitufted morphology typical of VIP-expressing interneurons (pial surface is upward). (*b*) Current–voltage plots obtained, in the presence of TTX (1 μM), from another cell in control conditions (open circles, input resistance: 133.16 M) and at the peak of the DAMGO response (filled circles). The third plot (filled squares) shows the DAMGO-induced current obtained by subtracting control values from those measured during DAMGO application. The reversal potential for the DAMGO-induced current (−81.9 mV) was close to equilibrium potential of potassium (−85 mV in our experimental conditions).

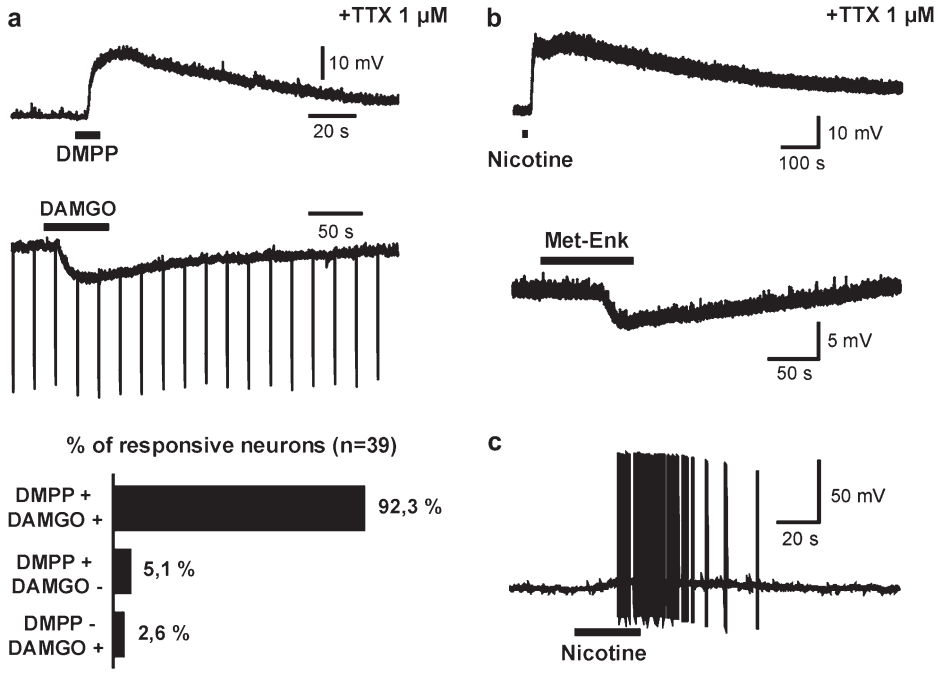

Figure 3. Nicotinic and µ-opioid agonists act on the same neocortical interneurons. Current-clamp recordings in (*a*, upper panels) show the responses of a neuron to sequential applications of the nicotinic agonist DMPP and the MOR-selective agonist DAMGO in the presence of TTX. In this neuron, DMPP (100 µM) induced a fast depolarization (19.2 mV), whereas DAMGO (2.5 µM) induced a hyperpolarization (−9.71 mV, steps of –50 pA were applied every 20 s). The lower panel shows the extensive overlap of nicotinic- and µ-opioid–responsive populations. The example of responses to nicotine (100 µM) and Met-Enk (30 µM) shown in (*b*) illustrates their similarity with those induced by DMPP and DAMGO, respectively. In this neuron, sequential nicotine and Met-Enk application induced a 21.6 mV depolarization and a 4.9 mV hyperpolarization, respectively. As illustrated by the current-clamp recording in (*c*), application of nicotine at low concentration (1 µM) resulted in a depolarization leading to a sustained action potential discharge in responsive interneurons.

layer I interneurons tested responded to both DMPP and DAMGO (n = 10). Both DMPP and DAMGO responses persisted in the presence of TTX (1 µM, n = 10). As previously reported (Xiang et al. 1998; Porter et al. 1999; Christophe et al. 2002), nicotinic-responsive interneurons, found in all layers, were depolarized by DMPP applications (19.2 ± 1.1 mV, n = 10). In contrast, DAMGO responses consisted of slow hyperpolarizations (–10.4 ± 1.9 mV, n = 10). DMPP and DAMGO effects were mimicked by nicotine (100 µM, n = 3) and the endogenous MOR agonist methionine-enkephalin (Met-Enk, 30 µM, n = 6), respectively (Fig. 3*b*). Consistent with the expression of the high affinity α4, α5, and β2 subunits (Ramirez-Latorre et al. 1996; Marubio and Changeux 2000) in nicotinic-responsive neocortical interneurons (Porter et al. 1999; Christophe et al. 2002), a low dose of nicotine (1 µM) also depolarized these neurons and triggered action potentials (n = 3, Fig. 3*c*).

The almost complete overlap between nicotinic and µ-opioid responses indicates that interactions between corresponding neurotransmitter pathways or their related drugs occur at the cellular level in the neocortex.

Integration of Nicotinic and µ-Opioid Signals

Consequences of nicotinic receptor and MOR colocalization in neocortical interneurons were next investigated. Nonpyramidal neurons were recorded in current-clamp mode and exposed to the nicotinic agonist DMPP (100 µM), in the absence or in the presence of DAMGO (2.5 µM, Fig. 4). In the presence of TTX (1 µM, see example in Fig. 4*a*), DMPP elicited a depolarization of responsive interneurons (10.9 ± 5.7 mV), which was reduced to 28% of control during DAMGO application (3.1 ± 2.1 mV) and recovered after 15 min of DAMGO washout (8.2 ± 3.6 mV, n = 5, Fig. 4*b*). In the absence of TTX, DMPP application elicited a sustained action potential discharge (see example in Fig. 4*b*). This DMPP response was prevented by DAMGO and recovered after DAMGO washout (n = 4). These results indicate that interneurons integrate nicotinic and µ-opioid signals at the somatodendritic level.

IPSCs elicited by cholinergic agonists in neocortical neurons are TTX sensitive (Xiang et al. 1998) and thus stem from somatodendritic excitation of GABAergic interneurons leading to action potential discharge. In order to evaluate the influence of nicotinic and µ-opioid interactions on neocortical network activity, IPSCs were recorded in pyramidal cells that constitute one of the postsynaptic targets of both VIP-expressing interneurons (Hajos et al. 1988; Peters and Harriman 1988; Peters 1990) and layer I interneurons (Chu et al. 2003). DMPP applications (100 µM) were performed in the absence or in the presence of DAMGO (2.5 µM), whereas IPSCs were recorded in voltage-clamp mode. This set of experiments was performed in the presence of D-AP5 (20 µM) and CNQX (10 µM) to prevent glutamatergic transmission. DMPP stimulation of nicotinic-responsive interneurons induced, in the pyramidal neuron shown in Figure 5*a*,*b*, a large increase in IPSC frequency and amplitude. This DMPP effect was suppressed in the presence of DAMGO and recovered after DAMGO washout. Similar effects of DAMGO on the DMPP-induced increase of IPSCs were observed in 6 additional pyramidal cells and are summarized in Figure 5*c*. Mean inter-IPSC interval obtained from these 7 neurons during DMPP stimulation varied from 0.17 ± 0.0 s for control DMPP application, to 0.62 ± 0.04 s in the presence of DAMGO, and to 0.22 ± 0.01 s following DAMGO washout (Mean inter-IPSC interval preceding DMPP application

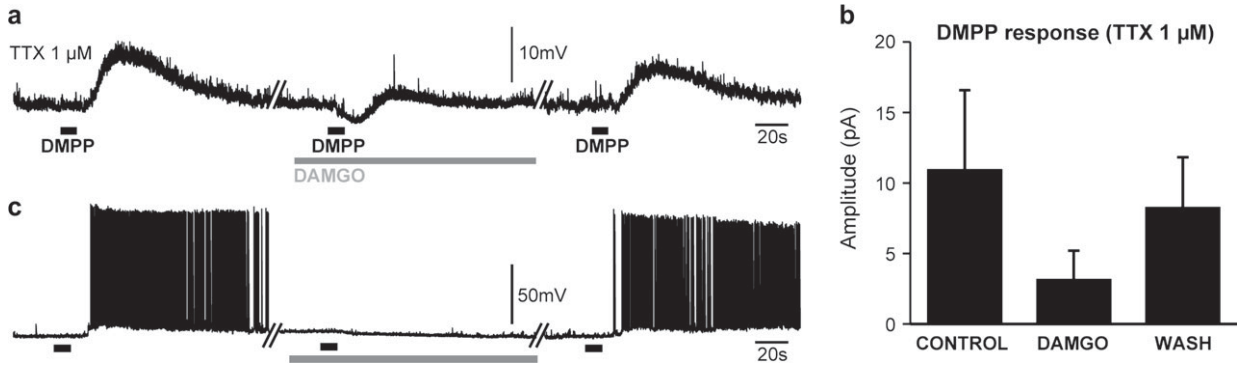

Figure 4. Interneurons integrate nicotinic and μ-opioid responses. (*a*) In the presence of TTX, DMPP (100 μM) elicited a membrane depolarization that was decreased in the presence of DAMGO (2.5 μM) and recovered after DAMGO washout. In this interneuron, the summation of DAMGO-induced hyperpolarization and of DMPP-induced depolarization resulted in a minimal deviation from the preset membrane potential. (*b*) In the presence of TTX, the amplitude of DMPP-induced depolarization was reversibly decreased by the application of DAMGO ($n = 5$). (*c*) In the absence of TTX, DMPP elicited an action potential discharge that was prevented in the presence of DAMGO and recovered after DAMGO washout. In this interneuron, the depolarizing effect of DMPP was virtually abolished in the presence of DAMGO.

in control conditions: 1.08 ± 0.10 s). Mean IPSC amplitudes varied from 17.49 ± 0.27 pA for control DMPP application, to 12.56 ± 0.31 pA in the presence of DAMGO, and to 15.90 ± 0.33 pA after DAMGO washout (Mean IPSC amplitude preceding DMPP application in control conditions: 12.23 ± 0.39 pA). These results show that modulation of interneuron activity via MOR and nicotinic receptors influences neocortical network activity. Furthermore, they confirm that expression patterns of these receptors overlap extensively and allow the selective integration of nicotinic and μ-opioid stimuli by a single GABAergic interneuron population.

Nicotinic Activation of Endogenous μ-Opioid Transmission

The expression of the MOR endogenous agonist Enk in a large proportion of MOR-expressing neurons suggests that nicotinic stimulation of these neurons can induce the release of Enk and consequently activate MORs. To test this assumption, we investigated the effects of the MOR-selective antagonist CTOP on DMPP-induced GABAergic postsynaptic currents recorded in pyramidal cells. The changes in IPSC frequency elicited by prolonged DMPP applications (100 μM, 30 s application), either in the absence (control, $n = 11$) or in the continuous presence of CTOP (1 μM, $n = 11$), are illustrated in Figure 6. In control conditions, DMPP application elicited a biphasic response consisting of an initial increase of IPSC frequency, followed by a depression of GABAergic inhibitory inputs (Fig. 6*a*). Indeed, the mean IPSC interval decreased to 42.49 ± 0.04% of its initial value (pre: 1.48 ± 0.49 s, Fig. 6*b*) during the first phase and subsequently increased to 222.4 ± 0.07% of the pre-DMPP level during the second period. In the presence of CTOP, the first phase was potentiated. Then, in contrast with control conditions, the IPSC frequency subsequently returned to the pre-DMPP value without undershooting the baseline (Fig. 6*a*). In CTOP conditions, the mean inter-IPSC interval first decreased to 28.78 ± 0.02% of its initial value (1.05 ± 0.40 s) and subsequently returned to its initial level (98.93 ± 0.03%, Fig. 6*b*).

These results suggest that stimulation of nicotinic-responsive interneurons led to Enk release and subsequent MOR activation, which in turn resulted in the inhibition of these interneurons. Hence, the neocortical μ-opioid system mediates an activity-dependent, inhibitory feedback onto nicotinic-responsive interneurons.

Discussion

In the neocortex, we found a selective expression of MOR in interneurons responsive to nicotinic agonists throughout layers I–V. Enk was frequently expressed in MOR-expressing interneurons but was also observed in MOR-negative neurons. MOR agonists elicited a hyperpolarizing response that prevented the action potential discharge induced by nicotinic stimulation. MOR agonists also blocked the IPSC increase elicited in pyramidal neurons by application of a nicotinic agonist. Finally, nicotinic stimulation triggered a μ-opioid inhibitory feedback on MOR-expressing interneurons through the release of endogenous Enk.

Expression Patterns of MOR and Enk

We found that in layers II–V, the MOR mRNA is primarily expressed in IS/RSNP VIP-positive interneurons, which frequently express CCK and CR and show a low occurrence of the SOM, NPY, and CB mRNAs. These results confirm a previous immunocytochemical report on MOR-expressing neurons (Taki et al. 2000) and are consistent with the known firing patterns and expression profile of VIPergic interneurons (Kawaguchi and Kubota 1996; Cauli et al. 1997, 2000; Porter et al. 1998, 1999). Although the detection of the MOR mRNA by scPCR was suboptimal, the detection of VIP in most DAMGO-responsive neurons in layers II–V confirms that MOR is primarily expressed in VIPergic interneurons in neocortical layers II–V. The MOR mRNA was additionally expressed in layer I interneurons characterized by a high occurrence of the NPY and CR mRNAs, which all responded to DAMGO. Layer I interneurons frequently express CR (Gonchar and Burkhalter 1999). Interestingly, these interneurons often exhibit neurogliaform morphology (DeFelipe and Jones 1988; Christophe et al. 2002) that correlates with the expression of NPY in the hippocampus (Price et al. 2005). Although layer I interneurons exhibit heterogeneity in their firing patterns and morphology (Zhou and Hablitz 1996a, 1996b; Chu et al. 2003), their extensive responsiveness to nicotinic agonists (Christophe

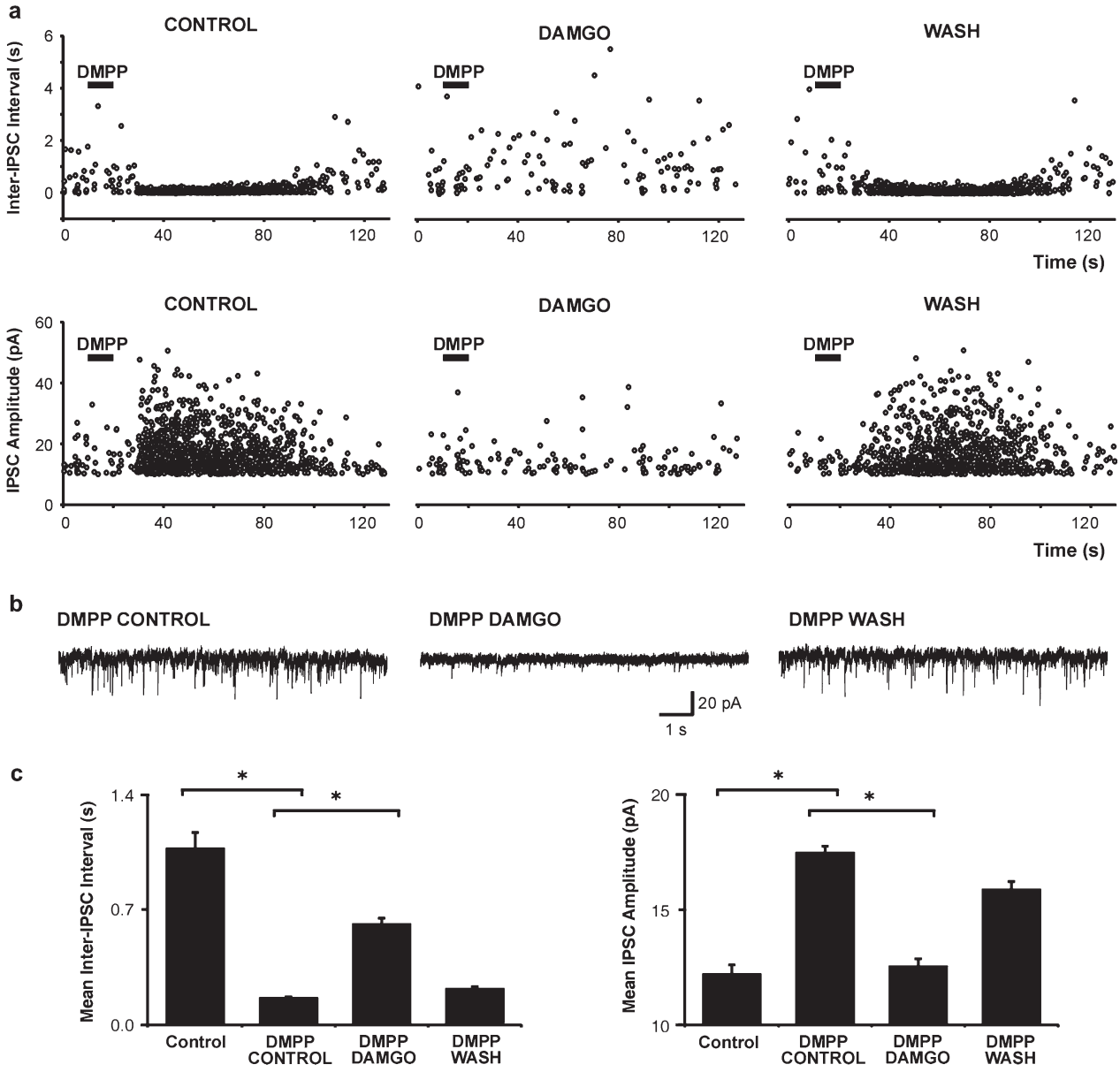

Figure 5. MOR controls the GABAergic output of nicotinic-responsive interneurons. DMPP-induced enhancement of spontaneous IPSCs in a pyramidal neuron was reduced in the presence of DAMGO and recovered after DAMGO washout. (*a*) Scatter plots showing the change in inter-IPSC interval (upper panel) and IPSC amplitude (lower panel) in response to DMPP application (100 μM), in control condition (left panel), upon DAMGO application (2.5 μM, middle panel) and after DAMGO washout (right panel). (*b*) Spontaneous IPSCs recorded in this neuron 30 s after the DMPP application in each condition. (*c*) Mean inter-IPSC interval and IPSC amplitude for data pooled from 7 cells in each condition. Asterisk, $P \leq 0.05$, Kruskal–Wallis one way analysis of variance on ranks followed by a Dunn's test.

et al. 2002) and to DAMGO indicates that almost all these neurons express both MOR and nicotinic receptors.

Consistent with a previous report (Taki et al. 2000), we found a high occurrence of the Enk mRNA in MOR-positive interneurons, with the notable exception of layer I cells. However, the presence of Enk in other neocortical neurons, including pyramidal cells, suggests that Enk expression is broader than appreciated by immunocytochemistry, as earlier observed by in situ hybridization (Harlan et al. 1987). Indeed, Enk is abundantly expressed in the neocortex where it is found at a concentration of 2.6 nmole/g protein as measured by radioimmunoassay (Rossier et al. 1977; Lindberg et al. 1979). For comparison (Crawley 1985), it is about 4 times more abundant than VIP (below 0.7 nmole/g protein), although immunocytochemistry reveals fewer cells positive for Enk than for VIP (Taki et al. 2000). Furthermore, colchicine pretreatment allows Enk immunoreactivity to become detectable in pyramidal cells (McGinty et al. 1984). Hence, we propose that Enk is expressed in multiple neocortical neuronal types including pyramidal neurons, albeit at lower levels than in MOR-positive interneurons.

Neocortical μ-Opioid Transmission

Previous studies have established that μ-opioid agonists disinhibit the hippocampal network by inhibiting interneurons (Zieglgansberger et al. 1979; Madison and Nicoll 1988; Capogna et al. 1993). Our observations indicate that in the neocortex, μ-opioid agonists selectively inhibit interneurons excited by nicotinic agonists. Indeed, the overlap of nicotinic and μ-opioid responsiveness encompassed a discrete interneuron population

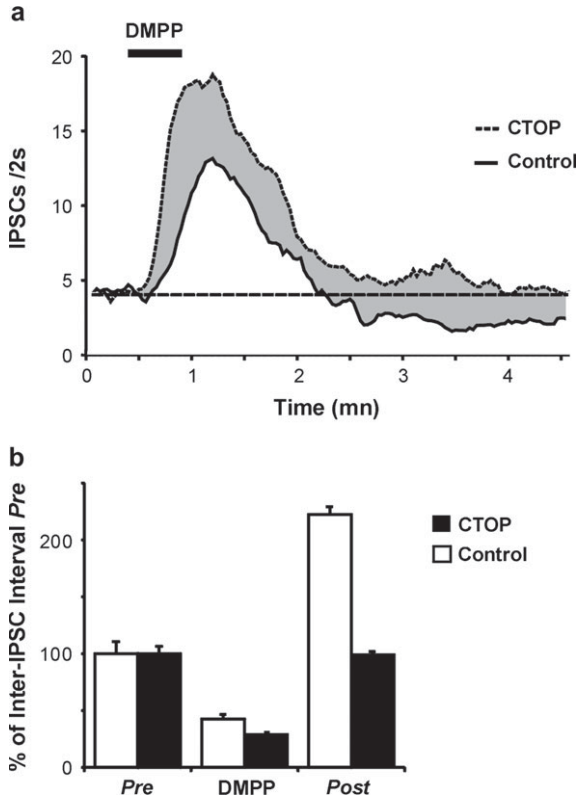

Figure 6. Nicotinic stimulation activates the endogenous μ-opioid system. Effect of DMPP (100 μM, 30 s application) on IPSC frequency in pyramidal cells in the absence (control, $n = 11$) or in the continuous presence of the MOR-selective antagonist CTOP (1 μM, $n = 11$). (*a*) Mean IPSC frequencies are expressed as the number of IPSCs per 2 s. DMPP increased IPSC frequency in both control and CTOP conditions. In control conditions, IPSC frequency subsequently fell below the baseline. This effect was prevented in the presence of CTOP. The gray area between the control and CTOP curves indicates the effect of MOR activation by endogenous Enk. (*b*) Same results presented as mean inter-IPSC interval measured before (pre, 0–30 s), during (DMPP, 50–100 s), and after (post, 180–280 s) the peak response to DMPP. Interevent intervals are expressed as percentages of the pre values. Note that post inter-IPSC interval differed significantly from pre values in control ($P < 0.001$) but not in CTOP conditions ($P = 0.88$, 2-way analysis of variance completed by the Holm–Sidak method of comparison).

comprising cell types that reportedly exhibit nicotinic sensitivity (Porter et al. 1999; Christophe et al. 2002). In these interneurons, μ-opioid agonists induced a hyperpolarizing response due to the opening of a potassium conductance, which was able to prevent action potential firing elicited by DMPP. Accordingly, DAMGO markedly decreased IPSCs evoked by DMPP in pyramidal cells. The present results further suggest that endogenous Enk released by nicotinic stimulation activates MOR, which in turn decreases IPSCs originating from nicotinic-responsive interneurons. Neuropeptide release requires a high level of activity and depends upon a sustained elevation of intracellular calcium (Zupanc 1996; Ludwig and Pittman 2003; Baraban and Tallent 2004). Upon nicotinic stimulation, the main source of Enk release in the neocortex is presumably VIP-expressing neurons. However, in addition to cholinergic inputs, VIP-expressing neurons integrate glutamatergic and serotonergic inputs that trigger intracellular calcium increase via ionotropic and metabotropic receptors (Staiger et al. 1996; Hajos et al. 1997; Porter et al. 1998; Cauli et al. 2000; Ferezou et al. 2002). In vivo, the release of Enk and thus the GABAergic contribution of MOR-expressing interneurons to the neocortical network are presumably controlled by summation of multiple local and afferent signals. The broad distribution of Enk suggests that other neocortical neuronal types participate in this process.

Network Implications

The present results indicate that layer I and VIPergic interneurons are the main targets of μ-opioid transmission in the neocortex. These interneuron populations influence the activity of pyramidal cells at all cortical layers (Hajos et al. 1988; Peters and Harriman 1988; Peters 1990; Kawaguchi and Kubota 1997; Zhu 2000; Larkum and Zhu 2002; Chu et al. 2003). However, because both interneuron types also innervate other interneurons (Hajos et al. 1988; Peters and Harriman 1988; Peters 1990; Kawaguchi and Kubota 1997; Christophe et al. 2002), the net effect of their activation or inhibition on pyramidal cell excitability is difficult to appreciate. Nonetheless, our findings suggest that sustained cholinergic stimulation of Layer I and VIP-expressing neurons results in a biphasic inhibitory/disinhibitory action on the network. During the disinhibitory phase, μ-opioid transmission is able to reshape inhibition patterns and thus signal processing in the neocortical network by switching off the GABAergic output of Layer I and VIPergic interneurons. It is noteworthy that in addition to Enk, VIPergic interneurons also contain neurokinin B, corticotropin-releasing factor, and CCK, which selectively increase the excitability of pyramidal neurons (Gallopin et al. 2005). The population of VIP-expressing neurons thus appears as an important source for the coordinated effects of several excitatory/disinhibitory neuropeptides in the neocortex.

The μ-Opioid Involvement in Nicotine Effects

VIP-expressing and layer I interneurons coexpress the α4, α5, and β2 nicotinic receptor subunits (Porter et al. 1999; Christophe et al. 2002) and MOR and thus constitute the primary target of both nicotine and opiates (Matthes et al. 1996; Marubio and Changeux 2000; Picciotto et al. 2000; Salas et al. 2003) in the neocortex. The present results suggest that, in this structure, nicotine intake is able to activate endogenous μ-opioid transmission. Our findings thus provide a mechanistic explanation as to how μ-opioid transmission can mediate part of nicotine effects and may help to explain the similarities between tobacco and opiate addiction (Pomerleau 1998; Mathieu-Kia et al. 2002).

Notes

We thank T. Gallopin, P. Schweitzer, G. Koob, P. Kenny, and J. Roeper for their valuable help and P. Gouédard for assistance with the database. This work was supported by Centre National de la Recherche Scientifique. *Conflict of Interest*: None declared.

Funding to pay the Open Access publication charges for this article was provided by Grant-in-Aid for Scientific Research on Priority Areas (Molecular Brain Science) from the Ministry of Education, Culture, Sports, Science and Technology of Japan (No. 17024055).

Address correspondence to Dr Bertrand Lambolez, NPA, CNRS UMR 7102, UPMC, 9 quai St Bernard, 75005 Paris, France. Email: bertrand.lambolez@snv.jussieu.fr.

References

Baraban S, Tallent M. 2004. Interneuron diversity series: interneuronal neuropeptides—endogenous regulators of neuronal excitability. Trends Neurosci. 27:135–142.

Berrendero F, Kieffer BL, Maldonado R. 2002. Attenuation of nicotine-induced antinociception, rewarding effects, and dependence in mu-opioid receptor knock-out mice. J Neurosci. 22:10935–10940.
Berrendero F, Mendizabal V, Robledo P, Galeote L, Bilkei-Gorzo A, Zimmer A, Maldonado R. 2005. Nicotine-induced antinociception, rewarding effects, and physical dependence are decreased in mice lacking the preproenkephalin gene. J Neurosci. 25:1103–1112.
Bochet P, Audinat E, Lambolez B, Crépel F, Rossier J, Iino M, Tsuzuki K, Ozawa S. 1994. Subunit composition at the single-cell level explains functional properties of a glutamate-gated channel. Neuron. 12:383–388.
Capogna M, Gahwiler BH, Thompson SM. 1993. Mechanism of mu-opioid receptor-mediated presynaptic inhibition in the rat hippocampus in vitro. J Physiol (Lond). 470:539–558.
Cauli B, Audinat E, Lambolez B, Angulo MC, Ropert N, Tsuzuki K, Hestrin S, Rossier J. 1997. Molecular and physiological diversity of cortical nonpyramidal cells. J Neurosci. 17:3894–3906.
Cauli B, Porter JT, Tsuzuki K, Lambolez B, Rossier J, Quenet B, Audinat E. 2000. Classification of fusiform neocortical interneurons based on unsupervised clustering. Proc Natl Acad Sci USA. 97:6144–6149.
Chomczynski P, Sacchi N. 1987. Single-step method of RNA isolation by acid guanidinium thiocyanate- phenol-chloroform extraction. Anal Biochem. 162:156–159.
Christophe E, Roebuck A, Staiger JF, Lavery DJ, Charpak S, Audinat E. 2002. Two types of nicotinic receptors mediate an excitation of neocortical layer I interneurons. J Neurophysiol. 88:1318–1327.
Chu Z, Galarreta M, Hestrin S. 2003. Synaptic interactions of late-spiking neocortical neurons in layer 1. J Neurosci. 23:96–102.
Connors BW, Gutnick MJ. 1990. Intrinsic firing patterns of diverse neocortical neurons. Trends Neurosci. 13:99–104.
Crawley J. 1985. Comparative distribution of cholecystokinin and other neuropeptides. Why is this peptide different from all other peptides. In: Vanderhaeghen JJ, Crawley J, editors. Annal of the New-York academy of sciences. New-York: New-York academy of sciences. p. 1–8.
Dantzker JL, Callaway EM. 2000. Laminar sources of synaptic input to cortical inhibitory interneurons and pyramidal neurons. Nat Neurosci. 3:701–707.
DeFelipe J. 1993. Neocortical neuronal diversity: chemical heterogeneity revealed by colocalization studies of classic neurotransmitters, neuropeptides, calcium-binding proteins, and cell surface molecules. Cereb Cortex. 3:273–289.
DeFelipe J, Jones EG. 1988. Cajal on the cerebral cortex. New York: Oxford University Press. p. 158, 208.
Ferezou I, Cauli B, Hill EL, Rossier J, Hamel E, Lambolez B. 2002. 5-HT3 receptors mediate serotonergic fast synaptic excitation of neocortical vasoactive intestinal peptide/cholecystokinin interneurons. J Neurosci. 22:7389–7397.
Gallopin T, Geoffroy H, Rossier J, Lambolez B. 2005 Dec 7. Cortical sources of CRF, NKB, and CCK and their effects on pyramidal cells in the neocortex. Cereb Cortex. doi: 10.1093/cercor/bhj081.
Gee CE, Chen CL, Roberts JL, Thompson R, Watson SJ. 1983. Identification of proopiomelanocortin neurones in rat hypothalamus by in situ cDNA-mRNA hybridization. Nature. 306:374–376.
Giraud P, Castanas E, Patey G, Oliver C, Rossier J. 1983. Regional distribution of methionine-enkephalin-Arg6-Phe7 in the rat brain: comparative study with the distribution of other opioid peptides. J Neurochem. 41:154–160.
Gonchar Y, Burkhalter A. 1999. Connectivity of GABAergic calretinin-immunoreactive neurons in rat primary visual cortex. Cereb Cortex. 9:683–696.
Hajos F, Staiger JF, Halasy K, Freund TF, Zilles K. 1997. Geniculo-cortical afferents form synaptic contacts with vasoactive intestinal polypeptide (VIP) immunoreactive neurons of the rat visual cortex. Neurosci Lett. 228:179–182.
Hajos F, Zilles K, Schleicher A, Kalman M. 1988. Types and spatial distribution of vasoactive intestinal polypeptide (VIP)-containing synapses in the rat visual cortex. Anat Embryol. 178:207–217.
Harlan RE, Shivers BD, Romano GJ, Howells RD, Pfaff DW. 1987. Localization of preproenkephalin mRNA in the rat brain and spinal cord by in situ hybridization. J Comp Neurol. 258:159–184.
Kaneko T, Murashima M, Lee T, Mizuno N. 1998. Characterization of neocortical non-pyramidal neurons expressing preprotachykinins A and B: a double immunofluorescence study in the rat. Neuroscience. 86:765–781.
Kawaguchi Y. 1993. Groupings of nonpyramidal and pyramidal cells with specific physiological and morphological characteristics in rat frontal cortex. J Neurophysiol. 69:416–431.
Kawaguchi Y. 1995. Physiological subgroups of nonpyramidal cells with specific morphological characteristics in layer II/III of rat frontal cortex. J Neurosci. 15:2638–2655.
Kawaguchi Y. 1997. Selective cholinergic modulation of cortical GABAergic cell subtypes. J Neurophysiol. 78:1743–1747.
Kawaguchi Y, Kubota Y. 1996. Physiological and morphological identification of somatostatin- or vasoactive intestinal polypeptide-containing cells among GABAergic cell subtypes in rat frontal cortex. J Neurosci. 16:2701–2715.
Kawaguchi Y, Kubota Y. 1997. GABAergic cell subtypes and their synaptic connections in rat frontal cortex. Cereb Cortex. 7:476–486.
Kubota Y, Hattori R, Yui Y. 1994. Three distinct subpopulations of GABAergic neurons in rat frontal agranular cortex. Brain Res. 649:159–173.
Lambolez B, Audinat E, Bochet P, Crepel F, Rossier J. 1992. AMPA receptor subunits expressed by single Purkinje cells. Neuron. 9:247–258.
Larkum ME, Zhu JJ. 2002. Signaling of layer 1 whisker-evoked Ca^{2+} and Na^{+} action potentials in distal and terminal dendrites of rat neocortical pyramidal neurons in vitro and in vivo. J Neurosci. 22:6991–7005.
Lindberg I, Smythe SJ, Dahl JL. 1979. Regional distribution of enkephalin in bovine brain. Brain Res. 168:200–204.
Ludwig M, Pittman QJ. 2003. Talking back: dendritic neurotransmitter release. Trends Neurosci. 26:255–261.
Madison DV, Nicoll RA. 1988. Enkephalin hyperpolarizes interneurones in the rat hippocampus. J Physiol (Lond). 398:123–130.
Malin DH. 2001. Nicotine dependence: studies with a laboratory model. Pharmacol Biochem Behav. 70:551–559.
Marubio LM, Changeux JP. 2000. Nicotinic acetylcholine receptor knockout mice as animal models for studying receptor function. Eur J Pharmacol. 393:113–121.
Mathieu-Kia AM, Kellogg SH, Butelman ER, Kreek MJ. 2002. Nicotine addiction: insights from recent animal studies. Psychopharmacology. 162:102–118.
Matthes HW, Maldonado R, Simonin F, Valverde O, Slowe S, Kitchen I, Befort K, Dierich A, Le Meur M, Dolle P, et al. 1996. Loss of morphine-induced analgesia, reward effect and withdrawal symptoms in mice lacking the mu-opioid-receptor gene. Nature. 383:819–823.
McCormick DA, Connors BW, Lighthall JW, Prince DA. 1985. Comparative electrophysiology of pyramidal and sparsely spiny stellate neurons of the neocortex. J Neurophysiol. 54:782–806.
McCormick DA, Prince DA. 1985. Two types of muscarinic response to acetylcholine in mammalian cortical neurons. Proc Natl Acad Sci USA. 82:6344–6348.
McGinty JF, van der Kooy D, Bloom FE. 1984. The distribution and morphology of opioid peptide immunoreactive neurons in the cerebral cortex of rats. J Neurosci. 4:1104–1117.
Pan YX, Xu J, Mahurter L, Bolan E, Xu M, Pasternak GW. 2001. Generation of the mu opioid receptor (MOR-1) protein by three new splice variants of the Oprm gene. Proc Natl Acad Sci USA. 98:14084–14089.
Papadopoulos GC, Parnavelas JG, Cavanagh ME. 1987. Extensive co-existence of neuropeptides in the rat visual cortex. Brain Res. 420:95–99.
Peters A. 1990. The axon terminals of vasoactive intestinal polypeptide (VIP)-containing bipolar cells in rat visual cortex. J Neurocytol. 19:672–685.
Peters A, Harriman KM. 1988. Enigmatic bipolar cells of rat visual cortex. J Comp Neurol. 267:409–432.
Peters A, Jones EG. 1984. Classification of cortical neurons. In: Peters A, Jones EG, editors. Cerebral cortex, Vol. 1, cellular components of the cerebral cortex. New York: Plenum. p. 107–121.

Picciotto MR, Caldarone BJ, King SL, Zachariou V. 2000. Nicotinic receptors in the brain. Links between molecular biology and behavior. Neuropsychopharmacology. 22:451–465.
Pomerleau OF. 1998. Endogenous opioids and smoking: a review of progress and problems. Psychoneuroendocrinology. 23:115–130.
Porter JT, Cauli B, Staiger JF, Lambolez B, Rossier J, Audinat E. 1998. Properties of bipolar VIPergic interneurons and their excitation by pyramidal neurons in the rat neocortex. Eur J Neurosci. 10:3617–3628.
Porter JT, Cauli B, Tsuzuki K, Lambolez B, Rossier J, Audinat E. 1999. Selective excitation of subtypes of neocortical interneurons by nicotinic receptors. J Neurosci. 19:5228–5235.
Price CJ, Cauli B, Kovacs ER, Kulik A, Lambolez B, Shigemoto R, Capogna M. 2005. Neurogliaform neurons form a novel inhibitory network in the hippocampal CA1 area. J Neurosci. 25:6775–6786.
Ramirez-Latorre J, Yu CR, Qu X, Perin F, Karlin A, Role L. 1996. Functional contributions of alpha5 subunit to neuronal acetylcholine receptor channels. Nature. 380:347–351.
Rossier J, Vargo TM, Minick S, Ling N, Bloom FE, Guillemin R. 1977. Regional dissociation of beta-endorphin and enkephalin contents in rat brain and pituitary. Proc Natl Acad Sci USA. 74:5162–5165.
Salas R, Orr-Urtreger A, Broide RS, Beaudet A, Paylor R, De Biasi M. 2003. The nicotinic acetylcholine receptor subunit alpha 5 mediates short-term effects of nicotine in vivo. Mol Pharmacol. 63:1059–1066.
Somogyi P, Tamas G, Lujan R, Buhl EH. 1998. Salient features of synaptic organisation in the cerebral cortex. Brain Res Brain Res Rev. 26:113–135.
Staiger JF, Zilles K, Freund TF. 1996. Innervation of VIP-immunoreactive neurons by the ventroposteromedial thalamic nucleus in the barrel cortex of the rat. J Comp Neurol. 367:194–204.
Stuart GJ, Dodt HU, Sakmann B. 1993. Patch-clamp recordings from the soma and dendrites of neurons in brain slices using infrared video microscopy. Pflugers Arch. 423:511–518.
Taki K, Kaneko T, Mizuno N. 2000. A group of cortical interneurons expressing mu-opioid receptor-like immunoreactivity: a double immunofluorescence study in the rat cerebral cortex. Neuroscience. 98:221–231.
Thomson AM, Deuchars J. 1994. Temporal and spatial properties of local circuits in neocortex. Trends Neurosci. 17:119–126.
Toledo-Rodriguez M, Goodman P, Illic M, Wu C, Markram H. 2005. Neuropeptide and calcium binding protein gene expression profiles predict neuronal anatomical type in the juvenile rat. J Physiol. 567:401–413.
Williams JT, Christie MJ, Manzoni O. 2001. Cellular and synaptic adaptations mediating opioid dependence. Physiol Rev. 81:299–343.
Xiang Z, Huguenard JR, Prince DA. 1998. Cholinergic switching within neocortical inhibitory networks. Science. 281:985–988.
Zieglgansberger W, French ED, Siggins GR, Bloom FE. 1979. Opioid peptides may excite hippocampal pyramidal neurons by inhibiting adjacent inhibitory interneurons. Science. 205:415–417.
Zhou FM, Hablitz JJ. 1996a. Morphological properties of intracellularly labeled layer I neurons in rat neocortex. J Comp Neurol. 376:198–213.
Zhou FM, Hablitz JJ. 1996b. Layer I neurons of rat neocortex. I. Action potential and repetitive firing properties. J Neurophysiol. 76:651–667.
Zhu JJ. 2000. Maturation of layer 5 neocortical pyramidal neurons: amplifying salient layer 1 and layer 4 inputs by Ca^{2+} action potentials in adult rat tuft dendrites. J Physiol. 526:571–587.
Zupanc GK. 1996. Peptidergic transmission: from morphological correlates to functional implications. Micron. 27:35–91.

The Journal of Neuroscience, September 1, 2002, 22(17):7389–7397

5-HT_3 Receptors Mediate Serotonergic Fast Synaptic Excitation of Neocortical Vasoactive Intestinal Peptide/Cholecystokinin Interneurons

Isabelle Férézou,[1] Bruno Cauli,[1] Elisa L. Hill,[1] Jean Rossier,[1] Edith Hamel,[2] and Bertrand Lambolez[1]

[1]*Laboratoire de Neurobiologie et Diversité Cellulaire, Centre National de la Recherche Scientifique, Unité Mixte de Rechérche 7637, Ecole Superieure de Physique et Chíme Industrielles de la ville de Paris, 75005 Paris, France, and* [2]*Complex Neural Systems Neurobiology Unit, Montreal Neurological Institute, McGill University, Montreal, Quebec, Canada H3AZB4*

Neocortical neurons expressing the serotonin 5-HT_3 receptor (5-HT_3R) were characterized in rat acute slices by using patch-clamp recordings combined with single-cell RT-PCR and histochemical labeling. The 5-HT_{3A} receptor subunit was expressed selectively in a subset of GABAergic interneurons coexpressing cholecystokinin (CCK) and vasoactive intestinal peptide (VIP). The 5-HT_{3B} subunit was never detected, indicating that 5-HT_3Rs expressed by neocortical interneurons did not contain this subunit. In 5-HT_{3A}-expressing VIP/CCK interneurons, serotonin induced fast membrane potential depolarizations by activating an inward current that was blocked by the selective 5-HT_3R antagonist tropisetron. Furthermore, we observed close appositions between serotonergic fibers and the dendrites and somata of 5-HT_3R-expressing neurons, suggestive of possible synaptic contacts. Indeed, in interneurons exhibiting rapid excitation by serotonin, local electrical stimulations evoked fast EPSCs of large amplitude that were blocked by tropisetron. Finally, 5-HT_3R-expressing neurons were also excited by a nicotinic agonist, indicating that serotonergic and cholinergic fast synaptic transmission could converge onto VIP/CCK interneurons. Our results establish a clear correlation between the presence of the 5-HT_{3A} receptor subunit in neocortical VIP/CCK GABAergic interneurons, its functional expression, and its synaptic activation by serotonergic afferent fibers from the brainstem raphe nuclei.

Key words: neocortex; GABAergic interneurons; vasoactive intestinal peptide; cholecystokinin; single-cell RT-PCR; raphe nucleus; serotonin; 5-HT_3 receptor; 5-HT_{3A} and 5-HT_{3B} subunits; tropisetron; EPSC; nicotinic receptor

Neurons of the neocortex are classified as pyramidal cells or nonpyramidal cells according to their morphology. Pyramidal cells accumulate glutamate and are the main excitatory cortical neuron, whereas most nonpyramidal cells use GABA as a neurotransmitter and are believed to be inhibitory interneurons (Peters and Jones, 1984). The large diversity of neocortical GABAergic interneurons has led to several classifications (Houser et al., 1983; Hendry et al., 1989; Connors and Gutnick, 1990; Kawaguchi, 1993; Cauli et al., 1997, 2000; Kawaguchi and Kubota, 1997; Somogyi et al., 1998). However, the specific function of interneuron subtypes in the physiology of the neocortex remains to be established. Understanding how the excitability of interneuron subtypes is regulated by extracortical inputs therefore may contribute to elucidating their specific role.

It is well documented that serotonergic neurons of the midbrain raphe nuclei innervate neocortical nonpyramidal cells. At the electron microscopy level it has been demonstrated that serotonergic fibers can form conventional synapses on their cortical targets, suggesting that this subcortical projection may exert a fast modulation of interneuron excitability (Papadopoulos et al., 1987a; DeFelipe et al., 1991; Paspalas and Papadopoulos, 2001). The neurotransmitter serotonin (5-HT) interacts with several receptors, all of which are G-protein-coupled, with the exception of the 5-HT_3 receptor (5-HT_3R), which is a cation-selective ligand-gated ion channel suggested to mediate fast synaptic transmission (Derkach et al., 1989; Maricq et al., 1991; Sugita et al., 1992). Two 5-HT_3R subunits have been cloned, 5-HT_{3A}, which forms functional homomeric 5-HT_3Rs, and 5-HT_{3B}, which can assemble with 5-HT_{3A} subunits into heteromeric receptors (Davies et al., 1999; Hanna et al., 2000). *In situ* hybridization and immunocytochemical analyses have shown that 5-HT_3Rs are expressed selectively by a subgroup of GABAergic interneurons characterized by the expression of cholecystokinin (CCK) and located predominantly in neocortical layers II and III (Morales and Bloom, 1997). Although 5-HT_3R-mediated responses have been reported in the neocortex (Roerig et al., 1997; Zhou and Hablitz, 1999), a clear correlation between fast excitatory effects mediated by 5-HT_3Rs and a neuronal population remains to be established.

In the present study we combined patch-clamp recordings followed by single-cell reverse transcription and multiplex PCR (single-cell RT-mPCR; Lambolez et al., 1992; Ruano et al., 1995) analyses to identify and characterize 5-HT_3R-expressing neocortical neurons in rat acute slices. We found that functional postsynaptic 5-HT_3R expression was restricted to a small subset of GABAergic interneurons that coexpressed CCK and vasoactive

Received May 3, 2002; revised June 11, 2002; accepted June 14, 2002.

This work was supported by Centre National de la Recherche Scientifique (France) and European Union Grant QLG3-CT-1999-00649. I.F. and E.L.H. were supported by Ministère de la Recherche (France); E.H. was funded by a Blaise Pascal International Research Chair from the Région Ile de France. We thank Nora Fehlbaum, Zsolt Lenkei, Armelle Rancillac, Richard Schwartzmann, Paul Schweitzer, and Jim Surmeier.

Correspondence should be addressed to Dr. Bertrand Lambolez, Laboratoire de Neurobiologie et Diversité Cellulaire, Ecole Superieure de Physique et Chimie Industrielles, 10 Rue Vauquelin, 75005 Paris, France. E-mail: bertrand.lambolez@espci.fr.

Table 1. PCR primers and FRET probes

	Size	PCR	FRET probes
GAD 65	391	Sense[b], 713: TCTTTTCTCCTGGTGGTGCC	3′ FITC, 848: TTTCTCTCAAGAAGGGAGCTGCA
#M72422		Antisense[b], 1085: CCCCAAGCAGCATCCACAT	5′ R705, 872: CCTTGGGGATCGGAACAGACA
GAD 67	600	Sense[a], 713: TACGGGGTTCGCACAGGTC	3′ FITC, 930: CCTGGGGGAGCCATATCCAA
#M76177		Antisense, 1294: same as GAD65	5′ R705, 951: ATGTACAGCATCATGGCGGCTC
CaB	432	Sense[a], 134: AGGCACGAAAGAAGGCTGGAT	3′ FITC, 263: TCCTGCTGCTCTTTCGATGCC
#M27839		Antisense[a], 544: TCCCACACATTTTGATTCCCTG	5′ R705, 285: GCAACTGAAGTCCTGCGAGGAA
PV	381	Sense, 247: ACAAAGACGCTGATGGCTGC	3′ FITC, 283: GACGGCAAGATTGGGGTTGA
#M12725		Antisense, 607: CGTGGTCCTTCGCTCTCTCTC	5′ R705, 304: GAATTCTCCACTCTGGTGGCCG
CR	309	Sense[a], 142: CTGGAGAAGGCAAGGAAAGGT	3′ FITC, 248: TTGAGATGGCAGAGCTGGCG
#X66974		Antisense[a], 429: AGGTTCATCATAGGGACGGTTG	5′ R705, 269: AGATCCTGCCAACCGAAGAGAAT
NPY	359	Sense[a], −45: GCCCAGAGCAGAGCACCC	3′ FITC, 17: AACGAATGGGGCTGTGTGGA
#M15880		Antisense[a], 292: CAAGTTTCATTTCCCATCACCA	5′ R705, 38: TGACCCTCGCTCTATCCCTGC
SOM	209	Sense[a], 43: ATCGTCCTGGCTTTGGGC	3′ FITC, 105: GCAGAAGTCTCTGGCGGCTG
#K02248		Antisense[a], 231: GCCTCATCTCGTCCTGCTCA	5′ R705, 126: CACCGGGAAACAGGAACTGGC
VIP	286	Sense[a], 167: TGCCTTAGCGGAGAATGACA	3′ FITC, 199: TGTGTCCAGAAATGCCAGGCA
#X02341		Antisense[a], 434: CCTCACTGCTCCTCTTCCCA	5′ R705, 221: GCTGATGGAGTTTTCACCAGCG
CCK	216	Sense[a], 174: CGCACTGCTAGCCCGATACA	3′ FITC, 198: CCAGCAGGTCCGCAAAGCT
#K01259		Antisense[a], 373: TTTCTCATTCCGCCTCCTCC	5′ R705, 218: CCTCTGGCCGCATGTCCG
5-HT_3A	411	Sense, 1105: TTCCAAGCCAACAAGACTGATG	3′ FITC, 1127: ACTGCTCAGCCATGGGAAACC
#U59672		Antisense, 1499: AGGGGACTGGGGTTGCTC	5′ R705, 1149: CTGCAGCCATGTCGGAAGCC
5-HT_3B	275	Sense, 51: CACAGCGACACCTCAGCCT	Position 1: first base of the start codon
#NM_022189		Antisense, 304: TGGCACTGAGAGGGAGAGAGAT	

[a]Cauli et al. 1997.
[b]Bochet et al. 1994.

intestinal peptide (VIP). Furthermore, we present functional and anatomical evidence of the fast synaptic excitation of 5-HT_3R-expressing interneurons by 5-HT-containing afferent fibers. Finally, 5-HT_3R-expressing interneurons are also responsive to a nicotinic agonist, suggesting that serotonergic and cholinergic fast synaptic transmission could converge onto the same subpopulation of neocortical interneurons.

MATERIALS AND METHODS

Slice preparation. Young Wistar rats (postnatal day 14–21) were anesthetized deeply with a mixture of ketamine (65 mg/kg) and xylazine (14 mg/kg) and decapitated. Subsequently, 300-μm-thick parasagittal sections of cerebral sensorimotor cortex were prepared as described previously (Cauli et al., 1997). The slices were incubated at room temperature (20–25°C) in artificial CSF (ACSF) containing (in mM): 126 NaCl, 2.5 KCl, 1.25 NaH_2PO_4, 2 $CaCl_2$, 1 $MgCl_2$, 26 $NaHCO_3$, 20 glucose, and 5 pyruvate, which was bubbled with a mixture of 95% O_2/5% CO_2.

Whole-cell recordings. Slices were transferred to a chamber and perfused at 1–2 ml/min with ACSF at room temperature. Patch pipettes (6–8 MΩ), pulled from borosilicate glass, were filled with 8 μl of internal solution containing (in mM): 123 K-gluconate, 21 KCl, 3 $MgCl_2$, 0.5 EGTA, and 10 HEPES plus 2 mg/ml biocytin (Sigma, St. Louis, MO). In the internal solution used for recording evoked postsynaptic currents (see below), KCl was replaced by K-gluconate (144 mM final). The pH was adjusted to 7.2 and osmolarity to 285/295 mOsm. Whole-cell recordings were made from neocortical neurons identified under infrared video microscopy with Nomarski optics (Stuart et al., 1993) and with a patch-clamp amplifier (Axopatch 200A, Axon Instruments, Foster City, CA). Resting membrane potential was measured just after passing in whole-cell configuration, and only cells with a resting membrane potential more hyperpolarized than −50 mV were analyzed. All membrane potentials were corrected for junction potential (−11 mV). Cells were maintained at a holding potential of −71 mV by continuous current injection, and their firing behavior was tested by applying depolarizing current pulses. Action potential discharges were recorded by using the I-clamp fast mode of the amplifier. The signals were filtered at 5 kHz, digitized at 10 kHz, saved to a PC, and analyzed off-line with Acquis1 software (Gérard Sadoc, Gif-Yvette, France).

The nicotinic receptor agonist 1–1-dimethyl-4-phenyl-piperazinium iodide (DMPP), 5-hydroxytryptamine hydrochloride (5-HT), and the 5-HT_3R agonist 1-(m-chlorophenyl)-biguanide hydrochloride (m-CPBG; Sigma) were added either to the bathing solution or were applied by pressure from a large pipette onto the recorded neuron. The 5-HT_3R antagonist 3-tropanyl-indole-3-carboxylate hydrochloride (tropisetron, ICS 205-930; Sigma) was added to the bathing solution.

Electrical stimulations were performed in the presence of D(−)-2-amino-5-phosphopentanoic acid (D-AP-5) and 6-cyano-7-nitroquinoxaline-2,3-dione (CNQX; Tocris, Ballwin, MO) by using conventional glass electrodes filled with ACSF. The holding potential of the recorded neurons was adjusted to the reversion potential of inhibitory currents in our experimental conditions (−78 mV). We did not use $GABA_A$ receptor antagonists in these experiments because of their reported lack of selectivity within the $GABA_A$, nicotinic, and 5-HT_3 receptor channel superfamily (Mayer and Straughan, 1981; Demuro et al., 2001; Erkkila et al., 2001). Stimulations (0.1–1 mA, 0.3 msec) were applied every 15 sec by using a stimulation isolation unit (Isolator-11, Axon Instruments). For each cell several locations of the stimulating electrode in the rostral local environment of the recorded neurons (60–100 μM) were tested for their ability to evoke postsynaptic currents. Hyperpolarizing voltage steps (5 mV) were applied before each stimulation to monitor passive electrical properties of the recorded cell as well as the stability of access resistances. Series resistances ranged from 15 to 30 MΩ, and a 50–70% compensation was achieved routinely by using the amplifier adjustments.

Cytoplasm harvesting and reverse transcription. At the end of the recording as much as possible of the content of the cell was aspirated into the recording pipette by the application of a gentle negative pressure in the pipette while maintaining the tight seal. Then the pipette was removed delicately allowing, in most instances, outside-out patch formation. Next, the content of the pipette was expelled into a test tube, and reverse transcription (RT) was performed in a final volume of 10 μl as described previously (Lambolez et al., 1992).

Multiplex PCR. Two steps of mPCR were performed essentially as described previously (Ruano et al., 1995). The cDNAs present in 10 μl of the reverse transcription reaction first were amplified simultaneously by using all of the primer pairs described in Table 1 (for each primer pair the sense and antisense primers were positioned on two different exons). *Taq* polymerase (2.5 U; Qiagen GmbH, Hilden, Germany) and 10 pmol

of each primer were added to the buffer supplied by the manufacturer (final volume, 100 μl), and 20 cycles (94°C for 30 sec; 60°C for 30 sec; 72°C for 35 sec) of PCR were run. Second rounds of PCR were performed by using 2 μl of the first PCR product as a template. In this second round each cDNA was amplified individually with its specific primer pair by performing 35 PCR cycles (as described above). Then 10 μl of each individual PCR was run on a 2% agarose gel, with ϕx174 digested by *Hae*III as a molecular weight marker and was stained with ethidium bromide.

Identification of the PCR products. PCR-generated fragments obtained from each cell were analyzed by fluorescence resonance energy transfer (FRET) between two adjacent oligoprobes (purchased from Genset, Paris, France; see Table 1) internal to the amplified sequence. The upstream probe was FITC-labeled at the 3′ end (donor; excitation, 470 nm), and the downstream probe was Red705-labeled at the 5′ end (acceptor; emission, 710 nm). FRET between the two fluorophores, which can occur only when both probes are hybridized to their cognate PCR fragment, was measured with a LightCycler instrument (Roche Diagnostics GmbH, Mannheim, Germany) that used the following protocol. At the end of the second PCR, 18 μl of the PCR was mixed with the oligoprobes (each at 0.2 μM final) and EDTA (2 mM final) in a final volume of 20 μl. After 10 sec of denaturation at 95°C and 1 min of hybridization at 50°C, the FRET was measured continuously during a ramp to 95°C (1°C/sec) and analyzed with the manufacturer's software.

Test of the RT-mPCR protocol. The RT-mPCR protocol was tested on 500 pg of total RNA purified from rat neocortex (Chomczynski and Sacchi, 1987). All of the transcripts were detected from 500 pg of neocortical RNA, except for the 5-HT_{3B} subunit, which was detected from 10 ng of whole brain RNA. The absence of 5-HT_{3B} mRNA detection from neocortical RNA is consistent with a recent report showing the very low abundance of 5-HT_{3B} transcripts in the rat CNS (Wang et al., 2001). The sizes of the PCR-generated fragments were as predicted by the mRNA sequences (see Table 1), and their identity was confirmed by FRET between adjacent oligoprobes (as described above).

Intracellular labeling and immunocytochemistry. The slices containing cells recorded and filled with biocytin were fixed overnight in 4% paraformaldehyde in PBS at 4°C, rinsed six times in 0.1 M phosphate buffer for 10 min, incubated for 30 min in PBS containing 70% methanol, and rinsed three times in PBS supplemented with 0.1 M gelatin and 0.25% Triton X-100 (GT-PBS) for 10 min. For the immunostaining of 5-HT fibers, before biocytin revelation, the slices were incubated overnight with rabbit antisera raised against serotonin (1:10,000; Diasorin, Stillwater, MN) in GT-PBS. Slices then were washed four times in GT-PBS for 10 min and incubated for 4 hr at room temperature with Streptavidin Alexafluor 488 (1:1000; Molecular Probes, Leiden, The Netherlands) and Cy3-conjugated goat anti-rabbit IgG (1:400; Chemicon, Temecula, CA); they were diluted in GT-PBS and subsequently were rinsed twice in PBS. The slices were mounted in Vectashield (Vector, Burlingame, CA) medium for observation, and labeled cells were reconstructed with a confocal microscope (Leica, TCS NT, Mannheim, Germany).

RESULTS

The 5-HT_3R is expressed by a subset of VIP/CCK interneurons

To identify and characterize 5-HT_3R-expressing neocortical neurons, 13 pyramidal neurons and 94 interneurons from neocortical layers I, II, III, and V were visually selected via infrared video microscopy, electrophysiologically characterized, and analyzed by single-cell RT-mPCR. All cells were classified as irregular spiking (IS), fast spiking (FS), regular spiking nonpyramidal (RSNP), or pyramidal neurons according to their action potential firing behavior (McCormick et al., 1985; Cauli et al., 1997, 2000; Porter et al., 1998) after application of depolarizing current pulses. The molecular analysis protocol was designed to probe for the mRNA expression of the 5-HT_{3A} subunit of the 5-HT_3R in addition to nine interneuron markers [GAD 65; GAD 67; three calcium binding proteins: parvalbumin (PV), calretinin (CR), and calbindin (CB); and four neuropeptides: neuropeptide-Y (NPY), somatostatin (SOM), cholecystokinin (CCK), and vasoactive intestinal peptide (VIP)].

The 5-HT_{3A} mRNA expression was restricted to a small subset of neocortical neurons (n = 19 of 107) exhibiting the firing properties of RSNP (n = 14) or IS (n = 5) interneurons. The molecular profile of 5-HT_{3A}-expressing neurons is summarized in Figure 1*A*. The high occurrence of GAD 65, GAD 67, VIP, and CCK (95, 89, 95, and 100%, respectively) indicated that the 5-HT_3R was expressed selectively by GABAergic interneurons that coexpressed VIP and CCK (VIP/CCK interneurons). As documented previously (Morales and Bloom, 1997), 5-HT_{3A}-expressing neurons also showed substantial expression of CB and CR (37 and 53%, respectively). Among VIP/CCK interneurons (n = 41) we did not observe significant differences between the expression profiles of 5-HT_{3A}-positive and 5-HT_{3A}-negative interneurons. 5-HT_{3A} was expressed in 33% of the sampled CCK-expressing interneurons and in 27% of those containing VIP (data not shown). In addition, 5-HT_{3B} subunit expression was tested in 56 of the 107 neurons that were tested for 5-HT_{3A} expression. 5-HT_{3B} was never detected, even in five 5-HT_{3A}-positive cells, suggesting that the 5-HT_3Rs expressed in neocortical interneurons were composed primarily of the 5-HT_{3A} subunit.

Figure 1*B,C* shows the molecular profiles of the two neuronal populations that expressed the 5-HT_{3A} subunit: IS interneurons (n = 12) and RSNP VIP/CCK cells (n = 32). Consistent with previous studies (Porter et al., 1998; Cauli et al., 2000), IS interneurons frequently expressed VIP and CCK (83 and 75%, respectively). Although our present sample of IS and RSNP VIP/CCK cells differed by the occurrence of CR, NPY, and SOM (Fig. 1*B,C*), they exhibited a similar incidence of 5-HT_{3A} expression (42 and 38%, respectively). Indeed, previous studies have shown that these two interneuron populations form a relatively homogeneous cell type (Cauli et al., 2000).

Functional 5-HT_3R expression by VIP/CCK neocortical interneurons

The functionality of the 5-HT_3Rs that were expressed by neocortical interneurons was tested by local pressure application of 5-HT (200 μM, 50 msec) in 48 of the 107 neurons that were analyzed by single-cell RT-mPCR (see above).

In nine interneurons (7 RSNP and 2 IS cells; see examples in Fig. 2*A*), 5-HT applications induced a rapid membrane potential depolarization resulting, in most instances, in action potential discharge (Fig. 2*B1,B2*). Voltage-clamp recordings from the same neurons showed that 5-HT applications elicited inward currents, with peak amplitudes ranging from −22 to −319 pA (mean, −125 pA) and a time course similar to that of the depolarization (rise time, 2.5–5 sec and decay time, 15–30 sec; see examples in Fig. 2*C1,C2*). We observed that repetitive applications of 5-HT at 2 min intervals resulted in inward currents with no substantial change in peak amplitude (data not shown). Responses to 5-HT applications were blocked totally by the bath application of the highly potent and selective 5-HT_3R antagonist tropisetron (10 nM) (Fig. 2*C1,C2*). Recovery of the 5-HT-induced currents was not observed even after 25 min of tropisetron washout. This was consistent with previous studies that showed only partial recovery after 0.5–1.5 hr of tropisetron washout (Ropert and Guy, 1991; Kawa, 1994; McMahon and Kauer, 1997). RT-mPCR analyses of 5-HT_3-responsive cells consistently revealed the expression of the 5-HT_{3A} subunit in addition to GAD65 and/or GAD67, VIP, and CCK (Fig. 2*D1,D2*). Conversely, the 5-HT_{3A} mRNA was never detected in unresponsive neurons. Occasionally 5-HT application induced a slowly developing depolarization (n = 1) or hyperpo-

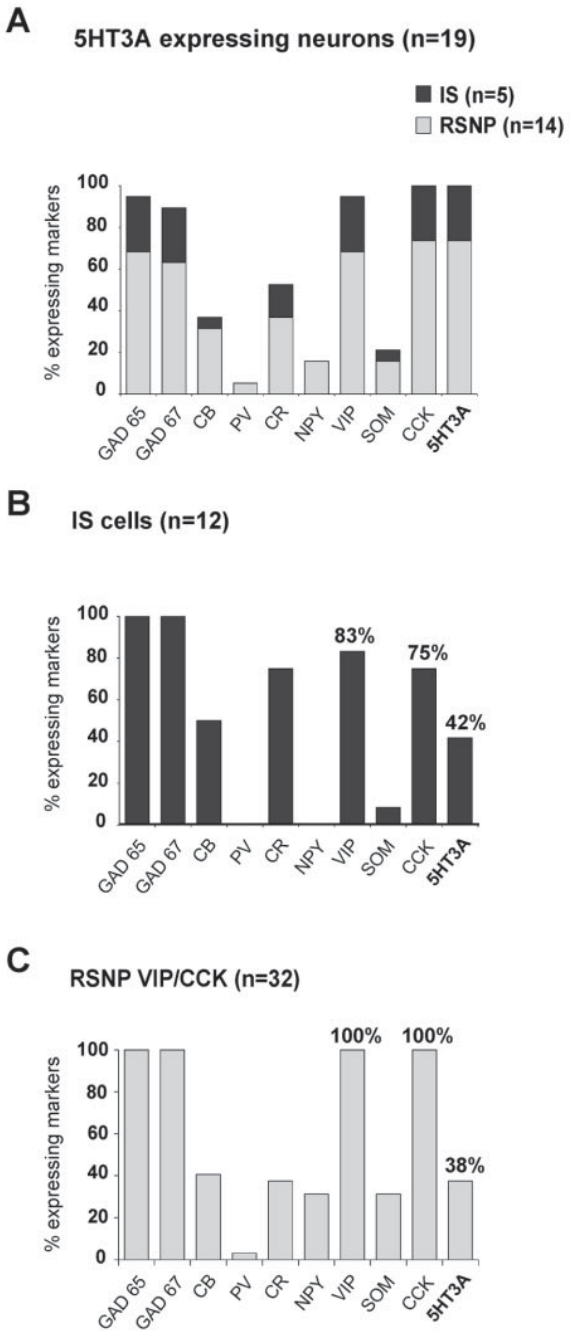

Figure 1. 5-HT_3R is expressed selectively in a subset of GABAergic interneurons coexpressing VIP and CCK. Single-cell RT-mPCR analyses of 107 neocortical neurons, including 13 pyramidal cells and 94 interneurons, revealed 5-HT_{3A} expression in five IS and 14 RSNP interneurons. The histogram in *A* illustrates the percentage of 5-HT_{3A}-expressing IS (*dark gray*) and RSNP (*light gray*) neurons that expressed each of the biochemical markers. The high occurrence of GAD 65, GAD 67, VIP, and CCK (95, 89, 95, and 100%, respectively) indicated that 5-HT_3R expression was restricted to a subset of neocortical GABAergic interneurons coexpressing VIP and CCK. 5-HT_3-expressing interneurons were also characterized by a low occurrence of PV, SOM, and NPY (5, 16, and 21%, respectively) and the relatively frequent expression of CB and CR (37 and 53%, respectively). *B, C*, Two histograms illustrating the molecular profiles of IS interneurons and VIP/CCK RSNP cells. The 5-HT_{3A} mRNA was detected in 42% of IS and 38% of RSNP VIP/CCK interneurons. No significant difference was observed between 5-HT_{3A}-expressing and 5-HT_{3A}-nonexpressing IS and RSNP VIP/CCK neurons. The 5-HT_{3B} subunit was never detected (56 neurons tested).

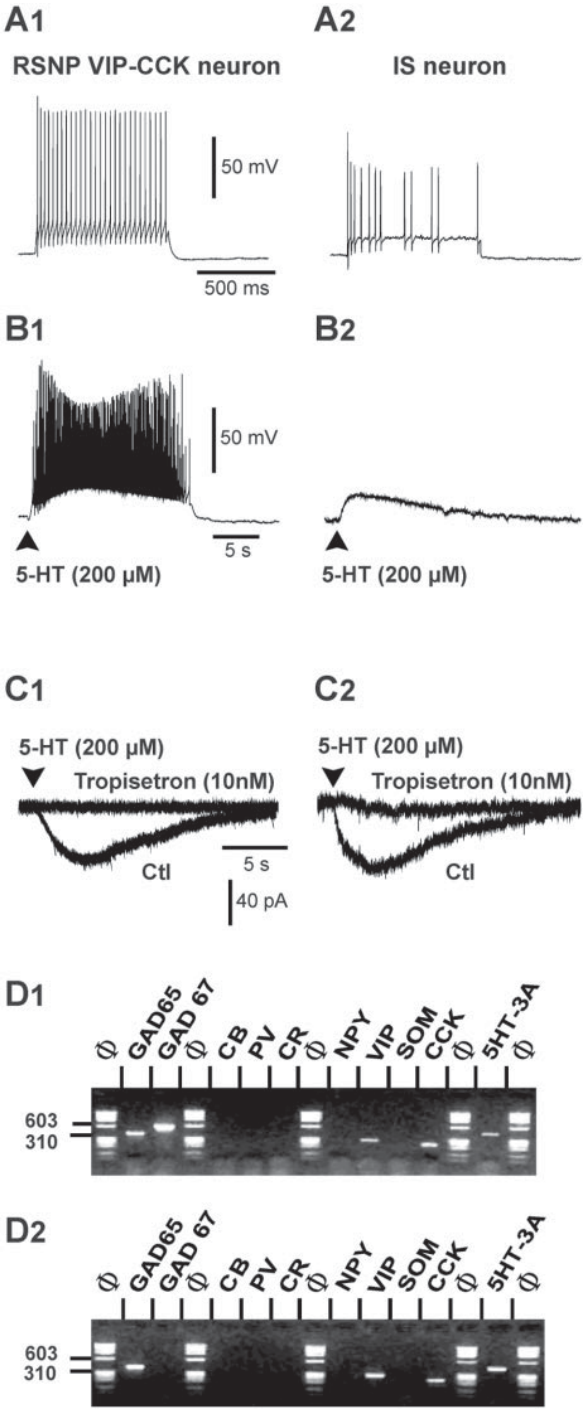

Figure 2. Functional 5-HT_3R expression by VIP/CCK interneurons. *A*, In current-clamp mode the RSNP and IS neurons were identified by their firing properties after depolarizing current injections (100 pA; holding potential, −71 mV). The RSNP neuron exhibited a 50.9% reduction of firing frequency along the discharge (*A1*), and the IS neuron showed an initial burst of action potentials followed by irregularly emitted action potentials (*A2*). *B*, Local pressure applications of 5-HT (200 μM, 50 msec) induced fast membrane potential depolarizations in these neurons (*B1, B2*). Note the action potential discharge in *B1*. *C*, In voltage clamp (holding potential, −71 mV) the 5-HT applications induced inward currents (*C1*, −68.5 pA; *C2*, −67.5 pA) that were blocked by bath application of tropisetron (10 nM). *D*, Agarose gel analysis of PCR products obtained from these two 5-HT_3-responsive neurons (*D1, D2*) revealed the expression of the 5-HT_{3A} subunit together with GAD65 (and GAD67 in *D1*), VIP, and CCK.

larizations ($n = 2$) of small amplitude. These slow responses were not associated with 5-HT_3R expression (data not shown).

Consistent with the GABAergic nature of 5-HT3R-expressing cells, the selective agonist mCPBG has been reported to induce IPSCs in neocortical neurons (Zhou and Hablitz, 1999). Indeed, the bath application of mCPBG (100 μM, 15 sec) in the presence of CNQX (10 μM) and D-AP-5 (50 μM) increased the frequency of spontaneous IPSCs in three of seven interneurons that were tested (data not shown). In these neurons recorded in voltage-clamp mode at a holding potential of −80 mV, mCPBG induced a mean 3.3-fold increase in the frequency of IPSCs but did not affect their amplitudes. Hence, these observations demonstrated a good correspondence between the 5-HT_{3A} expression and physiological 5-HT_3R responses, indicating that the 5-HT_{3A} subunit expressed by VIP/CCK GABAergic interneurons forms functional 5-HT_3Rs.

Close apposition of serotonergic fibers with dendrites and somata of 5-HT_3R-expressing neurons

Within the neocortex, serotonergic (5-HT) fibers originating from the brainstem raphe nuclei project broadly and diffusely and constitute the only source of 5-HT (Mulligan and Tork, 1988; Seguela et al., 1989; DeFelipe et al., 1991; Hornung and Celio, 1992; Smiley and Goldman-Rakic, 1996). To investigate whether these fibers could exert fast synaptic excitation of 5-HT_3R-expressing interneurons, we combined intracellular biocytin labeling of recorded neurons with 5-HT immunostaining. 5-HT_3R-expressing interneurons were identified by the local pressure application of mCPBG (100 μM, 50 msec). Like for 5-HT, responses to mCPBG consisted of rapid membrane potential depolarizations leading to action potential discharges (Fig. 3*A1,B1*). Examples of confocal reconstructions are shown for two mCPBG-responsive RSNP neurons from layer V (Fig. 3*A2*) and layer II (Fig. 3*B2*). Neurons responsive to mCPBG ($n = 8$) exhibited a bipolar/bitufted morphology, typical of VIP/CCK interneurons (Morrison et al., 1984; Kawaguchi and Kubota, 1996; Bayraktar et al., 1997, 2000; Kubota and Kawaguchi, 1997; Porter et al., 1998). Immunocytochemical staining of 5-HT revealed an intricate network of thin, varicose, and tortuous fibers for which the overall distribution and orientation pattern were consistent with earlier descriptions (Lidov et al., 1980; Papadopoulos et al., 1987a). The density of 5-HT fibers coursing in the vicinity of the labeled neurons was highly variable (Fig. 3*A2,B2*). However, in each case it was possible to highlight close appositions of 5-HT-containing varicosities onto the soma and dendrites of mCPBG-responsive neurons (as seen at higher magnification in Fig. 3*A3–A7,B3,B4*), suggestive of possible synaptic contacts.

Evoked synaptic responses mediated by the 5-HT_3R

To assess the presence of functional serotonergic synapses, we attempted to stimulate 5-HT fibers by performing local electrical stimulation in the vicinity of 5-HT_3R-expressing interneurons. In this set of experiments 99 neurons were recorded in current-clamp mode and, after characterization of their firing properties, were exposed to bath application of 5-HT (10 μM, 10 sec). In this case 5-HT was preferred to mCPBG because this latter agonist induced significantly longer desensitization (data not shown) (see also Kawa, 1994). Electrical stimulation of 5-HT fibers was attempted for four IS and 20 RSNP interneurons that exhibited rapid depolarization in response to 5-HT application. Voltage-clamp recordings of these neurons were performed in the presence of D-AP-5 (20 μM) and CNQX (10 μM) to prevent glutamatergic transmission and at a holding potential of −78 mV, which corresponded to the reversal potential of $GABA_A$ receptor-mediated events. The effective block of glutamatergic and GABAergic postsynaptic currents in these conditions was verified in each recorded cell (data not shown). Because it is not possible to predict the exact trajectory of 5-HT fibers in acute neocortical slices, electrical stimulations were applied at different sites in the rostral environment of the recorded neurons (distance between stimulating and recording electrodes varied from 60 to 100 μm). For five 5-HT-responsive RSNP neurons the electrical stimulations evoked fast EPSCs of large amplitude that were blocked by tropisetron. Examples of these evoked EPSCs recorded in a layer II RSNP cell are shown in Figure 4. Local electrical stimulation applied in layer I ~100 μm away from the soma of this cell induced fast EPSCs (Fig. 4*A*, *black arrow*) with a latency of 2.3 ± 0.2 msec (measured between the beginning of the stimulation artifact and the peak of the EPSCs) and a steady amplitude of −287 ± 13 pA (mean ± SD for 10 successive events) (Fig. 4*A,C*). The rise time (10–90%) of EPSCs was 0.29 msec, and their decay

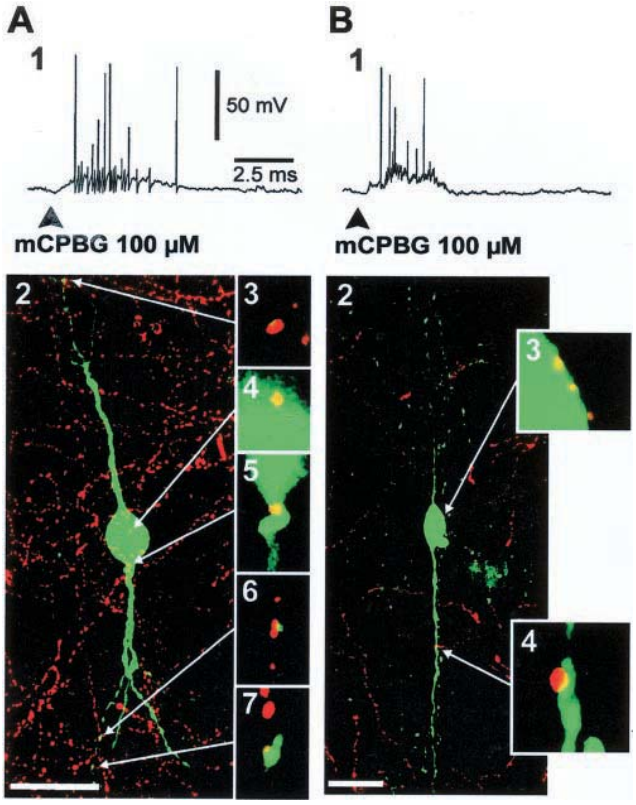

Figure 3. 5-HT-containing fibers form close appositions with 5-HT_3-responsive neurons. Confocal reconstruction shows two mCPBG-responsive neurons from layers V (*A2*) and II (*B2*) labeled by biocytin (*green*) and immunostained 5-HT-containing fibers (*red*). Responses to local pressure applications of mCPBG (100 μM, 50 msec), a selective 5-HT_3R agonist, consisted of membrane potential depolarizations surmounted by action potentials (*A1, B1*). Confocal reconstructions shown in *A2* and *B2* (scale bars, 20 μm) consisted of a *z*-series of 48 and 28 images, respectively, projected in one layer via the maximum intensity method (the spacing of successive *z*-images was 1 μm). mCPBG-responsive neurons exhibited a bipolar morphology, typical of VIP/CCK-expressing interneurons. 5-HT immunostaining showed thin varicose fibers coursing in the vicinity of these neurons. As seen at higher magnification (6×) on unitary *z*-images, 5-HT-containing varicosities were in close apposition to the soma (*A4, A5, B3*) or dendrites (*A3, A6, A7, B4*) of mCPBG-responsive neurons.

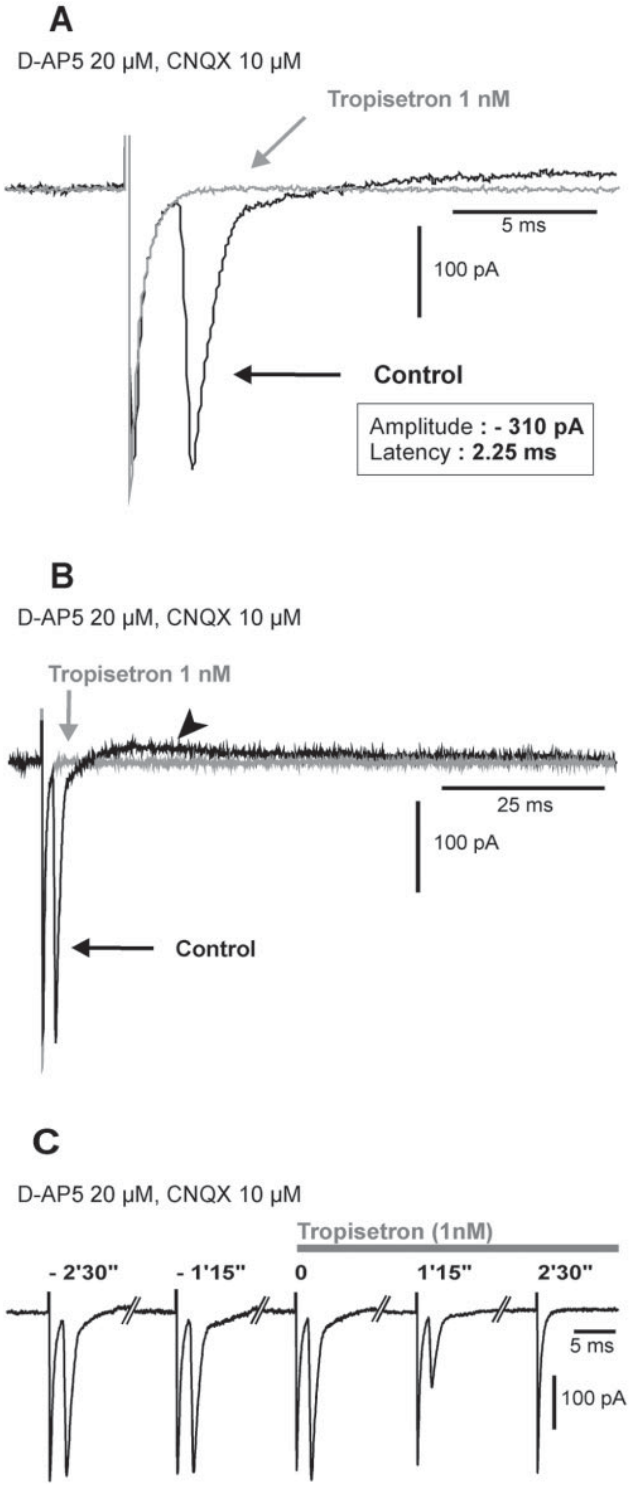

Figure 4. Serotonergic synaptic transmission in 5-HT_3-responsive cells. A 5-HT-responsive RSNP interneuron located in layer II was recorded in voltage-clamp mode at a holding potential of −78 mV (corresponding to the reversal potential of $GABA_A$-mediated events). Electrical stimulation (0.2 mA; 0.067 Hz) applied in layer I, ~100 μm above the soma of this neuron, evoked D-AP-5/CNQX-resistant EPSCs. The example of evoked D-AP-5/CNQX-resistant EPSCs shown in *A* had an amplitude of −310 pA and a latency to peak of 2.25 msec. For this EPSC the rise time was 0.29 msec (10–90%), and the decay was fit with two exponentials with time constants of 0.65 msec (87%) and 2.63 msec (13%). The same EPSC shown in *B* at a different time scale was followed by a slowly inactivating outward current (17 pA; *arrowhead*). Both the EPSC and the outward current were blocked completely by the 5-HT_3R antagonist tropisetron (*A, B*). *C* shows the steady amplitude of the evoked EPSCs (mean, −287 ± 13 pA for 10 successive events) that were blocked completely by tropisetron 2.5 min after the beginning of the bath application.

was well fit with two exponentials, with time constants of 0.62 ± 0.03 msec (84% of decay) and 3.16 ± 0.73 msec (16% of decay, mean ± SD, for 10 successive events). A slowly inactivating outward current was apparent at the end of the EPSCs (13.9 ± 3.7 pA) (Fig. 4*B*, *arrowhead*). It is likely that this outward current partly contributed to the very fast decay of the EPSCs.

As shown in Figure 4*A,B*, these D-AP-5/CNQX-resistant postsynaptic currents were blocked completely by bath application of tropisetron (1 nM), suggesting that both inward and outward currents resulted from the activation of 5-HT_3Rs. It is known that 5-HT_3Rs are highly permeable to calcium (Yang et al., 1992; Brown et al., 1998). The slowly inactivating outward current therefore might be attributable to calcium-activated potassium conductances (Sah, 1996). Figure 4*C* shows the steady amplitude of the 5-HT_3R postsynaptic responses and their complete block by tropisetron 2.5 min after the beginning of the bath application. Similar results were obtained for the other four cells showing D-AP-5/CNQX-resistant evoked EPSCs.

In our sample of five neurons showing D-AP-5/CNQX-resistant EPSCs, the mean EPSC amplitude was −240.8 ± 50 pA, and the mean latency to peak was 1.6 ± 0.9 msec (ranging from 0.8 to 3.1 msec). Mean decay time constants were 0.71 ± 0.03 msec (fast exponential, 84%) and 4.84 ± 1.96 msec (slow exponential, 16%). The mean amplitude of the slowly inactivating outward current was 5.25 ± 2.04 pA. The D-AP-5/CNQX-resistant evoked postsynaptic currents of all five cells were blocked totally by the bath application of tropisetron (1 nM) in 2–3 min, indicating that they were mediated by 5-HT_3R activation. The 5-HT_3R-mediated EPSCs exhibited an "all-or-none" behavior because their amplitude did not vary according to the stimulation intensity. Furthermore, within each neuron the response-to-response amplitude variability was very small (6 ± 3%), and, once effective location and intensity of stimulation was found, no transmission failure was observed. The latencies appeared to be correlated to the distance of the stimulation electrode from the recorded neurons. The low conduction velocity of 5-HT fibers (Jones, 1982; Goldfinger et al., 1992), together with their tortuous topology, also could explain the large latency variability. We did not detect D-AP-5/CNQX-resistant evoked postsynaptic currents in any of the remaining 19 cells that responded to 5-HT application (see above). In addition, three IS, nine RSNP, and four pyramidal neurons that did not respond to 5-HT bath application were also tested as negative controls. No D-AP-5/CNQX-resistant postsynaptic currents were recorded in these cells.

These results indicated that 5-HT_3Rs can mediate fast synaptic excitation of 5-HT_{3A}-expressing VIP/CCK neocortical interneurons by fibers originating from the raphe nucleus.

Convergence of fast serotonergic and nicotinic pathways on a subset of VIP/CCK interneurons

It has been shown previously that nicotinic receptor agonists selectively excite a subpopulation of GABAergic interneurons coexpressing VIP and CCK via the activation of somatodendritic nicotinic receptors containing the α4, α5, and β2 subunits (Porter et al., 1999). To establish whether 5-HT_3 and nicotinic receptors

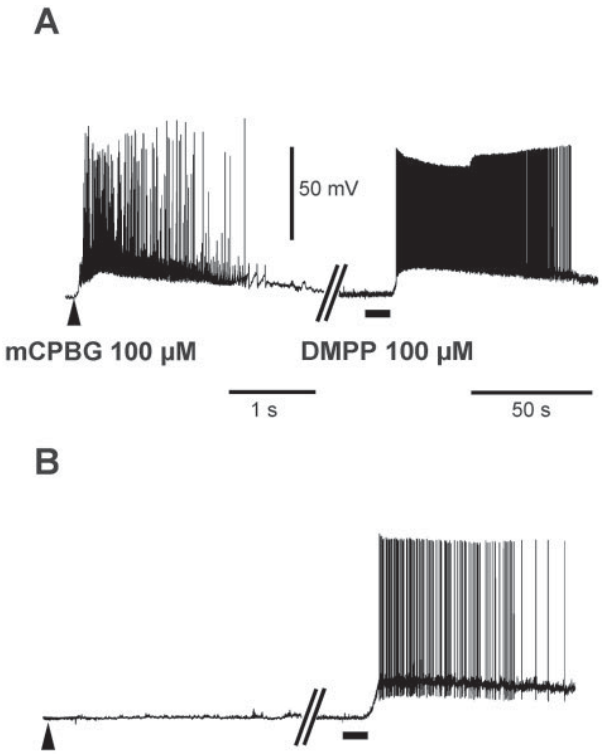

Figure 5. 5-HT_3R expression is restricted to a subset of DMPP-sensitive interneurons. On 86 recorded neurons we successively applied mCPBG (local pressure application, 100 μM; 50 msec) and the nicotinic agonist DMPP (bath application, 100 μM). All of the mCPBG-responsive neurons (n = 7) also responded to DMPP (*A*). However, 42 neurons responded only to DMPP (*B*), and 37 neurons did not show any response (data not shown). DMPP responses were not affected by tropisetron (1 nM; data not shown).

are expressed by the same interneurons, we sequentially applied mCPBG (100 μM; local pressure application), and the nicotinic agonist DMPP (100 μM; bath application) to another set of nonpyramidal neurons (n = 86, including 79 RSNP, 3 FS, and 4 IS cells). All of the mCPBG-responsive neurons (n = 7) also responded to DMPP (Fig. 5*A*). Forty-two neurons responded only to DMPP (Fig. 5*B*), and 37 neurons were not responsive to either mCPBG or DMPP (data not shown). Neurons responsive only to mCPBG were not observed in our sample. Neurons responding only to DMPP showed a lower occurrence of CCK (35% in 20 neurons that were analyzed molecularly; data not shown) compared with 5-HT3R-expressing neurons (100%; see above). No other significant difference was observed among their firing patterns, morphologies, or molecular profiles. Therefore, these data indicated that 5-HT_3R-expressing neurons represented a subset of DMPP-responsive interneurons. It must be noted that no nicotinic receptor-mediated EPSC was observed in the above stimulation experiments despite the reported existence of cholinergic synaptic junctions in the neocortex, albeit at a low incidence (Chedotal et al., 1994; Umbriaco et al., 1994). The fact that DMPP responses were not affected by tropisetron (1 nM; n = 3 responsive neurons; data not shown) confirms that the above D-AP-5/CNQX-resistant EPSCs indeed were mediated by 5-HT_3Rs.

DISCUSSION

In the present study we found that, in the rat neocortex, 5-HT_3R expression was restricted to a subset of IS and RSNP GABAergic interneurons that coexpressed VIP and CCK. The occurrence of evoked fast EPSCs mediated by 5-HT_3Rs in these interneurons suggested that they received synaptic inputs from the raphe nuclei, as further emphasized by the presence of close appositions between 5-HT-immunostained nerve terminals and 5-HT_3R-responsive neurons. Finally, 5-HT_3R-responsive interneurons represented a subset of interneurons responding to nicotinic agonists.

5-HT_3R is expressed selectively by a subset of VIP/CCK-expressing GABAergic interneurons

Using single-cell RT-mPCR, we probed for the expression of both 5-HT_{3A} and 5-HT_{3B} subunits in neocortical neurons. We found that the expression of the 5-HT_{3A} subunit was selective for VIP/CCK-expressing GABAergic interneurons. In contrast, no 5-HT_{3B} transcripts were detected, either at the single neuron level or in total neocortical RNA preparations (see Materials and Methods). Together, the present results agree with previous findings of the neocortical expression of 5-HT_3Rs demonstrated by radioligand binding, *in situ* hybridization, and immunocytochemistry (Kilpatrick et al., 1987, 1988; Barnes et al., 1990; Gehlert et al., 1991; Laporte et al., 1992; Morales et al., 1996a, 1998; Morales and Bloom, 1997) but further indicate that these receptors are composed primarily with the 5-HT_{3A} subunit.

Consistent with previous studies, we detected 5-HT_3R expression only in CCK-containing GABAergic interneurons that also expressed CB and CR (Morales et al., 1996a; Morales and Bloom, 1997). 5-HT_3-expressing neurons represented 33% of our CCK-positive interneurons, in accordance with an earlier study (Morales and Bloom, 1997). Assuming that CCK is expressed by 10% of interneurons (Demeulemeester et al., 1988) and that interneurons represent 20% of neocortical neurons, 5-HT_3R would be expressed in 0.7% of the neurons in the neocortex. In the present study we found that 5-HT_3R-containing interneurons were also characterized by VIP expression, which is coexpressed mainly with CCK in the neocortex (Papadopoulos et al., 1987b; Kubota and Kawaguchi, 1997; Cauli et al., 2000). 5-HT_{3A}-expressing neurons represented 27% of our sampled VIP-positive neurons. A similar assumption as above with VIP (present in ~20% of neocortical interneurons; Kubota et al., 1994; Cauli et al., 1997) indicates the expression of 5-HT_3R in 1% of the neurons in the neocortex. 5-HT_3R-expressing neurons therefore would represent 0.7–1% of neocortical neurons.

5-HT_3R-expressing neurons exhibited IS or RSNP firing properties with an IS/RSNP proportion (0.35) similar to that we reported previously for VIP/CCK interneurons (0.5; Cauli et al., 2000). Conversely, the proportion of 5-HT_3-positive cells in our sampled IS neurons (42%) was equivalent to that observed in RSNP VIP/CCK interneurons (38%). Together, the present results support our previous studies indicating that neocortical IS and RSNP VIP/CCK interneurons form a relatively homogeneous cell type (Cauli et al., 2000), also characterized by the selective expression of postsynaptic nicotinic receptors (Porter et al., 1999).

Selective excitation of neocortical VIP/CCK interneurons mediated by the 5-HT_3Rs

We observed an excellent correlation between 5-HT-evoked rapid depolarizing responses blocked by tropisetron and the expression of the 5-HT_{3A} subunit in VIP/CCK interneurons. This clearly indicated that the 5-HT_3R-mediated excitation of these interneurons was attributable to the activation of postsynaptic

receptors. This is in agreement with immunocytochemical studies that described a dense labeling of neocortical interneuron somata with 5-HT_3R antibodies (Morales et al., 1996b; Morales and Bloom, 1997; Jakab and Goldman-Rakic, 2000). A similar excitation of interneurons via somatodendritic 5-HT_3Rs has been reported in hippocampal (Kawa, 1994; McMahon and Kauer, 1997) and neocortical layer I (Zhou and Hablitz, 1999) interneurons. As described by these authors, 5-HT_3R activation resulted in an inward current that showed a large amplitude variability from one cell to another (from 22 to 319 pA). The present results provide a direct correlation between the expression of native 5-HT_{3A} receptors and their ligand-gated ion channel function.

Coexpression of 5-HT_3Rs and nicotinic receptors in VIP/CCK interneurons

Because IS interneurons and RSNP cells coexpressing VIP and CCK had been shown previously to be responsive selectively to nicotinic stimulation (Porter et al., 1999), we investigated whether the same interneurons could be excited by both 5-HT_3R and nicotinic agonists (mCPBG and DMPP, respectively). We found that all mCPBG-responsive cells also responded to DMPP and therefore represented a subgroup (14%) of DMPP-responsive neurons. This finding discloses a remarkable convergence between putative serotonergic and cholinergic fast transmission in the same interneuron subtype.

Nicotinic receptors expressed by VIP/CCK interneurons are formed with a combination of the α4, α5, and β2 subunits (Porter et al., 1999). It has been shown that the 5-HT_{3A} subunit can coassemble with the α4 nicotinic subunit in heterologous expression systems to form functional hybrid receptors that are activated by 5-HT_3R agonists, but not by nicotinic agonists (van Hooft et al., 1998; Kriegler et al., 1999). Our results suggest that both the nicotinic α4 and the 5-HT_{3A} subunits can be expressed in the same interneurons and thus open the possibility that such hybrid receptors exist in native conditions. The absence of discriminative pharmacological tools did not allow us to investigate the existence of 5-HT_{3A}–α4 hybrid receptors. However, if 5-HT_{3A}-expressing interneurons contain such hybrid receptors, they also express "pure" nicotinic receptors, because all of them also responded to DMPP.

5-HT_3Rs mediate fast synaptic excitation of VIP/CCK neocortical interneurons

Many histochemical studies have reported a dense innervation of neocortical interneurons by serotonergic fibers originating from the midbrain raphe nuclei (Mulligan and Tork, 1988; Seguela et al., 1989; DeFelipe et al., 1991; Hornung and Celio, 1992; Smiley and Goldman-Rakic, 1996). In addition, at the electron microscopy level it has been shown that some of the 5-HT varicosities form identifiable synapses onto their cortical targets (Descarries et al., 1975; Papadopoulos et al., 1987a; Seguela et al., 1989; Smiley and Goldman-Rakic, 1996; Paspalas and Papadopoulos, 2001). In the present study, using two-channel confocal microscopy, we observed close appositions of 5-HT fibers on the dendrites and somata of 5-HT_3R-expressing interneurons, suggestive of possible synaptic contacts.

In five neurons showing fast depolarizing responses to 5-HT, electrical stimulation evoked robust D-AP-5/CNQX-resistant EPSCs of large amplitude. The complete block of these currents by the highly selective antagonist tropisetron indicated that they resulted from the activation of 5-HT_3Rs. The short mean latency to peak of these EPSCs (1.6 msec), together with the absence of serotonergic neocortical intrinsic neurons, indicates that the tropisetron-sensitive EPSCs were attributable to the stimulation of 5-HT fibers originating from the raphe nuclei. Although 5-HT_3R-mediated synaptic responses have been reported previously (Sugita et al., 1992; Roerig et al., 1997), we establish here a clear correlation between the functional expression of the 5-HT_{3A} receptor subunit in VIP/CCK GABAergic interneurons and its synaptic activation by serotonergic afferent fibers.

The most remarkable characteristics of the 5-HT_3R-mediated EPSCs were their "all or none" behavior and their high amplitude, suggesting that they resulted from the stimulation of a single 5-HT fiber, which probably excited the neuron via multiple synaptic contacts. Indeed, the amplitude of the EPSCs (-240 ± 50 pA) was always superior to that necessary to induce action potential discharge in these neurons (below 50 pA at a membrane potential of -71 mV), suggesting that a single raphe serotonergic neuron could synchronize the activity of its VIP/CCK neocortical interneuron target.

Because 5-HT_3Rs appear to mediate fast direct synaptic excitation from the raphe nucleus to neocortical interneurons, their selective expression by the VIP/CCK GABAergic subtype may have important functional implications. It is known that peptidergic release requires higher levels of activity than that of classical neurotransmitters (for review, see Zupanc, 1996). It might be hypothesized that, with the excitation via 5HT_3Rs, VIP/CCK interneurons would reach the activity threshold of CCK release. Synaptic activation of neocortical VIP/CCK interneurons by the raphe serotonergic system therefore might provide a functional and cellular explanation to the well known involvement of both 5HT_3R and CCK in anxiety and other emotional disorders (for review, see van Megen et al., 1996).

REFERENCES

Barnes JM, Barnes NM, Champaneria S, Costall B, Naylor RJ (1990) Characterization and autoradiographic localization of 5-HT_3 receptor recognition sites identified with [^{3}H]-(*S*)-zacopride in the forebrain of the rat. Neuropharmacology 29:1037–1045.

Bayraktar T, Staiger JF, Acsady L, Cozzari C, Freund TF, Zilles K (1997) Colocalization of vasoactive intestinal polypeptide, γ-aminobutyric acid, and choline acetyltransferase in neocortical interneurons of the adult rat. Brain Res 757:209–217.

Bayraktar T, Welker E, Freund TF, Zilles K, Staiger JF (2000) Neurons immunoreactive for vasoactive intestinal polypeptide in the rat primary somatosensory cortex: morphology and spatial relationship to barrel-related columns. J Comp Neurol 420:291–304.

Bochet P, Audinat E, Lambolez B, Crepel F, Rossier J, Iino M, Tsuzuki K, Ozawa S (1994) Subunit composition at the single-cell level explains functional properties of a glutamate-gated channel. Neuron 12:383–388.

Brown AM, Hope AG, Lambert JJ, Peters JA (1998) Ion permeation and conduction in a human recombinant 5-HT_3 receptor subunit (h5-HT_{3A}). J Physiol (Lond) 507[Pt 3]:653–665.

Cauli B, Audinat E, Lambolez B, Angulo MC, Ropert N, Tsuzuki K, Hestrin S, Rossier J (1997) Molecular and physiological diversity of cortical nonpyramidal cells. J Neurosci 17:3894–3906.

Cauli B, Porter JT, Tsuzuki K, Lambolez B, Rossier J, Quenet B, Audinat E (2000) Classification of fusiform neocortical interneurons based on unsupervised clustering. Proc Natl Acad Sci USA 97:6144–6149.

Chedotal A, Umbriaco D, Descarries L, Hartman BK, Hamel E (1994) Light and electron microscopic immunocytochemical analysis of the neurovascular relationships of choline acetyltransferase and vasoactive intestinal polypeptide nerve terminals in the rat cerebral cortex. J Comp Neurol 343:57–71.

Chomczynski P, Sacchi N (1987) Single-step method of RNA isolation by acid guanidinium thiocyanate-phenol-chloroform extraction. Anal Biochem 162:156–159.

Connors BW, Gutnick MJ (1990) Intrinsic firing patterns of diverse neocortical neurons. Trends Neurosci 13:99–104.

Davies PA, Pistis M, Hanna MC, Peters JA, Lambert JJ, Hales TG, Kirkness EF (1999) The 5-HT_{3B} subunit is a major determinant of serotonin receptor function. Nature 397:359–363.

DeFelipe J, Hendry SH, Hashikawa T, Jones EG (1991) Synaptic rela-

tionships of serotonin-immunoreactive terminal baskets on GABA neurons in the cat auditory cortex. Cereb Cortex 1:117–133.
Demeulemeester H, Vandesande F, Orban GA, Brandon C, Vanderhaeghen JJ (1988) Heterogeneity of GABAergic cells in cat visual cortex. J Neurosci 8:988–1000.
Demuro A, Palma E, Eusebi F, Miledi R (2001) Inhibition of nicotinic acetylcholine receptors by bicuculline. Neuropharmacology 41:854–861.
Derkach V, Surprenant A, North RA (1989) 5-HT_3 receptors are membrane ion channels. Nature 339:706–709.
Descarries L, Beaudet A, Watkins KC (1975) Serotonin nerve terminals in adult rat neocortex. Brain Res 100:563–588.
Erkkila BE, Wotring VE, Weiss DS (2001) Picrotoxin inhibits $\alpha 3\beta 4$ nicotinic acetylcholine receptors. Soc Neurosci Abstr 35.16.
Gehlert DR, Gackenheimer SL, Wong DT, Robertson DW (1991) Localization of 5-HT_3 receptors in the rat brain using [^{3}H]LY278584. Brain Res 553:149–154.
Goldfinger MD, Roettger VR, Pearson JC (1992) Theoretical studies of impulse propagation in serotonergic axons. Biol Cybern 66:399–406.
Hanna MC, Davies PA, Hales TG, Kirkness EF (2000) Evidence for expression of heteromeric serotonin 5-HT_3 receptors in rodents. J Neurochem 75:240–247.
Hendry SH, Jones EG, Emson PC, Lawson DE, Heizmann CW, Streit P (1989) Two classes of cortical GABA neurons defined by differential calcium binding protein immunoreactivities. Exp Brain Res 76:467–472.
Hornung JP, Celio MR (1992) The selective innervation by serotoninergic axons of calbindin-containing interneurons in the neocortex and hippocampus of the marmoset. J Comp Neurol 320:457–467.
Houser CR, Hendry SH, Jones EG, Vaughn JE (1983) Morphological diversity of immunocytochemically identified GABA neurons in the monkey sensory-motor cortex. J Neurocytol 12:617–638.
Jakab RL, Goldman-Rakic PS (2000) Segregation of serotonin 5-HT_{2A} and 5-HT_3 receptors in inhibitory circuits of the primate cerebral cortex. J Comp Neurol 417:337–348.
Jones RS (1982) Responses of cortical neurones to stimulation of the nucleus raphe medianus: a pharmacological analysis of the role of indoleamines. Neuropharmacology 21:511–520.
Kawa K (1994) Distribution and functional properties of 5-HT_3 receptors in the rat hippocampal dentate gyrus: a patch-clamp study. J Neurophysiol 71:1935–1947.
Kawaguchi Y (1993) Groupings of nonpyramidal and pyramidal cells with specific physiological and morphological characteristics in rat frontal cortex. J Neurophysiol 69:416–431.
Kawaguchi Y, Kubota Y (1996) Physiological and morphological identification of somatostatin- or vasoactive intestinal polypeptide-containing cells among GABAergic cell subtypes in rat frontal cortex. J Neurosci 16:2701–2715.
Kawaguchi Y, Kubota Y (1997) GABAergic cell subtypes and their synaptic connections in rat frontal cortex. Cereb Cortex 7:476–486.
Kilpatrick GJ, Jones BJ, Tyers MB (1987) Identification and distribution of 5-HT_3 receptors in rat brain using radioligand binding. Nature 330:746–748.
Kilpatrick GJ, Jones BJ, Tyers MB (1988) The distribution of specific binding of the 5-HT_3 receptor ligand [^{3}H]GR65630 in rat brain using quantitative autoradiography. Neurosci Lett 94:156–160.
Kriegler S, Sudweeks S, Yakel JL (1999) The nicotinic $\alpha 4$ receptor subunit contributes to the lining of the ion channel pore when expressed with the 5-HT_3 receptor subunit. J Biol Chem 274:3934–3936.
Kubota Y, Kawaguchi Y (1997) Two distinct subgroups of cholecystokinin-immunoreactive cortical interneurons. Brain Res 752:175–183.
Kubota Y, Hattori R, Yui Y (1994) Three distinct subpopulations of GABAergic neurons in rat frontal agranular cortex. Brain Res 649:159–173.
Lambolez B, Audinat E, Bochet P, Crepel F, Rossier J (1992) AMPA receptor subunits expressed by single Purkinje cells. Neuron 9:247–258.
Laporte AM, Koscielniak T, Ponchant M, Verge D, Hamon M, Gozlan H (1992) Quantitative autoradiographic mapping of 5-HT_3 receptors in the rat CNS using [^{125}I]iodo-zacopride and [^{3}H]zacopride as radioligands. Synapse 10:271–281.
Lidov HG, Grzanna R, Molliver ME (1980) The serotonin innervation of the cerebral cortex in the rat—an immunohistochemical analysis. Neuroscience 5:207–227.
Maricq AV, Peterson AS, Brake AJ, Myers RM, Julius D (1991) Primary structure and functional expression of the 5HT_3 receptor, a serotonin-gated ion channel. Science 254:432–437.
Mayer ML, Straughan DW (1981) Effects of 5-hydroxytryptamine on central neurones antagonized by bicuculline and picrotoxin. Neuropharmacology 20:347–350.
McCormick DA, Connors BW, Lighthall JW, Prince DA (1985) Comparative electrophysiology of pyramidal and sparsely spiny stellate neurons of the neocortex. J Neurophysiol 54:782–806.
McMahon LL, Kauer JA (1997) Hippocampal interneurons are excited via serotonin-gated ion channels. J Neurophysiol 78:2493–2502.
Morales M, Bloom FE (1997) The 5-HT_3 receptor is present in different subpopulations of GABAergic neurons in the rat telencephalon. J Neurosci 17:3157–3167.
Morales M, Battenberg E, de Lecea L, Bloom FE (1996a) The type 3 serotonin receptor is expressed in a subpopulation of GABAergic neurons in the rat neocortex and hippocampus. Brain Res 731:199–202.
Morales M, Battenberg E, de Lecea L, Sanna PP, Bloom FE (1996b) Cellular and subcellular immunolocalization of the type 3 serotonin receptor in the rat central nervous system. Brain Res Mol Brain Res 36:251–260.
Morales M, Battenberg E, Bloom FE (1998) Distribution of neurons expressing immunoreactivity for the 5HT_3 receptor subtype in the rat brain and spinal cord. J Comp Neurol 402:385–401.
Morrison JH, Magistretti PJ, Benoit R, Bloom FE (1984) The distribution and morphological characteristics of the intracortical VIP-positive cell: an immunohistochemical analysis. Brain Res 292:269–282.
Mulligan KA, Tork I (1988) Serotoninergic innervation of the cat cerebral cortex. J Comp Neurol 270:86–110.
Papadopoulos GC, Parnavelas JG, Buijs RM (1987a) Light and electron microscopic immunocytochemical analysis of the serotonin innervation of the rat visual cortex. J Neurocytol 16:883–892.
Papadopoulos GC, Parnavelas JG, Cavanagh ME (1987b) Extensive coexistence of neuropeptides in the rat visual cortex. Brain Res 420:95–99.
Paspalas CD, Papadopoulos GC (2001) Serotoninergic afferents preferentially innervate distinct subclasses of peptidergic interneurons in the rat visual cortex. Brain Res 891:158–167.
Peters A, Jones EG (1984) Classification of cortical neurons. In: Cerebral cortex, Vol 1, Cellular components of the cerebral cortex (Peters A, Jones EG, eds), pp 107–121. New York: Plenum.
Porter JT, Cauli B, Staiger JF, Lambolez B, Rossier J, Audinat E (1998) Properties of bipolar VIPergic interneurons and their excitation by pyramidal neurons in the rat neocortex. Eur J Neurosci 10:3617–3628.
Porter JT, Cauli B, Tsuzuki K, Lambolez B, Rossier J, Audinat E (1999) Selective excitation of subtypes of neocortical interneurons by nicotinic receptors. J Neurosci 19:5228–5235.
Roerig B, Nelson DA, Katz LC (1997) Fast synaptic signaling by nicotinic acetylcholine and serotonin 5-HT_3 receptors in developing visual cortex. J Neurosci 17:8353–8362.
Ropert N, Guy N (1991) Serotonin facilitates GABAergic transmission in the CA1 region of rat hippocampus *in vitro*. J Physiol (Lond) 441:121–136.
Ruano D, Lambolez B, Rossier J, Paternain AV, Lerma J (1995) Kainate receptor subunits expressed in single cultured hippocampal neurons: molecular and functional variants by RNA editing. Neuron 14:1009–1017.
Sah P (1996) Ca^{2+}-activated K^+ currents in neurones: types, physiological roles, and modulation. Trends Neurosci 19:150–154.
Seguela P, Watkins KC, Descarries L (1989) Ultrastructural relationships of serotonin axon terminals in the cerebral cortex of the adult rat. J Comp Neurol 289:129–142.
Smiley JF, Goldman-Rakic PS (1996) Serotonergic axons in monkey prefrontal cerebral cortex synapse predominantly on interneurons as demonstrated by serial section electron microscopy. J Comp Neurol 367:431–443.
Somogyi P, Tamas G, Lujan R, Buhl EH (1998) Salient features of synaptic organization in the cerebral cortex. Brain Res Brain Res Rev 26:113–135.
Stuart GJ, Dodt HU, Sakmann B (1993) Patch-clamp recordings from the soma and dendrites of neurons in brain slices using infrared video microscopy. Pflügers Arch 423:511–518.
Sugita S, Shen KZ, North RA (1992) 5-Hydroxytryptamine is a fast excitatory transmitter at 5-HT_3 receptors in rat amygdala. Neuron 8:199–203.
Umbriaco D, Watkins KC, Descarries L, Cozzari C, Hartman BK (1994) Ultrastructural and morphometric features of the acetylcholine innervation in adult rat parietal cortex: an electron microscopic study in serial sections. J Comp Neurol 348:351–373.
van Hooft JA, Spier AD, Yakel JL, Lummis SC, Vijverberg HP (1998) Promiscuous coassembly of serotonin 5-HT_3 and nicotinic $\alpha 4$ receptor subunits into Ca^{2+}-permeable ion channels. Proc Natl Acad Sci USA 95:11456–11461.
van Megen HJ, Westenberg HG, den Boer JA, Kahn RS (1996) Cholecystokinin in anxiety. Eur Neuropsychopharmacol 6:263–280.
Wang SD, McCollum N, Morales M (2001) Differential expression of the 5-HT_3 receptor subunits A and B in CNS and PNS. Soc Neurosci Abstr 600.6.
Yang J, Mathie A, Hille B (1992) 5-HT_3 receptor channels in dissociated rat superior cervical ganglion neurons. J Physiol (Lond) 448:237–256.
Zhou FM, Hablitz JJ (1999) Activation of serotonin receptors modulates synaptic transmission in rat cerebral cortex. J Neurophysiol 82:2989–2999.
Zupanc GK (1996) Peptidergic transmission: from morphological correlates to functional implications. Micron 27:35–91.

Journal of Neuroscience Methods 257 (2016) 76–96

Contents lists available at ScienceDirect

Journal of Neuroscience Methods

journal homepage: www.elsevier.com/locate/jneumeth

Computational Neuroscience

Spatially Structured Sparse Morphological Component Separation for voltage-sensitive dye optical imaging

Hugo Raguet[a], Cyril Monier[b], Luc Foubert[b], Isabelle Ferezou[b], Yves Fregnac[b], Gabriel Peyré[a,*]

[a] CNRS and Ceremade, Université Paris-Dauphine, Place du Maréchal De Lattre De Tassigny, 75775 Paris Cedex 16, France
[b] Unit of Neuroscience, Information and Complexity, CNRS UPR-3293, 1 Avenue de la Terrasse, 91198 Gif-sur-Yvette, France

HIGHLIGHTS

- We present a new tool to denoise and remove artifacts from voltage-sensitive dye optical imaging.
- It is based on a mathematical modeling of the signal and artifacts formation process.
- It makes use of state of the art convex optimization techniques.
- An automatic parameter selection process through risk estimation is embedded into the method.
- It is validated on synthetic as well as real VSDOI data.

ARTICLE INFO

Article history:
Received 16 June 2015
Received in revised form
23 September 2015
Accepted 23 September 2015
Available online 3 October 2015

Keywords:
Voltage-sensitive dye optical imaging
Sensory cortical dynamics
Orientation maps
Sparse component separation

ABSTRACT

Background: Voltage-sensitive dye optical imaging is a promising technique for studying in vivo neural assemblies dynamics where functional clustering can be visualized in the imaging plane. Its practical potential is however limited by many artifacts.
New method: We present a novel method, that we call "SMCS" (Spatially Structured Sparse Morphological Component Separation), to separate the relevant biological signal from noise and artifacts. It extends Generalized Linear Models (GLM) by using a set of convex non-smooth regularization priors adapted to the morphology of the sources and artifacts to capture.
Results: We make use of first order proximal splitting algorithms to solve the corresponding large scale optimization problem. We also propose an automatic parameters selection procedure based on statistical risk estimation methods.
Comparison with existing methods: We compare this method with blank subtraction and GLM methods on both synthetic and real data. It shows encouraging perspectives for the observation of complex cortical dynamics.
Conclusions: This work shows how recent advances in source separation can be integrated into a biophysical model of VSDOI. Going beyond GLM methods is important to capture transient cortical events such as propagating waves.

1. Introduction

This work is focused on the processing of *voltage-sensitive dye optical imaging* (VSDOI) recordings. This experimental method can in theory, combine the mesoscopic spatial scale of optical imaging with the real-time temporal resolution of direct electrophysiological measurements. The VSDOI signal is however contaminated by a strong noise and artifacts, and suffers from a poor understanding of the signal formation process, as we detail in this section.

1.1. The VSDOI experimental method

1.1.1. Principles

Sensitivity to membrane potential of some fluorescent dyes is known for long (at least back to Cohen et al. (1974)), and its use

* Corresponding author. Tel.: +33 01 44 05 48 71.
E-mail addresses: hugo.raguet@gmail.com (H. Raguet), cyril.monier@unic.cnrs-gif.fr (C. Monier), luc.foubert@unic.cnrs-gif.fr (L. Foubert), isabelle.ferezou@unic.cnrs-gif.fr (I. Ferezou), yves.fregnac@unic.cnrs-gif.fr (Y. Fregnac), gabriel.peyre@ceremade.dauphine.fr (G. Peyré).
URL: http://www.ceremade.dauphine.fr/ peyre/ (G. Peyré).

http://dx.doi.org/10.1016/j.jneumeth.2015.09.024
0165-0270/

nature neuroscience

Dendritic channelopathies contribute to neocortical and sensory hyperexcitability in *Fmr1*$^{-/y}$ mice

Yu Zhang[1,2,7,8], Audrey Bonnan[1,2,7,8], Guillaume Bony[1,2,8], Isabelle Ferezou[3,7], Susanna Pietropaolo[4,5], Melanie Ginger[1,2], Nathalie Sans[1,2], Jean Rossier[3,7], Ben Oostra[6], Gwen LeMasson[1,2] & Andreas Frick[1,2]

Hypersensitivity in response to sensory stimuli and neocortical hyperexcitability are prominent features of Fragile X Syndrome (FXS) and autism spectrum disorders, but little is known about the dendritic mechanisms underlying these phenomena. We found that the primary somatosensory neocortex (S1) was hyperexcited in response to tactile sensory stimulation in *Fmr1*$^{-/y}$ mice. This correlated with neuronal and dendritic hyperexcitability of S1 pyramidal neurons, which affect all major aspects of neuronal computation, from the integration of synaptic input to the generation of action potential output. Using dendritic electrophysiological recordings, calcium imaging, pharmacology, biochemistry and a computer model, we found that this defect was, at least in part, attributable to the reduction and dysfunction of dendritic h- and BK_{Ca} channels. We pharmacologically rescued several core hyperexcitability phenomena by targeting BK_{Ca} channels. Our results provide strong evidence pointing to the utility of BK_{Ca} channel openers for the treatment of the sensory hypersensitivity aspects of FXS.

FXS is the most common heritable form of intellectual disability and is the leading known monogenic cause for autism spectrum disorders (ASD), with a third of FXS patients fulfilling the criteria for ASD[1,2]. FXS is caused by transcriptional silencing of *Fmr1*, which encodes the fragile X mental retardation protein (FMRP, reviewed in ref. 3). Hypersensitivity to sensory stimuli is a prominent feature of FXS and ASD[1,2,4]. In FXS patients, these symptoms include tactile defensiveness, sensory avoidance and enhanced responses to stimuli of various sensory modalities (for example, see refs. 5–7; reviewed in ref. 8). Consistent with clinical studies, *Fmr1*$^{-/y}$ mice (the mouse model for FXS) exhibit enhanced sensitivity to weak auditory stimuli[9–12], and there is increasing evidence that the neocortex of *Fmr1*$^{-/y}$ mice is hyperexcitable[11,13–15]. Recent studies have suggested that circuits of the somatosensory cortex are altered under baseline conditions in *Fmr1*$^{-/y}$ mice, pointing to a causative role for neocortical circuit defects in sensory hypersensitivity in FXS[13–15]. Perturbed plasticity during critical periods and an altered balance of excitation to inhibition[13,14,16,17] have been suggested to contribute to this phenomenon. However, almost nothing is known about the cellular-dendritic mechanisms underlying the hyperexcitability of neocortical circuits in FXS. This knowledge is essential for designing appropriate pharmaceutical therapies for the treatment of sensory hypersensitivity and neocortical hyperexcitability in FXS.

FMRP is an RNA-binding protein and a central player in neuronal function, where it regulates the translation, trafficking and stability of target RNAs[3]. Recent studies have suggested an additional function for FMRP as a regulator of the activity of certain ion channels[18,19]. The targets of FMRP (at the mRNA or protein level) include several voltage-gated ion channels (VGICs) that are crucial determinants of neuronal and dendritic excitability and it is increasingly recognized that certain features of FXS may be a result of underlying channelopathies (reviewed in refs. 20,21). Although alterations in dendritic function have been demonstrated in the CA1 region of the hippocampus of *Fmr1*$^{-/y}$ mice[22,23], nothing is known regarding the pathophysiology of dendritic function in the somatosensory cortex in FXS.

Dendrites of neocortical pyramidal neurons receive synaptic inputs from hundreds to thousands of neurons from a variety of brain regions. Their fundamental role is to integrate these synaptic inputs, permitting the generation of an appropriate action potential (AP) output (reviewed in ref. 24). Synaptic integration is the result of complex computations performed in the dendrites and is strongly determined by their intrinsic excitability (reviewed in refs. 21,25,26). Dendritic excitability is a result of the expression levels and biophysical properties of a variety of VGICs in their membrane (reviewed in ref. 26), and any pathological change in these VGICs would therefore markedly affect dendritic function in individual neurons, thereby affecting information processing in neocortical circuits.

We sought a cellular correlate for circuit level changes underlying S1 hyperexcitability in *Fmr1*$^{-/y}$ mice. We focused on the period following critical phase plasticity when the basic hardwiring of circuits is established[16,27,28] and when pharmacological intervention could be targeted to adolescent or adult patients. At the neuronal population

[1]INSERM, Neurocentre Magendie, Physiopathologie de la plasticité neuronale, U862, Bordeaux, France. [2]University of Bordeaux, Neurocentre Magendie, Physiopathologie de la plasticité neuronale, U862, Bordeaux, France. [3]Laboratoire de Neurobiologie, ESPCI ParisTech CNRS UMR 7637, Paris, France. [4]University of Bordeaux, INCIA, Talence, France. [5]CNRS, INCIA, UMR 5287, Talence, France. [6]Department of Clinical Genetics, Erasmus MC, Rotterdam, the Netherlands. [7]Present address: Department of Physiology, Development and Neuroscience, University of Cambridge, Cambridge, UK (Y.Z.), Max Planck Florida Institute for Neuroscience, Jupiter, Florida, USA (A.B.), Unité de Neurosciences Information et Complexité, CNRS UPR 3293, Gif-sur-Yvette, France (I.F.), Centre de Psychiatrie et Neurosciences, INSERM U894, Université Paris Descartes, Paris, France (J.R.). [8]These authors contributed equally to this work. Correspondence should be addressed to A.F. (andreas.frick@inserm.fr).

Received 4 August; accepted 14 October; published online 10 November 2014; doi:10.1038/nn.3864

Holographic laser Doppler imaging of microvascular blood flow

C. Magnain,[1] A. Castel,[1] T. Boucneau,[1] M. Simonutti,[2] I. Ferezou,[3] A. Rancillac,[3] T. Vitalis,[3] J. A. Sahel,[2] M. Paques,[2] and M. Atlan[1,*]

[1]*Institut Langevin, Centre National de la Recherche Scientifique (CNRS) UMR 7587, Institut National de la Santé et de la Recherche Médicale (INSERM) U 979, Université Pierre et Marie Curie (UPMC), Université Paris Diderot, Ecole Supérieure de Physique et de Chimie Industrielles (ESPCI ParisTech), 10 Rue Vauquelin, 75005 Paris, France*
[2]*Institut de la Vision, INSERM UMR-S 968, CNRS UMR 7210, UPMC, 17 Rue Moreau, 75012 Paris, France*
[3]*Brain Plasticity Unit, CNRS UMR 8249, ESPCI ParisTech, 10 Rue Vauquelin, 75005 Paris, France*
**Corresponding author: michael.atlan@espci.fr*

Received September 15, 2014; accepted September 17, 2014;
posted October 10, 2014 (Doc. ID 223162); published November 17, 2014

We report on local superficial blood flow monitoring in biological tissue from laser Doppler holographic imaging. In time-averaging recording conditions, holography acts as a narrowband bandpass filter, which, combined with a frequency-shifted reference beam, permits frequency-selective imaging in the radio frequency range. These Doppler images are acquired with an off-axis Mach–Zehnder interferometer. Microvascular hemodynamic components mapping is performed in the cerebral cortex of the mouse and the eye fundus of the rat with near-infrared laser light without any exogenous marker. These measures are made from a basic inverse-method analysis of local first-order optical fluctuation spectra at low radio frequencies, from 0 Hz to 100 kHz. Local quadratic velocity is derived from Doppler broadenings induced by fluid flows, with elementary diffusing wave spectroscopy formalism in backscattering configuration. We demonstrate quadratic mean velocity assessment in the 0.1–10 mm/s range *in vitro* and imaging of superficial blood perfusion with a spatial resolution of about 10 micrometers in rodent models of cortical and retinal blood flow.

OCIS codes: (090.0090) Holography; (040.2840) Heterodyne; (170.1470) Blood or tissue constituent monitoring; (170.3340) Laser Doppler velocimetry.
http://dx.doi.org/10.1364/JOSAA.31.002723

1. INTRODUCTION

A. Motivations

The role of the microcirculation is increasingly being recognized in the pathophysiology of cardiovascular diseases, e.g., hypertension [1–3] and diabetes [4–6]. In the eye, assessing retinal blood flow can be potentially useful for understanding diabetic retinopathies [7] and studying the relationships between vascularization and glaucoma [8–12]. Moreover, extensive use of optical methods is made for monitoring skin microvascular endothelial (dys)function [13–18]. Prevalent optical techniques to monitor microvascular blood flow in clinical studies are laser Doppler probes and spatial speckle contrast imaging. The former is characterized by its high temporal resolution and the latter enables wide-field imaging of superficial microvascular networks. High sensitivity in low light, high temporal resolution, high spatial resolution, and the ability to perform quantitative measurements are a requirement for blood flow monitoring schemes. Most current techniques are limited in their spatial resolution or temporal resolution or both. Hence wide-field optical imaging techniques using laser light and sensor arrays to probe local dynamics with potentially high spatial and temporal resolution are attracting attention for the measurement of blood flow [19].

B. Relationship between Local Motion and Optical Fluctuations

The radio frequency (RF) spectrum of dynamic light fluctuations is affected by microvascular hemodynamics and hence is a subject of great interest for blood flow imaging applications. The laser Doppler technique measures Doppler shifts and broadenings of quasi-elastically scattered light. Depending on the detection configuration, single scattering or multiple scattering can be targeted to yield Doppler spectra. The observation and interpretation of Doppler broadening of a scattered laser light beam by a fluid in motion *in vitro* [20] and *in vivo* [21] has led to the physical modeling of laser Doppler velocimetry [22,23]. Mapping retinal hemodynamics *in vivo* has many biomedical applications such as diagnosis of retinal microvasculature disorders [24–26]. Optical instrumentation is well adapted to noninvasive retinal blood flow imaging, because the eye fundus vascular tree is visible through the cornea and is thus potentially accessible for light imaging. The Doppler shift of a monochromatic optical radiation scattered by a moving target is the scalar product of the optical momentum transfer with the target velocity. Doppler shifts are cumulative. In the case of multiple scattering, algebraic Doppler shifts add up throughout each optical path, and the broadening of the backscattered radiation still carries a

1084-7529/14/122723-13$15.00/0

Development/Plasticity/Repair

Neurotransmitter Release at the Thalamocortical Synapse Instructs Barrel Formation But Not Axon Patterning in the Somatosensory Cortex

Nicolas Narboux-Nême,[1,2,3] Alexis Evrard,[4,8,9] Isabelle Ferezou,[5] Reha S. Erzurumlu,[6] Pascal S. Kaeser,[7] Jeanne Lainé,[1,2,3] Jean Rossier,[5] Nicole Ropert,[4,8,9] Thomas C. Südhof,[7] and Patricia Gaspar[1,2,3]

[1]Institut National de la Santé et de la Recherche Médicale, UMR-S 839, 75005 France, [2]Université Pierre et Marie Curie, Paris, 75005, Paris, France, [3]Institut du Fer à Moulin, 17, rue du Fer à Moulin, 75005, Paris, France, [4]Institut National de la Santé et de la Recherche Médicale, U603, Laboratory of Neurophysiology and New Microscopies, 75006 Paris, France, [5]CNRS, UMR 7637, Laboratoire de Neurobiologie, ESPCI ParisTech, 75005, Paris, France, [6]Department of Anatomy and Neurobiology, University of Maryland School of Medicine, Baltimore, Maryland 21201, [7]Howard Hughes Medical Institute, Stanford University, Stanford, California 94305-5453, [8]CNRS, UMR 8154, Paris, France, and [9]Université Paris Descartes, 75006, Paris, France

To assess the impact of synaptic neurotransmitter release on neural circuit development, we analyzed barrel cortex formation after thalamic or cortical ablation of RIM1 and RIM2 proteins, which control synaptic vesicle fusion. Thalamus-specific deletion of RIMs reduced neurotransmission efficacy by 67%. A barrelless phenotype was found with a dissociation of effects on the presynaptic and postsynaptic cellular elements of the barrel. Presynaptically, thalamocortical axons formed a normal whisker map, whereas postsynaptically the cytoarchitecture of layer IV neurons was altered as spiny stellate neurons were evenly distributed and their dendritic trees were symmetric. Strikingly, cortex-specific deletion of the RIM genes did not modify barrel development. Adult mice with thalamic-specific RIM deletion showed a lack of activity-triggered immediate early gene expression and altered sensory-related behaviors. Thus, efficient synaptic release is required at thalamocortical but not at corticocortical synapses for building the whisker to barrel map and for efficient sensory function.

Introduction

Genetic alterations of synaptic transmission underlie a number of developmental disorders, such as autism spectrum disorders or mental retardation (Bourgeron, 2009). However, the role of hard-wired defects of neural circuits in these affections remains unclear. Neural activity is involved in neuronal network wiring but no visible change in brain development was observed upon abolishing synaptic release (Verhage et al., 2000; Molnár et al., 2002). Since neurotransmitters and electrical activity have direct effects on morphogenetic processes such as neuronal growth (Zhang and Poo, 2001), guidance (Hanson and Landmesser, 2004; Nicol et al., 2007), or gene transcription (Borodinsky et al., 2004), a large part of the developmental effects of neural activity could be independent of synaptic activity. However, the role of synaptic release in later activity-dependent refinement of neural circuits could not be examined because of early lethality.

Neurotransmitter release is controlled by proteins that prime vesicles to the presynaptic active zone, where they control vesicle fusion following Ca^{2+} rise (Sudhof, 2004). Among these proteins, the Rab3 interacting molecules (RIM) family includes seven isoforms, two of which, RIM1 and RIM2, are expressed broadly in the brain (Schoch et al., 2006). RIM1 and RIM2 are central organizers of presynaptic release, interacting with a number of active zone proteins as well as synaptic vesicle proteins (Mittelstaedt et al., 2010). Loss of function studies revealed that RIMs are required for the docking of synaptic vesicles and for the assembly of calcium channels in the presynaptic active zone (Deng et al., 2011; Han et al., 2011; Kaeser et al., 2011). RIM1/RIM2 double knock-out mice show a massive reduction in the priming and calcium-triggering of neurotransmitter release (Schoch et al., 2006; Kaeser et al., 2011).

Ablation of RIMs at selected synapses should allow determining the role of calcium-dependent neurotransmitter release on late phases of neural wiring. We used the rodent primary somatosensory barrel cortex as a model in which neural activity plays a role in sculpting barrels within the posteromedial barrel subfield (Erzurumlu and Kind, 2001; Wu et al., 2011). Barrels are columnar processing units that respond preferentially to the stimulation of individual whiskers. The development of a barrel is initiated by the clustering of thalamocortical (TC) axon terminals, followed by an arrangement of the cortical layer IV neurons

Received Jan. 24, 2012; revised March 9, 2012; accepted March 15, 2012.

Author contributions: P.G. designed research; N.N.-N., A.E., I.F., R.S.E., J.L., and N.R. performed research; P.S.K., J.R., and T.C.S. contributed unpublished reagents/analytic tools; N.N.-N., A.E., I.F., R.S.E., J.L., and P.G. analyzed data; N.N.-N., A.E., I.F., R.S.E., N.R., T.C.S., and P.G. wrote the paper.

This work was supported by Institut National de la Santé et de la Recherche Médicale, Université Pierre et Marie Curie, the Fondation Jerome Lejeune, Domaine d'Intérêt Majeur Neurosciences Région île de France; Agence Nationale pour la Recherche (ANR605-neur-046), Ecole des Neurosciences de Paris and NIH/NINDS R01 NS039050 (R.S.E.). We thank Alexandra Rebsam for critical reading of the manuscript and Gaelle Angenard for technical help.

Correspondence should be addressed to Patricia Gaspar, INSERM U839, 17 rue du Fer à Moulin, 75005, Paris, France. E-mail: patricia.gaspar@inserm.fr.

I. Ferezou's present address: UNIC, CNRS, UPR-3293, 91198, Gif-Sur Yvette, France.

DOI:10.1523/JNEUROSCI.0343-12.2012

 0270-6474/12/326183-14$15.00/0

frontiers in
NEURAL CIRCUITS

ORIGINAL RESEARCH ARTICLE
published: 10 August 2012
doi: 10.3389/fncir.2012.00050

Activation of cortical 5-HT$_3$ receptor-expressing interneurons induces NO mediated vasodilatations and NPY mediated vasoconstrictions

Quentin Perrenoud, Jean Rossier, Isabelle Férézou†, Hélène Geoffroy, Thierry Gallopin, Tania Vitalis and Armelle Rancillac*

Laboratoire de Neurobiologie, CNRS UMR 7637, ESPCI ParisTech, Paris, France

Edited by:
Bruno Cauli, UPMC, France

Reviewed by:
Kathleen S. Rockland, Massachusetts Institute of Technology, USA
Salah El Mestikawy, Université Pierre et Marie Curie, France
Helene Girouard, Universite de Montreal, Canada

***Correspondence:**
Armelle Rancillac, Laboratoire de Neurobiologie, CNRS UMR 7637, ESPCI ParisTech, 10 rue Vauquelin, 75005 Paris, France.
e-mail: armelle.rancillac@espci.fr

†Present address:
Isabelle Férézou, Unité de Neurosciences Information et Complexité, Centre National de la Recherche Scientifique, Gif sur Yvette, France.

GABAergic interneurons are local integrators of cortical activity that have been reported to be involved in the control of cerebral blood flow (CBF) through their ability to produce vasoactive molecules and their rich innervation of neighboring blood vessels. They form a highly diverse population among which the serotonin 5-hydroxytryptamine 3A receptor (5-HT$_{3A}$)-expressing interneurons share a common developmental origin, in addition to the responsiveness to serotonergic ascending pathway. We have recently shown that these neurons regroup two distinct subpopulations within the somatosensory cortex: Neuropeptide Y (NPY)-expressing interneurons, displaying morphological properties similar to those of neurogliaform cells and Vasoactive Intestinal Peptide (VIP)-expressing bipolar/bitufted interneurons. The aim of the present study was to determine the role of these neuronal populations in the control of vascular tone by monitoring blood vessels diameter changes, using infrared videomicroscopy in mouse neocortical slices. Bath applications of 1-(3-Chlorophenyl)biguanide hydrochloride (mCPBG), a 5-HT$_3$R agonist, induced both constrictions (30%) and dilations (70%) of penetrating arterioles within supragranular layers. All vasoconstrictions were abolished in the presence of the NPY receptor antagonist (BIBP 3226), suggesting that they were elicited by NPY release. Vasodilations persisted in the presence of the VIP receptor antagonist VPAC1 (PG-97-269), whereas they were blocked in the presence of the neuronal Nitric Oxide (NO) Synthase (nNOS) inhibitor, L-NNA. Altogether, these results strongly suggest that activation of neocortical 5-HT$_{3A}$-expressing interneurons by serotoninergic input could induces NO mediated vasodilatations and NPY mediated vasoconstrictions.

Keywords: neurovascular coupling, mCPBG, serotonin, U46619, Pet1 knock-out mouse, vasoactive intestinal peptide, brain slices, neurogliaform cells

INTRODUCTION

Within the cerebral cortex, different types of GABAergic inhibitory interneurons have been described according to their distinctive morphological, molecular, and electrophysiological characteristics (Cauli et al., 1997; Markram et al., 2004; Vitalis and Rossier, 2011). Although the final classification scheme of cortical interneurons is still a matter of debate (Ascoli et al., 2008), data from *in vitro* and *in vivo* experiments tend to demonstrate that distinct subpopulations of inhibitory interneurons exert specific functional roles in the integrative processes of the cortical network (Whittington and Traub, 2003; Markram et al., 2004; Fanselow and Connors, 2010; Gentet et al., 2010; Mendez and Bacci, 2011). Furthermore, some GABAergic interneurons have been reported recently to be involved in the control of cerebral blood flow (CBF) through their ability to express and release vasoactive molecules (Cauli et al., 2004; Cauli and Hamel, 2010). However, further characterization of these vasoactive interneurons subpopulations remains to be established.

Interestingly, the robust cortical serotoninergic innervation from raphe nuclei (Reinhard et al., 1979; Steinbusch, 1981; Tork, 1990), which modulate cortical activity (Takeuchi and Sano, 1984; Papadopoulos et al., 1987; DeFelipe et al., 1991) and CBF (Rapport et al., 1948; Cohen et al., 1996; Riad et al., 1998), preferentially targets inhibitory interneurons (DeFelipe et al., 1991; Smiley and Goldman-Rakic, 1996; Paspalas and Papadopoulos, 2001). However, the processes by which 5-hydroxytryptamine (serotonin, 5-HT) acts on the cortical network and CBF are complex and deserve to be further understood. Indeed, responses to 5-HT seem to depend upon the nature of the receptors involved, and the recruited neuronal populations (Underwood et al., 1992; Cohen et al., 1996; Foehring et al., 2002).

Serotonin can notably induce a fast excitation of specific interneuron subpopulations through the activation of the 5-hydroxytryptamine 3A receptor (5-HT$_{3A}$) (Ferezou et al., 2002; Lee et al., 2010) which is the only ionotropic serotonergic receptor (Barnes and Sharp, 1999; Chameau and van Hooft, 2006). In the mouse primary somatosensory cortex, the 5-HT$_{3A}$ receptor is expressed by two distinct types of interneurons (Vucurovic et al., 2010). The first one was characterized by a bipolar/bitufted morphology, an adaptative or bursting firing behavior and the

Journal of Neuroscience Research

Journal of Neuroscience Research 88:487–499 (2010)

Degenerative Abnormalities in Transgenic Neocortical Neuropeptide Y Interneurons Expressing Tau-Green Fluorescent Protein

Armelle Rancillac,[1]* Jeanne Lainé,[2] Quentin Perrenoud,[1] Hélène Geoffroy,[1] Isabelle Ferezou,[1] Tania Vitalis,[1] and Jean Rossier[1]

[1]Laboratoire de Neurobiologie, CNRS UMR 7637, ESPCI ParisTech, Paris, France
[2]Laboratoire de Neurobiologie du cervelet, Université Pierre et Marie Curie Paris 6, Faculté de Médecine Pitié Salpétrière, Paris, France

The introduction of a reporter gene into bacterial artificial chromosome (BAC) constructs allows a rapid identification of the cell type expressing the gene of interest. Here we used BAC transgenic mice expressing a tau-sapphire green fluorescent protein (GFP) under the transcriptional control of the neuropeptide Y (NPY) genomic sequence to characterize morphological and electrophysiological properties of NPY-GFP interneurons of the mouse juvenile primary somatosensory cortex. Electrophysiological whole-cell recordings and biocytin injections were performed to allow the morphological reconstruction of the recorded neurons in three dimensions. Ninety-six recorded NPY-GFP interneurons were compared with 39 wild-type (WT) NPY interneurons, from which 23 and 19 were reconstructed, respectively. We observed that 91% of the reconstructed NPY-GFP interneurons had developed an atypical axonal swelling from which emerge numerous ramifications. These abnormalities were very heterogeneous in shape and size. They were immunoreactive for the microtubule-associated protein tau and the lysosomal-associated membrane protein 1 (LAMP1). Moreover, an electron microscopic analysis revealed the accumulation of numerous autophagic and lysosomal vacuoles in swollen axons. Morphological analyses of NPY-GFP interneurons also indicated that their somata were smaller, their entire dendritic tree was thickened and presented a restricted spatial distribution in comparison with WT NPY interneurons. Finallly, the morphological defects observed in NPY-GFP interneurons appeared to be associated with alterations of their electrophysiological intrinsic properties. Altogether, these results demonstrate that NPY-GFP interneurons developed dystrophic axonal swellings and severe morphological and electrophysiological defects that could be due to the overexpression of tau-coupled reporter constructs.

Key words: somatosensory cortex; bacterial artificial chromosome; Neurolucida reconstructions; scRT-PCR; patch-clamp; axonal swellings; spheroids; thickenings and tauopathy

γ-Aminobutyric acid (GABA)-ergic interneurons constitute only a minor fraction of the total number of neurons in the mammalian neocortex (15–25%; Fairen et al., 1984) but are crucial for normal brain function (McBain and Fisahn, 2001; Whittington and Traub, 2003). Despite their small number, these interneurons are remarkably diverse in their morphological, electrophysiological, and molecular properties (Fairen et al., 1984; DeFelipe, 1993; Cauli et al., 1997; Kawaguchi and Kubota, 1997; Gupta et al., 2000; Markram et al., 2004; Ascoli et al., 2008).

A subclass of these cortical interneurons is indeed characterized by the expression of neuropeptide Y (NPY), although it presents quite various intrinsic properties (Hendry et al., 1984; Cauli et al., 1997; Karagiannis et al., 2009). NPY expression is therefore likely a property shared by functionally diverse neuronal subpopulations that have just been recently classified into three main types in the rat (Karagiannis et al., 2009).

Here, we were interested in further characterizing this heterogeneous population in the mouse primary somatosensory cortex. For this purpose, we wanted to benefit from the use of transgenic mice selectively expressing the green fluorescent protein (GFP) in NPY-expressing neurons, which cannot otherwise be easily

Additional Supporting Information may be found in the online version of this article.

Contract grant sponsor: French National Research Agency; Contract grant number: ANR-06-NEURO-033-01.

*Correspondence to: Armelle Rancillac, Laboratoire de Neurobiologie, CNRS UMR 7637, ESPCI ParisTech, 10 rue Vauquelin, 75005 Paris, France.
E-mail: armelle.rancillac@espci.fr

Received 15 April 2009; Revised 26 June 2009; Accepted 7 July 2009

Published online 14 October 2009 in Wiley InterScience (www.interscience.wiley.com). DOI: 10.1002/jnr.22234

ORGANIC LETTERS

2009
Vol. 11, No. 21
4822−4825

Straightforward Synthesis of the Near-Infrared Fluorescent Voltage-Sensitive Dye RH1691 and Analogues Thereof

Raphaël Lebeuf, Isabelle Férézou,[†] Jean Rossier,[†] Stellios Arseniyadis,* and Janine Cossy*

Laboratoire de Chimie Organique, ESPCI ParisTech, CNRS, 10 rue Vauquelin, 75231 Paris Cedex 05, France, and Fondation Pierre-Gilles de Gennes pour la Recherche, 29 rue d'Ulm, 75005 Paris, France

stellios.arseniyadis@espci.fr; janine.cossy@espci.fr

Received August 8, 2009

ABSTRACT

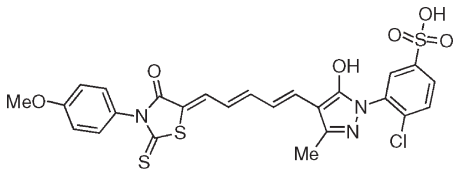

RH1691

A highly straightforward synthesis of the near-infrared voltage-sensitive dye RH1691 is reported featuring two sequential anionic additions of *C*-nucleophilic heterocycles on a cyanine. This convergent approach led to the synthesis of four new probes, which also exhibit fluorescence in the near-infrared region.

One of the most challenging objectives of modern neuroscience is to understand the neuronal bases of behavior. It is therefore crucial to perform functional studies of the cerebral cortex as it is the most integrative structure of the brain involved in many cognitive functions such as processing of sensory information and generation of motor commands. During the past two decades, massive efforts have been made to record single cortical neurons in the intact brain and to investigate how the properties of these neurons and their intricate synaptic connections combine to form networks allowing the processing of information. Recently, the remarkable development of real time cortical imaging[1] with voltage-sensitive dyes[2] has opened new avenues in this field allowing the recording of cortical ensemble activity with a temporal resolution reaching a millisecond and a spatial resolution of a few tens of micrometers.[2b,3−5] This experimental approach is based on the use of dyes that bind to the external surface of excitable membranes without interrupting their normal function and act as transducers that transform changes in membrane potential into optical signals. Various molecules presenting such properties have been developed,[6]

[†] Laboratoire de neurobiologie et diversité cellulaire, ESPCI ParisTech, CNRS, 10 rue Vauquelin, F-75231 Paris Cedex 05, France.

10.1021/ol901846g CCC: $40.75
Published on Web 09/25/2009

(1) (a) Grinvald, A.; Anglister, L.; Freeman, J. A.; Hildesheim, R.; Manker, A. *Nature* **1984**, *308*, 848–850. (b) Orbach, H. S.; Cohen, L. B.; Grinvald, A. *J. Neurosci.* **1985**, *5*, 1886–1895. (c) Arieli, A.; Sterkin, A.; Grinvald, A.; Aertsen, A. *Science* **1996**, *273*, 1868–1871. (d) Kleinfeld, D.; Delaney, K. R. *J. Comp. Neurol.* **1996**, *375*, 89–108. (e) Tsodyks, M.; Kenett, T.; Grinvald, A.; Arieli, A. *Science* **1999**, *286*, 1943–1946. (f) Spors, H.; Grinvald, A. *Neuron* **2002**, *34*, 301–315. (g) Seidemann, E.; Arieli, A.; Grinvald, A.; Slovin, H. *Science* **2002**, *295*, 862–865. (h) Slovin, H.; Arieli, A.; Hildesheim, R.; Grinvald, A. *J. Neurophysiol.* **2002**, *88*, 3421–3438. (i) Petersen, C. C. H.; Grinvald, A.; Sakmann, B. *J. Neurosci.* **2003**, *23*, 1298–1309. (j) Petersen, C. C. H.; Hahn, T. T. G.; Mehta, M.; Grinvald, A.; Sakmann, B. *Proc. Natl. Acad. Sci. U.S.A.* **2003**, *100*, 13638–13643. (k) Derdikman, D.; Hildesheim, R.; Ahissar, E.; Arieli, A.; Grinvald, A. *J. Neurosci.* **2003**, *23*, 3100–3105.

(2) (a) Shoham, D.; Glaser, D. E.; Arieli, A.; Kenet, T.; Wijnbergen, C.; Toledo, Y.; Hildesheim, R.; Grinvald, A. *Neuron* **1999**, *24*, 791–802. (b) Grinvald, A.; Hildesheim, R. *Nat. Rev. Neurosci.* **2004**, *5*, 874–885.

(3) Kleinfeld, D.; Waters, J. *Neuron* **2007**, *56*, 760–762.

J Neurophysiol 97: 3751–3762, 2007.
First published March 14, 2007; doi:10.1152/jn.01178.2006.

Combined Voltage and Calcium Epifluorescence Imaging In Vitro and In Vivo Reveals Subthreshold and Suprathreshold Dynamics of Mouse Barrel Cortex

Thomas Berger,[1,3] Aren Borgdorff,[1] Sylvain Crochet,[1] Florian B. Neubauer,[3] Sandrine Lefort,[1] Bruno Fauvet,[1] Isabelle Ferezou,[1] Alan Carleton,[2] Hans-Rudolf Lüscher,[3] and Carl C. H. Petersen[1]
[1]*Laboratory of Sensory Processing and* [2]*Flavour Perception Group, Brain Mind Institute, Ecole Polytechnique Federale de Lausanne, Lausanne; and* [3]*Institute of Physiology, University of Bern, Bern, Switzerland*

Submitted 6 November 2006; accepted in final form 10 March 2007

Berger T, Borgdorff A, Crochet S, Neubauer FB, Lefort S, Fauvet B, Ferezou I, Carleton A, Lüscher H-R, Petersen CC. Combined voltage and calcium epifluorescence imaging in vitro and in vivo reveals subthreshold and suprathreshold dynamics of mouse barrel cortex. *J Neurophysiol* 97: 3751–3762, 2007. First published March 14, 2007; doi:10.1152/jn.01178.2006. Cortical dynamics can be imaged at high spatiotemporal resolution with voltage-sensitive dyes (VSDs) and calcium-sensitive dyes (CaSDs). We combined these two imaging techniques using epifluorescence optics together with whole cell recordings to measure the spatiotemporal dynamics of activity in the mouse somatosensory barrel cortex in vitro and in the supragranular layers in vivo. The two optical signals reported distinct aspects of cortical function. VSD fluorescence varied linearly with membrane potential and was dominated by subthreshold postsynaptic potentials, whereas the CaSD signal predominantly reflected local action potential firing. Combining VSDs and CaSDs allowed us to monitor the synaptic drive and the spiking activity of a given area at the same time in the same preparation. The spatial extent of the two dye signals was different, with VSD signals spreading further than CaSD signals, reflecting broad subthreshold and narrow suprathreshold receptive fields. Importantly, the signals from the dyes were differentially affected by pharmacological manipulations, stimulation strength, and depth of isoflurane anesthesia. Combined VSD and CaSD measurements can therefore be used to specify the temporal and spatial relationships between subthreshold and suprathreshold activity of the neocortex.

INTRODUCTION

Many computations in the neocortex are thought to occur on the millisecond timescale within maps composed of cortical columns. Most current techniques to investigate cortical processing offer limited spatial resolution because of the low density of recording electrodes or theoretical difficulties of defining the signal sources. Optical methods, however, offer both sufficient temporal and spatial resolution for real-time analysis of cortical processing.

Two of the most dynamic parameters in the active brain are membrane potential (V_m) and intracellular calcium concentration ($[Ca^{2+}]_i$). Both of these can be imaged optically by the introduction of fluorescent probes into the brain. Voltage-sensitive dyes (VSDs) insert into the plasma membrane and change their fluorescence intensity dependent on the potential across the lipid bilayer. Previous studies recorded VSD signals in invertebrate preparations (Antic and Zecevic 1995; Salzberg et al. 1973), from cultured cells (Bullen and Saggau 1998), brain slices (Antic et al. 1999; Contreras and Llinas 2001; Laaris and Keller 2002; Petersen and Sakmann 2001), and in vivo (Borgdorff et al. 2007; Civillico and Contreras 2006; Derdikman et al. 2003; Ferezou et al. 2006; Grinvald et al. 1984; Kleinfeld and Delaney 1996; Petersen et al. 2003a,b; Shoham et al. 1999). The VSD JPW1114 (also known as di-2-ANEPEQ) has proven useful as a dye for intracellular application in individual nerve cells, allowing the spatiotemporal analysis of electrical signaling in dendrites (Antic and Zecevic 1995; Antic et al. 1999). The VSD RH1691 is optimized for in vivo measurements (Shoham et al. 1999) and, when topically applied to the neocortex, it can resolve cortical activity with millisecond and subcolumnar resolution (Grinvald and Hildesheim 2004). Fluorescent calcium-sensitive dyes (CaSDs) such as Fluo-3 and Oregon Green BAPTA-1 (OGB-1) have been developed that respond rapidly and selectively to changes in the cytosolic free calcium ion concentration (Tsien 1980). CaSDs can be applied extracellularly in a membrane-permeable ester form, which is subsequently cleaved intracellularly by esterases releasing the functional fluorescent CaSD (Tsien 1981). Recently, network activity was imaged with CaSD both in brain slices and in the intact brain (Borgdorff et al. 2007; Kerr et al. 2005; Nimmerjahn et al. 2004; Ohki et al. 2005; Peterlin et al. 2000; Stosiek et al. 2003; Wachowiak and Cohen 2001; Yaksi and Friedrich 2006).

In this study, we combined epifluorescence VSD and CaSD imaging together with whole cell (WC) V_m recordings to allow a quantitative comparison of what is measured using these techniques, focusing on their application to the study of the mouse barrel cortex (Petersen 2003; Woolsey and Van der Loos 1970). We recorded VSD and CaSD signals in three different experimental conditions: in single cells, in brain slices, and in vivo. In single cells, we studied the dynamic range of VSDs and CaSDs during controlled membrane potential changes. In the barrel cortex in vitro, we characterized the link of the VSD and CaSD signals to sub- and suprathreshold electrophysiological network activity and thereafter studied the spatial spread of synaptic activity and action potentials. We next transferred these methods to make in vivo optical measurements of activity in layer 2/3 barrel cortex of anesthetized mice, analyzing both the evoked and the spontaneous spatiotemporal dynamics of the VSD and CaSD signals. The data are

Address for reprint requests and other correspondence: C. Petersen, Laboratory of Sensory Processing, Brain Mind Institute, SV-BMI-LSENS, Station 15, Ecole Polytechnique Federale de Lausanne, CH-1015 Lausanne, Switzerland (E-mail: carl.petersen@epfl.ch).

J Neurophysiol 97: 2580–2589, 2007.
First published January 31, 2007; doi:10.1152/jn.00603.2006.

Functional CB1 Receptors Are Broadly Expressed in Neocortical GABAergic and Glutamatergic Neurons

Elisa L. Hill,[1] Thierry Gallopin,[1] Isabelle Férézou,[1] Bruno Cauli,[1] Jean Rossier,[1] Paul Schweitzer,[2] and Bertrand Lambolez[1]

[1]*Laboratoire de Neurobiologie et Diversité Cellulaire, Centre National de la Recherche Scientifique Unité Mixte de Recherche 7637, Ecole Supérieure de Physique et de Chimie Industrielles, Paris, France; and* [2]*Molecular and Integrative Neurosciences Department, The Scripps Research Institute, La Jolla, California*

Submitted 9 June 2006; accepted in final form 31 January 2007

Hill EL, Gallopin T, Férézou I, Cauli B, Rossier J, Schweitzer P, Lambolez B. Functional CB1 receptors are broadly expressed in neocortical GABAergic and glutamatergic neurons. *J Neurophysiol* 97: 2580–2589, 2007. First published January 31, 2007; doi:10.1152/jn.00603.2006. The cannabinoid receptor CB1 is found in abundance in brain neurons, whereas CB2 is essentially expressed outside the brain. In the neocortex, CB1 is observed predominantly on large cholecystokinin (CCK)-expressing interneurons. However, physiological evidence suggests that functional CB1 are present on other neocortical neuronal types. We investigated the expression of CB1 and CB2 in identified neurons of rat neocortical slices using single-cell RT-PCR. We found that 63% of somatostatin (SST)-expressing and 69% of vasoactive intestinal polypeptide (VIP)-expressing interneurons co-expressed CB1. As much as 49% of pyramidal neurons expressed CB1. In contrast, CB2 was observed in a small proportion of neocortical neurons. We performed whole cell recordings of pyramidal neurons to corroborate our molecular findings. Inhibitory postsynaptic currents (IPSCs) induced by a mixed muscarinic/nicotinic cholinergic agonist showed depolarization-induced suppression of inhibition and were decreased by the CB1 agonist WIN-55212-2 (WIN-2), suggesting that interneurons excited by cholinergic agonists (mainly SST and VIP neurons) possess CB1. IPSCs elicited by a nicotinic receptor agonist were also reduced in the presence of WIN-2, suggesting that neurons excited by nicotinic agonists (mainly VIP neurons) indeed possess CB1. WIN-2 largely decreased excitatory postsynaptic currents evoked by intracortical electrical stimulation, pointing at the presence of CB1 on glutamatergic pyramidal neurons. All WIN-2 effects were strongly reduced by the CB1 antagonist AM 251. We conclude that CB1 is expressed in various neocortical neuronal populations, including glutamatergic neurons. Our combined molecular and physiological data suggest that CB1 widely mediates endocannabinoid effects on glutamatergic and GABAergic transmission to modulate cortical networks.

INTRODUCTION

Cannabinoid substances act at CB1 receptors to impair brain functioning in a variety of cognitive and performance tasks, including memory, learning, and attention (Iversen 2003); and endogenous ligands for these receptors, the endocannabinoids, have emerged as transmitters regulating neuronal activity (Freund et al. 2003). CB1 is found throughout the brain and is present at a high density in neocortex and hippocampus (Herkenham et al. 1990). In these brain areas, CB1 immunoreactivity is mostly found on large cholecystokinin (CCK)-expressing interneurons but not vasoactive intestinal peptide (VIP)- or somatostatin (SST)-expressing interneurons (Bodor et al. 2005; Katona et al. 1999; Tsou et al. 1999). The CB1 mRNA is expressed in pyramidal neurons (Marsicano and Lutz 1999; Matsuda et al. 1993), but CB1 immunoreactivity has often been undetected in these neurons (Bodor et al. 2005; Katona et al. 1999; Tsou et al. 1999). Although the presence of CB1 immunoreactivity at hippocampal excitatory presynaptic terminals has been recently reported (Katona et al. 2006; Kawamura et al. 2006), the extent of cortical CB1 expression in pyramidal neurons remains unclear.

Numerous electrophysiological studies have investigated the influence of cannabinoids in brain preparations. In neocortex and hippocampus, cannabinoids acting at CB1 depress inhibitory and excitatory synaptic transmission (Auclair et al. 2000; Bender et al. 2006; Davies et al. 2002; Fortin and Levine 2006; Piomelli 2003; Sjostrom et al. 2003, 2004). The use of CB1 knock-out mice further established the occurrence of functional CB1 on forebrain glutamatergic neurons (Domenici et al. 2006; Kawamura et al. 2006; Marsicano et al. 2003; Takahashi and Castillo 2006). Yet the CB1 expression patterns in glutamatergic neurons remain unclear, and this prompted us to investigate the expression of CB1 in pyramidal neurons of the neocortex.

Endocannabinoids act as retrograde messengers to elicit the phenomenon of depolarization-induced suppression of inhibition (DSI) (Wilson and Nicoll 2001). DSI has been observed in neocortex (Bodor et al. 2005; Trettel and Levine 2002, 2003; Trettel et al. 2004), and activation of cholinergic receptors is often required to obtain significant DSI (Martin and Alger 1999), implicating acetylcholine-responsive interneurons expressing CB1 to contribute to DSI (Trettel et al. 2004). Neocortical interneurons expressing cholinergic receptors typically co-express SST or VIP (Gulledge et al. 2006; Kawaguchi 1997; Porter et al. 1999), suggesting that these interneuron populations also possess CB1 in contradiction with the reported presence of CB1 mainly on large CCK neurons. Therefore we investigated the expression of CB1 in SST and VIP interneuron populations.

Cannabinoids also act at CB2, which is principally found outside the brain, but mediates part of cannabinoid effects on cerebellar granule cells (Skaper et al. 1996) and brain stem neurons (Van Sickle et al. 2005). Although CB2 is only present at low level in the cortex (Van Sickle et al. 2005), we probed its expression in parallel with that of CB1.

Address for reprint requests and other correspondence: B. Lambolez, NPA, CNRS UMR 7102, UPMC, 9 quai St Bernard 75005 Paris, France (E-mail: bertrand.lambolez@snv.jussieu.fr).

The costs of publication of this article were defrayed in part by the payment of page charges. The article must therefore be hereby marked "*advertisement*" in accordance with 18 U.S.C. Section 1734 solely to indicate this fact.